John Dowden

Editor

The Theory of Laser Materials Processing

Heat and Mass Transfer in Modern Technology

Springer

Springer Series in

MATERIALS SCIENCE 119

Springer Series in

MATERIALS SCIENCE

Editors: R. Hull   R.M. Osgood, Jr.   J. Parisi   H. Warlimont

The Springer Series in Materials Science covers the complete spectrum of materials physics, including fundamental principles, physical properties, materials theory and design. Recognizing the increasing importance of materials science in future device technologies, the book titles in this series reflect the state-of-the-art in understanding and controlling the structure and properties of all important classes of materials.

John Dowden (Ed.)

The Theory of Laser Materials Processing

Heat and Mass Transfer in Modern Technology

Springer

Professor J. M. Dowden
Department of Mathematical Sciences
University of Essex
Colchester
Essex CO4 3SQ
United Kingdon

Series Editors:

Professor Robert Hull
University of Virginia
Dept. of Materials Science and Engineering
Thornton Hall
Charlottesville, VA 22903-2442, USA

Professor R.M. Osgood, Jr.
Microelectronics Science Laboratory
Department of Electrical Engineering
Columbia University
Seeley W. Mudd Building
New York, NY 10027, USA

Professor Jürgen Parisi
Universität Oldenburg, Fachbereich Physik
Abt. Energie- und Halbleiterforschung
Carl-von-Ossietzky-Strasse 9–11
26129 Oldenburg, Germany

Professor Hans Warlimont
Institut für Festkörper
und Werkstofforschung,
Helmholtzstrasse 20
01069 Dresden, Germany

Preface

The use of lasers in materials processing has become widespread in recent years, so that an understanding of the nature of heat and mass transfer in this branch of modern technology is of increasing importance. The aim of the authors of this book is to concentrate on the physical processes; these can be developed from a mathematical point of view, or from direct experimentally-derived observation. The two approaches are complementary; each can provide insights and the synthesis of the two can lead to a very powerful understanding of the processes involved. Mathematical modelling of physical processes has had an important role to play in the development of technology over the centuries and particularly so in the last one hundred and fifty years or so. It can be argued that it is more important today than ever before since the availability of high-speed computers allows accurate numerical simulation of industrial processes at a fraction of the cost of the corresponding experiments. This is one aspect of mathematical modelling, high profile and much valued, but it is not the only one.

In the past mathematical modelling had to rely on qualitative investigation, very special analytical solutions, or inaccurate and time-consuming calculations performed with little in the way of tabulated or mechanical assistance. Log tables and slide rules are still remembered by people working today, though there are surely few who regret their disappearance.

The value and distinctive function of methods based on the analytical approach is now becoming much clearer, now that they are no longer expected to produce detailed imitations of what happens in real experiments of industrial processes, a function now fulfilled mostly by numerical methods, considered below. The emphasis today is on their ability to confirm and extend our understanding of the basic physical mechanisms involved in the processes of interest. These are essential for any intelligent use of numerical simulation.

The argument about the value of teaching people how to do arithmetic themselves without the aid of a calculator seems to be passing into history,

but it is an important one and provides a simple analogy. If someone does not have a feeling for numbers and the way arithmetic works, they will all too easily fail to spot an error produced by a machine. Computers are not infallible – and neither are those who build or program them. Computers are now taking on less mundane mathematical tasks and the same controversies are appearing in connection with algebraic manipulation. Equally, and with even greater penalties in terms of cost in the event of errors, the same considerations apply to numerical simulation of major industrial processes. Awareness of the analytical solutions can be invaluable in distinguishing the right from the wrong, i.e. for the practitioner to understand the basis of the work, and to have an idea of the kinds of outcomes that are plausible – and to recognise those which are not.

The phrase "mathematical modelling" is, however, ambiguous, perhaps more now than it has ever been. There is an enormous amount of work done today on simulation based on the use of very powerful computer programs, and it is quite correctly referred to as mathematical modelling. The programs are sometimes constructed in-house but are usually commercial packages. This is an entirely valid approach with specific (generally commercial) objectives. In general there are two uses. The dominant objective is numerical agreement with a particular experiment in the first instance, leading to predictive commercial use in the second instance. The second objective is the clarification of physical mechanisms, aimed at the generation of understanding of complex interconnected processes, rather than the exact reproduction of a particular experiment. It is sometimes overlooked that, with sufficient care, a numerical approach is equally valid in the investigation of physical fundamentals. Numerical simulation is not a central topic of this book, but because of its crucial importance to each of the two uses to which numerical modelling can be put, it is vital that the computational basis of the work should be completely sound. In addition, the level of process detail which can be considered by the numerical approach usually exceeds what is possible with the analytical approach significantly, leaving little choice but to revert to the numerical treatment when investigating the interconnections between processes. It is for these reasons that the book concludes with a chapter on comprehensive numerical simulation.

In many ways, the approach adopted here is complementary to the more phenomenological approach. It is always important in a field which has very direct industrial applications to bear in mind how techniques such as those described here will be used, but it is essential not to lose sight of the fundamentals. There are serious safety implications; there are cost implications; there are moral implications; there are considerations of the appropriateness of the technology to the application under consideration. A proper respect for all these requires an understanding of the fundamentals.

We are all too well aware that this book does little more than scratch the surface of the problems involved in a fundamental understanding of these phenomena. If we have provided ideas and information that cause others to

test them experimentally or intellectually, agree with them or dispute them vigorously, and develop them further, we will consider that we have achieved our aim.

Colchester

April, 2008   *John Dowden*

Contents

1

Mathematics in Laser Processing

John Dowden

Department of Mathematical Sciences, University of Essex, Colchester,
Essex CO4 0LP, UK. `dowdj@essex.ac.uk`

Abstract. Methods by which physical laws can be converted into mathematical form as partial differential equations are discussed. Associated with these equations are boundary conditions, or the conditions to be applied at the interface between regions in which different regimes apply, represented by a discontinuity in some or all aspects of the variables describing the mathematical system. The manner in which the form of these conditions can be deduced is considered. The principles described are illustrated by application to some of the physical laws at the centre of laser technology.

1.1 Mathematics and its Application

The study of the theory of a technological discipline nearly always requires a return to its underlying physical principles. These in turn are usually expressed in their most general form in terms of standard language: the many different forms in which Newton's Laws of Motion are expressed provide a familiar example. All too often, however, the use of standard language proves to be far too cumbersome for the further investigation of technological processes and problems. In practice, *Mathematics* has been found to provide a convenient and concise tool for the purpose, as it has in science as a whole. The well-known assertion that "Mathematics is the Language of Science" is often attributed to Galileo (in his book, *The Assayer*) although it would be more accurately expressed, and closer to Galileo's original statement, to say that the language of science is mathematics.[1]

Mathematics is now proving to be an invaluable tool in the investigation of subjects which had not formerly been thought of as natural fields for its use. It is an intellectual discipline in its own right independently of science, as Galileo recognised, or from any other discipline in which it is used as a

---

[1] Indeed, Galileo went even further. The Assayer contains his well-known statement that mathematics is the language of God. (http://en.wikipedia.org/wiki/The_Assayer).

tool, but there has been a long history of beneficial interaction between it and its fields of application. Physics, engineering and modern technology are examples of the greatest importance.

Thus it is that the underlying physical principles of the theory of the applications of laser technology are well suited to expression in mathematical form, and their consequences investigated using mathematical techniques. Many of the laws of physics are expressed, either explicitly or implicitly, in terms of macroscopic objects or concepts. These are not necessarily the best starting point for mathematical investigation. In the past, it has been found helpful to convert them into other forms, in terms of concepts defined as abstractions; an example of such an abstraction is the mathematical process of differentiation. Similarly, numerical methods often resort to a kind of half-way house since digital computers are unable to deal with the true mathematical limit, a concept which rarely, if ever, has any real physical meaning; one only has to consider the concept of the density of an object at a point to realise that there are problems, when the atomic model of matter is called to mind.

This chapter therefore deals with the way in which some well-known physical laws can be converted into idealised mathematical forms expressed in terms of differential equations.

When attempts are made to solve differential equations, it rapidly becomes obvious that an important part of the statement of the mathematical problem consists of the boundary conditions, or, if there are surfaces at which discontinuities occur, the appropriate interface conditions. The derivations of these from the underlying principles are considered in the same way that the equations themselves are derived.

The language of mathematics is used freely in this book, in addition to the standard terminology of the fields of study of the individual chapters. On the whole, specialist (or relatively rare) terminology is not defined if it is standard in the field under discussion, and a reader who encounters a word that is unfamiliar is encouraged to look for its definition in the literature of the field; the World Wide Web will be found to be an invaluable resource in this connection – in doing so, the reader may also find a great deal of helpful additional material.

An exception is being made of the term "ansatz", which is current amongst theoretical physicists. One definition is given in the On-Line edition of the Oxford English Dictionary, but a much better one is provided by Wikipedia, which gives its meaning as

"In physics and mathematics, an **ansatz***... is an educated guess that is verified later by its results. An* ansatz *is the establishment of the starting equation(s) describing a mathematical or physical problem. It can take into consideration boundary conditions. After an ansatz has been established, the equations are solved for the general function of interest. Typically, a word problem starts by writing down the* ansatz *with subsequent refinement leading to the solution of the problem."*

(http://en.wikipedia.org/wiki/Ansatz). There is no really satisfactory single word available in the less specialist mathematical literature, and it is used from time to time in this book in the sense described. As the Wikipedia definition says so well, it encapsulates one of the fundamental methods by which solutions to mathematical problems may be obtained. A colloquial alternative might be "inspired guess" – but it is an inspired guess that has to be rigorously justified.

The approach adopted here is in many ways complementary to that adopted in works such as those of Steen [1] and von Allmen and Blatter [2]. Steen's work, for example, is much more pragmatic. It must never be forgotten that laser technology is a rapidly evolving field with applications of the utmost importance, so it is essential to bear in mind the ways in which the theory will be used. Conversely, it is essential for the developer and indeed the end-user not to lose sight of the fundamentals; without understanding, there is always the danger of inadvertent error.

1.2 Formulation in Terms of Partial Differential Equations

1.2.1 Length Scales

Most laws in physics, at least at the macroscopic level, are statements about ideal objects; to be of interest they must nonetheless represent something with some kind of tangible reality. Examples are the "bodies" that appear in Newton's Laws of Motion and his Theory of Gravitation, electric charge, magnetic poles, and so on. Often these concepts are sufficient in themselves to solve important problems, but there are a great many circumstances where it is simply not practicable to deal with large numbers of these ideal objects. The behaviour of a moving liquid provides a familiar example, where the concept of an atom might be thought of as providing a point mass, but is really very little help at the basis for the analysis of weather forecasting, for example. The differences between the length and time scales of the basic entities and the subject of study are just too great. The problem is frequently tackled by re-phrasing the laws in such a way that they can cope with large numbers of the basic entities at once, and in that way statements are obtained which are usually best expressed in mathematical form with the use of integrals, often over an arbitrary surface, or volume in space. Some of the laws of electromagnetism, Faraday's law for example, are really integral statements in themselves and are therefore naturally expressed in mathematical form in this way.

Although the expression of physical laws as integrals is elegant, such a formulation has not, in the past at least, provided an easy way to solve problems since appropriate techniques did not exist. The traditional way round the problem was to convert the integral statements into differential equations. Since the days of Newton and Leibnitz a vast array of techniques have been developed to solve problems using the analytical techniques of differential

calculus. These have been applied very successfully, and were more or less the only resource available until the advent of high speed computers.

All the same there can be a philosophical problem with the approach since differential calculus has at its heart the use of the limiting process as some quantity tends to zero; it might be a length, or a time, or a volume... but whichever it is, there is a difficulty when one remembers that very often the formulation as an integral was used to avoid problems associated with small entities. The modelling approach behind calculus techniques assumes that there are properties (mass density, for example) that have a clear trend to their properties as the size of the volume (in the case of mass density) decreases; it is then assumed that the apparent trend can be extrapolated downwards to a vanishingly small size, even though such a process is impossible when thought of in terms of the more fundamental physical entities (atoms, for example). It is then possible to construct a value at a point, derivatives, etc. It is assumed that this *continuum approximation* can be used to deduce properties of the system that, on a large scale, are not inconsistent with the properties of the real system; the assumption is made even though the process of taking progressively smaller scales does not produce any kind of regularity in the limit in reality. The assumption itself is sometimes called the "continuum hypothesis" (not to be confused with Cantor's continuum hypothesis in set theory). See for example, Batchelor [3], §1.2. In the case of gases, the approximation can only be used if the *Knudsen number* is small. The Knudsen number, Kn, is the ratio of the molecular mean free path length to a characteristic physical length scale of the problem under consideration and is useful in the description of the flow of low-density gases. In particle dynamics, the mean free path (m) is

$$\frac{k_B T}{\pi \sigma^2 p \sqrt{2}}$$

where k_B (J K^{-1}) is Boltzmann's constant, σ (m) is the particle diameter and p (Pa) is the total pressure.

1.2.2 Conservation Equations and their Generalisations

A number of ideas of fundamental importance in the sciences take the form of conservation statements, a well-known example being the principle of conservation of energy. A very much larger class of fundamental ideas in physics however can be thought of as statements of the ways in which some quantity is not conserved; there may be processes whereby it is generated or destroyed or, equivalently, transferred into or out of another system that is analysed separately. The process by which such statements can be converted into partial differential equations is described in detail in Sect. 2.1.1 of [4]; it can be summarised as follows.

In the absence of generation or destruction terms, they are referred to as *conservation* equations. It is a not ideal terminology, not least because

the most famous conservation equation of all, the equation of conservation of energy for a single particle moving in a conservative field of force, is not of this form as usually stated. When generation or destruction terms are present, terminology for the resulting equations is not standard. Possibilities are to refer to them as *balance*, *generation* or *transfer* equations. The terminology that will be preferred here is to call them *generalised conservation equations* or, following [5], just *conservation equations*; both generation and destruction effects can then be included, distinguishing them only by the sign of the relevant term.

For many quantifiable physical properties $\mathcal{Q}$ there is a relation between the way in which it increases (or decreases) in V and the manner in which $\mathcal{Q}$ is introduced into V. Such a relationship can be summarised by saying that

- The net rate of increase of $\mathcal{Q}$ in V is equal to the net rate of generation of $\mathcal{Q}$ inside V and on its surface S, less its net rate of outward flow across S. (1.1)

The process of derivation of the mathematical form of such a statement can be summarised as follows.

First, in the case when all aspects of the physical process can be adequately described in terms of continuous functions, an assumption of sufficient differentiability will be made. The method will only be applied to properties that can be properly described in terms of scalars, vectors, or tensors of any order. When it is helpful to do so, the notation of rectangular Cartesian tensors will be employed, including the use of Einstein's summation convention with a comma separator to indicate differentiation. A vector $\mathbf{v}$, for example, has three components v_i $(i = 1\dots 3)$ and its divergence will be written

$$\nabla \cdot \mathbf{v}, \quad v_{j,j} \quad \text{or} \quad \frac{\partial v_j}{\partial x_j}.$$

Suppose $\mathcal{Q}$ is defined at every point in some region of space V contained within the domain of investigation D, and that

- there is a density k_* units of $\mathcal{Q}$ per unit volume at each point of V, where k_* is a tensor of order $r \geq 0$ with $*$ indicating an appropriate set of r subscripts;
- there is a flow Q_{*i} defined at each point of D so that the direction of flow and magnitude of the quantity whose density is measured by k_* is Q_{*i} units of $\mathcal{Q}$ per unit area per unit time;
- at an element with an outward unit normal $\mathbf{n}$ of the surface S of V, there is a rate of generation $G_{*j} n_j$ units of $\mathcal{Q}$ per unit area of S per unit time.
- a net number q_* units of $\mathcal{Q}$ are generated per unit volume per unit time.

In these statements the region V can be any region, big or small, contained within D, so that it and its bounding surface S can be conceptual rather than physically distinct entities, and S is a part of V. Again, they will be considered
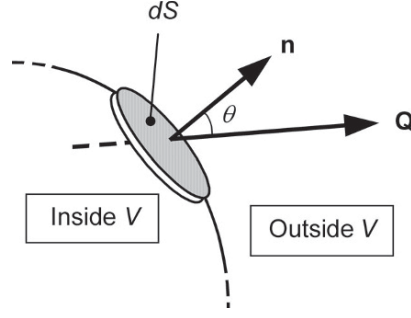
Fig. 1.1. Flow out of V across S in the case when the flow is a vector, $\mathbf{Q}$. The component of $\mathbf{Q}$ in the direction of $\mathbf{n}$ is $\mathbf{Q}\cos\theta$. © *2001 From* [4]. *Reproduced by permission of Taylor & Francis LLC, a division of Informa plc.*

to be fixed in space for the moment, though that also is a condition which can be relaxed. The general configuration is shown in Fig. 1.1 for flow across S in the case when the flow is a vector, $\mathbf{Q}$. The same applies to the surface generation term except that in that case $\mathbf{G}$ cannot be considered as crossing the surface, but rather as being generated at it.

In the third property of the four properties of $\mathfrak{Q}$, the discussion will be limited to the case where G_{*i} is independent of the orientation of the surface element. The third property is essentially the same as the second but the distinction is helpful when it comes to the physical origins of the respective terms; the two forms are usually thought of in quite different ways. The third is somewhat similar to Newton's Third Law of Motion, in that it shows how regions may be combined in the same way that the Third Law of Motion shows how bodies may be aggregated.

For a true conservation condition, G_{*i} and q_* are both identically zero.

Mathematically, the generalised conservation statement can be written

$$\frac{d}{dt}\int_V k_* dV = \int_V q_* dV - \int_S Q_{*j} n_j dS + \int_S G_{*j} n_j dS. \qquad (1.2)$$

The two last terms in the equation correspond to the second and third of the properties above and are very similar in a formal sense; as already noted, they are worth distinguishing since they tend to arise for physically different reasons.

Since the region V is required to be fixed in space, the time derivative can be taken inside the integral. Suppose that $G_{*i} - Q_{*i}$ is a continuously differentiable field defined in a neighbourhood of V. Gauss's Theorem can be applied to the two surface integrals so that equation (1.2) can be written

$$\frac{1}{V}\int_V \left(\frac{\partial k_*}{\partial t} + \frac{\partial Q_{*j}}{\partial x_j} - \frac{\partial G_{*j}}{\partial x_j} - q_* \right) dV = 0. \qquad (1.3)$$

This result is true whatever the size or shape of V provided only that it lies in D. If the volume V is taken to contain a particular point $\mathbf{x}$, and all points of V are within a distance d of it, the limit as d tends to zero of the left hand side has the value of the integrand at $\mathbf{x}$, provided that it is continuous. The argument can be applied at any point $\mathbf{x}$ of D and so (1.2) has the equivalent mathematical form

$$\frac{\partial k_*}{\partial t} + \frac{\partial Q_{*j}}{\partial x_j} = q_* + \frac{\partial G_{*j}}{\partial x_j}. \qquad (1.4)$$

1.2.3 Governing Equations of Generalised Conservation Type

Table 1.1 provides some examples.

Comments in connection with some of these examples are necessary.

Flow of a Viscous Fluid

In the case of the Navier-Stokes equations (1.6) the bulk viscosity μ_B (also known as the volume viscosity) is also mentioned in Sect. 6.1.1. Formally at least, it can be incorporated into the pressure term if the context is such that no pressure values have absolute meaning; by contrast, that is not so in the case of atmospheric pressure for example, or the definition of pressure that follows (4.3). When an absolute definition of pressure is essential, the additional term involving μ_B should be included, but even so it is often left out. In incompressible flow, for which $u_{k,k} = 0$, it can in any case be ignored.

Viscous Heat Flow

As it stands, the form of the equation of heat conduction, (1.7), is appropriate to solids and liquids. In the case of gases, the heat flow is proportional to a pressure gradient as well as the temperature gradient [5, 6]; this additional contribution is known as the viscous heat flow. Although it is formally a second order effect in terms of its derivation in a kinetic theory description of gas flow and an expansion in powers of the Knudsen number, it can sometimes be comparable to the first order term, Fourier's law. The Knudsen number, Kn, is the ratio of the molecular mean free path length to a characteristic physical length scale and is useful in the description of the flow of low-density gases. For example, for the flow caused by a pressure gradient in a gas the viscous heat flow term is

$$\frac{\theta_4}{2}\frac{\mu}{\rho}\nabla p, \qquad (1.10)$$

where, in the case of Maxwellian molecules, θ_4 has the value 3; see [3]; consequently it needs to be added to the Fourier's law term in the equation. Here, μ is the stress viscosity, ρ is the mass density and p is the pressure of the gas. Since the thermal conductivity λ and the viscosity μ are both proportional

Table 1.1. Some governing equations considered as examples of generalised conservation conditions. SI base units are assumed.

k_*	Q_{*j}	q_*	G_{*j}	
		Dynamics of a Newtonian Fluid [3], ch 3		
Density, ρ	Mass flow rate, ρu_j	–	–	
	Equation of conservation of mass: $\dfrac{\partial \rho}{\partial t} + \nabla \cdot (\rho \mathbf{u}) = 0$			(1.5)
Momentum density, ρu_i	Momentum flow rate, $\rho u_i u_j$	Body forces, ρF_i	Stress, $\sigma_{ij} = -p\delta_{ij} + \mu_B u_{k,k}\delta_{ij} + d_{ij}$	

Navier-Stokes equations:

$$\frac{\partial \rho u_i}{\partial t} + (\rho u_i u_j)_{,j} = \rho F_i - p_{,i} + (\mu_B u_{j,j})_{,i} + \left\{ \mu \left(u_{i,j} + u_{j,i} - \frac{2}{3} u_{k,k}\delta_{i,j} \right) \right\}_{,j} ; \qquad (1.6)$$

u is the velocity, μ is the coefficient of (dynamic) viscosity and p is the pressure; $d_{ij} = \mu \left(u_{i,j} + u_{j,i} - \frac{2}{3} u_{k,k}\delta_{i,j} \right)$ is the deviatoric stress tensor and μ_B the bulk viscosity.

		Heat conduction in a moving medium [3], ch 3		
Internal energy per unit volume, ρE	Convection and Fourier's Law, $\rho E u_j - kT_{,j}$	Sources of thermal energy, q	–	
	$\dfrac{\partial}{\partial t}(\rho E) + (\rho E u_j)_{,j} = q + (kT_{,j})_{,j}$			(1.7)

T is the temperature and k the coefficient of thermal conductivity.

		Electromagnetic Theory		
Net charge Density, ρ_{charge}	Current density, **j**	–	–	
	$\dfrac{\partial \rho_{charge}}{\partial t} + j_{k,k} = 0.$			(1.8)

		Linear thermoelasticity in an isotropic medium at rest		
Momentum density, $\rho \dfrac{\partial \xi_i}{\partial t}$	–	Body forces, ρF_i	Stress (with strain relation and thermal expansion), $p_{ij} = \lambda e_{kk}\delta_{ij} + 2\mu e_{ij} - \frac{1}{3}\alpha(3\lambda + 2\mu)(T - T_0)\delta_{ij}$	

$$\rho \frac{\partial^2 \xi_i}{\partial t^2} = \rho F_i + (\lambda + \mu)\xi_{j,ji} + \mu \xi_{i,jj} - \frac{1}{3}\alpha(3\lambda + 2\mu)T_{,i} \qquad (1.9)$$

λ and μ are the Lamé constants, ξ the displacement, e_{ij} the strain tensor given by $e_{ij} = \frac{1}{2}(\xi_{i,j} + \xi_{j,i})$, T the temperature, and α the volume coefficient of expansion.

to the molecular mean free path, this term, the viscous heat transfer, cannot be neglected in comparison with the Fourier's law term in the hydrodynamic limit (in which the Knudsen number tends to zero); see [6]. Under conditions in which the pressure is comparable to or greater than atmospheric pressure, so that the density of the gas is not low, the viscous heat flow term is likely to be small; for example, for air at standard temperature and pressure, the ratio of the viscous heat flow to the Fourier contribution is of the order of $10^{-3}\Delta p/\Delta T$, but it is clear from this that if the pressure differences are of the order of $1\,\mathrm{bar}$, say, and the temperature differences on the same length scale are not too great, this ratio would indicated that the viscous heat flow was of importance. If conditions were near to a vacuum so that the gas density was small, the term might even become dominant.

Conservation of Electric Charge

The equation of conservation of net charge, (1.8) in the table, provides part of the theoretical justification for the existence of Maxwell's displacement current, an essential component of Maxwell's equations. They, like the field equation formulation of Newton's theory of gravitation, have their origins in the behaviour of an abstract test particle. The statements are then converted into differential form by a similar technique that is based on the use of Stokes's Theorem rather than Gauss's Theorem. The process is described briefly in §1.5.

Linear Thermo-Elasticity in a Moving Frame of Reference

It is sometimes helpful to use the equations of linear thermo-elasticity in a moving frame of reference. The linearisation depends only on the stress and strain tensors being small so, provided that the underlying motion of the entire work piece consists only of a combination of a velocity and a rotation, (1.9) in Table 1.1 can be used in a modified form. Suppose that there is a uniform, possibly time-dependent, velocity $\mathbf{U}(t)$ and a time-dependent angular velocity $\boldsymbol{\omega}(\tau)$ about a fixed point, $\mathbf{x}^0$ in the equivalent unstrained material. At the point $\mathbf{x}$ there is a small displacement $\boldsymbol{\xi}(\mathbf{x},t)$ in the real material from the equivalent ideal unstrained material. Write

$$V_i = U_i\left(t\right) + \varepsilon_{ijk}\omega_j\left(t\right)\left(x_k - x_k^0\right);$$

$\mathbf{V}$ is thus the velocity of points in the ideal material, and is caused by a body force $\mathbf{F}^0$. An additional small body force $\mathbf{F}$ must be added to this to produce the small displacement $\vec{\boldsymbol{\xi}}$. $\mathbf{V}$ and $\mathbf{F}^0$ are related by

$$\rho\left\{\frac{\partial V_i}{\partial t} + \frac{\partial}{\partial x_j}\left(V_iV_j\right)\right\} = F_i^0.$$

This equation can be subtracted from the one which results from using the generalised conservation argument (for small displacements from the

undistorted motion) obtained by considering

$$k_i = \rho \left(V_i + \frac{\partial \xi_i}{\partial t} + V_k \frac{\partial \xi_i}{\partial x_k} \right),$$

$$Q_{ij} = k_i k_j / \rho, \quad q_i = \rho \left(F_i^0 + F_i \right) \text{ and } G_{ij} = p_{ij}$$

where p_{ij} is given in Table 1.1. Equation (1.4) then shows, to the small disturbance approximation, that the left-hand side of (1.9) in the table is replaced by

$$\rho \left\{ \left(\frac{\partial}{\partial t} + V_j \frac{\partial}{\partial x_j} \right)^2 \xi_i + \frac{\partial}{\partial x_j} \left[V_i \left(\frac{\partial}{\partial t} + V_k \frac{\partial}{\partial x_k} \right) \xi_j \right] \right\}.$$

Note that $\nabla \cdot \mathbf{V} = 0$. The body-force term ρF_i on the right must be understood as any small force in addition to $\mathbf{F}^0$, the force that is necessary to account for the acceleration implied by the presence of the terms in $\mathbf{U}$ and $\boldsymbol{\omega}$. These last two quantities must not depend on position in space and the constitutive equation for the stress must depend only on the symmetric part of the displacement gradient (a consequence of the Principle of Material Frame-Indifference, a principle which is still a subject of some controversy, but seems unlikely to be found unsatisfactory in the context of macroscopic material processing involving solids and liquids.)

1.2.4 Gauss's Law

There are a number of physical laws whose mathematical form is very similar to generalised conservation equations, but which are not usually thought of as such, even though in some respects that is what they are. The reason is that the very existence of the underlying quantity, usually a scalar whose spatial density is q, itself produces effects that can be described in terms of a vector field $\mathbf{Q}$; it has the property that the flux of $\mathbf{Q}$ out of any volume V is proportional to the total amount of the quantity contained in V. They are thus generalised flux conservation laws. In the absence of q, it is then flux along a tube whose sides are parallel to $\mathbf{Q}$ which is conserved. It follows that

$$\int_S \mathbf{Q} \cdot \mathbf{n} dS = \alpha \int_V q \, dV.$$

It is always a part of the definition of $\mathbf{Q}$ that the constant of proportionality, α, depends only on the system of units chosen. The same mathematical arguments as those used above show that there is a corresponding differential form for these conditions, given by

$$\nabla \cdot \mathbf{Q} = \alpha q.$$

Table 1.2 gives some examples.

Table 1.2. Examples of generalised flux conservation laws.

q_*	Q_{*j}	α
Newton's Theory of Gravitation		
Mass density, ρ	Gravitational field, $\mathbf{F}$	$-4\pi G$
$\nabla \cdot \mathbf{F} = -4\pi G \rho$; G is the universal gravitational constant.		
Electromagnetic Theory		
(Absence of monopoles) 0	Magnetic flux density, $\mathbf{B}$	$-$
Gauss's law for magnetism: $\nabla \cdot \mathbf{B} = 0$		(1.11)
Charge density, ρ_{charge}	Electric displacement field, $\mathbf{D}$	1
Gauss's law: $\nabla \cdot \mathbf{D} = \rho_{charge}$		(1.12)

1.3 Boundary and Interface Conditions

1.3.1 Generalised Conservation Conditions

A problem is described not only by the governing equations in the interior of the medium under consideration, but also by the initial conditions, the conditions at the external boundaries of the problem and any internal boundaries between regions with different properties. These initial and interface conditions are every bit as important as the governing equations [4], p56. Although the initial conditions quite often lapse into unimportance with the passage of time, the interface conditions must always be taken into account.

The form of the initial conditions to be imposed will depend on the structure of the governing equations and the kind of problem to be solved. To some extent they will always depend on previous history, though often in only very simple ways. The equation of heat conduction, for example, will normally only need to have the initial temperature distribution specified, but even in simple problems care must always be taken to ensure that assumptions made are justified and consistent with the mathematical model that it is proposed to use, as well as being a proper description of the physical processes involved.

Boundary and interface conditions must likewise be considered carefully; failure to do so can lead to many different problems. There might be no solution, many solutions when only one is expected or, most dangerously of all, a solution may be obtained that is in fact invalid but appears reasonable at a casual in glance.

Many interface conditions are based on the same ideas of conservation or lack of it that were considered in the previous section, and the appropriate
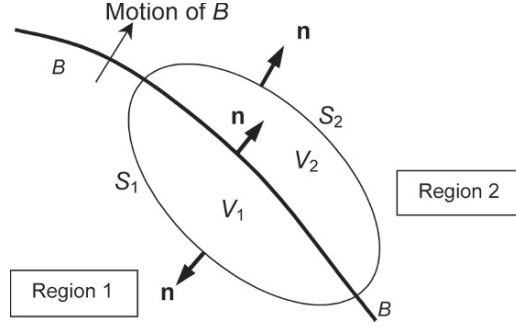
Fig. 1.2. The control volume V, whose surface S is divided into two sections S_1 and S_2 by the moving interface B. The figure shows the convention for the directions of the normals $\mathbf{n}$ on each of the surfaces B, S_1 and S_2; S_1 and S_2 are fixed.

mathematical form can be obtained in much the same way. The underlying statement is indeed identical and the initial starting-point in mathematical form is almost the same as (1.1). There is one important difference however and that is to the fourth of the properties listed. At a boundary or interface, B, there may be generation of $\mathcal{Q}$ which occurs only there; suppose that it has a magnitude Δq_* per unit area of B. Perhaps the most familiar example is the release of latent heat as steam condenses to water.

The necessary interface condition can be found by considering a volume V with a fixed surface S which encloses the moving interface B separating region 1 from region 2 in the manner shown in figure 1.2. The property $\mathcal{Q}$ is considered to be crossing B from V_1 to V_2 so that $V = V_1 \cup V_2$ and $S = S_1 \cup S_2$. Suppose that B is moving with a velocity $\dot{n}$ in the direction of its normal from V_1 into V_2; the unit normal $\mathbf{n}$ on B is likewise directed from V_1 to V_2.

The mathematical form of the generalised conservation statement (1.1) for the entire volume remains identical except that there is the additional term

$$\int_B \Delta q_* \, dS$$

on its right-hand side. V can now be split into its components V_1 and V_2 which are bounded by $S_1 \cup B$ and $S_2 \cup B$ respectively. Now notice that, for example,

$$\frac{d}{dt} \int_{V_1} k_* dV = \int_{V_1} \frac{\partial k_*}{\partial t} dV + \int_{V_1} k_* \frac{d}{dt}(dV) = \int_{V_1} \frac{\partial k_*}{\partial t} dV + \int_B [k_*]_1 \, \dot{n} \, dS.$$

$$(1.13)$$

In the case of V_2 the expression is similar except that the sign of the last term on the right is negative because of the convention adopted for the sign of $\dot{n}$.

The notation $[\ldots]_1$ is the value of the enclosed quantity in region 1 for example, and $[\ldots]_1^2$ is its value in region 2 minus its value in region 1. Equation (1.3) can be applied to V_1 and V_2 separately and both subtracted

from (1.13) to show that

$$\int_B [k_*]_1 \, \dot{n} \, dS - \int_B [k_*]_2 \, \dot{n} \, dS = \int_B [Q_{*j} - G_{*j}]_1 \, n_j dS - \int_B [Q_{*j} - G_{*j}]_2 \, n_j dS$$

$$+ \int_B \Delta q_* \, dS.$$

The whole equation can be written as a single integral over B, divided by its magnitude. Then so long as the integrand is continuous and the limit as the area of B tends to zero is taken in such a way that the distance of every point on B from an arbitrarily specified point on it tends to zero, the interface condition can be expressed as

$$[-k_* \dot{n} + (Q_{*j} - G_{*j}) \, n_j]_1^2 = \Delta q_*. \tag{1.14}$$

An alternative approach to the derivation of (1.14) can be found in [4]. It can often be convenient to express the normal in term of the gradient of an expression for the surface S. Suppose it is given by the equation $S(\mathbf{x}, t) = 0$, then

$$n_j = \pm \frac{S_{,j}}{\sqrt{S_{,k}^2}} \quad \text{and} \quad \dot{n} = \mp \frac{1}{\sqrt{S_{,k}^2}} \frac{\partial S}{\partial t}.$$

The choice of sign is necessary to ensure compatibility with the convention for the normal; $\dot{n}$ should be positive when the boundary is moving in the direction in which $\mathbf{n}$ points. A few examples of the use of (1.14) are shown in Table 1.3.

Characteristic interface conditions for Gauss's laws for gravitation, magnetism and electric fields in the absence of surface effects at the boundary are similarly

$$[\mathbf{F} \cdot \mathbf{n}]_1^2 = 0, \quad [\mathbf{B} \cdot \mathbf{n}]_1^2 = 0 \text{ and } [\mathbf{D} \cdot \mathbf{n}]_1^2 = 0.$$

They are easily modified by the addition of extra terms when surface effects are present.

1.3.2 The Kinematic Condition in Fluid Dynamics

At an interface between a fluid and another medium it is usual to specify that the tangential component of velocity is continuous across the separating surface, so that

$$[\mathbf{u} \cdot \mathbf{t}]_1^2 = 0 \tag{1.19}$$

where $\mathbf{u}$ is the velocity vector and $\mathbf{t}$ is any vector tangent to the surface. The background and reasons for such a condition are well presented in [3], p 149 and Sect. 1.9. In summary, at any discontinuity across a material

Table 1.3. Some interface conditions as examples of generalised conservation conditions; the notation is the same as that used in Table 1.1.

Dynamics of a Newtonian Fluid [3]

$$\Delta q_* = 0,$$

Mass conservation: $[\rho\,(u_j n_j - \dot{n})]_1^2 = 0.$ (1.15)

$\Delta q_* = n_i\,(\gamma n_{j,j} + n_j \gamma_{,j}) - \gamma_{,i}$ where γ is the coefficient of surface tension.

Momentum transfer: $[\rho u_i\,(u_j n_j - \dot{n}) + p n_i - d_{ij} n_j]_1^2$
$$= n_i\,(\gamma n_{j,j} + n_j \gamma_{,j}) - \gamma_{,i}.$$ (1.16)

The normal and tangential components of this condition simplify to
$[\dot{m} n_i u_i + p - n_i d_{ij} n_j]_1^2 = \gamma n_{j,j}$ if $\dot{m} = [\rho\,(u_j n_j - \dot{n})]_1 = [\rho\,(u_j n_j - \dot{n})]_2$,
$[t_i d_{ij} n_j]_1^2 = t_i \gamma_{,i}$ where use is made of (1.15) and (1.19);
t_i is the ith component of a unit tangential vector.

Heat conduction in a moving medium [3]

$$\Delta q_* = -\dot{m} L_1^2.$$
The Stefan condition: $[k n_j T_{,j}]_1^2 = \dot{m} L_1^2$ (1.17)

where $\dot{m}$ is $[\rho\,(u_j n_j - \dot{n})]_1 = [\rho\,(u_j n_j - \dot{n})]_2$ and
L_1^2 is the latent heat of transition from phase 1 to phase 2 (i.e. in the direction of the normal **n**).

Electromagnetic Theory

When $\Delta q_* = 0$:
$$[\rho_{charge}\dot{n} - j_k n_k]_1^2 = 0.$$ (1.18)

surface, molecular transport would rapidly give rise to a very large stress at the surface, whose effect would be to tend to eliminate the relative velocity. In the case of a boundary separating a fluid and a solid, the condition that the tangential component of velocity should be continuous is known as the *no-slip condition*.

The same argument can be used to support (1.19) in the case of two different substances, and of a single substance in different phases, including the case when matter crosses the phase boundary, but it is then less satisfactory. The validity of the no-slip condition between a solid and a fluid was discussed at length in the nineteenth century, but the result has been adequately confirmed by experiment, and its practical success. It cannot be regarded as having the same firm theoretical foundations as the other conditions and there are circumstances where it may not apply, either for pragmatic reasons, of because it has been found to be false. An example of the first occurs when the inviscid fluid model is used as an approximation, in which case (1.19) cannot be employed. The inviscid model of fluid flow at normal temperatures ignores the region very close to the boundary in which normal molecular

interactions occur, so that the arguments supporting the no-slip condition still apply, but are supposed to have no influence beyond a short distance from the interface.

The inviscid model is an example where (1.19) applies but is ignored for compatibility with a useful approximation in the solution procedure for the problem under consideration. A circumstance in which it does not necessarily apply, however, occurs in the case of low-density gases, where the mean velocity of a molecule can vary significantly in distances comparable with the mean free path. In this case there can be a non-zero change in velocity and a temperature difference between the gas and the solid or liquid adjacent to it [5,6]. The question is considered further in §4.3.1 in connection with the Knudsen layer.

1.4 Fick's Laws

The heat conduction equation (1.7) is an example of a diffusive process. Suppose $\mathcal{Q}$ is some quantifiable substance which is conserved. Examples might be thermal energy, particles diffusing through some medium, or a contaminating chemical. If it has a concentration C and $\mathcal{Q}$ is conserved, then its flow rate $\mathbf{q}_c$ is related to C by *Fick's First Law*,

$$\mathbf{q}_c = -D\nabla C \qquad (1.20)$$

relative to the underlying medium, which is normally assumed to be at rest. In (1.20) D is a diffusion coefficient. Conservation of $\mathcal{Q}$, by (1.4) in the absence of any generation processes, gives

$$\frac{\partial C}{\partial t} + \nabla \cdot \mathbf{q}_c.$$

If this equation is combined with (1.20), *Fick's Second Law* is obtained,

$$\frac{\partial C}{\partial t} = D\nabla^2 C, \qquad (1.21)$$

provided the diffusion constant D can be regarded as a constant.

1.5 Electromagnetism

1.5.1 Maxwell's Equations

A number of physical laws are usually stated in the form that no work is done when a unit test particle acted on by a force field $\mathbf{F}$ is moved round any closed path in space. Another way of stating the result is to say that $\mathbf{F}$ is

conservative. Such a statement can be expressed in mathematical form as

$$\int_C \mathbf{F} \cdot \mathbf{dr} = 0$$

where C is such a path. It can be converted into the form of a differential equation as follows. Suppose that C is simple and smooth but otherwise arbitrary in size, orientation and location, and that it can be spanned by a surface at every point of which $\mathbf{F}$ is differentiable. In that case Stokes' Theorem shows that

$$\int_S \nabla \times \mathbf{F} \cdot \mathbf{n}\, dS = 0 \qquad (1.22)$$

where $\mathbf{n}$ is the unit normal to S. Then consider a particular point in space and construct a circular path of radius a about the point in a plane with a fixed (but otherwise arbitrary) normal. Divide (1.22) by the area of the circle and take the limit as a tends to zero, to show that the integrand must vanish. Since the direction of the normal is arbitrary it follows that

$$\nabla \times \mathbf{F} = \mathbf{0} \qquad (1.23)$$

everywhere in the domain in which $\mathbf{F}$ has the required properties. Consequently, $\mathbf{F}$ can be expressed as the gradient of a scalar. It is a standard result for conservative fields that is sometimes taken as their definition, although the more usual definition is that they are expressible as the gradient of some scalar field, usually referred to as the potential (conventions vary on the sign of the potential however). The terminology is independent of the physical interpretation of these scalar and vector fields.

If, by extension, a finite amount of work is done equal to the flux of a second field, $\mathbf{Q}$ say, across a surface spanning the path C and lying in the domain of definition of $\mathbf{F}$, and the flux is otherwise independent of the choice of S, then

$$\int_C \mathbf{F} \cdot \mathbf{dr} = \int_C \mathbf{Q} \cdot \mathbf{n}\, dS.$$

Stokes' theorem can be applied in the same way as before to show that

$$\nabla \times \mathbf{F} = \mathbf{Q} \qquad (1.24)$$

in the domain of definition of $\mathbf{F}$ and $\mathbf{Q}$. The divergence of a vector field which is the curl of another vector field is identically zero; necessarily, therefore,

$$\nabla \cdot \mathbf{Q} = 0. \qquad (1.25)$$

A vector field that satisfies such a condition is said to be solenoidal, and again the terminology is used irrespective of the physical interpretation.

Comparison with the ideas of §1.2.2 shows that it might sometimes be helpful to think of $\mathbf{Q}$ as a rate of flow of some conserved quantity in a steady state, or when the density of the conserved quantity is constant in time.

The field theory formulation of Newton's theory of gravitation is of this type. The work done by a gravitational field $\mathbf{F}$ on a particle moving in a closed path C is zero, and so the argument just given shows that

$$\nabla \times \mathbf{F} = \mathbf{0}.$$

There therefore exists a gravitational potential, and as a result of Gauss's law for the gravitational field (see Table 1.1), it satisfies Poisson's equation. The classical form for the law of Conservation of Energy for a single particle moving under the action of a gravitational field only is then a consequence of Newton's Second Law of Motion.

The application of the idea to electromagnetism is rather more involved. Faraday's law states that the induced electromotive force in a closed loop is proportional to the rate of change of the magnetic flux through it. It is supplemented by Lenz's law which adds that the polarity of the induced electromotive force induces a current whose magnetic field opposes the change which produced it. These laws can be summarised by saying that if $\mathbf{F}$ (above) is taken as the electric field $\mathbf{E}$, $\mathbf{B}$ is the magnetic flux vector, and $\mathbf{Q}$ is proportional to $\partial \mathbf{B}/\partial t$, then the latter is proportional to $\nabla \times \mathbf{E}$. Lenz's law means that the sign of the constant is negative and in SI base units its magnitude is one, so that

$$\nabla \times \mathbf{E} = -\frac{\partial \mathbf{B}}{\partial t}. \tag{1.26}$$

In the case of the magnetic field $\mathbf{H}$ the starting point is Ampère's Circuit Law which says that in a steady state the circulating magnetic field $\mathbf{H}$ in a closed path C is proportional to the total electric current $\mathbf{J}$ linked with C. Thus, in the same way as for Faraday's law, take $\mathbf{F}$ to be $\mathbf{H}$ and $\mathbf{Q}$ to be $\mathbf{j}$. In SI base units, the constant of proportionality is one (and is positive) so that

$$\nabla \times \mathbf{H} = \mathbf{j}.$$

The result is clearly unsatisfactory when conditions are changing with time, since the form of the law implies that $\nabla \cdot \mathbf{j} = 0$ contrary to (1.8) in Table 1.1. Maxwell saw, however, that the difficulty could be resolved by the addition of an extra term to the equation; suppose it is the vector $\mathbf{X}$, and appears on the right of the equation. Then necessarily $\nabla \cdot \mathbf{X} = -\nabla \cdot \mathbf{j}$ and so from (1.8) and Gauss's law, (1.12),

$$\nabla \cdot \left\{ \mathbf{X} - \frac{\partial \mathbf{D}}{\partial t} \right\} = 0.$$

Thus $\mathbf{X} = \partial \mathbf{D}/\partial t$ to which could in principle be added a solenoidal field which necessarily vanishes whenever conditions are steady, but it is not required. Maxwell's extension to Ampère's law therefore results in the equation

$$\nabla \times \mathbf{H} = \mathbf{j} + \frac{\partial \mathbf{D}}{\partial t}. \tag{1.27}$$

To these equations must be added a couple of constitutive equations to relate $\mathbf{B}$ to $\mathbf{H}$, and $\mathbf{E}$ to $\mathbf{D}$. For example, in free space they are

$$\mathbf{B} = \mu_0\mathbf{H} \text{ and } \mathbf{D} = \varepsilon_0\mathbf{E} \tag{1.28}$$

where $\mu_0 = 4\pi \times 10^{-7}\,\text{H m}^{-1}$ is the permeability of a vacuum (the magnetic constant); if c is the speed of light, the permittivity of a vacuum, ε_0, is equal to $\mu_0 c^{-1}$. In most circumstances of interest, to these must be added a relation between $\mathbf{j}$ and other quantities.

1.5.2 Ohm's Law

The classical Ohm's law for a simple conducting medium is the best known relation between the current $\mathbf{j}$ and other field quantities. In vector form it states that $\mathbf{j} = \sigma\mathbf{E}$. where σ ($\Omega^{-1}\text{m}^{-1}$) is the resistivity of the material; the reciprocal of the resistivity is the conductance. The law is adequate for most purposes in a solid or a liquid, but is often unsatisfactory in a gas, especially if the gas is totally or partially ionised.

The general form of such a relation is complicated, but Spitzer [7] p 28 shows that its form can be simplified if it is assumed that (i) the equations are linearised, (ii) the plasma is fully ionised and electrically neutral (an approximation that has to be verified *a posteriori*) and a scalar pressure is used. In that case the relation for a fully ionised plasma becomes

$$\frac{m_e}{e^2 n_e}\frac{\partial \mathbf{j}}{\partial t} + \frac{\mathbf{j}}{\sigma} = \mathbf{E} + \mathbf{u} \times \mathbf{B} - \frac{1}{en_e}\mathbf{j} \times \mathbf{B} + \frac{1}{en_e}\nabla p_e - \frac{m_e}{e\rho}\nabla p_i \tag{1.29}$$

where p_e and p_i are the electron and ion pressures, ρ is the mass density of the vapour (from [7] on the assumption that $\rho = m_i n_e$ if $Z = 1$, there are no neutral ions, and the gas is electrically neutral), m_e and $-e$ are the mass and charge of an electron respectively, and n_e is the number density of electrons. The third term on the right of (1.29) corresponds to the Hall effect.

The coefficient of the first term is very small indeed (and the term would in any case be zero in a steady state) and the last term is small compared to the previous terms, so these two may be neglected. A rough estimate for the conductivity $\sigma(\Omega^{-1}\text{m}^{-1})$ can be estimated as follows; see [7], p 138–139; also see [8]. A Lorenz gas is a hypothetical fully ionised gas in which the positive ions are at rest and the electrons do not interact with each other; if the electric field is small enough, the electrical conductivity, σ_L, is given for such a gas by

$$\sigma_L = 32\varepsilon_0^2\sqrt{8\pi k_B^3 T^3}\Big/\left(e^2 Z\sqrt{m_e}\ln\Lambda\right)$$

where Z is the ionic charge, k_B is Boltzmann's constant, ε_0 is the permittivity of free space and Λ is a temperature-dependent parameter whose logarithm is of order 5 and varies only slowly with temperature at atmospheric pressure

and temperatures of the order of 10^4 K. Cohen [8] gives

$$\Lambda = \frac{3\pi \left(2\varepsilon_0 k_B T\right)^{3/2}}{e^3 n_e^{1/2}}.$$

The conductivity of an ionised gas can then be found in terms of σ_L from the relation $\sigma = \gamma_E \sigma_L$ where γ_E depends on the ionic charge, Z. When $Z = 1$, γ_E has the value 0.582 and

$$\sigma \approx 0.0153 T^{3/2}/\ln \Lambda \ \Omega^{-1}\mathrm{m}^{-1}. \tag{1.30}$$

References

1. Steen WM (1998) Laser Material Processing, 2nd edn. Springer, Berlin
2. von Allmen M, Blatter A (1995) Laser Beam Interaction with Materials: Physical Principles and Applications. Springer, Berlin
3. Batchelor GK (1967) An Introduction to Fluid Dynamics. Cambridge University Press, Cambridge
4. Dowden JM (2001) The Mathematics of Thermal Modeling: An Introduction to the Theory of Laser Material Processing. Chapman Hall/CRC, Boca Raton, Florida
5. Sone Y (2002) Kinetic Theory and Fluid Dynamics. Birkhäuser, Boston ch 5
6. Sharipov F (2004) Heat transfer in the Knudsen layer. Physical Review E60: 061201, 1–4
7. Spitzer L (1962) Physics of fully ionized gases. Interscience, New York
8. Cohen RS, Spitzer L, Routly PMcR (1950) The electrical conductivity of an ionized gas. Phys Rev 80: 230–238

Simulation of Laser Cutting

Wolfgang Schulz[1,2], Markus Nießen[2], Urs Eppelt[2] and Kerstin Kowalick[3]

[1] Fraunhofer Institute for Laser Technology, ILT Aachen
   `wolfgang.schulz@ilt.fraunhofer.de`
[2] Nonlinear Dynamics of Laser Processing, RWTH Aachen University
   `markus.niessen@ilt.fraunhofer.de urs.eppelt@ilt.fraunhofer.de`
[3] Chair for Laser Technology, RWTH Aachen University
   `kerstin.kowalick@llt.rwth-aachen.de`

Abstract. Laser cutting is a thermal separation process widely used in shaping and contour cutting applications. There are, however, gaps in understanding the dynamics of the process, especially issues related to cut quality. This work describes the advances in fundamental physical modelling and process monitoring of laser cutting, as well as time varying processes such as contour cutting. Diagnosis of ripple and dross formation is advanced to observe the melt flow and its separation simultaneously as well as the spatial shape of the cut kerf.

The cutting process is described with a spatial three-dimensional Free Boundary Problem for the motion of one phase boundary. In such dissipative dynamical systems a finite dimensional *inertial manifold* exists which contains the attractor of the system. The existence of a finite dimensional inertial manifold means that the motion of a finite set of degrees of freedom can give a good approximation to the complete solution. Asymptotic methods are used to identify the degrees of freedom, and integral methods are applied to derive their equations of motion. Experimental findings about the morphology of ripple formation guide the modelling approach and motivate the investigation of what is known as the one phase problem. Solving inverse problems and the properties of the thermal boundary layers are discussed. The model reproduces details of the U-shaped ripples evolving at the cut surface.

In discussion of what is known as the two phase problem the properties of the melt flow are included. The additional degrees of freedom are the melt film thickness, the mass flow and the temperature at the melt film surface. The onset of evaporation and the increase in capillary forces are the two physical phenomena relevant to the build-up of adherent dross. The dynamic model predicts a modulation frequency for the laser power that leads to almost complete suppression of adherent dross in contour cutting. Heat transport in thin film flow is investigated demonstrating how to control the error of reduced models by spectral methods.

To find the properties of the gas flow leading to melt ejection is a fundamental task in cutting. The interaction of the gas flow with the condensed phase is mediated by two quantities, namely the pressure gradient and the shear stress along the liquid surface. Results of a detailed analysis of the momentum boundary layer of the gas flow is compared with numerical calculations using the Euler equations as well as the viscous effects described by the compressible Navier-Stokes equations. Deflection

and separation of a supersonic gas jet emanating from a nozzle and propagating into the cut kerf is investigated using Schlieren photography and theoretical analysis. Looking for the different situations present in cutting and trepanning, the formation of horizontal structures in the ripple pattern in the cut is discussed. The effect of design and alignment parameters on nozzle performance in cutting are investigated and two dominant effects are discussed, namely the feedback of the gas flow into the nozzle and deflection of the gas flow away from the cutting front. Discussion of the onset of dross formation is extended to include compressible gas flow in the simulation such that the nozzle pressure enters the calculation of the processing domain for a dross-free cut.

2.1 Introduction

Laser processing dominates the market for industrial laser applications, with metal sheet cutting more important than metal sheet welding and marking, as well as other applications that are not yet widespread. Scientific research and development are related to monitoring and quality assurance. Today the development of the technology high-performance cutting machines, which is already well established, is moving towards a so-called autonomous machine, which is thought to incorporate cognition of the underlying physical mechanisms. Related fundamental research activities are focussed on the influence of fluctuations of the parameters and the resulting dynamical features of the process as well as scatter in cutting results. The dominant dynamical features of the process are ripple formation [1] and adherent dross [2, 3] – in contour cutting [4], processing at high cutting speeds, precision machining of microstructures [5, 6]. The applicability to high-quality cutting of diode pumped solid state lasers [7] and fibre lasers in the multi kW power range is also under investigation and researchers are exploiting their potential. The fundamental physical processes – also present in caving, welding and drilling – are related to the movement of free boundaries separated by the melt flow establishing the dynamical shape of the cutting front. Fundamental results are available for the physics of thin film flow [8]–[13], wetting [14, 15] and flow separation [16]–[19], as well as evaporation and condensation [20]–[24]. Specific investigations deal with the development and application of mathematical methods for the analysis of partial differential equations (asymptotic methods [25]–[27], integral (variational) [28, 29] and spectral methods [30]) and Free Boundary Problems [29], which yield the formulation of approximate (asymptotically exact) models [25, 26], [31]–[33]. Numerical methods for tracking of free boundaries (Level Set method [34, 35], and adaptive sparse grids [36, 37]) are applied. The comparison of approximate models with advanced numerical simulations and experimental identification [4, 38] by diagnostic methods with temporal and spatial resolution is used to improve understanding and to determine the physical limits of cutting-machine performance.

Historically, investigations of fundamental experiments [39]–[42] and modelling are carried out to discover the different physical mechanisms

contributing to the technical process. The physical foundations and their possible application to thermal processing are given by van Allmen [43]. In the monograph of Steen [44] the dominant physical processes and their technical relevance for laser applications are discussed. The main modelling activities up to 1994 are reviewed by Steen [45]. Comprehensive surveys [46] of the practical tasks for laser cutting are available.

The physical mechanisms dominant in cutting – such as the balance of the thermal energy heating up the material to be cut, the two phase transitions of melting and evaporation, the melt flow and its hydrodynamical stability [47] as well as the flow of the assist gas in cutting related to momentum and heat transfer [48] from the inert gas jet to the melt – are explored through experimental evidence and have been discussed in connection with the early models. The thin melt film is driven by a supersonic gas jet which is in contact with the melt at the free moving liquid surface. Depending on the position and type of the gas nozzle, as well as the shape of the cutting front, the gas pressure and the shear stress on the melt film can change, and the compressible flow can separate from the cut metal sheet. Performing numerical simulations of supersonic gas flow and using the Schlieren method [42], [49]–[52], characteristics of the complex gas jet such as supersonic domains, shocks, expansion waves and flow separation have become more well understood. Turbulent effects of the gas flow have been discussed [53]. The main interest then changed from the discussion of specific problems to the question of how to give a closed formulation of the process, and what are the additional effects introduced by the coupling of the physical processes. It became essential to distinguish between the independent parameters of the process such as cutting speed, laser power, intensity distribution etc., and quantities, which evolve during the process and have to be calculated as part of the solution, such as the slope of the cutting front, the melt film thickness, the surface temperature, the width of the cut kerf [54]–[58] etc. Additional effects of the reactive gas cutting process have been investigated [53], [59]–[61]. The oxygen and iron concentrations within the liquid oxide layer were investigated [62]–[64] and yield the reaction rate and hence the energy released by the exothermal reaction. By comparing the action of the oxygen gas jet in laser cutting and in autogenous gas cutting the high performance laser gas cutting process, referred to as burning stabilised gas cutting, was invented [65] and later applied in industry.

2.1.1 Physical Phenomena and Experimental Observation

Direct observation of the melt flow as well as the formation of dross and striations is observable during a special type of laser cutting referred to as trimming or trim-cutting. Temporally and spatially resolved diagnosis of ripple and dross formation during trim-cutting (Fig. 2.1a) was introduced by Zefferer [66]. Zefferer combined the observation of thermal radiation emitted from the cutting front and light from an external illumination source reflected by the cut surface. This technique was subsequently applied by other scientists
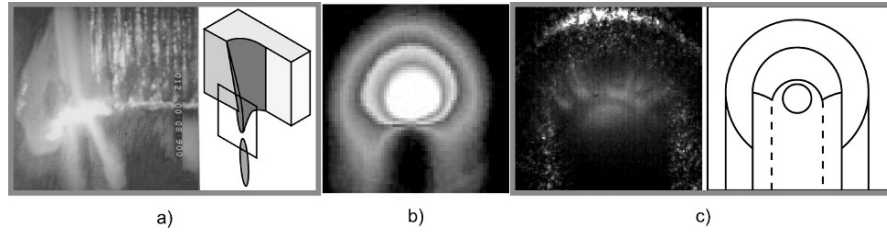
Fig. 2.1. Observation of ripple and dross formation. a) Trim-cutting using in addition external illumination by a flash lamp [66]. Separation of the melt flow, droplet and dross formation as well as ripple formation. Observation of a real cut with an optical set-up coaxial with the laser beam axis. Without b) and with c) external illumination.

to cutting [67] as well as welding [38]. Trimming of sheet metal means cutting along the edge of the work piece, such that the corresponding trim-cut evolves with a one-sided cutting front producing only one cut surface. To allow visual inspection during cutting and to avoid expansion of the gas jet the open side of the trim-cut is covered by a plate made out of transparent material. Two drawbacks remain present in the diagnosis of trim-cutting introduced by the transparent plate, namely the high temperature at the cutting front, which limits the proximity of the plate and the sensitivity of the gas flow to position and bending of the plate. There are plausible and interesting ideas how to improve the trim-cut technique, such as using materials with low melting temperature ($T_m = 96\,^\circ\mathrm{C}$ Rose's alloy) to reduce the overall thermal load of the transparent plate [68].

The ideas of Zefferer [66] and Beersiek [38] and the first demonstrations were improved by Moalem [69] and further refinements today open the possibility of simultaneously observing thermal emission from the liquid surface, separating molten material and vapour flow as well as the shape of the moving front and thermal expansion of the solid on top of the sheet in the environment of the melting front during real processing (Fig. 2.1c). Observation in the coaxial direction with respect to the laser beam axis can be carried out by recording thermal emission from the cutting front (Fig. 2.1b), which gives detailed information about the dynamics of the surface temperature. As the main result, the signal amplitude of fluctuations depends on the cutting speed being more pronounced for low cutting speed. However, while recording the thermal emission only, it is hard to see features of the spatial shape of the cutting front such as the width of the cut at the top and bottom surface. More detailed results are demonstrated by Moalem [69] combining the attenuated thermal signal with the spectral filtered reflection of an external light source (Fig. 2.1c). As shown in the sketch in Fig. 2.1c of the cutting front the different areas can be clearly distinguished in the camera recordings.

At least three different ripple patterns are observable, referred to as ripples of first, second, and third kind (Fig. 2.2a). They evolve subsequently with
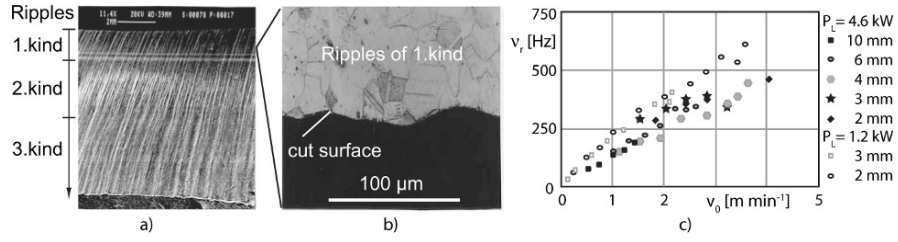
Fig. 2.2. Ripple morphology: a) At least three different kinds of ripples can be distinguished. b) For ripples of the first kind no resolidified melt can be observed and c) the averaged ripple frequency increases linearly with cutting speed.

increasing sheet thickness and cutting speed. Ripples of the first kind appear at the top of the cut edge and up to feed rates of 4 m/min especially. Almost no resolidified material can be observed on metallurgical inspection of the cross section near the top of the cut edge (Fig. 2.2b). The averaged ripple frequency increases nearly linearly with respect to the cutting speed up to a value of about 500 Hz at 4 m/min (Fig. 2.2c). Ripples of the second kind are characterised by double the ripple frequency of the first kind, and with increasing cutting speed their onset is shifted towards the top surface of the sheet metal. Ripples of the third kind are characterised by the dominance of resolidified molten material. To probe more deeply into the mechanisms leading to ripple formation requires the identification of the different types of ripple morphology and the relating of these findings to the processing parameters. Zefferer [66] compared the ripple frequency ν_r with the modulation frequency ν_{mod} and pointed out, that the visibility of ripples strongly depends on their shape. For this reason he introduced the notion of natural ripples and natural ripple frequency, which have been firmly established to be a consequence of natural fluctuations of the processing parameters or the temporally varying gas flow. U-shaped ripples with a sharp tip are clearly visible to the naked eye down to extremely small ripple amplitudes of about $<10\,\mu$m. As result, the ripple frequency depends linearly on modulation frequency (Fig. 2.3a). However, directly observable ripples show this behaviour only in a narrow interval of modulation frequencies around the natural ripple frequency of a few hundred Hz observed for unmodulated laser radiation. Indeed the laser radiation fluctuates and induces ripple formation even for unmodulated power. In spite of that, any modulation frequency induces a movement of the melting front resulting in ripple formation at the cut surfaces. The observability of ripples at low modulation frequency suffers from their large wavelength as well as their smooth and wavy shape. At large modulation frequency the ripple amplitude goes down to a μm scale and a microscope is necessary for observation. It is therefore misleading to ignore the strongly reduced visibility of ripples at high and low frequencies. The waviness of the cut surface as a consequence of low values for the modulation frequency is clearly visible at
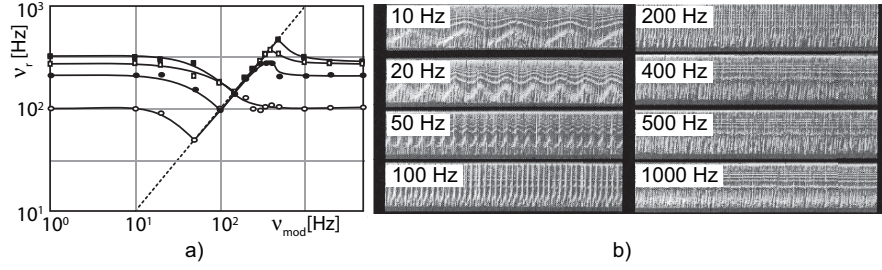
Fig. 2.3. Ripples of first kind: a) The averaged ripple frequency ν_r changes with modulation frequency ν_{mod} of the laser power and the cutting speed v_0 ($v_0 = 1.5$ (filled square), 1.25 (square), 1.0 (filled circle), 0.5 (circle) m min^{-1}). b) The ripple pattern for different values of the modulation frequency ν_{mod} ($v_0 = 1.25$ m min^{-1}). Laser power $P_L = 0.9 + 0.15 \cdot \sin(\nu_{mod} t)$ kW, sheet thickness $d = 2$ mm, stainless steel, gas pressure $P_k = 8 \cdot 10^5$ Pa.

low modulation frequency (Fig. 2.3b). For high modulating frequencies the corresponding small ripple amplitude is found to be superimposed on natural ripples. These experimental findings are related especially to the movement of the melting front only, and therefore significantly guide the modelling approach. They motivate a closer look at the so-called one-phase problem (Fig. 2.4) and the detailed structure of the solution describing the thermal boundary layers. Subsequent iterative extension of the model by increasing the spatial dimension and investigating the meaningful properties of liquid and gaseous phases turns out to be more favorable than trying to solve an apparently comprehensive model. The most challenging task in the diagnostics of cutting is observation of the gas and vapour flow. The Schlieren method [70, 71] is a powerful technique for investigating the properties of the supersonic gas jet as it flows along the surfaces of a cold prepared kerf (model kerf). This model kerf is made out of three layers, substituting the shape of the cut front as well as the two cut surfaces. Interpreting the results from the Schlieren method requires transferring the data from a model flow along a cold, simplified (sharp edges, flat surfaces) set-up to the real cutting situation. Indeed the Schlieren results suffer from the effects of surface temperature, which strongly increase the temperature and momentum boundary layer thicknesses. The shape of the real cutting front and the interaction of gas and liquid flow introduce additional open questions.

2.2 Mathematical Formulation and Analysis

A typical property of dissipative infinite dimensional dynamical systems is the existence of a finite dimensional attractor [25], which is a subset of the phase space attracting all trajectories. From the theory of finite dimensional dynamical systems it is well known that, in systems with different time scales
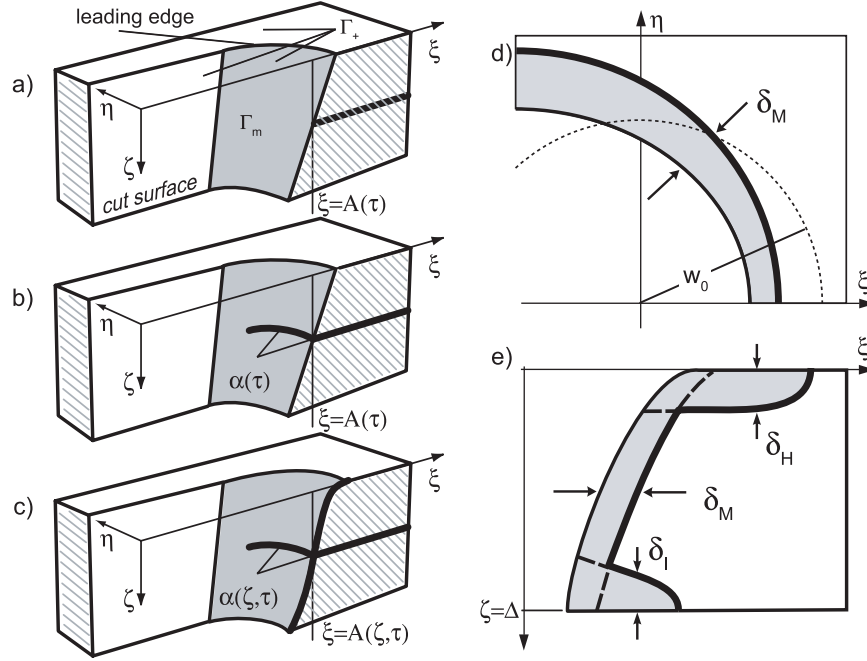
Fig. 2.4. Formulation of the one-phase Free Boundary Problem. The different length scales introduce a hierarchical structure of the solution: a) spatially one-dimensional model where the front position $\xi = A(\tau)$ and heat content $Q(\tau)$ are the free parameters, b) spatially two-dimensional model with curvature $\alpha(\tau)$ as additional free parameter, and c) the axially resolved two-dimensional model, which reproduce the axial shape of the melting front. d) Top view, lateral cross section with thermal boundary layer $\delta_M = \kappa/v_0$ and beam radius w_0. e) Side view, longitudinal section with thermal boundary layers δ_H due to pre-heating and δ_I due to thermal isolation. $x = \delta_M \xi$, $y = w_0 \eta$, $z = d\zeta$.

after the decay of the fast degrees of freedom, the dimension in phase space is reduced. By analogy, the analysis of some examples [26, 27, 31] of dissipative partial differential equations yields the result that the long time dynamic of such systems can also be concentrated in the neighbourhood of a manifold having a *finite* dimension. Such manifolds are called *inertial manifolds*. Obviously, the attractor is a part of the inertial manifold. In principle, the existence of a finite dimensional inertial manifold means that the motion of a finite set of degrees of freedom can give a good approximation to the complete solution. The contraction of phase space is also well known from systems of ordinary differential equations and the corresponding attractor is called the *central manifold*.

One example of such a behaviour is well known from the Boltzmann equation of kinetic theory. The solutions of this differential equation are known

as distribution functions, describing the probability amplitudes for a particle in phase space. In the short time limit, which corresponds to non-equilibrium, these solutions have a rather complex structure. In the long time limit, which corresponds to quasi-equilibrium (equilibrium of flows), the solution is completely described by the equilibrium distribution. The equilibrium distribution is parameterised by a small number of averaged quantities like the thermodynamical temperature and the hydrodynamical drift velocity. The dynamics of these parameters are governed by the simpler hydrodynamical equations of motion. For this example the approximate dynamical system is given by the hydrodynamical approximation of the kinetic equations, where the approximating step is the assumption of the local thermodynamical equilibrium. The solution of the hydrodynamical equations of motion plays the role of the inertial manifold of the Boltzmann equation.

For many partial differential equations of continuum physics the existence of an inertial manifold has been proved and their dimension estimated. From these estimates we can expect a decrease of the dimension in phase space with the dissipation in the system.

In some cases the inertial manifold is explicitly constructed; see for example [72] for the case of the Chaffee-Infante reactions-diffusion equation. Historically, essential advances in the understanding of physical processes and analysis of the partial differential equations are established by the application of integral methods. Famous examples are the quantum mechanical treatment of the Helium atom by Hylleraas [73] applying variational methods and the formulation of the Bénard Problem by Saltzmann [74] and Lorenz [75] using integral methods. It is shown that the motion of the complete system contracts on short time scales into a subspace of lower dimension. Hylleraas identified the three crucial characteristic dynamical variables for the description of the Helium atom, namely the orbital radii of the two electrons and their separation. The Lorenz system consists of three ordinary differential equations of first order with respect to time. The dynamics of these three characteristic dynamical variables or degrees of freedom only, are still able to reproduce the most important properties of the Bénard Problem.

Characteristic dynamical variables are encountered in long-time dynamics near the inertial manifold. The construction of equations of motion for the characteristic dynamical variables is also the crucial step for the testing and final identification of reduced models for Free Boundary Problems in thermal processing. The fundamental idea for deriving models with a reduced dimension in phase space is to find integral representations of the partial differential equations. The variational method introduced by Biot and Daughaday [28] allows the formulation of an integral equation which is equivalent to the Free Boundary Problem ((2.11)–(2.13), (2.34)–(2.35), (2.52)–(2.54)). The application of the variational method to the spatial one-dimensional Free Boundary Problem is given in [33]. The approximating step is the assumption of fast relaxation for the spatial distribution of the temperature, which is parameterised by slowly varying characteristic dynamical variables.

2.2.1 The One-Phase Problem

In cutting, the interaction of the gaseous, liquid and solid domains takes place only across spatially two-dimensional surfaces. The solid volume $\Omega(\tau)$ (Fig. 2.4) is bounded by the absorption front $\Gamma^+(\tau)$ and the bottom surface $\Gamma^-(\tau)$. A part of the absorption front is a free boundary called the melting front $\Gamma_m(\tau)$. Hence, adding the various effects of the gas- and melt flow only change the boundary values, while the structure of the model for the solid, called the one-phase model, remains unchanged. To find the properties of a comprehensive cutting model relies on the detailed analysis of the one-phase model, which was first formulated in 1997 by Enss et al. [32].

The phase boundary of the one-phase Free Boundary Problem can move into the material and erosion takes place or remains unchanged. Resolidification is not allowed. Mathematically the problem is formulated as follows (Fig. 2.4a). The material volume $\Omega(t) \subseteq R^2 \times (0, d)$ is bounded by the absorption front $\Gamma_+(t) = \partial\Omega(t) \cap \{z < d\}$ and the bottom surface of the solid material $\Gamma_-(t) = \partial\Omega(t) \cap \{z = d\}$. The intensity $I = I_0(t)f([\mathbf{x} - \mathbf{v}_0 t]/w_0)$ of the laser beam is characterised by its maximum value $I_0(t)$, the spatial distribution f ($0 \leq f \leq 1$) and the laser beam radius w_0. The laser beam is directed top to bottom with local direction $\mathbf{s} = \mathbf{s}(\mathbf{x}, t)$ ($|\mathbf{s}| = 1$) of the Poynting vector $\mathbf{S} = I_0 f \mathbf{s}$ and moves with velocity v_0 in the positive x-direction, $\mathbf{v}_0 = v_0 \mathbf{e}_x$. The absorbed heat flux $q_a = -A_p\, \mathbf{n} \cdot \mathbf{S}$ depends on the degree of absorption A_p, where $\mathbf{n} = \mathbf{n}(\mathbf{x}, t)$ is normal with respect to the absorption front $\Gamma_+(t)$. The velocity $-v_p\mathbf{n}$ of the free boundary is therefore related to the degree of absorption $A_p = A_p(\mu)$, which depends on polarisation p and wavelength of the laser beam as well as the angle of incidence ϑ ($\mu = \cos(\vartheta)$). The normal component $v_p \geq 0$ of the velocity is restricted to non-negative values, since resolidification is not allowed. The absorption front $\Gamma_+(t)$ can be subdivided into two regions: the melting front $\Gamma_m(t)$, where the temperature equals the melting point $T = T_m$ and erosion takes place ($v_p \geq 0$), and the rest $\Gamma_+(t) \setminus \Gamma_m(t)$ ($T < T_m$ and $v_p = 0$). The melting front $\Gamma_m(t)$ is the *free boundary* of the one-phase problem. The resulting shape of the cut surfaces – where ripples are formed – is a result of the motion of the border line $\partial\Gamma_m(t)$, which is located at the leading edge and is a part of the cut surface. With these definitions the one-phase Free Boundary Problem has the following general form: Find the solution of the heat conduction equation

$$\frac{\partial T}{\partial t} = \kappa \triangle T, \quad T = T(\mathbf{x}, t), \quad \mathbf{x} \in \Omega(t), \tag{2.1}$$

subject to the free boundary conditions

$$q_a - \lambda \nabla T \cdot \mathbf{n} = \rho \mathbf{H}_m v_p, \quad \mathbf{x} \in \Gamma_m(t)$$

$$T = T_m, \qquad \mathbf{x} \in \Gamma_m(t) \tag{2.2}$$

$$q_a - \lambda \nabla T \cdot \mathbf{n} = \mathbf{0}, \quad \mathbf{x} \in \Gamma_+(t) \setminus \Gamma_m(t)$$
$$\nabla T \cdot \mathbf{n} = \mathbf{0}, \quad \mathbf{x} \in \Gamma_-(t) \tag{2.3}$$
$$T_{|\mathbf{x}| \to \infty} = T_a, \quad \mathbf{x} \in \Omega(t).$$

Here T_a and T_m are the ambient- and the melting temperatures. H_m is the melting enthalpy, λ is the heat conductivity, ρ the density, $\kappa = \lambda/(\rho c)$ the thermal diffusivity and c the specific heat capacity. In comparison with the well known Stefan-problem, as represented by Elliot et al. [76] or Fasano et al. [77] there is a different and more complicated situation involved in thermal erosion by a moving heat source,

- the energy transfer takes place directly at the free boundary,
- the heat flux absorbed at the free boundary depends on the angle of incidence and via the intensity distribution $f(\mathbf{x}, t)$ on the position and
- the boundary conditions are changing discontinuously at the boundary $\partial \Gamma_m(t)$ of the melting front.

There are typically three clearly different spatial scales involved in cutting.

$$\delta_M \ll w_0 \ll d \tag{2.4}$$

namely, the thickness $\delta_M = \kappa/v_0$ of a thermal boundary layer at the melting front Γ_m and the spatial scales of the laser beam. The shape of the isophote of the laser beam also introduces entirely different length scales. Typically, the beam radius $w_0 \ll z_R$ is small compared with the Rayleigh length z_R and these scales give the characteristic measures for the shape of the capillary in welding or the melting front in cutting. The scales

$$t = \frac{\delta_M^2}{\kappa} \tau, \quad x = \delta_M \xi_\delta, \quad y = w_0 \eta, \quad z = d\zeta, \quad \theta = \frac{T - T_a}{T_m - T_a} \tag{2.5}$$

are therefore characteristic for cutting. The non-dimensional form of the heat conduction equation (2.1) in a frame of reference moving with the laser beam axis at velocity v_0

$$\frac{\partial \theta}{\partial \tau} = \left[\frac{\partial \theta}{\partial \xi_\delta} + \frac{\partial^2 \theta}{\partial \xi_\delta^2} \right] + \left(\frac{\delta_M}{w_0} \right)^2 \frac{\partial^2 \theta}{\partial \eta^2} + \left(\frac{\delta_M}{d} \right)^2 \frac{\partial^2 \theta}{\partial \zeta^2}, \tag{2.6}$$

clearly demonstrates the importance of the different length scales. In particular, the spatially one-dimensional properties in the feed direction are dominant for fast movement of the beam axis (the square brackets in (2.6)) and the lateral term $\delta_M/w_0 \ll 1$ as well as the axial terms $\delta_M/d \ll 1$ only contribute small corrections. The smallness relation $\delta_M \ll w_0 \ll d$ of the length scales induce a set of three one-phase models hierarchically ordered with respect to the corrections introduced by higher spatial dimensions. As indicated in Fig. (2.4) a)–c) the different magnitude of the contributions in (2.6) at the leading order gives the position $A(\tau)$ of the melting front with respect to the feeding direction (spatially one dimensional model),

the width or radius $\alpha(\tau)$ of the melting front in the η-direction (spatially two dimensional model) and its axial shape as part of the solution of the spatially three-dimensional model. The ratio δ_M/w_0 of the boundary layer thickness and the beam radius is called the inverse Péclet-number Pe^{-1} ($\mathrm{Pe} = w_0/\delta_M = w_0 v_0/\kappa$).

One-Dimensional One-Phase Model

The one-dimensional one-phase model is introduced in [33]. The idea by which the equations of motion for the melting front are derived and the fundamental properties of the solution are outlined. Consider the leading order of (2.6) with respect to the smallness relation $\delta/d \ll \delta/w_0 \ll 1$ the most fundamental limiting case of the boundary value problem can be extracted. The spatial one-dimensional problem

$$\frac{\partial\theta}{\partial\tau} = \frac{\partial\theta}{\partial\xi_\delta} + \frac{\partial^2\theta}{\partial\xi_\delta^2}\theta \mid_{\xi_\delta^2=1} = 1 \ , \qquad \theta \mid_{\xi_\delta^2 \to \infty} = 0 \tag{2.7}$$

has the general quasi-steady solution

$$\theta(\xi_\delta) = \exp[-\xi_\delta] \ , \quad \xi_\delta = \frac{x}{\delta} = \mathrm{Pe}\frac{x}{w_0} = \mathrm{Pe}\ \xi. \tag{2.8}$$

As a result, there are three parameters well suited to describing the structure of the exact quasi-steady solution (2.8) for the temperature in advance of the melting front thus motivating the ansatz

$$\theta_{app}(\xi, \tau) = \theta_s(\tau)\exp\left[-\frac{\xi - A(\tau)}{Q(\tau)}\right] \ , \quad \xi \geq A(\tau) \ , \tag{2.9}$$

which is characterised by three time-dependent characteristic variables, the surface temperature $\theta_s(\tau)$, the position of the melting front $A(\tau)$ and the thermal penetration depth $Q(\tau)$. In the spatial one-dimensional problem the change of boundary conditions can take place with respect to time only, and spatial coexistence is not covered. During the melting phase the surface temperature $\theta_s(\tau) = 1$ equals the melting temperature. $Q(\tau)$ is the penetration depth of the temperature. For $Q(\tau) = 1/\mathrm{Pe}$ the quasi-steady solution (2.8) is reproduced by (2.9) and the position $A(\tau) = \mathrm{Pe}\ \tau$ of the melting front moves together with the beam axis at the cutting speed $\mathrm{Pe} = (w_0/\kappa)v_0$. Of course, the spatially integrated temperature has the physical meaning of the energy content E,

$$E(\tau) = \int\limits_{A(\tau)}^{\infty} \theta_{app}(\xi, \tau)d\xi = \theta_s(\tau)Q(\tau) \ ; \tag{2.10}$$

the quantity $Q(\tau)$ during the melting phase ($\theta_s(\tau) = 1$) can also be interpreted as energy content. In the beginning of the material treatment or while the intensity is modulated, the dynamical system can remain in the heating phase.

The surface temperature $\theta_s(\tau) < 1$ is smaller than the melting temperature and the position of the front $A(\tau) = const.$ remains unchanged.

A detailed derivation of the equations of motion for the characteristic dynamical variables $\theta_s(\tau)$, $A(\tau)$ and $Q(\tau)$ using a variational approach is given in [33]. The equations of motion reduce to the system of ordinary differential equations (ODE-system),

heating phase $(\theta_s < 1)$ melting phase $(\theta_s = 1)$

$$\dot{\theta}_s = \frac{1}{(1 - b_1)Q}\left(\gamma f - b_1 \frac{\theta_s}{Q}\right) \qquad \dot{\theta}_s = 0 \tag{2.11}$$

$$\dot{A} = 0 \qquad\qquad \dot{A} = \frac{1}{1 + h_m - b_1}\left(\gamma f - b_1 \frac{1}{Q}\right) \tag{2.12}$$

$$\dot{Q} = \frac{1}{\theta_s}(\gamma f - \dot{\theta}_s Q) \qquad\qquad \dot{Q} = \gamma f - (1 + h_m)\dot{A}. \tag{2.13}$$

Here $\gamma f = \gamma(\tau)f(A(\tau) - \text{Pe }\tau)$ is the absorbed intensity and $b_1 = 3/5$.

The independent parameters of the problem are the Péclet-number Pe, the time-dependent maximum value $\gamma(\tau)$ of the intensity with distribution $f(x)$, and the inverse of the Stefan number h_m:

$$\text{Pe} = \frac{w_0 v_0}{\kappa}, \quad \gamma = \frac{A_p I_0}{\lambda(T_m - T_a)/w_0}, \quad h_m = \frac{H_m}{c(T_m - T_a)}. \tag{2.14}$$

The system (2.11)–(2.13) is an example of ordinary differential equations with a discontinuous right hand side [78]. The solution can switch between the heating phase and the melting phase (Fig. 2.5a) and is used to check the performance of numerical codes solving the corresponding partial differential equations (PDE-system). During the heating phase the surface temperature $\theta_s < 1$ is below the melting point and the front does not move $\dot{A} = 0$. In the melting phase the surface temperature $\theta_s = 1$ is equal to the melting point and the front moves $\dot{A} > 0$. As shown in Fig. 2.5a the initial heating phase terminates at $\tau_1 = 2.9\,\text{ms}$ while the surface at $A(\tau_1) = 0$ reaches the melting point $\theta(\xi = 0, \tau_1) = 1$. The system switches to the melting phase and part of the material is ablated $\dot{A} > 0$. At $\tau_I = 18\,\text{ms}$ thermal isolation at the bottom is already present.

Time Scale Separation

Consider the melting phase, where the front position $A(\tau)$ and the thickness $Q(\tau)$ of the thermal boundary layer relax towards the the quasi-steady state $\{\text{Pe}Q(\tau), A(\tau) - \text{Pe }\tau\} = \{1, 1\}$ (Fig. 2.5b). Time scale separation depending on Péclet-number Pe changes the relaxation path of the ODE system (2.11)–(2.13) towards the quasi-steady state $\{\text{Pe}Q(\tau), A(\tau) - \text{Pe }\tau\} = \{1, 1\}$ of the melting phase. Relaxation of the fast variable towards the slow surface and
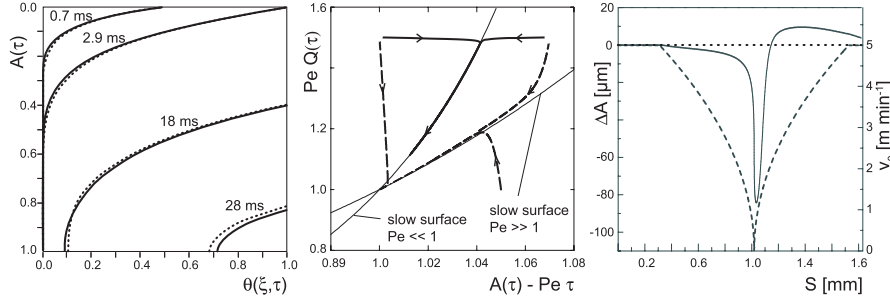
Fig. 2.5. a) The solution of the ODE-system (2.11)–(2.13) (dotted) is reproduced well by the numerical solution (solid) of the corresponding PDE-system. A spatially one-dimensional domain is heated and ablated by the action of the absorbed laser radiation with intensity $\gamma(\tau)$. b) Time scale separation depending on Péclet-number Pe changes the relaxation path. The solid lines correspond to the value $\text{Pe} = 1.5 \cdot 10^{-2}$; the dashed lines correspond to $\text{Pe} = 15$. c) To compensate for a dynamical variation of the cutting speed $v_0(\tau)$ (dashed) the intensity $\gamma(\tau)$ can be controlled. Quasi-steady control (solid) leads to strong deviation ΔA of the front position, while the deviation is suppressed using the inverse solution of the ODE-system for the control (dotted).

subsequent relaxation of both fast and slow variables towards the quasi-steady state is characteristic for the melting phase. The corresponding slow surfaces are indicated in Fig. (2.5b). The time scales $t_\kappa = \kappa/v_0^2$ and $t_{v_0} = w_0/v_0$ are characteristic for heat conduction and movement of the melting front position, respectively. The ratio $t_{v_0}/t_\kappa = \text{Pe}$ of these time scales provides the meaning of the Péclet-number Pe for the dynamical properties of the solution. Analysis using the theorem of Vasil'eva, Gradshtejn and Tichonov [79] yields the following results:

- For $\text{Pe} \gg 1$ first the energy content relaxes fast towards the quasi-steady value, which corresponds to the actual value of the distance $A_1 = A(\tau) - \text{Pe}\,\tau$ between the melting front and the laser beam axis. Further development of the system takes place along the slow surface

$$(1 + h_m)\dot{A} = \gamma f \;, \quad Q = \frac{(1 + h_m)}{\gamma f} \;, \quad \gamma f = \gamma f(A(\tau) - \text{Pe}\,\tau) \qquad (2.15)$$

in phase space.
- For $\text{Pe} \ll 1$ first the position $A(\tau)$ of the melting front relaxes fast to the quasi-steady value, which corresponds to the actual value of the energy content Q. Further development of the system takes place along the slow surface

$$\dot{Q} = b_1 \left(\frac{1}{Q} - \text{Pe} \right) \;, \quad \gamma f(A(\tau) - \text{Pe}\,\tau) = (1 + h_m - b_1)\text{Pe} + \frac{b_1}{Q}. \qquad (2.16)$$

in phase space.

The slow surfaces intersect at the stable quasi-steady point.

Let the initial value $Q(\tau = 0) > Q_{stat}$ for the energy content be larger than the quasi steady value $Q_{stat} = 1/\text{Pe}$. The distance $A(\tau) - \text{Pe}\ \tau$ of the front with respect to the laser beam axis then changes only slightly when $\text{Pe} \gg 1$. For small values $\text{Pe} \ll 1$ the front at first moves very rapidly out of the laser beam and further on approaches the quasi steady point together with its energy content, while moving slowly. For small values of the Péclet-number Pe, the position of the melting front responds more strongly to changes of the processing parameters than is the case for large values.

As a result of quantitative analysis of the ODE-system (2.11)–(2.13) the Péclet-number has to be compared with the scaled gradient $G := 1/f(\partial f/\partial \xi) = O(1)$ of the intensity distribution $f(\xi)$. For a Gaussian distribution this value is of the order of unity. Moreover, the fast and slow time scales can be given explicitly:

$$\text{Pe} \gg \frac{|G|}{b_1} : \quad t_{fast} = \frac{1 + h_m - b_1}{1 + h_m} \frac{\kappa}{b_1 v_0^2} , \quad t_{slow} = \frac{w_0}{|G| v_0} , \qquad (2.17)$$

$$\text{Pe} \ll \frac{|G|}{b_1} : \quad t_{fast} = \frac{1 + h_m - b_1}{1 + h_m} \frac{w_0}{|G| v_0} , \quad t_{slow} = \frac{\kappa}{b_1 v_0^2}. \qquad (2.18)$$

These characteristic times are comparable with experimentally observed times for the changes of the thermal emission of the melting front. Inserting typical values for the distance $A(\tau) - \text{Pe}\ \tau = 1$ between the front position and the laser beam axis gives the corresponding value for the gradient $|G| = 4$. The value $w_0 = 150\,\mu\text{m}$ for the laser beam radius, $v_0 = 5\,\text{cm}\,\text{s}^{-1}$ for the cutting speed and $\kappa = 6 \cdot 10^{-6}\,\text{m}^2\,\text{s}^{-1}$ for the thermal diffusivity gives the values $\text{Pe} = 1.25$, $b_1 \text{Pe}/|G| = 0.19 \ll 1$. As result, the characteristic times $t_{fast} = 0.4\,\text{ms}$ for relaxation of the melting front and $t_{slow} = 4.0\,\text{ms}$ for the relaxation of the penetration depth are found.

An Inverse Problem

A control problem relevant to contour cutting or during the start of a cut can be posed. Using the reduced equations of motion (2.11)–(2.13) allows the solution of the inverse problem for the control of the processing parameters. Let $R_L(\tau)$ be the position of the laser beam axis, which is accelerated $\ddot{R}_L(\tau) \neq 0$ with respect to the material. An inverse problem can be formulated as follows. Find the power $\gamma(\tau)$ as a function of time, for which the distance $A_1 = A(\tau) - R_L(\tau)$ between the position of the front $A(\tau)$ and the laser beam axis $R_L(\tau)$ remains constant. Let $c(\tau)$

$$c(\tau) = \frac{\gamma(\tau) f(A_1)}{1 + h_m} - \dot{R}_L(\tau) \qquad (2.19)$$

be the dynamical correction to the quasi steady control. Then the expression for the unknown power $\gamma(\tau)$ has the form

$$\gamma(\tau) = \frac{1 + h_m}{f(A_1)}(\dot{R}_L(\tau) + c(\tau)) \tag{2.20}$$

and the dynamical correction $c(\tau)$ is the solution of the initial value problem

$$\dot{c}(\tau) + b_1 c(\tau)\left[\dot{R}_L(\tau) + \frac{1 + h_m}{b_1}c(\tau)\right]^2 = \frac{b_1}{1 + h_m}\ddot{R}_L(\tau), \quad c(\tau = 0) = 0. \tag{2.21}$$

For uniform motion $\ddot{R}_L(\tau) = 0$, $\dot{R}_L(\tau) = \text{Pe} = const$, the correction $c(\tau) = 0$ is the unique solution and the power γ equals the quasi steady value $\gamma(\tau)f(A_1) = (1 + h_m)\,\text{Pe}$. Consider the deviation $\Delta A(\tau) = A_1 - [A(\tau) - R_L(\tau)]$ of the position of the front from its quasi steady value. The result for this deviation is shown in Fig. (2.5c) (solid line) as a function of the cut length S for the quasi steady control $\gamma(\tau) \propto \dot{R}_L(\tau)$. With values of the acceleration $\ddot{R}_L\kappa/w_0 = 0.5\,\text{g}$ of cutting machines attainable today, the deviations reach values which are of the order of the laser beam radius $w_0 = 100\,\mu\text{m}$.

Two-Dimensional One-Phase Model

The dynamics of the lateral extent of the cutting front (Fig. 2.4b, e) are described by equations of motion for the radius r_m of the melting front which may deviate from the beam radius w_0. To derive the equations for the radius $\alpha = r_m/w_0$, the boundary problem for a moving cylindrical source, frequently cited in the literature related to welding and cutting applications, is considered:

$$0 = \text{Pe}\frac{\partial\theta}{\partial\xi} + \frac{\partial^2\theta}{\partial\xi^2} + \frac{\partial^2\theta}{\partial\eta^2}\,, \qquad \rho^2 = \xi^2 + \eta^2 \geq \alpha^2 \tag{2.22}$$

$$\theta\mid_{\xi^2+\eta^2=\alpha^2} = 1\,, \quad \theta\mid_{\xi^2+\eta^2\to\infty} = 0 \tag{2.23}$$

where the lengths are scaled with the beam radius w_0. The solution can be given in explicit form and in plane polar coordinates $\{\rho, \varphi\}$ gives:

$$\theta(\rho, \varphi) = \exp[-\text{Pe}\,\rho\cos(\varphi)/2]\,S(\rho, \varphi), \qquad \rho > \alpha$$

$$S(\rho, \varphi) = \theta_0 K_0(\text{Pe}\,\rho/2) + 2\sum_{n=1}^{\infty}\theta_n K_n(\text{Pe}\,\rho/2)\cos(n\varphi), \tag{2.24}$$

$$\theta_n = \left[\frac{I_n(x)}{K_n(x)}\right]_{x=\text{Pe}\,\alpha/2}, \qquad n = 0, 1, 2, \ldots$$

Asymptotic analysis of the quasi-steady solution (2.24) with respect to the small parameter $\epsilon = 1/k$ gives an expression for temperature at the vertex

line $\{\rho, \varphi = 0\}$

$$\theta(\rho, \varphi = 0) \sim \frac{\exp[-2k\ (\rho/\alpha - 1)]}{\sqrt{2}\sqrt{\rho/\alpha - \beta_0}}, \quad \beta_0 = \frac{1}{2}, \quad k = \frac{\text{Pe}\,\alpha}{2} \to \infty. \qquad (2.25)$$

which indicates a lateral correction of square root type to the exponential dependence (2.28) which is well known from the spatial one-dimensional solution. The correction takes into account the additional heat flux necessary to reach the melting point on a boundary curve with radius α. Moreover, there is a shift β_0 with respect to the centre of the cylindrical axis with an asymptotic value of $\beta_0 = 1/2$. The asymptotic analysis suggests an approximate ansatz $\theta_{app}(\rho, \varphi, \tau)$ for the description of the time-dependent, two-dimensional melting front:

$$\theta_{app}(\rho, \varphi, \tau) = \left(\sqrt{\frac{\rho/\alpha - \beta}{1 - \beta}}\right)^{-1} \exp\left[-\frac{1 + \cos(\varphi)}{2} \frac{\rho/\alpha - 1}{Q/\alpha}\right] \qquad (2.26)$$

where the shift $\beta = \beta(Q/\alpha)$ depends on the ratio $Q/\alpha = \delta_M/r_m$ of the thickness δ_M of the thermal boundary layer and radius r_m of the cutting front at the vertex line $\varphi = 0$

$$\beta = \beta(x) = x \exp[x]\ E_1[x], \quad x = Q/\alpha, \quad Q = Q(\tau), \quad \alpha = \alpha(\tau); \qquad (2.27)$$

the parameters Q, α of the quasi-steady solution are identified as characteristic dynamical variables $Q(\tau)$ and $\alpha(\tau)$. The spatially one-dimensional solution is reproduced by the limiting case for large values of the radius α of the melting front:

$$\lim_{\alpha \to \infty} \theta_{app}(\nu + \alpha, \varphi = 0, \tau) = \lim_{\alpha \to \infty} \frac{\exp[-\frac{\nu}{Q}]}{\sqrt{1 + \frac{\nu/\alpha}{1 - \beta[Q/\alpha]}}} = \exp\left[-\frac{\nu}{Q}\right] \qquad (2.28)$$

where the abbreviation

$$\nu = \rho - \alpha\ , \quad \rho/\alpha = 1 + \nu/\alpha. \qquad (2.29)$$

for the distance ν from the boundary is introduced. Since the displacement β is non-negative $0 \le \beta \le 1/2$ and remains bounded, the temperature θ_{1D} is an upper bound $\theta_{app} \le \theta_{1D}$ for the temperature in advance of the curved melting front.

The ansatz (2.26) is used to derive the equations of motion for the two-dimensional one-phase model of the melting front by using a variational approach. To apply the variational approach as discussed in [33] means finding the so called thermal potential $\mathbf{h}$ by solving the equations

$$\theta = -\nabla \cdot \mathbf{h}\ , \quad \nabla \times \mathbf{h} = \mathbf{0} \qquad (2.30)$$

The expansion with respect to φ at the vertex line $\varphi = 0$ of the melting front

$$\theta(\rho, \varphi, \tau) = \theta_0(\rho, \tau) + \theta_2(\rho, \tau)\frac{\varphi^2}{2} + \cdots$$

$$h_\rho(\rho, \varphi, \tau) = h_{\rho 0}(\rho, \tau) + h_{\rho 2}(\rho, \tau)\frac{\varphi^2}{2} + \cdots \quad h_\varphi(\rho, \varphi, \tau) = h_{\varphi 1}(\rho, \tau)\varphi + \cdots$$

$$(2.31)$$

gives a system of equations with the radius ρ as an independent variable

$$0 = \frac{\partial}{\rho \partial \rho} h_{\varphi 1} - \frac{h_{\rho 2}}{\rho}$$

$$-\theta_0 = \frac{\partial}{\rho \partial \rho}(\rho h_{\rho 0}) + \frac{h_{\varphi 1}}{\rho}$$

$$-\theta_2 = \frac{\partial}{\rho \partial \rho}(\rho h_{\rho 2})$$

for the calculation of the Taylor coefficients in the expansion (2.31). Inserting the ansatz (2.26) into the formal solution

$$h_{\rho 0}(\rho, \tau) = \frac{1}{\rho} \int_\rho^\infty \theta_0(\rho', \tau)\rho' d\rho' + \frac{1}{\rho} \int_\rho^\infty h_{\varphi 1}(\rho', \tau)\, d\rho' \qquad (2.32)$$

$$h_{\varphi 1}(\rho, \tau) = -\frac{1}{\rho} \int_\rho^\infty h_{\rho 2}(\rho', \tau)\, d\rho' \ , \quad h_{\rho 2}(\rho, \tau) = \frac{1}{\rho} \int_\rho^\infty \theta_2(\rho', \tau)\, \rho' d\rho' \quad (2.33)$$

and direct integration yields an explicit expression for the thermal potential **h**. Applying the variational calculus discussed in [33] the final result for the equations of motion reads:

$$\dot{\alpha} = \frac{1}{1 + h_m}\left[\left(\gamma f_2 - \frac{b_2}{Q}\right) + \frac{1 + h_m + b_2}{1 + h_m - b_1}\left(\gamma f_0 - \frac{b_1}{Q}\right)\right] , \qquad (2.34)$$

$$\dot{A} = \frac{1}{1 + h_m - b_1}\left(\gamma f_0 - \frac{b_1}{Q}\right) , \quad \dot{Q} = b_1\left(\frac{1}{Q} - \dot{A}\right) . \qquad (2.35)$$

where $b_1 = 3/5$ and $b_2 = 1/10$. As a result, the dynamics of the spatially one-dimensional dynamical variables $\{A, Q\}$ is decoupled from the motion of the additional two-dimensional variable α. It is worth discussing the limiting case of large values of the Péclet-number. Owing to time scale separation as shown in Fig. 2.5b, the dynamical variables move on the slow surface: $(1 + h_m)\dot{A} = \gamma f$, $Q = (1 + h_m)/\gamma f$. Additionally, inserting a Gaussian intensity distribution $f(\mathbf{x}) = \exp(-2\mathbf{x}^2)$ in the intensity γf the Taylor coefficients f_0, f_2 are

$$f = f_0 + f_2 \frac{\varphi^2}{2}, \quad f_0 = \exp(-2\bar{A}^2), \quad f_2 = -4\alpha(\alpha - \bar{A})f_0. \qquad (2.36)$$

The distance $\bar{A} = A - R_L$ between the position of the front $\xi = A(\tau)$ and the moving laser beam axis $\xi = R_L(\tau)$ has been introduced. Finally, in the limiting case $\text{Pe} \to \infty$ the lateral equations of motion

$$\dot{\alpha} = \frac{\gamma f_0}{1 + h_m}[-4\alpha(\alpha - \bar{A}) + 1], \quad \bar{A} = A - R_L \qquad (2.37)$$

$$(1 + h_m)\dot{A} = \gamma f_0, \quad Q = \frac{1}{\bar{A}}, \qquad (2.38)$$

are solved explicitly. The stable ($\alpha \geq 0$) quasi-steady ($\dot{A} = \text{Pe}, \dot{\alpha} = 0$) solution reads

$$\alpha = \frac{1}{2}\bar{A} + \frac{1}{2}\sqrt{\bar{A}^2 + 1} \;, \quad \gamma f_0(\bar{A}) = (1 + h_m)\text{Pe} \;, \quad Q = \frac{1}{\text{Pe}}. \qquad (2.39)$$

For the quasi steady state the radius $\alpha > \bar{A}$ is larger than the distance $\bar{A}$ between the melting front and the laser beam axis. Since the lines of constant value for the intensity are circles, the radius of curvature of the isophote at the vertex line equals the distance $\bar{A}$. Comparison with numerical results shows that the radius α of curvature at the vertex line is already closely connected to the width of the cutting kerf.

The laser beam axis and the feeding direction span the xz-plane ($y = 0$ or $\eta = 0$). The intersection of the xz-plane and the cutting front gives a curve referred to as the ceiling line, or centre line of the cutting front. The dynamics of $\alpha(\tau)$ is closely related to the formation of ripples at the cut edge, if the radius of curvature $\alpha(\tau)$ at the ceiling line $\phi = 0$ is accepted as an approximation to the shape of the cutting front. The boundary $\partial\Gamma_m(t)$ is defined by the spatial coexistence of the boundary conditions (2.34, 2.35) for the melting phase, where the melting front moves $v_p > 0$, and the heating phase, where the cut edge evolves ($v_p = 0$). For the dynamical system, the non-dimensional velocity v_p of the boundary is $v_p = (\dot{A} - \dot{\alpha})\cos(\phi) + \dot{\alpha}$ which determines the azimuth angle $\phi = \bar{\phi}(\tau)$ where the boundary conditions are changing, namely $v_p(\bar{\phi}) = 0$,

$$\cos(\bar{\phi}) = \frac{-\dot{\alpha}}{\dot{A} - \dot{\alpha}}. \qquad (2.40)$$

The stationary solution ($\dot{A} = \text{Pe}, \dot{\alpha} = 0$) shows that $\bar{\phi}_{stat} = \pm\pi/2$ and any deviation from the stationary state leads to a dynamical response of the arc length $\alpha(\tau)2\bar{\phi}(\tau)$ of the melting front. In particular, the arc length can change faster than the cutting speed resulting in U-shaped ripples evolving at the cut surface.

Three-Dimensional One-Phase Model

The Free Boundary Problem for a single phase describing the axial motion of the melting front (Fig. 2.4) in the non-dimensional variables $\xi = x/w_0$,

$\zeta = z/d$ reads

$$\frac{\partial \theta}{\partial \tau} = \frac{\partial^2 \theta}{\partial \xi^2} + \left(\frac{w_0}{d}\right)^2 \frac{\partial^2 \theta}{\partial \zeta'^2},$$

$$\theta|_{\xi = a(\zeta')} = 1,$$

$$\gamma(\tau)\mu A(\mu)f(a(\zeta) - \mathrm{Pe}\tau) + \left[\frac{\partial \theta}{\partial \xi} - \left(\frac{w_0}{d}\right)^2 \frac{\partial \theta}{\partial \zeta'}\frac{\partial a}{\partial \zeta'}\right] = -h_m\frac{\partial a}{\partial \tau},$$

$$\left.\frac{\partial \theta}{\partial \zeta'}\right|_{\substack{\zeta' = 0 \\ \xi \geq a(0)}} = -\left(\frac{d}{w_0}\right)^2 \gamma A(1)f(\xi).$$

The asymptotic analysis $(w_0 \ll d)$ of this problem shows that outside the boundary layers at the top δ_H and bottom δ_I of the metal sheet the terms containing $(w_0/d)^2 \ll 1$ can be neglected. Therefore the axial dynamics of the melting front are determined predominantly by spatially one-dimensional heat conduction in the feed-direction [32, 33]. Within the upper boundary layer of thickness δ_H the temperature field is determined by preheating of the laser beam (Fig. 2.4e).

An approximate solution for $(w_0/d)^2 \ll 1$ can be derived by solving the preheating problem separately, which gives the initial value for the position $\xi = A(\zeta, \tau)$ of the axially distributed melting front. The interaction of the boundary layers δ_H and δ_M can be calculated by matching the thermal boundary layers.

Thermal Boundary Layers

There are three different thermal boundary layers involved in cutting (Fig. 2.4e). Ahead of the laser beam, heating (Neumann type) of the material surface takes place resulting in a thermal boundary layer of thickness $\delta_H = \mathrm{Pe}^{-1/2}$. The position where the surface temperature reaches the melting point is called the leading edge of the cutting front. The cut evolves at the leading edge. The cutting front is moving and so there is a second thermal boundary layer (Dirichlet type) with thickness $\delta_M = \mathrm{Pe}^{-1}$. At the lower surface $\zeta = \Delta$ the heat transition to ambient conditions is fairly small compared to the flux inside the metal; this state of near thermal isolation is the reason for the third thermal boundary layer whose thickness is δ_I. It is worth mentioning that the cutting model includes different types of boundary conditions at the top surface (Neumann type) and the melting front (Dirichlet type). Moreover, at the leading edge $\{\xi, \zeta\} = \{A(\zeta = 0), 0\}$ the different boundary conditions coexist spatially and interact. At the lower edge $\zeta = \Delta$ of the cutting front there are also two coexisting Neumann conditions with very different boundary values, namely the heat flux, which moves the melting front, coexists with the relatively small-valued thermal radiation condition; the latter may even be best represented by thermal isolation giving a homogeneous Neumann
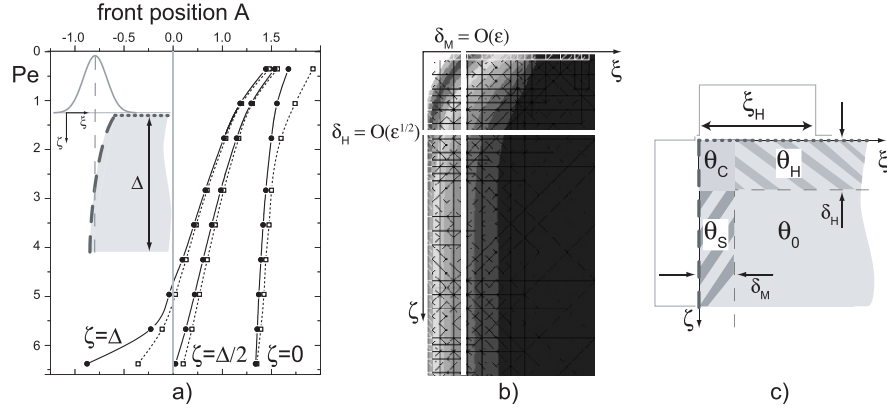
Fig. 2.6. Interaction of different thermal boundary layers with thickness δ_M, δ_H at the leading edge $\{\xi, \zeta\} = \{A(\zeta), 0\}$ and the lower edge $\zeta = \Delta$ of the cutting front depending on position $\zeta \in \{0, \Delta\}$ and Péclet-number Pe. a) The front position $\xi = A(\zeta)$ calculated without (dotted, reduced model) and with (solid, numerical model) interaction of the boundary layers. b) The numerical solution for the temperature (gray scale) reproduces the different scales $\delta_M = O(\epsilon)$ and $\delta_H = O(\epsilon^{1/2})$ which are derived from singular perturbation analysis for moderate values of the Péclet-number (Pe = 1). c) Singular perturbation analysis gives the temperature as the sum of three contributions $\theta_H, \theta_M, \theta_C$ related to pre-heating at the surface $\zeta = 0$, the heat flux at the melting front $\xi = A(\zeta)$ and a correction taking into account the interaction of the thermal boundary layers δ_H and δ_M.

condition. In consequence a third boundary layer δ_I exists. The different thickness $\delta_H, \delta_M, \delta_I$ of the thermal boundary layers tend to support three-dimensional effects for the heat transport. In contrast to heat transport with fixed boundaries, the solution of free boundary problems is sensitive to the effects of coexisting boundary conditions. In this case, the position $A(\zeta = 0)$ of the leading edge is an initial value for the quasi-steady shape of the melting front $A(\zeta)$, and its shape at the lower surface $\zeta = \Delta$ influences stability of the cut as well as wetting and separation of the melt flow.

The effects of three-dimensional heat transport at the leading edge $\{\xi, \zeta\} = \{A(\zeta = 0), 0\}$ and the lower edge $\zeta = \Delta$ of the cutting front depend on position $\zeta \in \{0, \Delta\}$ and on the Péclet-number Pe (Fig. 2.6a). In general, thermal boundary layers are singular perturbations of the heat conduction equation and are therefore hard to analyse by numerical methods. To find the structure of the solution near the leading edge, to be able to evaluate the accuracy of numerical results and to identify an ansatz for the reduced model, the asymptotic solution has to be analysed. Introducing the spatial scales $x = w_0 \xi$, $z = w_0 \zeta$ and the smallness parameter ϵ

$$\epsilon = \frac{1}{\text{Pe}}, \qquad \text{Pe} = \frac{w_0 v_0}{\kappa} \tag{2.41}$$

the quasi-steady model problem (Fig. 2.6c) can be restated as follows. Find the solution of the heat conduction equation

$$\frac{\partial \theta}{\partial \xi} + \epsilon \frac{\partial^2 \theta}{\partial \xi^2} + \epsilon \frac{\partial^2 \theta}{\partial \eta^2} = 0 \tag{2.42}$$

subject to the boundary conditions (Fig. 2.6c)

$$\frac{\partial \theta}{\partial \eta}\Big|_{\eta=0} = \begin{cases} -Q_H & \text{if } 0 < \xi < \xi_H, \quad Q_H > 0 \\ 0 & \text{otherwise} \end{cases} \tag{2.43}$$

$$\frac{\partial \theta}{\partial \xi}\Big|_{\xi=0} = -Q_M, \quad Q_M > 0 \tag{2.44}$$

$$\frac{\partial \theta}{\partial \eta}\Big|_{\eta=\Delta} = 0 \tag{2.45}$$

$$\theta(\xi, \eta)\Big|_{\xi \to \infty} = \theta_0. \tag{2.46}$$

In the singular limiting case $\epsilon \to 0$ the appropriate new scales δ_M and δ_H given by the thickness of the corresponding boundary layers

$$\hat{\xi} = \xi/\delta_M, \qquad \hat{\eta} = \eta/\delta_H, \qquad \delta_M = \epsilon, \qquad \delta_H = \sqrt{\epsilon} \tag{2.47}$$

are found. The solution emerges as the superposition

$$\theta(\xi, \eta) = \theta_0 + \theta_M \left(\hat{\xi} = \frac{\xi}{\delta_M} \right) + \theta_H \left(\xi, \hat{\eta} = \frac{\eta}{\delta_H} \right) + \theta_C \left(\hat{\xi}, \hat{\eta} \right) + O(\epsilon) \tag{2.48}$$

of the outer solution θ_0, which is determined by the boundary condition (2.46) and three contributions $\theta_M, \theta_H, \theta_C$ related to pre-heating at the surface $\zeta = 0$, the heat flux at the moving melting front $\xi = A(\zeta)$ and a correction θ_C which describes the interaction of the thermal boundary layers δ_H and δ_M near the leading edge $\{\xi, \zeta\} = \{A(\zeta = 0), 0\}$. As a result, the explicit solution reads:

$$\theta_M \left(\hat{\xi} \right) = \epsilon Q_M \exp(-\hat{\xi}) \tag{2.49}$$

$$\theta_H (\xi, \hat{\eta}) = \epsilon^{1/2} \, Q_H \left[\frac{2\sqrt{\xi_H - \xi}}{\sqrt{\pi} \exp\left(\frac{\hat{\eta}^2}{4\sqrt{\xi_H - \xi}} \right)} - \hat{\eta} \, \text{erfc}\left(\frac{\hat{\eta}^2}{2\sqrt{\xi_H - \xi}} \right) \right] \tag{2.50}$$

$$\theta_K \left(\hat{\xi}, \hat{\eta} \right) = -\epsilon^{3/2} \, \pi^{-1/2} \, Q_H \exp\left(-\frac{\hat{\eta}^2}{4} \right) \exp(-\hat{\xi}). \tag{2.51}$$

The numerical solution for the temperature (Fig. 2.6b, gray scale) reproduces the different scales $\delta_M = O(\epsilon)$ and $\delta_H = O(\epsilon^{1/2})$ which are derived from singular perturbation analysis. It is worth mentioning that the asymptotic values remain significant and give a suitable approximation even for moderate values of the Péclet-number (Pe = 1). As result of the singular perturbation
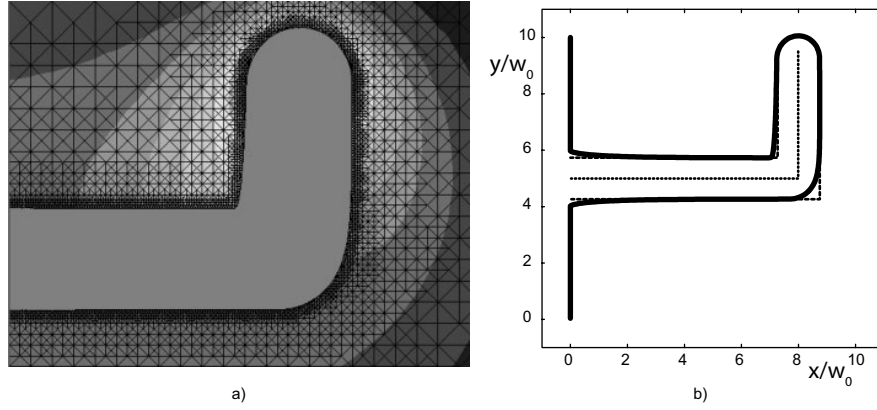
Fig. 2.7. a) Numerical calculation of temperature, motion of the cutting front and development of the cut surface. Detail at the corner of the cut. The intensity is considered to be constant and no ripple formation occurs. b) At the start of the cut and near the corner, the temperature and thermal boundary layers and also the cut shape (solid) deviate from the ideal shape (dotted). The trace of the laser beam axis is indicated as a dashed line.

analysis, numerical values for the spatial resolution in numerical calculations can be given, which are needed to resolve the thermal boundary layers.

The effects of the thermal boundary layer in the lateral direction are pronounced in the case of contour cutting. The lateral shape of the evolving cut kerf is relevant to the cut quality in connection with the evenness of the cut surface, and for melt flow which changes with the formation of the gas flow pattern. Numerical simulation (Fig. 2.7) of the Free Boundary Problem is carried out using a modified Level-Set method [34, 35] for the motion of the melting front and adaptive methods on hierarchically ordered and sparse grids [37] for accurate approximation of the temperature distribution within the boundary layers. Deviations from the ideal shape of the cut kerf are limited by the extent of the thermal boundary layers. The results indicate that at the start of the cut and near the corner, deviations of the boundary layer thickness from the ideal values are present, which can be calculated in detail by taking into account the local curvature.

2.2.2 The Two-Phase Problem

Approximate solutions of the variational equation describing long-time behaviour are found. The corresponding finite dimensional dynamical system describes the movement of time-dependent characteristic parameters, such as the front position A, front radius α, surface temperature θ_s and energy content Q. The extent of the model for the melt flow – one example of a sequel-process – can be treated in a similar way, by describing the dynamics of integrated

quantities like the melt film thickness h and mass flow m. The mass flow m is the melt velocity integrated with respect to the melt film thickness. The onset of evaporation at the irradiated metal surface is a further example of a sequel-process. Quality degradation such as scorings in oxygen cutting, unevenness in contoured fusion cutting and ripple formation from resolidifying melt are a direct consequence of melt flow.

The suitable dynamical variables are the melt film thickness $h(\tau)$, the mass flow $m(\tau)$ and the temperature $\theta_s(\tau)$ at the melt film surface. These variables are time-dependent parameters of the spatial distributions of the velocity and the temperature in the melt. The dynamics on shorter time scales governing relaxation to the equilibrium distributions can be described by spectral methods. Using the integral representation of the balance equations for mass, momentum, and energy the equations of motion for the dynamical variables $h(\tau)$, $m(\tau)$, $\theta_s(\tau)$ read

$$\mathrm{Re}\left(\frac{\partial m}{\partial \tau_l} + \frac{6}{5}\frac{\partial}{\partial \zeta}\left[\frac{m^2}{h}\right]\right) = -\frac{\partial \Pi_g}{\partial \zeta}h + 3\left(\frac{\Sigma_g}{2} - \frac{m}{h^2}\right), \quad \text{momentum} \qquad (2.52)$$

$$\frac{\partial h}{\partial \tau_l} + \frac{\partial m}{\partial \zeta} = v_P, \qquad\qquad\qquad\qquad\qquad \text{mass} \qquad (2.53)$$

$$\frac{1}{2}\frac{\partial}{\partial \tau_l}[\theta_s h g_1] + \frac{5}{8}\frac{\partial}{\partial \zeta}[\theta_s m g_2] = \frac{1}{Pe_l}\left[q_a - \frac{\theta_s}{h}g_3\right] \qquad \text{energy} \qquad (2.54)$$

$$m\big|_{\zeta=0} = h\big|_{\zeta=0} = \theta_s\big|_{\zeta=0} = 0. \qquad\qquad \text{initial values} \qquad (2.55)$$

The dynamical system (2.52)–(2.55) for the melt flow is coupled to the gaseous and the solid phases by the pressure gradient $\partial \Pi_g/\partial \zeta$ as well as by the shear stress Σ_g exerted by the gas flow and by friction at the melting front, respectively. The cutting problem is extended by the dynamical system for the motion of the melting front (2.34)–(2.35). Inserting the time dependent characteristic parameters into the ansatz for the spatial distribution allows the reconstruction of the three-dimensional representation of the movement in phase space. Two examples, namely the formation of ripples and adherent dross, will be used to demonstrate that the analysis in phase space – spanned by integral quantities – is more transparent than the interpretation of spatially three dimensional results from direct numerical integration.

The formation of ripples is a characteristic dynamical feature of the cutting process. Taking the melt flow into account (2.52)–(2.55) an additional property of the cutting process – the formation of ripples of the second kind – becomes part of the solution [4]. Ripples of the first kind, namely U-shaped ripples evolving at the cut surface (Fig. 2.8a), are reproduced by the dynamical system as a result of the moving melting front (2.40). In the upper part of the sheet the influence of the melt flow on the movement of the melting front is negligible, since the heat contained in the melt film, its thickness and the mass flow of molten material, remains fairly small. Heat transport by
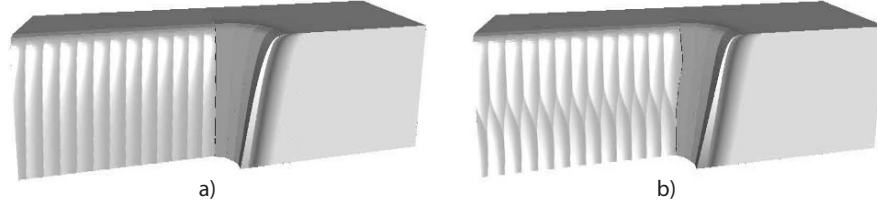
Fig. 2.8. Ripples of the first kind a) and second kind b) are reproduced by the dynamical system.
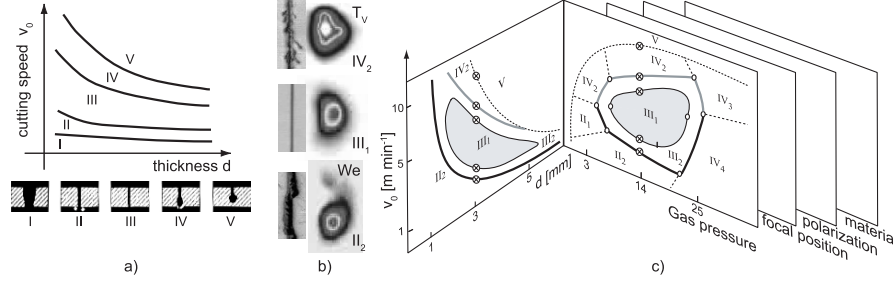
Fig. 2.9. Processing domains related to cut quality. Quality classes introduced by Arata [39] for oxygen cutting (a) are applicable to fusion cutting (b, c). There are at least two different kinds of dross observable, which are related to droplet formation by capillary forces (We, solid black) or by the onset of evaporation (T_V, solid gray). The maximum cutting speeds (dotted) are limited by material thickness and laser power.

convection in the melt film is involved when ripples of the second kind are formed (Fig. 2.8b). Any ripple of the first kind causes a melt wave propagating in the axial direction. The subsequent heat transport – convection in the axial direction – leads to an additional and delayed motion of the melting front by a heat wave (2.74) moving the melting front. As a result, the ripple frequency is doubled. Ripples of the third kind are a consequence of resolidified melt at the cut surfaces. Introduction of quality classes by Arata [39] is applicable to fusion cutting (Fig. 2.9a), class II, III, IV. The quality classes are related to the dynamical processing domains and can be identified with the underlying physical mechanisms. Three main processing domains in fusion cutting (Fig. 2.9b) are characterised by different morphologies of the adherent dross and become observable by online measurement of the thermal emission with a CCD-camera [4]. The ratio of the stagnation pressure ρu_m^2 of the melt flow at the bottom of the sheet metal and the counteracting capillary pressure σ/d_m is called the Weber number We

$$\mathrm{We} = \frac{\rho u_m^2}{\sigma/d_m} \tag{2.56}$$

where ρ, u_m, σ and d_m are the liquid density, velocity of melt, surface tension and thickness of the melt film, respectively. If the capillary forces become
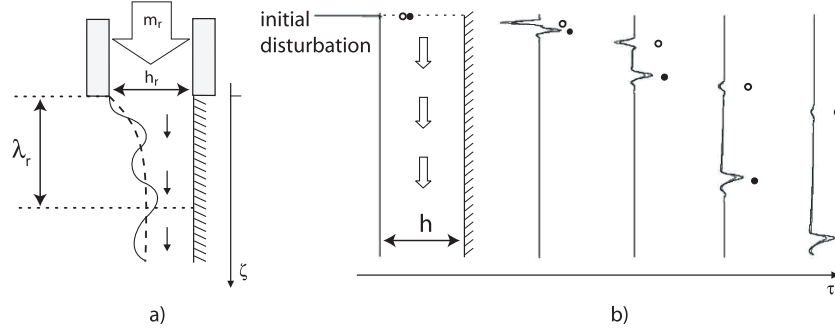
Fig. 2.10. (a) Water tap model. (b) Solution for the propagation of an initial perturbation from the linear stability analysis (dots) compared with the numerical solution (solid). The hollow λ_- and solid circles λ_+ give the time dependent position of the travelling melt wave from linear stability analysis.

comparable with the inertia of the melt We ≈ 1 then separation of the melt flow becomes unstable. The tendency to the formation of dross is estimated from the solution (Fig. 2.9c solid black curve, We) and occurs for low cutting speeds. The dross shows a circular shape and adheres on one side of the cutting kerf. The thermal emission recorded with the camera images shows low signal levels, strongly fluctuating and asymmetric with respect to the feeding direction. The interpretation for low values of the Weber number is that the CCD-image shows an asymmetric position of the single melt thread (Fig. 2.9b, We) and there is dross at one side of the kerf, called dross of kind 1. For increased cutting speeds the melt film starts to evaporate depending on cutting speed v_0 and thickness d of the sheet metal as the model predicts (Fig. 2.9c solid gray curve, T_V). With the onset of the evaporation pressure the CCD-image shows a symmetric splitting of the melt thread and dross at both sides of the kerf, referred to as dross of kind 2. Finally the maximum cutting speed achievable (Fig. 2.9c dotted curve) is given by energy balance. The correlation between the processing domains II (We) and IV (T_V), and the characteristics of the CCD-images and the formation of the different kinds of dross is striking. The equations of motion (2.52), (2.53) for mass flow $m = m(\zeta, \tau)$ and melt film thickness $h = h(\zeta, \tau)$ are analysed with respect to stability of the travelling melt waves (Fig. 2.10). A model problem – we call it the water tap model – is considered; it describes the outflow from an orifice with diameter h_r and mass flow m_r down a rigid wall in the ζ-direction, $\zeta \in [0, \infty)$. The flow is accelerated by a shear stress Σ at the free liquid surface and a no-slip condition is imposed at the rigid wall. The equations of motion for the water tap read:

$$\text{Re} \left(\frac{\partial m}{\partial \tau} + \frac{6}{5} \frac{\partial}{\partial \zeta} \left[\frac{m^2}{h} \right] \right) = \frac{3}{2} \Sigma - 3 \frac{m}{h^2} \tag{2.57}$$

$$\frac{\partial h}{\partial \tau} + \frac{\partial m}{\partial \zeta} = 0 \tag{2.58}$$

$$h(\zeta, \tau)\Big|_{\zeta=0} = h_r, \qquad m(\zeta, \tau)\Big|_{\zeta=0} = m_r(\tau) \tag{2.59}$$

$$h(\zeta, \tau)\Big|_{\tau=0} = h_r, \qquad m(\zeta, \tau)\Big|_{\tau=0} = m_r(\tau)\Big|_{\tau=0} \tag{2.60}$$

In the long time limit the thickness $h(\zeta, \tau)$ of the liquid undergoes relaxation towards the value h_∞ on the relaxation length λ_r. Linear stability analysis shows that there are two solutions with different velocities of propagation $\lambda^{(\pm)}$ which are related to fanned and damped disturbances of the liquid waves. Equations (2.57), (2.58)

$$u(\zeta, \tau) = \begin{pmatrix} m(\zeta, \tau) \\ h(\zeta, \tau) \end{pmatrix} = u_0(\zeta) + u_1(\zeta, \tau) \tag{2.61}$$

are linearised with respect to the deviation u_1 from the quasi-steady solution u_0

$$\frac{\partial u_1}{\partial \tau} + A(u_0)\,\frac{\partial u_1}{\partial \zeta} = B(u_0)\,u_1. \tag{2.62}$$

The eigenvalues $\lambda^{(\pm)}$ and eigenvectors $v_{(\pm)}$ of the matrix $A(u_0)$ are given by

$$\lambda^{(\pm)} = \frac{1}{5}\frac{m_0}{h_0}\left(6 \pm \sqrt{6}\right) > 0, \qquad v_{(\pm)} = \begin{pmatrix} \lambda^{(\pm)} \\ 1 \end{pmatrix}, \tag{2.63}$$

the velocities and the direction of propagation for the perturbation u_1, respectively. The dispersion relation for harmonic perturbations with respect to a constant melt film thickness with frequency ω and complex valued wave-number $k \in \mathbb{C}$ is

$$k^2 - \frac{k}{\lambda^{(+)}}\left[\omega\left(1 + \frac{1}{c}\right) - i\left(\tilde{b}_1 - \frac{\tilde{b}_2}{c}\right)\right] = -\frac{1}{\lambda^{(+)}}\left[\frac{\omega^2}{\lambda^{(-)}} - i\frac{\omega}{\lambda^{(-)}}(\tilde{b}_1 - \tilde{b}_2)\right], \tag{2.64}$$

$$c = \frac{6 - \sqrt{6}}{6 + \sqrt{6}}, \qquad \tilde{b}_{1,2} = \frac{1}{\mathrm{Re}}\frac{3}{5}\frac{m_0}{h_0^3}\left(4 \mp \sqrt{6}\right).$$

The solution shows growing $\mathrm{Im}(k_1) > 0$ and damped $\mathrm{Im}(k_2) < 0$ contributions. With increasing Reynolds number Re the absolute value $|k|$ of the solutions decays and the length scale for amplitude growth as well as for damping increases. As a result, the modulation frequency of the laser power producing one single wave crest of melt moving down the cutting front can be estimated by the ratio of velocity of propagation for the growing wave amplitude and the sheet thickness. This kind of power modulation is used to avoid the formation of adherent dross in contour cutting.
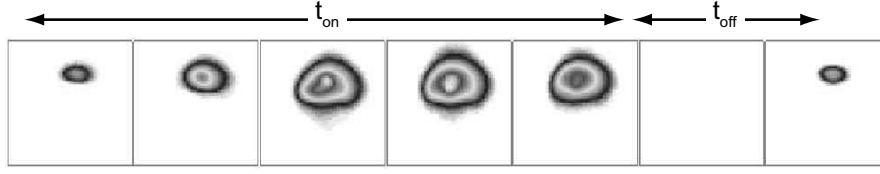
Fig. 2.11. The cutting process can evolve periodically using modulated laser power. The recorded CCD-images in this case show the typical properties of high quality cuts of class III known from CW operation. (cutting speed $1.2\,\mathrm{m/min}$, thickness $3\,\mathrm{mm}$, N_2 14 bar, nozzle diameter $1.4\,\mathrm{mm}$, maximum CO2 laser power $2.6\,\mathrm{kW}$/pulsed, duty cycle 70%, pulse frequency $450\,\mathrm{Hz}$, beam radius $150\,\mu\mathrm{m}$, Rayleigh length $2.2\,\mathrm{mm}$, focal position $-2.4\,\mathrm{mm}$, stainless steel (1.4301), CCD camera frame rate $2.9\,\mathrm{kHz}$).

The capillary forces become dominant for low cutting speeds and for cw operation. The melt flow does not separate completely from the sheet metal. Low cutting speeds are encountered in contour cutting and therefore a reliable control strategy is of interest. For this task it is crucial to differentiate between the cutting speed v_0 and the velocity $v_p(t)$ of the cutting front. From the results about the capillary forces (Fig. 2.9) the formation of adherent dross is related to small values of the Weber number $\mathrm{We} \propto u_m^2 d_m$, which has to be kept at values larger than unity. Modulation of the laser power results in a correspondingly modulated velocity $v_p(t)$ of the melting front and hence the time dependent mass flow $u_m d_m = v_p(t)d \gg v_0 d$ can be significantly larger than its value $v_0 d$ averaged with respect to the time of the modulation period. The modulation parameters, namely pulse duration and the duty cycle, can be chosen such that only one wave of ejected melt is produced during each laser pulse. The laser pulse duration t_{on} has to be matched to the typical time d/u_m for the propagation of a melt wave propagating down the melting front with sheet thickness d. Additionally, the cycle time $T = t_{on} + t_{off}$ has to meet the time averaged energy balance, such that the cut length $\int v_p(t')dt' = v_0 T$ matches the movement of the laser beam axis with velocity v_0. Using these constraints, the parameters for the pulse mode operation, namely pulse duration and duty cycle, are determined. Figure 2.11 gives an example for a cut at a low cutting speed $v_0 = 1.2\mathrm{m/min}$ performed with modulated laser power which remains dross-free. The CCD-images show that the melt thread remains at the centre of the cutting front as for cw-cutting and parameters corresponding to quality class III in Fig. 2.9.

Heat Transport in Thin Film Flow

Taking into account the liquid flow in cutting requires extending the one-phase problem by introducing the heat transport through the melt film. To investigate the dominant effects of heat transport in thin film flow the heat transport through a liquid layer with an established Couette-flow profile is a

suitable model problem. The convective heat transport in thin film flow and the accuracy of equations for the boundary layer dynamics reduced by spatial integration, are two fundamental aspects which can be discussed in detail. The corrections to the spatially integrated equations of motion are found by applying a spectral method, which can be applied in a similar way to more detailed formulations of the problem. Consider a viscous, incompressible fluid flowing on an infinitely extended horizontal plane under the influence of a constant shear force, created by a homogeneous gas flow along the surface. We assume that the gas pressure along the surface is constant. The momentum balance of the Navier-Stokes equations

$$\text{Re}(u_t + uu_z + vu_x) = -p_z + u_{zz} + u_{xx}, \tag{2.65}$$

$$\text{Re}(v_t + uv_z + vv_x) = -p_x + v_{zz} + v_{xx} \tag{2.66}$$

with no-slip boundary conditions at the rigid wall $x = 0$ and continuity boundary condition at the free surface $x = h(z, t)$

$$u = v = 0, \quad x = 0, \qquad h_t + uh_z = v, \quad x = h(z, t) \tag{2.67}$$

has Couette flow as the well known stationary solution [80, 81]:

$$v(x, z) = 0, \qquad u(x, z) = x, \qquad h(z) = 1. \tag{2.68}$$

The heat conduction in the melt film [82] is described by the partial differential equation

$$\frac{\partial \theta}{\partial t} + \text{Pe}\, u \frac{\partial \theta}{\partial z} + \text{Pe}\, v \frac{\partial \theta}{\partial x} = \frac{\partial^2 \theta}{\partial x^2} \tag{2.69}$$

with boundary conditions

$$\theta|_{x=0} = 0, \qquad \left.\frac{\partial \theta}{\partial x}\right|_{x=h} = \gamma(t) f(z). \tag{2.70}$$

Here Re, Pe denote the Reynolds and Péclet-number respectively. We consider the instantaneous solution $\theta_0(x, z, t) = \gamma(t) f(z) x$ of (2.69). The function θ_0 satisfies (2.69) for Pe = 0 in the stationary case and the boundary conditions (2.70). Looking for a solution of the form $\theta(x, z, t) = \theta_0(x, z, t) + \theta_1(x, z, t)$, the function θ_1 satisfies the inhomogeneous equation with homogeneous boundary conditions:

$$\frac{\partial \theta_1}{\partial t} + \text{Pe}\, u \frac{\partial \theta_1}{\partial z} - \frac{\partial^2 \theta_1}{\partial x^2} = -\frac{\partial \theta_0}{\partial t} - \text{Pe}\, u \frac{\partial \theta_0}{\partial z} \tag{2.71}$$

$$\theta_1|_{x=0} = 0, \qquad \left.\frac{\partial \theta_1}{\partial x}\right|_{x=h} = 0 \tag{2.72}$$

We look for a spectral decomposition $\theta_1(x, z, t) = \sum a_k(z, t) w_k(x)$ of θ_1, where $k \in \{0, 1, \ldots, \infty\}$ and $w_k(x)$ are the eigenfunctions of the eigenvalue problem

$$w_k''(x) = -\lambda_k u(x) w_k(x), \qquad w_k(0) = 0, \qquad w_k'(h) = 0, \tag{2.73}$$

including the convective transport proportional to the flow velocity $u(x)$. Normalising, and introducing the quantity e_k so that

$$\int_0^h w_j(x) w_k(x) u(x) dx = \delta_{jk}, \qquad e_k = \sqrt{3} \mathrm{Ai}'(-h\lambda_k^{1/3}) - \mathrm{Bi}'(-h\lambda_k^{1/3}),$$

the eigenvalues $\lambda_k(h)$ are determined by the transcendental equation $e_k = 0$ having an infinite number of solutions. The two lowest solutions $k = 0, 1$ of this equation for $h = 1$ are $\lambda_0 = 3.47662\ldots$ and $\lambda_1 = 44.1385\ldots$ and are separated by an order of magnitude. The corresponding eigenfunctions have the form

$$w_k(x; h) = N_k(h)^{-1/2} \left[\sqrt{3} \mathrm{Ai}(-\lambda_k(h)^{1/3}x) - \mathrm{Bi}(-\lambda_k(h)^{1/3}x) \right],$$

where $N_k(h)$ represents the normalisation constant. As a result, the equations of motion for the spectral components $a_k(z, t)$

$$c_k \frac{\partial a_k(z, t)}{\partial t} + \mathrm{Pe} \frac{\partial a_k(z, t)}{\partial z} + \lambda_k a_k(z, t) = q_k(z, t; \mathrm{Pe})$$

$$c_k = \int_0^h w_k^2(x; h) dx = N_k(h)^{-1} \left\{ h e_k^2 - \left(\frac{43}{\lambda_k(h)} \right)^{1/3} \frac{1}{\Gamma(1/3)^2} \right\} \tag{2.74}$$

$$q_k(z, t, \mathrm{Pe}) = -\gamma'(t) f(z) \int_0^h x w_k(x; h) dx - \mathrm{Pe}\, \gamma(t) f'(z) \int_0^h x u(x) w_k(x; h) dx$$

have the form of a wave equation and the wave velocity c_k of the k-th mode depends on the thickness h of the melt film. Temporal $\gamma'(t)$ and spatial $\mathrm{Pe} f'(z)$ changes of the absorbed intensity together with the flow velocity Pe enter the source term $q_k(z, t, \mathrm{Pe})$ for the spectral components of the heat wave. The quasi-steady solution $\gamma'(t) = 0$ of (2.74) can be integrated directly thus giving

$$a_k(z) = \gamma \left[\frac{\sqrt{2\pi}\lambda_k}{4\mathrm{Pe}} \exp\left\{ \frac{\lambda_k^2 - 8z\lambda_k \mathrm{Pe}}{8\mathrm{Pe}^2} \right\} \left(1 + \mathrm{erf}\left(\frac{4\mathrm{Pe}\, z - \lambda_k}{2\sqrt{2}\mathrm{Pe}} \right) \right) - e^{-2z^2} \right] \tag{2.75}$$

$$\times \int_0^h x u(x) w_k(x; h) dx. \tag{2.76}$$

To evaluate the accuracy of the equations of motion for boundary layer dynamics reduced by spatial integration we apply the method of integrated
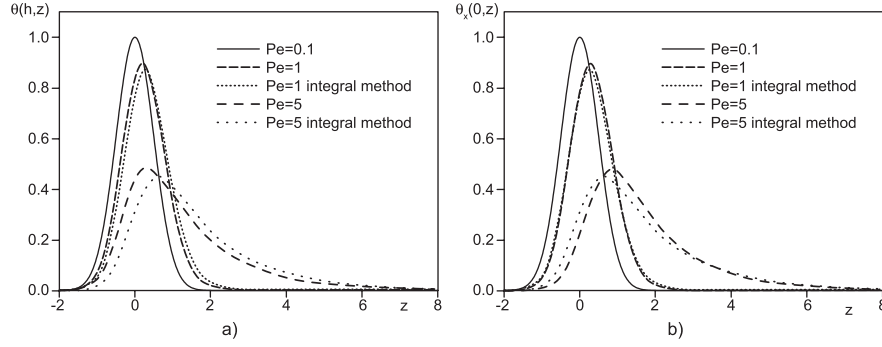
Fig. 2.12. Comparison of the solutions from the integral method (dotted) with the spectral method (dashed) for Pe $= 1.5$. As reference, the solution from the spectral method is given for a low value of the Péclet-number Pe $= 0.1$. a) The temperature $\theta(h, z)$ at the liquid surface $x = h$ and b) the heat flux $\theta_x(0, z)$ at the solid boundary $x = 0$.

balance [82] to the heat conduction equation (2.69) as an approximate approach. The heat conduction equation is integrated with respect to the melt film thickness $x \in \{0, h\}$ obtaining

$$\frac{\partial}{\partial t} \int_0^h \theta \, dx + \text{Pe} \frac{\partial}{\partial z} \int_0^h x\theta \, dx = \gamma(t)f(z) - \frac{\partial \theta}{\partial x}\Big|_{x=0}.$$

Assuming time scale separation such that the surface temperature $\widehat{\theta}$ is the slow variable and the spatial distribution is the fast variable, the temperature is given by a linear function $\theta(x, z, t) = \widehat{\theta}(z, t)x$ of the spatial coordinate x. The integrated balance becomes an equation for the surface temperature $\widehat{\theta}$:

$$\frac{h^2}{2} \frac{\partial \widehat{\theta}}{\partial t} + \text{Pe} \frac{h^3}{3} \frac{\partial \widehat{\theta}}{\partial z} = \gamma(t)f(z) - \theta_0(z, t). \tag{2.77}$$

In particular, for the Gaussian distribution $f(z)$ and constant maximum intensity $\gamma(t) = \gamma = const.$ the result is given by

$$\widehat{\theta}(z) = \frac{3\sqrt{2\pi}\gamma}{4h^3\text{Pe}} \exp\left\{ \frac{9}{8h^6\text{Pe}^2} - \frac{3z}{h^3\text{Pe}} \right\} \text{erfc}\left(\frac{3\sqrt{2}}{4h^3\text{Pe}} - \sqrt{2}z \right). \tag{2.78}$$

The resulting surface temperature $\theta(x = h, z)$ and the heat flux $\theta_x(0, z)$ at the solid boundary $x = 0$ reconstructed from the spectral and integral method (Fig. 2.12) show displacement by convection and widening by diffusion of heat compared with the absorbed intensity. The results agree very well and the error introduced by the integral approximation can be determined using spectral methods. Both methods are suitable to evaluate numerical calculations. The equation of motion (2.77) from the integrated balance shows a pronounced

dependence on the melt film thickness h. The spectral approach already show-ing the effects of temporal variations of the intensity can be directly extended to include spatial variations of the melt film thickness $h(z,t)$ as well. Spatial variations of the melt film thickness $h(z,t)$ in fact change the structure of the mathematical problem qualitatively by introducing coupling of the equations for the spectral components $a_k(z,t)$.

2.2.3 Three-Phase Problem

To find the properties of the gas flow leading to melt ejection is a fundamen-tal task in cutting. The interaction of the gas flow with the condensed phase is mediated by two quantities, namely the pressure gradient and the shear stress along the liquid surface. There remain a couple of intriguing questions about the effects of the gas flow on the melt flow and their relation to qual-ity criteria in cutting such as ripples of the third kind and dross formation. These quantities are related to separation and resolidification of the melt. In particular, separation of the supersonic gas flow from the cutting front are observed using Schlieren photography [42, 66, 68]. Other effects like the feed-back of a wavy melt surface on gas flow are not considered in detail. However, discussion of the properties of supersonic gas flow in cutting suffers from the numerical difficulties involved [83]. Compared to well established simulations of compressible flow in aerofoil construction the situation in cutting is much more difficult due to the widely different temperature scales and spatial scales involved. The smallest temporal and spatial scales involved in cutting are related to gas flow phenomena and the most detailed properties of the shape of the condensed boundary, namely the liquid surface at the melting front, have to be addressed. In particular, to probe deeper into medical or photo-voltaic applications like fine cutting of metallic stents or silicon wafers requires the inclusion of evaporation and flow of gas and vapour at a tube wall, or wafer thickness in the range of a few hundreds of micrometers (Fig. 2.13). Therefore, for the analysis of the gas flow phenomenon it is crucial to support the development and evaluation of numerical schemes by rigorous mathemat-ical analysis. To find the details of the analysis of compressible non-viscous flow described by the Euler equations, boundary layer theory and improved experimental methods are used to guide efforts to extend numerical methods for the solution of the compressible Navier-Stokes equations.

Momentum Boundary Layer of the Gas Flow

Using asymptotic analysis of the compressible Navier-Stokes equations the viscous effects near the condensed boundary can be described by a set of coupled ordinary differential equations. The structure of the solution for the momentum boundary layer can be found and moreover, explicit expressions for the shear stress $\tau_g(\xi)$ at the condensed boundary $\eta = 0$ and the thickness $\delta_g(\xi)$ of the viscous boundary layer in the flow direction ξ can be derived. Near
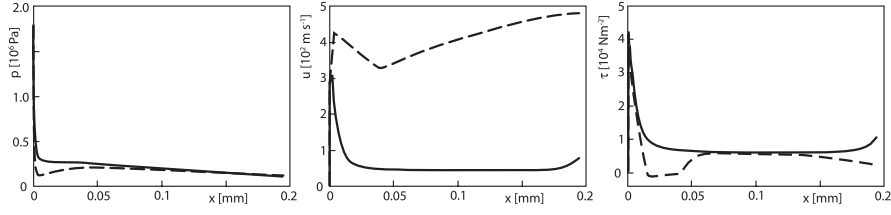
Fig. 2.13. Pressure p, velocity u and shear stress τ at the condensed surface in fine cutting. Numerical solution for the compressible flow calculated with the Navier-Stokes equations (solid) and the non-viscous Euler equations (dashed). The shear stress τ from the solution of the Euler equations is calculated using the Prandtl boundary layer expression given in (2.91).

the condensed surface viscous forces slow down the velocity of the cutting gas and a boundary layer for the momentum evolves. The thickness δ_G of the momentum boundary layer is characterised by the distance from the condensed surface where the flow changes from viscosity to inertia dominated. For laminar flows the ratio $\epsilon = \delta_G/L$ of the thickness δ_G and the length L along the flow becomes a smallness parameter for the Navier-Stokes equations. In the limiting case $\epsilon \to 0$ the compressible Navier-Stokes equations take the form of the well known Prandtl boundary layer equations for compressible flows:

$$\partial_t \rho + \nabla(\rho \boldsymbol{v}) = 0, \tag{2.79}$$

$$\rho(\partial_t + \langle \boldsymbol{v}, \nabla \rangle)u + \partial_x p = \partial_y \mu \, \partial_y u, \tag{2.80}$$

$$\partial_y p = 0, \tag{2.81}$$

$$\rho(\partial_t + \langle \boldsymbol{v}, \nabla \rangle)h - u\partial_x p = \mu(\partial_y u)^2 + \frac{1}{\mathrm{Pr}}\partial_y \lambda \, \partial_y h, \tag{2.82}$$

for the four dependent quantities density ρ, velocity $\boldsymbol{v} = \boldsymbol{v}(x, y)$ and gas pressure p, subject to the no-slip boundary conditions

$$\boldsymbol{v}(x, y) \mid_{y=0} = 0, \quad T(x, y) \mid_{y=0} = T_s(x) \tag{2.83}$$

at the condensed surface $y = 0$, where $T_s(x)$ is the temperature of the condensed surface. The boundary conditions for large values of $y \to \infty$ are given by the properties of the outer flow.

$$\boldsymbol{v}(x, y) \mid_{y \to \infty} = \boldsymbol{v}_\infty(x), \quad T(x, y) \mid_{y \to \infty} = T_\infty(x), \tag{2.84}$$

$$\rho(x, y) \mid_{y \to \infty} = \rho_\infty(x) \tag{2.85}$$

The Prandtl number $\mathrm{Pr} = \mu c_p/\lambda$ is the ratio of dynamical viscosity μ times specific heat capacity c_p and heat conductivity λ. Here u, v are the components of the velocity $\boldsymbol{v} = (u, v)$ parallel and perpendicular to the condensed boundary $y = 0$, respectively. The specific enthalpy $h = e + p/\rho$ of

the gas depends on the internal energy $e = e(T) = c_v p/\rho$ $(c_v = (\gamma - 1)^{-1})$, where the temperature T is related to density and pressure via the equation of state $(p = \rho \tilde{R} T,\ \tilde{R}$ specific gas constant). As a consequence of the boundary layer approximation the pressure does not change $\partial_y p = 0$ within the boundary layer. The mass balance (2.79) can be satisfied by introducing a potential $\Psi(x, y)$, such that $\partial_y \Psi = \rho u$ and $\partial_x \Psi = -\rho v$. Introducing the transformation $\{\xi, \eta\} = \{\xi(x), \eta(x, y)\}$ for the spatial variables

$$\xi(x) = \int_0^\infty \mu_\infty \rho_\infty u_\infty dx', \quad \eta(x, y)\sqrt{2\xi(x)} = u_\infty \int_0^y \rho dy' \qquad (2.86)$$

the Prandtl boundary layer equations (2.79)–(2.82) are reduced to an equivalent form for two dependent quantities $g(\xi, \eta), f(\xi, \eta)$ as discussed by Rogers [84]. The most interesting result is found by considering the limiting case for slowly varying properties of the outer non-viscous flow characterised by the values ρ_∞, u_∞, μ_∞, h_∞ and H_∞ far outside the viscous boundary layer. The total enthalpy $H_\infty = h_\infty + \boldsymbol{v}^2/2$ of the outer flow includes the contribution $\boldsymbol{v}^2/2$ from the stagnation pressure. More precisely, the boundary values for the viscous flow within the boundary layer change with the spatial coordinate ξ in the flow direction on a length scale large compared to the boundary layer thickness itself. Consequently, the solution for $f = f(\eta)$ and $g = g(\eta)$ describing the gas flow within the boundary layer can be seen to depend on ξ only as a parameter. The boundary layer flow can be found by solving a set of coupled ordinary differential equations

$$f_{\eta\eta\eta} + f f_{\eta\eta} + \beta(g - f_\eta^2) = 0, \qquad \beta = \beta(\mathsf{Ma}_\infty, \gamma) \qquad (2.87)$$

$$g_{\eta\eta} + \Pr f g_\eta + (\Pr - 1)\bar{\sigma}(f_\eta f_{\eta\eta})_\eta = 0, \qquad \bar{\sigma} = \bar{\sigma}(\mathsf{Ma}_\infty, \gamma) \qquad (2.88)$$

where Ma_∞ and γ are the Mach-number and the adiabatic coefficient, subject to the boundary conditions

$$f(\eta = 0) = 0, \qquad f_\eta(\eta = 0) = 0, \quad g(\eta = 0) = \frac{h(T(\xi, 0))}{H_\infty(\xi)} \qquad (2.89)$$

$$f_\eta(\eta \to \infty) = 1, \qquad g(\eta \to \infty) = 1 \qquad (2.90)$$

at the condensed surface (2.89) describing the no-slip condition $f_\eta = u$ and prescribing the surface temperature $T(\xi, 0)$ as well as the properties of the outer flow (2.90). As a result, the explicit expressions for the shear stress $\tau_g(\xi)$ and the thickness $\delta_g(\xi)$ of the viscous boundary layer read

$$\tau_g(\xi) = c_\tau \frac{\mu(\xi, 0)\rho(\xi, 0)u_\infty(\xi)}{\sqrt{2\xi}}, \qquad c_\tau = f_{\eta\eta}(0) \qquad (2.91)$$

$$\delta_g(\xi) = c_\delta \frac{\sqrt{2\xi}}{\rho_\infty(\xi)u_\infty(\xi)}, \qquad c_\delta = \left[\int_0^\infty \frac{H_\infty}{h_\infty}(g - f_{\eta\eta}^2) - f_\eta(1 - f_\eta)d\eta\right] \qquad (2.92)$$
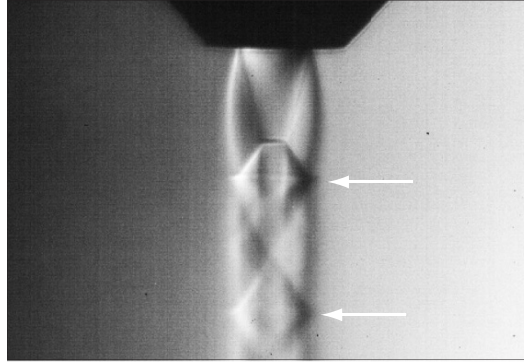
Fig. 2.14. Density gradient of a supersonic gas jet. The positions of two Mach discs are indicated (white arrows).

where the factors c_τ and c_δ reflect the details within the boundary, are of the order of unity, and give only a small correction to the scales depending on ξ. Comparing the numerical solution for the compressible flow along the free boundary calculated from the Navier-Stokes equations and the inviscid Euler equations (Fig. 2.13) shows deviations for pressure p and shear stress τ only in the regions where the flow undergoes large spatial variations due to expansion from the stagnation point near the upper edge $x = 0$ and separation at the lower edge $x = 0.2\,\mathrm{mm}$. The velocity u of the Euler flow corresponds to the outer flow velocity u_∞ and from the Navier-Stokes flow it does not reaches the no-slip boundary value $u = 0$, depending on the spatial extent of the boundary cell element. The Prandtl boundary layer approximation gives a useful scale for the driving force exerted by the shear stress τ_g given in (2.91) that guides the development of reliable numerical schemes. As result, the numerical scheme can be used to reproduce the limiting case of a viscous boundary layer.

Deflection and Separation

A supersonic gas jet emerging from a nozzle into the ambient gas forms an interacting wave and flow pattern. The wave pattern within the jet consists of shock and expansion waves as well as Mach discs (Fig. 2.14, white arrows). The outer boundary of the jet forming the flow pattern is characterised by a curved contact discontinuity between the gas jet and the ambient gas. For free expansion of the jet, the shock and expansion waves have an almost linear spatial shape and the contact discontinuity is curved. Across the contact discontinuity the gas density as well as the velocity component in the tangential direction changes discontinuously while pressure and the normal component of the velocity are continuous. The shape of the contact discontinuity depends on the nozzle parameters and thus is a free surface within the ambient gas. The

a)   b)
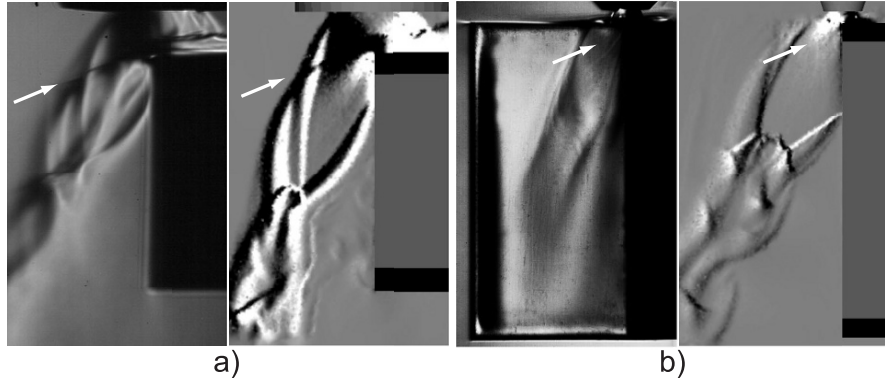
Fig. 2.15. Density gradient of the gas flow through a model kerf. Comparison of Schlieren photography and simulation both showing the oblique shock (white arrows) above the rigid body deflecting the gas jet a) without glass plates and free expansion to the sides (sheet thickness $d = 6\,\text{mm}$) and b) with glass plates confining the kerf on both sides (sheet thickness $d = 2\,\text{mm}$). Nozzle diameter $D_3 = 1.5\,\text{mm}$, displacement $V_x = V_y = 0\,\text{mm}$, stand-off distance $A = 0.75\,\text{mm}$, nozzle pressure $p_K = 15 \cdot 10^5\,\text{Pa}$, kerf width $500\,\mu\text{m}$.

resulting flow pattern undergoes cyclic changes. At the edge of the orifice, where the contact discontinuity evolves, the nozzle pressure changes to the ambient pressure discontinuously and therefore the contact discontinuity as well as a converging shock spatially coexist. Expansion waves arise during the transition from the converging shock wave to the contact discontinuity. With increasing distance from the orifice the expansion waves are reflected at the contact discontinuity, leading to local minima of pressure at positions where the gas jet reaches its maximum diameter. The reflected expansion waves together with the converging shocks build a disc-like shock called the Mach disc. A cyclic change from reflected shocks and expansion waves forms the diamond-like characteristic structure observed by Schlieren photography. The jet is accelerated and decelerated between sonic and supersonic flow regions, where sonic flow is established at the Mach discs.

Schlieren diagnostics and simulation are performed for the gas flow impinging on an edge and for a gas flow in a prepared kerf (model kerf) made out of three layers substituting the shape of the cut front. Agreement between Schlieren photography and simulation is striking (Fig. 2.15).

An additional oblique shock is formed between body and nozzle when the gas jet impinges on a rigid body. The oblique shock deflects and accelerates the gas jet into the kerf. The jet is partially aligned to the body and deflected by the oblique shock. Although the oblique shock leads to a deflection of the jet, the wave pattern of the deflected jet remains qualitatively unchanged. As a consequence the aligned part of the jet is related to the driving forces for melt acceleration along the rigid body, i.e. the pressure gradient and shear stress. Strength and shape of the oblique shock depend on the nozzle position
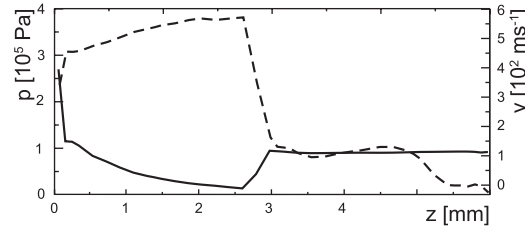
Fig. 2.16. Pressure and tangential velocity component along the edge related to Fig. 2.15 a). A jump in the gas flow properties occurs at the point of separation ($z \approx 2,6\,\text{mm}$).

and parameters as well as on the body's shape. The range of jet alignment also depends on the nozzle position and parameters as well as on the body shape; the driving forces can therefore be adjusted by a proper choice of nozzle position and parameters. The main difference between the flows along the rigid body without glass plates and free expansion to the sides (Fig. 2.15a) and the flow through the model kerf with two glass plates bounding the kerf on both sides (Fig. 2.15b) is the magnitude of the gas pressure behind the oblique shock. For the model kerf the pressure p is larger ($p \sim 10 \cdot 10^5\,\text{Pa}$) than the pressure ($p \sim 3 \cdot 10^5\,\text{Pa}$) without lateral kerf walls. Consequently, the flow within the kerf separates far down the front of the model kerf at a separation depth $d_s \sim 5.7\,\text{mm}$ (Fig. 2.19) compared to $d_s \sim 2.6\,\text{mm}$ (Fig. 2.16).

The spatial extent of shock and expansion wave patterns is well reproduced in the upper part of the kerf, while in the lower part the contrast of the experimental results suffers additionally from larger amplitudes of the non-stationary oscillating flow. The simulation gives the instantaneous flow while the experimental observation is averaged with respect to time. Simulation therefore shows that the instantaneous density changes even in the lower part of the kerf are much stronger than expected from Schlieren photography. Improved recording of the flow using high-speed videography reproduce the oscillatory behaviour of the gas flow. While strong reflections occur in channel flow, these reflections perpendicular to the kerf walls are suppressed in the vicinity of the cutting front. Simulations and experimental observations show that the shape of the deflecting oblique shock changes depending on the shape of the kerf. The shape of the oblique shock and the subsequent expansion taking place in the direction of the open side of the cut kerf tends to suppress the appearance of reflections perpendicular to the kerf walls. Induced by a shock, the gas flow separates from the wall and the depth d_s of separation can be determined from the wave pattern. Numerical results reproduce the jump-like change of the gas flow where the flow separates from the rigid body (Fig. 2.16). The pressure gradient changes its sign and the velocity component tangential to the wall is slowed down considerably. The driving forces on a melt film induced by the gas flow change suddenly in a drastic way, leading to a deceleration of the melt flow as well as to a growing thickness of the melt
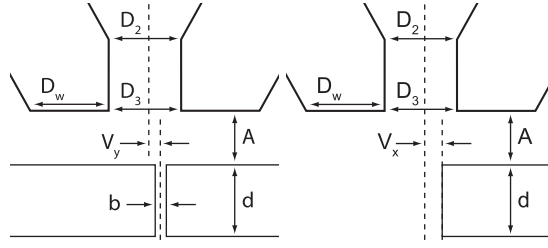
Fig. 2.17. The parameters for design and alignment of a conical-cylindrical nozzle with respect to the cut kerf.
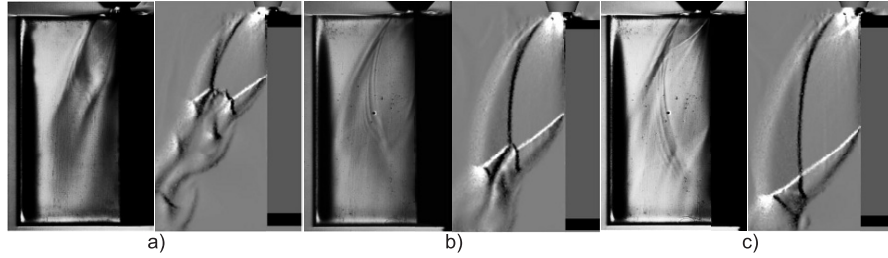
Fig. 2.18. Density gradient of the gas flow within a kerf. Comparison of Schlieren photography and simulation for different values V_x of displacement. a) $V_x = 0(a)$, 0.35 (b), 0.75(c) mm. Nozzle diameter $D_3 = 1.5$ mm, displacement $V_y = 0$ mm, stand-off distance $A = 0.75$ mm, nozzle pressure $p_K = 15 \cdot 10^5$ Pa, kerf width 500 μm, sheet thickness of $d = 20$ mm.

film. The measured depth d_s of separation changes significantly when a flow around an edge is compared with a flow through a model kerf. The depth d_s of separation is significantly larger in the case of the model kerf, showing that an analysis of a flow around an edge will not give valid results when flow situations in a cutting kerf are considered.

The analysis of gas flows through the model kerf is detailed with respect to the nozzle displacement V_x (Fig. 2.17). The agreement of experiment and simulation concerning the depth where separation of the gas flow from the condensed surface sets in (Fig. 2.19) and the related wave pattern (Fig. 2.18) is extremely good. A larger nozzle pressure p_K leads to an increase of the separation depth d_s. Reducing the stand-off distance A can increase the depth of separation as well, until feedback into the nozzle takes place due to stagnation of the gas flow at the sheet metal. For the chosen experimental setup the onset of feedback can be observed for stand-off distances smaller than $A < 0.5$ mm. Experimental results and the simulation indicate that the depth of separation is dominantly influenced by the nozzle displacement V_x. The effect of jet deflection is minimised by reducing the overlap between nozzle and material.
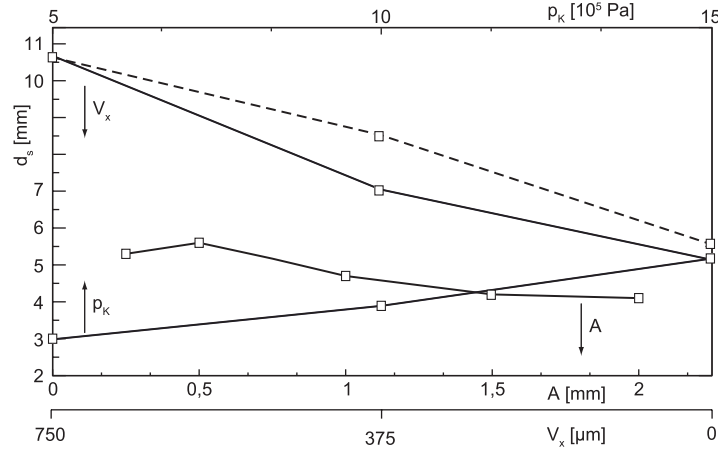
Fig. 2.19. The depth d_s where the gas flow separates from the condensed surface depends on nozzle pressure p_K, the stand-off distance A and the nozzle displacement V_x. Experimental results (solid) and the simulation (dashed) indicate that the depth d_s of separation is dominantly influenced by the nozzle displacement V_x.

Obviously, the displacement V_x and the width b of the cut kerf cannot be prescribed directly, are a part of the solution, and depend on different processing parameters such as cutting speed, spatial distribution of the laser radiation etc. Moreover, with increasing depth of separation the flow tends to lower oscillatory amplitudes. From these findings it is quite clear that high-quality cutting relies on a gas flow where it does not separate from the front and the flow relaxes to a quasi-steady state on time scales much shorter than those prescribed by other parameters such as cutting speed and laser power. It remains an intriguing problem to find the time scales of relaxation and the dynamical properties of the gas flow depending on the parameters of nozzle design and alignment.

Gas Flow in Cutting and Trepanning

Periodically repeated reflection of shocks and compression waves along the side walls are observed in Schlieren photography and are related to the formation of horizontal structures of the ripple pattern in the real cutting situation. Looking at the different situations present in cutting and trepanning, the main difference for the gas flow is related to the open kerf in cutting compared with the circular hole in trepanning. Simulation shows that the shape of the deflecting oblique shock is related to the shape of the kerf. Subsequent expansion taking place in the direction of the open side of the cut kerf tends to suppress the appearance of strong reflections perpendicular to the kerf walls. However, in trepanning the extent of the circular cut can be small enough to enhance the strength of shocks reflected from the condensed
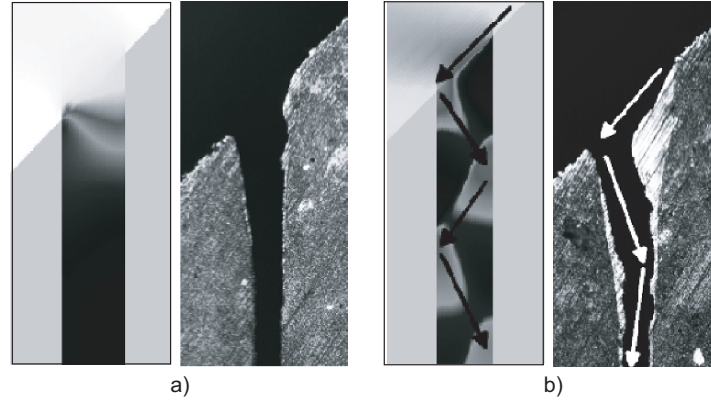
Fig. 2.20. Reflection of shocks and compression waves takes place in trepanning of inclined sheet metal leading to separation of the gas flow and pronounced periodic axial variation of the pressure (simulation) and periodic formation of recast layers (cross section). a) Nozzle alignment towards the right-hand upper edge of the circular cut (wall position on the right side of the cut) and b) nozzle axis aligned to the laser beam axis.

wall behind the actual position of the cutting front (Fig. 2.20). This behaviour can be observed in trepanning, where a drill hole is widened by performing a trim cut along the circular wall. In particular, performing trepanning and having the laser beam axis inclined with respect to the sheet metal surface the effect of reflected compression waves is further enhanced leading to periodic changes of the driving forces for the melt flow and corresponding changes in the thickness residual recast layers. If the distance for expansion of the gas flow by widening the hole diameter or by proper alignment of the nozzle by shifting the nozzle wall towards the right-hand upper edge of the circular drilled wall (Fig. 2.20a) is increased, the reflections in the gas flow are absent and resoldification can be avoided.

Simulation of the three dimensional problem including the moving cutting front and the gas flow calculated with the compressible Navier-Stokes equations are carried out to compare the effects of the driving forces in the axial and lateral directions along the cutting front (Fig. 2.21). As a consequence of the processing parameters the gas flow does not separate from the cutting front. The pressure gradient as well as the gas velocity are directed dominantly in the axial direction. There are no shocks at the cut surfaces and even the pressure and velocity vary smoothly along the cutting front and the cut surfaces.

Spatial variations of pressure and velocities of the gas flow taken from the results in Fig. 2.21 are compared (Fig. 2.22). The ratio of lateral (gray curves) and axial quantities (black curves) are of the same order of magnitude as the ratio $2\pi w_0 d^{-1} \sim 0.18$ of the lateral $2\pi w_0$ and axial d length of the cutting front. Due to the presence of the cut surfaces the oblique shock is enhanced
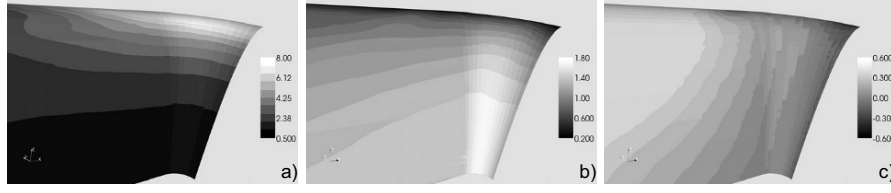
Fig. 2.21. Simulation of the three dimensional problem including the gas flow from the compressible Navier-Stokes equations. a) Pressure p $[10^5\,\mathrm{Pa}]$ and tangential components b) v_{axial} $[3.3 \cdot 10^2\,\mathrm{m\,s^{-1}}]$ and c) $v_{lateral}$ $[3.3 \cdot 10^2\,\mathrm{m\,s^{-1}}]$ of the gas velocity in the axial and lateral directions, respectively. ($D_3 = 1.5\,\mathrm{mm}$, $A = 0.75\,\mathrm{mm}$, $d = 4\,\mathrm{mm}$, $p_K = 15 \cdot 10^5\,\mathrm{Pa}$, N_2, $w_0 = 300\,\mu\mathrm{m}$, $P_L = 4\,\mathrm{kW}$, $v_0 = 1.5\,\mathrm{m\,min^{-1}}$, $d = 4\,\mathrm{mm}$).
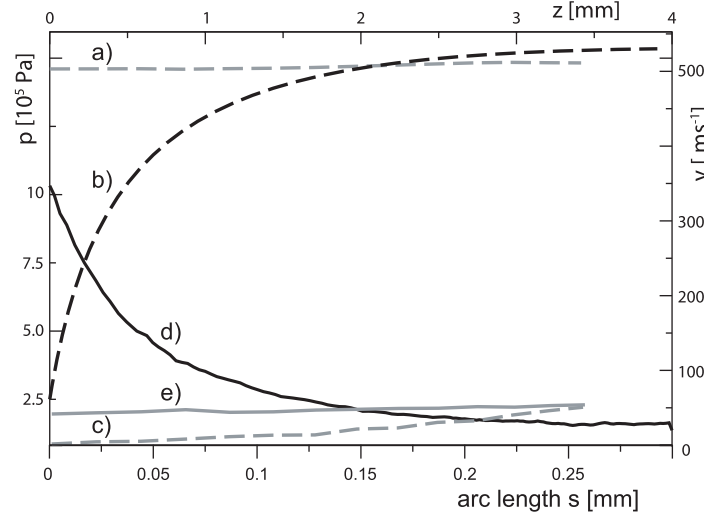
Fig. 2.22. Pressure p (solid, d), e)) and tangential components $v_{axial}, v_{lateral}$ of the velocity v (dashed, a), b), c)) are given depending on the lateral (gray) direction measured by the arc length s at a depth of $z_0 = 2\,\mathrm{mm}$ (a) $v_{axial}(s, z_0)$, c) $v_{lateral}(s, z_0)$, e) $p(s, z_0)$) and the axial direction (black) at the ceiling line $s = 0$) as a function of the depth z b) $v_{axial}(s = 0, z)$, d) $p(s = 0, z)$). ($D_3 = 1.5\,\mathrm{mm}$, $A = 0.75\,\mathrm{mm}$, $d = 4\,\mathrm{mm}$, $p_K = 15 \cdot 10^5\,\mathrm{Pa}$, N_2, $w_0 = 300\,\mu\mathrm{m}$, $P_L = 4\,\mathrm{kW}$, $v_0 = 1.5\,\mathrm{m}$ $\mathrm{min^{-1}}$, $d = 4\,\mathrm{mm}$).

leading to a large pressure $p \sim 10 \cdot 10^5\,\mathrm{Pa}$ at the top of the cut compared with the maximum pressure $p \sim 3 \cdot 10^5\,\mathrm{Pa}$ for the case where free expansion perpendicular to the cutting direction takes place (Fig. 2.16).

There is an extended range of processing parameters, where the two-dimensional properties of the gas flow already reproduce the qualitative behaviour of the three dimensional flow (Fig. 2.23). In general, the spatial changes of gas pressure p along the cutting front change by an order of magnitude. As a rule of thumb, for a typical situation in cutting the pressure
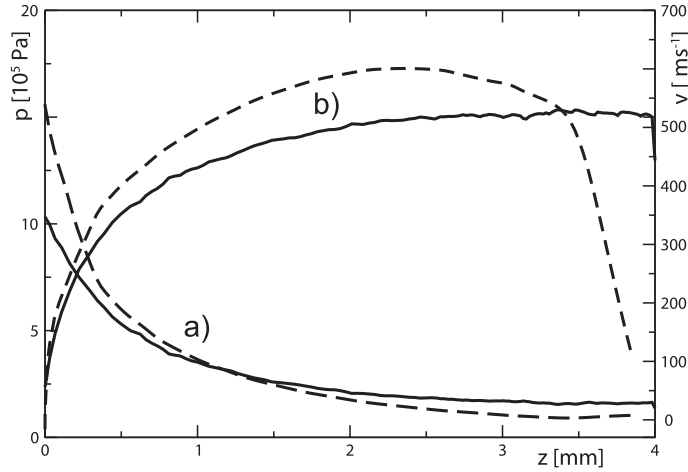
Fig. 2.23. Simulation of the three dimensional problem including the compressible Navier-Stokes equations. Comparison of gas flow taking place at a spatially two- (dashed) and three-dimensional (solid) domain. The values for the three-dimensional flow are taken from the ceiling line. (a) Pressure $p\,[10^5\,\mathrm{Pa}]$ and b) axial component $v\,[\mathrm{m\,s^{-1}}]$ of the gas velocity.

p along the cutting front changes at an average rate of about $\sim\!10^8\,\mathrm{Pa\,m^{-1}}$ which equals 1 bar mm^{-1}. The value of $10^8\,\mathrm{Pa\,m^{-1}}$ corresponds to a cutting depth $z > 0.5\,\mathrm{mm}$ in Fig. 2.23 (a, solid line). The maximum value of the pressure gradient located near the upper edge of the front is up to ten times larger, but the extent of this region of high pressure gradient is limited to a few hundred microns, as shown in Fig. 2.25.

Alignment of Nozzle Position and Cutting Front

The effect of design and alignment parameters on nozzle performance in cutting are investigated in more detail. Two dominant effects are discussed, namely the feedback of the gas flow into the nozzle and deflection of the gas flow away from the cutting front. Feedback into the nozzle sets in due to stagnation of the gas flow at the sheet metal. Feedback diminishes both the mass flow out of the nozzle orifice and the outflow velocity. With increasing deflection, first the driving forces along the cutting front (pressure gradient and shear stress) are reduced and finally the gas flow separates before reaching the full cut depth.

As is well known from experimental evidence, the simulation also shows that it is advantageous to use a conical nozzle design in cutting instead of the Laval or Laval-Venturi design. The Laval nozzle generates larger gas velocities and lower gas pressure at the orifice, which turns out to be of minor importance due to the stagnation-type flow evolving at the sheet metal surface and the subsequent transition of the flow through an oblique shock into the cutting
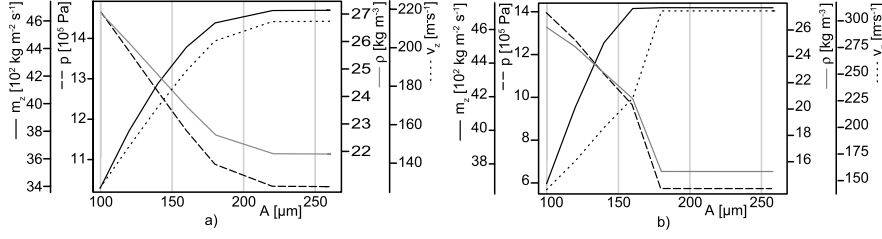
Fig. 2.24. Feedback into the nozzle due to stagnation of the gas flow at the sheet metal surface. The mass flow m_z out of the nozzle, the pressure p, the density ρ and the gas velocity v_z at the nozzle exit are integrated with respect to the diameter D_3 of the orifice, and their dependence on the stand-off distance A is given. a) Conical nozzle ($D_2 > D_3$) and b) conical-cylindrical nozzle ($D_2 = D_3$). $D_2 = D_3 = 0.24$ mm, $A = 0.175$ mm, $d = 0.26$ mm, $p_K = 19 \cdot 10^5$ Pa (Argon).

kerf; moreover, the pressure gradient at the cutting front is smaller for the Laval design. In particular, the alignment parameters: stand-off distance A of the nozzle with respect to the surface of the sheet metal, and the displacement V_x of the nozzle axis and the cutting front, are more sensitive for the Laval nozzle.

The parameters of the conical nozzle are given by the thickness of the nozzle wall D_w, diameters D_2, D_3 of the orifice and stand-off distance A as well as the kerf parameters width and depth b, d of the cut and displacements V_x, V_y with respect to feed and lateral direction as sketched in Fig. 2.17. Additional parameters such as length of the cylindrical part between D_2 and D_3 of the orifice and the length of the conical part above D_2 are of less importance.

The simulation results are related to feedback into the nozzle caused by stagnation of the gas flow at the sheet metal, and the resulting pressure, velocity, density and mass flow out of the nozzle and along the cutting front.

The gas velocity at the orifice reaches the velocity of sound $c = \sqrt{\gamma p / \rho}$ for a conical nozzle. However, feedback due to stagnation is present due to the compressibility of the gas and a sufficiently large stand-off distance is necessary to avoid the unwanted counteracting effect.

The displacement V_x of the nozzle with respect to the feed direction dominantly changes the driving forces for the melt flow (Fig. 2.25). Variations along the front are pronounced for the pressure gradient p_z, while the axial component v_z of the gas velocity changes only slightly.

Dross Formation Depending on Gas Pressure

Discussion of the onset of dross formation is carried out with respect to cutting speed v_0 and sheet thickness d (Fig. 2.9), where the driving forces exerted
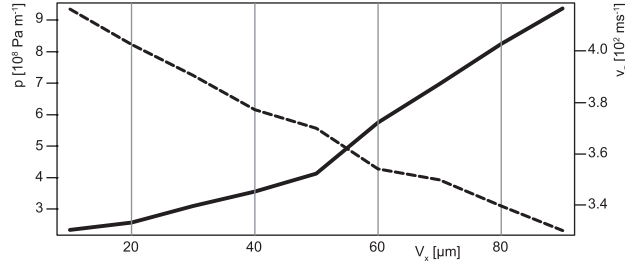
Fig. 2.25. Pressure gradient p_z (solid) and gas velocity v_z (dashed) depending on the displacement V_x between nozzle axis and front. $D_2 = D_3 = 0.24\,\mathrm{mm}$, $A = 0.175\,\mathrm{mm}$, $d = 0.26\,\mathrm{mm}$, $p_K = 19 \cdot 10^5\,\mathrm{Pa}$ (Argon).

on the melt flow were estimated by their scales only. The analysis can be extended to include compressible gas flow in the simulation so that the nozzle pressure p_K enters the calculation of the processing domain (Fig. 2.26b). The transitions to the adjacent domains II and IV related to droplet formation and evaporation are characterised by low values for the Weber number (We ≤ 1, domain II) and the onset of evaporation ($\Theta_s \geq 1$, domain IV). Both quantities are determined by the gas flow via the free quantities' outflow velocity $u = u_m/u_0$ and thickness $h = d_m/d_{m0}$ of the melt film (Fig. 2.26c). The scale u_0 for the outflow velocity results from global mass balance in the melt film. The scale d_{m0} for the melt film thickness is obtained from the momentum in the outflow direction at the ceiling line (centre line) of the cutting front and depends on dynamical viscosity η, cutting speed v_0, sheet thickness d and a typical value for the driving forces. Here, the dominant driving force, shear stress τ_g or the pressure gradient dp_g/dz exerted to the melt film surface by the cutting gas, has to be inserted. The scales for the Weber number We (droplet formation) and the surface temperature T_s (evaporation) are thus

$$\mathrm{We} = \frac{\rho}{\sigma}u_0^2 d_{m0}, \qquad\qquad u_0 = v_0\frac{d}{d_{m0}}, \qquad\qquad (2.93)$$

$$\Theta_s = \frac{T_s - T_m}{T_v - T_m} = \exp\left(\frac{v_0 d_{m0}}{\kappa}\right), \quad d_{m0,\tau}^2 = 2\frac{\eta v_0 d}{\tau_g}, \quad d_{m0,p}^3 = \frac{\eta v_0 d}{dp_g/dz} \quad (2.94)$$

where σ is the surface tension of the liquid and T_v, T_m denote the evaporation and melting temperature, respectively. As a result, the simulation reproduces the experimental results for the onset of evaporation and droplet formation as functions of the cutting speed v_0 and sheet thickness d (Fig. 2.26 a). Additionally, the simulation shows that the processing domain III has the tendency to be closed for decreasing nozzle pressure at $p_K \sim 3 \cdot 10^5\,\mathrm{Pa}$. The most interesting result is related to the sensitivity of the outflow velocity u and thickness h of the melt film on the nozzle pressure p_K. Scatter of the processing parameters shows different sensitivity with respect to their actions on the outflow velocity and the melt film thickness. The values for the processing parameters
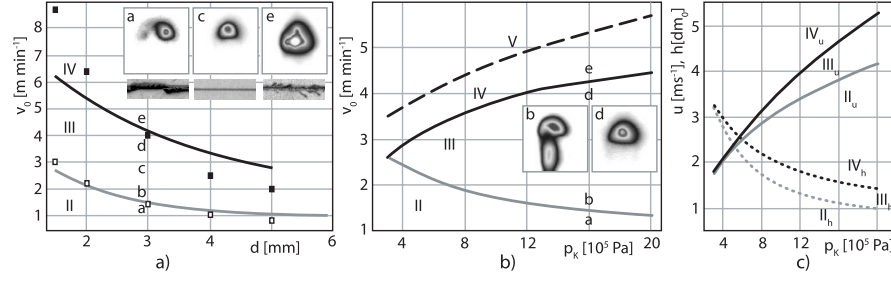
Fig. 2.26. The processing domain III for determination for a cut free of dross. Dross of kind 1 (domain II: droplet formation, gray, insert a) and kind 2. (domain IV, onset of evaporation, black, insert e). CCD-images of the thermal emission from the cutting front. a) Comparison of experiment (squares) and simulation (solid lines). Nozzle pressure $p_K = 14 \cdot 10^5$ Pa. b) The calculated boundaries of the processing domains depending on nozzle pressure at sheet thickness $d = 3$ mm. c) Outflow velocity u (solid) and thickness h (dotted) of the melt film depending on nozzle pressure at $d = 3$ mm. (CO$_2$ laser, $P_L = 2.6$ kW, $w_0 = 150$ μm, $z_R = 2.2$ mm, focal position $z_0 = d/2$, stainless steel.)

within the dross free processing domain III 1 indicated in Fig. 2.9c) and the allowable fluctuations leading to adherent dross can be derived. Consequently, the confidence interval (the distance between region III 1 and III 2) can be determined.

To probe more deeply into the understanding of dross formation requires identification of additional features of the dross morphology, and the detailing and identification of the dominance of either the fluctuations or the temporal averaged parameter settings of the contributing mechanisms.

2.3 Outlook

Laser cutting machines account for the highest percentage of the laser market for industrial applications. In spite of the technical success already achieved, laser cutting is expected to exploit additional future potential offered by new laser systems such as multi-kW fibre laser and cutting machines with improved performance. To simplify handling and trouble-shooting the machine suppliers aim to introduce cognition in relation to the process into the machine, and development efforts are directed towards an "autonomous cutting machine". One crucial step towards a cutting machine having more autonomous properties consists of extending knowledge about the processing domains and including a larger set of the processing parameters. For example, models for the propagation of laser radiation could take into consideration more details than just free propagation and the geometric optics of reflections. Extending the number of parameters spanning the phase space of the processing domains also means including not only a sufficient number of parameters

but also understanding the influence of their fluctuations. To know more details about the accuracy necessary for a safe parameter-setting requires the ability to distinguish between fluctuations of processing parameters, the scatter of residual cut quality, and the sensitivity of the dependence of the cut quality on the processing parameters.

While some properties of macro cutting can be applied to processing of small sheet thickness, simulation of fine cutting remains a challenge. To probe deeper into medical or photovoltaic applications like fine cutting of metallic stents or silicon wafers requires the inclusion of evaporation and flow of gas and vapour at a tube wall, or wafer thickness in the range of a few hundreds of micrometres. Processes of this kind are at the border line between drilling and cutting, since vapour flow from evaporation and gas flow from the nozzle are involved simultaneously.

The need for more detailed analysis of numerical schemes, their performance as well as their reliability in solving coupled dynamical equations with very different length scales along the free boundaries, becomes apparent. The smallest length scales of a few tenth of μm for the momentum boundary layer up to scales of about ten mm corresponding to the sheet thickness favour advanced developments including cartesian grid methods, discontinuous Galerkin methods and adaptive grid refinement. Such methods are not directly applicable at present and appropriate modification of them requires detailed mathematical analysis.

2.4 Acknowledgements

References

1. Friedrich R, Radons G, Ditzinger T, Henning A (2000) Ripple formation through an interface instability from moving growth and erosion sources. Phys Rev Lett 85(23): 4884–7
2. Makashev NK, Asmolov NS, Blinkov VV, Boris AY, Buzykin OG, Burmistrov AV, Gryaznov MR, Makarov VA (1992) Gas hydrodynamics of metal cutting by CW laser radiation in a rare gas. Sov J Quant Electr 22: 847–852
3. Nemchinsky VA (1997) Dross formation and heat transfer during plasma arc cutting. J Phys D: Appl Phys 30: 2566–2572
4. Poprawe R, König W (2001) Modeling, Monitoring and Control in High Quality Laser Cutting. Annals of the CIRP 50(1): 137–140

5. Klimentov SM, Garnov SV, Kononenko TV, Konov VI, Pivovarov PA, Dausinger F (1999) High rate deep channel ablative formation by picosecond-nanosecond combined laser pulses. Applied Physics A 69: 633–636

6. Hellrung D, Gillner A, Poprawe R (1997) Laser beam removal of micro-structures with Nd:YAG lasers. Proc Lasers in Material Processing Laser'97, Munich, SPIE 3097: 267–273.

7. Schulz W, Poprawe R (2000) Manufacturing with Novel High Power Diode Lasers. IEEE JSTQE 6(4): 696–705

8. Jurman LA, McCready MJ (1989) Study of waves on thin liquid films sheared by turbulent gas flow. Phys Fluids A 1: 522–536

9. Hsieh DY (1990) Mechanism for instability of fluid flow down an inclined plane. Phys Fluids A 11145–1148

10. Miesen R, Boersma BJ (1995) Hydrodynamic stability of a shared liquid film. J Fluid Mech 301: 175–202

11. Oron A, Davies SH, Bankoff SG (1997) Long-scale evolution of thin liquid films. Rev Mod Phys 69: 931–980

12. Aksel N (2000) Influence of the capillarity on a creeping film flow down an inclined plane with an edge. Archive of Applied Mechanics 70: 81–90

13. Scholle M, Aksel N (2001) An exact solution of viscocapillary flow in an inclined channel. Z angew Math Phys 52: 749–769

14. de Gennes PG (1985) Wetting: statics and dynamics. Rev Mod Phys 57: 827–863

15. Schäffer E, Wong P (1998) Dynamics of contact line pinning in capillary rise and fall. Phys Rev Lett 80: 3069–3072

16. Pritchard WG (1984) Some viscous-dominated flows. In: Ciarlet PG, Roseau M (eds.) Trends and Applications of Pure Mathematics to Mechanics. Lecture Notes in Physics, Berlin, Springer-Verlag, 195: 305–332

17. Pritchard WG, Saavedra P, Scott LR, Tavener SJ (1994) Theoretical issues in the modelling of viscous free-surface flows. In: Brown RA, Davies SH (eds), Free Boundaries in Viscous Flows. Springer-Verlag, New York 29–48

18. Eggers J (1997) Tropfenbildung. Phys Bl 53: 431–434

19. Eggers J (1997) Nonlinear dynamics and break-up of free surface flows. Rev Mod Phys 69: 865–929

20. Aoki K, Sone Y (1991) Gas flows around the condensed phase with strong evaporation or condensation – Fluid dynamics equation and its boundary condition on the interface and their application. In: Gatignol R, Soubbaramayer (eds), Advances in Kinetic Theory and Continuum Mechanics, Proceedings of a Symposium Held in Honor of Professor Henri Cabannes at the University Pierre et Marie Curie, Paris. Springer, Berlin, 43–54

21. Ytrehus T (1997) Molecular-flow effects in evaporation and condensation at interfaces. Multiphase Science and Technology 9: 205–327

22. Rose JW (1999) Condensation heat transfer. Heat and Mass Transfer, Springer 35: 479–485

23. Rose JW (2000) Accurate approximate equations for intensive sub-sonic evaporation. Int J Heat and Mass Transfer 43: 3869–3875

24. Aoki K, Bardos C, Takata S (2003) Knudsen Layer for Gas Mixtures. Journal of Statistical Physics 112(3): 629–655

25. Temam R (1988) Infinite-dimensional Dynamical Systems in Mechanics and Physics. Springer-Verlag, New York

26. Constantin R, Foias C, Nicolaenko B, Temam R (1989) Integral Manifolds and Inertial Manifolds for Dissipative Partial Differential Equations. Springer-Verlag, New York
27. Robinson JC (1995) Finite-dimensional behavior in dissipative partial differential equations. Chaos 5: 330–345
28. Biot MA (1970) Varational Principles in Heat Transfer. Oxford University Press, Oxford
29. Elliot CM, Ockendon JR (1982) Weak and variational methods for moving boundary problems. Pitman, Boston
30. Canuto C, Hussaini MY, Quateroni A, Zang TA (1988) Spectral methods in fluid dynamics. Springer Verlag
31. Sirovich L, Knight BW, Rodriguez JD (1990) Optimal low-dimensional dynamical approximations. Quart Appl Math 48: 535–548.
32. Enß V, Kostrykin V, Schulz W, Zimmermann C, Zefferer H, Petring D (1997) Thermal treatment using laser radiation: Laser beam fusion cutting. In: Mathematik - Schlüsseltechnologie für die Zukunft, Hoffmann K-H, Jäger W, Lohmann Th, Schunk H. Springer Verlag, Berlin, 161–174
33. Schulz W, Kostrykin V, Zefferer H, Petring D and Poprawe R (1997) A Free Boundary Problem Related to Laser Beam Fusion Cutting: ODE Approximation. Int J Heat Mass Transfer 40(12): 2913–2928
34. Sethian JA (1999) Level Set Methods and Fast Marching Methods. Cambridge University Press, Cambridge
35. Adalsteinsson D, Sethian JA (1999) The fast construction of extension velocities in level set methods. J Comp Phys 148: 2–22
36. Yserentant H (1986) On the multi-level splitting of finite element spaces. Numer Math 49: 379–412
37. Zenger C (1991) Sparse grids. In Hackbusch W (ed), Parallel Algorithms for Partial Differential Equations: Proceedings of the 6-th GAMM-Seminar, Kiel, January. Notes on Numerical Fluid Mechanics, Vieweg, Braunschweig, 31241–251
38. Beersiek J, Schulz W, Poprawe R, Mueller R, Duley WW (1997) On-line monitoring of penetration depth in laser beam welding. Proc ICALEO97, San Diego, USA
39. Arata Y, Maruo H, Miyamoto I, Takeuchi S (1979) Dynamic behavior in Laser Gas Cutting of Mild Steel. Trans JWRI 8(2): 15–26
40. Arata Y, Maruo H, Miyamoto I, Takeuchi S (1979) Fundamental research of laser gas cutting II. J High Temp Soc 5: 2
41. Olsen FO (1980) Cutting with polarized laser beams. DVS-Berichte 63: 197
42. Fieret J, Terry MJ, Ward BA (1987) Overview of flow dynamics in gas assisted laser cutting. Proc SPIE High Power Lasers 801: 243–250
43. van Allmen M (1989) Laser Beam Interactions with Materials. Springer Verlag
44. Steen WM (1991) Laser Material Processing. Springer Verlag
45. Steen WM, O'Neill W (1994) Review of mathematical models of laser cutting. In: Lasers in Engineering, Mordike BL (ed), Gordon and Breach Publishers, Review of Mathematical Models of High Power Laser Materials Processing 3(4): 281–297
46. Powell J (1993) CO_2 Laser Cutting. Springer, London
47. Vicanek M, Simon G, Urbassek HM, Decker I (1987) Hydrodynamical instability of melt flow in laser cutting. J Phys D: Appl Phys 20: 140–145

48. Vicanek M, Simon G (1987) Momentum and heat transfer from an inert gas jet to the melt in laser cutting. J Phys D: Appl Phys 20: 1191–1196
49. Petring D, Abels P, Beyer E, Herziger G (1988) Werkstoffbearbeitung mit Laserstrahlung, Teil 10: Schneiden von metallischen Werkstoffen mit CO_2-Hochleistungslaserstrahlung. Feinwerktechnik und Meßtechnik 96: 364
50. Berger P, Herrmann M, Hgel H (1990) Untersuchungen von Laserschneiddsen. In: Waidelich W (ed), Proc LASER89, Springer, Berlin, 630
51. Zefferer H, Petring D, Beyer E (1991) DVS-Berichte 135: 210
52. Man HC, Duan J, Yue TM (1999) Analysis of the dynamic characteristics of gas flow inside a laser cut kerf under high cut-assist gas pressure. J Phys D: Appl Phys 321469–1477
53. O'Neill WO, Steen WM (1992) The dynamical effects of gas jets in laser cutting. Proc ICALEO92, Orlando
54. Shachrai A (1979) Application of high power lasers in manufacturing. Annals of the CIRP 28: 2
55. Petring D, Abels P, Beyer E (1988) The absorption distribution as a variable property during laser beam cutting. Proc ICALEO 88, Santa Clara
56. Schulz W, Becker D (1989) On laser fusion cutting: a closed formulation of the process. Bergmann HW (ed), Proc European Scinetific Laser Workshop, Lisbon, Sprechsaal Pub. Group, Coburg, 178–200
57. Olsen FO (1994) Fundamental mechanisms of cutting front formation in laser cutting. In Laser Materials Processing: Industrial and Microelectronics Applications. Proc SPIE 2207: 402–413
58. Kaplan AFH (1996) An analytical model of metal cutting with a laser beam. J Appl Phys 79(5): 2198–2208
59. Chen SL, Steen WM (1991) The theoretical investigation of gas assisted laser cutting. Proc ICALEO91, San Jose
60. Kovalenko V, Romanenko V, Chuck N (1992) Mathematical modelling at metal laser cutting quality evaluation. Proc LAMP92, Nagaoka, 393
61. O'Neill WO, Steen WM (1995) A three dimensional analysis of gas entrainment operating during the laser cutting process. J Phys D: Appl Phys 26: 12–16
62. Wagner C (1973) The formation of thin oxide films on metals. Corrosion Science 1323–52
63. Schulz W, Simon G, Vicanek M, Decker I (1987) Influence of the oxidation process in laser gas cutting. Proc High Power Lasers and Laser Machining, Den Haag, SPIE 801: 331–336
64. Franke J, Schulz W, Petring D, Beyer E (1993) Die Rolle der exothermen Reaktion beim Laserstrahlbrennschneiden. Proc LASER93 562–567
65. Franke J, Schulz W, Herziger G (1993) Burnoff-stabilized laser beam oxygen cutting - a new process. Welding and Cutting 45:490-493, & 45: E161–E162
66. Zefferer H, Petring D, Schulz W, Schneider F,Herziger G (1993) Laserstrahlschmelzschneiden - Diagnostik und Modellierung des Schmelznachlaufes und der Riefenbildung. In: Geiger M, Hollmann F (eds), Strahl-Stoff-Wechselwirkung bei der Laserstrahlbearbeitung. Ergebnisse des Schwerpunktprogramm(1993)s der Deutschen Forschungsgemeinschaft DFG 1991 bis 1992. Meisenbach, Bamberg 123–128
67. Grop A, Hutfless J, Schuberth S, Geiger M (1995) Laser beam cutting. J Opt Quant Electronics 27: 1257–1271

68. Yudin PV, Petrov AP, Kovalev OB (2007) Experimental modelling and high speed photographic studies of gas laser cutting of sheet metal. Congress on high-speed photography and photonics, Proc SPIE, 6279(17): 1–11

69. Moalem A (2005) Koaxiale Fremdbeleuchtung zur Überwachung des Schneidens und Schweissens mit Laserstrahlung. Diploma thesis, RWTH Aachen University

70. Ward BA (1984) Proc Int Conf on Application of Lasers and Electro-Optics (Boston, MA) (Boston, MA: Laser Institute of America), 730

71. Zefferer H , Petring D, Beyer E (1991) Investigation of the gas flow in laser beam cutting. Deutscher Verband für Schweißtechnik e.V. DVS, Düsseldorf: 3. Internationale Konferenz Stahltechnik '91, Düsseldorf: DVS-Verlag

72. Jolly MS (1989) Explicit construction of an inertial manifold for a reaction diffusion equation. J Diff Eq 78: 220–261

73. Hylleraas EA (1929) The Schrödinger Two-Electron Atomic Problem. Adv Quantum Chem 1: 15

74. Saltzmann B (1962) Finite Amplitude Free Convection as an Initial Value Problem. J Atmos Science 19: 329

75. Lorenz EN (1963) Deterministic Nonperiodic Flow. J Atmos Science 20130

76. Elliot CM, Ockendon JR (1982) Weak and variational methods for moving boundary problems. Pitman, Boston

77. Fasano A, Primicerio M (1977) General free-boundary value problems for the heat equation, I, II, III. J Math Anal Appl 57: 694–723, & 58: 202–231, & 59: 1–14

78. Filippov AF(1988) Differential equations with Discontinuous Righthand Sides. Kluwer, Dodrecht

79. Arnold VI, Afraimovich VS, L'yashenko YSI, Shilnikov LP (1994) Bifurcation Theory. In: Dynamical Systems V, Arnold VI (ed), Springer, Berlin

80. Batchelor GK (1967) An Introduction to Fluid Dynamics. Cambridge Univ Press, Cambridge

81. Miles JW (1960) The hydrodynamic stability of a thin film of fluid in uniform shearing motion. J Fluid Mech 8: 593–610

82. Schulz W, Becker D, Franke J, Kemmerling R and Herziger G (1993) Heat conduction losses in laser cutting of metals. J Phys D: Appl Phys 26: 1375–1363

83. Gross MS, Black I, Mueller WH (2004) Determination of the lower complexity limit for laser cut quality modelling. Modelling Simul Mater Sci Eng 12: 1237–1249

84. Rogers DF (1992) Laminar flow analysis. Cambridge University Press, Cambridge

85. Geiger M (1993) Texte zum Berichtskolloquium der DFG im Rahmen des Schwerpunktprogramms. In: Hollmann F (ed): Strahl–Stoff–Wechselwirkung bei der Laserstrahlbearbeitung 1991-1992. Meisenbach Verlag, Bamberg, 123–128

86. Sepold G (1998) Texte zum Abschlußkolloquium der DFG im Rahmen des Schwerpunktprogramms. In: Geiger M (ed): Strahl–Stoff–Wechselwirkung bei der Laserstrahlbearbeitung. IDEE & DRUCK, Bremen

87. Horn A, Mingareev I, Miyamoto I (2006) Ultra-fast diagnostics of laser-induced melting of matter. JLMN-Journal of Laser Micro/Nanoengineering 1(3): 264–268

3

Keyhole Welding: The Solid and Liquid Phases

Alexander Kaplan

Luleå University of Technology, SE-97 187 Luleå, Sweden.
`alexander.kaplan@ltu.se`

Abstract. Deep penetration laser welding relies on the evaporation of material by a high power laser beam in order to drill a vapour capillary, usually referred to as a *keyhole*. During continuous welding the keyhole is kept open by the pressure in the vapour which evaporates continuously from its wall; the pressure acts continuously against the surface tension pressure that favours contraction. In contrast to pulsed wave (pw-) laser welding, during continuous wave (cw-) laser welding quasi-steady state conditions of the accompanying temperature field, and thus of the shape of the keyhole and melt pool, are established. Nevertheless, in the keyhole and melt pool complex fluid mechanical mechanisms take place. The most important thermodynamic and melt flow phenomena in keyhole laser welding will be briefly discussed. For some of them mathematical models and calculation results will be presented, complementing a comprehensive survey that was published earlier [1].

Notation employed in this chapter is given in Table 3.1.

3.1 Heat Generation and Heat Transfer

3.1.1 Absorption

During absorption [2, 3], i.e. interactions of photons with matter at the solid or liquid surfaces or in the plasma volume, the optical energy of the laser beam is partially converted into heat. The heat so generated drives the thermodynamics of the welding process. In deep penetration laser welding absorption is a highly complex mechanism [4] composed of contributions from the direct absorption of the laser beam at the keyhole wall (the main governing mechanism), absorption during multiple scattering, absorption in the metal plasma and absorption at the top surface of the work piece. The remaining part of the laser beam radiation is lost by reflection at the surface, multiple back reflections through the top of the keyhole and transmission through the keyhole; the last only applies when the keyhole penetrates right through the work piece. The amount of absorbed energy is most simply expressed as the product of the incident laser beam power multiplied by an overall absorptance. The latter is usually quoted as a percentage, and is sufficient for simpler

Table 3.1. Notation.

Symbol	Units	Meaning	Symbol	Units	Meaning
A	%	absorptance	r_f	m	focal radius
A_w	m^2	weld cross section area	r_{kh}, R_{kh}	m	keyhole radius
c_p	$\mathrm{J\,kg^1\,K^{-1}}$	specific heat capacity	r_L	m	laser beam radius
c_p^*	$\mathrm{J\,kg^{-1}\,K^{-1}}$	artificially enhanced specific heat capacity	t	s	time
D	m	sheet thickness	T	K	temperature
d_w	m	filler wire diameter	T_a	K	ambient temperature
E_L	J	laser beam pulse energy	l	–	subscript for liquid phase, liquidus
h_c	$\mathrm{W\,m^{-2}\,K^{-1}}$	convective heat transfer coefficient	s	–	subscript for solid phase, solidus
i	–	radial index	v	–	subscript for evaporation
I_{ij}	$\mathrm{W\,m^{-2}}$	beam power density at i,j	v	$\mathrm{m\,s^{-1}}$	welding speed
I_L	$\mathrm{W\,m^{-2}}$	laser beam power density	v_w	$\mathrm{m\,s^{-1}}$	filler wire feeding rate
I_{La}	$\mathrm{W\,m^{-2}}$	absorbed beam power density	w_g	m	joint gap width
$\mathrm{I_0(\ )}$	–	modified Bessel function of first kind, zero order	x	m	coordinate in welding direction
j	–	time index	x_f	m	keyhole front location
k	–	index	x_r	m	keyhole rear location
K	$\mathrm{W\,m^{-1}\,K^{-1}}$	thermal conductivity	y	m	coordinate lateral to welding
$\mathrm{K_0(\ )}$	–	modified Bessel function of second kind, zero order	z	m	vertical coordinate
$\mathrm{K_1(\ )}$	–	modified Bessel function of second kind, first order	β	–	vertical keyhole wall angle
L_m	$\mathrm{J\,kg^{-1}}$	latent heat of melting	δ	–	ellipsis, aspect ratio of the axes
Pe	–	Péclet number	ε	–	emissivity factor
Pe_f	–	Péclet number at keyhole front	ρ	$\mathrm{kg\,m^{-3}}$	specific mass density

Table 3.1. *Continued*

Symbol	Units	Meaning	Symbol	Units	Meaning
P_L	W	laser beam power	σ_{SB}	$\mathrm{W\,m^{-2}\,K^{-4}}$	Stefan-Boltzmann constant
q_v	$\mathrm{W\,m^{-2}}$	heat flux at the evaporation front	η	–	ellipsis, azimuthal angle
R	m	radial coordinate	κ	$\mathrm{m^2\,s^{-1}}$	thermal diffusivity

modelling such as the moving point source or moving line source models. For more accurate study of heat conduction, however, the spatial (and temporal) distribution of the absorbed laser beam power across the keyhole wall surface is also of importance. Models in which a point and a line source of heat are superimposed [5], or several point sources are superimposed [6], take this into account. Other models implicitly calculate the distribution of the absorbed power [4], as will be described below.

In particular, the absorptivity of a material (at any location) is determined by its optical constants n and k that are functions of the material, the laser wavelength, the temperature, and the angle of incidence. Moreover, the surface topography and chemistry (usually in the form of oxides) alter the local absorptance [7, 8].

For a given temperature distribution of the absorptivity, the absorptance distribution as a function of space and time will result iteratively from the temperature field that is generated. During the initiation of laser welding (and during pulsed laser welding) the absorptance and its influence on the heat conduction can be calculated from a semi-analytical mathematical model [4], described below.

3.1.2 Heat Conduction and Convection

The heat generated by absorption is conducted into the metal sheets by thermal conduction accompanied by convection, i.e. relative motion of the material, in particular the welding speed.

For an established quasi-steady state keyhole during cw-laser welding the temperature field is governed by conduction of the absorbed laser beam power (distributed over the keyhole wall) and by convection at the welding speed and accompanying melt pool motion.

Steady State 3D-Solutions Based on Moving Point Sources of Heat

For constant welding speed, frequently used simple models [9, 10] are the moving point source of heat

$$T\left(x,y,z\right) = T_a + \frac{2AP_L}{Kr} \exp\left(-\frac{v\left(x+r\right)}{2\kappa}\right)$$

with $r = \sqrt{x^2 + y^2 + z^2}$ and the moving line source of heat,

$$T(x, y) = T_a + \frac{AP_L}{d2\pi K} \exp\left(-\frac{vx}{2\kappa}\right) K_0 \left(-\frac{v\sqrt{x^2 + y^2}}{2\kappa}\right),$$

where $K_0(\ )$ is the modified Bessel function of the second kind and zero order.

As a result of the singularity at the origin, these solutions are inaccurate close to the heat source. A more accurate solution (without the singularity) is given by the moving Gaussian source of heat, see [11], where integration involving a Green's function takes into account an absorbed laser beam power density of Gaussian character. A numerical integral has to be evaluated, but in contrast to the moving point source the beam radius is taken into account, giving solutions that are quite accurate even close to the laser beam. This model was extended by superposition [12] of different Gaussian distributions at the surface, making it possible to model almost any arbitrary cw beam power density distribution, such as line-shaped beams, doughnut beams or other multimode beams. The method has proved to be very powerful. In particular, it was demonstrated that approximating higher order modes by a Gaussian beam can under certain circumstances cause fundamental errors.

A very flexible approach is the superposition of moving point sources of heat enabling the simulation of more complex temperature fields and shapes [6], particularly vertical heat flow, as illustrated in Fig. 3.1:
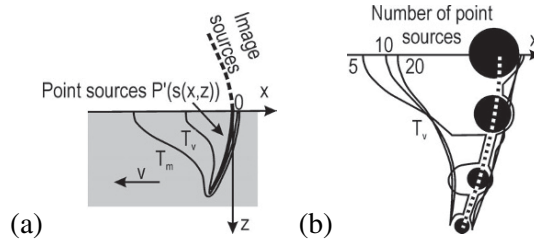
Fig. 3.1. Model of superposition of moving point sources of heat and resulting isotherms: (a) melting and evaporation isotherm, (b) evaporation isotherm dependent on the number of sources employed.

This model approach is suitable for many different complex situations, e.g. for conduction-like laser welding, Fig. 3.2a, or for deeper partial penetration welding, Fig. 3.2b, where the upper region is dominated by planar 2D-heat flow, while the lower region is governed by 3D-heat flow. Figure 3.2c shows homogeneously distributed heat sources, resulting in planar flow behaviour, while a nail-shaped weld penetrating completely through the work piece, as in Fig. 3.2d, has the opposite behaviour to Fig. 3.2b. Twin-sided simultaneous welding with two nail-head shapes is shown in Fig. 3.2e.

The method of superimposing moving point sources of heat nevertheless produces a great many simplifications, but it allows the straightforward
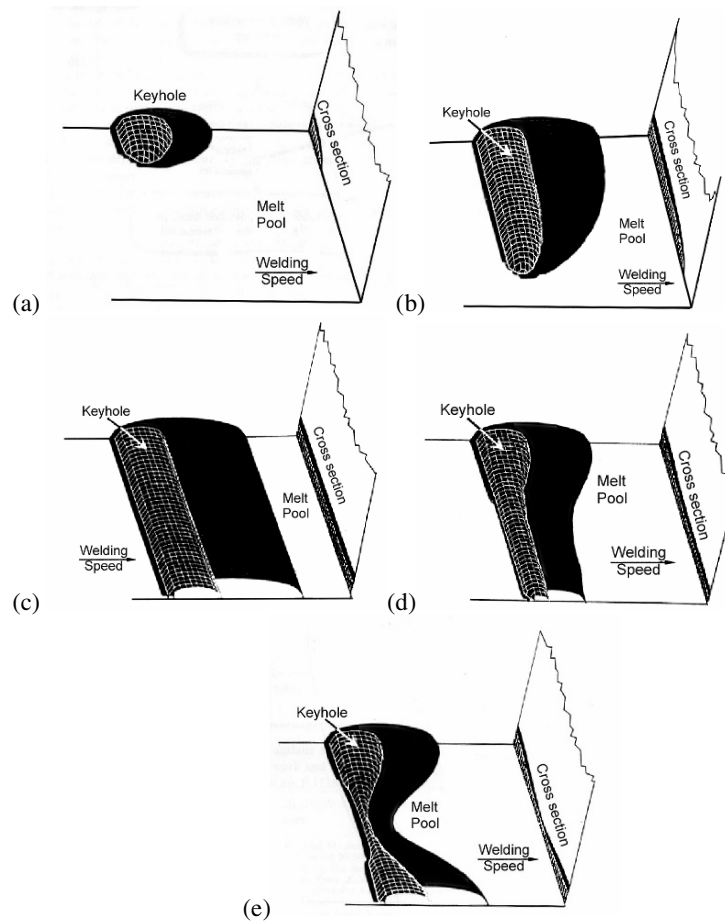
Fig. 3.2. Calculated shape of the melt pool and keyhole based on superposition of moving point sources of heat: (a) low power (500 W), not welded through, (b) moderate power (1500 W), not welded through, (c) high power (2500 W), welded through, (d) welded through, widening at the top, (e) widening at top and bottom (e.g. twin-sided welding). *Reprinted from* [6], *copyright (1998) with permission from Old City Publishing.*

creation of reasonably realistic temperature fields, and in turn cooling rates; the latter are of importance in the calculation of the metallurgical behaviour, for example.

Steady State 2D-Heat Conduction from a Moving Cylinder at Constant Temperature

Another powerful analytical solution is the moving cylinder (the keyhole cross section), where the surface of a cylinder is set at a constant temperature; this

might be the evaporation temperature in the case of a keyhole. An analytical expression [13] describes the accompanying planar temperature field $T(x, y)$ which only depends on the Péclet number

$$\mathrm{Pe} = \frac{vR}{2\kappa},$$

where R is the keyhole radius, v the welding speed and κ the thermal diffusivity. This model assumes a certain keyhole, thus the power per unit depth results (from the heat flux, i.e. the azimuthal integration of the normal temperature gradient at the boundary). More sophisticated is the assumption of a moving ellipse [14] instead of a cylinder, providing an additional geometrical parameter of freedom. The calculated dimensionless heat flux q at the ellipse (keyhole wall) as a function of the azimuthal angle η is shown in Fig. 3.3 for different Péclet numbers Pe and elliptical aspect ratios $\delta = a/b$, if a is a coordinate in the welding direction and b a coordinate perpendicular to it.

As can be seen, the aspect ratio δ of the ellipse has some influence on the azimuthal heat flux distribution, while high Péclet numbers lead to a strong azimuthal asymmetry. For an ellipse that is strongly elongated in the lateral direction, Fig. 3.3b, the maximum heat flux is no longer located at the leading edge, but at the side.

A highly accurate solution for the temperature field $T(x, y)$ in the horizontal plane can be computed numerically, as has been done by several authors for a given (usually circular) keyhole cross section, e.g. by the Finite Control Volume Method; here, 2D-melt flow around the keyhole was taken into account [15] as will be described later. Figure 3.4 shows the resulting isotherms of the temperature field in the melt pool, calculated for steel for a keyhole diameter of $200\,\mu$m and a welding speed of $3\,$m/min. Comparison with the (thermodynamically identical) analytical solution for the moving cylinder shows very good numerical agreement as long as the melt flow speeds are not too high. Nevertheless, in addition to the melt flow, the numerical solution can take into account the latent heat of melting and temperature dependent material properties. For higher speeds and more intense melt flow, numerical analysis can explain the sharp rear shape of the resolidification isotherm rather than the round one seen in Fig. 3.4.

Sophisticated Quasi-3D-Model Based on the Moving Line Source of Heat

The keyhole geometry can be calculated [4, 15] in the x, z-plane point-by-point by applying a local energy balance between the incident laser beam radiation,

$$I_L(r, z) = \frac{2P_L}{r_f^2(z)\,\pi} \exp\left(-\frac{2r^2}{r_f^2(z)}\right),$$

and the heat flux required locally to reach evaporation temperature at a given welding speed. The heat flux is derived from the moving line source model
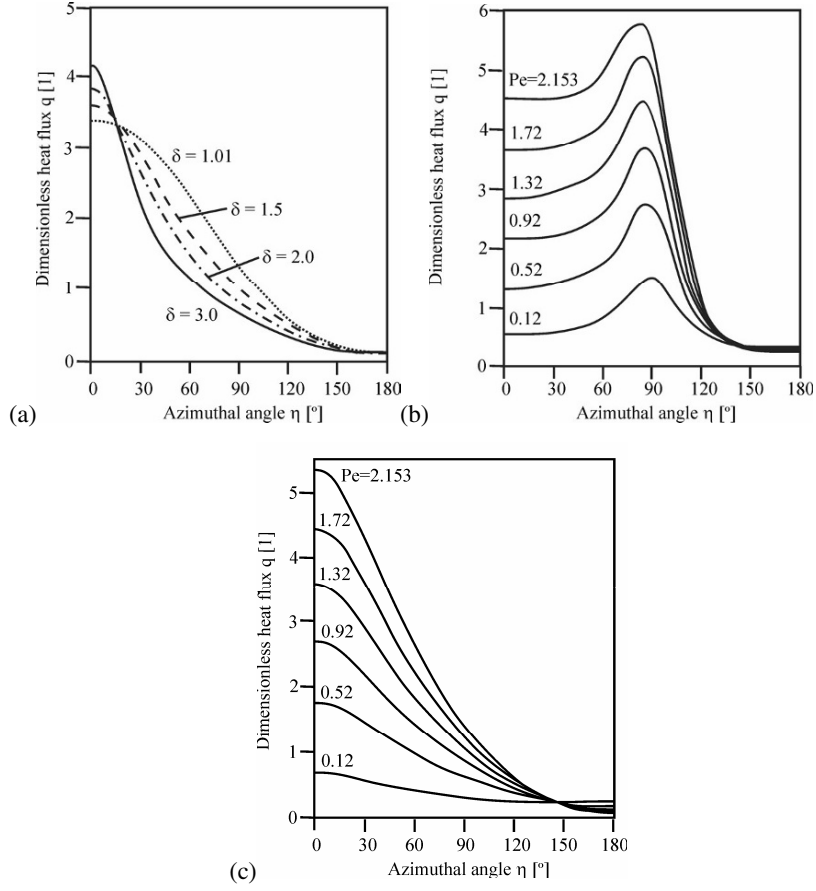
Fig. 3.3. Calculated results of the dimensionless heat flux at the surface as a function of the azimuthal angle for the model of a moving ellipse at constant surface temperature: (a) different elongation aspect ratios δ of the ellipse for Pe = 1.32, (b) different Pe-numbers for a laterally elongated ellipse (keyhole) with δ = 0.25 and (c) for a longitudinally elongated ellipse with δ = 1.5. *Reprinted from* [14], *copyright (1997) with permission from Institute of Physics Publishing Ltd.*

of heat flow (applied in each plane of vertical discretisation, by matching the length of the evaporation isotherm), for example, at the front wall of the keyhole to

$$q_{v,front}\left(x_f\right) = (T_v - T_a)\,\frac{\rho c_p v}{2}\left[1 + \frac{\mathrm{K}_1\left(\mathrm{Pe}_f\right)}{\mathrm{K}_0\left(\mathrm{Pe}_f\right)}\right],$$

where

$$\mathrm{Pe}_f = \frac{vx_f}{2\kappa}$$

is the Péclet number for the keyhole front wall location $x_f(z)$.
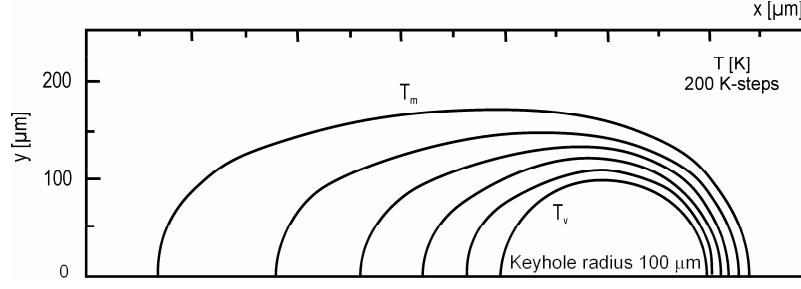
Fig. 3.4. Isotherms of the temperature field accompanying a circular moving keyhole, calculated by the FCV-method (keyhole diameter $2r_{kh} = 200\,\mu$m, welding speed $v = 3\,$m/min, low C steel) [15].

With the use of approximations to the value of the Bessel function, simplified expressions can be derived for the heat flux at the front and rear side, respectively:

$$q_{v,front} = (T_v - T_a)\frac{\rho c_p v}{2}\left[2 + \left(\frac{vR_{kh}}{2\kappa}\right)^{-0,7}\right]$$

and

$$q_{v,rear} = (T_v - T_a)\frac{\rho c_p v}{2}\left(\frac{vR_{kh}}{2\kappa}\right)^{-0,7}.$$

The fluxes of the absorbed beam power (taking into account different absorption mechanisms) and the heat flux (required for maintaining the evaporation temperature) are balanced by the angle of inclination $\beta(z)$ of the keyhole wall, calculated separately at the front and rear walls:

$$A\left(\beta\right)I_L\left(x,z\right) = q_v\left(R_{kh}\left(z\right)\right)\tan\left(\beta\left(z\right)\right);$$

$A(\beta)$ can take into account different absorption contributions, in particular the local angle-dependent Fresnel-absorption.

In each horizontal plane the keyhole wall angle and the approximate temperature field can be calculated, making use of the vertical discretisation. The keyhole geometry described by $x_f(z)$ and $x_r(z)$ is found by integration from both sides, $+x$ and $-x$ at $z = 0$, towards incrementally lower x- and higher z-values respectively. At each location the keyhole wall angle $\beta(z)$ in the xz-plane is calculated from the above energy balance, enabling successive calculation of the keyhole shape from the top surface until both curvatures meet at the bottom of the keyhole (or until they end at the bottom surface of the work piece).

The model consists of many submodels [4, 15] that allow high modelling flexibility [16] in choosing between high accuracy and simplicity.

The fluid flow as well as phenomena related to pressure at the rear wall of the keyhole are not taken into account in this model. A simplified estimate of

the extension of the weld pool caused by thermocapillary flow was developed by introducing an enhanced thermal conductivity in the upper region [17].

3.1.3 Surface Convection and Radiation

The absorbed laser power generates a distributed heat source as the governing boundary condition for the heat flow. Conservation of energy for quasi-steady state conditions requires equivalent heat losses at the boundaries. During laser materials processing, however, the heat input is highly concentrated and thus dominant, while the heat losses are distributed over large surface areas and have therefore a less significant influence on the temperature field. In contrast, the main cooling mechanism locally affecting heat conduction is dispersion of heat into the surrounding extended metal sheet, which remains close to room temperature. The heat can dissipate freely within the work piece and infinite sheet size is often a valid approximation. This divergent flow is seen to be dominant when compared to flow across the surface boundaries resulting from forced gas convection and thermal radiation. Moreover, the method of clamping the work piece can significantly conduct off heat, leading to a complex three-dimensional heat flow.

Losses by surface convection to the ambient atmosphere or, in particular, to the shielding gas flow, can be taken into account in a linear manner by introducing a heat transfer coefficient h_c, which must be determined empirically:

$$-K\nabla T = h_c \left(T - T_a \right).$$

The hot metal vapour or plasma streaming out of the keyhole in deep penetration laser welding [4, 15] can have the opposite effect of conducting additional heat to the surface. As known from high speed imaging, this flow is rather unpredictable and fluctuates considerably; it is not yet well understood.

The same boundary condition can be additively extended to include radiative surface losses by thermal emission obeying the Stefan-Boltzmann law (according to Planck's radiation law):

$$-K\nabla T = \varepsilon \sigma_{SB} \left(T^4 - T_a^4 \right).$$

However, the absolute magnitude of convective and radiative surface losses is so small (a few Watts) that it is often neglected and a simple no-heat-flux boundary condition is applied:

$$\mathbf{n} \cdot \nabla T = 0$$

where $\mathbf{n}$ is a vector in the normal direction. Only in exceptional circumstances is any boundary of the work piece close to the processing zone, causing a significant stagnation of the heat flow and a corresponding increase in temperature. For analytical heat source models the method of mirror images can be applied to simulate a no-heat-flux condition across an edge in an easy manner [6, 9, 18]. However, normally the metal sheets provide sufficiently large regions around the processing zone to enable wide dissemination of the heat flow.

3.1.4 Phase Transformations

During laser materials processing a series of phase transformations can take place, often in both directions: melting and resolidification, evaporation and condensation, metallurgical phase transformations (e.g. from ferrite to austenite and vice versa), or chemical reactions (e.g. oxidation). According to the direction of evolution of enthalpy and Gibb's free energy, phase transformations either liberate or consume energy. In a temperature field, this source or sink of energy through phase transformations leads to a corresponding jump of the temperature gradient; in a medium at rest which does not change density as a result of the change,

$$-K_s\mathbf{n} \cdot \nabla T_s = -K_l\mathbf{n} \cdot \nabla T_l + \rho v L_m$$

where v is the normal velocity of the phase-front in the direction $\mathbf{n}$, the unit normal to it. In FEM-simulations it is common to introduce an artificially increased (or lowered) heat capacity in a narrow temperature interval around the phase transformation temperature to simulate the consumption (or generation) of heat:

$$c_p^* = \frac{L_m}{T_l - T_s};$$

see also Chapter 7. For analytical modelling very few solutions can take this phase transformation discontinuity into account. A generally applicable method that, however, has to be checked case by case with regard to accuracy and thus applicability, is an enthalpy transformation. The boundary problem is expressed in terms of enthalpy h instead of temperature T, i.e. an existing analytical solution for the T-field is expressed as an h-field instead. The resulting enthalpy field can then be transformed to a temperature field as shown in Chapter 7, inducing an artificial plateau at the phase transformation temperature for simulating the phase transformation.

It is easier to handle phase transformations at the surface, e.g. evaporation corresponds to heat flux losses that can often be directly subtracted from the absorbed power density of the beam, simply lowering the boundary condition [18].

3.1.5 Transient and Pulsed Heat Conduction

Transient conditions take place during pw-laser welding, during process initiation and termination, when there are strongly varying conditions (in the product geometry, for example), during process oscillations, etc. In many situations the quasi-steady-state conditions are sufficiently representative. For oscillating conditions powerful techniques for the solution of the heat conduction equation have been developed [13, 19], particularly by expanding the steady state solutions of moving sources of heat to allow for oscillating conditions. Another method to treat oscillating conditions as well as stability
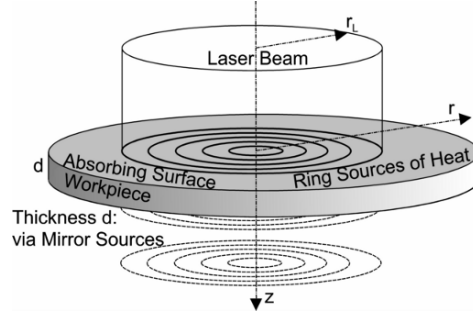
Fig. 3.5. Mathematical model [18] and geometry of pulsed heating of a (laterally infinite) work piece by a circular laser beam, by superposition of instantaneous ring sources of heat of different radius and energy, including mirror sources for the finite sample thickness d. *Reprinted from [18], copyright (2005) with permission from Elsevier.*

criteria is the perturbation method that does not require a quantitative numerical solution of the physical state. Instead it focuses on dynamic behaviour, particularly the stability of oscillations.

Model for Initiation of Laser Spot Welding

For single pulse laser welding (spot welding, with no relative motion) a model was developed [18] that calculates heat conduction for a flat-surfaced work piece (i.e. before keyhole drilling) by taking into account the surface absorptance $A(r,t)$ as a function of space and time, as a result of the temperature dependence of the absorptance, $A(T)$. If the solution for an instantaneous ring source of heat [10],

$$T_{ij}\left(r, z; t\right) = \frac{\Delta Q_{ij}}{8\rho c_p \left(\pi\kappa\left(t - t_j\right)\right)^{3/2}} \exp\left[-\frac{r^2 + r_i^2 + z^2}{4\kappa\left(t - t_j\right)}\right] I_0\left(\frac{rr_i}{2\kappa\left(t - t_j\right)}\right),$$

is used, superposition of such individually matched ring sources

$$\Delta Q_{ij} = 2A_{ij}I_{ij}2\pi r_i\Delta r_i\Delta t_j$$

in space (radius r_i) and time (instant t_j), by integrating over the radial coordinate as shown in Fig. 3.5, and iteratively over time, allows calculation of the resulting temperature field (discretised formulation of the corresponding integral):

$$T\left(r, z; t\right) = T_a + \sum_j \sum_i T_{ij}\left(r, z; t\right) + \sum_k \sum_j \sum_i T_{ij}\left(r, z - 2kd; t\right)$$

The finite thickness d of the work piece (assumed laterally infinite) is taken into account by the method of mirror sources [9]. In the calculation each ring
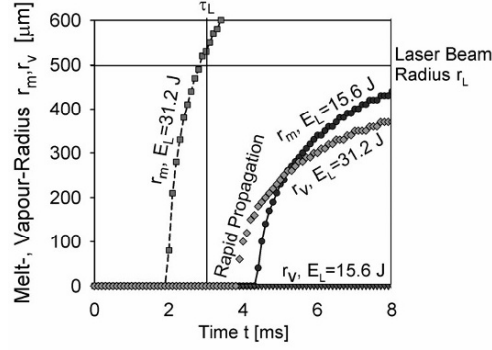
Fig. 3.6. Calculated radius, r_m and r_v, of the surface melting and evaporation domains as a function of time for two laser pulse energies E_L. *Reprinted from* [18], *copyright (2005) with permission from Elsevier.*

source has a portion ΔQ of energy and represents a radial interval Δr around the location r_i and a time interval Δt around the instant t_j of the entire absorbed heat input of the laser pulse.

It should be emphasised that this superposition provides a high degree of flexibility for modelling almost any (radially symmetric) power density distribution in space (beam profile $I_L(r)$) and time (pulse profile $I_L(t)$).

From the various calculated results in [18], one for AuNi-coated copper is shown in Fig. 3.6. For two laser beam pulse energies the melting radius at the surface is plotted as a function of time. For higher beam energies, the evaporation temperature will be reached and the development of the evaporation domain radius (assuming no changes in shape of the surface) is also shown.

The analysis allows detailed study of the absorptance as a function of space and time. A steep increase in the absorptance during melting (as the Au-layer disappears and the heated Cu increases its absorptance) significantly accelerates the heating process. Correspondingly, beyond the melting threshold the melting radius grows rapidly, making the process highly sensitive to disturbances. This was recognised as a source of unreliability and a serious industrial problem; it was possible to study it and performance was successfully improved by lowering the sensitivity of the surface conditions that in turn lower the absorptance. Figure 3.7 illustrates the theory for the initiation of pulsed laser welding, derived from the model. The impact of small absorbing pollutions (hot spots) and the threshold to keyhole formation can be explained, for example.

3.1.6 Geometry of the Liquid Pool

Heat conduction, along with convection, governs the geometry of the interface domains of the phase transformations, particularly the shape of the keyhole
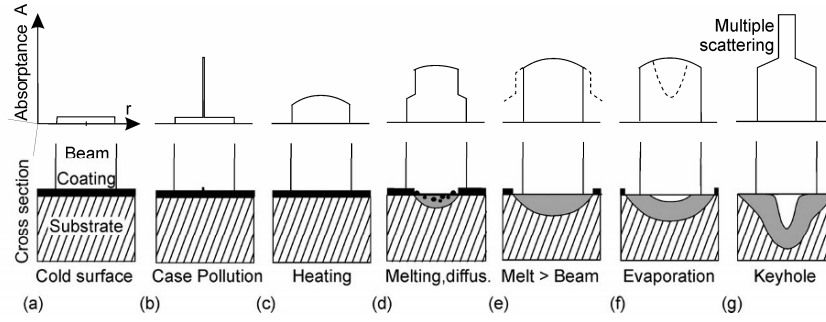
Fig. 3.7. Theory of the radial absorptance (upper figure) and material cross section (lower figure) for seven different stages of pulsed laser processing: (a) room temperature, with correspondingly low absorptance, (b) central spot of high absorptance, (c) increased absorptance during heating, (d) diffusion of the coating during melting, (e) melt spot exceeding the beam size, (f) evaporation losses, (g) keyhole formation with multiple reflections enhancing the absorptance. *Reprinted from* [18], *copyright (2005) with permission from Elsevier.*

and of the molten pool during laser welding, but also the Heat Affected Zone. The cross section achieved during the process, which is often a design goal, is a projection of the three-dimensional interface, e.g. the weld seam shape or the hardened track. Moreover, the temperature gradients at the interface determine the metallurgical structure. Another important role of the geometry of the melt pool is its influence on fluid flow, which is determined by its inner shape - the keyhole wall - and its outer shape, the solid-liquid interface.

For low welding speed when the Péclet number is small, heat conduction dominates over convection and the isotherms are close to a rotationally symmetric shape around the laser beam axis and the conditions are correspondingly less constrained.

In contrast, at high speed the isotherms become significantly asymmetric and elongated; see for example Fig. 3.2 and Fig. 3.4, even though the speed is only moderate. The fluid flow and vapour conditions become highly constrained by strong directional forces and mechanisms.

Mass Balance of a Welding Joint

Figure 3.8a illustrates a typical laser butt weld cross section. The shape of the weld cross section is governed to first order by conservation of mass (cross section area). For the case shown here of zero gap, material has flowed down due to root drop-out as is typical for aluminium welds due to its physical properties, such as large melting interval and low viscosity; material is therefore missing at the top surface, leading to depletion or undercut. An increasing of the average gap width, as seen in Fig. 3.8b, would correspondingly increase the material deficit (cross section area) and in turn the trend to undercutting at the top surface, independently of the process itself. In contrast, the addition
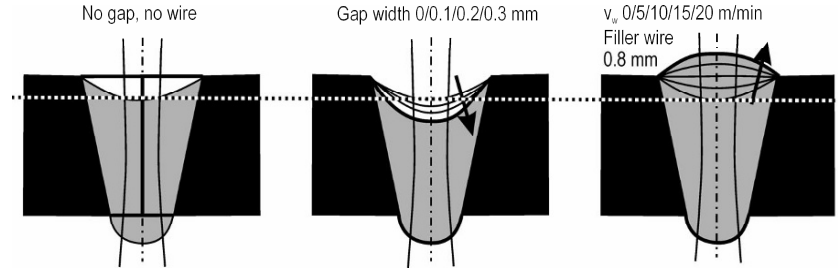
Fig. 3.8. Calculated weld seam cross section for (a) zero gap, (b) different gap widths, (c) different filler wire speed v_w (wire diameter 0.8 mm).

of filler wire (either cold wire or arc-augmented wire-addition during hybrid welding), as shown in Fig. 3.8c, raises the top surface, avoids undercutting and permits shape reinforcement of a desired height.

The cross sectional area added by wire feeding depends on the process. It is proportional to the wire feeding rate and inversely proportional to the welding speed, and is thus governed by the ratio v_w/v. The change in the cross section area of a weld by the above two phenomena can be expressed by a mass balance (reformulated in terms of area):

$$\Delta A_w = \frac{d_w^2 \pi v_w}{4v} - w_g d.$$

While butt and overlap joints (mostly) correspond to highly symmetric conditions in the processing direction, other joint geometries lead to lateral asymmetry, as in the case of fillet joints or tailored blanks, which often makes mathematical modelling more difficult.

The liquid pool geometry is one of the main links between heat conduction and melt flow and plays an essential role in the phenomena discussed in the following section.

3.2 Melt Flow

The shape of the melt pool as defined by the keyhole (the liquid-vapour interface), its melting and resolidification front (the solid-liquid interface) and its surface (the liquid-gas interface) is mainly the result of heat conduction, accompanied by convection caused by the relative motion of the work piece and the laser beam and various melt flow phenomena.

For the most common case of cw-laser welding heat conduction leads to quasi-steady state conditions relative to the laser beam. Besides free surface conditions, certain phenomena, such as evaporation at the keyhole wall or flow of the shielding gas, govern the fluid mechanical boundary conditions of the melt pool that in turn induce melt pool motion. Although the melt
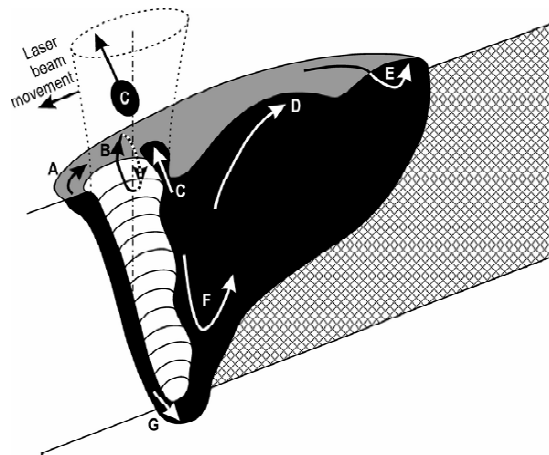
Fig. 3.9. Different melt flow phenomena during laser welding: A: melt passing around the keyhole, B: Marangoni flow, C: drop ejection, D: humping, E: rear flow stagnation, F: inner eddies, G: root drop-out.

flow is usually considered relative to the keyhole for the sake of simplicity (so that a coordinate system moving with the laser beam, keyhole and melt pool is generally used), it should not be forgotten that this relative motion is superimposed on the welding speed. This means eddies induced by Marangoni flow, for example, are really of spiral type viewed relative to the work piece.

For pw-laser welding, and in particular for single pulse laser welding, the conditions are highly transient and even more complex. One example, namely the keyhole collapse [20] during single spot laser keyhole welding that often ends in the formation of a pore, is described in Chapter 7. Spatter ejection during drilling of the keyhole is also typical, as the transient conditions are not in balance, in contrast to cw-laser welding, and often lead to a considerable excess of evaporation recoil forces that accelerate the melt. Pulsed conditions also take place during laser hybrid welding where periodically drops detach from the feeding wire that move towards the melt and interact with it.

Inside the melt pool different types of melt flow can take place. A number of important flow phenomena selected are illustrated in Fig. 3.9 and will be briefly described in the following.

A. Melt flow redirected to pass around the keyhole.
B. Marangoni flow driven by surface tension gradients.
C. Uncontrolled violent melt motion and drop ejection behind the keyhole.
D. Humping due to accumulating downstream flow.
E. Stagnation point for accelerated flow, causing undercuts and a central peak.
F. Inner eddies, driven by vertical downstream flow at the keyhole rear wall.
G. Root drop-out by gravity and by the keyhole front film ejected by ablation pressure.

3.2.1 Melt Flow Passing Around the Keyhole

For an established keyhole the welding speed drives the molten material towards the keyhole front. As only a small portion of the upstream melt evaporates, conservation of mass and the reduction of the melt flow cross section through the keyhole requires acceleration to take place so that the melt can pass around or under the keyhole; the process is illustrated as mechanism A in Fig. 3.9. The driving force for this acceleration is the evaporation recoil pressure at the front of the keyhole, controlled by the incident laser beam power and by the local keyhole wall angle. As a regulating mechanism, the more the upstream melt tries to push the keyhole front wall forward, the more strongly is the laser beam locally absorbed; the keyhole wall reacts by evaporation and through the resulting ablation recoil pressure.

Numerical 2D-Simulation of the Melt Flow Around a Prescribed Keyhole Shape

The melt flow around the keyhole can be computed by numerical simulation, as will be presented using the method of Finite Control Volumes (FCV, very suitable for developing one's own tailored fluid mechanical codes). Reduce the problem to one in a horizontal plane (xy-coordinates) and assume a cylindrical keyhole of prescribed diameter (assumed to resist the melt motion by reason of its shape, which is maintained in reality by evaporation and the fluid pressure of the escaping vapour), the melt pool shape and the flow conditions can then be calculated for these simplified conditions; the results depend solely on the keyhole diameter, the welding speed and the material.

The temperature field and the resulting shape of the melt pool have already been shown in Fig. 3.4. Figure 3.10 shows the computed [15, 21] melt flow field (upper half: velocity vectors, lower half: lines of constant speed) for steel, with a keyhole diameter of $200\,\mu$m, and at a speed of $3\,$m/min.

It shows a rather narrow melt film in front of and beside the keyhole. High velocities are therefore required in these regions to maintain the mass balance. In the large melt pool behind the keyhole the melt slows down again before resolidification.

At lower speed the melt pool becomes wider. In particular the channel between the keyhole and the melting isotherm becomes wider, thus causing a less constrained flow of lower speed. For a larger keyhole a very narrow channel can result where a high pressure develops in order to drive the melt around the keyhole, to ensure conservation of mass. The high speed generated can lead to phenomena such as surface waves, undercuts with central peaks (mechanism E in Fig. 3.9) and humping (mechanism D in Fig. 3.9). Materials with higher thermal conductivity or with a larger difference between the melting and boiling temperatures like aluminium provide a much wider channel compared to steel for otherwise identical conditions. Correspondingly, relatively little
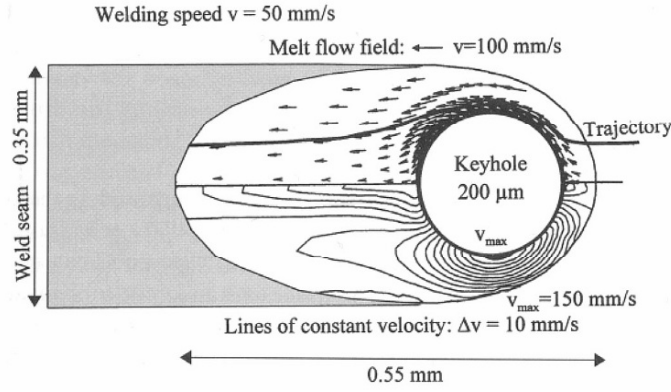
Fig. 3.10. Melt flow field (upper) and lines of constant speed (lower) calculated by the FCV-method for steel, $v = 3\,\mathrm{m/min}$, $2r_{kh} = 200\,\mu\mathrm{m}$ [15, 21].
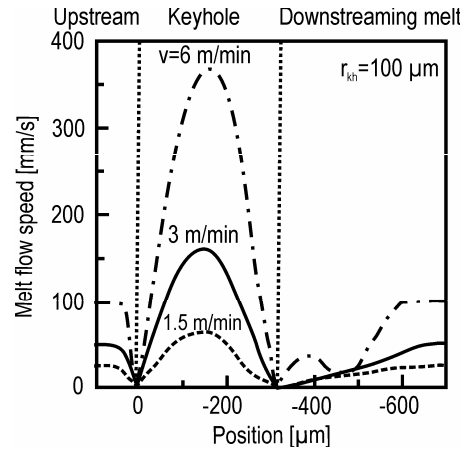
Fig. 3.11. Calculated (FCV-method) melt flow speed at the centreline ($y = 0$, position x) and along the keyhole wall when flowing around a cylindrical keyhole of diameter $2r_{kh} = 200\,\mu\mathrm{m}$, for three welding speeds v (low C-steel) [15].

acceleration is caused; nevertheless, the processing of aluminium is usually very unstable, because of the low viscosity, low surface tension, etc.

The high speed is a result of steep pressure gradients in the melt that in turn are caused by evaporation at the keyhole front. The evaporating keyhole front has a self-regulating mechanism for continuously redirecting the upstream melt laterally around the keyhole. The resulting speed of the melt at the centreline of the melt and along the keyhole boundary is plotted in Fig. 3.11; x is positive in front of the keyhole, $x = 0$ to $x = -314\,\mu\mathrm{m}$ is along one half of the keyhole circumference, and $x < -314\,\mu\mathrm{m}$ is behind the keyhole, for three different welding speeds.
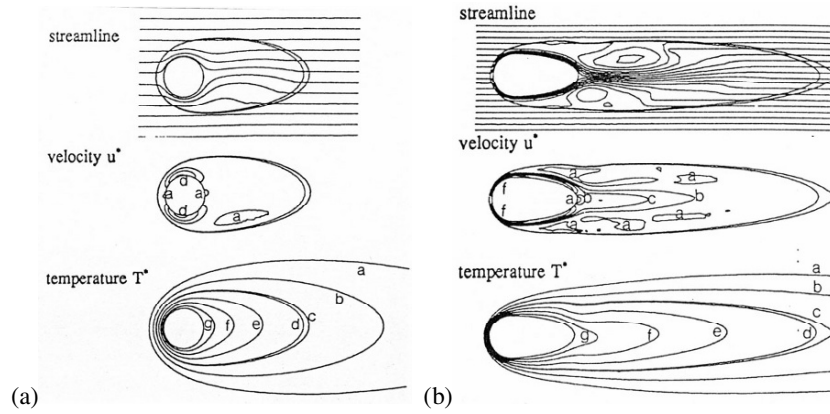
Fig. 3.12. Calculated (FE-method) streamline, velocity and temperature for (a) cylindrical keyhole, $2r_{kh} = 200\,\mu$m, $v = 5\,$m/min, Fe, (b) elongated keyhole, width $100\,\mu$m, length $250\,\mu$m, $v = 15\,$m/min, Fe; legend velocity u*: a = 0.5, b = 2, c = 3, d = 4, e = 5, f = 7, g = 9; legend temperature T*: a = 0.6, b = 0.8, c = 0.99, d = 1.01, e = 1.2, f = 1.4, g = 1.6 [22].

The narrow channel between the keyhole and the melt front, and the correspondingly constrained flow, can have a significant impact on several melt flow phenomena. Despite the highly non-linear nature of viscous fluid flow, the flow behaviour around the keyhole often follows a fairly regular behaviour, as can be seen from Fig. 3.11. Based on the stagnation pressure of the welding speed v,

$$p_{d0} = \rho\frac{v^2}{2},$$

a general linear approach to finding the pressure along the keyhole can be formulated [15]. Behind the keyhole the melt slows down again in the large melt pool followed by resolidification. Various simulations with somewhat differing results can be found in the literature for this boundary value problem. Figure 3.12 shows the streamlines and absolute velocity values of an FE-based flow field calculation [22] and the corresponding temperature field.

For a circular keyhole and low speed, Fig. 3.12a, the flow is similar to the above results, although a slight jet remains in the wake. For high welding speed, see Fig. 3.12b for an elongated keyhole, the acceleration beside the keyhole leads to strong jets that have a significant impact on the wake and can in practice cause humping (mechanism D), i.e. the formation of large, regular drops at the weld surface. Even for moderate welding speed the accelerated flow can significantly affect the resulting shape of the weld, by the formation of a central peak for example, accompanied by undercuts; see mechanism E in Fig. 3.9 (described below) that can originate from the mechanism A described above. Recently, thanks to more computation power being available, even three-dimensional simulations were successfully carried

out [23, 24], making it possible to explain further phenomena such as the formation of vortices, induced for example by Marangoni flow, which lead to three-dimensional trajectories, or the separation of the keyhole during overlap welding with a gap.

3.2.2 Marangoni Flow Driven by Surface Tension Gradients

A phenomenon well known from arc welding is thermocapillary flow or Marangoni convection, often calculated by numerical methods [25]. This kind of flow is driven by surface tension gradients which impose a boundary condition of shear force type on the melt flow; this gradient is generated by the temperature dependence of the surface tension. A negative temperature coefficient for the surface tension is the more common case, which results in a lower surface tension in the middle of the melt pool and a higher surface tension towards the solid-liquid boundary. A corresponding flow develops radially outwards. Conservation of mass combined with the necessary existence of a stagnation point at the solid-liquid interface results in eddies developing in which the melt flows downwards (the possibility of upward flow is limited by surface tension). It then returns to the centre in deeper regions and flows up again; see mechanism B in Fig. 3.9. This kind of eddy (due to the fact that welding speed eddies become advancing spirals) supports heat conduction radially away from the keyhole, thus widening the weld pool and making it more shallow. This mechanism may be one of the origins for the often typical nail shape (or wine glass shape) of the weld. While FEA computation enables highly accurate solutions, the widening can be taken into account in relatively simple models as well, by introducing (and matching) an increased thermal conductivity [17], for example, or by superimposing artificial point sources of heat [5, 6].

Under certain circumstances, namely if the temperature coefficient of the surface tension is positive (as in the case of the addition of surface active elements such as sulphur or oxygen to steel, for example), the flow is directed in the opposite direction, so that at the surface it flows towards the centre of the melt pool where it is redirected downwards, leading to deeper weld pools. Combinations of both directions of flow can take place in the same melt pool.

Marangoni convection is a complex but important phenomenon which is always present and often dominant during laser welding. Today, high speed imaging allows a better understanding of this mechanism and its interaction with the other melt pool flows.

3.2.3 Uncontrolled Violent Melt Motion and Drop Ejection Behind the Keyhole

While the location of the front wall of the keyhole is strongly controlled by interaction with the absorbed laser beam, the position of the rear wall is less well determined. The wall more or less reacts to the developing vapour

pressure that keeps the keyhole open against surface tension contraction. The rear keyhole wall is the boundary to the weld pool at the rear side, where the melt extension is much larger compared to the thin region in front of and beside the keyhole.

Different complex flow phenomena were revealed behind the keyhole, both through numerical FEA simulation [26] and through high speed imaging [26, 27]. In particular, these flows under rather uncontrolled (large pool) boundary conditions often turn out to lead to an upstream flow against the upper rear edge of the keyhole where drop formation is initiated. Depending on the violence of the melt flow, kinetic energy can dominate over surface tension and lead to the formation of necks and separation of droplets that are ejected as spatter [26, 27]; see mechanism C in Fig. 3.9. Moreover, surface waves directed backwards into the melt pool can be generated. By employing a carefully adjusted gas jet directed at this edge to control the fluid dynamics (as opposed to ordinary shielding gas flow, which has less scope for control), it was recently demonstrated [26] that this uncontrolled behaviour can be tamed, leading to a very smooth flow without spatter. Moreover, slight inclination of the laser beam in or against the welding direction affects the flow and the amount of spatter ejection [27].

3.2.4 Humping Caused by Accumulating Downstream Flow

Humping is a phenomenon often experienced in laser welding, particularly at very high speeds. It is characterised by the regular development of large drops on the melt pool; see mechanism D in Fig. 3.9. These periodically resolidify at the top weld surface, thus leading to an unacceptable weld quality.

Recently, three different types of humping were distinguished [26]–[28]. In particular, strong acceleration of the melt under a blind keyhole followed by subsequent stagnation far behind the keyhole was observed at high welding speed with the aid of high speed imaging. Moreover, in contrast to (or in combination with) drops at the surface formed by humping, channels can form between the resolidifying drop and the lateral boundaries of the weld. In the weld seam they appear as cavities or severe undercuts.

3.2.5 Stagnation Point for Accelerated Flow, Causing Undercuts and a Central Peak

The weld often tends to a central peak so that there are undercuts at the sides; see mechanism E in Fig. 3.9. This effect is similar to humping, but less pronounced. It occurs when any melt flow is accelerated towards the resolidification front. It usually has a shape convergence towards the centreline, as in Fig. 3.10, for example, and makes resolidification at the sides of the weld pool more difficult. Instead, at the top surface the flow is redirected along the solid-liquid boundary towards the centreline where, due to flow from both sides, stagnation slows down and stops the flow, or redirects it vertically downwards

(and is forced upwards against the surface tension force; see mechanism E in Fig. 3.9), where it sooner or later will resolidify.

This phenomenon results in undercuts at the sides and a peak in the centre of the weld, as can be observed in the weld seam cross section. The cause of this phenomenon is the high speed of the melt that can be generated by the flow around the keyhole (mechanism A), by the Marangoni mechanism (mechanism B), by the different humping mechanisms (D) or by the shearing force of the shielding gas.

Besides trying to suppress high melt flow speeds by controlling the above mechanisms, a broader stagnation front at the resolidifying rear boundary can prevent this mechanism coming into effect, with its unwanted weld surface shape.

3.2.6 Interior Eddies, Driven by Vertical Downstream Flow at the Keyhole's Rear Wall

From high speed X-ray imaging with tracer particles [27] it was revealed that the melt can accelerate strongly vertically downwards in front of and particularly behind the keyhole. While the former can be explained by the stagnation situation and melt film ejection by ablation pressure, the latter is more difficult to imagine. Evidently, such a flow leads to eddies inside the melt pool, in order to satisfy mass conservation. Stagnation and redirection at the lower boundaries of the melt pool occurs, as shown for mechanism F in Fig. 3.9. This type of flow also has a transportation effect on bubbles near the keyhole bottom that can tend to become pores.

3.2.7 Root Drop-out by Gravity and the Keyhole Front Film Ejected by Ablation Pressure

As mentioned above, the melt film in front of and beside the keyhole is more strongly controlled (by the laser beam) than is the large melt pool. In particular, the evaporation recoil pressure at the keyhole wall continuously tries to maintain a balance against collapsing melt flow and surface tension forces.

The excess of recoil pressure from evaporation acts as a force on the melt film that causes vertical melt film ejection by ablation pressure in addition to the horizontal redirecting mechanism, A. Consequently, the melt can either be accelerated to the top or bottom. The former can cause spatter, which can be amplified by the impact of impinging droplets during laser hybrid welding, as observed by high speed imaging. The latter often leads to root drop out as illustrated by mechanism G in Fig. 3.9. It is caused by ablation pressure augmented by the gravitational force. Their effect is only partially balanced by the surface tension of the root droplet. Again, momentum imparted by incident drops during hybrid welding can also support the mechanism. The evolution of root drop-out together with surface lowering and wire addition has already been described in Section 3.1.6.

3.2.8 Concluding Remarks

While heat conduction phenomena during laser beam welding are easier to understand, with the exception of convection in the melt flow, the above account describes only some of the melt flow phenomena that can occur. For example, the description of another melt flow mechanism, in this case the collapse of the keyhole causing pores, can be found in Chapter 7.

The superposition of all these mechanisms and their non-linear fluid-mechanical nature leads to extremely complex conditions and flow fields that are today only partially understood. Mathematical modelling and simulation as well as high speed imaging are suitable methods for improved understanding and control of these phenomena; such understanding is important since these phenomena often determine the resulting weld quality.

References

1. Kapadia P, Dowden J (1994) Review of mathematical models of deep penetration laser welding. Lasers in Engineering 3(3–4): 187–280
2. Bergström D, Powell J, Kaplan A (2005) Laser absorption measurements in opaque solids. Proc NOLAMP 10. Luleå (S), Ed: Kaplan AFH, Luleå TU (S) 10: 91–116
3. Prokhorov AM, Konov VI, Ursu I, Mihailescu (1990) In: Laser heating of metals. Adam Hilger, Bristol (UK)
4. Kaplan A (1994) A model of deep penetration laser welding based on calculation of the keyhole profile. J Phys D: Appl Phys 27: 1805–1814
5. Steen WM, Dowden J, Davis M, Kapadia P (1988) A point and line source model of laser keyhole welding. J Phys D: Appl Phys 21: 1255–1260
6. Resch M, Kaplan AFH (1998) Heat conduction modelling of laser welding. Lasers in Engineering 7(3–4): 229–240
7. Bergström D, Powell J, Kaplan AFH (2007) The absorptance of steels to Nd:YLF and Nd:YAG laser light at room temperature. Appl Surf Sci 253: 5017–5028
8. Bergström D, Powell J, Kaplan AFH (2007) Light scattering and absorption in Gaussian random rough metal surfaces using the geometric optics approximation. J Appl Phys 101(11): 113504–113514
9. Rosenthal D (1946) The theory of moving sources of heat and its application to metal treatments. Trans ASME 48: 849–865
10. Carslaw HS, Jaeger JC (1959) Conduction of heat in solids. Oxford Clarendon, Oxford
11. Cline HE, Anthony TR (1977) Heat treating and melting material with a scanning laser or electron beam. J Appl Phys 48(9): 3895–3900
12. Kaplan AFH (1997) Surface processing by non-Gaussian beams. Appl Phys Lett 70(2): 264–266
13. Simon G, Gratzke U, Kroos J (1993) Analysis of heat conduction in deep penetration welding with a time-modulated laser beam. J Phys D: Appl Phys 26(5): 862–869

14. Baeva M, Baev P, Kaplan A (1997) An analysis of the heat transfer from a moving elliptical cylinder. J Phys D: Appl Phys 30(8): 1190–1196

15. Kaplan A (1994) Modellrechnung und numerische Simulation von Absorption, Wärmeleitung und Strömung des Laser-Tiefschweißens (in German), PhD-thesis (Dissertation), Vienna University of Technology, Vienna (A)

16. Kaplan AFH (2004) Semi-analytical modeling of the process interaction zone. Proc. WCCM VI/APCOM'04, Beijing (CHI), Singh University Press & Springer-Verlag, Berlin (D)

17. Lampa C, Kaplan AFH, Powell J, Magnusson C (1997) An analytical thermo-dynamic model of laser welding. J Phys D: Appl Phys 30: 1293–1299

18. Kaplan AFH (2005) Modelling the absorption variation during pulsed laser heating. Appl Surf Sci 241(3–4): 362–370

19. Dowden J, Kapadia P (1999) Oscillations of a weld pool formed by melting through a thin work piece. Lasers in Engineering 8(4): 311–318

20. Kaplan AFH, Mizutani M, Katayama S, Matsunawa A (2002) Unbounded keyhole collapse and bubble formation during pulsed laser interaction with liquid zinc. J Phys D: Appl Phys 35: 1218–1228

21. Lampa C, Kaplan AFH, Resch M, Magnusson C (1998) Fluid flow and resolidification in deep penetration laser welding, Lasers in Engineering 7(3–4): 241–253

22. Beck M, Berger P, Dausinger F, Hügel H (1991) Aspects of keyhole/melt interaction in high speed laser welding. Proc SPIE 1397, Ed: Orza JM, Domingo C, Bellingham (WA) 769–774

23. Fuhrich Th, Berger P, Hügel H (2002) Numerical calculation of the weld pool in deep penetration laser welding. Proc Mathematical modelling of weld phenomena 6, ed: Cerjak H, Bhadeshia HKDH, Maney Pub, London (UK) 93–119

24. Otto A, Geiger M (2007) From basic research to industrial applications – new developments for laser welding, Proc. LIM – Lasers in Manufacturing, Munich (D), ed: Vollertsen F et al., WLT, Bremen (D) 5–11

25. Choo RTC, Szekely J (1994) Possible role of turbulence in GTA weld pool behavior. Welding Journal 73(2): 25s–31s

26. Fabbro R, Slimani S (2007) Melt pool dynamics during deep penetration cw Nd:YAG laser welding. Proc LIM – Lasers in Manufacturing, Munich (D), ed: Vollertsen F et al., WLT, Bremen (D) 259–264

27. Katayama S, Kawahito Y, Mizutani M (2007) Plume behaviour and melt flows during laser and hybrid welding. Proc LIM – Lasers in Manufacturing, Munich (D), ed: Vollertsen F et al., WLT, Bremen (D) 265–271

28. Neumann S, Thomy C, Seefeld T, Wagner F (2007) Experimental investigation of the humping effect in welding with highest beam quality. Proc. LIM – Lasers in Manufacturing, Munich (D), ed: Vollertsen F et al., WLT, Bremen (D) 273–276

4

Laser Keyhole Welding: The Vapour Phase

John Dowden

Department of Mathematical Sciences, University of Essex, Colchester, Essex CO4 3SQ, UK. `dowdj@essex.ac.uk`

Abstract. Several aspects of the properties of the keyhole and its relationship to the weld pool in laser keyhole welding are considered. The aspect of most immediate importance is the exchange of energy between the laser beam itself and the molten material of the weld pool. Many mechanisms are involved, but the two considered here are the process of direct absorption at the keyhole wall (Fresnel absorption) and the two-stage process of absorption of energy by inverse bremsstrahlung into the ionised vapour that forms in the case of the longer-wavelength lasers such as the CO_2 laser, followed by thermal conduction to the wall. Consideration is given to the role of the Knudsen layer at the boundary. The possibility that the exchange may be influenced by the vapour flow in the keyhole is considered. More generally, the dynamics of the flow is investigated and the balances necessary to keep the keyhole open are investigated. A simple model of the interaction of the vapour with the molten material in the weld pool is proposed which can be used to investigate their interaction. Order of magnitude estimates suggest that it is far from simple but that some simplifying approximations are possible.

The chapter ends with some basic models of electromagnetic effects in an ionised vapour as an introduction to the comprehensive analysis provided in chapter 6.

4.1 Notation

The symbols employed for the physical constants and the main variables used in this chapter, and their SI base units, are given in Table 4.1. Other symbols are defined when they are first introduced; subscripts and primes may be added to the symbols for related variables in specific contexts.

4.2 The Keyhole

The broad qualitative aspects of what happens in the keyhole in laser keyhole welding are reasonably clear, but the details are complex and are not too well understood. Experiments show that the keyhole is usually not in a steady

Table 4.1. Notation.

Symbol	Units	Meaning	Symbol	Units	Meaning
c	$\mathrm{m\,s^{-1}}$	speed of light	γ	$\mathrm{N\,m^{-1}}$ $(\mathrm{kg\,s^{-2}})$	coefficient of surface tension
e	$\mathrm{C\,(A\,s)}$	magnitude of the charge of an electron	ε_0	$\mathrm{F\,m^{-1}}$ $(\mathrm{A^2\,kg^{-1}\,m^{-1}\,s^4})$	permittivity of free space, $= 8.854 \times 10^{-12}\,\mathrm{F\,m^{-1}}$ $= \mu_0^{-1} c^{-2}$ where $\mu_0 = 4\pi \times 10^{-7}\,\mathrm{H\,m^{-1}}$
k_B	$\mathrm{J\,K^{-1}}$ $(\mathrm{kg\,m^2\,s^{-2}\,K^{-1}})$	Boltzmann's constant	λ	$\mathrm{W\,m^{-1}\,K^{-1}}$ $(\mathrm{kg\,m\,s^{-3}\,K^{-1}})$	thermal conductivity
$m_e,\ m_n,$ m_i	kg	mass of an electron, a neutral atom, an ion	μ	$\mathrm{Pa\,s}$ $(\mathrm{kg\,m^{-1}\,s^{-1}})$	dynamic viscosity
P	Pa $(\mathrm{kg\,m^{-1}\,s^{-2}})$	pressure	μ_r	–	(real) refractive index
p_0	Pa	ambient pressure	ν	$\mathrm{m^2\,s^{-3}}$	kinematic viscosity, μ/ρ
R	$\mathrm{m\,s^{-1}}$	radial co-ordinate	ρ	$\mathrm{kg\,m^{-3}}$	mass density
$\mathbf{v}$	$\mathrm{m\,s^{-1}}$	velocity vector	ρ_{charge}	$\mathrm{C\,m^{-3}}$ $(\mathrm{A\,m^{-3}\,s})$	charge density
v_r or u	$\mathrm{m\,s^{-1}}$	radial component of $\mathbf{v}$	ω	$\mathrm{s^{-1}}$	angular frequency of laser radiation
v_z or w	$\mathrm{m\,s^{-1}}$	axial component of $\mathbf{v}$	$\hbar$	$\mathrm{J\,s}$ $(\mathrm{kg\,m^2\,s^{-1}})$	Planck's constant/2π
z	$\mathrm{m\,s^{-1}}$	axial co-ordinate			
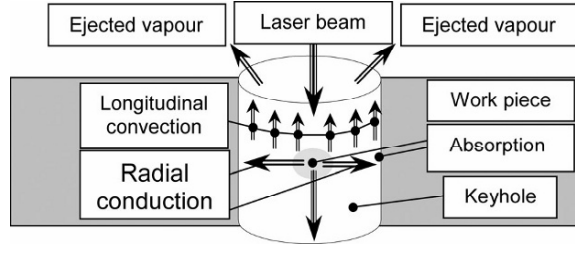
Fig. 4.1. The relative geometry of the work piece, laser and keyhole during laser keyhole welding, and the transfer processes involved.

state, even in a frame of reference that is stationary with respect to the laser beam, but much can be learned from a study of the steady state. In outline, the energy from the laser beam first enters the keyhole; much of it is then absorbed and reflected directly at the keyhole wall by the process of Fresnel absorption, but some of the power of the laser, depending on its wavelength, is absorbed into the partially ionised vapour that fills the keyhole. It is either re-radiated or else passed by thermal conduction in the vapour to the keyhole wall. For a CW CO_2 laser this fraction can be substantial, but is much less when the wavelength is shorter. This transfer process is illustrated in Fig. 4.1.

If time dependence is ignored, the main equations and the reasons for them can be found in [1] and in a form extended to variation along the keyhole in [2] and [3]. The power absorbed per unit volume by inverse bremsstrahlung, q, is given in terms of the absorption cross-section, σ, by

$$q = 4\pi U_{mean}\sigma n_e \quad \text{where} \quad \sigma = \frac{n_i Z^2 e^6 \left\{1 - \exp\left(-\hbar\omega/k_B T\right)\right\}}{6\mu_r \varepsilon_0^3 c\hbar\omega^3 m_e^2} \sqrt{\frac{m_e}{6\pi k_B T}}\bar{g}$$

(4.1)

where U_{mean} ($\mathrm{W\,m^{-2}}$) is the mean intensity of radiation in all 4π directions and Z is the average charge of the positive ions in units of proton charge. The Gaunt factors are the ratio of a corrected version of the formula to the classical result, and different factors are used for different interactions [4]; they are discussed in §6.5.1, but here the average value $\bar{g}$ of the appropriate factor is taken as unity. Thus

$$\sigma_0 \equiv \sigma \left/ \frac{n_i Z^2 e^6 \bar{g}}{6\mu_r \varepsilon_0^3 c\hbar\omega^3 m_e^2}\sqrt{\frac{m_e}{6\pi\hbar\omega}}\right. = \frac{1 - \exp\left(-1/T'\right)}{\sqrt{T'}} \quad \text{where} \quad T' = k_B T/\hbar\omega.$$

(4.2)

For a CO_2 laser with vapour at 10^4 K, the value of T' is 7.4. The assumption that the electron temperature is approximately the same as that of the ions and neutrals will be made, so that Saha's equation,

$$\frac{n_e n_i}{n_n} = n_0 N\left(T''\right),$$

can be used to relate the number densities of electrons, neutrals and ions, n_e, n_n and n_i respectively, if local thermodynamic equilibrium is assumed. In the equation,

$$n_0 = 2\frac{g_0^i}{g_0^n}\left(\frac{m_e I}{2\pi\hbar^2}\right)^{\frac{3}{2}}, \quad T'' = \frac{k_B T}{I}$$

and, approximately,

$$N\left(T''\right) = T''^{\frac{3}{2}}\exp\left(-\frac{1}{T''}\right) \approx T''^{\frac{3}{2}}; \tag{4.3}$$

I is the ionisation energy of the atoms of the vapour in the keyhole, which will be assumed to consist mainly of iron from the work piece. Number densities are related to charge density, mass density and pressure by

$$\rho_{charge} = e\left(Zn_i - n_e\right),$$

$$\rho = m_i n_i + m_n n_n + m_e n_e,$$

$$p = \left(n_i + n_n + n_e\right)k_B T.$$

Assume that $m_e \ll m_i = m_n$ and that $\rho_{charge} = 0$ so $Zn_i = n_e$; although the second of these assumptions is shown not to true in §4.7, it is none the less convenient and likely to be a good approximation in view of the high conductivity of an ionised vapour. The quasi-neutrality approximation can then be used. Assume also that $Z = 1$ provided the temperature is not too high, so

$$n_i = n_e = n_0\left\{S\left(T'', p''\right) - N\left(T''\right)\right\} \quad \text{and}$$
$$n_n = n_0\left\{2N\left(T''\right) + \frac{p''}{T''} - 2S\left(T'', p''\right)\right\}, \tag{4.4}$$

where

$$p'' = \frac{p}{n_0 I} \quad \text{and} \quad S\left(T'', p''\right) \equiv \sqrt{\frac{N\left(T''\right)p''}{T''} + N\left(T''\right)^2}.$$

The mass density is therefore given by

$$\rho = m_n n_0\left\{N\left(T''\right) + p''/T'' - S\left(T'', p''\right)\right\}. \tag{4.5}$$

Equations (4.3) and (4.4) applied to (4.1) and (4.2) show that

$$q_0\left(T'', p''\right) \equiv \frac{q}{4\pi U_{mean} D\left(T\right) n_0^2 \sigma_0\left(T'\right)}$$

$$= N\left(T''\right)\left\{2N\left(T''\right) + \frac{p''}{T''} - 2S\left(T'', p''\right)\right\}$$

where

$$D = \frac{Z^2 e^6 \overline{g}\,(T)}{6\mu_r \varepsilon_0^3 c\hbar\omega^3 m_e^2} \sqrt{\frac{m_e}{6\pi\hbar\omega}}.$$

For iron, T'' has the value 0.11 at 10^4 K, and at atmospheric pressure the value of p'' is about 6×10^{-7} while n_0 is about $10^{29}\,\mathrm{m}^{-3}$. The ionisation then tends to be low since $N \approx 4.1 \times 10^{-6}$ and $p''/T'' \approx 5.5 \times 10^{-6}$. The vapour itself is strongly conductive at these temperatures. Since the degree of ionisation is relatively low, the coefficient of thermal conductivity will be taken to have the form

$$B\sqrt{T} \quad \text{where} \quad B = 8.324 \times 10^2 \times m^{-1/2}\Omega^{-1}d^{-2}\mathrm{J\,m^{-1}\,s^{-1}K^{-3/2}}; \quad (4.6)$$

see [5]. In (4.6) m is the molecular weight of the gas, d (measured in pm) is the molecular diameter and Ω is weakly dependent on temperature. From [6], d for iron is about 140 pm, while at 5000 K, Ω is 0.6, and at 10^4 K, it is 0.5.

The results obtained so far must be combined with the equation of heat conduction (1.7), for which an approximation to the velocity components in the vapour is needed. An order of magnitude calculation suggests that the convection terms and the longitudinal conduction term have a fairly small effect compared to the lateral conduction term on the temperature distribution, but their inclusion would allow a qualitative evaluation of their effects.

Assume that the radially inward flow caused by ablation at the keyhole wall is not confined to a narrow layer but decreases more or less uniformly with distance from the wall; see Sect. 4.6.2 for further discussion of this aspect of the problem. If the pressure gradient in the keyhole is considered to have a minor role compared to the lateral conditions at the wall, and since the longitudinal viscous terms can be ignored by comparison with the radial ones, the longitudinal term in the Navier-Stokes equation is approximately

$$\frac{1}{r}\frac{\partial}{\partial r}\mu r \frac{\partial u_z}{\partial r} = 0 \quad \text{giving} \quad u_z = W\,(z)\,.$$

Since compressibility of the vapour is not central to the problem under consideration, ignore it so that $\mathbf{u} \cdot \nabla\rho \approx 0$; the equation of conservation of mass then shows that

$$\frac{1}{r}\frac{\partial}{\partial r}ru_r + \frac{\partial u_z}{\partial z} = 0 \quad \text{so} \quad u_r = -\frac{dW}{dz}r.$$

so the equation of heat conduction becomes

$$\rho C_p \left\{ -\frac{1}{2}\frac{dW}{dz}r\frac{\partial T}{\partial r} + W\frac{\partial T}{\partial z} \right\} = \frac{1}{r}\frac{\partial}{\partial r}\lambda r\frac{\partial T}{\partial r}. \quad (4.7)$$

The effects of longitudinal conduction have been ignored compared to the radial terms. Mass is not conserved along the length of the keyhole because of

ablation at the keyhole wall. If W is taken to be a linear function of z, dW/dz is a given constant so (4.7) becomes

$$\frac{1}{r'}\frac{\partial}{\partial r'}r'\sqrt{T''}\frac{\partial T''}{\partial r'} + PE\Sigma\left(T'',p''\right) =$$

$$vC_p'\rho'\left(T''\right)a'\left(z'\right)\left\{W'\left(z'\right)\left[a'\left(z'\right)\frac{\partial T''}{\partial z'} - \frac{da'\left(z'\right)}{dz'}\cdot r'\frac{\partial T''}{\partial r'}\right]\right.$$

$$\left.-\frac{1}{2}a'\left(z'\right)\frac{dW'\left(z'\right)}{dz'}r'\frac{dT''}{dr'}\right\} \tag{4.8}$$

in dimensionless form (see [1, 3]), where a_0 is for example the beam radius or the radius of the keyhole at the surface, $a(z) = a_0 a'(z')$ is the keyhole radius and W_0 is a velocity scale for W; ℓ is a characteristic longitudinal length scale such as the thickness of the work piece, the expected average depth of a blind keyhole or a suitable length scale deduced by consideration of the other dimensional and dimensionless groups in the problem. Additionally,

$$\Sigma\left(T'',p''\right) \equiv \bar{g}\left(T''\right)\frac{1 - \exp\left(-\hbar\omega/IT''\right)}{\sqrt{IT''/\hbar\omega}}N\left(T''\right)\left\{2N\left(T''\right) + \frac{p''}{T''} - 2S\left(T'',p''\right)\right\},$$

$$E \equiv \frac{n_0^2}{\pi B}\frac{Z^2 e^6}{6\mu_r\varepsilon_0^3 c\hbar\omega^3 m_e^2}\sqrt{\frac{m_e}{6\pi\hbar\omega}}\left(\frac{k_B}{I}\right)^{3/2}\mathrm{W}^{-1},\quad v = \frac{n_0 a_0^2 W_0}{\ell B}\sqrt{\frac{k_B^3}{I}},$$

$$C_p' = \frac{m_n}{k_B}C_p,\quad 4\pi U_{mean} = \frac{P}{\pi a^2}\quad\text{and}\quad z = \ell z',\quad r = a_0 r'.$$

E is about $8.775 \times 10^8\,\mathrm{W}^{-1}$ for iron vapour in CO_2 laser light. If z is measured positive downwards, da/dz will usually be negative and so will dW/dz for regions in which the flow in the keyhole is upwards. The dependence of $\bar{g}$ on T is not known, but its value seems to be close to one at the relevant temperatures. The specific heat C_p can be calculated from

$$C_p = \left(\frac{\partial H}{\partial T}\right)_p\quad\text{where}\quad H = \frac{5p}{2\rho} + \frac{In_i}{\rho}; \tag{4.9}$$

H is the enthalpy per unit mass, and the partial derivative can be calculated using (4.4) and the effective constitutive relation (4.5).

In principle, the pressure has to be related to the flow of the vapour in the keyhole, and will itself depend on both r and the longitudinal co-ordinate z. Although the viscous thermal flow term (1.10) should perhaps be included as well, an order of magnitude calculation suggests that the ratio of its value to the Fourier heat flow is likely to be an order of magnitude less than one. Its neglect is therefore convenient but not necessarily fully justified so whether or not it can be neglected will depend the purpose of the model. Sometimes the pressure can be regarded as not varying greatly from the average local value. As shown later though, that is not a good approximation for the fluid dynamic aspects of the problem, and the question of what holds the keyhole open.

Equation 4.8 has to be solved for the temperature T with appropriate boundary conditions at the keyhole wall.

4.3 The Keyhole Wall

4.3.1 The Knudsen Layer

When a gas or vapour occupies a region adjacent to a solid or liquid boundary, there is a thin layer, identified by Knudsen [7], in which the velocity distribution of the molecules of the gas is not Maxwellian. Since molecules immediately adjacent to the boundary cannot have a component of velocity relative to it that is directed towards it, there is an adjustment layer with a thickness of a few mean free paths before equilibrium is reached. The region is known as the *Knudsen layer*. The distribution of velocities immediately adjacent to the wall is usually assumed to be half-Maxwellian, an assumption which is well supported by observation. The hydrodynamic continuum approximation (§1.2.1), Kn ≪ 1, does not apply in the layer and if it is to be used elsewhere, discontinuity conditions have to be introduced. In laser processing consideration of the Knudsen layer can be important since strong vaporisation can occur on, for example, the keyhole wall in laser keyhole welding. The gas near the wall is not in translational equilibrium, which is reached in a few mean free paths as a result of particle collisions.

Ablation Through the Knudsen Layer

At the boundary between the liquid and vapour phases the material of the work piece crossing it experiences an intense phase change. It arrives at the boundary as a liquid with a normal component of velocity that it relatively close to the velocity of the interface itself, and leaves it as a vapour that is much less dense than the liquid; conservation of the mass flow rate therefore requires it to have a very much higher velocity. The random velocity fluctuations of the individual particles very close to the boundary cannot be considered to be isotropic as there will not be many back-scattered particles at the interface. The result is that a Knudsen layer forms in the vapour in which the transition from a non-equilibrium velocity distribution at the surface of the liquid region, to a local Maxwell-Boltzmann distribution some few mean free paths above the metal surface occurs. See for example [7]–[12].

Knight [11] has shown that the following discontinuity relationships hold. The subscript $_V$ indicates conditions on the vapour side of the Knudsen layer and $_L$ indicates conditions in the liquid immediately prior to vaporisation; ρ_{SV} is the density of saturated vapour at the temperature of the liquid at the interface, T_L, since Knight's analysis assumes that emitted particles were in equilibrium with the liquid before vaporisation. Figure 4.2 shows schematically the regions to which each of the subscripted variables applies.

The discontinuity in the temperature is given by

$$
\frac{T_V}{T_L} = \left\{ \sqrt{1 + \tfrac{1}{4}\pi m^2 \left(\frac{\gamma - 1}{\gamma + 1}\right)^2} - \tfrac{1}{2} m \frac{\gamma - 1}{\gamma + 1}\sqrt{\pi} \right\}^2 ,
$$
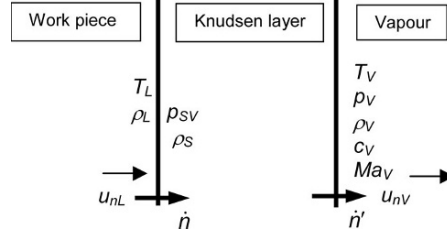
Fig. 4.2. The Knudsen layer, showing the regions to which the notation of §4.3 applies. T is the temperature, p the pressure, ρ the density, u the velocity, c the speed of sound and Ma the Mach number. Vaporising material moves from left to right and if conditions are steady in time, $\dot{n} = 0$.

and the discontinuity in density by

$$
\frac{\rho_V}{\rho_{SV}} = \sqrt{\frac{T_L}{T_V}} \left\{ \left(m^2 + \tfrac{1}{2}\right) \exp\left(m^2\right) \operatorname{erfc}\left(m\right) - \frac{m}{\sqrt{\pi}} \right\}
$$
$$
+ \frac{1}{2} \frac{T_L}{T_V} \left\{ 1 - m\sqrt{\pi} \exp\left(m^2\right) \operatorname{erfc}\left(m\right) \right\}
$$

where erfc is the complementary error function as defined in [13], and

$$
m = \frac{u_{nV}}{\sqrt{2RT_V}} = \mathrm{Ma}_V \sqrt{\frac{\gamma}{2}}
$$

R is the gas constant for the vapour, Ma_V is the vapour Mach number just outside the layer with a speed of sound given by

$$
c_{Va} = \sqrt{\gamma p_V / \rho_V} = \sqrt{\gamma R T_V};
$$

γ is the adiabatic index of the vapour and is usually given the value $5/3$ appropriate to a monatomic gas; u_{nV} is the normal velocity component in the vapour just outside the Knudsen layer. The normal components of gas velocity are related by the condition of conservation of mass, (1.15) modified for a layer of finite but varying thickness, so that

$$
\rho_L \left(u_{nL} - \dot{n}\right) = \rho_V \left(u_{nV} - \dot{n}'\right)
$$

where $\dot{n}$ is the velocity of the interface measured positive following the direction of motion of the ablated material and $\dot{n}'$ is the velocity of the outer edge of the Knudsen layer. Since $\rho_V \ll \rho_L$, $\dot{n}'$ can usually be ignored and indeed when conditions are steady in time, both it and $\dot{n}$ are zero, so $\rho_L u_{nL} = \rho_V u_{nV}$ if the system is stationary. The conditions depend strongly on the Mach number of the vapour flow based on the normal velocity u_{nV}.

Various simplifications have been proposed, based on slightly different assumptions. For example, Anisimov shows in [8] that in a vacuum $T_V = 0.67\, T_L$

and $\rho_V = 0.31\,\rho_{SV}$; the saturated vapour pressure p_{SV} corresponding to ρ_{SV} can be found from a vapour pressure relationship such as that given in [14] for example. Conditions inside a keyhole, however, are not those of a vacuum, and Finke et al. [10, 15] found the discontinuity conditions as functions of the Mach number numerically. Their results were calculated for values of the Mach number at the edge of the layer, u_{nV}/c_{Va}, in the range 0 to 1 and can be approximated by the following quadratic relations. If

$$x_1 = u_{nV}/c_{Va},\ 0 \le u_{nV} \le c_{Va} \quad \text{and} \quad x_2 = \tfrac{1}{4}\left(p_{SV}/p_V - 1\right),\ p_V \le p_{SV} < 5p_V$$

then

$$T_V/T_L = 1 - 0.31x_1 - 0.09x_1^2, \tag{4.10}$$

$$\rho_V/\rho_{SV} = 1 - 1.16x_1 + 0.56x_1^2, \quad T_V/T_L = 1 - 0.60x_2 + 0.24x_2^2,$$

$$\rho_V/\rho_{SV} = 1 - 1.03x_2 + 0.35x_2^2 \quad \text{and} \quad u_{nV}/c_{SV} = 1.47x_2 - 0.47x_2^2.$$

The same notation is used as in Fig. 4.2 and $c_{Va} = \sqrt{\gamma p/\rho}$ is the speed of sound. In these calculations, as in Knight's analysis, the normal component of velocity at the edge of the layer, u_{nV} (or equivalently the Mach number Ma_V), is a free parameter determined by the flow far from the boundary.

Thermal Flux and Viscous Slip in the Knudsen Layer

The no-slip condition (1.19) for a gas moving adjacent to a non-interacting fluid or solid boundary does not necessarily apply because of the presence of the Knudsen layer, and the appropriate viscous slip conditions and associated thermal flux have been studied in detail in [12] and [15] chs 3–6. The extension to the case when there is ablation or condensation at the interface, as in the case of the keyhole in laser welding where there is an asymptotic large tangential flow as well, has been investigated [16], ch 7. The results are not straightforward, but the arguments in favour of (1.19) in the absence of ablation apply with greater strength in the presence of vigorous ablation and it seems reasonable to assume that it can be used as an approximation. The same may not be true, though, when condensation occurs.

When there is no phase change at the boundary, the formal position is that (1.19) is replaced by a slip condition [17, 18]. There is a tangential slip velocity $\mathbf{u}$ (so that $\mathbf{u} \cdot \mathbf{n} = 0$) between the surface and the gas which must satisfy

$$\mathbf{u} \cdot \mathbf{t} = \sigma_p \frac{v_m}{p} n_i t_j d_{ij} + \sigma_T \frac{\mu}{\rho} \frac{1}{T} \mathbf{t} \cdot \nabla T \tag{4.11}$$

for any tangential vector $\mathbf{t}$, where $\mathbf{n}$ is a unit vector normal to the surface directed into the gas, d_{ij} is the deviatoric stress tensor defined in Table 1.1, σ_p is the viscous slip coefficient and σ_τ is the thermal slip coefficient (both of these are dimensionless); v_m is the most probable molecular velocity at the

local temperature T and m is the molecular mass of the gas. The density ρ and v_m are given by

$$\rho = \frac{pm}{k_B T} \quad \text{and} \quad v_m = \sqrt{\frac{2k_B T}{m}}.$$

Reference [19] provides a critical review of values; the value of σ_p depends on the diffuse fraction α in Maxwell's boundary condition which lies between 0 and 1; see [19], §3.8.2). It appears to be given fairly accurately by

$$\sigma_p = (2 - \alpha) \left\{ \sigma_p (1) - 0.1211 (1 - \alpha) \right\} / \alpha$$

and $\sigma_p(1)$ has a value close to unity; σ_T is given by $0.75 + b\alpha$ where b is given variously as 0.375 or 0.3993.

The theory so far has been derived for a solid boundary at rest, but the same ideas apply if the boundary were liquid and in motion, provided the slip velocity is understood to be relative to the (tangential) velocity of the boundary.

Related to (4.5) is the existence of a heat flux, $\mathbf{q}$, tangential to the surface (so $\mathbf{q} \cdot \mathbf{n} = 0$) in the Knudsen layer which is related to the viscous stress at the edge of the hydrodynamic regime by

$$\mathbf{q} \cdot \mathbf{t} = \kappa_s n_i t_j d_{ij}; \tag{4.12}$$

κ_s ($\mathrm{m^2\,s^{-1}}$) is a surface heat conductivity given by

$$\kappa_s = \frac{\mu v_0^2}{2p} \left(\tfrac{1}{2}\theta_4 - \sigma_T \right)$$

where θ_4 is the same constant that appears in (1.10) and has the value 3 for Maxwellian molecules [12], but will be different for other models.

Some modification is necessary to combine these results with the results of section (4.3.1) or the work of authors cited in, for example, [16] and [19], ch 7. At atmospheric pressure however, even at temperatures of the order of 10^4 K, the coefficients of $\partial u_\tau / \partial n$ and $\partial \ln T / \partial \tau$ in (4.11) and (4.12) are small. This suggests that the results relating to tangential mass and heat flows can be ignored when the process being studied takes place at or close to atmospheric pressure. In particular, it is likely that the no-slip condition (1.19) remains a good approximation.

4.3.2 Fresnel Absorption

When a laser beam is incident on a metallic surface, the wave is partly reflected and partly absorbed; the process is usually referred to as *Fresnel absorption*. The subject was analysed in detail by Stratton [20] and was applied in the case of p-polarised light to laser cutting by Schulz et al. [21]. It is assumed that the

light is absorbed by the classical Fresnel formulae and the light beam couples to the metal electron gas. This absorbs some of the intensity by Joule heating. The process gives absorption and reflection coefficients that are independent of the incident intensity, and depend on the angle of incidence θ of the laser beam measured from the normal to the surface and on the material-dependent quantity

$$\varepsilon^2 = \frac{2\varepsilon_2}{\varepsilon_1 + \sqrt{\varepsilon_1^2 + (\sigma_{st}/\omega\varepsilon_0)^2}}.$$

The quantities ε_1 and ε_2 are the real parts of the dielectric constants of the metal and the vapour respectively through which the beam is being transmitted and σ_{st} is the electrical conductance per unit depth of the work piece; ε_1 and ε_2 have typical values that are approximately unity while σ_{st} has a value of about $5.0 \times 10^5 \, \mathrm{W}^{-1}\,\mathrm{m}^{-1}$. A CO_2 laser with a wavelength of $10.6\,\mu\mathrm{m}$ has a value for ω of $1.78 \times 1014\,\mathrm{s}^{-1}$, and so ε has a value of about 0.08. In the case of laser cutting, p-polarised light is more effective than s-polarised light [22] and the reflection coefficient in that case is

$$R_s(\theta) = \frac{\cos^2\theta + (\varepsilon - \cos\theta)^2}{\cos^2\theta + (\varepsilon + \cos\theta)^2}.$$

For laser welding the roughly circular cross-section of the keyhole makes an assumption of circularly polarised light more appropriate; the reflection coefficient is then

$$R_c(\theta) = \frac{1}{2}\left(\frac{1 + (1 - \varepsilon\cos\theta)^2}{1 + (1 + \varepsilon\cos\theta)^2} + \frac{\cos^2\theta + (\varepsilon - \cos\theta)^2}{\cos^2\theta + (\varepsilon + \cos\theta)^2}\right).$$

A characteristic of both formulae is that when θ is near $^1/_2\pi$, so that the beam is close to grazing incidence, the reflection coefficient is remarkably small so that a high proportion of the intensity is absorbed. For a p-polarised beam, the minimum value of the reflection coefficient is

$$3 - 2\sqrt{2} \approx 0.17 \quad \text{when } \cos\theta = \varepsilon/\sqrt{2}$$

and for the circularly polarised case the stationary value is attained close to the same value of $\cos\theta$ when ε is small with a value depending on ε but close to 0.6. These should be compared to the values when θ is zero, which are approximately 0.85 in both cases when ε is 0.08.

This simple electromagnetic model for absorption at a metal surface is often used at the wavelength of a CO_2 laser; at that wavelength a simple model of electromagnetic interaction involving resistive dissipation is probably adequate. At shorter wavelengths, though, the model becomes less satisfactory; neither does it allow for surface impurities.
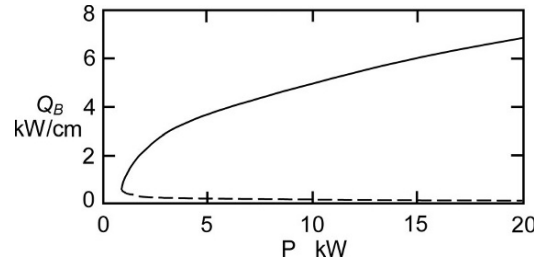
Fig. 4.3. Power absorbed per unit depth at the keyhole wall for iron vapour as a function of power at the given cross-section of the keyhole. ©*2001 From* [1]. *Reproduced by permission of Taylor & Francis LLC, a division of Informa plc.*

4.4 The Role of Convection in the Transfer of Energy to the Keyhole Wall

In the case of a CO_2 laser, inverse bremsstrahlung ensures a substantial degree of ionisation and resultant flow of thermal energy from the ionised vapour in the interior of the keyhole to the wall. At shorter wavelengths the effect becomes progressively less important; for a Nd:YAG laser it is known that some ionisation can occur but the rise in temperature is not significant. To find the temperature distribution and the flow of heat to the wall in the longer wavelength case, it is necessary to solve (4.8) with an appropriate boundary condition on the temperature to allow for the effect of the Knudsen layer; (4.10) provides an example. Supposing that the vapour consists effectively of single un-ionised iron atoms, the pressure is atmospheric, and u_{nV} is of the order of $1\,\mathrm{m\,s}^{-1}$ (see [23] and Sect. 4.6.3) x_1 is approximately $0.063/\sqrt{T_V}$. When substituted in (4.10) and taking T_L to be $2999\,\mathrm{K}$ these give a value of 10^{-3} for x_1 and $2998\,\mathrm{K}$ for T_V, the boundary condition to be imposed on (4.8), suggesting that the presence of the Knudsen layer has only a small effect on the solution. It is worth note that the speed of sound in unionised iron vapour at this temperature is nearly three times that for air at room temperature.

To find the heat transferred to the boundary by inverse bremsstrahlung, (4.8) has to be solved. At the CO_2 wavelength, an order of magnitude calculation suggests that the dominant term is the second on the left, with the convection terms on the right playing a relatively minor role. For first order estimates therefore they can be neglected. Reference [1] pp 205–240 gives the solution of this equation; Fig. 4.3 shows the heat flux to the keyhole wall which results in the case of iron vapour. The lower branch is an unstable alternative solution.

At atmospheric pressure and a temperature of $10^4\,\mathrm{K}$ the term $E\Sigma$ on the left of (4.8) has a value of $0.188\,\mathrm{kW}^{-1}$ for iron vapour; when $\ell = 1\,\mathrm{cm}$, $a_0 = 0.1\,\mathrm{mm}$, $W_0 = 300\,\mathrm{m\,s}^{-1}$ [23, 24] the value of υ is 177 and at the same
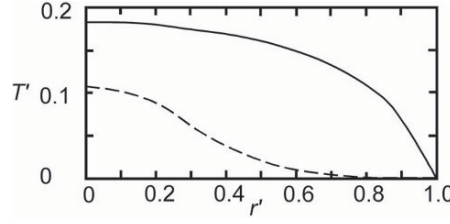
Fig. 4.4. Dimensionless temperature $y = [T(r) - T_V]/[T(0) - T_V]$ as a function of the dimensionless radial distance r/a. The cases when $v = 0$ and 200 (solid curve) are indistinguishable; the broken line shows the case when $v = 47000$; in the latter case Q_B is zero.

values as before for p and T, C'_p is equal to 29.2. The order of magnitude of the right hand side of the equation is then 6.2×10^{-4}. At lower temperatures, of the order of $5\,\mathrm{kK}$ at atmospheric pressure, the ratio of the convective term to the absorption term rises dramatically and is very high at the boiling temperature. Since the effect of the convective terms is cooling on balance, they may have a very substantial effect on the temperature distribution, and on the energy available to be absorbed by the work piece.

At the CO_2 wavelength, the convective term makes little practical difference to the temperature distribution. If a is assumed independent of z, W to be linear in z, and ℓ is the thickness of the work piece which is fully penetrated, W is given by

$$W(z') = \frac{z'}{z'_{stag}} - 1$$

where z'_{stag} is the position of the stagnation point and has the value $1/2$ in these circumstances. If the velocity scale W_0 is taken as the magnitude of the exit velocity at either end of the keyhole, a solution for T independent of z is then possible. The solid line in Fig. 4.4 represents the solution for the dimensionless radial temperature distribution when the power in the fundamental frequency is $5\,\mathrm{kW}$. From (4.1) it is clear that there is almost no contribution to inverse bremsstrahlung absorption from higher harmonics. The solid line represents both of the cases when W at $z = 0$ is $0\,\mathrm{m\,s^{-1}}$ ($v = 0$) and when it is $300\,\mathrm{m\,s^{-1}}$, a reasonably representative value in practice ($v = 200$; the two cases are indistinguishable. $T(0)$ is predicted to be $23\,\mathrm{kK}$; although this temperature may seem rather high, it should be noticed from the graph that the temperature falls off quite rapidly away from the axis, and in fact the average value is $15\,\mathrm{kK}$. Furthermore, for a conical blind keyhole the average temperature over the whole keyhole is then predicted to be of the order of $13\,\mathrm{kK}$. For lasers with higher fundamental frequencies much less energy is absorbed by inverse bremsstrahlung resulting in a much lower temperature on the axis and on average over the whole keyhole.

The quantity that is of importance is the net rate of flow of heat from the vapour to the metal per unit depth. It is given by

$$Q_B \equiv 2\pi a \left(-\lambda \frac{\partial T}{\partial r} + \rho H u_r \right) \bigg|_{r=a}$$

$$= 2\pi B \left(\frac{I}{k_B} \right)^{3/2} \left[-\sqrt{T''} \frac{\partial T''}{\partial r'} - v a'^2 \frac{dW'}{dz'} \left(\tfrac{5}{2} p'' + 2N + \frac{p''}{T''} - 2S \right) \right]_{r'=1}$$

$$(4.13)$$

where λ is given by (4.6) and H by (4.9). The critical quantity in determining the importance of thermal convection in the welding process is the ratio of the second of these terms to the first, since the second term has the effect of reducing the energy transferred into the work piece. With the same example as before of a 5 kW laser power into 1 cm of metal, the ratio is about 2% so that neglect of the convection term remains justifiable. The constant E is very strongly dependent of the wavelength of the laser used, and it falls rapidly with decreasing wavelength whereas the parameter v, which is largely determined by W_0 and is not strongly frequency dependent, is not affected to the same extent. A consequence is that the radial ablation velocity increasingly tends to suppress absorption by inverse Bresstrahlung when progressively higher wavelengths are used.

Included in Fig. (4.4) is the temperature profile which corresponds to a very much greater degree of convection; the particular instance shown is the limiting case in which Q_B as given by (4.13) is zero; in that case the power necessary to melt the work piece and provide the weld pool must be supplied entirely by Fresnel absorption at the keyhole wall. At higher levels of convection no solution is possible and the plasma is extinguished.

The same is generally true of longitudinal convection. From (4.8) its effects are of the same order of magnitude as those of radial convection, but the mathematical problem is harder since the equation becomes a parabolic partial differential equation with a singular point (at which the coefficient of the highest derivative in z' vanishes) occurs in the interior of the solution domain. One approach is to re-introduce the second derivatives in z' so that the elliptic structure of the equation is restored; they had been neglected since elsewhere their effect is negligible so this is not wholly satisfactory and would present problems in a numerical scheme of solution as well as introducing complications in an analytical approach. Alternatively, retain the parabolic form of the equation, exclude the singularity and insist on obtaining matching solutions in the two regions, with T and $\partial T/\partial z$ continuous at the stagnation point. These difficulties are, however, of a technical nature and have no underlying physical significance.

It seems that, for most purposes, the simplified model in which convection is ignored is probably adequate at present for the study of CO_2 laser welding.

Table 4.2. Some estimates for the maximum viscosity of ionised gases.

Source	Gas	$\mu\,(10^{-4}\,\mathrm{Pa\,s})$	At: (K)
Devoto [25, 26]	Argon	2 (order of magnitude)	–
Palmer & Wright [27]	Air-like mixture	2.3	10^4
Gupta [28]	Air-like mixture	2.5	10^4
Armaly [29]	Air-like mixture	2.3/2.5	$9/11 \times 10^3$
Wilke [30]	Air-like mixture	1.7	6×10^3
Murphy [31]	Air-like mixture	2.3	10^4

Equation (4.8) can therefore be replaced by

$$\frac{1}{r'}\frac{\partial}{\partial r'}r'\sqrt{T''}\frac{\partial T''}{\partial r'} + PE\Sigma\left(T'',p''\right) = 0. \tag{4.14}$$

4.5 Fluid Flow in the Keyhole

4.5.1 General Aspects

Equations (4.5)–(4.9) can be used to estimate the parameters of a partially singly ionised gas of iron atoms at atmospheric pressure and a temperature of 1000 K. The density $\rho \approx 7.22 \times 10^{-4}\,\mathrm{kg\,m^{-3}}$ from (4.5), the thermal conductivity $\lambda \approx 1\,\mathrm{kg\,m\,s^{-3}\,K^{-1}}$ from (4.6), and the specific heat $C_p \approx 24 \times 10^4\,\mathrm{m^2\,s^{-2}\,K^{-1}}$ from (4.9).

Table 4.2 shows values found in the literature, or deducible from it, for the dynamic viscosity of some air-like mixtures. Regarded as functions of temperature, T, the graphs for the viscosity, μ, have a very similar shape in all cases (35). A maximum value is reached as indicated in the table followed by a fairly rapid fall to a value under 0.3×10^{-4} Pa s at 2 kK or lower. A representative value of 2×10^{-4} Pa s can be taken for air or argon, and a corresponding value for iron vapour can be deduced which is perhaps nearer 3×10^{-4} Pa s, since the viscosity is approximately proportional to the square root of the molecular mass. If a typical value of $300\,\mathrm{m\,s^{-1}}$ for the axial velocity, W, in the keyhole is taken (see Amara and Bendib [24], for example) and a value of 10^{-4} m for the radius of the keyhole, a_0, the Reynolds number, Re, and the Prandtl number, Pr, have the following orders of magnitude,

$$\mathrm{Re}_{vapour} = \frac{2Wa_0\rho}{\mu} \approx 0.3 \quad \text{and} \quad \mathrm{Pr} = \frac{\mu C_p}{\lambda} \approx 75.$$

It seems that viscosity dominates over thermal conductivity and the flow is far from turbulent; the threshold for turbulent flow in a conventional pipe is at a Reynolds number of around 30, with fully developed turbulence only occurring for a very much higher value. For turbulence to occur in the keyhole it would be necessary for the flow velocity to be 100 times faster at the very
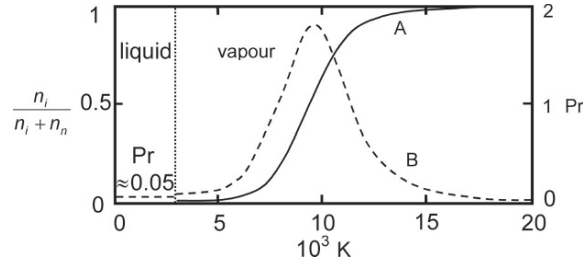
Fig. 4.5. (A) Degree of ionisation, $n_i/(n_i + n_n)$ and (B) the Prandtl number $\mathrm{Pr} = \nu/\kappa$ as functions of temperature at atmospheric pressure for iron vapour.
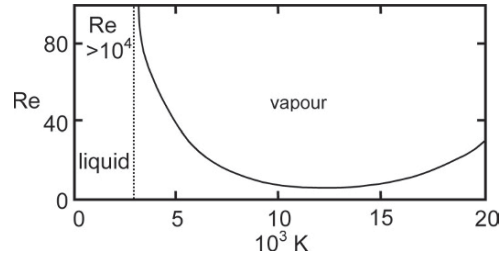
Fig. 4.6. Reynolds number $\mathrm{Re} = W\ell/\nu$ as a function of temperature (based on $W = 300\,\mathrm{m\,s^{-1}}$, $\ell = 0.1\,\mathrm{mm}$ in both the liquid and vapour regions).

least. There are some unexpected consequences for the study of the behaviour of the keyhole and the flow in the melt pool.

For example, consider the Reynolds Number in the melt pool; it is possible to estimate its order of magnitude. Amara and Bendib [24] quote experimentally observed keyhole vapour ejection velocities of the order of 100–$200\,\mathrm{m\,s^{-1}}$, while Amara, Fabbro and Bendib [23] produced a theoretical model that gives keyhole vapour velocities in the interior of the keyhole which can be many times greater than this at 1 bar. For the purposes of order of magnitude calculations here, take the kinematic viscosity in the molten region, ν_{liquid}, equal to $2.85 \times 10^{-7}\,\mathrm{m^2\,s^{-1}}$, $\ell = 0.5 \times 10^{-2}\,\mathrm{m}$ and $W_{liquid} = 300\,\mathrm{m\,s^{-1}}$ since the tangential component of velocity at the interface has to be continuous [1] p 205; ℓ is a measure of the size of the weld pool. With these values

$$\mathrm{Re}_{liquid} = \frac{U\ell}{\nu} \approx 5 \times 10^8$$

showing that the Reynolds number is very high and would still be high enough for turbulence to be expected in the melt pool even if the velocities were of the order of $\mathrm{cm\,s^{-1}}$ rather than hundreds of $\mathrm{m\,s^{-1}}$, and the radius of the keyhole were used rather than the dimensions of the melt pool.

Graphs of the degree of ionisation, the Prandtl number and the Reynolds number as functions of temperature at atmospheric pressure are shown in Figs. 4.5 and 4.6. Ionisation has a significant effect on Re and Pr, and hence
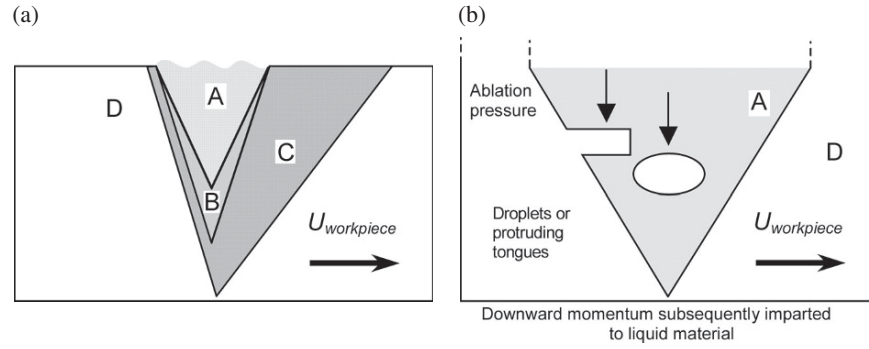
Fig. 4.7. Schematic diagrams of the welding region, showing (a) the four different regions and (b) the conversion of the energy of a downward-directed laser beam to downward momentum of liquid material near the bottom of a blind keyhole. $U_{workpiece}$ indicates the direction of translation of the work piece relative to the laser beam.

also on the Péclet number, $Pe = Re\ Pr$; curve A in Fig. 4.5 shows that the change from little ionisation to almost complete single ionisation takes place in the middle of the relevant temperature range.

4.5.2 Turbulence in the Weld Pool and the Keyhole

The graph of the Reynolds number in the two regions shows that the flow in the keyhole is dominated by viscosity and is not turbulent in the conventional sense. A suitably modified Poiseuille flow in the keyhole is therefore to be expected; the keyhole, however, is known to be a writhing, tortuous entity, far from dynamically stationary, with a great many of the characteristics commonly associated with turbulence. The reason for this lies in the molten region, not the keyhole itself. The Reynolds number close to the keyhole wall (based on the same length scale and velocity) is very high, with a value at the level associated with fully developed turbulence. In consequence, a strongly turbulent motion is to be expected near the keyhole wall in the liquid region though not in the vapour. The important difference between the two regions is that the density of the vapour is very much less than that of the liquid metal even though their axial velocities are comparable. The similarity of the velocities is a result of the tangential interface condition; see §§1.3.2 and 4.1.3.2. Consequently, the momentum per unit volume of the molten material is very much greater than that of the vapour, so the shape of the interface is dominated by the complex turbulent motion in the liquid, even though the dynamics of the flow in the vapour has the relative simplicity of a motion dominated by viscosity. As a result, it seems likely that the welding region for a blind keyhole can be divided schematically into regions as in Fig. 4.7a, with four separate regions when considered in a frame of reference at rest relative to the laser beam.

Region A. The highly viscous vapour region inside the keyhole.

Region B. A mixed region consisting intermittently at any given point of viscous vapour some of the time and near-inviscid liquid metal; its characteristics are not unlike those of turbulence, and can be considered in many ways as a turbulent mixture of two interacting phases of the material, mixed with any shielding gas or surrounding atmosphere that has found its way into the keyhole. There may be both evaporation and condensation occurring between the molten and gaseous phases of the material of the work piece.

Region C. A region consisting entirely of molten material. It probably has a turbulent region adjacent to region B and may have a mushy zone adjacent to region D.

Region D. The solid region of the work piece.

For a keyhole that penetrates the work piece completely the same general principles will hold, but region B will be thinner and the location of the exit of the keyhole will be more or less well defined unless penetration is only just achieved.

In the case of a keyhole that penetrates completely through the work piece with a substantial radius at the exit point, the laser is rapidly re-drilling the keyhole as soon as instabilities form; [32] gives an account of the mechanism for the generation and propagation of such disturbances. The keyhole thus retains its approximately cylindrical shape. If a significant degree of taper is expected so that penetration is barely achieved, or if the keyhole is blind, the lower part of the keyhole may be very unstable and the instabilities can produce bubbles towards the bottom of the keyhole [33, 34]. Under such conditions, any given point in space near the bottom of the keyhole may be occupied by vapour at one time and by liquid metal at another, a very special form of turbulence that is essentially two-phase flow with strong transitions from one phase to the other, with the formation of droplets a strong possibility.

The bottom end of a blind keyhole may move around erratically, and its boundary deform, in a manner reminiscent of chaotic behaviour; although its shape and position are given deterministically it appears to behave randomly. An interesting feature of such a situation is the possibility of a substantial downward force on adjacent regions of liquid material. Ablation on the upper surface of a protrusion from the keyhole wall or on a droplet occurs whenever the material is not shielded by molten material higher up the keyhole, but the ablation pressure which results does not balance the surface tension forces. A substantial excess pressure is produced in the liquid on upward-facing parts of the liquid while lower parts are shielded. The result is clearest in the case of droplets which will be impelled to move downwards (ultimately transferring their momentum to the melt pool), but the same applies to regions connected to the main body of fluid. In either case, there will be a net downward motion in the molten material [32]. As this occurs where the upward velocity of the

vapour in the keyhole is least, it can result in a net downward flow in the molten region through condition (1.9), rather than the anticipated upward flow that occurs elsewhere [35, 36]. The situation is illustrated schematically in Fig. 4.7b.

4.6 Further Aspects of Fluid Flow

4.6.1 Simplifying Assumptions for an Analytical Model

A simplified analytical model of the interactions of the keyhole and the molten material can be constructed by assuming that region B is thin; no distinction need be made between regions C and D; the keyhole is almost parallel-sided; flow parallel to the laser beam in the molten region is driven locally by the axial flow of the vapour in the keyhole; flow perpendicular to the laser beam is driven by the translation of the work piece and the need for most of the material to avoid the keyhole.

4.6.2 Lubrication Theory Model

A simple lubrication theory approach to modelling of flow in the keyhole can give some insight into the character of the flow. Take constant values for the density, ρ, and dynamical viscosity, μ so that the axial and radial components of the equations of motion and the equation of conservation of mass, are approximated by

$$\rho\left(u\frac{\partial u}{\partial r} + w\frac{\partial u}{\partial z}\right) = -\frac{\partial p}{\partial r} + \mu\left(\frac{\partial^2 u}{\partial r^2} + \frac{1}{r}\frac{\partial u}{\partial r} - \frac{u}{r^2}\right) \qquad (4.15)$$

$$\rho\left(u\frac{\partial w}{\partial r} + w\frac{\partial w}{\partial z}\right) = -\frac{\partial p}{\partial z} + \mu\left(\frac{\partial^2 w}{\partial r^2} + \frac{1}{r}\frac{\partial w}{\partial r}\right) \qquad (4.16)$$

$$\frac{\partial u}{\partial r} + \frac{u}{r} + \frac{\partial w}{\partial z} = 0; \qquad (4.17)$$

w is the axial velocity in the z-direction, u is the radial velocity in the r-direction and p is the pressure. Assume that the radius of the keyhole, $a(z)$, for a laser beam of radius a_0, is small compared to its length, ℓ, but retain the term in $\partial p/\partial z$ in (4.16) because of the possibility of a longitudinal pressure gradient term that is of the order of magnitude $(\ell/a_0)^2$ greater than the radial pressure gradient.

   If the Reynolds number is sufficiently low, neglect the left-hand sides of the first two equations and use the lubrication theory approximation; the assumption is made that the flow is locally the same as it would be if conditions were entirely uniform, with an effectively constant pressure gradient. There

is a regularity condition at $r = 0$ to be satisfied, and the pressure should be effectively the ambient pressure, p_0, at $z = 0$ and $z = \ell$. Continuity of stress is required at the keyhole wall; its normal component determines the position of the boundary, $r = a$. From (4.19) the tangential component has to be continuous at the boundary, and mass-flow has to be continuous. The conditions apply so long as the motion in the molten metal has any viscosity, whether or not the main body of the motion is separated from the boundary by a thin boundary layer. As a result, the equations of fluid dynamics for the molten region have to be solved and matched to the solution in the vapour region.

It is helpful to postpone the matching process and simply specify at this stage that on $r = a$, $u(a, z) = -U(z)$ and $w(a, z) = W(z)$. The linearised lubrication theory model (4.15)–(4.17) has the solution

$$u = -\tfrac{1}{2} r \frac{dW}{dz} + \frac{1}{4\mu} \left\{ \tfrac{1}{4} r \left(2a^2 - r^2 \right) \frac{d^2 p}{dz^2} + ar \frac{da}{dz} \frac{dp}{dz} \right\},$$

$$w = W + \frac{1}{4\mu} \frac{dp}{dz} \left(r^2 - a^2 \right),$$

with the pressure given by the differential equation

$$U = \tfrac{1}{2} a \frac{dW}{dz} - \frac{1}{4\mu} \left\{ \frac{a^3}{4} \frac{d^2 p}{dz^2} + a^2 \frac{da}{dz} \frac{dp}{dz} \right\} \quad \text{with} \quad p(0) = p(\ell) = p_0; \quad (4.18)$$

the last condition is a result of the requirement that $u(a, z) = -U$. One consequence is that

$$\delta p \equiv p - p_0 = O \left(\mu U \ell^2 / a_0^3 \right). \quad (4.19)$$

U and W are not independent and, in principle, an analysis of the liquid region is necessary to establish a connection.

4.6.3 Boundary Conditions

An important aspect of such a model is that part which gives the keyhole radius $a(z)$ and the ablation velocity at the wall, U. There are essentially two conditions, one a boundary condition that determines the location of the keyhole wall by a balance of forces; see Table 1.2. The other is the thermodynamic condition satisfied by material crossing the boundary wall. A simplified implementation of the former is to require that

$$\left\{ p(a) - p_0 - n_i d_{ij} n_j \right\} + \rho u_n \left(a \right)^2 = \frac{\gamma}{a}, \quad (4.20)$$

where $u_n = |\mathbf{n} \cdot \mathbf{u}(a, z)|$ and $\mathbf{n} \cdot \mathbf{u}(a, z) \approx -U - W(da/dz)$, so that the sign is positive when $\mathbf{n} \cdot \mathbf{u}(a, z)$ is directed outward, the direction of increasing value of the radial co-ordinate r. The effective coefficient of surface tension is γ; it may be less than the normal value since ablation is also taking place

at the surface so that the inter-molecular forces are much weakened. As a further approximation p_{liquid} will be taken to be equal to p_0, the atmospheric pressure. Consequently, the equation has terms whose orders of magnitude are in the ratio

$$\frac{\mu\ell^2 u_n}{\rho a_0^3} : \frac{\mu u_n}{\rho a_0} : u_n^2 : \frac{\gamma}{\rho a_0} \approx 10^5 u_n : 10 u_n : u_n^2 : 10^5 \qquad (4.21)$$

if all quantities are measured in SI base units. The last figure in the ratio is probably an overestimate for the reason given above. The term $n_i d_{ij} n_j$ in (4.18), which uses the notation of Table 1.1, is the normal component of the viscous stress and d_{ij} is the deviatoric part of the corresponding stress tensor; see [37] for the form of the individual stress components in polar co-ordinates. From its definition, it is of the order of $\mu U/a$ and is therefore small by comparison with δp whose order of magnitude is given by (4.19) to be of the order of magnitude of $\mu U \ell^2 / a_0^3$; it cannot necessarily be neglected.

The significance of the ratios (4.21) is most easily seen with the aid of a diagram representing the magnitudes of the various terms. In Fig. 4.8, the x-coordinate is $x = \log_{10}(u_n)$ and the y-coordinate is the magnitude of the components of the ratios on the right of the equation. In general, the uppermost line at any given value of x belongs to the dominant effect at that speed. Possible balances between terms occur when two or more such lines cross, and it is these points which represent a possible equilibrium state. Figure 4.8 shows that two different balances are possible in theory. The first is one in which the ablation forces balance the pressure ($x = 5$; put $u_n = 10^5$ in the ratio); since it requires the axial velocity to be of the order of $10^7 \, \mathrm{m \, s^{-1}}$ it can be rejected on the grounds that such high velocities are not observed in practice.

The second possibility is one in which there is a balance between the viscosity-driven pressure term and the ablation term (put $u_n = 1$ in the ratio), although this *cannot* be true near the exits, where $p = p_0$. The balance then determines the necessary ablation rate and the power needed to provide it.

Viscosity, therefore, is likely to dominate in the central section of the keyhole which is then kept open by a balance of the excess of the conventional pressure against the surface tension. The ablation velocity at the keyhole wall has to be of the order of $1 \, \mathrm{m \, s^{-1}}$ (with axial and hence ejection velocities of the order $10^2 \, \mathrm{m \, s^{-1}}$), figures which are broadly compatible with [23]. Such considerations do not apply at the exits of the keyhole, where $p(a) \approx p_0$; in these regions the keyhole has to be kept open by ablation pressure. The balance is now predominantly between the ablation term and the surface tension term (put $u_n = 10^{5/2}$ in the ratio). It does not necessarily result in excessively high axial velocities, though, since the exit region is short and indeed these velocities are still compatible with the results of [23]. It follows that it is necessary to retain at least the first and last two terms in (4.20) although the second can safely be ignored. Except at the bottom of a blind keyhole, and perhaps
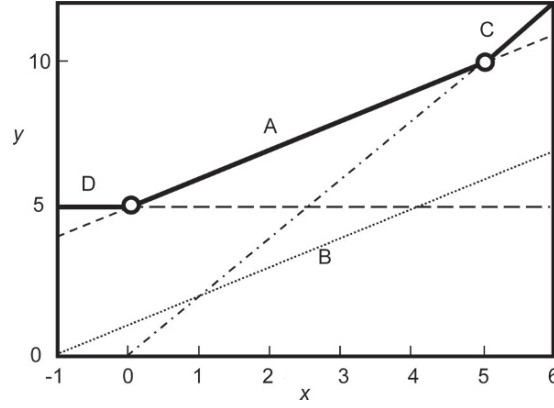
Fig. 4.8. Magnitudes of terms in the boundary condition (4.21). The magnitudes of the individual terms are shown by the straight lines A: $y = x + 5$ representing pressure effects; B: $y = x + 1$ representing viscous effects; C: $y = 2x$ representing ablation effects; D: $y = 5$ representing surface tension effects. The dominant terms at any given value of $x = \log_{10}(u_n)$ are shown bold and possible equilibrium balances by circles.

in the entry and exit regions, it is unlikely that a more accurate expression is needed for the surface tension term on the right. The arguments presented in §4.5.2 suggest that other considerations may apply at the bottom of a blind keyhole.

The model can be developed somewhat further with the conditions taken as

$$\delta p = \frac{\gamma}{a}, \quad \text{for } 0 < z < \ell, \tag{4.22}$$

the inequalities are strict and near the ends both of the principal radii of curvature may need to be taken into account, as well as the ablation term so that (4.22) should be replaced by

$$\delta p + \rho u_n^2 (a) = \gamma \left\{ \frac{1}{a\sqrt{1 + a'^2}} - \frac{a''}{\left(1 + a'^2\right)^{1/2}} \right\}, \quad \text{when } z \approx 0 \, \text{or} \, \ell \tag{4.23}$$

where dashes indicate differentiation with respect to z. It is also possible that in the vicinity of $z = z_0$, the bottom of a blind keyhole, the ablation pressure should also be taken into account and it would be necessary to make allowance for the inclination of the surface.

From (4.18), δp is given by solving the equation

$$\frac{d^2 \delta p}{dz^2} a^3 + 4a^2 \frac{da}{dz} \frac{d\delta p}{dz} + 16\mu \left(U - \tfrac{1}{2} a \frac{dW}{dz} \right) = 0. \tag{4.24}$$

Formally, the boundary conditions on this equation are

$$\delta p(0) = \delta p(\ell) = 0$$

but such conditions can only be applied in conjunction with (4.23). Otherwise the condition at $z = 0$ has to be taken as $\delta p = \gamma/a_0$ where a_0 is the beam radius, with a rapid transition region to the outside atmosphere; it is likely that the ablation pressure plays an important role here, and indeed may even provide the major balance. Similar considerations apply to the exit from the keyhole on the far side of the work piece with a_0 replaced by a_ℓ, though the ablation pressure is most unlikely to play a significant role here. If a difference of external pressure between the two ends of the keyhole exists, it can be taken into account. Seen from this point of view, (4.22) and (4.24) provide an equation linking a and $U - \frac{1}{2}aW'$ of the form

$$a\frac{d^2a}{dz^2} + 2\left(\frac{da}{dz}\right)^2 = \frac{16\mu}{\gamma}\left(U - \tfrac{1}{2}a\frac{dW}{dz}\right). \tag{4.25}$$

A second relation between U and a is the thermodynamic energy transfer condition between the laser, the ablated material, and the work piece. An example of a simple form of such a relation is provided in [1] pp 105 and 174–182. The Rosenthal line source solution [38, 39] is integrated about the laser axis to obtain the average temperature at a given distance from the axis in terms of the power absorbed per unit depth of the work piece, Q. The average keyhole radius, a, can be deduced for a given material with a boiling temperature T_B, so that an approximate relation is obtained between Q_{Th}, the associated value of Q, T_B and a of the form

$$T_B = T_0 + \frac{Q_{Th}}{2\pi\lambda}\mathrm{I}_0\left(\frac{U_{workpiece}a}{2\kappa}\right)\mathrm{K}_0\left(\frac{U_{workpiece}a}{2\kappa}\right)$$

If the power, P, at a given cross section is considered to be absorbed solely by Fresnel absorption at a rate Q_F per unit depth, it is approximated by $P = P_0(a/a_0)^{2(1-R)}$ where R is a representative value for $R_p(\theta)$ given in §4.3.2. If absorption by inverse bremsstrahlung is ignored and the power per unit depth Q_A needed to produce ablation is Q_A, $Q_F = Q_{Th} + Q_A$. These results can be combined to show that

$$2a'^{1-2R}\frac{da'}{dz'} + \frac{a'}{P'_{0L}}\left(U' + \frac{a_0}{\ell}\frac{da'}{dz'}W'\right) + \frac{F(a'\mathrm{Pe})}{P'_{0B}} = 0 \tag{4.26}$$

where

$$P'_{0L} = \frac{P_0(1-R)}{2\pi a_0\ell\rho L_v U_{scale}}, \quad P'_{0B} = \frac{P_0(1-R)}{2\pi\lambda\ell(T_B - T_0)}, \quad \mathrm{Pe} = \frac{U_{workpiece}a_0}{2\kappa_V}$$

and

$$L_v = c_{pS}(T_M - T_0) + c_{pL}(T_B - T_M) + L_M + L_V.$$

U_{scale} is a velocity scale for the radial vapour motion (e.g. that given above, with a value of the order of $1\,\mathrm{m\,s^{-1}}$) and is used to scale both U and W while

z is scaled with ℓ and a with a_0. $U_{workpiece}$ is the velocity of translation of the work piece relative to the laser and

$$F(x) = \frac{1}{\mathrm{I}_0(x)\,\mathrm{K}_0(x)} \sim 2x \quad \text{for } x \text{ large.}$$

The error in the approximation for $F(x)$ is only greater than 10% for x less 0.4, and decreases rapidly as x increases, being about 1% when x is 4. The three dimensionless numbers P'_{0L}, P'_{0B} and Pe are generally of the order of one.

The other interface conditions are continuity of tangential stress, continuity of tangential velocity and conservation of mass, respectively

$$\mu_L \left.\frac{\partial w_L}{\partial r}\right|_{r=a} = \mu \left.\frac{\partial w}{\partial r}\right|_{r=a}, \quad w(a) = W,$$

and

$$\rho_L \left(u_L(a) - w_L(a)\frac{da}{dz} \right) = \rho \left(-U - W\frac{da}{dz} \right)$$

where the subscript $_L$ indicates value in the molten region and the absence of a subscript indicates value in the vapour. The conditions are all expressed on the assumption that $a_0 \ll \ell$ and $\mathrm{O}(wa_0) = O(\ell u)$ in both liquid and solid regions.

4.6.4 Solution Matched to the Liquid Region

The interface conditions are not sufficient by themselves to close the model completely since it is necessary to solve the fluid equations in the liquid region. If, however, it is assumed that flow immediately adjacent to the keyhole is turbulent, an empirical relation from the study of turbulence can be used to provide an additional relation which avoids the difficulty. The difference between the wall velocity and the asymptotic velocity can be related to the wall stress by the approximate relation

$$\text{Asymptotic velocity} - \text{wall velocity} = k_0\sqrt{\text{wall stress/liquid density}}$$

where k_0 lies between about 0.035 and 0.05; Tritton [40], p 279.

For the layer on the liquid side of the keyhole wall, the difference between the wall velocity, W, and the axial velocity at the liquid/solid boundary (which is necessarily zero) is large so that if the turbulent layer is thin the asymptotic velocity of the turbulent layer at the keyhole relative to the velocity at the keyhole wall is not very different from W, and this empirical relation can be used as an approximation. For a thin turbulent layer in the molten metal next to the keyhole wall, it follows that W is given approximately by

$$W = -k_0\sqrt{\frac{\mu_V}{2\rho_L}\left|\frac{\partial w}{\partial r}\right|_{r=a}}\,\,\mathrm{sign}\left(\left.\frac{\partial w}{\partial r}\right|_{r=a}\right); \qquad (4.27)$$
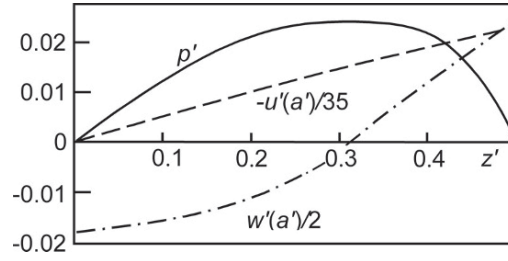
Fig. 4.9. Sample solution for the flow in the keyhole matched to the liquid region, using (4.27) to approximate effects of turbulent flow in the weld pool.

where $a_0 \ll \ell$; $\partial w/\partial r$ is obtained from (4.17), (4.18) and (4.22). Figure 4.9 shows a characteristic solution of (4.25)–(4.27) in dimensionless form, exhibiting features such as the following. There is a stagnation point at approximately half way down the keyhole, a pressure maximum at approximately the same place, and an outwardly-directed vapour flow at either end. It is interesting to notice that the magnitude of the radial velocity at the wall is least at the top of the keyhole and greatest at the bottom, though it must be remembered that the model requires a short adjustment region here to balance the surface tension forces in the absence of a compensating pressure effect.

When there is absorption of energy directly into the vapour in the keyhole that is sufficient to produce ionisation, even if only on a small scale, the radial and axial components of velocity of the vapour could affect the lateral conduction of heat to the keyhole wall. The discussion of §4.4 suggests that the effect can be ignored in many standard situations, but the model given in this section could be used to study cases where the effect needs to be taken into consideration.

4.7 Electromagnetic Effects

4.7.1 Self-Induced Currents in the Vapour

As distinct from the use of hybrid arc and laser beam welding, it has long been known that the introduction of an electric current can affect the characteristics of the resulting weld and alter its quality [41] as a result of the Lorentz forces. It is possible for example to increase the welding depth, or affect the size of the nail-head. An alternative approach is to consider the use of a magnetic field to influence the weld, a technique that is well-established in foundry technology and in arc welding processes, for example. Magnetic stirring during the laser welding of aluminium has been studied by Vollertsen and Thomy [42], and magnetically supported laser beam welding with a CO_2 laser was first studied by Kern et al. [43]. They showed that it is possible to suppress humping, improve top bead quality, modify the seam cross section,

reduce splashing, dampen plasma plume fluctuation and increase process stability; the polarity and orientation of the magnetic field made a considerable difference to the results. Kern had performed CO_2 laser beam welding experiments with a magnetic field applied perpendicular to the welding direction and noticed effects on the weld pool behaviour, whereas similar experiments with a Nd:YAG laser did not, from which the inference could be drawn that in the first case there must be significant current, but that the size of this current depended on the frequency of the laser light. Diagnostic measurements suggested that in the interaction zone of laser beam welding in the absence of a magnetic field there was a net current of 8 to 14 A. Experiments with electron beam welding suggested that the cause was the presence of a thermoelectric voltage between the melt and the base material of the order of $10^{-6}\,\mathrm{V\,K^{-1}}$. Ambrosy et al. [44] analysed the problem in terms of the generalised (macroscopic) Ohm's law in the plasma. An example of such a relation is provided by (1.27), which, in this form, applies to a fully ionised plasma, but a relation with similar structure will apply to a partially ionised vapour as well. The coefficient of $\mathbf{j} \times \mathbf{B}$ in this equation can be replaced by $\omega_{ec}/\sigma\nu_c$ where ω_{ec} is the electrical cyclotron frequency and ν_c is the collision frequency, with units $\mathrm{Wb^{-1}\,m^{-1}\,s^{-1}}$ and $\mathrm{m^{-3}\,s^{-1}}$ respectively.

If the current density $\mathbf{j}$ is considered in the absence of external electric and magnetic fields, the first three terms in (1.27) can only be present if the fields are induced by an intrinsic current and therefore cannot themselves cause it. A possible cause exists in the form of the fourth term on the right, and only requires the presence of a gradient of the electron pressure. Since it is temperature dependent, the effect requires the presence of a substantial plasma, as may be expected with a CO_2 laser beam where inverse bremsstrahlung absorption is strong but not at shorter wavelengths such as that of a Nd:YAG source; see (4.2) and [45], in accordance with their experimental results.

Equation (1.27) implies the existence of electromagnetic effects in the plasma, irrespective of whether there are externally imposed electric or magnetic fields. The complete set of equation for the electromagnetic dependent variables are appropriate forms of (1.11), (1.12), (1.26)–(1.28) and (1.29) for the unknowns $\mathbf{j}$, $\mathbf{B}$, $\mathbf{H}$, $\mathbf{E}$, $\mathbf{D}$ and ρ_{charge}. Equations (1.11) and (1.26) are not wholly independent, which accounts for the apparent discrepancy in the number of unknowns compared to the number of equations; in the steady state, (1.26) has only two independent components instead of three and in the time-dependent state (1.11) ensures that the same is true. Mathematically rather than physically (1.8) is a consequence of (1.12) and (1.27) and is therefore not an independent equation.

The equations explicitly contain the velocity field $\mathbf{u}$ and implicitly p and T; they are determined by suitable forms of (1.5), (1.6) and (1.7). The fluid mass density can be regarded as a convenient subsidiary variable, and is given by (4.5) in a gas.

The inclusion of ρ_{charge} in the list of unknowns in the problem together with the inclusion of the gradient of the electron pressure in (1.29) implies that

the convenient assumption that the ionised vapour is electrically neutral (see for example §4.2) is in general not true, although the high conductivity, σ, of an ionised vapour is likely to ensure that neutrality is a good approximation. Order of magnitude estimates confirm the assumption that ρ_{charge} has little effect on such processes.

Suppose that conditions are steady and no external fields are present. Although (1.29) can only be regarded as a rough guide for a partially ionised vapour, it can provide an illustration of possible mechanisms, even if these are not to be relied on in detail. An order of magnitude calculation then suggests that its terms are approximately in the ratio

$$0 : j : 10^2 \Delta V : 10^{-6} j : 10^{-13} j^2 : 10^2 : 0$$

where $\mathbf{E} = -\nabla V$ and $j = |\mathbf{j}|$. Multiplying by σ and taking the divergence shows that a balance between the 3$^{\text{rd}}$–6$^{\text{th}}$ terms must exist as well as one including the second. The principal balance therefore is one in which ΔV is of the order of $1\,\text{V}$, j is of the order of $100\,\text{A}\,\text{m}^{-2}$ and the only important terms in (1.29) are the 2$^{\text{nd}}$, 3$^{\text{rd}}$ and 6$^{\text{th}}$. The equations then simplify to

$$\rho_{charge} = -\nabla \cdot (\varepsilon \nabla V) \quad \text{and} \quad \nabla \cdot (\sigma \nabla V) = \nabla \cdot \left\{ \frac{k_B \sigma}{e} \frac{\nabla (n_e T)}{n_e} \right\}. \quad (4.28)$$

The current can be calculated from the approximate form of (1.29),

$$\mathbf{j} = \sigma \left\{ -\nabla V + \frac{1}{e n_e} \nabla p_e \right\} \quad (4.29)$$

and the charge density, if required, is given by

$$\rho_{charge} = -\nabla^2 \left\{ \int \frac{\varepsilon k_B}{n_e e} \frac{\partial}{\partial T} (n_e T) \, dT \right\}.$$

Thus

$$V = V_0(T) + V_1(\mathbf{x}) \quad \text{where} \quad V_0(T) = \int \frac{k_B}{e n_e} \frac{\partial}{\partial T} (n_e T) \, dT \quad (4.30)$$

where V_1 satisfies

$$\nabla \cdot (\sigma \nabla V_1) = 0. \quad (4.31)$$

Define V_0 to be zero at ambient temperature. Although it is assumed that the total pressure varies little from the atmospheric value, the partial pressures are temperature dependent.

Equation (4.28) must be solved for the potential V and matched to appropriate boundary conditions on the surface of the work piece and the walls of the keyhole. For there to be no current in the work piece it would be necessary for these to be an equipotential surface, a possibility which is not immediately self-evident. The numerical values for a typical keyhole weld with a CO_2 laser

Table 4.3. Values of voltage induced by electron pressure at atmospheric pressure, and resistivity.

T	300 K	800 K	3000 K	10000 K
Voltage: $V_0(T)$ from (4.30):	0 V	3.9 V	9.3 V	14.3 V
Resistivity $1/\sigma$ of plasma from (1.30):	$0.378\,\Omega\,\mathrm{m}$	0.087	$0.012\,\Omega\,\mathrm{m}$	$0.002\,\Omega\,\mathrm{m}$
Resistivity of iron:	$9.98\,\Omega\,\mathrm{m}$	$57.1\,\Omega\,\mathrm{m}$		
Typical resisitivity of an iron/nickel alloy	$34.3\,\Omega\,\mathrm{m}$			
Resistivity of air	$3 \times 10^{-5}\,\Omega\,\mathrm{m}$			
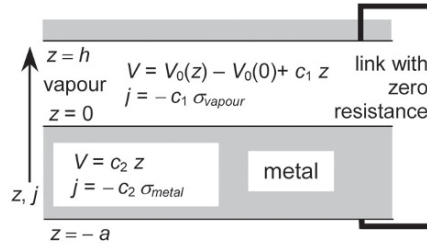
Fig. 4.10. Model problem for current and voltage induced by the gradient of the electron pressure in the vapour.

shown in Table 4.3 suggest that such a current may be possible, even if it is not particularly large. The imposition of an external magnetic field would then affect the velocity distribution in the weld pool.

Most of any return circuit will be through a mixture of the surrounding atmosphere, the shielding gas, and the partially ionised vapour. The metal vapour is much more conductive than the work piece and will play a significant part in such a circuit. The mathematical problem is to solve (4.29)–(4.31) with $\mathbf{j} \cdot \mathbf{n}$ and V continuous at the keyhole walls and the work piece's surface, and $V \to 0$ at infinity. A numerical solution is needed, but insight into the question of whether or not a non-zero current might be expected to flow as a result of the mechanism alone can be obtained from an idealised model problem.

For most of its length conditions in the keyhole are uniform with V_0 varying between about 9 V and 15 V between the keyhole wall and the axis of the keyhole, so consider a model consisting of the region above the work piece with an average value for V_0 at the keyhole exit and another, lower, average value over the rest of the surface of the work piece. Take an average value for the resistivity of the medium above the work piece, σ_{vapour}, and a higher one, σ_{metal}, for the resistivity of the work piece itself. Although this model is much simpler than reality, it is still more sophisticated than necessary. Figure 4.10 shows a one-dimensional idealisation that contains all the essential features. There is a plasma region above the plane $z = 0$ and a metal region below.

Both regions are bounded by surfaces which are connected by a link of zero resistance, so that they are electrically equivalent. In both regions (4.31) reduces to $d^2 V_1 / dz^2 = 0$.

The solutions for V and $j = |\mathbf{j}|$ are included in Fig. 4.10 in terms of the arbitrary constants c_1 and c_2. The continuity conditions on j and V at $z = 0$ (which may be thought of as equivalent to the work piece surface) and $z = h$ (equivalent to $z = -a$, equivalent to the end of the keyhole) give the values of the constants so that the current density in the system is

$$ j = \frac{V_0\left(h\right) - V_0\left(0\right)}{h/\sigma_{vapour} + a/\sigma_{metal}}. \tag{4.32} $$

In this instance at least, the gradient of the electron pressure leads to a net current without the need to impose an external current or an electric or magnetic field.

Although the gradient of the electron pressure may therefore be the cause of Kern's intrinsic current [43], Ambrosy et al. [44] have identified the thermal emission current density as probably the principal cause. The point is important since knowledge of the source of the current distribution in the weld pool is necessary before it is possible to ensure high quality weld seams.

There is a current density at the cathode surface (only) caused by escaping electrons whose magnitude is given by the Richardson-Dushman equation corrected for the Schottky effect as

$$ AT^2 \exp\left(-\frac{W - \Delta W}{k_B T}\right) \quad \text{where} \quad \Delta W = \sqrt{\frac{e^3 E}{4\pi\varepsilon_0}}. $$

E is the local electric field, $-e$ is the electronic charge, W is the electron work function of the surface (the minimum amount of energy needed for an electron to leave the surface) and A is Richardson's constant with a theoretical value given by

$$ \frac{m_e k_B^2 e}{2\pi^2 \hbar^3} \approx 1.20 \times 10^6 \, \text{A m}^{-2} \, \text{K}^{-2}, $$

although in practice its value depends on the material. The work function W is usually about half the ionisation energy of a free atom of the metal. For iron, for example, it is about $4.7 \, \text{eV}$ (7.5×10^{-19} J) [46], a value which is broadly characteristic of most common metals including unoxidised aluminium (about $4.2 \, \text{eV}$), although in the case of aluminium the value more than doubles when exposed to air so that it oxidises. The effect represents a modification to the condition on $\mathbf{j} \cdot \mathbf{n}$ at the interfaces. An estimate for the current generated gives a value of the order of $10^{-5} \, \text{A m}^{-2}$ compared to an estimate of the order of $10 \, \text{A m}^{-2}$ from (4.32).

4.7.2 The Laser Beam as a Current Guide

The fact that a laser beam of sufficiently low frequency, such a CO_2 laser, can have a high enough temperature to produce ionisation, with the resulting

low electrical resistance of a plasma or partially ionised vapour, means that in principle an electric current could be guided through an otherwise unionised atmosphere. Some theoretical work has been carried out on the idea [47, 48] and a patented application exists [49].

An energy balance equation can be set up for a cylinder of ionised vapour. If P is the total power at a given cross section of the cylinder and Q_B is the power absorbed per unit depth into the vapour by inverse bremsstrahlung at a given cross section; it can be estimated using (4.1)–(4.5). Power is lost from the arc through conduction, convection and radiation. Conduction of heat along the axis of the arc per unit length is likely to be small, but it is included as Q_{axial}. There will be a radiation loss $Q_{radiation}$ and a loss by convection and lateral conduction, $Q_{convection}$. They are balanced by power input to the arc as a result of ohmic heating from the current flowing in the arc, Q_{ohm}, and absorption of energy from the laser beam, Q_B. Then

$$\frac{dP}{dz} = -Q_B \quad \text{and} \quad Q_B + Q_{ohm} = Q_{axial} + Q_{radiation} + Q_{convection}.$$

Approximate the heating $\mathbf{E} \cdot \mathbf{j}$ per unit volume using Ohm's law, $\mathbf{j} = \sigma \mathbf{E}$, so that the ohmic heating per unit length of the arc in terms of the total current J is approximately

$$Q_{ohm} = J^2/\pi a^2 \sigma$$

where the conductivity σ is given by (1.30). Ignore the axial conduction term Q_{axial}. The component due to radiation might be expressed in the form

$$Q_{radiation} = 2\pi a R_c \sigma_{SB} T^4$$

where R_c is a coefficient which takes account of the fact that the cylindrical arc is not radiating like a black body and σ_{SB} is the Stefan-Boltzmann constant. Consideration of a partially ionised vapour using a quantum treatment is not straightforward, but [50] gives an example of an estimate for R_c obtained by a classical argument. It has the properties

$$R_c \sim 1 - 1/4s^2 \text{ as } s \to \infty \quad \text{and} \quad \sim 2s \text{ as } s \to 0 \quad \text{where } s = \tfrac{1}{4}\pi(n_n + n_i)d_a^2 a;$$

d_a is a suitable measure of the mean atomic diameter. For an arc with a radius of 1 mm at atmospheric pressure in air the value of R_c is close to 1.

To calculate the rate of loss of thermal energy per unit length of the arc as the result of thermal convection, an expression for the mass flow rate per unit area through the arc, $\dot{m}$, is required. If $\mathbf{n}$ is a unit vector in the direction of the laser beam and $\hat{\mathbf{g}}$ is a unit vector vertically upward, an estimate is

$$\dot{m} \approx \pi^{1/4} \sqrt{\frac{\rho \rho_0 g a}{|\mathbf{n} \times \hat{\mathbf{g}}|}}$$

if the density ρ of the hot ionised gas is small compared to the density ρ_0 of the surrounding gas and the angle of inclination of the arc to the horizontal is

not too great. The reasons are explained in the note at the end of the section. It should be regarded as the magnitude of a vector mass flux taking place in the upward vertical direction. To this must be added another vector mass flux which is the result of any wind. It has a magnitude $2a\,|\mathbf{n} \times (\mathbf{w} \times \mathbf{n})|$ per unit length of the arc and is in the direction mass flux per unit area of the wind, $\mathbf{w}$. The two quantities may be of the same order of magnitude. If the temperature of the arc is 10^4 K, the laser beam has a radius of 1 mm and the wind has a speed of $1\,\mathrm{m\,s^{-1}}$, the ratio of the two is $0.7 : 1$ with a magnitude for the latter of $2 \times 10^{-4}\,\mathrm{kg\,m^{-1}\,s^{-1}}$, so that in a wind of only quite moderate speed its cooling effect may dominate. A good deal of instability might therefore result if such an arc were to be employed in an open place; photographs tend to confirm it.

$Q_{convection}$ is the sum of $Q_{conv,lateral}$, the rate of loss of energy by thermal convection per unit length of the arc, and $Q_{conv,axial}$, a component of convection of thermal energy along the arc by the wind. If H is the increase in enthalpy per unit mass of the material passing through the arc, given approximately by (4.9), they are given by

$$Q_{conv,lateral} \equiv \left(H - \frac{p}{\rho}\right) |\mathbf{n} \times ((\dot{m}\hat{\mathbf{g}} + 2a\hat{\mathbf{w}}\,|\mathbf{n} \times (\mathbf{w} \times \mathbf{n})|) \times \mathbf{n})|$$

and

$$Q_{conv,axial} = \frac{d}{dz}\left\{\frac{\pi a}{2}\left(H - \frac{p}{\rho}\right)\left(-\dot{m}\hat{\mathbf{g}} \cdot \mathbf{n} + 2a\mathbf{w} \cdot \mathbf{n}\sqrt{1 - (\hat{\mathbf{w}} \cdot \mathbf{n})^2}\right)\right\}.$$

The equations can be solved for the temperature of the arc for a given beam radius and input power, and the relative magnitude of the various terms in the energy balance equation evaluated. With the temperature of the arc known as a function of distance along the arc, the maximum length of arc possible for a given power and beam radius, and the resistance of the arc, can be found.

Calculations given in [47] and [48] show that to obtain a path of the order of a metre or more in a gas such as air, very high powers are required for the laser beam, typically of the order of 100 kW or more, but that the resistance of the path can be very low with a total value for the whole path of a small fraction of an ohm. These distances are large compared to those currently used in materials processing, but the analysis demonstrates the way that a laser beam can influence the path of an electric current.

Note on Cooling by Thermal Convection

Consider the circular arc to be replaced by a square cross section with side d inclined at an angle θ to the horizontal so that $\cos\theta = |\mathbf{n} \times \hat{\mathbf{g}}|$, and suppose that

air at density ρ_0 enters across the bottom surface, is immediately converted to a density ρ and leaves across the top surface with that density. The height of the section is $d \sec \theta$ so the momentum balance requires that

$$p_{top} + \frac{\dot{m}^2}{\rho} + \rho g d \sec \theta = p_{bottom} + \frac{\dot{m}^2}{\rho_0}$$

provided the angle of inclination of the arc to the horizontal is not too great. Archimedes' Principle immediately adjacent to the arc gives

$$p_{bottom} = p_{top} + \rho_0 g d \sec \theta.$$

Solving these gives

$$\dot{m} = \sqrt{\rho_0 \rho g d \sec \theta} \approx \pi^{1/4} \sqrt{\frac{\rho \rho_0 g a}{|\mathbf{n} \times \hat{\mathbf{g}}|}} \quad \text{if } d^2 = \pi a^2.$$

References

1. Dowden JM (2001) The Mathematics of Thermal Modeling: An Introduction to the Theory of Laser Material Processing. Chapman Hall/CRC, Boca Raton, Florida
2. Dowden JM (2005) Analytical Modelling Of Energy Transfer Through The Vapour In Laser Keyhole Welding. In: Proc. 10th NOLAMP Conference, Luleå University of Technology, pp 127–138
3. Dowden JM (2006) Convection of energy in partially ionised vapour in laser keyhole welding. In: Brandt M, Harvey E (eds) Proc 2nd Pacific International Conference on Application of Lasers and Optics, Melbourne, paper No 402
4. Hughes TP (1975) Plasmas and Laser Light. Adam Hilger, London.
5. Hirschfelder JO, Curtis CF, Bird RB (1954) Molecular Theory of Gases and Liquids. Wiley, New York
6. Emsley J (1998) The Elements. Clarendon Press, Oxford
7. Knudsen M (1909) Die Molecularströmung der Gase durch Öffnungen und die Effusion. Annalen der Physik (Leipzig) 28(5): 999–1016
8. Anisimov SI (1968) Vaporization of metal absorbing laser radiation. Soviet Physics JETP 27(1): 182–183
9. Finke BR, Simon G (1990) On the gas kinetics of laser-induced evaporation of metals. J Phys D: Appl Phys 23: 67–74
10. Finke BR, Finke M, Kapadia PD, Dowden JM, Simon G (1990) Numerical investigation of the Knudsen-layer, appearing in the laser induced evaporation of metals. Proc European Congress on Optics, The Hague
11. Knight CJ (1979) Theoretical modeling of rapid surface vaporization with back pressure. AIAA Journal 17(5): 519–523
12. Sharipov F (2004) Heat transfer in the Knudsen layer. Physical Review E60: 061201, 1–4
13. Abramowitz A, Stegun IA (1965).Handbook of Mathematical Functions. Dover, New York, p 297

14. Anisimov et al. (1971) Effects of high power radiation on metals. Reproduced by National Technical Information Services, US Department of Commerce
15. Finke BR (1981) Untersuchung des Erosionjets bei der Destrahlung von Metallen mit Laserlicht hoher Intensität. Diploma Thesis, TU Braunschweig
16. Sone Y (2002) Kinetic Theory and Fluid Dynamics. Birkhäuser, Boston ch 3-6
17. Bayazitoglu Y, Tunc G (2002) An extension to the first order slip boundary conditions to be used in early transient regime. In: Proc 8th AIAA/ASME Joint Thermophysics and Heat Transfer Conference 24–26 June 2002, St Louis, Missouri. Paper no AIAA 2002–2779
18. Sharipov F (2003) Application of the Cercignani-Lampis scattering kernel to calculations of rarefied gas flows. II. Slip and jump coefficients. Eur J Mech B/Fluids 22: 133–143
19. Sharipov F, Seleznev V (1998) Data on internal rarefied gas flows. J Phys Chem Ref Data 27: 657–706
20. Stratton JA (1941) Electromagnetic theory. McGraw-Hill, New York, pp 500–511
21. Schulz W, Simon G, Urbassek HM, Decker I (1987) On laser fusion cutting of metals. J Phys D: Appl Phys 20: 481–488
22. Olsen FO (1980) Cutting with polarised laser beams. DVS-Berichte 63: 197–200
23. Amara EH, Fabbro R, Bendib A (2003) Modeling of the compressible vapour flow induced in a keyhole during laser welding. J Appl Phys 93(7): 4289–4296
24. Amara EH, Bendib A (2002). Modeling of vapour flow in deep penetration laser welding. J Phys D: Appl Phys 35(3): 272–280
25. Devoto RS (1967) Simplified expressions for the transport properties of ionized monatomic gases. Phys Fluids 10(10): 2105–2112
26. Devoto RS (1973) Transport coefficients of ionized argon. Phys Fluids 16(5): 616–623
27. Palmer GE, Wright ML (2003) Comparison of methods to compute high-temperature gas viscosity. J Thermophys & Heat Transfer, 17(2): 232–239
28. Gupta RN, Yos JM, Thompson RA, Lee K-P (1990) A review of reaction rates and thermodynamic and transport properties for an 11-species air model for chemical and thermal non-equilibrium calculations at 30000K. NASA RP-1232
29. Armaly BF, Sutton L (1980) Viscosity of multicomponent partially ionised gas mixtures. AIAA Paper 80-1495
30. Wilke CR (1950) A viscosity equation for gas mixtures. J Chemical Phys 18(4): 517–519
31. Murphy AB (1995) Transport coefficients of air, argon-air, nitrogen-air and oxygen-air plasmas. Plasma Chem. & Plasma Processing 15(2): 279–307
32. Matsunawa A, Semak V (1997) The simulation of front keyhole wall dynamics during laser welding. J Phys D: Appl Phys 30: 798–809
33. Dowden JM, Kapadia PD (1996) The instabilities of the keyhole and the formation of pores in the weld in laser keyhole welding. In: Mazumder J, Matsunawa A, Magnusson C (eds.) Proc. ICALEO'95. Laser Inst America, Orlando 80: 961–968
34. Dowden JM, Kapadia PD, Clucas A, Ducharme R, Steen WM (1996) Laser welding: On the relation between fluid dynamic pressure and the formation of pores in laser keyhole welding. J Laser Applics 8: 183–190
35. Kinoshita K, Mizutani M, Kawahito Y, Katayama S (2006) Phenomena of welding with high-power fiber laser. In: Ostendorf A, Hilton P, Lu Y (eds) Proc ICALEO 2007, Orlando USA, paper 902

36. Matsunawa A (2000) Possible Motive Forces of Liquid Motion in Laser Weld Pool. IIW Doc IV-770-2000/212-917-00. International Institute of Welding, Paris
37. Batchelor GK (1967) An Introduction to Fluid Dynamics. Cambridge University Press, Cambridge
38. Rosenthal D (1941) Mathematical theory of heat distribution during welding and cutting. Welding J 20(5): 220s–234s
39. Rosenthal D (1946) The theory of moving sources of heat and its application to metal treatments. Trans ASME 48: 849–866
40. Tritton DJ (1977) Physical Fluid Dynamics. Van Nostrand Reinhold: London
41. Ambrosy G, Berger P, Hügel H (2004) Electro-magnetically supported deep-penetration laser beam welding – Calculation of generated forces. In: Kaplan A (ed) Proc M^{4}PL 17. Luleå TU, paper 3
42. Vollertsen F, Thomy C (2006) Magnetic stirring during laser welding of aluminium. J Laser Applics 18(1): 28–34
43. Kern M, Berger P, Hügel H (2000) Magneto-fluid dynamic control of seam quality in CO_2 laser beam welding. Welding J 79(3): 72s–78s
44. Ambrosy G, Avilov V, Berger P (2007) Laser-induced plasma as a source for an electrical current in the weld pool. In: Kaplan A (ed) Proc M^{4}PL 20. Luleå TU, paper 2
45. Metzbower EA (1997) On the formation of the keyhole and its temperature. J Laser Applics 9(1): 23–33
46. Lide DR (1997) CRC Handbook of Chemistry and Physics 78th edn. CRC Press, Boca Ratan, p 12–124
47. Dowden JM, Kapadia PD (1998) A mathematical model of the use of a high-power laser to provide an electrical path of low resistance. In: Fabbro R, Kar A, Matsunawa A (eds) Proc ICALEO'97, Laser Inst. America, Orlando, 83e:C206-C215
48. Dowden JM, Kapadia PD (1998) The use of a high-power laser to provide an electrical path of low resistance. J Laser Applics 10(5): 219–223
49. Guinnessy P (1997) Set phasers to shock. New Sci 156: 6
50. Dowden JM, Kapadia PD (1994) Plasma arc welding: a mathematical model of the arc. J Phys D: Appl Phys 27: 902–910, Appendix 4

5

Basic Concepts of Laser Drilling

Wolfgang Schulz[1,2] and Urs Eppelt[2]

[1] Fraunhofer Institute for Laser Technology, ILT Aachen. `wolfgang.schulz@ilt.fraunhofer.de`
[2] Nonlinear Dynamics of Laser Processing, RWTH Aachen University. `urs.eppelt@ilt.fraunhofer.de`

Abstract. The state of the technology of μs pulse laser applications is dominated by single pulse drilling, percussion drilling and even trepanning used for high speed drilling with melt expulsion. However, short ps pulses have to be addressed anyway, since there are technical aspects in addition to achieve high speeds in drilling, namely, structuring and tapering while maintaining the mechanical integrity of operation. As an example, to avoid delamination of thermal barrier coatings while structuring the inlet of cooling holes in turbine manufacturing as well as to avoid cracking at the drilled wall forces the scientist to take into consideration the mechanisms of short pulse ablation at least in the case of ps pulses.

The variety of intriguing physical phenomena runs from recast formation (well known from the action of μs-pulses), via formation of cracks typical of ns- to ps-pulse duration, to homogeneous expansion, phase explosion and spallation characteristic of fs-pulses. The numerous phenomena are related to physical models describing propagation and absorption of radiation, ionisation, evaporation and non-linear transport of mass, momentum and energy. Technical achievements like lasers emitting 100 ps or shorter pulses and related experimental observations imply a future need for simulations to cope with the kinetic properties of beam-matter interaction. Temperatures approaching the critical state during ablation with pulse durations in a range from some ps to a few hundred ns raise the question whether Equation of State phenomena contribute to the overall appearance in drilling. In particular, beam aberrations instead of a free running or multiply reflected beam pattern are encountered in modelling independent of pulse duration. Beam aberrations are not only introduced by the action of beam guiding and forming optics, but also by spatially distributed feedback from the dynamical shape of the ablated material surface. Effects changing the phase distribution of the incident laser radiation are incorporated in the models for the first time: for example, some temporal and spatial changes in density in the gaseous phase. In drilling, the dynamical phenomena governing the shape of the drilled hole are identified experimentally and can be related to the processing parameters theoretically.

5.1 Introduction

Actually, modelling and simulation relevant to developing improved technical applications improved by extending the scientific basis from macro

applications into the field of shorter pulses of about a few nano-seconds and smaller length scales down to the wavelength of the radiation is considered. Some key physical phenomena become apparent and more dominant on smaller scales. As a result, there is also feedback from improved models on the micro-scale to simulations describing macro-applications. The analysis deals with the interaction of physical quantities including photon and wave properties of radiation, energy flow density and photon energy, via evaporation dynamics changing from quasi-steady to kinetic behaviour with shorter time scales and changing material properties while approaching the critical state at large temperatures, towards non-linear transport phenomena due to the fast movement of the ablation front in drilling with μs and ns pulses.

Research directions in the field of pulsed beam-matter interaction are twofold. While diagnostic methods are extended and refined to reveal additional phenomena and to improve understanding of them [1, 2], the investigation of phenomena that are already known are also detailed to achieve a mapping of the dominant phenomena to the causal radiation properties. To detail the relevance of the different physical phenomena requires the division of the parameter space spanned by the radiation properties and the processing parameters into subspaces, which are called processing domains. Different processing domains can be distinguished either by the different properties of the final processing result or by the corresponding path the system undergoes in the physical phase space during the interaction. As a result, a single processing domain is then characterised by a unique subset of selected physical phenomena, which are found to be dominant. Their typical time scales and intensity regimes are indicated. The theoretical goal is to reveal the specific model structure which reproduces the characteristics of the different processing domains. The approach consists of iterative extension, refinement and reduction of the specific physical models so that finally the essential physics is included, but there is no unnecessary complexity.

5.2 Technology and Laser Systems

The state of the technology of pulsed laser applications is dominated by single pulse and percussion drilling with μs-pulse duration used for high speed drilling with melt expulsion (Fig. 5.4). Drilling cooling holes and fuel filters as well as drilling holes for lubricant feed is performed with top-hat like spatial beam profiles [3]. Experiments for this application suggest the use of gas for drilling [4] to provide protection for the optical system from metallic melt ejection and to improve drilling quality when drilling break through occurs. Establishing high combustion temperatures for greater efficiency of aero-engines has raised the problem that plasma-sprayed Thermal Barrier Coatings TBC made out of zirconia are fault-prone to delamination when exposed to thermal gradients [5]. Use has been made of a high pulse energy $E_p < 50\,\mathrm{J}$ for high rate percussion drilling and it remains attractive, even when dealing with the properties of melt expulsion such as recast formation [6]; subsequent
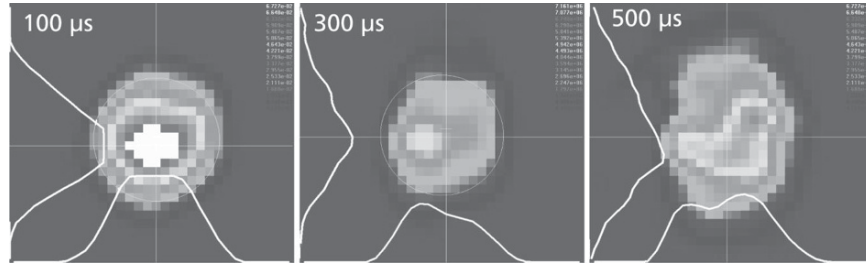
Fig. 5.1. Spatial distribution of intensity for laser system S1 at pulse duration $100, 300$ and $500\,\mu$s.

hot-cracking [7] as well as delamination of TBC remain an important problem. Reliable diagnostics of recast and cracking are improving continuously using microwave metrology, for instance [8]. It is worth mentioning that solving the additional task of structuring the inlet of cooling holes in turbine manufacture bearing in mind the TBC delamination task, favors a combination of short pulse ablation in the ps range with long pulses [9].

Flash lamp pumped laser systems with large pulse power at moderate up to high beam quality are applied on the industrial level [10]–[12]. For comparison with modelling and simulation a typical laser system is singled out. Such a laser system, referred to as laser system S1, combine beam quality $M^2 < 1.6$ with large pulse duration $t_p = 0.1$–$0.5\,$ms at high pulse power $P_{peak} = 2\,$kW. The maximum intensity I_0 at a focal length of $f = 100\,$mm is about $I_0 = 9 \cdot 10^7\,$W cm^{-2} (Rayleigh length $0.8\,$mm, focal radius $24\,\mu$m). It is worth mentioning that the spatial distribution of the intensity changes with pulse energy and pulse duration (Fig. 5.1). In particular, the nearly Gaussian intensity distribution at a pulse duration of $t_p = 100\,\mu$s approaches a rectangular shape at a pulse duration of $500\,\mu$s. The linear polarisation of the laser radiation facilitates pulse truncation or modulation of the temporal pulse shape using electro-optical devices, which is useful for probing deeper into the details of the temporal evolution of the drill-hole.

The state of the art in short pulse high power laser development is summarised in Fig. 5.2. Diffraction limited high beam quality fibre lasers, slab lasers and disk lasers can be obtained, and even rod lasers are still available. This new generation of radiation sources has been demonstrated and is increasingly available at an industrial level. From a scientific point of view these achievements are exciting, since high power, high beam quality laser radiation gives new opportunities to probe deeper into a wider variety of the phenomena encountered in laser-matter interaction. To approach the upper right part of Fig. 5.2 is the goal for future high precision high rate ablation applications. Nevertheless, many commercially available lasers are applied in niche markets today and are about to expand into new areas. The advent of promising technical applications [13] lies today in (a) ns and μs drilling of shaped holes by helical drilling [14], (b) drilling of extreme aspect ratios in
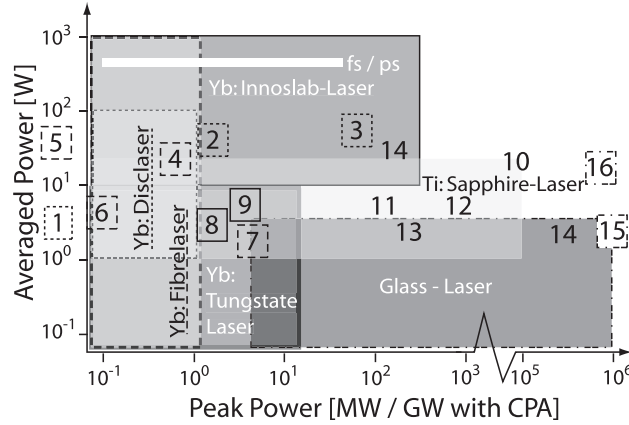
Fig. 5.2. Laser systems and industrial availability. With Chirped Pulse Amplification (with CPA) a factor 10^3 for the peak power is achievable. Yb:Disclaser (dotted): 1 Jenoptik, 2 Time-Bandwidth (without CPA), 3 TRUMPF (6.5 ps without CPA), Yb:Fibre laser (dashed): 4 Corelase, 5 IAP FSU Jena, 6 PolarOnyx, 7 Univ. of Michigan UoM, Yb:Tungstate Laser (solid bold), 8 Amplitude Systems, 9 Light Conversion, Ti:Sapphire-Laser (without borderline), 10 APRC Japan, 11 Coherent, 12 MBI Berlin, 13 Spectra Physics, 14 Thales 100/30, Glass Laser (dash-dotted) 15 Nova LLNL/Phelix GSI/Vulcan/RAP, 16 POLARIS FSU Jena, Yb:Innoslab (solid) current fs/ps-research (white bar) with specifications: $\tau_p \sim 1$ps (Yb:YAG), $\tau_p \sim 200$fs (Yb:KLG), $\nu_{rep} \in \{10\,\text{kHz}, 50\,\text{MHz}\}$, $P_{av} = 200$ W at $\lambda = 1030$ nm.

dielectrics/glass by ns-slab lasers [15], (c) nm-size periodic structuring of polymers by interferometric approaches, (d) ablation by ns- and ps-pulses for metal moulds [16], (e) generation of waveguide structures in glass by fs-pulses [17]. On the laboratory scale a next generation of diffraction-limited short pulse lasers is on the horizon [18]. In particular, ps-lasers at multi-hundred watts of average power with repetition rates of several MHz, fs-lasers at 400 W [15] average power, and green frequency-doubled lasers at 200 W are under construction. At the short pulse end, attosecond lasers have been demonstrated and will themselves open a new domain in the interaction of light and matter [19].

5.3 Diagnostics and Monitoring for μs Pulse Drilling

Numerous investigations of diagnostic methods and monitoring applied to laser applications which aim at a better understanding are reviewed [20, 21]. The observed physical quantities in drilling are the molten material splashing out of the drill entrance, the vapour jet above and below the drilled material and the thermal radiation emitted from the drill hole. In particular, lateral observation is applied to materials which are transparent to the thermal
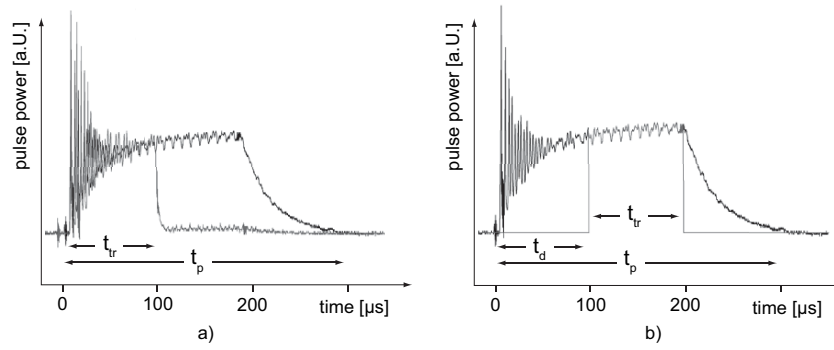
Fig. 5.3. Truncation of the pulse shape by electro-optic modulators.

radiation emitted by the plasma or the melt [10, 22, 23]. To find the relation between laser parameters and the temporal evolution of the hole is a fundamental task. The measurement of the drilling velocity or time dependent drilled depth usually requires the interpolation of data between different experimental runs by time-consuming preparation of sections, and the subsequent application of light microscopy. As an alternative to this time-consuming approach, drilling near the outer edge of a work piece allows the detection of the drilled depth during the process by observation of the thermal deformation of the material surface using high-speed videography [23].

To find the relation between laser parameters and the temporal evolution of the drill hole, electro-optic modulators are used to change the temporal pulse shape or to truncate a part of the laser pulse (Fig. 5.3). The direction of the linearly polarised electric field is rotated by the Kerr effect and then light is selected by a polariser. The particular advantage of extra-cavity electro-optic modulators is that the temporal pulse shape is modulated without changing the laser parameters such as the spatial distribution of the intensity (Fig. 5.1), since the laser parameters as well as the laser dynamics remain unaffected. As shown in Fig. 5.3 the original laser pulse with duration $t_p = 300\,\mu$s can be modulated by choosing a truncated pulse duration $t_{tr} = 100\,\mu$s with a delay t_d with respect to the original pulse; the maximum jitter of $6\,\mu$s is fairly acceptable. Using pulse truncation down to a duration $t_{tr} = 10\,\mu$s, the initial stages of the drill hole, especially the different dynamics of the evolution of the width and depth, can be analysed in detail (Fig. 5.13). Moreover, to single out the region of nearly constant pulse power (Fig. 5.15) as well as truncation of the temporal region where the pulse power decays (Fig. 5.16) reveals the effects of pulse shape on the overall appearance of the drill hole.

To improve quality assurance in drilling hollow components such as tubes or turbine blades, one technical task is to protect the rear side of the work piece. Different methods are investigated, such as the use of backer material which is removed after drilling, or using liquids to flood the internal volume.

Advances in the precise detection of the drill-through time are reported. Different approaches claim

- measurement of the delay an acoustic signal undergoes after reflection at the drilled wall
- inductive measurement of magnetic properties of the plasma
- optical detection of the thermal radiation emitted from the drill base in the coaxial or lateral direction with respect to the laser beam axis.

5.4 Phenomena of Beam-Matter Interaction

In optics generally photons or electromagnetic radiation are considered to interact with matter. The laser matured into a versatile light source and now continues to open up new opportunities for probing deeply into a variety of optical phenomena related to both photons and waves. Although numerous optical phenomena have already been found, and researchers have been exploiting their potential for technical applications for decades, it remains a challenge to set up a structuring or mapping (section 5.4.1) of the relation between well known phenomena and the radiation properties which cause them. Experimental diagnosis and theoretical analysis both suffer from the complication that the properties of laser radiation as well as the response of the material are dependent, at the very least, on time, space and energy. Moreover, pulse parameters such as pulse energy and pulse duration, as well as the spatial and temporal shape of the pulse, cannot be chosen independently but depend on the technical set-up of the radiation source and the dynamics of laser light generation. One of the numerous examples where details of the radiation properties become relevant to the interpretation of laser-matter interaction is the so-called pedestal pulse following the main laser pulse [24]. As a consequence of the pedestal pulse, the action of the main fs-pulse, which might be related to the processing domain referred to as "Cold Ablation" (Fig. 5.4) characterised by spallation, is obscured by the action of the longer ps-pedestal related to the processing domain known as "Hot Ablation" which mainly causes evaporation.

Bearing in mind, however, that the different phenomena take place simultaneously in different spatial regions as well as overlapping with respect to time and energy, it remains a challenge to distinguish the particular contribution of the different phenomena to the overall action of the laser pulse. In spite of that, there are selected parameter settings where only a small number of physical phenomena contribute; they can be distinguished by only four parameters, namely the photon energy, the energy flow density ϵ [$J \cdot m\,s^{-1} \cdot m^{-3}$] often called intensity I [Wm^{-2}] and the temporal and spatial extent of interaction often addressed as pulse duration and beam radius. It is therefore worth mentioning that there are indications of the existence of different physical domains of beam-matter interaction which can be classified by pulse duration (Fig. 5.4) and intensity (Fig. 5.6).
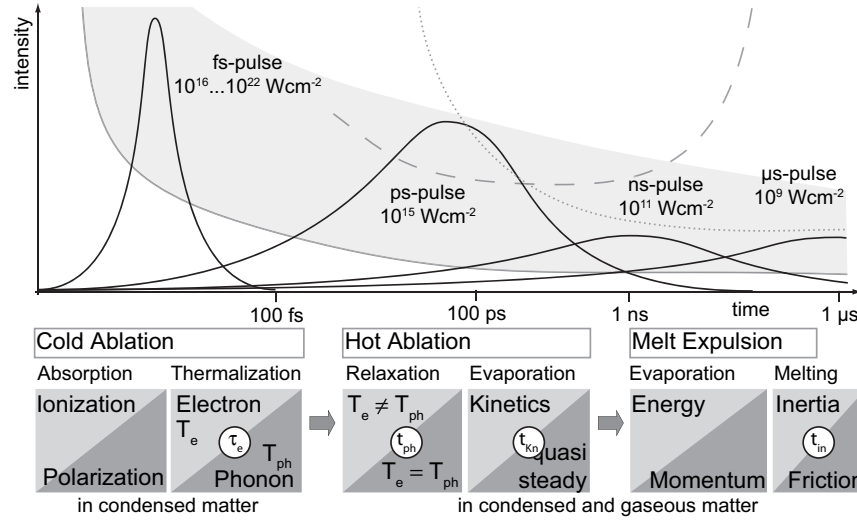
Fig. 5.4. Mapping of the three different physical domains – Cold Ablation, Hot Ablation and Melt Expulsion – with respect to the corresponding time scales. The ablation threshold (solid line), the maximum available pulse energy (grey) and the threshold for the critical state (dashed) of matter are indicated qualitatively. For long pulse durations the radiation also interacts with the ablated material in the gaseous phase (plasma threshold, dotted line). Typical time scales for thermalisation of electrons τ_e, relaxation of phonon temperature t_{ph}, for kinetics in the Knudsen layer approaching a quasi-steady state t_{Kn} and the onset of fully developed melt flow t_{in} limited by inertia are given.

5.4.1 Physical Domains – Map of Intensity and Pulse Duration

The interaction of radiation with matter in general takes place via excitation of electrons leading to polarisation and ionisation of atoms, molecules or condensed matter. Three physical domains distinguished by the corresponding time scales of their activation are indicated in Fig. 5.4, namely, Cold Ablation, Hot Ablation and Melt expulsion. Cold Ablation is characterised by beam-matter interaction taking place predominantly in the condensed state and the dynamics of subsequent ablation is governed by pure kinetic properties (section 5.4.5). Thermalisation of the photon energy absorbed by the electrons which leads to a thermodynamic equilibrium in the electron system, and which establishes an electron temperature T_e, takes place. One important method of describing kinetic properties is molecular dynamic simulation. Although Cold Ablation is analysed by molecular dynamic calculations [25]–[27] of the heavy particles, neglecting charged particles like electrons and ions, the results give remarkable insight. Hot Ablation sets in while the phonon system approaches local thermodynamical equilibrium with the initially heated electron system. The radiation interacts with both condensed

and gaseous matter. In Hot Ablation the condensed and gaseous phases do not reach a common equilibrium state, since they are separated by the evaporation front, which has the short time kinetic properties of a dynamical Knudsen layer. Melt Expulsion is characterised by reaching a fully developed continuum limit, where the long time limit of the kinetic Knudsen layer [28] across the evaporation front is also established. For ns-pulses evaporation takes a dominant role in the absorption of energy, but only a small amount of momentum is transferred to the melt and melt ejection sets in. With increasing pulse duration approaching the μs time scale, the energy is finally used mainly for melting, while evaporation acts as a powerful driving force introducing large momentum to the molten material via the recoil pressure at the liquid surface. Even in the range of dominant melting with increasing pulse duration a characteristic transition takes place, namely, from an inertia-dominated onset of melt flow at time scale t_{in} typical for sub-μs-pulses to fully developed melt ejection for μs-pulses and longer pulse durations. For μs-pulses melt flow is governed by the equilibrium between spatial changes of the recoil pressure and friction of the liquid at the solid melting front only. Further details are discussed in section 5.5.

Cold Ablation. Some more detailed relations and physical scales to support the understanding of the different physical domains can be given. For pulse durations t_p smaller than $t_p < 100\,$fs absorption of radiation initiates the processing domain called "Cold Ablation" (Fig. 5.4). In "Cold Ablation" the absorption of laser light by electrons and thermalisation – first between the electrons and later in the phonon system – are almost terminated while the matter remains in the condensed state. A few picoseconds later the phonon temperature rises and ablation of hot matter starts to take place. Typical atomic time scales for changes of the binding forces initiated by electron excitation or emission are comparable to the time $r_B/v_e \sim 2.5 \cdot 10^{-17}\,$s the electron needs for one round trip of the Bohr orbit with radius $r_B = 5.3 \cdot 10^{-11}\,$m and velocity $v_e = 2.2 \cdot 10^6\,\mathrm{m\,s^{-1}}$ [29]. In metals characterised by a large electron density, a pulse duration in the range of some femtoseconds is also a long time compared with the atomic scale r_B/v_e. Absorption and subsequent cold ablation can therefore happen without thermalisation of energy. Subsequent thermalisation of electrons by electron-electron collisions at $\tau_e \sim 10\,$fs is much faster than the thermalisation of phonons and thermalisation takes place separately with respect to time. It is worth mentioning that the time scale τ_e for relaxation of energy in the electron system

$$\tau_e = (\tau_{e-e}^{-1} + \tau_{e-ph}^{-1})^{-1} = (A\,T_e^2 + B\,T_{ph})^{-1}, \tag{5.1}$$

can be related to the final temperatures T_e and T_{ph} which the subsystems of electrons and phonons are approaching during thermalisation [30, 31]. The constants A and B are related to the electron-electron and electron-phonon collision frequencies, $\nu_{e-e} = A\,T_e^2$, $\nu_{e-ph} = B\,T_{ph}$. Values for the constants A and B are collected together in Table 5.1.

Table 5.1. Parameters of the hyperbolic two-temperature model at $T_e = T_{ph} = 300\,K$

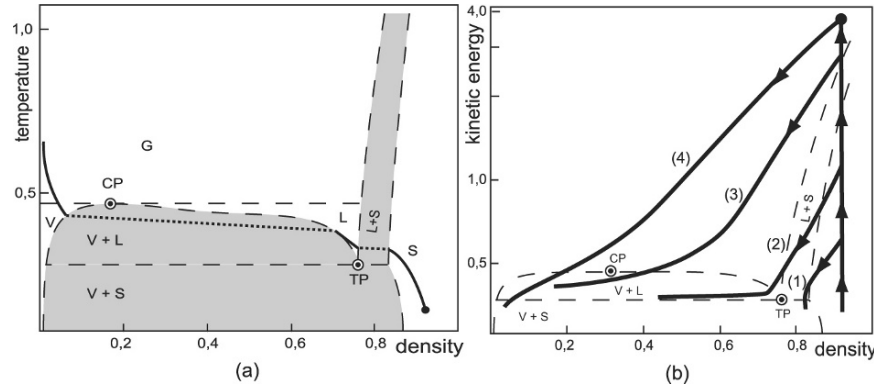|		Au	Al	Cu	Pb
A	$\mathrm{K^{-2}s^{-1}}$	$1.2 \cdot 10^7$	$2 \cdot 10^7$	$1 \cdot 10^7$	$0.9 \cdot 10^7$
B	$\mathrm{K^{-1}s^{-1}}$	$1.2 \cdot 10^{11}$	$7 \cdot 10^{11}$	$1.08 \cdot 10^{11}$	$47 \cdot 10^{11}$
$\tau_{\mathbf{Q}_e}$	fs	26	4.6	31	0.7
$t_e = C_e/h_{ex}$	ps	0.579	0.067	0.467	0.377
$t_{ph} = C_{ph}/h_{ex}$	ps	70.6	4.27	57.5	11.2

Fig. 5.5. (a) A typical path in the phase space for pulses longer than $t_p \gg 100\,\mathrm{ps}$ is related to the processing domain called "Melt Expulsion". Abbreviations are G Gaseous, V Vapor, L Liquid, S Solid, TP Triple Point, CP Critical Point. (b) The physical path in the phase space of a pre-selected material volume related to the action of a fs-pulse. The physical path is projected onto a sub-space spanned by kinetic energy instead of temperature and density. For reference, the binodal lines of the state of matter diagram for thermodynamical equilibrium are indicated (dashed). Depending on the energy absorbed, the dynamics of the matter volume follows four different paths in the physical phase space indicated by (1) spallation, (2) nucleation, (3) fragmentation and (4) vaporisation.

Molecular dynamic calculations for a fs-pulse [25] and a ps-pulse [26] showed that matter passes through one of at least four different possible paths in the physical phase space during beam-matter interaction (Fig. 5.5a). Typically, the material is modelled by Newton's equations of motion using a 2D-Lennard Jones potential with three parameters, namely binding energy ϵ of a few eV, atomic length scale σ of the order of a few Angstrom, and a cut-off radius. The calculated quantities such as kinetic energy and density are averaged with respect to an initially selected material volume and scaled by the binding energy ϵ and the initial density $1/\sigma^2$, respectively. Absorption of photons is approximated by an instantaneous energy transfer to the heavy

particles with a spatial distribution given by the Lambert-Beer law. The most interesting and plausible result from the molecular dynamic calculations is that the pulse energy is a dominant parameter for the selection of the path in phase space. At large energy density of the pulse far above the ablation threshold, different partial processes contribute their particular characteristics to the overall appearance of ablation. Even for small pulse duration in the range of tenths of femtoseconds the larger pulse energy leads to the temporal and spatial coexistence of different states of the gaseous phases as in the case of vaporisation (4) and fragmentation (3) as well as nucleation (2) of ablated particles (Fig. 5.5(a)).

Near the ablation threshold, spallation (1) is observed in the calculations, not only for fs-pulses [25] but also for ps-pulses [26, 27]. In spallation no gaseous phase is involved, while the thermo-mechanical load exceeds the yield stress of the material and removal like spalling of a thin metal disk is observed. The nucleation (2) path goes through the liquid phase as well as through the coexistence of a liquid-solid phase, and ends in the coexistence of a liquid-gas phase. Employing a phenomenological interpretation, nucleation is characterised by the development of vapour bubbles in homogeneously boiling molten material. For the last two ablation mechanisms, fragmentation (3) and vaporisation (4), ablation occurs outside the liquid-solid and liquid-vapour-coexistence regions, having the effect that the mass is separated from the surface just before relaxation to thermodynamic equilibrium becomes noticeable. The two paths are differentiated by cluster formation, which takes place in fragmentation (3) and is absent in vaporisation (4).

Hot Ablation. For pulse durations around $t_p = 100$ ps absorption of radiation initiates the processing domain called "Hot Ablation" (Fig. 5.4). Electron T_e and phonon T_{ph} temperatures are well defined thermodynamical parameters. Relaxation towards a common temperature $T = T_{ph} = T_e$ for electrons and phonons as well as the formation of a dissipative heat flux are the main physical effects encountered. In general, the initial heat flux Q_e of the electrons is much smaller than the spatial change $Q_e \ll -\lambda_e \nabla U_e / C_e \propto \nabla T_e$ of the energy U_e absorbed by the electrons. A detailed discussion of the dynamics involved by analysing the hyperbolic two-temperature model

$$\frac{\partial U_e}{\partial t} + \frac{\partial Q_e}{\partial z} = I_0 A_0 f(t)\alpha e^{-\alpha z} + h_{ex}(T_{ph} - T_e), \qquad (5.2)$$

$$\tau_{Q_e}\frac{\partial Q_e}{\partial t} + Q_e = -\lambda_e \frac{\partial T_e}{\partial z}, \qquad (5.3)$$

$$\frac{\partial U_{ph}}{\partial t} + \frac{\partial Q_{ph}}{\partial z} = h_{ex}(T_e - T_{ph}), \qquad (5.4)$$

$$\tau_{Q_{ph}}\frac{\partial Q_{ph}}{\partial t} + Q_{ph} = -\lambda_{ph} \frac{\partial T_{ph}}{\partial z}, \qquad (5.5)$$

is given by Kostrykin et al. [30]. Here the absorption of the laser radiation is described by the term $I_0 A_0 f(t) \alpha e^{-\alpha z}$, where $I_0 f(t)$ is the time-dependent intensity of the radiation, $A_0 = 1 - R_0$ is the degree of transmission at the surface related to the degree of reflection R_0, and α^{-1} is the penetration depth of the laser radiation. The thermal diffusivity of the phonons can be neglected compared to the electron diffusivity, $\lambda_{ph}/C_{ph} \ll \lambda_e/C_e$. The main questions arising from equ. 5.2–5.5 are related to the time scales for relaxation of electron temperature $t_e = C_e/h_{ex}$ and phonon temperature $t_{ph} = C_{ph}/h_{ex}$ towards a common value, as well as the relaxation time $\tau_{\mathbf{Q}_e}$ of the electron heat flux. The values of these coefficients at $T_e = T_{ph} = 300\,\mathrm{K}$ are presented in Table 5.1. Time scale separation for relaxation in the electron and phonon systems is pronounced. The long time limit for the heat flux Q_e of the electrons, which is given by Fourier's Law $Q_e = -\lambda_e \nabla U_e/C_e$, is established during the same very short time $\tau_{\mathbf{Q}_e} \sim \tau_e \sim 10\mathrm{fs}$ that the thermalisation of the electron system requires [30, 31]. For pulse durations much longer than $\tau_{\mathbf{Q}_e}$ the relaxation of the heat flow is negligible, thus showing that the standard parabolic two-temperature model of Anisimov is adequate, where the idealised assumption of instantaneous heat propagation is assumed [32]. As a result of time scale separation, for ps-pulses and the material data in Table 5.1, the electron temperature T_e is the fast variable with time scale t_e instantaneously following the dynamics of the phonon temperature, whose time scale turns out to be the slow variable with time scale $t_{ph} \gg t_e$ governing the dynamics during absorption and relaxation to a common temperature in metals.

Melt Expulsion. Kinetics in the Knudsen layer involved in evaporation and the numerous effects of the physical domain referred to as "Melt Expulsion" (Fig. 5.5b) are discussed in subsequent sections 5.4.2–5.4.5 and Sect. 5.5.

Ionisation and excitation depend not only on photon energy compared to atomic transitions energies, but also on the number density of photons, so that the intensity of the radiation induces quite different types of beam-matter interaction in metals. At least four domains can be differentiated with respect to intensity, which are characterised by heating of matter, the effects of sub- and super-atomic field strengths as well as the properties of relativistic particles (Fig. 5.6). At intensities lower than $10^{11}\,\mathrm{W\,cm^{-2}}$ absorption of infrared radiation in metals basically behaves optically linearly and elevated temperatures are established via Joule heating of the atoms by collisions with excited electrons from the conduction band. For pulse durations greater than 10ps the energy is dissipated in local thermal equilibrium. Thermal emission of electrons from condensed matter and collisional ionisation in metal vapours by the Richardson effect dominate the formation of ionised vapour or plasma. Corresponding thermal processes such as drilling and micro-processing are widely used in applications today.

At higher intensities above $10^{11}\,\mathrm{W\,cm^{-2}}$ multi-photon absorption or Multi-Photon Ionisation MPI in the infrared spectrum are observable [33].
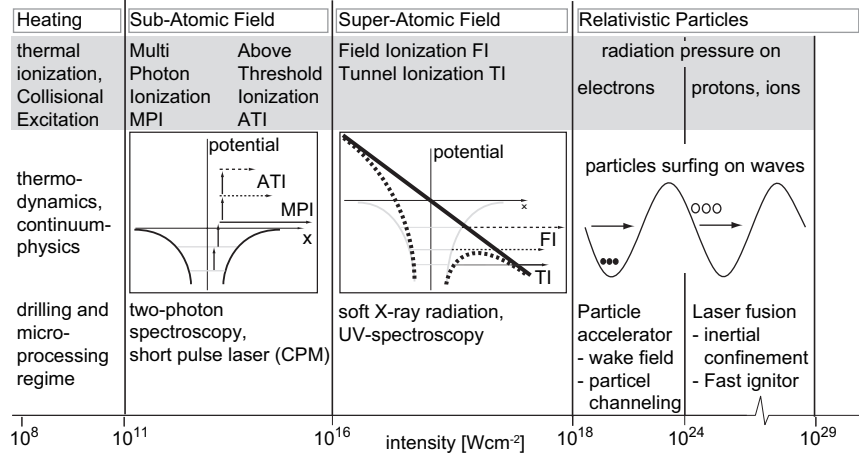
Fig. 5.6. Mapping of the different physical domains – Heating, Sub- and Super-Atomic Field Strength as well as Relativistic Particles – with respect to the corresponding intensity for metals.

The threshold intensity $I = n \cdot h\nu \cdot c$ for MPI of about $10^{11}\,\mathrm{W\,cm^{-2}}$ corresponds to a photon density $n = 4/3\pi\Delta s^3$. The spatial distance $\Delta s = c\Delta t_{virtual}/N$ between the photons moving at the speed of light c has to be as short as the photon travel distance $c\Delta t_{virtual}$ during the lifetime $\Delta t_{virtual}$ of virtual states in the atom divided by the number N of photons, which are needed to overcome the ionisation potential. Inserting $\Delta t_{virtual} = 10^{-15}\,\mathrm{s}$, $N = 5$ and the photon energy $h\nu = 1.5\,\mathrm{eV}$, then the spatial distance $\Delta s = 6 \cdot 10^{-8}\,\mathrm{m}$, the photon density $n \sim 10^{21}\,\mathrm{m^{-3}}$ and the threshold intensity $I = 7 \cdot 10^{10}\,\mathrm{W\,cm^{-2}}$ for MPI give plausible measures for the experimental evidence. The response of metals shows intensity-dependent optical properties. The non-linear effects are useful for increasing temporal and spatial resolution or selectivity in diagnosis and processing. Notable examples for increased temporal resolution are the colliding pulse mode CPM-laser and two-photon spectroscopy, or sub-wavelength modification which is based on increased spatial resolution. The data for threshold intensity I_{MPI} in Multi-Photon Ionisation of aluminium, copper and iron for the KrF- and TiSa-laser have been thoroughly investigated [34] and are collected in Table 5.2.

Above-Threshold Ionisation ATI is a kind of beam-matter interaction in which atoms subject to intense laser fields at intensities above $10^{12}\,\mathrm{W\,cm^{-2}}$ absorb more than the minimum number of photons required for ionisation. Since the first experimental discovery of ATI for Xenon atoms by Agostini in 1979 [35], ATI has been an important subject in ultrafast laser-atom interactions. Xenon with the ionisation potential of $12.27\,\mathrm{eV}$ absorbs twelve photons emitted from a Nd-glass laser, each having a photon energy of $1.17\,\mathrm{eV}$ at $10^{13}\,\mathrm{W\,cm^{-2}}$ of laser intensity. Both Multi-Photon Ionisation and

Table 5.2. Threshold intensity I_{MPI}, number of photons n involved and ionisation potential U_{ion} for multi-photon ionisation MPI of atoms. KrF-laser: wavelength 248 nm, photon energy 5 eV. TiSa-laser: wavelength 800 nm, photon energy 1.5 eV.

atom	U_{ion} [eV]	laser	N	I_{MPI} [W cm^{-2}]
Cu	7.73	KrF	2	$1.0 \cdot 10^9$
		TiSa	5	$5.0 \cdot 10^{11}$
Al	5.99	KrF	2	$2.3 \cdot 10^{10}$
		TiSa	4	$9.5 \cdot 10^{11}$
Fe	7.87	KrF	2	$1.0 \cdot 10^{10}$
		TiSa	7	$1.0 \cdot 10^{13}$

Above-Threshold Ionisation ATI are also involved in the formation of ionised processing gases.

The effect of Field Ionisation FI is revealed by the observation that fewer photons are necessary to ionise an atom than are required to overcome the energy U_{ion} for ionisation. Field Ionisation FI and Tunnel Ionisation TI come into play at intensities where the laser field E changes the atomic structure by ponderomotive forces. At intensities $I = (\epsilon_0 c/2) E_{atom}^2$ above $I > 10^{16}$ W cm^{-2} the electrical field strength becomes comparable with typical atomic fields $E_{atom} = (4\pi\epsilon_0)^{-1} e/r_B^2 \sim 5 \cdot 10^9$ V cm^{-1} depending on the Bohr radius $r_B = 5.3 \cdot 10^{-11}$ m [36]. In particular, the potential $U(x) = U_0(x) - eEx$ for an electron with charge e becomes asymmetric compared with the unperturbed potential $U = U_0(x)$. The energy U_{ion} for ionisation of Rydberg electrons and continuum electronic states is decreased by the ponderomotive energy U_p,

$$U_p = \frac{1}{m_e}\left(\frac{eE}{2\omega}\right), \qquad \gamma = \frac{U_{ion}}{2U_p} \tag{5.6}$$

which for free electrons in the laser field depends on electron mass m_e and charge e as well as the electric field amplitude E and photon energy $\hbar\omega$. The transition from dominant Field Ionization to tunnelling is characterised by $\gamma = 1$, where $\gamma = (U_{ion}/2U_p)$ is the well known Keldysh-parameter.

At 10^{18}–10^{19} W cm^{-2} the travel distance an electron needs to pick up its own rest energy $m_e c^2$ is only one wavelength λ of the incident visible light $eE\lambda = m_e c^2$ and the motion of the electron becomes relativistic. The energy of the wave becomes so large that the electron "surfs" on the wave. The wave exerts direct light pressure on the electron. The plasma and the particles become relativistic, the mechanisms lead to concepts and realisation for particle acceleration and to free electron lasers. If the field is a factor of 10^3 higher ($I = 10^{24}$ W cm^{-2}), the same effect occurs not only for electrons – they continue surfing at the bottom of this wave – but also

for heavy protons with mass m_p. The proton motion becomes relativistic $eE\lambda = m_p c^2$. Matter is directly compressed by the radiation in accordance with the fast ignitor concept of the Lawrence Livermore National Ignition Facility NIF. At about $10^{29}\,\mathrm{W\,cm^{-2}}$ the distance an electron needs to pick up its own rest energy is only its own de Broglie wavelength λ_{dB}. Thus the field comes into resonance with the matter wave. A change from collective absorption of electromagnetic radiation by electrons to a direct localised interaction of the photon with the particle has occurred, and electron-positron pairs are generated.

5.4.2 Beam Propagation

The effects of the wave-like, moving absorption front leading to dynamical aberrations of the laser radiation have to be analysed in comparison with free propagation in vacuo. The effects of the moving absorption front, where the laser is partially absorbed and reflected, on radiation propagation are rarely discussed beyond the level of geometric optics. Modelling and calculation of radiation propagation is feasible as long as well known model equations, such as Maxwell's equations, vector valued wave equations, and higher order Slowly-Varying-Envelope SVE-approximations or the geometrical optics approximation remain tractable by the available numerical methods. Numerical methods such as the Finite-Difference-Time-Domain FDTD-method, the Boundary-Element-Method BEM and the Beam-Propagation-Method BPM are sufficiently well developed in the literature to be applicable.

At the absorption front (the drill wall, the surface of the capillary in welding, or the cutting front), the laser radiation is reflected, absorbed or diffracted. Reflection and diffraction introduce changes in the laser beam. More precisely, the orientation and the absolute value of the Poynting vector are changed. The beam-forming effect of the absorption front has to be investigated in more detail by taking into account the wave properties of the radiation and the boundary conditions for strongly absorbing media. To solve Maxwell's equations directly the Finite-Difference-Time-Domain FDTD-method can be applied [37, 38]. The material equations of Drude and Lorentz are used to describe the electromagnetic properties of the metal or dielectric. Absorbing boundary conditions of so called "Perfectly Matching Layer" PML-type as well as periodic conditions work well at the external boundaries. Reflection, transmission and absorption of a plane wave incident on a plane surface are known analytically and serve as a test case. The accuracy of the numerical solution can be determined by comparison with the well known Fresnel Formulae (Fig. 5.7). Although the required spatial resolution in the range of 1/30-times the radiation wavelength is rather high, it is worth the cost of the calculation in order to gain a qualitative understanding.

Analysis of the structural stability of the physically approximated model equations for radiation propagation is carried out by revealing the changes
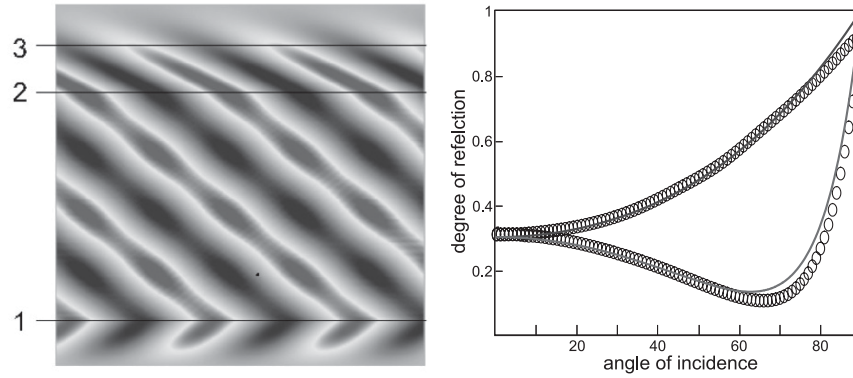
Fig. 5.7. Amplitude of a plane wave field emitted from boundary 1 incident on a plane surface (boundary 2) of a dielectric with periodic boundary conditions at the left and right boundaries calculated by the Finite-Difference-Time-Domain FDTD-method. The "Perfectly Matching Layer" PML is located above boundary 3. Comparison of the degree of reflection for a metal (complex refraction index $n = 1.42 + i \cdot 1.59$) calculated by the FDTD-method (circle) and the exact solution (solid line) from the Fresnel formulae as a function of the angle of incidence. Spatial resolution becomes important at glancing incidence.

in the solution depending on different physical model equations (Maxwell's equations, vector valued wave equations, the higher order SVE-approximation, the geometrical optics approximation). As a matter of fact, the accuracy of the different numerical methods such as the FDTD-method, the Boundary-Element-Method BEM and the Beam-Propagation Method BPM also have to be investigated.

5.4.3 Refraction and Reflection

The relevance of probing deeper into the details of radiation propagation becomes important if the optical path contains non-ideal optical objects such as density variations or particles within the gaseous phase. The cost of modification and adaptation of the model equations as well as the appropriate numerical methods are least in so far as ray-tracing can be used to describe the phenomena in question. For every additional order of reflection the cost increases in proportion to the number N of grid points. Calculating diffraction integrals means an increase to N^2. Finite-difference approaches are far more expensive, since the temporal evolution of the wave field has to be resolved, too. The aberration or beam forming due to metal vapour/plasma or a supersonic gas flow are investigated in detail. Radiation propagation in media with a spatially distributed index of refraction can be calculated by ray-tracing. The eikonal equation of geometrical optics is solved allowing for a spatially distributed index of refraction $n(\mathbf{r})$, where the arc length s along the ray $\mathbf{r}$ is
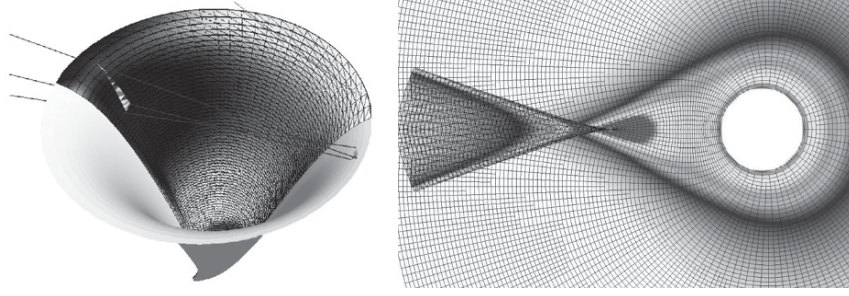
Fig. 5.8. Ray-tracing extended to inhomogeneous media and reconstruction of the multiply overlapping rays leading to caustic formation. A circular wave travelling outwards from the white circular area is diffracted by a spatially circular distribution of the index of refraction located left of the wave-emitting centre (white circle). Multiple reflections calculated by forward 3D-ray-tracing account for curvature and redistribution of power into a triangular surface grid.

introduced:

$$\frac{d}{ds}\left(n(\mathbf{r}(s))\frac{d\mathbf{r}(s)}{ds}\right) = \nabla n(\mathbf{r}(s)) \tag{5.7}$$

In inhomogeneous media $\nabla n(\mathbf{r}(s)) \neq 0$ the light rays become curved instead of being straight lines. The intensity is calculated solving the hierarchically ordered irradiance transport equations for the field amplitude [39]. To cope with the property of the solution that the wave fronts do not remain single valued but interfere with each other, the power of the refracted rays is projected and stored on a background grid. Methods for interpolation of point-wise defined quantities and adaptive approximation of functions by adaptive grid refinement are applied (Fig. 5.8).

It is worth mentioning that via the Cauchy dispersion relation the index of refraction n,

$$n - 1 = A\left(1 + \frac{B}{\lambda^2}\right), \tag{5.8}$$

depends on the material parameters A and B ($A = 87.80 \cdot 10^{-5}$ and $B = 22.65 \cdot 10^{-11}\,\mathrm{cm}^2$ for mercury vapour, $A = 29.06 \cdot 10^{-5}$ and $B = 7.7 \cdot 10^{-11}\,\mathrm{cm}^2$ for nitrogen, on radiation wavelength λ and is also related to the density ρ of the gaseous phase, where

$$\frac{n-1}{\rho} = \frac{n_0 - 1}{\rho_0}$$

which indeed changes in supersonic flow. Measured reference values n_0 and ρ_0 are available [40]–[42]. Analysis of refraction in inhomogeneous media combined with multiple reflections is used to reveal parameter ranges – known as

processing domains – where these effects show a dominant effect on the dynamical stability of the process. Improved understanding of radiation propagation is applied for a process-adapted design with beam-forming optics.

5.4.4 Absorption and Scattering in the Gaseous Phase

Absorption of infrared laser radiation in the metal vapour is governed by accelerated electrons colliding with atoms or ions. For the typical situation of drilling steel with μs-pulses, which is characterised by a pulse duration $t_p > 100\,\mu$s, pulse energy $E_p < 400\,$mJ and focal diameter $2w_0 = 40\,\mu$m of the laser beam, the metal plasma remains in local thermodynamic equilibrium and the number of multiply ionised ions is considerably smaller. The coefficient of absorption α of the metal vapour can therefore be approximated well by the Drude-model

$$\alpha = \frac{\omega_p^2\,\nu_e}{c(\omega^2+\nu_e^2)}, \quad \omega_p = \sqrt{\frac{n_e\,e^2}{\epsilon_0\,m_e}}, \quad n_e = n_e(T_g, \rho_g), \quad \nu_e = \nu_e(T_g, \rho_g) \qquad (5.9)$$

where ν_e is the collision frequency of electrons, ω the laser frequency and m_e the electron mass. The coefficient of absorption α depends on electron density n_e and on electron temperature T_e via the frequency ν_e of electron collisions. In consequence, the gas-dynamic state of the vapour enters the absorption coefficient α via the density ρ_g and temperature T_g. These quantities have to be estimated by calculations using the drilling model of section 5.5, for instance. The electron collision frequency ν_e is composed of two parts $\nu_e = \nu_{e,g} + \nu_{e,i}$, since electrons are dominantly colliding with atoms $\nu_{e,g}$ [43] and ions $\nu_{e,i}$ [44]

$$\nu_{e,g} = c_1\sqrt{T_e}\,n_g, \qquad c_1 = \frac{8\,(2\pi)^{3/2}r_{\text{Fe}}^2\sqrt{e}}{3\sqrt{m_e}} \approx 2.8\cdot10^{-13}\left[\frac{Hz}{m^3\sqrt{eV}}\right] \qquad (5.10)$$

$$\nu_{e,i} = c_2\frac{i^2\,n_i\,\ln(g)}{T_e^{3/2}}, \qquad c_2 = \frac{e^4(2\pi e)^{-3/2}}{3\varepsilon_0^2\sqrt{m_e}} \approx 1.6\cdot10^{-12}\left[\frac{eV^{3/2}}{m^3\,s}\right] \qquad (5.11)$$

$$g = 12\pi\,n_e\,\lambda_{Db}^3, \quad \lambda_{Db} = \sqrt{\frac{\varepsilon_0\,T_e}{n_e\,e^2}} \qquad (5.12)$$

where the atomic radius r_{Fe} for iron, the neutral atom density n_g, the degree of ionisation i, and the particle density n_i of ions, the Debye length λ_{Db}, the number g of electrons within the Debye sphere and the dielectric constant ε_0 are introduced. From 5.11 and 5.12 it turns out that for a small degree of ionisation i the contribution of the electron-ion collisions remains small compared to electron-atom collisions. As a result, the electron density $n_e(T_g, \rho_g)$ and the absorption coefficient $\alpha(T_g, \rho_g)$ can be calculated using the gas-dynamic state $\{T_g, \rho_g\}$ resulting from the evaporation model.

The coefficient of absorption α for the parameter range encountered in high speed drilling with Nd:YAG lasers $\lambda = 1\,\mu$m dominated by melt ejection
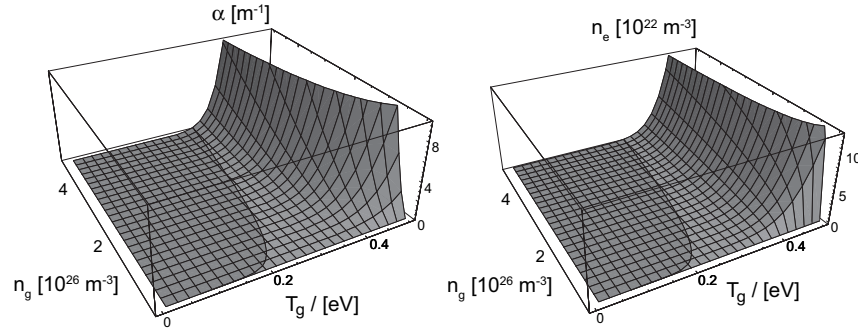
Fig. 5.9. Dependence of the coefficient of absorption α and electron density n_e on plasma temperature T_g and gas density n_g for stainless steel. Parameter range (dark-grey) is that encountered in high speed drilling dominated by melt ejection with intensities up to $I_0 < 10^{12}\,\mathrm{Wm^{-2}}$.

with intensities up to $I_0 < 10^{12}\,\mathrm{Wm^{-2}}$ is below $\alpha < 2\,\mathrm{m^{-1}}$. As a result, the absorption length is expected to be of the order of half a metre, much longer than the typical ablation depth or depth of a drilled hole. In consequence, plasma absorption in steel vapour produced at $\lambda = 1\,\mu\mathrm{m}$, $I_0 < 10^{12}\,\mathrm{Wm^{-2}}$ can be excluded from the list of dominant phenomena.

5.4.5 Kinetics and Equation of State

Energy and momentum is transported over a given distance L by the repeated movement of particles along a free path length λ between two subsequent collisions. Depending on the Knudsen number $\mathrm{Kn} = \lambda/L$, either the continuum assumption of fluid mechanics holds when $\mathrm{Kn} \ll 1$ or the kinetic properties of matter become essential when $\mathrm{Kn} \geq 1$. It is worth mentioning that the kinetic properties of matter are present not only for evaporation by fs-pulse duration at intensities larger than $10^{16}\,\mathrm{W\,cm^{-2}}$, but also play a dominant role in continuous evaporation at moderate intensities. Fluid mechanics fails as long as the distance L from the condensed surface remains comparable with the mean free path $\lambda_g \sim n_g^{-1/3}$ in the gaseous phase whose particle density is n_g. For laser drilling in condensed matter having a particle density n_c the Knudsen number $\mathrm{Kn} \ll 1$ is small, since the mean free path $\lambda_c \sim n_c^{-1/3}$ is small compared with the optical penetration depth α^{-1}. Immediately on the gaseous side of the condensed surface there is a layer formed known as the Knudsen layer, where the Knudsen number jumps to large values $\mathrm{Kn} \gg 1$, while the distance $L \ll \lambda_g$ remains small in the vicinity the condensed surface. The Knudsen number again approaches small values at distances $L \sim n\lambda_g$, which are a n-times the mean free path $\lambda_g = n_g^{-1/3}$ in the gaseous phase. In consequence, kinetic items are involved in any kind of condensed-gaseous phase change and the Navier-Stokes equations are not applicable. The task is

to find the kinetic details of the Knudsen layer, such as analysing the quasi-steady state of the Knudsen layer for example, and determining the time t_{Kn} the transition from a kinetic to a continuum state of the vapour takes. The transient time t_{Kn} for the build-up of a quasi-steady Knudsen layer (Fig. 5.4) has to be compared with pulse duration t_p. Separation of the time scales t_{Kn} and t_p is expected to change the overall result of evaporation.

The quasi-steady properties of the Knudsen layer are calculated using the Boltzmann equation for the kinetic distribution function $\Phi = \Phi(\mathbf{x}, \mathbf{V}_G)$. The function Φ describes the distribution of particles at position $\mathbf{x}$ with the hydrodynamical velocity $\mathbf{V}_G$ at the gaseous side of the Knudsen layer whose thickness is Δ_{vap}. The long time limit

$$\mathbf{V}_G \nabla \Phi = J(\Phi, \Phi), \quad \Phi|_{\mathbf{x} \in \Delta_{\text{vap}}} = \phi(\mathbf{V}_G), \quad \Phi|_{\mathbf{x} \to \infty} = \phi^{\text{MB}}(\mathbf{V}_G), \qquad (5.13)$$

has been solved numerically by Aoki [45], where the operator $J(\Phi, \Phi)$ is called the collision integral for relaxation of the distribution function Φ towards the Maxwell-Boltzmann equilibrium distribution $\phi^{\text{MB}}(\mathbf{V}_G)$ present on the gaseous side of the Knudsen layer. The result of the kinetic calculation gives a relation between the continuum properties of the gaseous phase outside the Knudsen layer (gas pressure P_G, temperature T_G, Mach-number $\text{Ma} = V_G/c(T_G)$) and the temperature T_L at the condensed or liquid side of the Knudsen layer.

$$P_G = G_1(\text{Ma}) \cdot P_{\text{sat}}(T_L) \qquad (5.14)$$

$$T_G = G_2(\text{Ma}) \cdot T_L \qquad (5.15)$$

where P_{sat} is the saturation pressure. For strong evaporation, referred to as the Chapman-Jouguet case

$$\mathbf{x} \in \Delta_{\text{vap}} : \ \text{Ma} = \frac{V_G}{c(T_G)} = 1. \qquad (5.16)$$

the Mach number $\text{Ma} = 1$ is already known. Here the gas-dynamics, in particular the gas pressure, do not change the evaporation process. It is worth mentioning that, for moderate evaporation, the Mach number $\text{Ma} < 1$ has to be determined and the additional information has to be taken from the gas flow outside the Knudsen layer

$$\mathbf{x} \in \Delta_{\text{vap}} : \ P_G = P_G(T_G, V_G) \qquad (5.17)$$

These model equations for quasi-steady evaporation correspond to the system path in the state diagram in Fig. 5.5b for large pulse duration. While the quasi-steady properties of the Knudsen layer are well known from the literature [28], the analysis related to the transient time t_{Kn} for the build-up of quasi-steady properties of the Knudsen layer remains an open question.

Moreover, relations depending on the state model, such as the ideal gas equation $P_G = \rho_G R_s T_G$ and other material properties like the enthalpies for
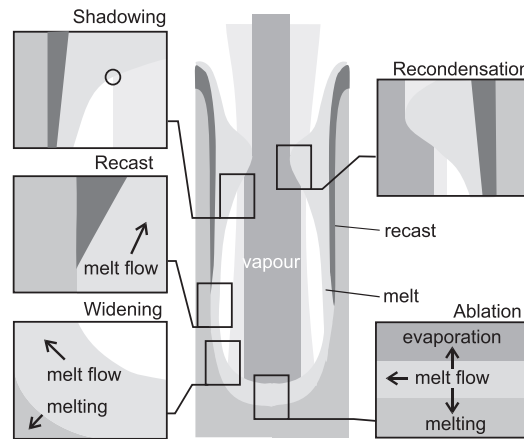
Fig. 5.10. Ablation at the drill base, widening by melt flow and narrowing by recast at the drill wall, shadowing the beam from the drill base, and recondensation of vapour.

phase transitions, become functions of temperature and pressure. Approaching the critical temperature the difference between the density of condensed matter and of the gas vanishes. Idealised state models are not applicable while approaching the critical temperature and more refined models have to be involved. In addition to molecular dynamic calculations, there are promising thermodynamical approaches like the Quotidian Equation of State QEOS developed by More et al. [46]

5.5 Phenomena of the Melt Expulsion Domain

In drilling with μs pulses the dynamical phenomena governing the shape of the drilled hole are identified experimentally and can be related to the processing parameters theoretically. Technical concern is focused on the build-up of recast at the drilled wall. Advances are made by relating the borders of the processing domain to dominant phenomena (Fig. 5.10) encountered in drilling such as ablation at the drill base, widening of the drill by melt flow and narrowing by recast at the drill wall, shadowing of the beam from the drill base near the entrance of the drill by the melt film and recast layer, recondensation of vapour at the drill wall and absorption by the plasma. After reaching a typical drilled depth recast formation sets in at the entrance of the drill hole (Figs. 5.12f, 5.15). Recast formation leads to deviation from a cylindrical drill and tends to narrow or even to close the entrance. Shadowing effects and strong aberration of the radiation take place. The distribution of the aberrated radiation determines the hole shape.
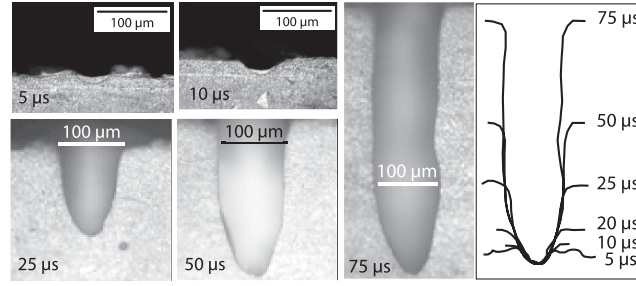
Fig. 5.11. Shape of the single pulse drills. Cross sections for truncated pulse durations $t_{tr} \in \{5, 75\}\mu$s, (*CMSX-4*, Nd:YAG laser, $t_p = 300\,\mu$s, $E_p = 325\,$mJ).

Mathematical model reduction is carried out using the existence of an inertial manifold, which is present in distributed dynamical systems dominated by diffusion [47, 48]. The corresponding long time limit of the underlying physical model is derived [18, 49, 50]. In principle, a spatially distributed dynamical system consists of an infinite set of dynamical parameters. Approaching the inertial manifold a substantial reduction in the number of degrees of freedom takes place. While the fast quantities undergo relaxation on the shortest time scales they are adiabatically linked to the small number of slowly varying quantities. Detailed exploitation of the time scale separation allows the analysis to be based on a model which shows no unnecessary complexity. Subsequent extensions including shorter time scales and the corresponding additional dynamical parameters can be carried out stepwise and with controlled error. Experimental evidence (Fig. 5.11) shows that the final shape of the drill base is established during the first few tenths of microseconds, which reinforces the mathematical arguments for a reduced model describing the dynamics of the drill base in the long time limit. Although temporal changes of the processing parameters on time scales larger than a few microseconds result in a dynamical evolution of the drill hole, the dynamical system does not leave the inertial manifold. These new scientific findings [9, 10] are shown by carefully taking into account the shadowing effects of melt flow and recast formation on radiation propagation; formerly they were obscured. Applying pulse durations in the range up to a few tenths of a ns the drill terminates in a transient regime in which the melt flow is not fully developed. The appearance of such a transient regime is seen to be a consequence of the time scales (5.25) of the model (Sect. 5.7.5) and can be observed in experiments (Fig. 5.18).

5.6 Mathematical Formulation of Reduced Models

The mathematical argument for the derivation of reduced models is the existence of an inertial manifold in dissipative dynamical systems of partial

differential equations [47, 48]. The concept of inertial manifolds is applicable to cutting, welding and drilling [51]. The long-time limit for a fast moving ablation front is given by a three-dimensional inertial manifold, an asymptotic subspace with the minimum number of degrees of freedom spanned by the position $A(t)$ and the global curvature $\alpha(t)$ of the absorption front as well as the heat content $Q(t)$ in the condensed phase. Deviations from the three-dimensional inertial manifold are due to spatial details like local curvature, and temporal effects such as the short rise time of the laser pulse whose effects decay on short time scales compared with the typical times for the movement of the slowest variables $A(t)$, $\alpha(t)$, $Q(t)$. Deviations from the inertial manifold are investigated by spectral decomposition of the diffusion operator.

5.6.1 Spectral Decomposition Applied to Dynamics in Recast Formation

For analysis of recast formation at the drill walls the curvature $\alpha(t)$ is negligible and $A(\tau)$ describes the position of the resolidification front. The time-scale t_{rec} for the build-up of the recast layer of thickness $A(\tau)$ at the drill wall can be found by analysis of the heat dissipation in the melt film and the solid, which become nonlinearly coupled through the movement of the recast front $\rho = A(\tau)$. The molten material flowing from the drill base leads to widening of the drill base and prepares the initial conditions ($\tau = 0$) for the melt flow and further heat dissipation into the solid at the drill wall. The liquid in the interval $\rho \in [-1, A(\tau)]$ covers the solid region $\rho \in [A(\tau), \infty]$. The recast front $\rho = A(\tau)$ starts to move with $\dot{A}(\tau) < 0$ into the liquid melt film. The liquid temperature $\theta_\ell(\rho, \tau)$ is described by a spectral decomposition using the eigenfunctions $\cos(\lambda_k \rho)$ of the diffusion operator whose eigenvalues are λ_k and mode amplitudes are $a_k(\tau)$. The dynamics of the temperature $\theta_s(\rho, \tau)$ in the solid are represented by changes of the penetration depth $Q(\tau)$ of the heat. The temperatures in the liquid and solid are coupled at the free moving boundary, namely the recast front whose position is given by $\rho = A(\tau)$:

$$\theta_\ell(\rho, \tau) = 1 + \sum_{k=0}^{\infty} a_k(\tau) \cos\left(\frac{(k + 1/2)\pi}{A(\tau)}\rho\right), \qquad \theta_s(\rho, \tau) = \exp\left(-\frac{\rho - A(\tau)}{Q(\tau)}\right)$$

$$(5.18)$$

Initially, when the recast front starts to move into the liquid, the liquid temperature $\theta_\ell(\rho, \tau) \geq 1$ is above the melting point $\theta = 1$ and heat is dissipated into the solid which remains at a lower temperature $\theta_s(\rho, \tau) \leq 1$. The initial conditions ($\tau = 0$), namely the values for a_k and A, Q, are given as a result from heat convection at the drill base and the heat released earlier into the solid, respectively. As boundary conditions at the drill wall, there is no heating by the laser beam, and the recast front $A(\tau)$ remains at melting temperature

$\theta = 1$ so that

$$\frac{\partial \theta_\ell}{\partial \rho}\Big|_{\rho=-1} = 0, \quad \theta_\ell\mid_{\rho=A(\tau)} = \theta_s\mid_{\rho=A(\tau)} = 1, \quad \theta_s\mid_{\rho\to\infty} = 0. \qquad (5.19)$$

The dynamics in the solid and liquid phase are nonlinearly coupled by the movement of the recast front at position $\rho = A(\tau)$ described by the Stefan boundary condition

$$\frac{\partial \theta_s}{\partial \rho}\Bigg|_{\rho=A(\tau)} - \frac{\partial \theta_\ell}{\partial \rho}\Bigg|_{\rho=A(\tau)} = h_m\,\dot{A}(\tau). \qquad (5.20)$$

The equations of motion for the degrees of freedom a_k, Q, A are derived by inserting the ansatz (5.18) into the heat conduction equations for the liquid (5.21) and the solid (5.22) as well as into the Stefan boundary condition (5.23):

$$\dot{a}_\ell + \left(\frac{\left(\ell + \frac{1}{2}\right)\pi}{A(\tau)}\right)^2 a_\ell = -\frac{\dot{A}(\tau)}{A(\tau)}\sum_0^\infty 2\pi\,g_{k\ell}\left(l + \frac{1}{2}\right)a_k, \qquad (5.21)$$

$$\dot{Q} = \frac{3}{5}\left(\frac{1}{Q} - \dot{A}\right), \qquad (5.22)$$

$$(1 + h_m)\,\dot{A} = -\dot{Q} + \sum_{k=0}^\infty a_k \cdot \left(\frac{\left(k + \frac{1}{2}\right)\pi}{A(\tau)}\right)\cdot(-1)^k \qquad (5.23)$$

where the initial conditions read $a_\ell|_{\tau=0} = a_{\ell 0}$, $Q(\tau)|_{\tau=0} = Q_0$, $A(\tau)|_{\tau=0} = 1$.

As a result, the relaxation of heat in the liquid $t_{rec1} = d_m^2/\kappa_\ell$ with melt film thickness d_m as well as in the solid $t_{rec2} = (\delta_s)^2/\kappa_s$ with penetration depth δ_s of the heat and the difference of the heat flux at the recast front contribute to the time scale of the dynamics. The time scale t_{rec} is given by the slowest contribution. The growth time-scale $|\dot{A}| \gg 1$ of the recast layer becomes small and is given by $t_{rec1} = d_m^2/\kappa_\ell$ for almost no heat release into the solid $t_{rec2} \ll t_{rec1}$ and no initial overheating of the liquid ($a_k(\tau = 0) = 0$). To slow down the build-up of a recast layer, $|\dot{A}| \ll 1$ and heating at the melt film surface along the drill wall has to balance the heat released into the solid.

5.7 Analysis

Modelling guided by experimental observation and comparison with simulation results gives seven fundamental findings which support understanding of the melt expulsion domain (Fig. 5.4), namely (1) the time-scales for initial heating and relaxation of melt flow during the rise time of the pulse, (2) the widening of the drill to a drill width up to approximately two times the beam diameter, (3) narrowing of the drill entrance due to recast formation as well as (4) suppression of recast by heating the drill walls during melt ejection,

(5) closure of the hole at a typical distance from the drill base, called lift-up height, by decelerated melt flow and recast formation, (6) non-local effects and the influence of pulse decay on the lift-up height, which changes the drill base from nearly circular to a more peaked shape subsequent to shadowing of the beam by the onset of closure, and (7) the transition time t_{in} for which the melt flow changes from inertia-dominated to friction-controlled.

5.7.1 Initial Heating and Relaxation of Melt Flow

Time-scales in the parameter range available for μs-pulses can be derived from the dynamical model. The time t_m to melting and to evaporation, t_v, are small compared with the time for relaxation t_{relax} of the melt flow. The time t_{relax} of a few microseconds is small compared with the time $t_\ell \simeq 100\,\mu$s the flow takes for moving up the drilled depth $\ell_B = 1\,$mm. In terms of the dependent quantities melt film thickness d_m and drilling velocity v_p – as well as the material properties: inverse Stefan-number h_m, kinematic viscosity ν, and evaporation temperature T_v – the time scales read

$$t_m = \frac{\pi}{4\kappa_s}\frac{\lambda^2(T_m - T_a)^2}{A_p^2 I_0^2}, \quad t_v = \frac{\kappa_\ell}{v_p^2}\ln\left(1 + \frac{\frac{T_v - T_m}{T_m - T_a}}{1 + h_m}\right),$$

$$t_{relax} = \frac{5}{12}\frac{d_m}{v_p}\frac{1}{1 + \frac{5}{8}\frac{\nu}{v_p w_0}}, \quad t_\ell = \frac{\ell_B}{\frac{w_0}{d_m}v_p},$$

$$(5.24)$$

The time t_m until melting is $t_m \approx 0.1\,\mu$s ($T_m = 1800\,$K, $\kappa_s = 10^{-5}\,$m^{2}s^{-1}, $A_p = 0.4$). Performing experiments with pulses truncated by a Pockels cell the evolution of the drill hole can be observed (Fig. 5.12 a–c). As a result, the time scales fit well with the experimental evidence. Using electro-optic pulse truncation (Fig. 5.3a)) the initial stages of the evolving drill hole can be analysed in detail. In particular, the different dynamics of width and depth at the drill base can be found (Fig. 5.13). The final width of the hole is first established on a typical time scale of a few tenths of a μs, while on the same time scale the depth changes from a slow parabolic rate of increase to a rapid linear increase. This experimental evidence for time-scale separation of the shape of the drill hole supports the setting up of a drilling model which is spatially integrated with respect to a fast dynamic relaxation shape of the drill base, called the spatially integrated model.

5.7.2 Widening of the Drill by Convection

There is no simple relation between the width of the laser beam and the drill, depending on the material properties and the laser radiation. The integrated model, which covers evaporation at the drill base and melt flow along the wall as well as recast formation, shows the widening of the drill base and gives fairly good results when compared with drilling experiments (Fig. 5.13).
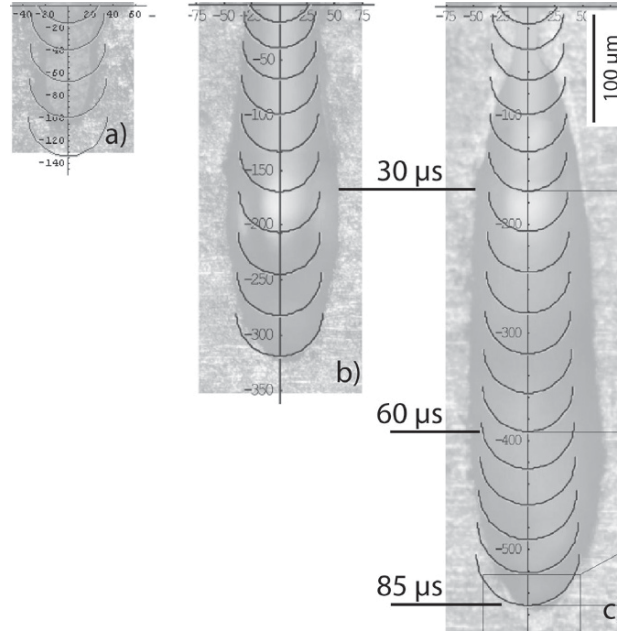
Fig. 5.12. Cross sections of truncated single pulse drills. Pockels cell with jitter $\Delta t_p = \pm 6 \, \mu$s. a)–c) Time increment $\Delta t = 5 \, \mu$s for simulation output. Truncated pulse duration $\{t_{tr} \in \{30, 60, 90 \, \mu$s $(X5CrNi18\text{-}10, t_p = 180 \, \mu$s, $E_p = 200 \, $mJ).
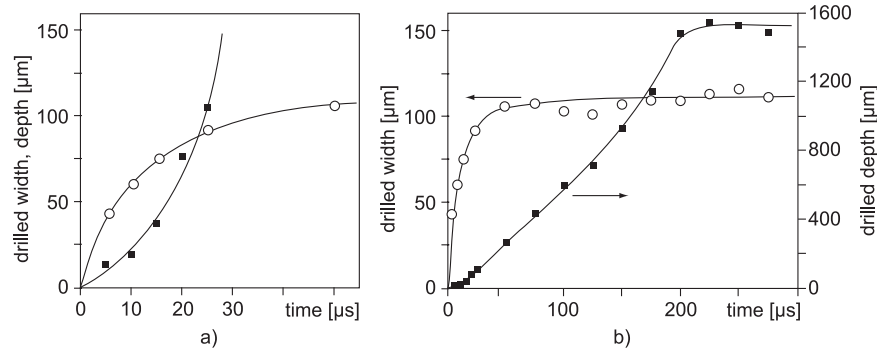

Fig. 5.13. The drilled depth (squares) and the width (circles) of the drill at the entrance. Truncation of the total pulse duration of $t_p = 300 \, \mu$s into truncated pulses of duration $t_{tr} \in \{10, 300\} \mu$s by electro-optic modulation of the resonator quality. Temporal increment Δt_{tr} for the truncated pulse durations is $\Delta t_{tr} = 10 \, \mu$s Results are given a) for the first $50 \, \mu$s and b) for the total pulse duration.

Global energy balance considerations yield the ratio $F(Pe_\ell) = P_K / P_\ell$ of convective P_K and dissipative power P_ℓ. It depends on the Péclet-number $Pe_\ell = (V_0 \, d_m)/\kappa$ only. P_ℓ is comparable to P_K and hence the ablated volumes per unit time inside and outside the w_0-environment around the beam axis
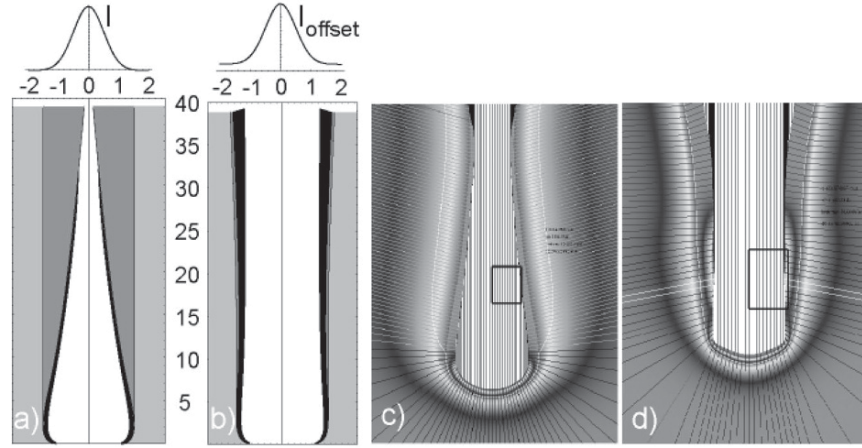
Fig. 5.14. Simulation of the integrated model a), b). Gaussian intensity profile without a) and with offset b) heating the wall: a) closure by recast (dark grey), b) heating the wall prevents recast formation, melt film (black). Length scale $w_0 = 20\,\mu$m. Simulation of the spatially resolved model c), d): Temperature in the solid: ambient (grey) to melting (light-grey) and liquid: melting (grey) to evaporation (light-grey) c) no shadowing, d) geometric optical shadowing.

are of the same order of magnitude. Energy balance and the Stefan condition at the melting front yield the widening Δr of the drill:

$$\Delta r = \left(\exp\left(\frac{Pe_\ell}{2} \right) - 1 \right) \cdot w_0. \tag{5.25}$$

As an example, for a drilling velocity $V_0 = 6\,\mathrm{m\,s^{-1}}$ and a laser beam radius $w_0 = 20\,\mu$m the widening $\Delta r \approx 0.82\,w_0 = 16\,\mu$m of the drill corresponds fairly well to the experimental evidence (Fig. 5.13). The measured values for the width are mostly above the predicted values of this model, which suggests that there are additional causes for widening such as recondensation of the evaporated material, plasma heating of the drill wall or beam aberration.

5.7.3 Narrowing of the Drill by Recast Formation

During drilling the laser beam predominantly heats the drill base and the melt cools down while flowing upwards along the walls resulting in recast formation on the additional time scale t_{rec}. To slow down the build-up of a recast layer (Fig. 5.14) heating at the melt film surface along the drill wall has to balance the heat release into the solid. As a result, typically a power of a few hundred Watts per mm drilled depth is sufficient to avoid recast formation. The spatially resolved model reproduces the onset of recast formation on the analytical scales and its tendency to narrow the drill and even to shadow the beam from the drill base (Fig. 5.14 c,d).
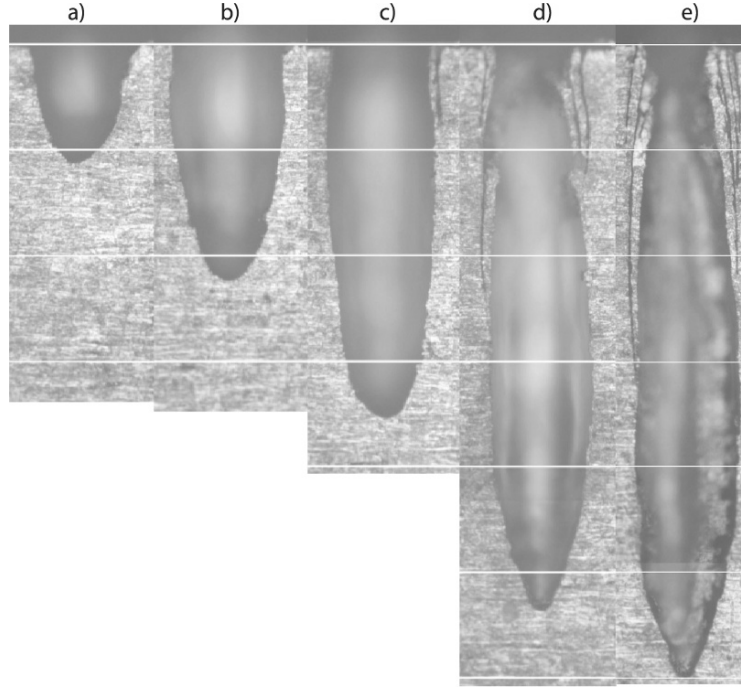
Fig. 5.15. Longitudinal sections showing recast layers at the entrance of the drill in percussion drilling with $n = 1$–5 pulses. No recast layer at a) $n = 1$ and b) $n = 2$ pulses. During every additional pulse a new layer of recast is formed: one, two, and three recast layer are observed for c) $n = 3$, d) $n = 4$, and e) $n = 5$ pulses, respectively. Horizontal white lines are separated by $100\,\mu$m. *X5CrNi18-10*, laser system S1, pulse energy $E_p = 200\,$mJ, pulse duration $t_p = 180\,\mu$s, truncated pulse width $t_{tr} = 30\,\mu$s.

The shape of the drill hole and formation of recast, which can also induce subsequent crack evolution, are the quality criteria known to be the most relevant to the action of μs-pulses. The mechanism for the build-up of recast is illustrated in the case of percussion drilling. With increasing pulse number n and drilled depth ℓ_B the formation of recast first sets in at the entrance to the drill. In particular, there is a typical value $\ell_B \geq \ell_{recast}$ for which every additional laser pulse generates a new recast layer at the entrance. As a result of percussion drilling, several recast layers overlap (Fig. 5.15). The number of recast layers equals the number of pulses after reaching the drilled depth $\ell_B = \ell_{recast}$. Using the laser system S1, the distance ℓ_{recast} between the drill base and the onset of recast at the drilled wall is about $\ell_{recast} = 375\,\mu$m.

The time scale $t_{recast} = d_m^2/\kappa$ for recast formation during melt flow along the drill wall is related to the melt film thickness d_m and the thermal diffusivity κ of the liquid metal. The distance $\ell_{recast} = r_B + v_m \cdot t_{recast}$ from the drill base with radius r_B where the recast sets in depends on the melt velocity v_m and the

time t_{recast}. For example, taking the velocity $v_m = 6\text{--}9\,\mathrm{m\,s^{-1}}$ and the melt film thickness $d_m = 20\text{--}30\,\mu\mathrm{m}$ from the spatially integrated dynamical model the time $t_{recast} = 40\text{--}90\,\mu\mathrm{s}$ and the distance $\ell_{recast} = 360\text{--}560\,\mu\mathrm{m}$ agree well with the experimental evidence from percussion drilling, where $\ell_{recast} = 375\,\mu\mathrm{m}$ is observed (Fig. 5.15d,e). By applying additional energy to the drill wall the formation of recast can be reduced significantly and the molten material separates from the drill [9, 52]. By heating the drill walls and slowing down the velocity of resolidification the drill walls are also free of recast for a greater drilled depth. The amount of power P_{heat} needed for heating the walls

$$P_{heat} = \rho H_m v_p \cdot F_{wall}, \qquad F_{wall} = 2\pi r_B (s - s_0) \tag{5.26}$$

depends on the density ρ, melting enthalpy H_m, the drilling velocity v_p and the surface area F_{wall} of the drilled wall. The dependent parameters radius r_B of the drill, and the arc lengths $s - s_0$ where resolidification takes place, enter through the surface area F_{wall} and are calculated by the integrated model (Fig. 5.14).

5.7.4 Melt Closure of the Drill Hole

Experimental observation – showing resolidified droplets beneath a closure – gives a hint that, starting at a critical depth L_{krit}, the drill hole can be closed by the melt. The melt flow slows down (5.31) at the entrance of the drill, the melt film thickness increases (5.29) with distance from the drill base, and finally starts to shadow the laser beam (Fig. 5.14c). Radiation heats the closure to evaporation temperature thus re-ejecting part of the molten closure (Fig. 5.14 d). This so called lift-up of the melt then happens periodically and leads to pronounced changes in the drill shape. The critical depth L_{crit} at which the drill starts to close can be estimated from the reduced model. The melt flow is driven by the gradient of the pressure Π_ℓ and shear stress Σ_g. The reduced model for melt flow is

$$Re\left(\frac{\partial m}{\partial \tau} + \frac{6}{5}\frac{\partial}{\partial \beta}\left(\frac{m^2}{h}\right)\right) = -\frac{\partial \Pi_\ell}{\partial \beta}h + \frac{3}{2}\Sigma_g - 3\frac{m}{h^2} \tag{5.27}$$

$$\frac{\partial h}{\partial \tau} + \frac{\partial m}{\partial \beta} = v_p(\beta, \tau) \tag{5.28}$$

where $m = m(\beta, \tau)$ and $h = h(\beta, \tau)$ denotes the mass flow and the melt film thickness, respectively.

The curvature K of the melt film surface enters the boundary condition for the pressure, when the melt flow slows down. The corresponding dimensionless group is called the Weber number We, scaling the ratio of hydrodynamic (ρV_0^2) and capillary pressure (σK). For We < 1 the surface tension σ tends

to form droplets and hinders separation. The pressure Π_ℓ is then given by

$$\Pi_\ell \; \to \Pi_\ell + \mathrm{We}^{-1}\frac{\partial^2 h}{\partial\beta^2}\,, \quad \mathrm{We} = \frac{\rho V_0^2}{\sigma K}. \qquad (5.29)$$

The resulting equation of motion is known as the Kuramoto-Sivashinsky equation, which describe unstable periodic orbits and the transition to turbulence of thin film flows.

For small Reynolds numbers ($\mathrm{Re} \to 0$) a separation of time scales of the dependent variables can be observed. From (5.27), (5.28) the slow manifold reads

$$m = \frac{\partial\Pi_\ell}{\partial\beta}\frac{h^3}{3} + \Sigma_g\frac{h^2}{2} \qquad (5.30)$$

The dynamics of melt flow is dominated by the melt film thickness as is well known from lubrication theory:

$$\frac{\partial h}{\partial\tau} + \frac{\partial}{\partial\beta}\left(\frac{\partial\Pi_\ell}{\partial\beta}\frac{h^3}{3} + \Sigma_g\frac{h^2}{2}\right) = v_p(\beta,\tau). \qquad (5.31)$$

Three major phenomena decelerate the melt at the drill wall: friction, resolidification at the wall and recondensation of the vapour. As a result, (5.27), (5.28) shows that the position $L_{krit} = \beta_{krit}w_0$ at which the drill is sealed by the melt,

$$L_{krit} = \frac{V_0\,w_0^2}{\nu}\frac{2}{5}m_0(1 - \varepsilon h_0), \qquad (5.32)$$

depends only on the inflow m_0 of mass and the melt film thickness h_0 from the drill base ($\varepsilon = d_m/w_0$). Shadowing of the radiation from the drill base by a large melt film thickness is also reproduced by the spatially resolved model (Fig. 5.14 c, d) and a pronounced feedback of shadowing onto the shape of the drill base and the acceleration of the melt is observed.

Electro-optic pulse truncation is used to single out the effect of decaying intensity at the end of the natural pulse shape on the spatial shape of the drill and recast formation at the drilled walls (Fig. 5.16). Two single-pulse drills are compared where the pulse energy 290 mJ and the pulse duration 290 µs are kept constant. For a pulse shape which includes the decaying part (Fig. 5.16a), the width of the drill changes and recast formation is pronounced, while for the truncated pulse without the decaying part, the hole is nearly cylindrical and the thickness of the recast layer is clearly reduced.

The onset of melt closure during drilling is observed at a pulse energy of $E_p = 200$ mJ and pulse duration $t_p = 180$ µs (Fig. 5.17). Estimating the drilling velocity from the resulting drilled depth in experiments averaged with respect to drilling time steps of 10 µs yields an initial drilling velocity $v_p < 1.5\,\mathrm{m\,s^{-1}}$ during the first 20 µs of the total pulse. At an elapsed time of 50 µs values of $v_p = 8\,\mathrm{m\,s^{-1}}$ are reached. For larger pulse duration the drilling
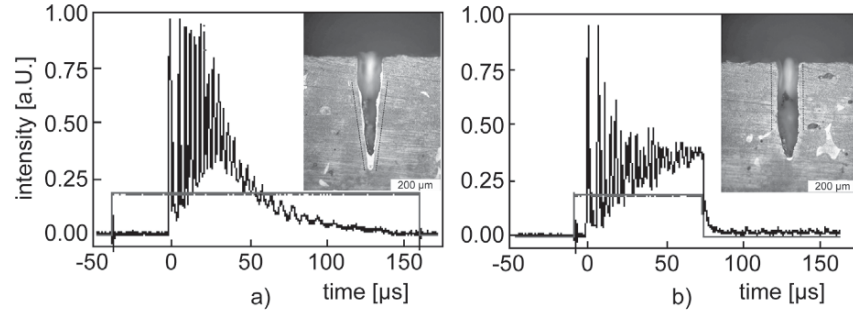
Fig. 5.16. Longitudinal sections showing the shape of the hole and recast at the drilled walls as a result of single pulse drilling with a) decaying intensity of the natural pulse shape and b) with electro-optic pulse truncation, the pulse having no decay. CMSX-4, laser system S1, pulse energy $E_p = 290\,\text{mJ}$, pulse duration $290\,\mu\text{s}$.
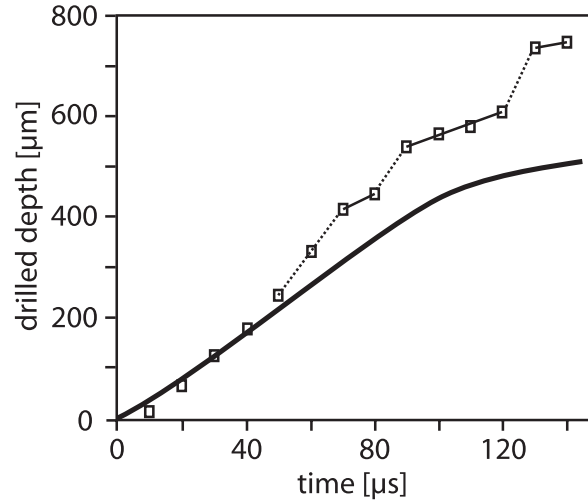

Fig. 5.17. Single pulse drilling with electro-optical pulse truncation. The pulse duration is increased by steps of $10\,\mu\text{s}$. The drilled depth ℓ_B calculated (solid line) from the spatially integrated dynamical model and experimental results (square). The repeated stepwise changes to larger drilling velocity observed in the experiments are indicated by the dotted lines (*X5CrNi18-10*, laser system S1, pulse energy $E_p = 200\,\text{mJ}$, pulse duration $t_p = 180\,\mu\text{s}$).

velocity starts to change stepwise between moderate values of $3.5\,\text{m\,s}^{-1}$ up to $13\,\text{m\,s}^{-1}$. The slowly changing, moderate values of the drilling velocity are in accordance with the spatially integrated dynamical model, while the repeated deviations to larger drilling velocities indicate the interaction of the laser beam with the onset of melt closures.
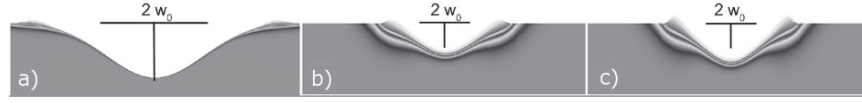
Fig. 5.18. Simulation of single pulse drilling: The melt flow is dominated by inertia of the liquid. Most of the molten material is evaporated and the rest does not escape far away from the beam axis. For pulse durations a) $t_p = 14\,\text{ns}$, b) 21 ns, c) 27 ns the melt flow is transient and widening is not yet pronounced. ($E_p = 0.5\,\text{mJ}$, $w_0 = 11\,\mu\text{m}$).

5.7.5 Drilling with Inertial Confinement – Helical Drilling

Drilling with ns-pulse duration intensities up to $I_0 = 10^{10}\,\text{W}\,\text{cm}^{-2}$ is encountered, but the molten material is not accelerated to high velocities as in drilling with μs-pulses. The well-known piston model and early FEM-calculations [53] already showed that the acceleration of the melt flow might dominate over the ablation results. However, advanced models can handle the pronounced sensitivity of the melt flow to the details of the intensity distribution (Fig. 5.18) and the nonlinear evaporation process. At the time scale t_{in} of sub-microseconds the melt flow is dominated by the inertia of the liquid and does not escape far away from the laser beam axis. This behaviour suggests that a moving beam can catch the recast from the preceding pulse and explains why helical drilling works with high-precision and almost no recast. During the pulse duration $t_p = 14$ns of one single pulse in helical drilling the momentum transferred to the molten material by the recoil pressure of evaporation is too small to overcome the inertia of the melt significantly. If the drill walls reach to a depth greater than the distance the melt can move, this strategy works well and almost all material is evaporated.

To improve precision the pulse duration can be reduced using short and ultra-short laser pulses [54, 55]. Alternatively, the laser beam can be moved as in helical drilling. The effect of rotational movement is demonstrated by comparing helical and percussion drilling with identical laser parameters. To get a circular drill profile independent of the symmetry of the laser beam cross section, the beam movement has to consist of two synchronised rotations. One rotation moves the beam axis across the work piece and another rotates the beam itself (Fig. 5.19). Like the cutting edges of a mechanical spiral bit, the same part of the laser beam is always in contact with the wall during one rotation. If beam rotation is absent, the cross section of the shape of the hole reproduces the beam profile. Both rotational movements can be realised with an image rotator such as the Dove prism. During one cycle of the prism, the beam itself is rotated two times. If the beam is shifted parallel to the optical axis the outgoing beam axis moves on a circular path with a rotational frequency twice the frequency of the Dove prism rotation. By tilting the beam with respect to the rotational axis, the outgoing beam describes a cone. The
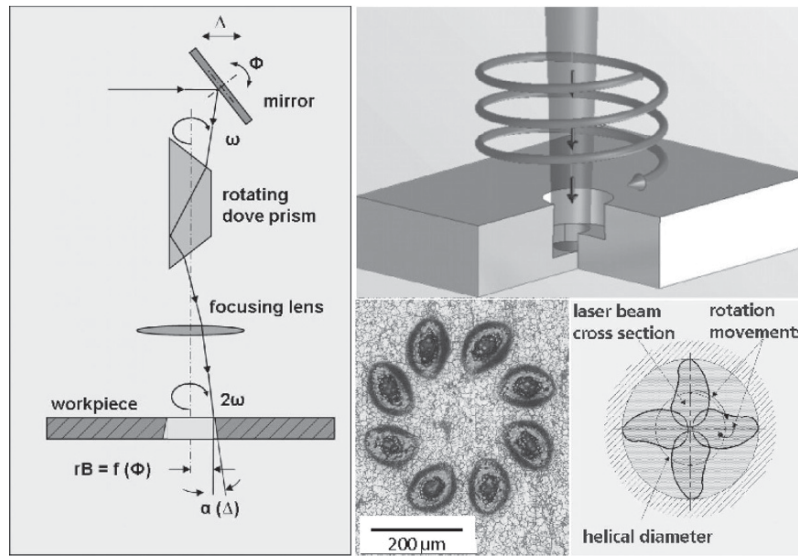
Fig. 5.19. Helical drilling: Principle, optical setup and beam rotation movement.

angle of the cone defines the entrance diameter and the shift results in the taper of the drill. By changing the two parameters, tilt and shift, cylindrical as well as conically shaped holes with positive or negative taper can be produced. If the parameters are changed during the drilling process, counterbores are also possible. The technical implementation of helical drilling optics has been developed by Fraunhofer-ILT [56]. A Dove prism is mounted into a high speed hollow shaft motor (Fig. 5.19). The shift of the laser beam is done by motorised movement of a laser mirror, and the tilt is done by a motorised wedge prism. All motors are controlled by an external control unit, which provides an interface for changing the parameters. A half-wave plate is also integrated into the hollow shaft motor, which rotates the polarisation synchronised to the laser beam. The drilling optics allow rotational frequencies of up to 20,000 rpm. The helical diameter has a range of 0 to $400\,\mu$m, and aspect ratios of the drillings up to $1:40$ for $2\,$mm material thickness can be achieved. Conical holes with an expansion ratio from entrance to exit in a range from $1:4$ to $2:1$ are possible. High precision helical drilling is achieved with the Dove prism optics (Fig. 5.20).

5.8 Outlook

Extending the actual state of modelling and simulation to pulse durations shorter than $\sim 500\,$ns requires careful comparison of the influence of the
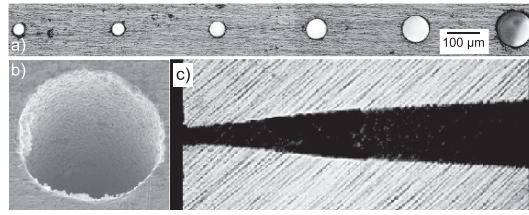
Fig. 5.20. Results for helical drilling: a) entrance diameter from 40 to 110 μm, tool steel, b) and c) hole surface in stainless steel, d) entrance diameter 80 μm, e) Cross section, entrance diameter 50 μm.

phenomena already included with at least three additional features, namely (1) beam propagation, (2) evaporation kinetics during relaxation of the Knudsen layer, and (3) changes of material properties due to elevated temperatures approaching the critical state. There will be additional exciting new insights from investigating in more detail how the radiation propagates including changes of amplitude and phase due to interaction with the shape and thermodynamical state of the drill. Kinetics during relaxation of the Knudsen layer in the vicinity of the drill base might change the most important quantities in drilling, namely energy and momentum during evaporation and recondensation. In particular, the double pulse technique – already under investigation – introduces first order effects to overall drilling performance and it remains an open question how to distinguish the contributions from plasma formation from evaporation itself. The effects of double-pulses and pulse bursts is interesting not only for drilling with sub-ns pulses in ablation, but also for fine cutting with μs pulses. Reaching a better understanding of power modulation will open a new field of processing strategies. With shorter pulses in the sub-ns range the rise time of the intensity becomes comparable with electron collision time in the gaseous phase. Spatial changes of the intensity also change the scale for the spatial coexistence of strong and weak evaporation. Changes of the vapour flow within the drill and subsequent recondensation at the drill wall is one of the consequences.

5.9 Acknowledgements

References

1. Horn A, Mingareev I, Miyamoto I (2006) Ultra-fast diagnostics of laser-induced melting of matter. JLMN-Journal of Laser Micro/Nanoengineering 1(3): 264–268
2. Horn A, Mingareev I, Werth A, Kachel M, Brenk U (2007) Investigations on ultrafast welding of glass-glass and glass-silicon. 9th International Conference on Laser Ablation, Teneriffe (Spain) 24–28 September 2007, in press.
3. Lehner C, Mann K, Kaiser E (2003) Bohren von Kühl und Schmierlöchern. In: Hügel H, Dausinger F, Müller M (eds), Tagungsband Stuttgarter Lasertage SLT03: 103–106
4. Schneider M, Berthe L, Fabbro R, Muller M, Nivard M (2007) Gas investigation for laser drilling. LIA Journal of Laser Applications 19(3): 165–169
5. Pashby IR, McNally CA (2004) Laser-drilling through Plasma-Sprayed Thermal Barrier Coatings on Nickel Based Superalloys. Proceedings of the 23rd International Congress on Applications of Lasers and Electro-Optics 2004, 5 pages
6. Sezera HK, Lia L, Schmidta M, Pinkertona AJ, Anderson B, Williams P (2006) Effect of beam angle on HAZ, recast and oxide layer characteristics in laser drilling of TBC nickel superalloys. Int J Machine Tools and Manufacture 46(15): 1972–1982
7. Matijasevic-Lux B, Neidel A, Riesenbeck E, Ullrich T, Völker J, Wallich S (2007) Hot cracking in the heat affected zone of laser drilled turbine blades made from the nickel-based superalloy Rene-80. Prakt Metallogr 449
8. Sezer HK, Li L, Wu Z, Anderson B, Williams P (2007) Non-destructive microwave evaluation of TBC delamination induced by acute angle laser drilling. Meas Sci Technol 18: 167–175
9. Willach J (2005) Herstellung von konturierten Bohrungen in Mehrschichtsystemen mit Nd:YAG-Laserstrahlung. PhD thesis, Chair Laser Technology LLT, RWTH Aachen University
10. Trippe L (2007) Reduzieren erstarrter Schmelze in der Bohrung beim Einzelpuls- und Perkussionsbohren mit Nd:YAG-Laserstrahlung. PhD thesis, Chair Laser Technology LLT, RWTH Aachen University
11. Dürr U (2004) Industrielles Laserbohren. Laser, (2): 18–21
12. Rapp J (2003) The laser with BOSCH – a flexible tool in serial production of an automotive supplier. First international Symposium on High-Power Laser Macroprocessing, Band 4831: 390–396
13. Poprawe R (2007) High Precision High-Speed Laser Ablation by Taylored Light. 9th Int Conf Laser Ablation COLA207, Tenerife, Spain, Sept 24–28
14. Gillner A, Wawers W (2006) Drilling holes. Industrial Laser Solutions, May 29–31
15. Shi P, Du K (2003) Subsurface precision maching of glass substrate by innovative lasers. Glass Sci Techn 76(2): 95–98
16. Gillner A, Yeh L, Dohrn A, Bayer A (2002) Laser micro manufacturing of moulds and forming parts. Proc LPM, LIA, SPIE 4830: 429–434
17. Kreutz EW, Horn A, Poprawe R (2005) Electron excitation in glasses followed by time- and space-measuring tools. Appl Surf Sci 248(1–4): 66–70
18. Meijer J, Du K, Gillner A, Hoffmann D, Kovalenko DS, Masuzawa T, Ostendorf A, Poprawe R, Schulz W (2002) Laser Machining by short and ultrashort pulses, state of the art. Ann CIRP, Keynote STC E 531–550

19. Baltuska A, Udem T, Uiberacker M, Hentschel M, Goulielmakis E, Gohle C, Holzwarth R, Yakovlev VS, Scrinzi A, Hansch TW, Krausz F (2003) Attosecond control of electronic processes by intense light fields. Nature Feb 6, 421(6923): 611–5

20. Hügel H, Dausinger F (2004) Fundamentals of laser-induced processes. In: Martienssen M, Poprawe R, Weber H, Herziger G, New Series Landolt-Börnstein: Laser Applications. (Series: Laser Physics and Applications, vol VIII/1C), 1. Aufl Springer, Berlin, 3–62

21. Wiesemann M (2004) Process monitoring and open-loop control. In: Martienssen M, Poprawe R, Weber H, Herziger G, New Series Landolt-Börnstein: Laser Applications. (Series: Laser Physics and Applications, vol VIII/1C), 1. Aufl Springer, Berlin 243–272

22. Schneider M, Fabbro R et al. (2005) Gas Investigation on Laser Drilling. LIA Proceedings ICALEO, CD-Version, 1094–1099

23. Walther K, Brajdic M, Kreutz EW (2006) Enhanced processing speed in laser drilling of stainless steel by spatially and temporally superposed pulsed Nd:YAG laser radiation. Int J Adv Man Tech 895–899

24. Semak VV, Campbell BR, Thomas JG (2006) On the possible effect of pedestal pulse on material removal by ultrahigh intensity laser pulses. J Phys D: Appl Phys 39: 3440–3449

25. Perez D, Lewis LJ (2003) Molecular dynamics studies of ablation of solids under femtosecond pulses. Phys Rev B67: 184102

26. Zhigilei LV, Garrison BJ (2000) Microscopic mechanisms of laser ablation of organic solids in thermal and stress confinement irradiatin regimes. J Appl Phys 88(3): 1281–1298

27. Urbassek M, Schäfer C, Zhigilei LV (2002) Metal ablation by picosecond laser pulses: A hybrid simulation. Phys Rev B 66: 115404

28. Aoki K, Bardos C, Takata S (2003) Knudsen Layer for Gas Mixtures. Journal of Statistical Physics 112(3/4): 629–655

29. Brabec T, Krausz F (2000) Intense few-cycle laser fields: Frontiers of nonlinear optics. Rev Mod Phys 72: 545

30. Kostrykin V, Niessen M, Jandeleit J, Schulz W, Kreutz EW, Poprawe R (1998) Picosecond laser pulses induced heat and mass transfer. In: High-Power Laser Ablation, Santa Fe, Phipps CR (ed), SPIE Proceedings vol 3343: 971–982

31. Wang X, Riffe D, Lee Y, Downer M (1994) Time resolved electron temperature measurement in highly excited gold target using femtosecond thermionic emission. Phys Rev B 50: 8016–8019

32. Anisimov S, Kapelovich B, Perel'man T (1974) Electron emission from metal surfaces exposed to ultrashort laser pulses. Sov Phys JETP 39: 375–377

33. Chin SL, Lambropoulos P (1984) Multiphoton Ionization of Atoms. Academic Press, Toronto

34. Walz S (2003) Laser-Neutralteilchen Massenspektrometrie, Thesis, Albert-Ludwigs-Universität Freiburg i Br

35. Agostini P, Fabre F, Mainfray G, Petite G, Rahman NK (1979) Free-Free Transitions Following Six-Photon Ionization of Xenon Atoms. Phys Rev Lett 42: 1127

36. Ammosov MV, Delone NB, Krainov VP (1986) Tunnel ionization of complex atoms and of atomic ions in an alternating electromagnetic field. Sov Phys JETP 64: 1191

37. Taflove A, Hagness SC (2005) Computational Electrodynamics: The Finite-Difference Time-Domain Method, 3rd ed. Artech House Publishers

38. Yu W, Mittra R, Su T, Liu Y, Yang Y (2006) Parallel Finite-Difference Time-Domain Method. Artech House Publishers

39. Teague MR (1983) Deterministic phase retrieval: a Green's function solution. J Opt Soc Am 73: 1434

40. Vasil'ev LA (1971) Schlieren Methods, Israel Programme for Scientific Translations, p 201

41. Bennett CE (1934) Precise Measurement of Dispersion in Nitrogen. Phys Rev 45(1): 200–207

42. Peck ER, Khanna BN (1966) Dispersion of Nitrogen. J Opt Soc Am 56(8) 1059–1063

43. Aden M (1994) Plasmadynamik beim laserinduzierten Verdampfungsprozess einer ebenen Metalloberfläche. Shaker Verlag

44. Ichimaru S (1973) Basic Principles of Plasma Physics: A statistical Approach. The Benjamin/Cummings Publishing Co

45. Aoki K, Sone Y (1991) Gas flows around the condensed phase with strong evaporation or condensation – Fluid dynamics equation and its boundary condition on the interface and their application. In: Gatignol R, Soubbaramayer (eds), Advances in Kinetic Theory and Continuum Mechanics, Proceedings of a Symposium Held in Honor of Professor Henri Cabannes at the University Pierre et Marie Curie, Paris, 1990. Springer, Berlin, 43–54

46. More RM, Warren KH, Young DA, Zimmerman GB (1988) A new quotidian equation of state (QEOS) for hot dense matter, Phys Fluids 31: 3059–3078.

47. Constantin R, Foias C, Nicolaenko B, Temam R (1989) Integral Manifolds and Inertial Manifolds for Dissipative Partial Differential Equations. Springer-Verlag, New York

48. Robinson JC (1995) Finite-dimensional behavior in dissipative partial differential equations. Chaos 5: 330–345

49. Poprawe R, Schulz W (2003) Development and application of new high-power laser beam sources. RIKEN Review No 50: 3–10

50. Kostrykin V, Schulz W, Niessen M, Michel J (2004) Short time dynamics in Laser Material Processing. In: Nonlinear Dynamics of Production Systems, Radons G, Neugebauer R (eds), Wiley-VCH, 443–452

51. Schulz W, Kostrykin V, Michel J, Niessen M (2004) Modelling and Simulation of Process Monitoring and Control in Laser Cutting. In: Radons G, Neugebauer R, Nonlinear Dynamics of Production Systems. Wiley-VCH, Weinheim 411–426, Michel J, Pfeiffer S, Schulz W, Niessen M, Kostrykin V, Approximate model for laser welding, – (2004) 427–442
Kostrykin V, Schulz W, Niessen M, Michel J, Short-time dynamics in laser material processing – (2004) 443–452

52. Schulz W, Willach J, Peterreit J, Trippe L, Kreutz EW (2004) Verfahren zum Bohren von metallischen Werkstoffen sowie von geschichteten metallischen Werkstoffen und solchen, die mindestens eine keramische Schicht aufweisen. German patent 10 2004 014 820

53. Ruf A, Breitling B, Berger P, Dausinger F, Hügel H (2003) Modeling and investigation of melt flow ejection dynamics for laser drilling with short pulses, 3rd Int Symp LPM, Miyamoto I, Kobayashi KF, Sugioka K, Poprawe R (eds). Proc SPIE vol 4830: 73–78

54. Dausinger F (2000) Laserverfahren für Mikrobohrungen. Springer-Verlag Berlin, Heidelberg
55. Kaspar J, Luft A, Nolte S, Will M, Beyer E (2006) Laser helical drilling of silicon wafers with ns to fs pulses: Scanning electron microscopy and transmission electron microscopy characterization of drilled through-holes. J Laser Applics 18(2): 85–92
56. Wawers W, Gillner A (2007) Device for drilling and removing material using a laser beam. Patent abstract WO/2007/000194

6

Arc Welding and Hybrid Laser-Arc Welding

Ian Richardson

Department of Materials Science and Engineering, Delft University of Technology, Mekelweg 2, 2628 CD Delft, The Netherlands. `i.m.richardson@tudelft.nl`

Abstract. Laser-arc hybrid welding has developed into a viable industrial technology in recent years, and is attracting increasing commercial interest. The physics of the underlying interactions is quite complex. In order to explore the relationships involved, it is useful to consider important aspects of laser and arc welding separately. The physics of laser welding has already been examined in Chaps. 3 and 4. A generic description of welding arcs is therefore provided here, which forms a basis for interpretation of laser-arc interactions and the hybrid welding conditions discussed in the final section of this chapter.

6.1 The Structure of the Welding Arc

Arcs belong to the class of self-sustaining reversible electrical discharges, which are characterised by plasma temperatures significantly above room temperature, high current densities at the electrodes (in comparison to other types of self-sustaining reversible electrical discharges, such as glow discharges) and relatively low voltages, of the order of a few volts to a few tens of volts. Arcs may operate over a wide range of currents from a few tens of milliampères, defining the lower boundary between arc and glow discharges, to currents of mega-amperes and above.

Arc properties and behaviour are very difficult to define precisely because of the large range of phenomena encompassed by the term. Various definitions have been proposed including the following descriptive example by Guile [1]:

"An arc is a discharge of electricity between electrodes in a gas or in a vapour from the electrodes which has a voltage drop at the cathode of the order of the excitation potential of the electrode vapour (viz: only of the order of 10 volts) and in which the current flowing can have any value almost without limit, above a minimum, which is about 100 milliamperes."

Welding arcs are generally subject to additional limitations including the need for spatial and temporal stability. The notation employed to describe arc and hybrid laser-arc welding is provided in Table 6.1. The subject of arc welding has been studied extensively for many years; nevertheless numerous works on

Table 6.1. Table of notation.

Symbol	Units	Meaning
Latin Symbols		
a	m	constant
a_o	m	Bohr radius ($= 5.3 \times 10^{-11}$)
A	$\mathrm{A\,m^{-2}\,K^{-2}}$	thermionic emission material constant
A_{ul}	$\mathrm{s^{-1}}$	transition probability
b	m	constant
B	T	magnetic flux density
c	$\mathrm{m\,s^{-1}}$	speed of light
$c_{f,r}$	m	constant
c_p	$\mathrm{J\,kg^{-1}\,K^{-1}}$	specific heat capacity at constant pressure
C	–	inertial coefficient
C_1	$\mathrm{m^{-3}}$	constant (eq. 6.71)
C_2	W	material constant (eq. 6.12)
C_μ	–	eddy viscosity proportionality constant ($= 0.09$)
d	m	material thickness
d_a	m	dendrite arm spacing
D_e	$\mathrm{m^2\,s^{-1}}$	electron diffusion coefficient
d_j	$\mathrm{m^{-1}}$	concentration gradients diffusion
D_{amb}	$\mathrm{m^2\,s^{-1}}$	ambipolar diffusion coefficient
D_{ij}	$\mathrm{m^2\,s^{-1}}$	ordinary diffusion coefficient
$\overline{D^x_{AB}}$	$\mathrm{m^2\,s^{-1}}$	combined ordinary diffusion coefficient
$\overline{D^P_{AB}}$	$\mathrm{m^2\,s^{-1}}$	combined pressure diffusion coefficient
$\overline{D^T_{AB}}$	$\mathrm{m^2\,s^{-1}}$	combined temperature diffusion coefficient
D^T_i	$\mathrm{kg\,m^{-1}\,s^{-1}}$	thermal diffusion coefficient
$D(E_s, W)$	–	electron tunnelling probability
e	C	magnitude of the charge on the electron
E	$\mathrm{V\,m^{-1}}$	electric field strength
E^a	$\mathrm{V\,m^{-1}}$	induced electric field
E_c	$\mathrm{V\,m^{-1}}$	complex electric field strength amplitude
E^e	$\mathrm{V\,m^{-1}}$	applied electric field
E_1	J	first ionisation energy
E_H	J	ionisation energy of hydrogen ($= 13.6\,\mathrm{eV}$)
E_{iu}	J	energy of the upper excited state
E_n	J	discrete energy level of an atom
E_o	$\mathrm{V\,m^{-1}}$	electric field strength amplitude
E_s	$\mathrm{V\,m^{-1}}$	electric field strength at a surface
$f_{f,r}$	–	fractional power to front and rear of Goldak ellipsoids
F_j	N	force
f_l	–	liquid fraction
F_p	m	focal length
f_s	–	solid fraction
$\overline{g_A}$	$\mathrm{m^{-2}\,s^{-1}}$	mean number flux of gas A
g_i	$\mathrm{m^{-2}\,s^{-1}}$	number flux of ith species
g_{iu}	–	statistical weight of the upper excited state (eq. 6.9)
g_l	–	liquid volume fraction
g_n	–	degeneracy of states of energy E_n
g_z	$\mathrm{m\,s^{-2}}$	acceleration due to gravity
$\bar{g}(\nu, T)$	–	average Gaunt factor
$\mathrm{g}(\nu, \mathrm{u}_1, \mathrm{u}_2)$	–	Gaunt factor

Table 6.1. *Continued*

Symbol	Units	Meaning
h	J s	Planck's constant
h, h_l	$\mathrm{J\,kg^{-1}}$	enthalpy
H_L	$\mathrm{J\,m^{-3}}$	latent heat of fusion
I	A	current
$I(x)$	$\mathrm{W\,m^{-2}\,sr^{-1}}$	radiance
I_o	$\mathrm{W\,m^{-2}\,sr^{-1}}$	radiative power density, laser power density
$I_\nu(r, \Omega)$	$\mathrm{J\,m^{-2}}$	specific intensity at a position r, frequency ν in the direction Ω
$I_\lambda^o(r)$	$\mathrm{W\,m^{-3}\,sr^{-1}}$	Plank function
$I_\nu^o(r)$	$\mathrm{J\,m^{-2}\,sr^{-1}}$	Plank function
J	$\mathrm{A\,m^{-2}}$	current density
J_T	$\mathrm{A\,m^{-2}}$	thermionic current density
k	$\mathrm{m^2\,s^{-2}}$	turbulent energy
k, k_n	$\mathrm{m^{-1}}$	wave vector
k_B	$\mathrm{J\,K^{-1}}$	Boltzmann's constant
k_c	$\mathrm{m^{-1}}$	curvature term (eq. 6.51)
m	–	complex refractive index
$\overline{m_{A,B}}$	kg	mass of gas A (or B)
m_e	kg	mass of an electron
$m_{i,j}$	kg	mass of an ion
$\dot{m}_v$	$\mathrm{kg\,s^{-1}}$	mass flux of vapour
M	$\mathrm{kg\,mol^{-1}}$	molar mass
n	$\mathrm{m^{-3}}$	number density
n	–	principal quantum number (eq. 6.20)
n_a	$\mathrm{m^{-3}}$	number density of unionised atoms
n_{cr}	$\mathrm{m^{-3}}$	critical number density
n_e	$\mathrm{m^{-3}}$	electron number density
$n_{e,LTE}$	$\mathrm{m^{-3}}$	equilibrium electron number density
n_i	$\mathrm{m^{-3}}$	number density of species i
n_{Im}	–	imaginary part of the refractive index
$\dot{n}_i$	$\mathrm{m^{-2}\,s^{-1}}$	number flux of particle species i
n_p	$\mathrm{m^{-3}}$	aerosol particle number density
n_{Re}	–	real part of the refractive index
n_T	$\mathrm{m^{-3}}$	number density of atoms + ions
$N(W, T_s, \phi)$	$\mathrm{J^{-1}\,m^{-2}\,s^{-1}}$	supply function
P	$\mathrm{N\,m^{-2}}$	pressure
p_1	–	constant (eq. 6.71)
$p(x')$	$\mathrm{kg\,m\,s^{-1}}$	electron momentum
P_a	$\mathrm{N\,m^{-2}}$	arc pressure
$P_{i,arc,laser}$	W	power
P_p	$\mathrm{N\,m^{-2}}$	vapour recoil pressure
P_o	$\mathrm{N\,m^{-2}}$	ambient pressure
Pr	–	Prandtl number
Pr_t	–	turbulence Prandtl number
P_s	W	input power
P_v	$\mathrm{N\,m^{-2}}$	saturation vapour pressure
q	$\mathrm{C\,m^{-3}}$	charge per unit volume
$q_{f,r}$	$\mathrm{W\,m^{-3}}$	Goldak power density distribution
q_r^{rad}	$\mathrm{W\,m^{-2}}$	radiative flux

Table 6.1. *Continued*

Symbol	Units	Meaning
Q	W m^{-2}	power density
Q_{arc}	W m^{-2}	arc power distribution
Q_{laser}	W m^{-2}	laser power distribution
Q_T	W m^{-2}	sum of laser and arc power densities
r	m	radius
r_a	m	arc radius
r_b	m	laser beam radius
r_{max}	m	maximum aerosol particle radius
r_{min}	m	minimum aerosol particle radius
R_{ij}, R_{ji}	s^{-1}	rate coefficients
s_i	–	stoichiometric coefficients
S_f	m^2	laser focal spot area
S_t	s^{-1}	strain rate
t	s	time
T	K	temperature
T_e	K	electron temperature
T_s	K	surface temperature
u	m s^{-1}	velocity
u_E	m s^{-1}	velocity due to electric field
u_m	m s^{-1}	metal surface velocity
u_r	m s^{-1}	radial velocity
u_s	m s^{-1}	surface velocity
u_t	m s^{-1}	as the characteristic turbulent velocity
u_T	m s^{-1}	thermal velocity
u_v	m s^{-1}	metal vapour velocity
u_w	m s^{-1}	welding speed
u_z	m s^{-1}	axial velocity
U	W m^{-3}	radiation source strength
V	V	voltage
V_r	m s^{-1}	relative velocity vector between liquid and solid phases
V_w, V_{sheath}	V	sheath voltage
W	J	electron energy
W_a	J	energy of an electron inside a metal
x	m	distance to arc axis (eq. 6.8)
x_j	–	number density ratio of jth species
y_{ref}	m	characteristic boundary layer length
Z_i	–	partition function
Z_j, Z_i	–	charge number
Z	–	ionic charge
z_i		degree of ionisation, net effective charge
Greek Symbols		
α	–	fine-structure constant ($= 1/137$) (eq. 6.18)
α	$\text{m}^2 \text{s}^{-1}$	thermal diffusivity
α_o	m	Bohr radius
β	$\text{m}^3 \text{K}^{-1}$	volumetric expansion coefficient
γ	N m^{-1}	surface tension coefficient
γ_g	–	Euler-Mascheroni constant
γ_i	–	quantum yield
γ_k	–	quantum yield

Table 6.1. *Continued*

Symbol	Units	Meaning
$\delta(z)$	m^{-1}	Dirac delta function
Δh	$\mathrm{J\,kg}^{-1}$	heat content per unit mass
ε	$\mathrm{m}^2\,\mathrm{s}^{-3}$	turbulent energy dissipation
$\varepsilon(r)$	$\mathrm{W\,m}^{-3}\,\mathrm{sr}^{-1}$	radial emission coefficient
ε_o	$\mathrm{A}^2\,\mathrm{s}^4\,\mathrm{kg}^{-1}\,\mathrm{m}^{-3}$	permittivity of free space ($= 8.854 \times 10^{-12}$)
ε_r	$-$	dielectric constant
ε_{ul}	$\mathrm{W\,m}^{-3}\,\mathrm{sr}^{-1}$	emission coefficient on electron transition between states u and l
η	$-$	process efficiency
κ	$\mathrm{W\,m}^{-1}\,\mathrm{K}^{-1}$	thermal conductivity
κ_K	$-$	von Karman's coefficient ($= 0.4$)
κ_ν	m^{-1}	radiative absorption coefficient
κ_λ	m^{-1}	spectral absorption coefficient
κ_ν^{bf}	m^{-1}	bound-free absorption coefficient
κ_ν^{ei}	m^{-1}	electron-ion absorption coefficient
κ_ν^{eo}	m^{-1}	electron-atom absorption coefficient
λ	m	wavelength
λ_L	$\mathrm{N\,m}^{-2}$	Lagrange multiplier
μ	$\mathrm{N\,s\,m}^{-2}$	dynamic viscosity
μ_B	$\mathrm{N\,s\,m}^{-2}$	coefficient of bulk viscosity
μ_F	J	Fermi energy
μ_o	$\mathrm{kg\,m\,s}^{-2}\,\mathrm{A}^{-2}$	permeability of free space ($= 4\pi \times 10^{-7}$)
μ_t	$\mathrm{N\,s\,m}^{-2}$	turbulent viscosity
ν	Hz	frequency
ν_{eo}	Hz	electron-neutral collision frequency
ν_{ul}	Hz	photon frequency
ρ	$\mathrm{kg\,m}^{-2}$	density
ρ_{ma}	$\mathrm{kg\,m}^{-2}$	aerosol mass density
ρ_∞	$\mathrm{kg\,m}^{-2}$	ambient gas density
σ	$\Omega^{-1}\,\mathrm{m}^{-1}$	electrical conductivity
σ_c	m^2	electron-atom collision cross section
σ_i	m^2	photo-ionisation cross section
$\sigma_{M,a}$	m^2	Mie absorption cross section
$\sigma_{M,s}$	m^2	Mie scattering cross section
$\sigma_{R,a}$	m^2	Rayleigh absorption cross section
$\sigma_{R,s}$	m^2	Rayleigh scattering cross section
σ_T	m^2	Thomson scattering cross section
ϕ	V	work function
τ_a	Pa	shear stress
χ'	$\mathrm{m}^3\,\mathrm{s}^{-1}$	recombination coefficient
ω	s^{-1}	angular frequency
ω_p	s^{-1}	plasma frequency

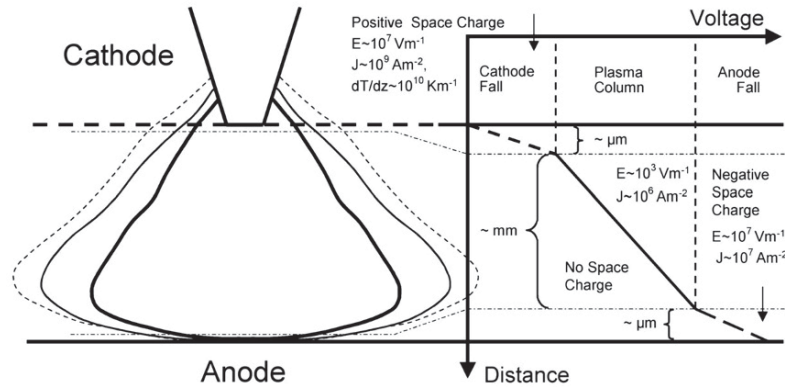| Abbreviations	
GMA	Gas metal arc
GTA	Gas tungsten arc
HAZ	Heat affected zone
LTE	Local thermal equilibrium
pLTE	Partial local thermal equilibrium
TIG	Tungsten inert gas (same as GTA)

Fig. 6.1. Schematic of a point-plane welding arc structure showing order of magnitudes of dimensions, current densities, and electric field strengths in the different arc regions.

the subject indicate that observation and experiment do not show any simple or well defined behaviour. On the contrary, the results provide a multitude of sometimes seemingly contradictory interdependencies, which vary enormously with prevailing conditions [1]. The physical mechanisms governing arc welding operations are numerous and involved, both within the arc and at the electrodes. Some of the observed behavioural variations can be directly ascribed to changes in conditions within the structure of the arc. Behaviour at the electrodes is known to have a major influence on arc characteristics and stability, although the exact nature of many of the interactions has yet to be fully explored.

From a macroscopic point of view the arc may be regarded as an energy converter. Energy is supplied in a controlled manner in the form of electrical input and is converted into heat and a broad range of electromagnetic radiation. The nature of the conversion process and the subsequent behaviour of the arc are determined to a large extent by the prevailing physical conditions (gas type, electrode composition, geometry etc). In order to gain some perspective on arc behaviour it is appropriate to explore the main gaseous discharge characteristics required for welding operations.

The following discussion will focus on the types of arc commonly employed in welding, that is, collision dominated, stable point-plane arcs burning between a rod-like welding electrode and a planar work-piece electrode.

6.1.1 Macroscopic Considerations

Like all gas discharges, the welding arcs can be described with reference to three principal regions, the cathode fall zone, the plasma column and the anode fall zone (Fig. 6.1). These regions are not distinct but merge in a physically continuous manner. The dimensions of each of the electrode zones are of the order 10^{-6} m. In contrast the plasma column can be several millimetres long.
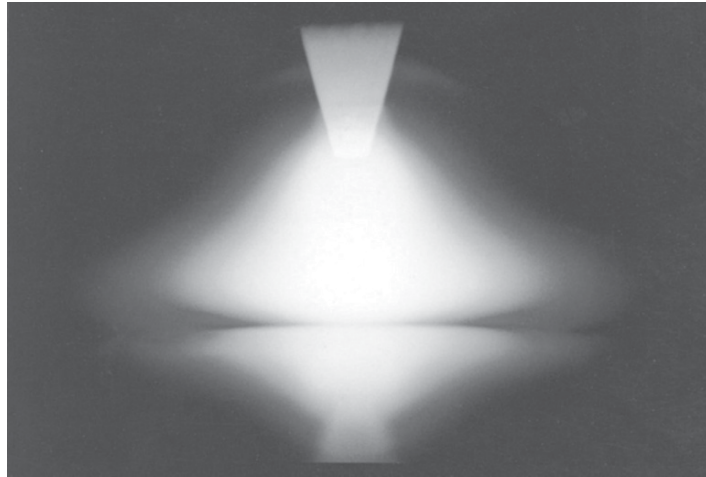
Fig. 6.2. Photograph of a 150 A argon gas tungsten arc burning on a stainless steel anode. The characteristic bell shape arises in part due to collision of a strong cathodic with a weak anodic plasma jet [2].

The anode and cathode fall zones are characterised by net local space charges within a few microns of the electrode surfaces. The discharge contracts, giving rise to high current densities, of the order 10^8 to $10^9\,\mathrm{A\,m^{-2}}$ at the cathode surface and $10^7\,\mathrm{A\,m^{-2}}$ at the anode surface, whilst in the plasma column the mean current density is of the order $10^6\,\mathrm{A\,m^{-2}}$. Differences in current density coupled with the self-induced magnetic field generate electromagnetic forces, acting from regions of high to low current density. These pump gas through the body of the discharge contributing to the characteristic bell shaped point-plane arc which arises (partly) as a result of colliding anode and cathode jets (Fig. 6.2).

Welding arcs are characterised by the transfer of mass between the electrodes. In consumable welding, the mass motion involves the transfer of molten metal from one electrode to another. The direction of motion is dependent on the mode of arc operation. In both consumable and non-consumable welding, gaseous products are transported through the arc. The forces generated depend on prevailing conditions near the electrodes as well as environmental conditions and boundary conditions at the edges of the discharge.

Gas flow is an important factor in welding due to its influence on process stability and resultant weld integrity. The structure and behaviour of the discharge is dependent on many factors including energy transport within the discharge, energy transfer efficiency at the electrodes, chemical reactions, species diffusion, and impurity entrainment.

To date, no comprehensive description of the physics of welding arc discharges has been constructed; the majority of approaches are based on simplifications, describing non-consumable arcs under equilibrium conditions [3].

Under such conditions the following continuity equations apply:

1) Mass must be conserved

$$\frac{\partial \rho}{\partial t} + \nabla \cdot (\rho \mathbf{u}) = 0, \tag{6.1}$$

where ρ is the mass density and $\mathbf{u}$ the velocity.

2) Charge must be conserved

$$\frac{\partial q}{\partial t} + \nabla \cdot \mathbf{J} = 0, \tag{6.2}$$

where q is the charge per unit volume and $\mathbf{J}$ the current density.

3) A generalised Ohm's law applies

$$\boldsymbol{J} = \sigma \left(\boldsymbol{E} + \boldsymbol{u} \times \boldsymbol{B} \right), \tag{6.3}$$

here σ is the electrical conductivity, $\mathbf{E}$ the electrical field strength and $\mathbf{B}$ the magnetic flux density.

4) Maxwell's equations apply

$$\nabla \times \mathbf{B} = \mu_o \mathbf{J} + \mu_o \varepsilon_o \frac{\partial \mathbf{E}}{\partial t},$$
$$\nabla \times \mathbf{E} = -\frac{\partial \mathbf{B}}{\partial t} \tag{6.4}$$

where μ_o is the magnetic permeability of free space and ε_o the permittivity of free space.

5) Momentum is conserved, described by the Navier-Stokes equation for incompressible flow

$$\rho \left(\frac{\partial \mathbf{u}}{\partial t} + \mathbf{u} \cdot \nabla \mathbf{u} \right) = -\nabla P + \mu \nabla^2 \mathbf{u} + \mathbf{J} \times \mathbf{B} + (\rho - \rho_\infty) \mathbf{g}_z, \tag{6.5}$$

where P is the pressure, μ the dynamic viscosity, ρ_∞ the gas density outside the discharge and $\mathbf{g}_z$ the acceleration due to gravity. Here inertial terms are balanced by a pressure gradient, viscous stress, electromagnetic forces and a buoyancy force. The assumption of incompressibility requires the divergence of the flow to be zero, and is acceptable provided changes in velocity do not have a significant influence on the internal energy (temperature).

6) Energy is conserved thus

$$\rho \mathbf{u} \cdot \nabla \left(h + \frac{\mathbf{u}^2}{2} \right) - \nabla \cdot (-\kappa \nabla T) + U = \mathbf{J} \cdot \mathbf{E}, \tag{6.6}$$

where κ is the thermal conductivity, h the enthalpy and U the radiation source strength (energy per unit volume). Here the energy generated by the flow of electric current is balanced by enthalpy, radiative and conductive terms.
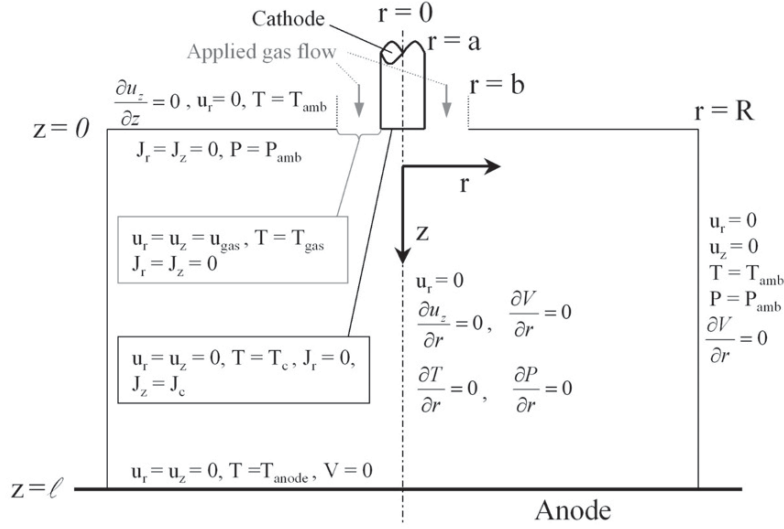
Fig. 6.3. Typical boundary conditions for numerical solution of the conservation equations governing a stationary, axi-symmetric point-plane arc. Subscript c refers to the cathode and amb to ambient conditions; ℓ is the distance between the cathode tip and anode plane.

In this description density, viscosity, thermal conductivity, enthalpy and radiation source strength are thermodynamic quantities, and hence functions of temperature and pressure only for any given material.

Simultaneous numerical solutions of (6.1) to (6.6) may be used to predict the first order behaviour, structure and energy exchanges occurring in the arc column, provided the arc is reasonably stable and that some equilibrium conditions are satisfied. Boundary conditions for the solution of a stationary axisymmetric discharge are given in Fig. 6.3 (see for example [4, 5]) and typical numerical solutions for a stationary tungsten inert gas (TIG) arc operating in an argon environment are shown in Fig. 6.4. In the simplest case, the axial current density at the cathode may be assumed to be constant, although better agreement between prediction and measurement is found if the cathodic current density follows a prescribed (for example a Gaussian) distribution, or is calculated directly from application of the governing equations to the body of the cathode.

The magnetohydrodynamic description outlined above does not take account of the non-equilibrium conditions occurring in the electrode fall zones, and the description breaks down rapidly in the absence of partial local thermal equilibrium, where a multi-fluid or rate equation based approach may be better suited.

In cases where incompressibility cannot be ignored, i.e. the divergence of the flow is non-zero, the Navier-Stokes equation (6.5) must be modified to
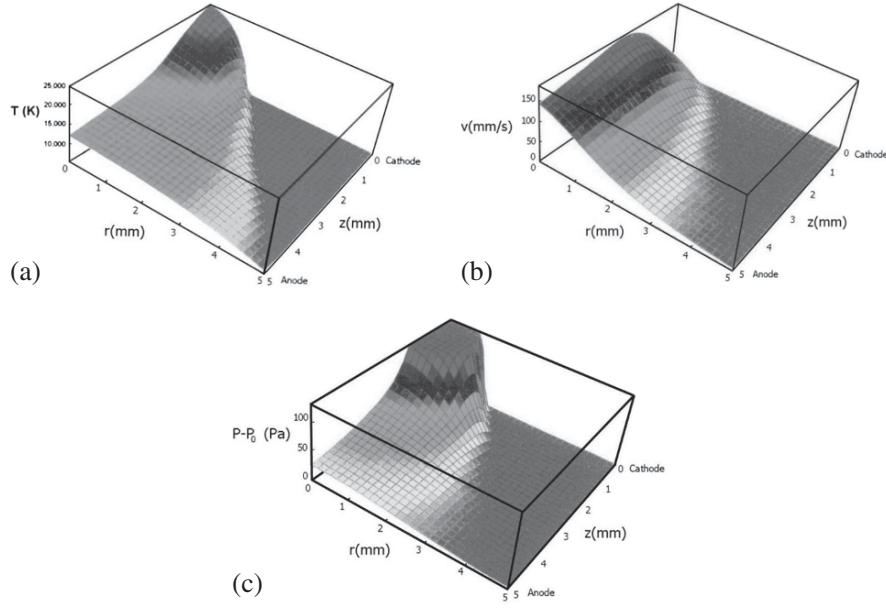
Fig. 6.4. Calculated (a) temperature (b) velocity and (c) pressure distributions for a stationary argon TIG arc. *Reproduced by kind permission of P.D. Kapadia.*

include extra viscous dissipation terms and takes the form

$$\rho \left(\frac{\partial \mathbf{u}}{\partial t} + \mathbf{u} \cdot \nabla \mathbf{u} \right) = - \nabla P + \mu \nabla^2 \mathbf{u} + \mathbf{J} \times \mathbf{B} + (\rho - \rho_\infty) \, \mathbf{g}_z + 2\nabla \mu \cdot \nabla \mathbf{u}$$

$$+ \nabla \mu \times (\nabla \times \mathbf{u}) + \tfrac{1}{3} \mu \nabla (\nabla \cdot \mathbf{u}) - \tfrac{2}{3} (\nabla \cdot \mathbf{u}) \nabla \mu$$

$$+ \mu_B \nabla (\nabla \cdot \mathbf{u}) + (\nabla \cdot \mathbf{u}) \nabla \mu_B \, , \tag{6.7}$$

where μ_B is the coefficient of bulk viscosity, which is assumed to be zero in the Stokes approximation [4].

6.1.2 Arc Temperatures and the pLTE Assumption

Knowledge of an arc temperature distribution provides an indication of the structure of the arc and also of the validity of the magnetohydrodynamic description. Predicted temperatures from the model of Lowke [5] are found to be in good agreement with temperatures measured by Haddad and Farmer [6] (Fig. 6.5). Maximum temperatures close to the cathode of a gas tungsten arc discharge exceed 20,000 K and temperature contours mirror the visible shape of the arc shown in Fig. 6.2. In this example, temperatures were measured by means of non-invasive emission spectroscopy, employing the Fowler-Milne method [7].
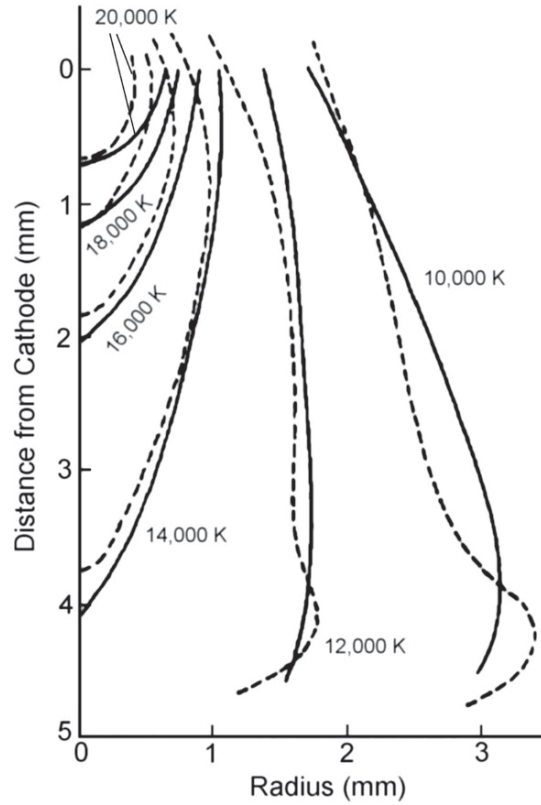
Fig. 6.5. Temperature contours of a 100 A, 5 mm long argon TIG arc. Dashed curves indicate experimental results [6], and solid curves calculations. © 2002 Institute of Physics Publishing *reproduced with permission from* [5].

A number of spectroscopic temperature measurement techniques are available based on the relationship between the measured radiance $I(x)$ and the radial emission coefficient $\varepsilon(r)$. Assuming an optically thin, cylindrically symmetric plasma, the radial distribution of the emission coefficient can be found from the Abel inversion of measured radiance

$$\varepsilon(r) = -\pi^{-1} \int\limits_{r}^{R} \frac{dI(x)}{dx} \left(x^2 - r^2\right)^{-0.5} dx, \tag{6.8}$$

where x is the perpendicular distance between the line of observation and the axis of symmetry, r the radius and R the outer limit of the source. The intensity of a spectral line emitted upon transition of an electron from an upper to a lower energy level is proportional to the population density of the upper energy level and the transition probability. If equilibrium is assumed to

hold, in other words a Boltzmann distribution is valid, then [8]

$$\varepsilon_{ul} = \frac{1}{4\pi} A_{ul} h \nu_{ul} \frac{n_i}{Z_i} g_{iu} \exp\left(-\frac{E_{iu}}{k_B T}\right),$$ (6.9)

where subscripts u and l refer to the upper and lower energy levels respectively. A_{ul} is the transition probability per unit time, h is Planck's constant, ν_{ul} is the frequency of the emitted photon, n_i the number density of the ith species, Z_i the partition function of the species calculated at temperature T, g_{iu} the statistical weight of the upper excited state E_{iu} the energy of the upper excited state and k_B is Boltzmann's constant.

In principle, when the emission coefficients have been measured experimentally, the temperature can be determined from (6.9); however, although frequencies, degeneracies and energy levels are often known with some precision, transition probabilities, partition functions and number densities are not always known with sufficient accuracy. To overcome difficulties with calculation of absolute line intensities, measurements may be based on relative intensities of two or more lines. In this case the ratio is independent of number densities and partition functions such that

$$\frac{\varepsilon_1}{\varepsilon_2} = \frac{A_1 \nu_1 g_1}{A_2 \nu_2 g_2} \exp\left(-\frac{E_1 - E_2}{k_B T}\right).$$ (6.10)

One problem with this approach is that the separation between the upper levels of the lines is generally of the same order or smaller than the thermal energies $(k_B T)$, making the emission coefficient ratio relatively insensitive to changes in temperature. Taking neutral argon lines at $425.94\,\text{nm}$ and $430.01\,\text{nm}$ for example, an increase in temperature from $10,000\,\text{K}$ to $20,000\,\text{K}$ alters the ratio $\varepsilon_1/\varepsilon_2$ by only 15% [9]. Improved accuracy can be obtained by measuring several line intensities and forming a Boltzmann plot [10], which yields a slope proportional to the inverse temperature, viz:

$$\ln\left(\frac{\varepsilon}{\nu A g}\right) = -\frac{E}{k_B T} + \ln\left(\frac{h n_i}{4\pi Z_i}\right).$$ (6.11)

Here the second term on the right hand side is independent of the transition lines observed. Unfortunately, this method requires measurement of a large number of transition lines, significantly increasing the time required for experimental observation, and is only feasible for highly stable discharge configurations.

The expression for the radial emission coefficient (6.9) may be written in a simplified form

$$\varepsilon(T) = C_2 \frac{n_i(T)}{Z_i(T)} \exp\left(-\frac{E_{iu}}{k_B T}\right),$$ (6.12)

where C_2 is a constant depending only on the properties of the radiating species. The function passes through a maximum at the *normal* temperature

when the increase due to the exponential term is balanced by a reduction of the particle density with temperature, resulting from both reduced density and transformation due to species ionisation. Provided the axial arc temperature exceeds the *normal* temperature, the off-axis maximum in the radial emission coefficient can be used to calibrate the radial intensity distribution. This method, known as the Fowler-Milne method [7], eliminates the need for transition probabilities and absolute equipment calibration, although the temperature dependent number density and partition function must be known. The former can be calculated from the Saha equation [8], which implicitly assumes quasi-neutrality in the plasma

$$\frac{n_e n_i}{n_{i-1}} = 2 \frac{Z_i(T)}{Z_{i-1}(T)} \left(\frac{2\pi m_e k_B T}{h^2} \right)^{3/2} \exp\left(-\frac{E_{i-1}}{k_B T} \right). \tag{6.13}$$

Here n_e is the electron density, m_e the electron mass, n_i the species density and i denotes the degree of ionisation of the species. The partition function is defined as

$$Z_i(T) = \sum_n g_n \exp\left(-\frac{E_n}{k_B T} \right), \tag{6.14}$$

where g_n is the degeneracy of states of energy E_n. The number of discrete energy levels of an isolated atom is infinite. For a plasma, the ionisation energy is reduced due to polarisation effects of neighbouring charged particles, thus only energy levels below the reduced ionisation limit need be included. Unfortunately, there are no experimental measurements of reduced ionisation potentials, and differences in calculated particle densities arise as a result of different criteria chosen to truncate the partition function series [10].

Despite the inherent reliance of numerical models and many experimental measurement techniques on the existence of local thermal equilibrium (LTE), or at least partial local thermal equilibrium (pLTE) for which a Boltzmann distribution exists amongst the excited states of the plasma, the existence of such a condition has been questioned on both theoretical and experimental grounds. Cram et al. [11] calculated the population density of excited states from a collisional-radiative model. Under kinetic equilibrium conditions

$$\sum_{j \neq i} (n_j R_{ji} - n_i R_{ij}) = 0, \tag{6.15}$$

where $n_i(r)$ is the population density of state i at position r. R_{ij} is the rate coefficient, comprising terms in spontaneous emission, stimulated emission and excitation and de-excitation due to particle collisions. A solution of the radiative transfer equation provides values of the net radiative (Biberman-Holstein) coefficients.

$$\frac{\partial I_\nu(r, \Omega)}{\partial l} = -\kappa_\nu(r) \left[I_\nu(r, \Omega) - I_\nu^o(r) \right], \tag{6.16}$$

where $I_\nu(r, \Omega)$ is the specific intensity at a position r, frequency ν in the direction indicated by the vector Ω. The absorption coefficient κ_ν involves continuum and line absorption terms and the source term $I_\nu^o(r)$ is given by the Planck function

$$I_\nu^o(r) = \frac{2h\nu^3}{c^2} \left[\exp\left(\frac{h\nu}{k_B T_e}\right) - 1 \right]^{-1}, \tag{6.17}$$

where c is the speed of light, and T_e the electron temperature. Differences between the population densities calculated using the LTE assumption and those of the collisional-radiative model have been found in the outer regions of the arc for electron temperatures below 8,000 K and associated electron densities below $10^{21}\,\mathrm{m}^{-3}$. This is attributed to enhanced excitation of higher atomic states by intense radiation emitted from the core of the arc. Strong excitation of the 4s levels occur when electron collisions are insufficient to maintain an equilibrium population due to Ar I resonance lines. Similarly, photo-recombination is responsible for exciting the ground state of the Ar II ions and the associated resonance lines enhance excitation of the excited Ar II states [11]. The electron density is below the level required for equilibrium between the ground state and excited states [10, 12]. At best, equilibrium can apply only between excited states; i.e., partial local thermal equilibrium.

Greim [8] indicates that the following condition on the electron density n_e must be satisfied for LTE to apply:

$$n_e \geq \frac{5}{8\pi^{0.5}} \left(\frac{\alpha}{a_o}\right)^3 \left(\frac{E_1}{E_H}\right)^3 \left(\frac{k_B T}{E_H}\right)^{0.5}$$

$$\geq 9.2 \times 10^{23} \left(\frac{E_1}{E_H}\right)^3 \left(\frac{k_B T}{E_H}\right)^{0.5}, \tag{6.18}$$

where α is the fine-structure constant, a_o is the Bohr radius, E_H the ionisation energy of hydrogen and E_1 the plasma (first) ionisation energy. For an argon plasma with $E_1 = 2.52 \times 10^{-18}\,\mathrm{J}$, (6.18) reduces to

$$n_e \geq 3.6 \times 10^{21}\, T^{0.5}, \tag{6.19}$$

which is not attainable under welding arc conditions at atmospheric pressure.

For pLTE, the electron density condition is given by the approximation [8]

$$n_e \geq 7 \times 10^{24} \frac{z^6}{n^{8.5}} \left(\frac{k_B T}{E_H}\right)^{0.5}, \tag{6.20}$$

where z is the number of effective charges and n the principal quantum number. Electron densities for a given principle quantum number should meet or exceed the calculated limit to ensure that 90% of the population in that state is in equilibrium with higher discreet states and with the free electrons.
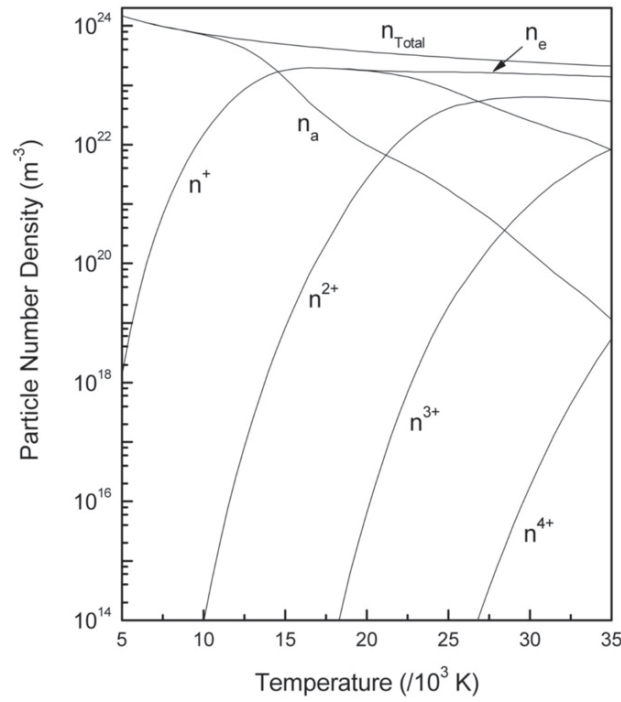
Fig. 6.6. Argon plasma particle number densities plotted from the data in [13].

Particle number densities for an argon plasma, based on the data provided in [13] are shown in Fig. 6.6.

Experimental evidence for departures from pLTE has been presented by several authors [14]–[19]. Farmer and Haddad [14], determined argon atom number densities from experiments involving Rayleigh scattering and compared the associated temperatures with those derived by the Fowler-Milne spectroscopic technique. Significant differences, attributed to the breakdown of the Boltzmann distribution, were reported for temperatures below 9,000 K. A comparison of the maximum value of the normalised radial emission coefficient (for a 5 mm long, 200 A argon TIG arc) as a function of axial position [15], showed that although the radial emission coefficient remains constant close to the anode, departures are seen within 1.5 mm of the cathode, where the maximum value falls as the cathode is approached.

Degout and Catherinot [9] determined electron density distributions in an argon TIG arc from spectroscopic measurements of Stark broadening and compared results with absolute and two line spectroscopic methods. They concluded that pLTE did not hold anywhere within the column of 4 mm long argon arcs in the current range 25 to 35 A. Supporting results are reported by Thornton [10, 19] who measured the temperature of a 100 A, 5 mm long
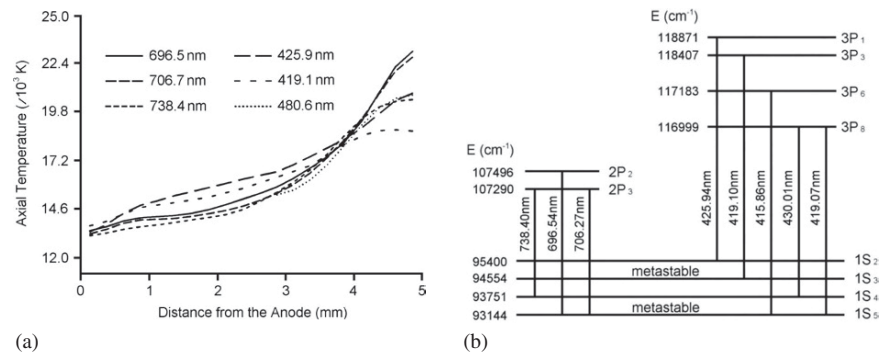
Fig. 6.7. a) Temperatures on the axis of a 100 A, 5 mm long argon TIG arc measured for different spectral lines using the Fowler-Milne method [10] and b) a partial energy level diagram for neutral argon.

argon TIG arc using the Fowler-Milne method and found that temperatures within 1 mm of the cathode vary by up to 4,000 K dependent on the emission line employed, whilst variations of more than 1,000 K exist within the body of the discharge (Fig. 6.7). Thornton suggests that departures from pLTE within 1 mm of the cathode could be related to the reduction in electron density at temperatures exceeding 17,000 K, assuming ionisation equilibrium.

The presence or absence of pLTE in welding arc discharges has not yet been definitively established, either theoretically or experimentally. Based on the available evidence, it is certain that LTE is violated almost everywhere and it appears highly likely that significant departures from pLTE exist close to the cathode. For the remaining body of the discharge, pLTE departures, if present, are likely to be small and limited to arcs with currents of a few tens of ampères. Under these conditions it is convenient to consider such departures as errors in the derived temperature, and to model the arc based on a pLTE assumption; however, it should be noted that this may not always yield a physically relevant description of arc behaviour.

6.1.3 Multi-Component Plasmas

Arc temperatures and local thermal equilibrium considerations have been discussed so far with reference to a monatomic gas. In practical welding applications, the plasma is inevitably a mixture of atomic and molecular species, the composition of which can be influenced by a number of factors including (i) the choice of shielding gas mixture, (ii) evaporation of material from the weld pool, governed primarily by weld pool chemistry, thermal distribution on the pool surface and fluid flow within the pool, and (iii) entrainment of atmospheric contaminants into the arc jet, which is a function of the shielding geometry, the momentum of the cold gas flow and velocity distribution of the arc plasma.

The local composition of a multi-species plasma is influenced by diffusive separation of component species, the plasma cannot therefore be assumed to adopt a uniform compositional distribution. For a plasma close to thermal equilibrium, the distribution function of species is assumed to be Maxwellian, perturbed by forces arising from concentration, pressure, temperature and electric field gradients associated with transport phenomena. The resultant redistribution leads to de-mixing, which in turn can influence the structure of the arc and the associated heat transfer properties.

When considering a plasma with q species, $\frac{1}{2}(q^2 - q)$ linearly independent ordinary diffusion coefficients and $(q - 1)$ linearly independent thermal diffusion coefficients are required to characterise the diffusion behaviour. The diffusion coefficients have to be calculated for each temperature and gas composition in the plasma, leading to $(q-1)$ species conservation and momentum conservation equations [20, 21]. In this context, a species is defined here to include electrons and any molecule, atom, or ion exhibiting a distinct structure. The large number of species present in welding plasmas means that calculations are time consuming and complex, and have yet to be reported for many welding arc compositions. Treatments can be greatly simplified if diffusion is described in terms of the gases rather than the many species present. Such an approach has been developed for a binary gas mixture by Murphy [21]–[24] where the $\frac{1}{2}(q^2 + q - 2)$ diffusion coefficients are replaced by four combined coefficients representing (i) a combined ordinary diffusion coefficient; (ii) a combined pressure diffusion coefficient; (iii) a combined thermal diffusion coefficient, describing, diffusion of the two gases due to concentration, pressure, and temperature gradients; and (iv) the electrical conductivity, describing diffusion of charged particles due to the applied electric field.

The number flux g_i of species i relative to the mass-average velocity in the presence of a temperature gradient, is given by [22] as

$$g_i \equiv n_i u_i = \frac{n^2}{\rho} \sum_{j=1}^{q} m_j D_{ij} d_j \; - \; \frac{D_i^T}{m_i} \nabla \ln T, \qquad (6.21)$$

where n_i is the species number density, u_i the diffusion flux of species i relative to the mass average velocity, ρ the mass density, T the temperature and m_j the mass of the jth species. D_{ij} is the ordinary diffusion coefficient and D_i^T the thermal diffusion coefficient. The term d_j describes the diffusion forces due to gradients in concentration $x_j = n_j/n$, pressure P and external forces F_j

$$d_j = \nabla x_j + \left(x_j - \frac{\rho_j}{\rho} \right) \nabla \ln P - \frac{\rho_j}{\rho P} \left(\frac{\rho}{m_j} F_j - \sum_{l=1}^{q} n_l F_l \right). \qquad (6.22)$$

Identifying the external forces with applied E^e and induced E^a electric fields to account for ambipolar diffusion yields

$$d_j = \nabla x_j + \left(x_j - \frac{\rho_j}{\rho} \right) \nabla \ln P - \frac{n_j Z_j e}{n k_B T} \left(E^e + E^a \right), \qquad (6.23)$$

where $Z_j e$ is the charge on the particle. The induced electric field E^a arises due to the tendency of electrons to diffuse more rapidly than ions and acts to slow electron diffusion whilst speeding up ion diffusion.

For a mixture of gases A and B the mean number flux $\overline{g_A}$ of gas A is given by

$$\overline{g_A} = \sum_{i=2}^{q} s_i g_i = \frac{n^2}{\rho} \overline{m_B} \left(\overline{D_{AB}^x} \nabla \overline{x_B} + \overline{D_{AB}^P} \nabla \ln P \right) - \left(\frac{\overline{D_{AB}^T}}{\overline{m_A}} \right) \nabla \ln T,$$

(6.24)

where s_i are the stoichiometric coefficients and the bar indicates that the parameters represent the gas rather than a species. The summation excludes $i = 1$ which refers to the electron contribution. Defining

$$\alpha_i = \sum_{j=1}^{q} n_j m_j Z_j D_{ij}$$

$$\beta = -\sum_{i,j=1}^{q} Z_i Z_j n_j m_j D_{ij},$$

(6.25)

and including the influence of the electric field in the ordinary and thermal diffusion coefficients

$$D_{ij}^a = D_{ij} + \frac{\alpha_i}{\beta} \sum_{l=1}^{q} Z_l D_{lj}$$

$$D_i^{Ta} = D_i^T + \frac{\alpha_i m_i}{\beta} \sum_{l=1}^{q} \frac{Z_l D_l^T}{m_l},$$

(6.26)

the combined ordinary, pressure and thermal diffusion coefficients may be expressed [22] as

$$\overline{D_{AB}^x} = \frac{1}{\overline{m_B}} \sum_{i=2}^{p} s_i \sum_{j=1}^{q} m_j D_{ij}^a \frac{\partial x_j}{\partial \overline{x_B}}$$

$$\overline{D_{AB}^P} = \frac{1}{\overline{m_B}} \sum_{i=2}^{p} s_i \sum_{j=1}^{q} m_j D_{ij}^a \left(x_j - \frac{\rho_j}{\rho} + P \frac{\partial x_j}{\partial P} \right)$$

(6.27)

$$\overline{D_{AB}^T} = \overline{m_A} \sum_{i=2}^{p} s_i \left(\frac{D_i^{Ta}}{m_i} - \frac{n^2}{\rho} \sum_{j=1}^{q} m_j D_{ij}^a T \frac{\partial x_j}{\partial T} \right).$$

Reference [25] gives the electrical conductivity as

$$\sigma = \frac{e^2 n}{\rho k_B T} \sum_{j=2}^{q} \left(n_j m_j Z_j D_{1j} - Z_j \sum_{i=1}^{q} n_i m_i Z_i D_{ji} \right).$$

(6.28)

The influence of diffusion driven de-mixing in plasmas is significant under some welding conditions, for example when welding some coated materials or when welding with argon-hydrogen gas mixtures, and is also important for non-welding applications such as chemical synthesis and waste destruction. Murphy [26] reports that for 200 A, 5 mm long TIG arc burning in an argon-helium shielding gas containing 10% helium by mass, the helium mass fraction is increased at the arc centre by 120% to 150%, and depleted in the outer regions of the arc by about 20%. The change in composition is accompanied by an increase in plasma flow velocity of the order 20% at atmospheric pressure [27]. This behaviour has been observed to generate high momentum plasma flows at elevated pressures, and has been exploited to extend the range of applicability of plasma keyhole welding to pressures above 90 bar [28]. For an argon-nitrogen mixture containing 20% nitrogen by mass, an increase of about 25% in nitrogen mass fraction is seen close to the axis of a 200 A TIG arc due to frictional forces driven by collisions between argon and nitrogen species. At arc radii between about 1 and 2 to 3 mm, a 10% mass fraction depletion is observed, whilst in the outer fringes, the nitrogen mass fraction is again greater than in the input gas mixture. This is caused by diffusion, driven by the mole fraction gradient, which displaces nitrogen to regions of lower temperature, below the re-combination temperature. In general de-mixing does not have a large influence on temperatures; however, in some cases, the change in gas composition can result in significant changes in energy transport. For example for argon-hydrogen arcs, the distribution of the thermal flux to the anode can be modified causing up to 50% increased thermal flux close to the arc axis, whilst for nitrogen arcs, this increase is of the order 10% [27].

The combined diffusion coefficient approach has been extended to describe diffusion under non-equilibrium plasma conditions. The magnitudes of the combined ordinary and thermal diffusion coefficients decrease as the plasma departs from equilibrium [20, 29], i.e. as the ratio of electron to heavy particle temperature increases. This is particularly relevant close to the cathode in arc welding.

6.2 The Arc Electrodes

The structure of an arc is determined to a significant extent by the boundary conditions at the electrodes, which in turn are governed by a large number of factors including electrode compositions, temperature distributions, chemical reactions, geometry and physical state (solid, liquid, vapour), all of which can undergo rapid and relatively large spatial and temporal variations. Local electrode conditions are governed by the composition and by the energy balance at the electrode surfaces, which includes terms describing particle collisions (neutral and metastable atoms and charged particles), radiation, chemical reactions, Joule heating, convection, mass transfer, conduction and vaporisation. The arc plasma changes structure close to the electrodes to ensure continuity at the interface.
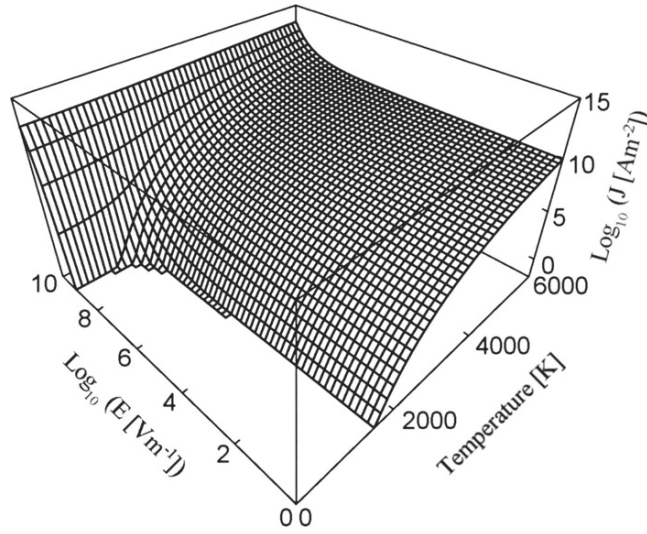
Fig. 6.8. Current density as a function of temperature and electric field strength for an arc burning on a cathode with a 4.5 eV work function. © 2002 Institute of Physics Publishing *reproduced with permission from* [32].

6.2.1 The Cathode

The extent of the cathode fall region can be estimated from the values of the cathode voltage drop and electric field strength (Fig. 6.1), which imply a thickness of approximately 10^{-6} m; this is at most of the order of the mean free paths of the component particle species, indicating a negligible collision rate and energy transfer within this region [30].

The current density at the cathode surface is the sum of the ionic and electronic terms, where the latter includes contributions from both primary and secondary emission mechanisms. For refractory cathodes, emission behaviour is often described by the Richardson-Dushman equation for thermionic emitters modified to include a Schottky contribution. Taking account of secondary terms the electronic current density J takes the form [31]

$$J = e \sum_i \gamma_i \dot{n}_i + AT^2 \exp\left(-\frac{e\phi}{k_B T} + \frac{e}{k_B T} \left(\frac{eE}{4\pi\varepsilon_r\varepsilon_o} \right)^{0.5} \right), \qquad (6.29)$$

where γ_i is the quantum yield and $\dot{n}_i$ the number flux of particle species i arriving at the cathode surface (including photons), ϕ is the work function, A a material constant and ε_r the dielectric constant. The relative influences of electric field strength and temperature are shown in Fig. 6.8.

The high temperature at the cathode is maintained by the energy flux carried by particles diffusing to the cathode surface, driven by density and potential gradients; on reaching the cathode these are neutralised, absorbed

or undergo de-excitation. The particle flux required for current continuity exceeds the supply from the plasma column and the combined cathode sheath and pre-sheath potential reflects the energy required to generate sufficient flux in the vicinity of the cathode due to collisions between the gas and emitted electrons.

In order to provide an adequate model of the cathode sheath region, the population densities, distributions and collision cross-sections of all species present should be determined together with the energy balance equation. Several models of varying degrees of complexity have been reported [30]–[37] and many factors play a role. For example, the presence of ions close to the cathode surface leads to a two stage resonant tunnelling process, involving metal to ion and ion to sheath steps, which effectively lower the local potential barrier. A rate equation approach [34] has been adopted to show that the resonant contribution significantly exceeds the non-resonant term and that ion neutralisation and re-ionisation play an important role in the space charge region. This observation is in agreement with predictions from the earlier model of Hsu and Pfender [35], which indicate a sharply increasing ion flux within $10\,\mu$m of the cathode surface. The temperature is reported to rise sharply away from the surface, increasing from the melting temperature of the electrode to 10^4 K over a distance of around $5\,\mu$m [33].

For non-thermionic cathodes, similar physical considerations apply; however, it is generally accepted that the balance shifts toward the domination of field emission as the primary mechanism. The Murphy and Good equation is often employed [38, 39], which takes the form

$$J = e \int_{-W_a}^{\infty} D(E_s, W)\, N(W, T_s, \phi)\, dW, \qquad (6.30)$$

where $D(E_s, W)$ is the electron tunnelling probability and $N(W, T_s, \phi)$ is the number of Fermi-Dirac distributed electrons incident on the barrier per unit time per unit area having energy between W and $W + dW$. The effective potential energy of the electrons inside the metal is $-W_a$; T_s is the cathode surface temperature and E_s the electric field strength at the surface. The Richardson-Schottky expression is recovered when $E_s \to 0$. The effect of ions close to the cathode surface can be taken into account by multiplying the right hand side of the above expression by an enhancement factor dependent on temperature, ion density and ionic charge. In the above expression

$$D(Es, W) = \left[1 + \exp\left(-i\frac{4\pi}{h} \int_{x_1}^{x_2} p(x')dx' \right) \right]^{-1}$$

and

$$N(W, T_s, \phi)dW = \frac{4\pi m k_B T}{h^3} \ln\left\{ 1 + \exp\left(-\frac{(W - \mu_F)}{k_B T} \right) \right\} dW \qquad (6.31)$$

where m_e is the electronic mass and μ_F the Fermi energy, x' the direction normal to the cathode surface and the integration limits x_1 and x_2 are defined at zeros in the square of the momentum function [38]. This description is valid for a simple boundary.

6.2.2 The Anode

In common with the cathode region, the arc contracts near the anode and a thin, non-equilibrium region exists close to the electrode surface. The high current density compared with the plasma column drives an electromagnetic anode jet, which opposes the (generally) stronger cathode jet, contributing to the typical bell shaped discharge (Fig. 6.2). Unlike the cathode, the current at the anode surface is carried almost entirely by electrons. Positive ions are created within the anode sheath primarily due to collisions and the sheath exhibits a concentration gradient ranging from almost zero at the anode surface to approximately equal numbers of ions and electrons adjacent to the plasma column. The energy balance in the sheath region, together with continuity considerations determine the detailed structure of the sheath.

The energy flux at the anode includes terms for radiation arriving from the plasma, radiative emission from the surface [33], collisions with neutral and metastable particles, and electron condensation; the latter being the dominant term [40]. The current density in the anode sheath includes a diffusion term, which dominates at low temperatures in the absence of equilibrium, when the electrical conductivity would otherwise be insufficient to maintain the current flow. The current density may be expressed as.

$$J = -\sigma E + e D_e \nabla n_e, \tag{6.32}$$

where D_e is the electron diffusion coefficient. The electron continuity equation is dependent on the ambipolar diffusion coefficient D_{amb}, which accounts for electron diffusion in the local electric field, and may be written [41]–[43]

$$\nabla \cdot D_{amb} \nabla n_e + \chi' \left[n_{e,LTE}^2 - n_e^2 \right] = 0, \tag{6.33}$$

where $n_{e,LTE}$ is the equilibrium electron number density and χ' is the recombination coefficient, which takes the form given by Hinnov and Hirschberg [43, 44]

$$\chi' = 1.1 \times 10^{-20} n_e T_e^{-9/2} \ [\text{m}^3\text{s}^{-1}]. \tag{6.34}$$

Some uncertainty exists over the numerical factor in the above expression; a value of 1.1×10^{-24}, derived from the same source is quoted in [43], whilst [45] quotes 8.72×10^{-22}, which includes corrections for additional terms.

Boundary conditions applied to solve (6.33) assume that n_e takes the equilibrium value at the plasma interface, whilst at the electrode surface

$$n_e = \frac{J_T}{e \, u_T}, \tag{6.35}$$

where J_T is the thermionic emission current density and u_T the thermal velocity which is $u_T = (8k_B T / \pi m_e)^{0.5}$ [41]. Solutions of the continuity equation [46] lead to negative electric field strengths in the anode sheath and negative effective electrical conductivities for the diffuse anode root typically observed during welding [33], [45]–[48]. For constricted arc roots, positive electric field strengths are predicted and both positive and negative conditions have been inferred from measurements based on Langmuir probe [47] and Thomson scattering experiments [48].

6.3 Molten Metal Flow

6.3.1 The Arc Generated Weld Pool

Fluid flow in the weld pool may be modelled using the same basic continuity equations used to describe the body of the arc (see Sect. 6.1 and examples in [49]–[53]). For the majority of models, a laminar flow regime is assumed. A number of forces act on the pool; these include the Lorentz force F_{em}, which has a vertical component driving flow downward from the centre of the weld pool, proportional to $J_r B_\theta$. The buoyancy force F_B is given by

$$F_B = -\rho_m \, g_z \beta \, (T - T_m) \,, \tag{6.36}$$

where T_m is the melting temperature of the pool ρ_m the density at the melting point and β the volume expansion coefficient. The surface tension force is usually added as a boundary condition and is dependent on the shape of the pool surface. The associated Marangoni-driven flow [49] may be described as

$$-\mu \frac{\partial u_s}{\partial n} = \tau_a + \frac{d\gamma}{dT} \frac{\partial T}{\partial s}, \tag{6.37}$$

where u_s is the surface velocity and τ_a the shear stress acting on the base plate. The static force balance accounting for surface deformation may be written as

$$\gamma \left\{ r \frac{\partial^2 z}{\partial r^2} + \frac{\partial z}{\partial r} \left(1 + \left(\frac{\partial z}{\partial r} \right)^2 \right) \right\} = r \left(1 + \left(\frac{\partial z}{\partial r} \right)^2 \right)^{\frac{3}{2}} \{ \rho g_z z - P_a + \lambda_L \} \,, \tag{6.38}$$

where P_a is the arc pressure and λ_L is the Lagrange multiplier, which is modified between iterations to satisfy the required continuity constraints. The work-piece is assumed to act as a uniform current sink with zero potential gradient at all boundaries except the weld pool surface; current flow due to the location of the return connection to the welding power source, which is known to be influential in practical welding applications, is therefore ignored. Kim and Na [49] predict outward toroidal fluid flows and weld pool surface oscillations due to current pulsing for TIG arcs operating on a 304 stainless

steel substrate. The outward flow leads to the formation of wide and shallow weld pools. For peak pulsed currents up to 160A and a 2mm long argon arc, the heat flux and current distribution have the same radii and a Gaussian like distribution, with peak values in the range 1.8 to $9.3 \times 10^{-6}\,\mathrm{W\,m^{-2}}$ and 1.8 to $9.6 \times 10^{-6}\,\mathrm{A\,m^{-2}}$ respectively. The arc pressure peaks at the pool centre and lies in the range 50 to 550 Pa, whilst the shear stress due to the gas flow across the anode surface peaks at a radius of just over 1mm and lies in the range 35 to 90 Pa. Fluid flow velocities, both inside the weld pool and on the surface are of the order 0.1 to $0.25\,\mathrm{m\,s^{-1}}$.

Some attention has been paid to the possibility of turbulent flow in the weld pool, which has been examined by among others Chakraborty et al. [53], who included a Reynolds stress term $\partial(-\overline{\rho u_i' u_j'})/\partial x_j$ in the Navier-Stokes equations. Here i and j indicate directions and the prime indicates velocity fluctuations. Turbulence is modelled using the classical eddy viscosity k-ε model, where the Reynolds stress term is given by

$$(-\overline{\rho u_i' u_j'}) = \mu_t \left(\frac{\partial \overline{u}_i}{\partial x_j} + \frac{\partial \overline{u}_j}{\partial x_i} \right) - \frac{2}{3}\delta_{ij}\rho k, \qquad (6.39)$$

and the turbulent viscosity μ_t is dependent on the liquid fraction f_l

$$\mu_t = C_\mu \sqrt{f_l} \rho \, \frac{k^2}{\varepsilon}, \qquad (6.40)$$

providing a smooth transition from the solid to the liquid state. Here C_μ is the eddy viscosity proportionality constant, k denotes the turbulent kinetic energy and ε the turbulent kinetic energy dissipation rate. The turbulent heat flux $(-\overline{u_j' T'})$ appearing in the energy balance equation is

$$(-\overline{u_j' T'}) = \frac{\mu_t}{\rho \, \mathrm{Pr}_t} \frac{\partial \overline{T}}{\partial x_j}, \qquad (6.41)$$

where Pr_t is the turbulent Prandtl number (taken to be 0.9). The standard governing equations for k and ε are employed and values of k and ε have been estimated based on a scaling analysis. The surface velocity of the weld pool is found to be

$$u_s \approx \left(\frac{\eta Q}{\pi r_a^2 \rho c_p} \frac{\partial \gamma}{\partial T} \frac{1}{\mu} \right)^{0.5}, \qquad (6.42)$$

where Q is the arc power, η the process efficiency and r_a the arc radius. The characteristic boundary layer length is

$$y_{ref} \approx \left(\frac{\eta Q}{\pi r_a^2 \rho c_p} \frac{r_a c_p}{u_s \Delta h} \right), \qquad (6.43)$$

where Δh is the heat content per unit mass. In a quasi-steady state the rate of turbulent energy production is approximately the same as the dissipation

rate hence

$$C_\mu \frac{k^2}{\varepsilon} S_t^2 = C_\mu \frac{k^2}{\varepsilon} \left(\frac{u_s}{y_{ref}} \right)^2 \approx \varepsilon, \qquad (6.44)$$

where S_t is the strain rate. Defining u_t as the characteristic turbulent velocity fluctuation

$$u_t = \kappa_K C_\mu^{0.5} u_s, \qquad (6.45)$$

where κ_K is von Kármán's coefficient, k and ε are respectively

$$k \approx u_t^2 = \kappa_K^2 C_\mu u_s^2;$$

$$\varepsilon \approx \frac{u_t^3}{\kappa_K y_{ref}} = C_\mu^{0.5} k \frac{u_s}{y_{ref}}. \qquad (6.46)$$

The position of the maximum dissipation of turbulent energy within the weld pool is dependent on the prevailing surface tension gradient. In the case of an inward toroidal flow (positive $\partial\gamma/\partial T$), k and ε are reported to reach maxima near the melt front due to the high local thermal gradients and velocities driven by the Marangoni flow. Conversely for an outward toroidal flow (negative $\partial\gamma/\partial T$), the turbulent kinetic energy and dissipation terms are highest close to the weld pool edges transverse to the welding direction, again where the temperature gradients are high. As the turbulent kinetic energy generation is proportional to the square of the strain rate, the maximum velocities occur in the regions of highest temperature gradients and are therefore coincident with the regions of maximum energy dissipation.

In the case of positive $\partial\gamma/\partial T$ (inward toroidal flow) the weld pool penetration reaches a maximum further away from the pool centre than is observed in a laminar flow regime, and penetration is reduced due to the reduced momentum of the fluid carrying heat from the surface of the pool in the downward direction. The molten zone of the turbulent weld pool is also shorter than in the laminar case, which may be attributed to increased thermal diffusion. For a negative surface tension gradient, the maximum penetration is greater for turbulent flow than for laminar flow, due to increased thermal diffusion and reduced momentum [53, 54].

6.3.2 Metal Transfer

Whilst many of the studies carried out on laser-hybrid welding have focused on non-consumable welding processes, there has been a considerable rise in interest in laser-GMA welding for commercial applications in recent years. Modelling of the GMA welding process has received considerable attention, particularly with regard to metal droplet development and metal transfer, which is based on a combination of static and dynamic forces; see for example [55]–[60].

Hu and Tsai [60] solve the continuity equations including terms for the liquid and solid regions in the time dependent momentum equations

$$
\frac{\partial\left(\rho u_r\right)}{\partial t} + \nabla \cdot \left(\rho V u_r\right) = \nabla \cdot \left(\mu_l \frac{\rho}{\rho_l} \nabla u_r\right) - \frac{\partial P}{\partial r} - \frac{\mu_l}{K} \frac{\rho}{\rho_l}\left(u_r - u_{r,s}\right)
$$

$$
-\frac{C\rho^2}{K^{0.5}\rho_l}\left|u_r - u_{r,s}\right|\left(u_r - u_{r,s}\right) - \nabla \cdot \left(\rho f_s f_l V_r u_r\right) - J_z B_\theta
$$

$$
\frac{\partial\left(\rho u_z\right)}{\partial t} + \nabla \cdot \left(\rho V u_z\right) = \nabla \cdot \left(\mu_l \frac{\rho}{\rho_l} \nabla u_z\right) - \frac{\partial P}{\partial z} - \frac{\mu_l}{K} \frac{\rho}{\rho_l}\left(u_z - u_{z,s}\right)
$$

$$
-\frac{C\rho^2}{K^{0.5}\rho_l}\left|u_z - u_{z,s}\right|\left(u_z - u_{z,s}\right) - \nabla \cdot \left(\rho f_s f_l V_r u_r\right) + J_r B_\theta + \rho g_z \beta\left(T - T_o\right),
$$

$$(6.47)$$

and energy expression

$$
\frac{\partial\left(\rho h\right)}{\partial t} + \nabla \cdot \left(\rho V h\right) = \nabla \cdot \left(\frac{\kappa}{c_p} \nabla h\right) + \nabla \cdot \left(\frac{\kappa}{c_p} \nabla\left(h_s - h\right)\right) - \Delta H_L \frac{\partial f_l}{\partial t} - U
$$

$$
- \nabla \cdot \left[\rho\left(V - V_s\right)\left(h_l - h\right)\right] + \frac{J_r^2 + J_z^2}{\sigma} + \frac{5 k_B}{c_p e}\left(J_r \frac{\partial h}{\partial r} + J_z \frac{\partial h}{\partial z}\right), \qquad (6.48)
$$

Here V_r is the relative velocity vector between the liquid and solid phases, subscripts s and l refer to the solid and liquid respectively β is the thermal expansion coefficient f the mass fraction and H_L the latent heat of fusion and the heat capacity c_p is that of the solid material. The factor K represents permeability in the mushy zone, which can be described in terms of fluid flow through a porous media. From the Carman-Kozeny equation

$$
K = \frac{d_a^2\, g_l^3}{180(1 - g_l)^2}, \qquad (6.49)
$$

where d_a is the dendrite arm spacing and g_l the liquid volume fraction. The inertial coefficient $C = 0.13\, g_l^{-3/2}$. The third and fourth terms on the right hand sides of (6.47) describe the first and second order drag forces in the mushy zone. The fifth terms describe the interaction between the solid and liquid phases. The second term on the right hand side of (6.48) represents the net Fourier diffusion flux, whilst the sixth is the energy flux associated with relative phase motion. The model includes a non-collisional sheath with a current density

$$
J = e n_e \left(\frac{k_B T_e}{2\pi m_e}\right)^{0.5} \exp\left(\frac{e V_{sheath}}{k_B T_e}\right) - \frac{1}{4} e n_e \left(\frac{k_B T_e}{m_i}\right)^{0.5}, \qquad (6.50)
$$

where the terms on the right hand side of the expression represent the electronic and ionic contributions respectively. The energy balance at the cathode

and anode is modified to include additional source terms to describe heating due to neutral particles, charge transport across the sheath and radiative cooling. A volume of fluids method is used to solve the system of equations and cells containing free surfaces, associated with the evolving metal droplet and weld pool, have an associated pressure which is the product of the surface tension and a curvature term k_c expressed in terms of the unit normal vector $\mathbf{n}$,

$$k_c = \frac{1}{|\mathbf{n}|} \left[\left(\frac{\mathbf{n}}{|\mathbf{n}|} \cdot \nabla \right) |\mathbf{n}| - (\nabla \cdot \mathbf{n}) \right]. \qquad (6.51)$$

In the arc region, the influence of metal vapour in the plasma was neglected. The model is able to predict the influence of current on droplet transfer and the motion of the liquid weld pool due to droplet impingement, which excites surface oscillations. The model also explained the formation of small secondary or satellite droplets, often observed in practice, which form because of the high electromagnetic pinch force in the small necking area after the detachment of the primary droplet.

6.4 Unified Arc and Electrode Models

Modelling of the welding arc is motivated by a number of goals, amongst which are a desire to understand the physics of the arc and to explain the behaviour of the discharge under different operating conditions. Another rationale is to predict the performance of welding processes based on physical principles. This remains a daunting task because of the complexity of processes involved and their widely differing length and time scales. With the continuing improvement in numerical efficiency and computational speed, models unifying discharge and electrode conditions have become feasible in the past decade and some aspects of welding process behaviour are now amenable to numerical prediction.

Some simplifications are inevitable when modelling a complex system. For example, Zhu et al. [46] present an analysis of free burning arcs including the electrodes with an emphasis on anode properties. The non-equilibrium sheath region at the anode is treated by approximation in which the iteration grid size is chosen large enough to include the electron diffusion region (estimated to be of the order $40\,\mu\mathrm{m}$), the electrical conductivity is assumed to be equal to that of the adjacent plasma and the energy balance equation is solved for zero electric field strength. Simplification of the cathode sheath structure has also been described [43] where the energy balance equation in the sheath is neglected, as are space charge considerations and the ionisation term due to electron acceleration in the electric field. In this work only the electron continuity equation involving ambipolar diffusion was considered together with thermal ionisation and recombination. Electron emission is assumed to be thermionic and radiative heating of the electrodes was neglected. Current densities are derived for
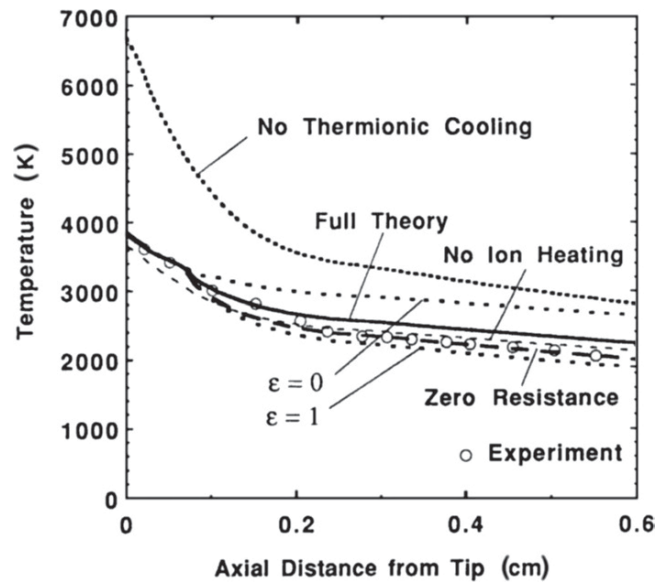
Fig. 6.9. Predicted temperatures on the cathode surface for a 200 A argon TIG arc indicating the role of various heat-transfer processes. Experimental points (circles) are taken from [61]. © 2002 Institute of Physics Publishing *reproduced with permission from* [43].

the combined arc and electrode region from the current continuity equation, without prior assumption of the current density distribution at the cathode surface. The relative influence of several factors on the surface temperature of the cathode are shown in Fig. 6.9 [43]. It can be seen that results are fairly insensitive to the heating effects of the ions and to Ohmic heating (zero resistance). Emissivity has a notable influence and has been calculated for the extremes of 0 and 1, whilst the largest influence is seen from the transpiration (thermionic) cooling term, which is critical for the prevention of melting at the electrode surface.

The influence of welding parameters on weld pool formation has been examined in a number of studies [41], [62]–[70]. Goodarzi et al. [62, 63] employed a simplified treatment of the cathode and anode sheaths and showed a maximum anode heat flux at an electrode angle of about 60° for a 200 A, 2 mm long argon TIG arc; whilst for 5 and 10 mm arc lengths, the heat flux shows a much weaker tip angle dependency. Shear stress on the anode surface due to convective gas flow is predicted to decrease from 250 to 200 Pa as electrode tip angle increases from 10° to 60° for a 2 mm arc length. The same trend is observed for longer arcs, although the peak shear stress, which occurs at an arc radius of around 1.25 mm, is reduced to 210 to 175 Pa for a 5 mm long arc. The results contrast somewhat with those of Tanaka et al. [65] where a peak shear stress of 38 Pa is predicted for a 5 mm long, 150 A argon TIG arc. A number of factors may contribute to this discrepancy, including

differences in sheath treatments at the electrodes and neglect of buoyancy in the arc plasma by Goodarzi et al. [62].

Ushio et al. [41] predict weld pool fluid flow with positive and negative surface tension gradients, corresponding to inward and outward toroidal flows (high and low sulphur conditions) on a 304 stainless steel. Resulting fusion zone shapes are in qualitative agreement with experimental observations. In a later paper, the authors examine possible mechanisms responsible for increases in weld penetration due to the addition of a surface flux [66]. The following four mechanisms are proposed: (i) a change in surface tension which reverses the temperature dependent surface tension gradient to generate an inward flow; (ii) electron depletion in the outer fringes of the arc due to liberated flux ions, resulting in an increase in current density; (iii) reduced surface tension resulting in greater pool depression and (iv) insulation of the weld pool surface away from the arc axis due to the presence of an oxide layer. Mechanisms (i) and (iv) are shown to be possible contributory factors. Electron depletion due to the ion flux (ii) was accounted for by adding terms for oxygen - electron collisions and oxygen ion – metal atom electron liberation to the electron continuity equation. The resulting calculations however showed that this is not a significant mechanism. The limitation of the model to a flat anode surface assumption meant that it was not possible to assess the pool depression and arc pressure influence, although experimental observations suggest that such an influence is small at welding currents below 150 A. This also suggests that increases in arc velocity due to core acceleration driven by de-mixing processes is likely to be small, although this aspect was not explicitly included in the model.

Multi-component plasmas have been included in the unified models of Lago et al. [69, 70] and Tanaka et al. [71]. In the former work, the mass flux $\dot{m}_v$ from the vaporising anode surface is represented by

$$\dot{m}_v = \frac{1}{1 - X_i} \rho D_v \frac{\partial X_i}{\partial z}, \tag{6.52}$$

evaluated at the anode surface. Here D_v is the diffusion coefficient of the metal vapour in the plasma and the X_i is the vapour mass fraction given by

$$X_i = \frac{P_v M_m}{P_v M_m + (1 - P_v)M_p}, \tag{6.53}$$

where P_v is the saturation vapour pressure and M the molar masses of the metal and plasma (subscripts m and p respectively). Metal vapour ingress into the arc is shown to be limited to the region adjacent to the anode surface due to the dominance of the cathode jet [69, 71]. The presence of the vapour leads to a reduction in plasma temperature, which may be explained in terms of the lower ionisation potential compared with the plasma.

Unified arc and electrode models offer the potential to explore the influence of physical phenomena and boundary conditions on arcs and weld pools. To

date, most of the unified models reported assume a stationary anode surface, which is likely to underestimate the influence of arc shear on weld pool flow. Free surfaces have however been considered for the description of metal droplet transport in Gas Metal Arc (GMA) welding [55, 56, 60, 72] to describe the evolution, of the metal droplet as well as droplet absorption at the molten weld pool surface. In these models the influence of the droplet on the plasma is considered but the plasma is treated as an LTE fluid and vaporisation and diffusion of metallic components within the plasma, which may be expected to have a significant influence, are generally ignored.

6.5 Arc Plasma – Laser Interactions

The combination of a laser with an arc discharge for welding purposes was first described by Steen and co-workers in the late 1970s [73, 74]. Since that time, considerable attention has been paid to the experimental characteristics and possible applications of hybrid laser-arc processes. A number of different process combinations have been examined including lasers with the gas tungsten arc, gas metal arc and plasma arc welding processes, with a range of geometries and laser wavelengths. In the following discussion, attention will be focus primarily gas (CO_2) and solid-state (Nd:YAG) laser interactions with the welding arc.

When a laser beam and a plasma interact, a number of effects are possible. The laser beam may be absorbed in the arc plasma, scattered or defocused, generally resulting in a decrease in laser power impinging on the work piece in comparison to laser operation in the absence of the arc. From the perspective of the arc, energy can be absorbed from the laser beam in the plasma column, resulting in a change in electrical structure, flow field and temperature. Laser energy may also be absorbed at the arc root, changing the structure of the sheath, the energy transport to the work-piece surface, and modifying the temperature, fluid flow behaviour and metallic vapour distribution in the up-stream plasma. In the case of a cathodic work-piece, laser radiation will also modify the electron emission mechanisms, increasing thermionic emission due to a local increase in surface temperature and will modify the ionic contribution to thermo-field emission due to changes in the particle energy distribution in the cathode sheath.

The balance of radiative energy gain and loss by the plasma may be expressed by replacing the radiative source strength in the energy balance equation (6.6) by a term describing the divergence of the radiative flux q_r^{rad}. Deron et al. [75] define this term for a one-dimensional axisymmetric plasma as

$$\frac{1}{r}\frac{d}{dr}\left(rq_f^{rad}\right) = \int_{\lambda^{-1}} d\lambda^{-1}\,\kappa_\lambda(r)\left\{4\pi I_\lambda^o(r) - \int_{r'}\kappa_\lambda(r')I_\lambda^o(r')\exp\left(-\Theta\right)\frac{dr'}{\parallel r'-r\parallel^2}\right\},$$

(6.54)

where

$$\Theta = \int\limits_{s=0}^{\|r'-r\|} \kappa_\lambda \left(r + s\frac{r'-r}{\|r'-r\|} \right) ds.$$

Here $\kappa_\lambda(r)$ is the spectral absorption coefficient of the plasma at position r, and wavelength λ, $I_\lambda^o(r)$ the Planck function at temperature $T(r)$ and s the optical path.

6.5.1 Absorption

Laser light is absorbed in a plasma as a result of inverse bremsstrahlung due to bound-free and free-free transitions. For typical welding arc plasmas with a Maxwellian electron velocity distribution and relatively low electron temperatures (no more than a few eV), the linear absorption coefficient for light of frequency ν due to electron ion collisions is given by [76, 77]

$$\kappa_\nu^{ei} = \bar{g}(\nu, T) \left(\frac{2\pi m_e}{3k_B T_e} \right)^{0.5} \left(\frac{Z^2}{n_{Re}} \right) \frac{n_e n_i e^6}{6ch(2\pi\varepsilon_o\nu)^3 m_e^2} \left[1 - \exp\left(-\frac{h\nu}{k_B T} \right) \right],$$
(6.55)

where n_{Re} is the real part of the complex refractive index of the plasma Z the ion charge and $\bar{g}(\nu, T)$ the averaged Gaunt factor; see also §4.2. This expression is only valid provided the radiation field does not perturb the electron velocity distribution from a Maxwellian state. The influence of the radiation can be assessed by examining the ratio of electron velocities due to thermal and electric field contributions. The acceleration experienced by an electron in the radiant electric field is $eE_o\sin(\omega t)$ and the corresponding maximum speed u_E is $|eE_o/m_e\omega|$. The electric field is related to the intensity I_o (power per unit area) by $I_o = 1/2\varepsilon_o c E_o^2$ and the thermal velocity u_T is of the order $(3k_B T_e/m_e)^{0.5}$, the ratio of electrical to thermal velocities is therefore

$$\frac{u_E}{u_T} = \frac{\lambda}{T_e^{0.5}} \frac{e}{\pi c} \left(\frac{I_o}{6m_e\varepsilon_o ck_B} \right)^{0.5} \ll 1$$
(6.56)

for CO_2 and Nd:YAG laser radiation at any temperature with reasonable electron density and for laser power densities to $10^{12}\,\mathrm{W\,m^{-2}}$ or higher. The averaged Gaunt factor in (6.55) is often expressed as

$$\bar{g}(\nu, T) = \frac{\sqrt{3}}{\pi} \ln\left[\left(\frac{2}{\gamma_g} \right)^{\frac{5}{2}} \left(\frac{k_B T_e}{m_e} \right)^{\frac{3}{2}} \left(\frac{2\varepsilon_o m_e}{Ze^2\nu} \right) \right],$$
(6.57)

where γ_g is the Euler-Mascheroni constant ($= 1.781$), and is valid provided $h\nu \ll k_B T_e$, which is just about acceptable at temperatures above $10^4\,\mathrm{K}$ for CO_2 laser radiation at $10.64\,\mu\mathrm{m}$, but is not valid for Nd:YAG laser radiation at

the low electron temperatures ($\leq 2\,\mathrm{eV}$) typically encountered in arcs. For the shorter wavelength Nd:YAG radiation of $1.06\,\mu\mathrm{m}$, the Born approximation is also invalid at such low temperatures and a quantum mechanical description is required.

For a non-relativistic electron making a transition from speed u_1 to speed u_2 [76], the Gaunt factor due to Sommerfeld is

$$g(\nu, u_1, u_2) = \frac{\sqrt{3}\,\pi x \dfrac{d}{dx}\left| F\left(i\eta_1, i\eta_2, 1; x\right)\right|}{\left\{\exp(2\pi\eta_1) - 1\right\}\left\{1 - \exp(-2\pi\eta_2)\right\}}, \qquad (6.58)$$

where

$$\eta_{1,2} = \frac{Ze^2}{2\varepsilon_o h v_{1,2}}; \quad x = -\frac{4\eta_1\eta_2}{\left(\eta_2 - \eta_1\right)^2}$$

and

$$F(\alpha, \beta, \gamma; x) = 1 + \frac{\alpha\beta}{\gamma}\frac{x}{1!} + \frac{\alpha(\alpha+1)\beta(\beta+1)}{\gamma(\gamma+1)}\frac{x^2}{2!} + \ldots.$$

A functionally equivalent form, avoiding the differential term in the above expression was employed by Paulini and Simon [77] for numerical simplicity

$$g(\nu, u_1, u_2) = \frac{\sqrt{3}\,\pi\eta_2\eta_1}{\left\{\exp(2\pi\eta_1) - 1\right\}\left\{1 - \exp(-2\pi\eta_2)\right\}}\frac{\Psi(i\eta_1, i\eta_2)}{(\eta_2 - \eta_1)}, \qquad (6.59)$$

with

$$\Psi(i\eta_1, i\eta_2) = F^2\left(\left(1 - i\eta_1\right), -i\eta_2, 1 : x\right) - F^2\left(\left(1 - i\eta_2\right), -i\eta_1, 1; x\right)$$

For a Maxwellian distribution of electron velocities, the average Gaunt factor is

$$\bar{g}(\nu, u_1, u_2) = \exp\left(\frac{h\nu}{k_B T_e}\right)\int\limits_{\frac{h\nu}{k_B T_e}}^{\infty} g(\nu, u_1, u_2)\exp(-\tau)d\tau, \qquad (6.60)$$

where

$$\tau = \frac{E}{k_B T}; \quad E = \tfrac{1}{2}mu_1^2; \quad E - h\nu = \tfrac{1}{2}mu_2^2$$

Many approximations can be found in the literature, ranging from the purely numerical expressions to simplifications of the Sommerfeld quantum mechanical description, (6.58). For example, Seyffarth and Krivtsun [78] present a frequency independent factor proportional to $\ln\left(Tn^{-1/3}\right)$, Wang and Rhodes [79] quote a factor proportional to $\ln(T^{4/3}P_e^{-1/3})$ where P_e is the electron pressure, whereas Greim [8] indicates a $\ln\left(T^3\lambda^2\right)$ dependency where $\omega \ll \omega_p$, which is invalid for CO_2 or Nd:YAG lasers irradiating welding arcs for which the plasma frequency ω_p is of the order 10^{12} to $10^{13}\,\mathrm{s}^{-1}$. A numerical approximation for the Gaunt factor is presented by Stallcop and Billman [80],
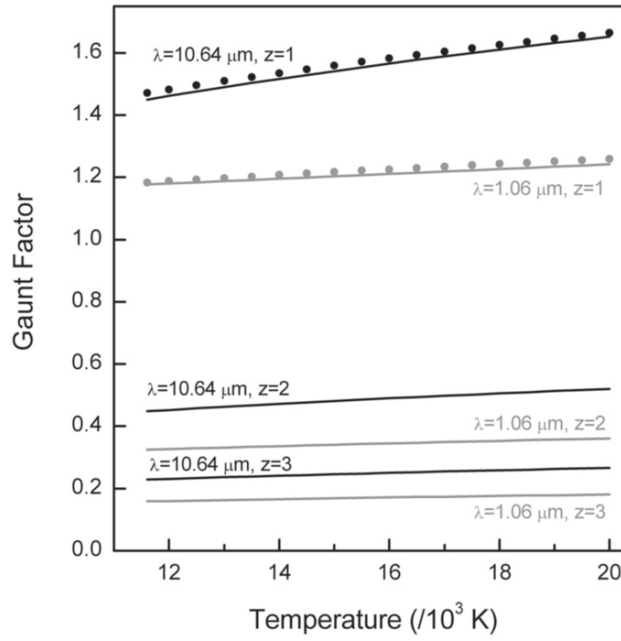
Fig. 6.10. Gaunt factors for different wavelengths and charges for an argon plasma. Points are plotted from the numerical approximation in [77] and lines from (6.61) [80].

Table 6.2. Coefficients $a_{n,m}$ for calculation of the Gaunt factor: (6.61) [80].

m	0	1	2
n	$0.1\,\mu\mathrm{m} \leq \lambda \leq 1\,\mu\mathrm{m}$		
0	1.1740	0.0662	0.0217
1	0.1982	0.4819	0.2240
2	0.3230	0.0454	−0.0831
	$1\,\mu\mathrm{m} \leq \lambda \leq 100\,\mu\mathrm{m}$		
1	1.1750	0.0789	0.1842
2	0.1812	0.5586	0.0304
3	0.3305	0.0203	0.0657

for electron temperatures $\geq 1\,\mathrm{eV}$, which takes the form

$$g(\lambda, T) = \sum_{n,m} a_{n,m} (\log_{10} T/Z^2)^n (\log_{10} Z^2 \lambda)^m \qquad (6.61)$$

where Z is the ionic charge and coefficients $a_{n,m}$ are given in table 6.2. and typical values are shown in Fig. 6.10.

A number of expressions for absorption coefficient may be found in the literature, which differ from (6.8) in greater or lesser detail (see for

example [78]–[80]). For example, Deron et al. [75] present the same expression without accounting for refractive index or net charge (the (Z^2/μ) term. These authors also describe absorption coefficients for electron-atom κ_ν^{eo} and bound-free κ_ν^{bf} contributions of the form:

$$k_\nu^{eo} = \frac{4e^2 n_e n_o}{3\pi\varepsilon_o hc\nu^3} \left(\frac{k_B T}{2\pi m_e}\right)^{\frac{3}{2}} \sigma_c(T) \left[1 - \exp\left(-\frac{h\nu}{k_B T}\right)\right] \left[1 + \left(1 + \frac{h\nu}{k_B T}\right)^2\right],$$

$$\kappa_\nu^{bf} = \left[1 - \exp\left(\frac{h\nu}{k_B T}\right)\right] \sum_i n_i \sigma_i(\nu), \tag{6.62}$$

where $\sigma_c(T)$ is the electron-atom collision cross section [81] and $\sigma_i(\nu)$ photo-ionisation cross-section. For CO_2 and Nd:YAG laser irradiation of a gas plasma, κ_ν^{bf} is small. Temperature dependent absorption coefficients for an argon plasma are shown in Fig. 6.11.

The complex refractive index of an isotropic plasma can be expressed as the difference of the real and imaginary components by Appleton's equation [82, 83]

$$\Phi = \left(\frac{\omega_p^2}{\omega^2 + \nu_{eo}^2}\right)$$

$$n_{Re} = \left\{\frac{1}{2}(1 - \Phi) + \frac{1}{2}\left[(1 - \Phi)^2 + \frac{\nu_{eo}^2}{\omega^2}(\Phi)^2\right]^{0.5}\right\}^{0.5} \tag{6.63}$$

$$n_{Im} = \left\{-\frac{1}{2}(1 - \Phi) + \frac{1}{2}\left[(1 - \Phi)^2 + \frac{\nu_{eo}^2}{\omega^2}(\Phi)^2\right]^{0.5}\right\}^{0.5},$$

where ν_{eo} is the electron-neutral collision frequency, ω the angular frequency of the incident radiation and ω_p the plasma frequency. Unfortunately, the expression for ν_{eo} given in [82] is dimensionally incorrect; however, the collision frequency can be estimated from

$$\nu_{eo} = n_o \sigma_c \left(\frac{3k_B T_e}{m_e}\right)^{0.5}, \quad \omega_p = \left(\frac{n_e e^2}{\varepsilon_o m_e}\right)^{0.5}, \tag{6.64}$$

where σ_c is the electron-atom collision cross section [81]. The critical damping factor γ_c of a plasma is related to the number density of atoms and ions n_T and can be estimated from

$$\gamma_c \approx \sigma_c n_T \left(\frac{3k_B T}{m_e}\right)^{0.5}. \tag{6.65}$$

For an argon plasma, angular plasma frequencies range from $6.9 \times 10^{12}\,\text{s}^{-1}$ at 10,000 K to a maximum of 2.5×10^{13} at around 16,500 K falling to $2.4 \times 10^{13}\,\text{s}^{-1}$ at 20,000 K. The angular frequency of the laser radiation is $2.8 \times 10^{14}\,\text{s}^{-1}$ and
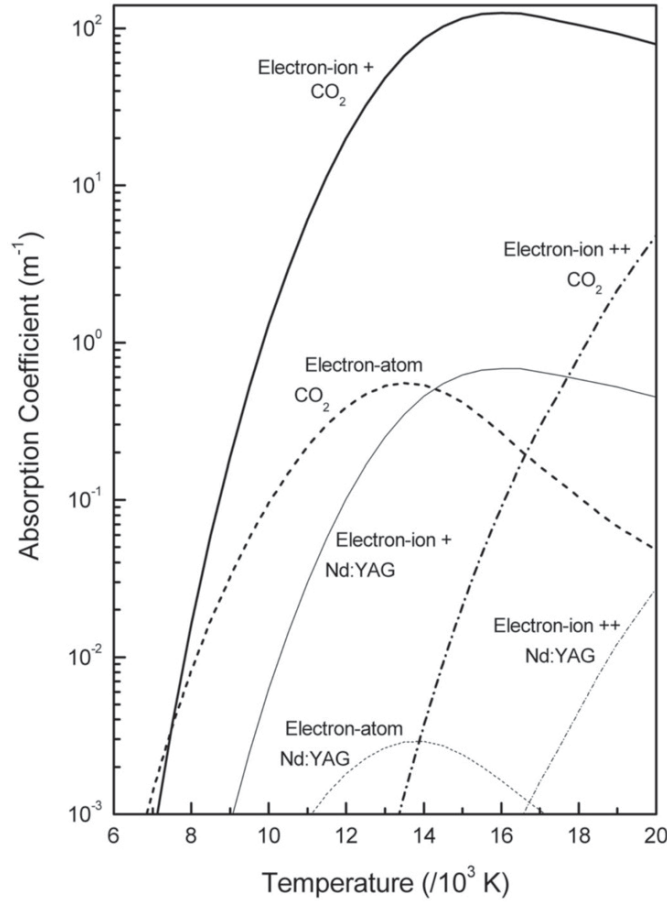
Fig. 6.11. Calculated absorption coefficients based on (6.55) and (6.62) using number densities from [13] and collision cross sections from [81].

$2.8 \times 10^{13}\,\mathrm{s}^{-1}$ for Nd:YAG and CO_2 lasers respectively. In both cases $\omega > \omega_p$, $\gamma_c \ll \omega_p$ and the plasma is dispersive. For the CO_2 laser, as ω approaches ω_p, and the plasma approaches resonance.

The real part of the refractive index remains very close to unity, whilst the absorption coefficient κ_ν [84], which can be approximated by

$$\kappa_\nu = \frac{4\pi n_{\mathrm{Im}}}{\lambda}, \tag{6.66}$$

is small for Nd:YAG laser radiation; the laser therefore undergoes minimal defocusing in the plasma. For the longer wavelength CO_2 radiation, the real part of the refractive index also remains close to unity, whilst the absorption coefficient becomes non-negligible as plasma temperature increases.

6.5.2 Scattering

The principal scattering mechanisms relevant to laser-arc plasma interactions are Rayleigh scattering, involving particles much smaller than the wavelength of the incident radiation, and Mie scattering from particles of a similar size or larger than the incident wavelength. Thomson scattering from electrons is independent of wavelength and has a cross-section σ_T [76], which is negligibly small.

$$\sigma_T = \frac{8\pi}{3} \left(\frac{e^2}{4\pi\varepsilon_o m_e c^2} \right) = 6.65 \times 10^{-29} \, [\text{m}^2], \tag{6.67}$$

Rayleigh scattering occurs from particles that act as dipoles in the electric field. For uniform spherical particles of radius r, both scattering and absorption can take place, which is dependent on the complex refractive index m of the plasma, but not on the internal refractive index of the scattering particles. The respective scattering and absorption cross sections are [85]

$$\sigma_{R,s} = \frac{3}{2\pi} \left(\frac{2\pi}{\lambda} \right)^4 \left(\frac{4\pi r^3}{3} \right)^2 \left| \frac{m^2 - 1}{m^2 + 2} \right|^2$$

$$\sigma_{R,a} = \frac{6\pi}{\lambda} \left(\frac{4\pi r^3}{3} \right) \text{Im} \left(\frac{m^2 - 1}{m^2 + 2} \right). \tag{6.68}$$

Greses and co-workers [86, 87] indicate that for a laser wavelength of $1.03\,\mu\text{m}$ and iron vapour with a complex refractive index m of $3.81 + 4.44i$ and particle radius of 20 nm, the scattering cross-section is $6.9 \times 10^{-19}\,\text{m}^2$ and the absorption cross-section is $5.7 \times 10^{-17}\,\text{m}^2$ and measured beam attenuations of 4% to 40% are reported for a range of Nd:YAG laser welding conditions. The linear attenuation coefficient is the product of the cross-section and the particle density, which for an iron vapour plume in laser welding is of the order $10^{18}\,\text{m}^{-3}$ [87]. Similar orders of magnitude may be expected for laser-TIG and laser-plasma hybrid welding where the laser heat source has a significantly higher surface power density than the arc source. In the case of consumable arc welding, the particle size distribution [88] is much broader than that measured during laser welding [87], with peak number densities occurring for particles in the range 0.1 to $0.5\,\mu\text{m}$ [88, 89].

Mie scattering, from particles of diameter similar to or greater than the incident wavelength, can also be treated as scattering from discrete dipoles. However, such large particles are represented by dipole arrays instead of single dipoles. For particles irradiated by non-polarised light, the scattering and absorption cross-sections [90] are

$$\sigma_{M,s} = \frac{8\pi r^6}{3} \left(\frac{2\pi}{\lambda} \right)^4 \left| \frac{m^2 - 1}{m^2 + 2} \right|^2$$

$$\sigma_{M,a} = \frac{8\pi^2 r^3}{\lambda} \text{Im} \left[\left(\frac{m^2 - 1}{m^2 + 2} \right) \left(1 + \frac{2\pi r}{\lambda} \left(\frac{m^2 - 1}{m^2 + 2} \right) \frac{m^4 + 27m^2 + 38}{2m^2 + 3} \right) \right], \tag{6.69}$$

The corresponding linear attenuation coefficients can be found by multiplying the cross-sections by the particle density or, for non-uniform particle sizes, a particle distribution function $n_p(r)$ (in units of m^{-3}), which describes the number of particles per unit volume and per unit radius as a function of the radius r. Thomas [90] provides a simple size distribution function for aerosols with a range of particle radii

$$n_p(r) = Ar^\alpha \exp(-br^\gamma), \tag{6.70}$$

where A, b, α, and γ are constants and the particle number density is $n_p = A\gamma^{-1}b^{-(\alpha+1)/\gamma}\Gamma((\alpha+1)/\gamma)$. Mie scattering in laser welding has been studied by Hansen and Duley [91], with particular reference to the vapour in the keyhole during welding. These authors describe the particle density with an expression of the form $n_p(r) = C_1 r^{p_1}$ where C_1 and p_1 are constants, and examined the relative roles of scattering and absorption due to Nd:YAG and CO_2 laser irradiation. The mass density of aerosol material ρ_{ma} is described by

$$\rho_{ma} = \begin{cases} \dfrac{4\pi C_1 \rho}{3(p_1+4)}\left(r_{max}^{p_1+4} - r_{min}^{p_1+4}\right) & p_1 \neq -4 \\[2ex] \dfrac{4\pi C_1 \rho}{3}\ln\left[\dfrac{r_{max}}{r_{min}}\right] & p_1 = -4 \end{cases}, \tag{6.71}$$

where ρ is the internal density of the aerosol particles and subscripts max and min refer to the maximum and minimum particle sizes. The linear absorption and scattering coefficients are proportional to the ratio ρ_{ma}/ρ and attenuation for Nd:YAG laser radiation becomes significant when ρ_{ma}/ρ approaches 10^{-4}, corresponding to particle number densities of 1.9×10^{14} and 1.9×10^{11} m^{-3} for particle sizes of 0.5 and $5\,\mu m$ respectively. These compare with particle densities of the order 10^{12} to 10^{11} m^{-3} reported for GMA welding [87], indicating that Mie Scattering can potentially modify the power density distribution during laser-GMA welding. Absorption by the aerosol particles results in heating which is estimated to be of the order $10^7\,K\,s^{-1}$ ($\rho_{ma}/\rho = 10^{-4}$, $\lambda = 10.6\,\mu m$, $I_o = 10^{10}\,W\,m^{-2}$), particles therefore vaporise in $< 1\,ms$. The contribution of Mie scattering will therefore be determined to a large extent by the rate of particle production. Mie scattering in CO_2 laser welding has been observed experimentally by Tu et al. [92] using a $363.8\,nm$ wavelength probe laser close to the edge of the plume, where transmittance fell to below 20%, compared with over 60% in the plume centre.

6.6 Laser-Arc Welding

Various terminologies are used to classify laser-arc interactions including laser enhanced arc welding and arc augmented laser welding. The first of these indicates that the majority of the power is derived from the arc discharge, whilst

the opposite is true for the latter. In the intermediate regime, the generic term laser-hybrid welding is generally employed, which also encompasses the arc and laser dominated regimes.

Steen and coworkers [73, 74] first showed that in comparison to laser welding alone, arc augmented laser welding can deliver increased welding speeds of 50 to 100% when combining a CO_2 laser with a TIG arc. They also showed increased penetration and observed that the arc root on a planar anode showed affinity for the laser focal spot. Compared with non-augmented laser welding, a further benefit of greater tolerance to joint geometry variations for combined process operation has been found. The commercial development of laser-arc welding began only after the widespread industrial acceptance of laser welding in the early 1990s, and to some extent rested on the development of laser optics and arc welding torches suitable for combined process applications. In recent years, a great deal of research effort has been expended on assessment of these processes to characterise their performance and explore potential advantages. Practical aspects of laser-arc applications are addressed in many published works, which are reviewed for example in [93]. The limited literature available addressing hybrid process modelling focuses either on laser-plasma interactions or discusses the influence of combined heat sources.

In an uncoupled model of heat transfer in laser-TIG welding Chen et al. [94, 95] describe the laser and arc as independent heat sources, with a reduction of the arc radius to account for the influence of the laser on the arc. The laser energy is distributed inside the keyhole according to

$$Q_{laser} = I_o \exp\left(-2\frac{r^2}{r_b^2}\right) \exp\left(-\kappa_\nu z\right)$$

$$r^2 = (x - u_w t)^2 + y^2$$

(6.72)

where u_w is the welding speed, I_o the peak power density at the beam centre and r_b the beam radius. The beam power P_{laser} is therefore

$$P_{laser} = \int\limits_0^Z \int\limits_0^{2r_b} Q_{laser} 2\pi r\, dr\, dz.$$

(6.73)

In this model, energy from the arc is assumed to be distributed over the weld pool surface according to

$$Q_{arc} = \frac{3\eta VI}{\pi r_a^2} \exp\left(-3\frac{r^2}{r_a^2}\right),$$

(6.74)

where V is the voltage, I the current, η the process efficiency and r_a the arc radius. The thermal distribution in the work-piece was derived for prescribed heat fluxes at the upper and lower surfaces. Predictions from this simple model indicate that at the surface, the heating rate and maximum surface
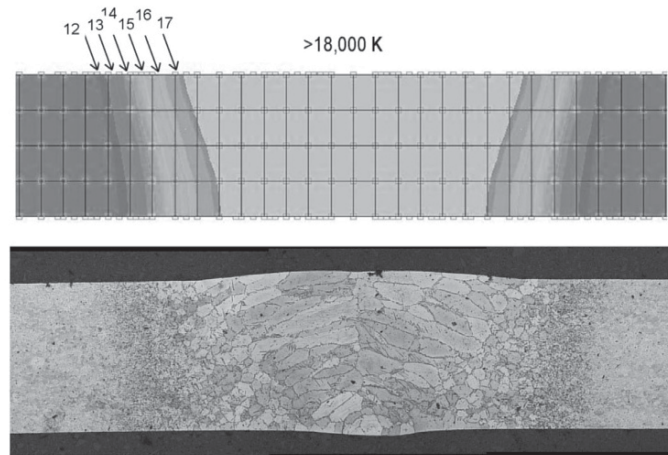
Fig. 6.12. Predicted thermal distribution and associated microstructure for a laser-TIG weld made on a 1 mm thick low carbon steel (FeP04) at $20\,\mathrm{mm\,s^{-1}}$ travel speed [96]. Numbers indicate temperatures ($/10^3\,\mathrm{K}$).

temperature for a 1 kW laser beam ($r_b = 1\,\mathrm{mm}$) is dominated by the laser conditions, whist the arc has comparatively little influence. Inside the keyhole, the heating rate due to hybrid operation rises faster with increasing depth than that found for laser welding without arc augmentation, resulting in deeper penetration. Penetration increases initially with arc current, but decreases again at high current, which is ascribed to arc broadening due to laser power absorption. The link between laser power and arc radius is unfortunately not described in this work.

Numerical simulation of heat flow in conduction mode laser-GTA welding has also been reported by Hu [96], where the arc heat source is represented by a Gaussian surface flux term, and the laser heat source by a Gaussian volume flux term. The thermal gradient in the heat affected zone of a hybrid weld was simulated using measured values of laser beam and arc root radii and energy transfer coefficients as model inputs. Although fluid flow was not explicitly incorporated in the calculation, the temperature profiles of the weld metal and heat-affected zone agree well with measured thermal distributions and reflect the structure observed in associated weld metal cross sections. A comparison of time spent at temperatures giving rise to significant grain growth showed a reduction of 40% when comparing arc and hybrid welds on a 1 mm thick low carbon steel, resulting in reduced HAZ grain size, consistent with experimental observation. An example of the model temperature profile and corresponding weld microstructure is shown in Fig. 6.12.

A similar study has been reported for a Nd:YAG laser and GMA arc hybrid process by Reutzel et al. [97] in which the thermal distributions for the arc,

the laser and the hybrid condition are described by Goldak double ellipsoid volumetric terms [98] viz:

$$q_{f,r}(x,y,z,t) = \frac{6\sqrt{3}f_{f,r}P_s}{abc_{f,r}\pi^{1.5}} \exp\left(-3\frac{x^2}{a^2} - 3\frac{y^2}{b^2} - 3\frac{(z+u_w t)^2}{c_{f,r}^2}\right), \quad (6.75)$$

where u_w is the welding velocity in the z direction, P_s the input power, a, b and $c_{f,r}$ are constants, subscripts f and r refer to the front and rear ellipsoids and $f_{f,r}$ to the fraction of the total heat input assigned to each ellipsoid such that $f_f + f_r = 2$. Good agreement was reported for the arc case; however the model predicted weld pool widths 35% greater than those obtained from experiments for full penetration laser welds in a 5 mm thick steel substrate. Direct combinations of laser and arc parameters were found to be inappropriate to describe the hybrid case, which required adjustment of the distribution parameters. These observations are in agreement with the expectation that the combined presence of a laser and arc result in a modified power distribution, which in turn has an influence on convective heat transport (fluid flow) in the weld pool.

The hydrodynamic processes in a weld pool have been considered semi-analytically by Zaĭkin et al. [99]. Radial fluid velocities on the surface of the weld pool were measured by direct observation, whilst axial velocities were inferred by scaling the radial values by the pool depth divided by the pool radius. The average vapour recoil pressure $\langle P_p \rangle$ is estimated from

$$\langle P_p \rangle = P_o + \frac{u_m u_v}{S_f}, \quad (6.76)$$

where u_m is the velocity of the metal, u_v the velocity of vapour expansion and S_f the focal spot area. Changes in mean vapour recoil pressure due to a measured fluid flow velocity of $0.75\,\mathrm{m\,s^{-1}}$ are in the order $1\,\mathrm{kPa}$. Variation in mass transport within the weld pool results in periodic changes of the vapour recoil pressure due to oscillation of the volume of the keyhole. For a CO_2 laser power density of $2 \times 10^{10}\,\mathrm{W\,m^{-2}}$, experimentally measured oscillation frequencies in the range 10^2 to $10^3\,\mathrm{Hz}$ were found, which satisfy the condition $g\rho/\gamma k_n \ll 1$, where ρ is the density, γ the surface tension and k_n the wave number, and hence may be described as capillary waves. It is possible that such waves form due to the periodic absorption and defocusing of the laser by the plasma jet, the properties of which then oscillate due to the periodic change in metallic vapour concentration expelled from the keyhole.

The influence of synergistic interactions between a laser and an arc has also been studied semi-analytically by Paulini and Simon [77] who examined the energy balance at the anode for a laser–TIG process. Their model assumes a Gaussian current density distribution at the work piece surface, with an arc radius of $2\,\mathrm{mm}$. The laser power distribution is also assumed to be Gaussian, with a radius of $0.1\,\mathrm{mm}$, and absorption takes place due to inverse bremsstrahlung and Fresnel processes (see §4.3.2) for perpendicularly

incident light. Latent heat and fluid flow are neglected and it is assumed that the weld pool surface is substantially unaffected by the laser beam; i.e., that no keyhole forms. The problem then reduces to finding a solution for the stationary heat conduction equation with a summed laser and arc power distribution $Q_T(x, y)$

$$u_w \frac{\partial T}{\partial x} = \alpha \nabla^2 T + \frac{Q_T(x, y)}{\rho \, C_p} \delta(z), \tag{6.77}$$

where α is the thermal diffusivity, u_w the welding speed and $\delta(z)$ the Dirac delta function. For a work piece of finite thickness d, and a boundary condition of zero thermal gradient at the lower surface of the plate ($z = -d$), an analytical solution can be found of the form [100, 101]

$$T = T_o + \sum_{i=laser,arc} \left(\frac{P_i}{\kappa \, r_i \, \pi^{1.5}} \sum_{n=-\infty}^{\infty} \int_o^{\infty} \frac{d\tau}{1 + \tau^2} \exp \{\Xi(\tau, n)\} \right)$$

$$\Xi(\tau, n) = \left\{ \frac{-\tau^2}{1 + \tau^2} \left[\left(\frac{x}{r_i} - \frac{r_i u_w}{4\alpha\tau^2} \right)^2 + \left(\frac{y}{r_i} \right)^2 \right] - \tau^2 \left(\frac{z}{r_i} - 2n\frac{d}{r_i} \right)^2 \right\}$$
$$\tag{6.78}$$

where κ is the thermal conductivity and the heat sources are moving in the positive x direction. The minimum arc power required to make a full penetration weld occurs when the melting isotherm intersects the lower surface of the work piece at a single point. For typical welding speeds of a few millimetres per second and in the absence of a laser, arc powers in the range 200 to 500 W are required to penetrate a 1 mm thick steel sheet, and surface temperatures lie in the range 1900 to 2100 K, well below the vaporisation temperature, which is of the order 3000 K. Some constraint is required to specify arc and laser powers uniquely for laser enhancement of the TIG arc, and this is chosen as the condition under which the weld pool surface ($z = 0$) reaches the vaporisation temperature. Upon vaporisation, metal ions are released into the arc, altering the arc structure and modifying the energy density at the work-piece surface. For a minimal full penetration condition, the laser power required to achieve surface vaporisation is substantially independent of welding speed and for a steel work piece is 65 W for a Nd:YAG laser and 130 W for a CO_2 laser. For aluminium alloys, the minimum laser powers increase by a factor of 6 whilst for copper, the minimum requirement is over 2 kW at 10.6 μm and over 3 kW at 1.06 μm [77]. The threshold laser powers are strongly dependent on the chosen arc and laser radii and on the temperature averaged material properties employed, and neglect laser absorption and scattering from the arc plasma. However, they indicate that for welds made on steel, changes in arc structure and energy transport may be expected at relatively modest beam powers.

Experimental measurements indicating changes in arc structure due to laser enhancement have been reported by Hu and den Ouden [102] who show direct photographic evidence of arc contraction due to metal vapour liberation and report calorimetric measurements of heat transfer to the work piece in laser, arc and hybrid welds. The heat dissipation measurements show no difference in heat transfer between the sum of the laser and arc sources acting separately and a hybrid process operation. However, the melting efficiency, defined as the percentage ratio of power required to heat and melt the weld volume obtained per unit time to the total power transferred to the work piece per unit time, is found to be 30 to 50% above the melting efficiency for the equivalent laser and arc conditions where the processes operate separately. These observations are consistent with the role of metal vapour in the arc plasma and have been confirmed by Langmuir and surface probe measurements made in TIG arcs with and without laser addition, which show a decrease in the conductive radius and increase in current density in the laser-arc condition.

The interaction between a laser beam and an arc plasma column, has been examined by Dowden and Kapadia [103] by means of an analytical energy balance approach, where consideration is given to extreme conditions. Ohmic heating dominates at the plasma temperatures occurring in an arc without laser irradiation, producing sufficient heating for ionisation and current flow. At low laser powers the laser acts to stabilise the plasma and helps to define the arc path, but provides only a small fraction of the energy required for ionisation. In contrast, at high plasma temperatures and laser powers, inverse bremsstrahlung provides a significant contribution to the energy required for current continuity. Under such conditions, inverse bremsstrahlung can dominate, opening a high conductivity path for current flow. However, laser powers of the order several tens to hundreds of kilowatts are necessary to achieve such a condition and these lie above the limits usually available for welding applications.

Plasma interactions at laser powers of up to $1.5\,\mathrm{kW}$ have been examined by Startsev et al. [104] for a co-axial and axisymmetric hybrid plasma configuration, involving a cylindrical hollow cathode. The interaction was modelled by inclusion of an absorption coefficient in the energy balance equation, which (c.f. (6.6)) took the form

$$\frac{\partial}{\partial z}\left(\rho c_p T\, r\, u_z\right) - \frac{\partial}{\partial r}\left(-\rho c_p T\, r\, u_r\right) - \frac{\partial}{\partial z}\left(\frac{\mu}{\mathrm{Pr}} r \frac{\partial}{\partial z}\left(c_p T\right)\right)$$

$$- \frac{\partial}{\partial r}\left(\frac{\mu}{\mathrm{Pr}} r \frac{\partial}{\partial r}\left(c_p T\right)\right) + r\left(\sigma E^2 + \kappa_\nu Q_{laser} - U\right) = 0, \qquad (6.79)$$

where Pr is the Prandtl number and Q_{laser} the incident laser power density. The propagation of the laser is treated as a quasi-planar electromagnetic wave

propagating in the z direction, thus

$$\frac{\partial^2 E_c}{\partial z^2} + 2ik\frac{\partial E_c}{\partial z} + \frac{1}{r}\frac{\partial}{\partial r}\left(r\frac{\partial E_c}{\partial r}\right) + k^2\left(-\frac{n_e}{n_{cr}} + i\frac{\kappa_\nu}{k}\right)E_c = 0, \qquad (6.80)$$

where E_c is the complex amplitude of the electric field, k the wave vector, n_e the electron number density, n_{cr} the critical electron number density. The first term in the right most parentheses, involving electron density ratio describes refraction, whilst the second term describes absorption. The plasma is assumed to be in pLTE and the electron density is therefore derived from the Saha equation. The electric field amplitude is related to the laser power density Q_{laser} by

$$Q_{laser} = \frac{1}{2}\left(\frac{\varepsilon_o}{\mu_o}\right)^{0.5} E_c^2, \qquad (6.81)$$

and the argon plasma radiation is related to the temperature by

$$U = \frac{280P^2 z_i}{(T \times 10^{-4})^{2.5}}\left(1 + 2.7 \times 10^{-6}T\right), \qquad (6.82)$$

where P is the pressure and z_i the degree of ionisation. The laser beam profile is assumed to be Gaussian with a focal spot radius of r_f at a focal plane $z = F_p$ (in the absence of a plasma) and the spatial distribution of the complex amplitude of the electric field is defined as

$$E_c = \left(\frac{4P_{laser}}{\pi r_f^2}\left(\frac{\mu_o}{\varepsilon_o}\right)^{0.5}\right)^{0.5}\frac{r_f}{r_z}\exp\left(-\frac{r^2}{r_z^2} + i\left(\frac{kr^2}{2R_z} - \varphi_z\right)\right), \qquad (6.83)$$

where

$$r_z^2 = r_f^2\left(1 + \left(\frac{z - F_p}{z_f}\right)^2\right); \quad R_z = (z - F_p)\left(1 + \left(\frac{z_f}{z - F_p}\right)^2\right);$$

$$\varphi_z = \tan^{-1}\left(\frac{z - F_p}{z_f}\right); \quad z_f = \frac{1}{2}kr_f^2. \qquad (6.84)$$

This system of governing equations has been solved numerically for suitable boundary conditions using an iterative technique, whereby a solution for the arc is sought, followed by a solution for the laser propagation; see (6.81). The process is repeated until all the required convergence criteria are satisfied. The results indicate a significant temperature rise in the core of the arc. For a cathode with a 4 mm internal diameter and 6 mm external diameter, an arc length of 5 mm and an argon plasma, the core arc temperatures are 10,000 to 12,000 K for currents of 50 to 200 A, in the absence of the laser. With the 1.5 kW CO_2 laser, the core temperature rises to 18,000 to 21,000 K, which is accompanied by enhanced ionisation and hence greater electrical

conductivity. As a result, the current density at the anode increases from $7 \times 10^6 \,\mathrm{A\,m^{-2}}$ to $4.5 \times 10^7 \,\mathrm{A\,m^{-2}}$ for a 100 A arc and the voltage drop in the arc column decreases by 25 to 50%. Whilst the current path changes, the gas flow is only weakly affected, with axial and radial velocities changing by less than 5%. The absorption coefficient and refractive index of the plasma are dependent on temperature and show significant spatial variation within the arc column. Increasing current results in increased absorption, but also in increased refraction due to the temperature dependence of the dielectric permeability which governs the refractive index; see for example (6.63) and (6.64). For a 200 A arcing condition, this results in self-focusing of the beam on the arc axis and enhanced beam intensity in comparison to laser conditions in the absence of the arc [104].

A number of related works consider the influence of beam-plasma interactions in specialised welding torch designs, see for example [78], and discuss power distribution at the weld pool and inside the bodies of arc generating torches. However, none of these address the influence of laser conditions on changes to the heat distribution at the work piece surface. Whilst laser-material interactions and arc structures have been explored in some detail, understanding of laser-arc hybrid welding process interactions and their consequences for weld formation and process stability is only just beginning. A deeper understanding of the influence of metal vapour on the energy transport within the welding plasma, particularly with regard to diffusion driven structural changes in multi-component mixtures is required. Prediction of the influence of beam-plume interactions on energy transport to the work piece and fluid flow within the weld pool, taking account of relevant physical phenomena, remains a considerable challenge for the future.

References

1. Guile AE (1969) Arc Cathode and Anode Phenomena. International Institute of Welding (IIW) Document 212-170-69
2. Zijp JP (1990) Heat Transport During Gas Tungsten Arc Welding. PhD thesis, Delft University of Technology, The Netherlands
3. Lancaster J (1984) The Physics of Welding. Pergamon Press
4. Ducharme R, Kapadia P, Dowden J, Thornton M, Richardson IM (1995) A Mathematical Model of the Arc in Electric Arc Welding, Including Shielding Gas Flow and Cathode Spot Location. J Phys D: Appl Phys 28(9): 1840–1850
5. Kovitya P, Lowke JJ (1985) Two-dimensional Analysis of Free Burning Arcs in Argon. J Phys D: Appl Phys 18: 53–70
6. Haddad GN, Farmer AJD (1984) Temperature Determinations in a Free-Burning Arc: I. Experimental Techniques and Results in Argon. J Phys D: Appl Phys 17: 1189–1196
7. Olsen HN (1959) Thermal and Electrical Properties of an Argon Plasma. Phys Fluids 2(6): 614–623
8. Greim HR (1964) Plasma Spectroscopy. McGraw-Hill

9. Degout D, Catherinot A (1986) Spectroscopic Analysis of the Plasma Created by a Double-Flux Tungsten Inert-Gas (TIG) Arc Plasma Torch. J Phys D: Appl Phys 19(5): 811–823

10. Thornton MF (1993) Spectroscopic Determination of Temperature Distributions for a TIG Arc. PhD thesis, Cranfield Institute of Technology, UK

11. Cram LE, Poladian L, Roumeliotis (1988) Departures from Equilibrium in a Free-Burning Argon Arc. J Phys D: Appl Phys 21: 418–425

12. Gomés AM (1983) Criteria for Partial LTE in an Argon Thermal Discharge at Atmospheric Pressure; Validity of the Spectroscopically Measured Electronic Temperature. J Phys D: Appl Phys 16: 357–378

13. Drellischak KS, Knopp CF and Cambel AB (1962) Partition Functions and Thermodynamic Properties of Argon Plasma. Gas Dynamics Laboratory, Nothwestern University, Illinois, USA. Report No A-3-62

14. Farmer AJD, Haddad GN (1988) Rayleigh-Scattering Measurements in a Free-Burning Argon Arc, J Phys D: Appl Phys 21(3): 426–431

15. Farmer AJD, Haddad GN (1984) Local Thermodynamic-Equilibrium in Free-Burning Arcs in Argon. Applied Physics Letters 45(1): 24–25

16. Bakshi V, Kearney RJ (1989) An Investigation of Local Thermodynamic Equilibrium in an Argon Plasma Jet at Atmospheric Pressure. J Quant Spect Rad Trans 41(5): 369–376

17. Snyder SC, Lassahn GD, Reynolds LD (1993) Direct Evidence of Departures from Local Thermal Equilibrium in a Free-burning Arc-discharge Plasma. Phys Rev E 48 5: 4124–4127

18. Kitamura T, Takeda K, Shibata K (1998) Deviation from Local Thermal Equilibrium State in Thermal Plasma. ISIJ International 38(11): 1165–1169

19. Thornton MF (1993) Spectroscopic Determination of Temperature Distributions for a TIG Arc J Phys D: Appl Phys 26: 1432–1438

20. Rat V, Aubreton J, Elchinger MF, Fauchais P, Murphy AB (2002) Diffusion in Two-temperature Thermal Plasmas 66: 056407

21. Murphy AB (1996) Modelling and Diagnostics of Plasma Chemical Processes in Mixed-Gas Arcs. Pure and Appl Chem 68(5): 1137–1142

22. Murphy AB (1993) Diffusion in Equilibrium Mixtures of Ionized Gases. Phys Rev E 44(5): 3594–3603

23. Murphy AB (1996) A Comparison of Treatments of Diffusion in Thermal Plasmas. J Phys D: Appl Phys 29(7): 1922–1932

24. Murphy AB and Arundell CJ (1994) Transport Coefficients of Argon, Nitrogen, Oxygen, Argon-nitrogen, and Argon-oxygen Plasmas. Plasma Chem Plasma Process 14(4): 451–490

25. Devoto RS (1966) Transport Properties of Ionized Monatomic Gases. Phys Fluids 9(6): 1230–1240

26. Murphy AB (1996) The Influence of Demixing on the Properties of a Free Burning Arc. Appl Phys Lett 69(3): 323–330

27. Murphy AB (1997) Demixing in Free-burning Arcs. Phys Rev E 55(6): 7473–7494

28. Greses-Juan J (1999) Examination of Adaptive control Strategies for Hyperbaric Keyhole Plasma Arc Welding. MSc thesis, Cranfield University, UK

29. Aubreton A, Elchinger MF (2003) Transport Properties in Non-equilibrium Argon, Copper and Argon–copper Thermal Plasmas, J Phys D: Appl Phys 36(15): 1798–1805

30. Rethfeld B, Wendelstorf J, Klein T, Simon G (1996) A Self-Consistent Model for the Cathode Fall Region of an Electric Arc. J Phys D: Appl Phys 29: 121–128
31. Chen MM, Thorne RE, Wyner EF (1976) Resolution of Electron Emission Mechanisms in an Argon Arc with Hot Tungsten Cathode, J Appl Phys 47(12): 5214–5217
32. Klein T, Paulini J, Simon G (1994) Time-resolved Description of Cathode Spot Development in Vacuum Arcs. J Phys D: Appl Phys 27: 1914–1921
33. Morrow R, Lowke JJ (1993) A One-Dimensional Theory for the Electrode Sheaths of Electric-Arcs. J Phys D: Appl Phys 26(4): 634–642
34. Spataru C, Teillet-Billy D, Gauyacq JP, Teste P, Chabrerie JP (1997) Ion-assisted Electron Emission from a Cathode in an Electric Arc, J Phys D: Appl Phys 30: 1135–1145
35. Hsu KC, Pfender E (1983) Analysis of the Cathode region of a Free Burning High Intensity Argon Arc. J Appl Phys 54(7): 3818–3824
36. Delalondre C, Simonin O (1990) Modeling of High-Intensity Arcs Including a Non-equilibrium Description of the Cathode Sheath. Journal De Physique 51(18): C5199–C5206
37. Wendelstorf J (2000) Ab Initio Modelling of Thermal Plasma Gas Discharges (Electric Arcs). PhD thesis, University of Braunschweig, Germany
38. Murphy EL, Good RH (1956) Thermionic Emission, Field Emission and the Transition Region. Phys Rev 102(6): 1464–1473
39. Coulombe S, Meunier JL (1997) A Comparison of Electron-emission Equations used in Arc-cathode Interaction Calculations. J Phys D: Appl Phys 20(30): 2905–2910
40. Quigley MBC, Richards PH, Swift-Hook DT, Gick AEF (1973) Heat-Flow to the Workpiece from a TIG Welding Arc. J Phys D: Appl Phys 6(18): 2250–2258
41. Ushio M, Tanaka M, Lowke JJ (2004) Anode Melting from Free-Burning Argon Arcs. IEEE Trans Plasma Sci 32(1): 108–117.
42. Tanaka M, Ushio M, Wu CS (1999) One-dimensional Analysis of the Anode Boundary Layer in Free-burning Argon Arcs. J Phys D: Appl Phys 32: 605–611
43. Lowke JJ, Morrow R, Haidar J (1997) A Simplified Unified Theory of Arcs and their Electrodes. J Phys D: Appl Phys 30: 2033–2042
44. Hinnov E, Hirschberg JG (1962) Electron-ion Recombination in Dense Plasmas. Phys Rev 125(3): 795–801
45. Jenista JJ, Heberlein VR (1997) Numerical Model of the Anode Region of High Current Electric Arcs. IEEE Trans Plasma Sci 25(5): 883–890
46. Zhu P, Lowke J J, Morrow R, Haider J (1995) Prediction of Anode Temperatures of Free Burning Arcs. J Phys D: Appl Phys 28: 1369–1376
47. Sanders NA, Pfender E (1984) Measurement of Anode Falls and Anode Heat Transfer in Atmospheric Pressure High Intensity Arcs. J Appl Phys 55(3): 714–722
48. Yang G, Heberlein J (2007) Anode Attachment Modes and their Formation in a High Intensity Argon Arc. Plasma Sources Sci Technol 16: 529–542
49. Kim W-H, Na S-J (1998) Heat and Fluid Flow in Pulsed Current GTA Weld Pool. Int J Heat and Mass Trans 41: 3213–3227
50. Zhang W, Kim C-H, DebRoy T (2004) Heat and Fluid Flow in Complex Joints During Gas Metal Arc Welding Part I: Numerical Model of Fillet Welding. J Appl Phys 95(9): 5210–5219

51. Wu CS, Yan F (2004) Numerical Simulation of Transient Development and Diminution of Weld Pool in Gas Tungsten Arc Welding. Modelling Simul Mater Sci Eng 12: 13–20
52. Mishra S, DebRoy T (2005) A Heat-transfer and Fluid-flow Based Model to Obtain a Specific Weld Geometry using Various Combinations of Welding Variables. J Appl Phys 98: 044902
53. Chakraborty N, Chakraborty S, Dutta P (2004) Three-dimensional Modeling of Turbulent Weld Pool Convection in GTAW Processes. Numerical Heat Transfer A 45: 391–413
54. Jaidi J, Dutta P (2004) Three-dimensional Turbulent Weld Pool Convection in Gas Metal Arc Welding Process. Sci Technol Weld Join 9(5): 407–414
55. Hu J, Tsai HL (2007) Heat and Mass Transfer in Gas Metal Arc Welding. Part I: The Arc. Int J Heat & Mass Trans 50: 808–820
56. Hu J, Tsai HL (2007) Heat and Mass Transfer in Gas Metal Arc Welding. Part II: The Metal. Int J Heat & Mass Trans 50: 833–846
57. Richardson IM, Norrish J, Hermans HJM (2006) The Mechanism and Significance of Drop Spray Transfer in GMAW, International Institute of Welding (IIW) Document XII-1893-06
58. Choi BK, Ko SH, Kim YS (1998) Dynamic Simulation of Metal Transfer in GMAW – Part 1: Globular and Spray Transfer Modes. Weld J 77: 38s–44s
59. Fan HG, Kovacevic R (2004) A Unified Model of Transport Phenomena in Gas Metal Arc Welding Including Electrode, Arc Plasma and Molten Pool. J Phys D: Appl Phys 37: 2531–2544
60. Hu J, Tsai HL (2006) Effects of Current on Droplet Generation and Arc Plasma in Gas Metal Arc Welding J: Appl Phys 100: 053304
61. Haidar J, Farmer AJD (1993) A Method for the Measurement of the Cathode Surface Temperature for a High-current Free-burning Arc. Rev Sci Instrum 64: 542–7
62. Goodarzi M, Choo R, Toguri JM (1997) The Effect of the Cathode Tip Angle on the Gas Tungsten Arc Welding Arc and Weld Pool: I. Mathematical Model of the Arc. J Phys D: Appl Phys 30: 2744–2756
63. Goodarzi M, Choo R, Takasu T, Toguri JM (1998) The Effect of the Cathode Tip Angle on the Gas Tungsten Arc Welding Arc and Weld Pool: II. The Mathematical Model for the Weld Pool. J Phys D: Appl Phys 31: 569–583
64. Tanaka M, Ushio M, Lowke JJ (2004) Numerical Study of Gas Tungsten Arc Plasma with Anode Melting. Vacuum 73: 381–389
65. Tanaka M, Ushio M, Lowke JJ (2004) Numerical Analysis for Weld Formation Using a Free-burning Helium Arc at Atmospheric Pressure. JSME Int J Series B 48(3): 397–404
66. Lowke JJ, Tanaka M, Ushio M (2004) Mechanisms Giving Increased Weld Depth Due to a Flux. J Phys D: Appl Phys 38: 3438–3445
67. Lowke JJ, Tanaka M (2007) Predictions of Weld Pool Profiles using Plasma Physics. J Phys D: Appl Phys 40: R1–R23
68. Tanaka M, Tashiro S, Lowke JJ (2007) Predictions of Weld Formation using Gas Tungsten Arcs for Various Arc Lengths from Unified Arc-electrode Model. Sci Technol Weld Join 12(1): 2–9
69. Lago F, Gonzalez JJ, Freton P, Gleizes A (2004) A Numerical Modelling of an Electric Arc and its Interaction with the Anode: Part I. The Two-dimensional Model. J Phys D: Appl Phys 37: 883–897

70. Gonzalez JJ, Lago F, Freton P, Masquère M, Franceries X (2005) Numerical Modelling of an Electric Arc and its Interaction with the Anode: Part II. The Three-dimensional Model – Influence of External Forces on the Arc Column. J Phys D: Appl Phys 38: 306–318
71. Tanaka M, Yamamoto K, Tashiro S, Nakata K, Ushio M, Yamazaki K, Yamamoto E, Suzuki K, Murphy AB, Lowke JJ (2007) Metal Vapour Behaviour in Thermal Plasma of Gas Tungsten Arcs During Welding. International Institute of Welding (IIW) Document 212-1107-07
72. Quinn TP, Szanto M, Gilad I, Shai I (2205) Coupled Arc and Droplet Model of GMAW. Sci Technol Weld Join 10(1): 113–119
73. Steen WM, Eboo M (1979) Arc Augmented Laser-Welding. Metal Construction 11(7): 332–335
74. Steen WM, Eboo M, Clarke J (1978) Arc Augmented Laser Welding. Proc 4th Int Conf Advances in Welding Processes, Harrogate, UK, 9-11 May. Paper 17: 257–265
75. Deron C, Rivière P, Perrin M-Y, Soufiani A (2006) Coupled Radiation, Conduction, and Joule Heating in Argon Thermal Plasmas. J Thermophys & Heat Trans 20(2): 211–219
76. Hughes TP (1975) Plasmas and Laser Light, Adam Hilger
77. Paulini J, Simon G (1993) A Theoretical Lower Limit for Laser Power in Laser-enhanced Arc Welding. J Phys D: Appl Phys 26: 1523–1527
78. Seyffarth P, Krivtsun IV (2002) Laser-Arc Processes and their Applications in Welding and Material Treatment. Welding and Allied Processes Volume 1. Taylor & Francis
79. Wang T-S, Rhodes R (2003) Thermophysics Characterization of Multiply Ionized Air Plasma Absorption of Laser Radiation. J Thermophys & Heat Trans 17(2): 217–224
80. Stallcop JR, Billman KW (1974) Analytical Formulae for the Inverse Bremsstrahlung Absorption Coefficient. Plasma Physics 16: 1187–1189
81. Devoto RS (1973) Transport Coefficients of Ionised Argon. Phys Fluids 16(5): 616–623
82. Mathuthu M, Raseleka RM, Forbes A, West N (2006) Radial Variation of Refractive Index, Plasma Frequency and Phase Velocity in Laser Induced Air Plasma. IEEE Trans Plasma Sci 34(6): 2554–2560
83. Howlader MK, Yang Y, Roth JR (2005) Time-Resolved Measurements of Electron Number Density and Collision Frequency for a Fluorescent Lamp Plasma Using Microwave Diagnostics. IEEE Trans Plasma Sci 33(3): 1093–1099
84. Lacroix D, Jeandel G, Boudot C (1998) Solution of the Radiative Transfer Equation in an Absorbing and Scattering Nd:YAG Laser-induced Plume. J Appl Phys 84(5): 2443–2449
85. Kokhanovsky AA (1999) Optics of Light Scattering Media. John Wiley & Sons and Praxis Publishing
86. Greses J (2003) Plasma/Plume Effects in CO_2 and Nd:YAG Laser Welding. PhD thesis, Cambridge University, UK
87. Greses J, Hilton PA, Barlow CY, Steen WM (2002) Plume Attenuation under High Power Nd:YAG Laser Welding. J Laser Appl 16(1): 9–15
88. Zimmer AT, Biswas P (2001) Characterization of the Aerosols Resulting from Arc Welding Processes. J Aerosol Science 32: 993–1008

89. Hewett P (1995) The Particle Size Distribution, Density, and Specific Surface Area of Welding Fumes from SMAW and GMAW Mild and Stainless Steel Consumables. American Industrial Hygiene Association, Journal, 56: 128–135
90. Thomas ME (2006) Optical Propagation in Linear Media. Oxford University Press
91. Hansen F, Duley WW (1994) Attenuation of Laser Radiation by Particles During Laser Materials Processing. J Laser Appl 6(3): 137–143
92. Tu J, Miyamoto I, Inoue T (2002) Characterizing Keyhole Plasma Light Emission and Plasma Plume Scattering for Monitoring 20 kW class CO_2 Laser Welding Processes. J Laser Appl 14(3): 146–153
93. Bagger C, Olsen F (2005) Review of Laser Hybrid Welding. J Laser Appl 17(1): 2–14
94. Chen Y, Li L, Fang J, Feng X, Wu L (2003) Temperature Field Simulation of Laser-TIG Hybrid Welding. China Welding 12(1): 62–66
95. Chen Y, Li, L, Fang J, Feng X (2003) Numerical Analysis of Energy Effect in Laser-TIG Hybrid Welding. J Mater Sci Technol 19 Suppl 1: 23–26
96. Hu B (2002) Nd:YAG Laser-assisted Arc Welding. PhD thesis Delft University of Technology, The Netherlands
97. Reutzel EW, Kelly SM, Martukanitz RP, Bugarewicz MM and Michaleris P (2005) Laser-GMA [MIG/MAG] Hybrid Welding: Process Monitoring and Thermal Modelling. In: David SA, DebRoy T, Lippold JC, Smartt HB, Vitek JM (eds) Proc 7th Int Conf Trends in Welding Research, Pine Mountain, GA, USA, 16-20 May 2005. Publ: Materials Park, OH 44073-0002, USA; ASM International; 2006, pp 143–148
98. Goldak J, Chakravarti A, Bibby M (1984) A New Finite Element Model for Welding Heat Sources. Met Trans B 15B: 299–305
99. Zaikin AE, Katulin VA, Levin AV, Petrov AL (1991) Hydrodynamic Processes in a Melt Bath under Laser-arc Interaction Conditions. Sov J Quantum Electron. 21(6): 635–639
100. Gratzke U, Kapadia PD, Dowden J (1991) Heat-Conduction in High-Speed Laser-Welding. J Phys D: Appl Phys 24(12): 2125–2134
101. Cline HE, Anthony TR (1977) Heat Treating and Melting Material with a Scanning Laser or Electron-Beam. J Appl Phys 8(9): 3895–3900
102. Hu B, den Ouden G (2005) Synergic Effects of Hybrid Laser/Arc Welding. Sci Technol Weld Join 10(4): 427–431
103. Dowden J, Kapadia PD (1998) The use of a High Power Laser to Provide an Electrical Path of Low Resistance. J Laser Appl 10(5): 219–223
104. Startsev VN, Martynenko DP, Leonov AF (2000) Investigation of Characteristics of an Arc Column in Laser Arc Welding using Numerical Simulation. High Temp 38(1): 24–29

7

Metallurgy of Welding and Hardening

Alexander Kaplan

Luleå University of Technology SE-97 187 Luleå, Sweden.
`alexander.kaplan@ltu.se`

Abstract. For laser welding and for laser hardening the resulting mechanical properties of the product can be expressed by the shape and metallurgy of the processed cross section. Both are determined by heat conduction, in particular by resolidification, by diffusion and by the crystallographic material behaviour, governed by the local thermal cycle of the material. In the following, a brief survey on the physical mechanisms responsible for the metallurgy [1, 2] at the macro- and micro-scale will be given, mainly referring to ferritic low alloy steel as the most relevant material. Many aspects are relevant to both welding and hardening, while some aspects are process-specific. For certain phenomena selected mathematical models are presented that enable quantitative calculation and description of the phenomena.

The notation employed in this chapter is to be found in Table 7.1.

7.1 Thermal Cycle and Cooling Rate

Two basic types of laser operation can be distinguished: While pulsed wave (pw) laser processing corresponds to a highly transient situation, the more commonly applied continuous wave (cw) laser beam causes quasi-steady state conditions, in particular a quasi-steady state temperature field accompanying the absorbed laser beam that acts as the heat source. A high processing speed is typical for laser processing, causing a thermal cycle with a steep rise in front of the laser beam and a less pronounced decay, with a very high cooling rate compared to other thermal techniques.

Highly suitable models for describing the thermal cycle of cw-laser beam processing to first order are the models of a moving point source and a moving line source, for surface and in-depth laser beam absorption, respectively, described in Chapter 3. Moreover, superposition of several heat sources allows high modelling flexibility.

Figure 7.1a shows typical thermal cycles resulting from the moving point source of heat (here: superposition of five heat sources laterally arranged in a row) for three different processing speeds. As can be seen, higher temperatures cause a steeper gradient and higher cooling rates, as plotted in Fig. 7.1b.

Table 7.1. Notation.

Symbol	Units	Meaning	Symbol	Units	Meaning
A	%	absorptance	p	$\mathrm{N\,m^{-2}}$	pressure
c	$\mathrm{m^{-3}}$	concentration	p_a	$\mathrm{N\,m^{-2}}$	ambient pressure
c_c	$\mathrm{m^{-3}}$	critical concentration	p_s	$\mathrm{N\,m^{-2}}$	surface pressure
c_e	$\mathrm{m^{-3}}$	sample composition	p_{sat}	$\mathrm{N\,m^{-2}}$	saturation pressure
c_p	$\mathrm{J\,kg^{-1}\,K^{-1}}$	specific heat capacity	p_g	$\mathrm{N\,m^{-2}}$	gas pressure
c_p^*	$\mathrm{J\,kg^{-1}\,K^{-1}}$	artificially enhanced specific heat	$\mathbf{q}_c$	$\mathrm{m^{-2}\,s^{-1}}$	concentration flux
D	$\mathrm{m^2\,s^{-1}}$	diffusion constant	q	W	beam power
D_0	$\mathrm{m^2\,s^{-1}}$	pre-exponential for diffusion of carbon	Q	$\mathrm{J\,mol^{-1}}$	Activation energy
f_f	%	fraction ferrite	R	m	radius, curvature
f_i	%	fraction pearlite	r_B	m	beam radius
f_m	%	fraction martensite	R_g	$\mathrm{J\,mol^{-1}\,K^{-1}}$	Gas constant
g	m	grain size	t	s	time
h	$\mathrm{J\,kg^{-1}}$	enthalpy	T	K	temperature
h_l	$\mathrm{J\,kg^{-1}}$	liquidus enthalpy	T_s	K	surface temperature
h_s	$\mathrm{J\,kg^{-1}}$	solidus enthalpy	T_m	K	melting temperature
H	HV	hardness	$u_{s,n}$	$\mathrm{m\,s^{-1}}$	normal speed at the surface
H_m	HV	hardness martensite	v	$\mathrm{m\,s^{-1}}$	processing speed
H_f	HV	hardness ferrite	α	–	equivalent kinetic heat cycle constant
I	s	kinetic strength of the heat cycle	λ	m	pearlite plate spacing
k	$\mathrm{J\,K^{-1}}$	Boltzmann constant	ρ_l	$\mathrm{kg\,m^{-3}}$	specific mass density
$\dot{M}$	$\mathrm{kg\,s^{-1}}$	mass flow rate	τ	s	time constant of thermal cycle
N_{sg}	–	number of shielding gas atoms	Φ_s	$\mathrm{m^2\,s^{-1}}$	flow potential at the surface
L_m	$\mathrm{J\,kg^{-1}}$	latent heat of melting	σ	$\mathrm{N\,m^{-1}}$	surface tension
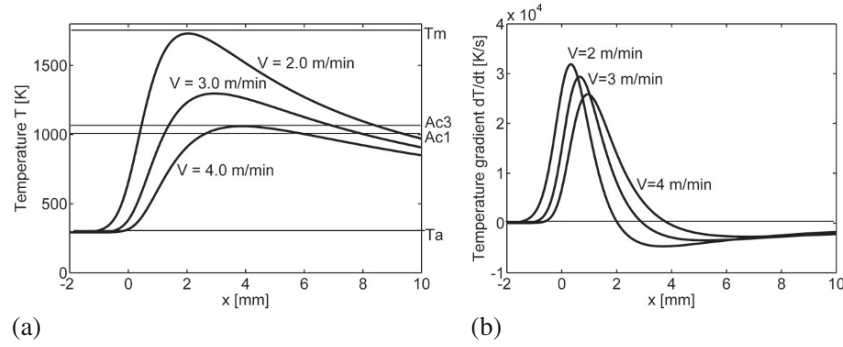
Fig. 7.1. Calculated (a) thermal cycle and (b) cooling rates vs. horizontal coordinate in processing direction for three speeds (the model consists of five superimposed moving point sources laterally arranged in a row).

The resolidification interface and its cooling rate distribution mainly determine the metallurgical structure across the cross section generated by the resolidification process, basically following the adequate time-temperature-transformation (TTT)-diagram for cooling and the phase diagram [1, 2]. Beside resolidification and phase transformations, diffusion governs the resulting metallurgy. Consideration of the local thermodynamics is essential. For laser processing of low C steel high cooling rates typically result in the formation of the brittle martensite phase.

7.2 Resolidification

Depending on the speed of resolidification and on the local thermodynamic state (supercooling) of the metal, two basic types of resolidification can be distinguished, namely planar propagation of the resolidification front (for high cooling rate) and dendritic growth [1].

When the temperature decays below the melting temperature, local supercooling of the material leads to resolidification, which releases the latent heat of melting. This corresponds to a discontinuous change of the temperature gradient across the front (the Stefan condition). Most analytical models cannot take into account latent heat, while numerical methods such as Finite Element Analysis (FEA) often apply an artificially enhanced specific heat capacity in a narrow temperature interval ΔT close to the melting point, thus simulating the consumption or release of latent heat, for melting or cooling, respectively:

$$c_p^* = \frac{L_m}{\Delta T}.$$

Another simplified method for taking the latent heat into account during modelling is to calculate in terms of enthalpy h rather than temperature T

(but otherwise using the same solutions and equivalent boundary conditions) and subsequently to transform the resulting enthalpy field to a temperature field by the relations

$$h \leq h_s : T = \frac{h}{c_p}$$

$$h_s \leq h \leq h_l : T = \frac{L_m}{c_p}$$

$$h_l \leq h : T = \frac{h - L_m}{c_p}.$$

This transformation permits the use of analytical equations and at the same time takes into account the latent heat of phase transformations; it introduces, however, the inaccurate simplification of inducing a temperature plateau around the transformation point instead of a stepwise change in the temperature gradient. Nevertheless, it often allows a more accurate calculation to be achieved with analytical equations, in a simple manner.

Model for the Resolidification Path

The resolidifcation path can be derived [3] by gradual integration of the normal vector of the temperature gradient at the resolidification front $T = T_\mathrm{m}$ of a temperature field $T(x, y, z; t)$. The integration starts at the laterally outermost locations of the melt pool and ends in the centre of the weld (for symmetric conditions). The calculated (solid lines) and experimentally observed (photograph and dotted lines) cooling patterns for laser welding of austenitic stainless steel are shown in Fig. 7.2 for horizontal and vertical cross sections at low and high welding speeds.

A more sophisticated model of resolidification [4] even takes into account the grain orientation (at the outer starting point), leading to slight fluctuations in the resolidification path.

7.3 Metallurgy

7.3.1 Diffusion

The metallurgy of a laser processed material is strongly governed by local diffusion processes that in turn are driven by thermal and chemical gradients.

The diffusion mechanism and the concentration distribution $c(x, y, z; t)$ to be calculated is basically described by Fick's first and second laws:

$$\mathbf{q}_c = -D\nabla c$$

$$\frac{\partial c}{\partial t} = D\nabla^2 c;$$

(a)

(b)

(c)

(d)
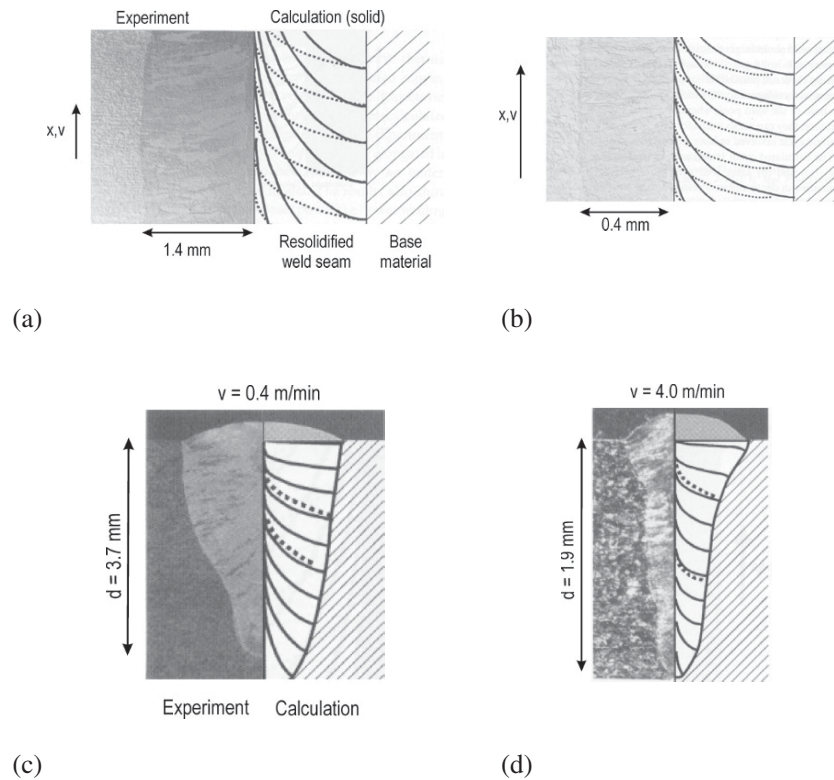
Fig. 7.2. Experimental (left, and dotted line) and calculated (right, solid line) resolidification pattern for two welding speeds: (a) horizontal cross section of the weld seam, $v = 0.4\,\mathrm{m/min}$, (b) horizontal, $v = 4.0\,\mathrm{m/min}$, (c) vertical, $v = 0.4\,\mathrm{m/min}$, (d) vertical, $v = 4.0\,\mathrm{m/min}$ (austenitic stainless steel, laser power: 1400 W) © *1997 Old City Publishing Inc. reproduced with permission from* [3].

see Sect. 1.4. The diffusion constant C is basically a measure for the mobility of a certain chemical element in some different atomic environment, e.g in a crystal lattice or in a liquid of a different element. The diffusion constant D can depend strongly on the temperature.

7.3.2 Fe-Based Alloys

Low Alloy Steel

The most common materials for laser transformation hardening and for laser welding are low alloy steels, and are therefore Fe-based alloys. Their metallurgy [1, 2] follows the FeC-phase diagram. According to the eutectic pearlite phase at 0.8%(wt.) carbon, we can divide them into hypoeutectic and hypereutectic steels, below and above this C-concentration, respectively.

A third important type of Fe-based alloy to be distinguished is cast iron in its different configurations (spherical, lamellar, etc.), containing more than 2% (wt.) Fe.

The fundamental metallurgical phases of steel are α-ferrite and γ-austenite. A low C-steel of ferritic nature can be laser transformation hardened by a thermal cycle during which it remains above the A_{c3}-temperature for sufficiently long. This enables the C-atoms to dissolve in the austenitic crystallographic γ-phase. During subsequent rapid quenching the lack of time for diffusion forces the formation of martensite, as the C-atoms remain in the α-lattice in a constrained manner, leading to correspondingly high hardness.

High Strength Steel and its Multi Scale Modelling

Recently, high strength steel became a highly promising engineering material. The different grades of high strength steel (AHSS, UHSS, etc.) can be included under the heading of alloyed steel, as the DP (Duplex Phase) and TRIP steel contain several metallurgical phases that lead to a more complex behaviour in metallurgy and fracture mechanics. Multi-scale modelling, i.e. modelling both at the atomic scale and at the macro-scale and, if needed, at some scales in between, is a highly sophisticated approach to the holistic study of the metallurgy in the context of its macro-continuum mechanical behaviour. It is, for example, suitable for high strength steel [5], where metallurgical phases with different mechanical properties are adjacent to each other and interact during load.

Finite Element simulation of stress formation and the strain response of a weld under load is a common method for the study of these problems, and is often applied on the macro continuum scale. One difficulty is meshing at locations with small dimensions/curvatures or large deformations. Moreover, valid material properties are needed, often being obtained from empirically derived material models. For single phase metals the stress-strain curve is often developed from an empirical model based on the chemical composition, while modelling of the physics is based on the density of dislocations and mobility of the grain boundaries.

For multi phase materials like high strength steels (DP, TRIP), however, and for the different zones of a weld (weld metal, HAZ, base metal) the identification is difficult as the micro-polycrystalline structure is heterogeneous, which requires modelling of the material properties at one or more micro-scale levels.

Both plastic deformation and fracture have their origin at the atomic scale. While deformation is caused by the propagation of dislocations (sliding at the atomic level), governed by the Rice criterion [5], atomic aggregates are split into two parts during fracture of a crystal, as can be calculated by using a universal relation for the binding energy leading to a newly created surface energy. The imperfections of real crystals, such as impurity or interstitial atoms, vacant lattice sites and dislocations, have to be taken into account.

A method which has often been used recently to model formability at the micro-scale is the Representative Volume Element (RVE) method for solving the crystal plasticity constitutive equations. Many RVE models have been developed, but they suffer from a lack of an accurate description in 3D space of the grain location, size or orientation, as they need to consider the strong interaction with adjacent grains.

High strength steel is basically designed to avoid propagation of dislocations by introducing propagation obstacles such as multi-phases or dispersed primary (μm-scale) or secondary (10 nm-scale) particles. For very high strength steel the steel maker Arcelor modelled the kinetics of cementite dissolution and austenite growth during heating (e.g. intercritical annealing of TRIP steel) by solving the mass balance and diffusion equations (e.g. for C or Mn) with respect to (interlamellar) space and time at the grain scale, driven by the gradients of the chemical potential.

For ultra high strength steel Hao et al. [5] introduced a calculation from first principles for the computation of the binding energy relations for the iron matrix (normal adhesion and sliding) and for the interfacial decohesion between the alloy matrix and the dispersed particles (TiC, TiN). Possible different orientations between the crystals can then be studied in terms of lowest energy. Gliding simulation has been rigorously studied by applying the principle-based simulation method for the stacking fault mechanism in face centred cubic (fcc) crystals, whereas few results are reported for iron body centred cubic (Fe-bcc) crystals. For calculating the sliding action, including the dispersed particle disturbances, Hao [5] calculates the interatomic energy and repelling forces as a function of the interatomic distances by introducing the Needleman potential (quantum mechanically, inserted into Schrödinger's equation) for describing the TiC-interface.

Calculation of these lattice-particle interactions at the atomic level is complicated, but essential for understanding and control of separation or dislocation propagation, as it is the key for setting goals for the development of advanced high strength steel types. For example, for Advanced High Strength Steel (AHSS) J. F. Gould [6] thermodynamically determined the critical cooling rate of martensite.

Stainless Steel

High alloy steel has a great many variations. Stainless steel (Fe-based with CrNi- or Cr-alloy), particularly its most common form containing 18% Cr and 10% Ni, is governed by its austenitic γ-phase. For laser welding of stainless steel, e.g. for the AISI 304-grade the hot cracking susceptibility caused by primary metastable austenite was modelled [7] by applying a recently modified version of the KGT (Kurz-Giovanola-Trivedi) model. This model is suitable for rapid solidification processes like laser welding, taking into account the transition of the primary phase on solidification. For given Gibbs-Thompson coefficient and entropy of fusion, the dendrite growth rate, dendrite tip radius
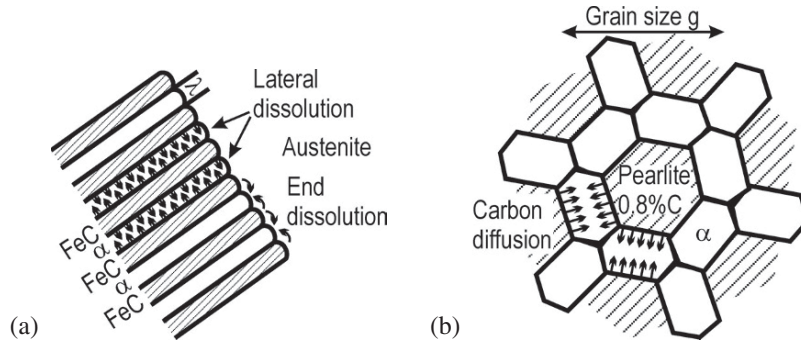
Fig. 7.3. Diffusion between metallurgical phases: (a) the transformation of pearlite to austenite, (b) the homogenisation of a hypoeutectoid steel. *Reprinted from* [8], © (1984) *with permission from Elsevier.*

and undercooling temperature can be calculated, enabling the division in turn of the laser weld cross section into areas of primary α-ferrite (FA) and primary γ-austenite (AF) solidification modes, and determining the distribution of e.g. N.

7.3.3 Model of the Metallurgy During Transformation Hardening of Low Alloy Steel

For laser transformation hardening of ferritic steel a very powerful heat conduction model along with local diffusion equations at the grain size level was developed, both for hypoeutectoid [8] and hypereutectoid steel [9]. Figure 7.3a shows the lamellar diffusion mechanism for the transformation of pearlite to austenite, where the diffusion distances λ are short and the transformation is rapid. Figure 7.3b shows the homogenisation of the grain structure of a hypoeutectoid steel where the diffusion distances scale as the austenite grain size g, so that the transformation is slow.

The kinetic strength of the thermal cycle is defined by

$$I = \int_0^{\infty} \exp\left(-\frac{Q}{R_g T(t)}\right) dt,$$

which can be approximated by

$$I = \alpha \tau \exp\left(-\frac{Q}{R_g T_P}\right),$$

where Q is the activation energy for the transformation and T_p is the peak temperature of the cycle. For a pearlite spacing λ within a colony of the type shown in Fig. 7.3a, the peak superheating temperature T_p required to cause the transformation from pearlite to austenite can then be calculated

by using the relation:

$$\lambda^2 = 2D_0 \alpha \tau \exp\left(-\frac{Q}{R_g T_P}\right).$$

For calculating the homogenisation of austenite, Fig. 7.3b, for a hypoeutectoid plain carbon steel, subsequent to the rapid transformation of pearlite to austenite described above, part or all of the ferrite may transform to austenite. Subsequently the carbon diffuses into regions with low carbon concentration and during the cooling cycle all regions with a carbon content greater than a critical value c_c (here: 0.05% by weight) transform to martensite while the rest reverts to ferrite. The time dependent solution of the diffusion equation yields an approximate parabolic solution for the boundary of the C-diffusion region as a function of time:

$$x = \frac{2}{\sqrt{\pi}} \ln\left(\frac{c_e}{c_c}\right) \sqrt{Dt}.$$

The volume fraction of martensite is therefore given by

$$f = f_m - (f_m - f_i)\exp\left[-\frac{12 f_i^{2/3}}{\sqrt{\pi} g} \ln\left(\frac{c_e}{c_c}\right)\sqrt{Dt}\right]$$

for isothermal treatment (in an environment of constant temperature), while in a thermal cycle the quantity Dt is replaced by $D_0 I$.

Both martensite and ferrite contribute to the total hardness which is given by

$$H = f H_m + (1 - f) H_f$$

where $H_f = 150\,\text{MPa}$ and H_m can be expressed as a polynomial of the mean carbon content from empirical data.

The thermal cycle (see also Chapter 3) can be described, for example, by the moving point heat source model, by the moving Gaussian source model, or by a line source of finite length at the surface moving normal to its orientation, which is a valid approximation for high speed. The last model was applied to the diffusion equations given above to calculate the amount of martensite and the corresponding hardness over depth; the result is shown on a logarithmic scale in Fig. 7.4 for three different laser beam radii, as a function of the laser beam energy density, and is calculated for a hypoeutectoid steel with a carbon content of 0.6% by weight.

As can be seen, the hardness decays with depth and above a certain energy threshold melting takes place. The diffusion model can also be applied for calculating the fraction of martensite in the heat affected zone (HAZ) during laser welding and other laser processes. The model explains for example why steels with a carbon content below 0.1% (by weight) do not respond to transformation hardening. A similar diffusion-based model was also derived for hypereutectoid steel [9].
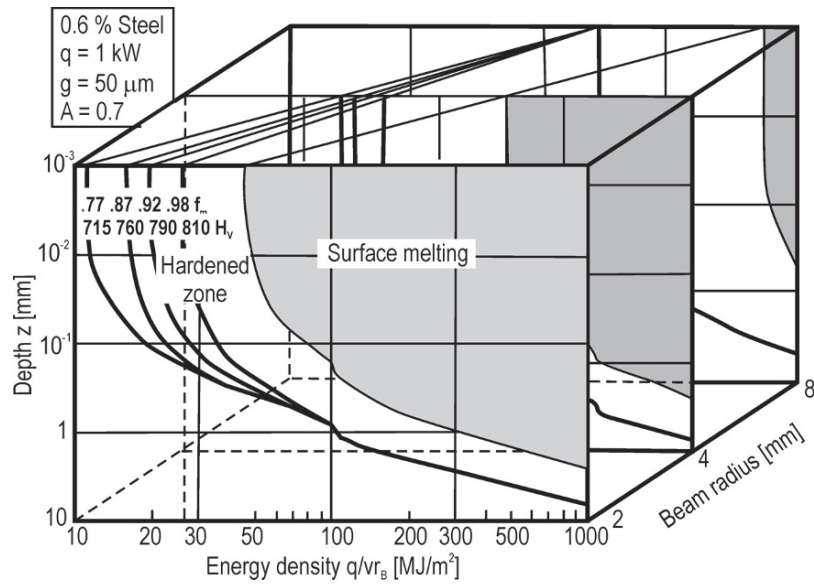
Fig. 7.4. Fraction of martensite f_m and corresponding hardness H_v calculated as a function of depth for three different laser beam radii and as a function of the energy density during laser transformation hardening of a hypoeutectoid steel with 0.6% (wt) C. *Reprinted from* [8], © (1984) *with permission from Elsevier.*

7.3.4 Non-Fe-Based Alloys

The most common non-ferritic metals on which laser welding is used are aluminium and titanium alloys, both offering low mass density and are therefore particularly suitable for light weight construction. For the same reason Mg-alloys are also becoming increasingly popular. Cu and its alloys, particularly brass and bronze, are frequently applied in the electronics industry, often in combination with other metals where they may be coated by thin Ni-, Au- or Ag-films, for example.

Aluminium alloys can be divided into non-hardenable and hardenable (Si-based) alloys, moreover they are classified according to their alloying elements. Most common are the AA5XXX and AA6XXX alloys with Mg and MgSi as the main alloying elements, the latter being hardenable. Several hardening mechanisms can take place in aluminium, one of which is precipitation hardening for example.

Welded joints of aluminium with steel are desirable, but they are difficult to make as the process forms intermetallic FeAl-needles that are brittle in nature, so that the joints tend to crack rather easily. High speeds are therefore aimed at during laser welding, as they keep the intermetallic phase layer thin (a few microns).
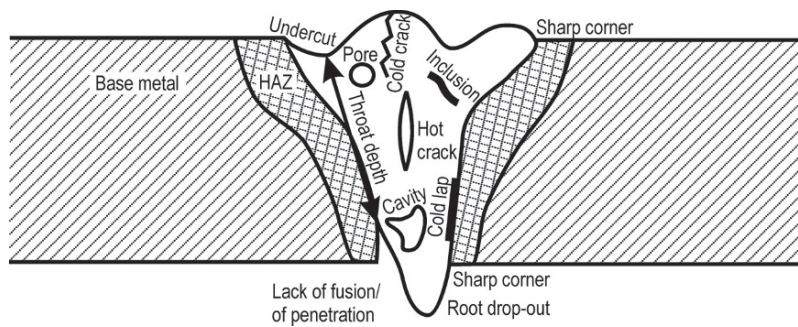
Fig. 7.5. Cross section of a laser weld with different kinds of defects that could appear.

The most common Ti-alloys are pure titanium and TiAl4V. A certain feature of Ti is its susceptibility to reaction with nitrogen, thus forming a hard nitride layer on the surface.

7.4 Defects

The quality of a weld is mainly determined by its mechanical properties that describe mechanical behaviour under load conditions, standardised in terms of the corresponding fracture mechanics. Fracture behaviour and its limits depend on the shape of the weld cross section, on the throat depth, on the metallurgy of the welded zone and on welding defects.

Various kinds of welding defects can be distinguished, as illustrated in Fig. 7.5.

- Large geometrical defects: undercuts, lack of fusion, cold laps, etc.
- Cracks: hot cracks, cold cracks.
- Inclusions: e.g. slag.
- Pores: H-pores, other spherical gas pores, irregular cavities.

Large Geometrical Defects

The shape of the weld essentially determines its behaviour during load of the welded product when in use. The (minimum) throat depth (mainly: penetration) is the main strength criterion, but in addition the surface shape at the top and root of the weld and any large geometrical defects can be crucial for stress formation and crack initiation during load, and thus for possible failure. In particular, small radii and sharp corners (root drop-out or undercuts, for example) acting as stress raisers have to be avoided [10]–[12]. Often it can depend on the particular load situation as to whether a certain geometry should be classified as a defect or not. Moreover, residual stress and

distortion can be counted as welding defects. Welding standards are guidelines which attempt to generalise a certain failure criterion when dimensioning a product, however; due to the complexity of fracture mechanics the accuracy of standards is often limited.

Figure 7.6 illustrates critical geometries of the shape of the weld for butt and fillet joint types [13] and indicates the basic physical mechanisms responsible for the geometrical details. In Fig. 7.6a an overmatched butt joint is shown, with reinforcement shapes at the top and root of the weld, as is typical for laser hybrid welding. The energy of the laser beam and of the arc and the mass from the filler wire govern the shape. The geometry is asymmetric but similar for fillet joints, Fig. 7.6b. Top surface shapes as in Fig. 7.6c are often created, however, with undercuts at the sides and a central peak or even with a significant regularly occurring humping drop. One theoretical explanation is illustrated in Fig. 7.6d where the typical gradually narrowing geometry of the resolidification front does not support simultaneous resolidification across its width. Instead, the melt continues to flow to the central stagnation point where it is forced to slow down; it then accumulates there before resolidification, leading to an excess of material in the form of a peak in the centre, but with a lack of material (undercut) at the sides.

The shape of the weld is a macroscopic criterion for judging the quality of a weld, rather than being counted as a microscopic defect. Nonetheless, even a knowledge of microscopic shape details can become essential. Note that a weld surface has a fractal nature (as do most surfaces and shapes in nature, e.g. coastlines). The surface roughness is composed of substructures, qualitatively repeating at smaller scales, which can again be regarded as a rough surface profile. It is not evident which substructure determines the mechanical behaviour, as each of them can in principle be regarded as a sharp curvature and in turn as a stress raiser. Knowledge of which is essential for fracture mechanics.

Cracks

Hot cracks, often looking like vertical elongated voids in the centre of the weld (but actually being a long channel along the length of the weld), are formed during resolidification. The resolidification process starts from the outer lateral boundary of the weld and gradually grows towards the centre. During resolidification shrinking of the melt takes place, a geometrical micro-movement that can be supported by tensile stress. When arriving at the centre, both resolidifying paths cannot meet, as they lack material due to shrinking, thus causing a void, the hot crack, as studied for stainless steel [7], for example. Typical measures taken to prevent hot cracks occurring are for example the proper employment of compressive stress or the addition of filler wire with a slightly different melting point.

Cold cracks originate from residual stress induced during the thermal cycle in the resolidified material. Cracking can happen even long after the material
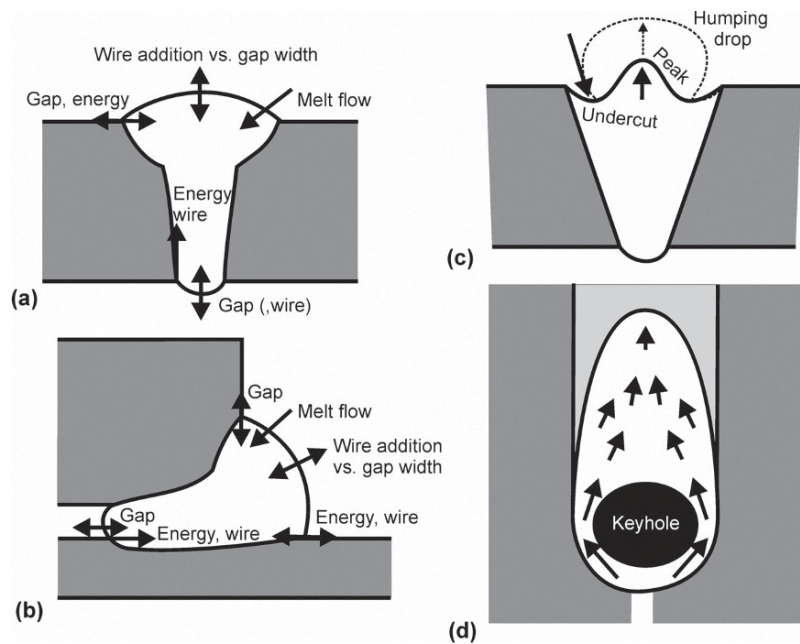
Fig. 7.6. Theory of the governing mechanisms for the shape of a laser (hybrid) weld: (a) butt joint, (b) fillet joint, (c) butt joint with undercuts and central elevation, (d) melt flow and stagnation, forcing a central peak accompanied by undercuts at the sides.

has cooled down. Cracking corresponds to a propagation of dislocations at the atomic level. Fine grain sizes have a stronger resistance to crack propagation, as the grain boundaries redistribute and possibly block the propagating stress and dislocation.

Thus if a technique is used which ensures the presence of fine grains, high strength will result.

Inclusions and Pores

Inclusions can occur as the result of slag (oxide) formation at the surface for example, merging into the resolidifying melt. During mechanical load causing stress formation and deformation, the boundary of inclusions can have a similar effect of lowering the mechanical strength and initiating cracking in the same way that pores do [14].

One type of cavity that is often counted as a pore is a cavity created by the trapping of a dynamic process, in particular a collapse of part of the keyhole (its bottom section, for example) during sudden resolidification. Moreover, lack of fusion and cold laps often appear as a non-spherical cavity that can have a rather irregular or elongated shape (or even be hardly visible,

but lack fusion, i.e. atomic bonding). The irregular shape indicates that the resolidification speed was greater than surface tension driven contraction mechanisms.

Further different types of pores can be distinguished. Pores of spherical shape are formed by gas inclusion during the molten phase, where sufficient time leads to a spherical equilibrium shape before being trapped during resolidification. One typical mechanism is the formation of small hydrogen pores in aluminium, as the solubility of hydrogen is high in the liquid phase but drops significantly during resolidification. Nowadays the amount of hydrogen in the aluminium and shielding gas can be reduced to avoid the effect. Another mechanism for the formation of spherical pores is the inclusion of shielding gas, which has been detected experimentally [15] and is described below in more detail.

Modelling of Pore Formation by Inert Gas Inclusions

A mathematical model for one particular mechanism for pore formation is presented in the following, namely pore formation by trapping of shielding gas during a keyhole collapse, particularly during the termination of laser keyhole spot welding. Any metal vapour inside a bubble, surrounded by its liquid phase will rapidly recondense during cooling, thus it cannot act as a force sustaining a bubble. In contrast, trapping of shielding gas, usually of an inert gas such as Ar and/or He, produces a cavity that develops into a spherical bubble that becomes trapped during resolidification. For pulsed laser keyhole spot welding the formation of a spherical bubble caused by the collapse of the keyhole can be modelled; the initial stage during or just after switching off the laser beam is shown in Fig. 7.7a and the final stage with the formation of the pore in Fig. 7.7b. While the left half of each of the images in Fig. 7.7 illustrate the real conditions of the melt constrained by its surrounding solid, an initial study was carried out in a large liquid pool, shown in the right half of the image in Fig. 7.7, as this eliminates a series of uncertainties, particularly if done in liquid Zn [16]. The study enabled highly accurate modelling of the situation under such simplified and controllable conditions and therefore provided qualitative and quantitative understanding of many governing mechanisms.

Figure 7.8a shows high speed X-ray transmission imaging of the keyhole, carried out at Osaka University, Japan [17, 18], viewed from the side for pulsed laser keyhole spot welding of steel and for its termination, leading to a spherical pore. Figure 7.8b show the same mechanism, but under the simpler condition of drilling the keyhole in a liquid Zn-pool [16]–[19], leading to a stable spherical bubble.

Switching off the laser beam means termination of the evaporation whose recoil pressure counteracted the surface tension forces and thus kept the keyhole open. The model [16] calculates surface tension driven keyhole collapse, Fig. 7.8c, via the Young-Laplace equation (surface tension forces due to the

Fig. 7.7. Modelling of (a) keyhole collapse after pulse termination, (b) which frequently ends in a pore (right half: simplified conditions in a liquid; left half: real liquid conditions surrounded by a constraining solid) © (2002) Institute of Physics Publishing *reproduced with permission from* [16].

curvature R, composed of the two tangential components R_φ, R_θ) that describes the excess of the liquid surface pressure p_s against the gas pressure p_g:

$$p_s - p_g = p_a + \sigma \left(\frac{1}{R_\varphi} + \frac{1}{R_\theta} \right) - p_{sat}(T_s).$$

The time-dependent Bernoulli equation for the flow potential field Φ along a streamline, particularly at the keyhole/bubble surface is

$$\frac{\partial \Phi_s}{\partial t} = \frac{p_s - p_g}{\rho_l} - \frac{u_{s,n}^2}{2};$$

it permits the calculation of the velocity field $u_{s,n}$ of the keyhole/bubble surface

$$u_{s,n}(z;t) = \frac{\dot{M}}{4\pi\rho_l} \left(\frac{1}{R_\varphi^2} + \frac{1}{R_\theta^2} \right).$$

From the above equations the contraction of a keyhole, the formation of its neck, the inclusion of cavities and their contraction to spherical bubbles can be calculated.

Beside the contraction of the keyhole to a bubble, the model also enables the calculation of the gas composition (in this case, the zinc metal vapour
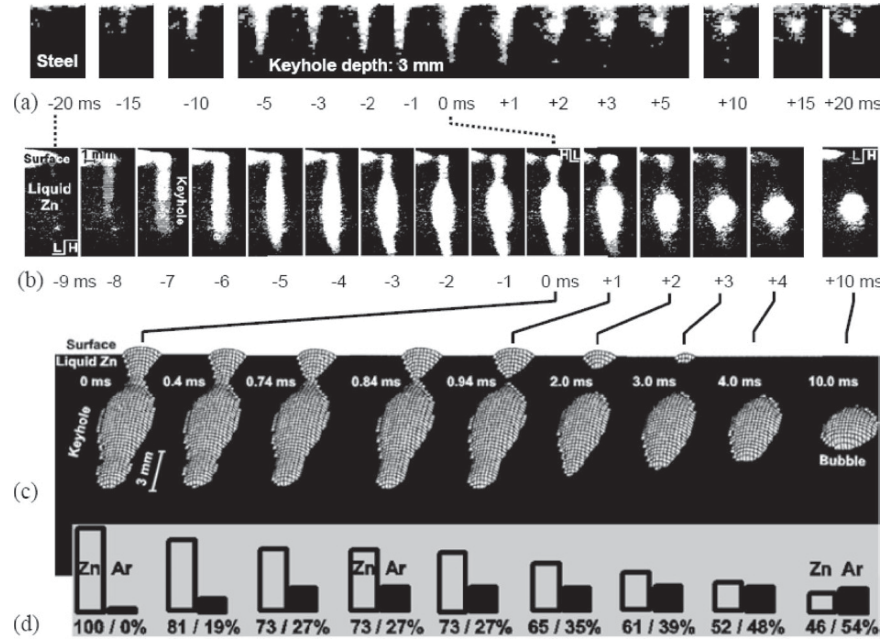
Fig. 7.8. Time-dependent X-ray images of the keyhole shape: initiation (drilling, $t < 0$) and termination (collapse, $t > 0$) (a) in steel (20 ms pulse), (b) in liquid Zn (simplified conditions, 10 ms pulse), (c) corresponding calculated keyhole collapse, with resulting spherical bubble, (d) calculated gas composition in the keyhole/bubble during the collapse. *From* [17], (2002) *with the kind authorisation of the International Institute of Welding (IIW).*

and the argon shielding gas) as a function of time, see Fig. 7.8c, governed by recondensation due to the cooling cycle and in turn governing the size of the spherical bubble.

After switching off the laser beam, the evaporation mechanism stops. Instead, due to cooling of the material the surface temperature $T_s(t)$ at the keyhole wall decays, causing recondensation of the metal vapour. The vapour pressure inside the keyhole drops following the saturation pressure relation $p_{sat}(T_{sat})$. This pressure drop drives ambient gas out of the keyhole, i.e. any shielding gas (being at atmospheric pressure) which has entered the keyhole.

For bottleneck keyhole shapes such as those illustrated in Fig. 7.8b,c for example, once the neck closes due to surface tension driven contraction, the shielding gas (of amount N_{sg}) is trapped. Further contraction leads to a spherical bubble and a pore (of final radius R when reaching the resolidification temperature T_m) filled solely with shielding gas N_{sg} (as the metal vapour recondenses), in pressurev balance with the surface tension σ so that

$$p_a + \frac{2\sigma}{R} = p_{\text{sat}}(T_m) + \frac{3N_{\text{sg}}}{4R^3\pi}kT_m.$$
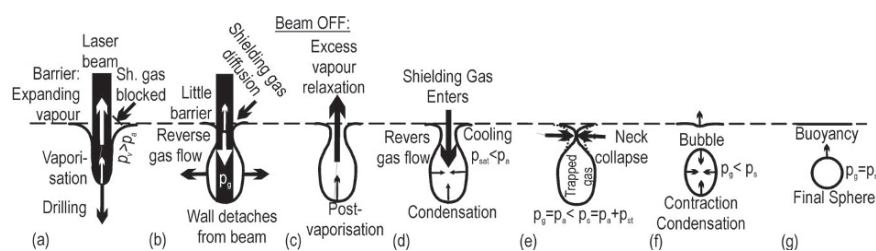
Fig. 7.9. Theoretical description of keyhole collapse and the resulting pore formation during pulsed laser keyhole spot welding. © (2002) Institute of Physics Publishing *reproduced with permission from* [16].

A corresponding theory of the different mechanisms involved for developing a spherical bubble and pore is illustrated in Fig. 7.9. The characteristic time constants for the different phenomena can be identified [16]. The theory also explains the entrainment of the shielding gas as rapid vapour recondensation, after switch-off of the laser pulse lowers the gas pressure inside the keyhole, driving the surrounding shielding gas into the keyhole.

References

1. Bengtsson B, Li W-B, Easterling K E (1983) Phase transformation in solids, Tsakalakos Th (ed), New York
2. Shewman PG (1963) Diffusion in solids. McGraw-Hill, New York
3. Lampa C, Kaplan AFH, Powell J, Magnusson C (1997) Fluid flow and resolidification in deep penetration laser welding. Lasers in Engineering 7: 241–252
4. Ploshikhin VV, Bergmann HW (1999) Influence of the process parameters on the grain structure in welds with a constant fusion zone width. Lasers in Engineering 8: 285–294
5. Hao S, Liu WK, Moran B, Vernerey F, Olson GB (2004) Multi-scale constitutive model and computational framework for the design of ultra-high strength high toughness steels. Comput Meth Appl Mech Eng 193: 1865–1908
6. Gould JF, Khurana SP, Li T (2006) Predictions of microstructures when welding automotive advanced high strength steel. Weld J 85: 111s–116s
7. Nishimoto K, Mori H (2004) Hot cracking susceptibility in laser weld metal of high nitrogen stainless steel. Sci Techn Adv Mat 5: 231–240
8. Ashby MF, Easterling KE (1984) The transformation hardening of steel surfaces by laser beams – I. hypo-eutectoid steels. Acta metall 32(11): 1935–1948
9. Li W-B, Easterling KE, Ashby MF (1986) Laser transformation hardening of steel – II. hypereutectoid steels. Acta metall 34(8): 1533–1543
10. Wouters M, Powell J, Kaplan AFH (2006) The influence of the joint gap on the strength of hybrid Nd:YAG laser-MIG welds, Journal of Laser Applications 18(3): 181–184
11. Young WC (2002) Roark's formulas for stress and strain. 7th edition, McGraw-Hill, New York

12. Mackerle J (2002) Finite element analysis and simulation of welding – an addendum: a bibliography (1996–2001). Mod Simul Mat Sci Eng 10: 295–318
13. Kaplan AFH, Nilsson K, Powell J (2007) Shaping of hybrid welds and gap sensitivity. Proceedings LIM – Lasers in Manufacturing, Munich (D), Vollertsen F (ed), 73–77
14. Prahl U, Papaefthymiou S, Uthaisansuk V, Bleck W, Sietsma J, van der Zwaag S (2007) Micromechanics-based modelling of properties and failure of multiphase steels. Comp Mat Sci 39: 17–22
15. Katayama S, Matsunawa A, Kojima K (1999) CO_2 laser weldability of aluminium alloys (2nd report): defect formation conditions and causes. Welding Research Abroad 45(6–7): 44–59
16. Kaplan AFH, Mizutani M, Katayama S, Matsunawa A (2002) Unbounded keyhole collapse and bubble formation during pulsed laser interaction with liquid zinc. J Phys D: Appl Phys 35: 1218–1228
17. Kaplan AFH, Mizutani M, Katayama S, Matsunawa A (2002) Analysis of different methods for the prevention of pore formation in keyhole laser spot welding. Welding in the World (Special Issue) 46: 39–50
18. Kaplan AFH, Mizutani M, Katayama S, Matsunawa A (2002) Keyhole laser spot welding. Proc. ICALEO 2002, Scottsdale (AR), Laser Institute of America, Orlando (FL)
19. Kaplan AFH, Mizutani M, Katayama S, Matsunawa A (2002) On the mechanism of pore formation during keyhole laser spot welding. Proc LAMP 2002, Osaka (JAP), Osaka University, Osaka (JAP)

8

Laser Cladding

Dietrich Lepski and Frank Brückner

Fraunhofer Institute for Material and Beam Technology, Winterbergstraße 28,
Dresden. `dietrich.lepski@iws.fraunhofer.de`,
`frank.brueckner@iws.fraunhofer.de`

Abstract. Laser cladding is a modern technology whose uses include, for example, the creation of protective coatings to reduce wear and corrosion on engine parts and tools. The aircraft and automotive industries are examples of industries in which it is much used. This account considers the theory of a number of aspects of the process in detail. The first to be studied is the interaction of the laser beam directly with the powder that is being deposited; the effects of gravity, beam shadowing, and particle heating are investigated. This is followed by a discussion of the mechanisms by which the particles adhere to the surface of the work piece and are absorbed into it. In order to understand the process, a study of the melt pool and the associated temperature distribution is necessary; it is then possible to infer the final bead geometry. An inevitable consequence of a thermal process such as laser cladding is the induced thermal stress and resulting distortion of the work piece. The fundamentals are discussed, a numerical model presented and in addition a simple heuristic model is given. The use of induction-assisted laser cladding as a means of preventing the formation of cracks is discussed.

8.1 Introduction

Laser cladding is a modern technology for the deposition of wear and corrosion protective coatings on engine parts and tools, applied especially in the aircraft and automotive industries. It is used even for the repair of wear damaged parts of turbines and forming tools as well as in rapid prototyping and rapid tooling. It allows many different substrate and coating materials to be combined, ranging from cobalt or nickel based hard alloys on steels to ceramic coatings on aluminium. In this context, however, results of numerical calculations and experiments will be presented solely for cobalt alloy coatings (Stellites) on steel substrates (AISI1045 or AISI304). A list of abbreviations is provided in Table 8.1 and of the notation employed in this chapter in Table 8.2.

In laser cladding the powdery coating material is blown through a nozzle into a melt pool on the work piece surface generated by the laser beam (Fig. 8.1). We are therefore speaking of a welding process which is able to

Table 8.1. Abbreviations.

Abbreviation	Meaning
AC	Alternating current
BEM	Boundary Element Method
EDX	Energy Dispersive X-ray spectroscopy
FEM	Finite Element Method
PTA	Plasma-Transferred Arc
TTT diagram	Time-Temperature Transformation diagram
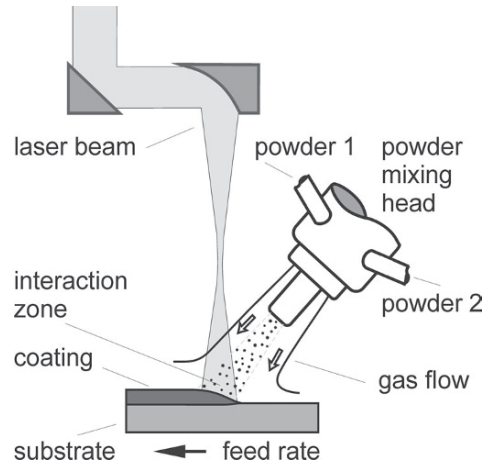
Fig. 8.1. Scheme of laser cladding with off-axis powder supply.

yield a very strong joint between substrate and coating without a substantial dilution of the coating with substrate material. Such a dilution could impair the intended properties of the coating.

In addition to the possibility of excellent process control, it is the sharply concentrated heat input which is responsible for the high precision and the comparatively low heat input connected with the technologies of laser materials processing. The large temperature gradients associated with the process, however, are also the cause of high thermal stresses which may even lead to cracking, delamination, and large bending distortion. Tensile stresses in the coating are unavoidably caused by thermal contraction during cooling after the coating has been deposited in the liquid state, but they can be influenced by controlling the thermal history of the work piece properly.

Thus the desired quality and precision can be reached only if the process parameters are carefully chosen on the basis of a thorough understanding of all the physical phenomena involved. That knowledge can be obtained by modelling. In this chapter (semi-)analytical models are presented which make the physics of the laser cladding technology more transparent, even though purely numerical methods promise more accurate results.

Table 8.2. Notation.

Symbol	Unit	Meaning
A	mm^2	area
A_P	mm^2	particle cross section area
$\overline{A_P}$	mm^2	space angle average of A_P
$\mathcal{A}$	1	absorptivity
$\underline{\underline{\mathbf{C}}}$	Pa	Hook's tensor (fourth rank)
E	Pa	Young's modulus
$F_{0,1}^{x,y}$		residuals of force balance $\rightarrow$ zero
$G_R(\vec{\mathbf{r}})$	K W^{-1}	Rosenthal's solution of the steady state heat flow
$\underline{\mathbf{I}}$	1	second rank unit tensor
J	g s^{-1}	mass flow, powder rate
L_m	J g^{-1}	latent heat of melting
Ma	1	Marangoni number
N_P	1	number of particles
$P(x)$	1	polynomial
P	W	laser beam power
Pr	1	Prandtl number
Q	1	characteristic number in thermocapillary flow
R	mm	characteristic length of the melt pool
R_P	mm	particle radius
R_0	mm	initial particle radius, Weibull parameter
R_N	mm	radius of coaxial nozzle
$R_{x,y}$	mm	radii of curvature of the distorted plate
$d\vec{\mathbf{S}}$, dS	mm^2	surface area element
S_P	mm^2	particle surface area
T	°C	temperature
T	K	absolute temperature
T_0	°C	arbitrary reference temperature
T_a	°C	ambient temperature
T_m	°C	melting point
T_P	°C	particle temperature
T_P^i	°C	initial particle temperature
T_{MS}	°C	martensite transformation start temperature
T_{MF}	°C	martensite transformation finishing temperature
$\mathrm{Tr}(\boldsymbol{\sigma})$	Pa	trace of the stress tensor
V	mm^3	volume
V_P	mm^3	particle volume
$\overline{V_P}$	mm^3	average particle volume
$W_{1,2}(R_P)$	mm^{-1}	Weibull type particle size distributions $W(R_P){=}\mathrm{d}n_P/\mathrm{d}R_P$
a	mm	ellipsoid half axis length (x)
b	mm	ellipsoid half axis length (y)
c	mm	ellipsoid half axis length (z)
c_P	J g^{-1} K^{-1}	specific heat
d	mm	plate thickness
$\vec{\mathbf{e}}_x, \ldots$	1	unit vectors
$f(x,y,z)$	1	ellipsoid shape function

Table 8.2. *Continued*

Symbol	Unit	Meaning
f_A	1	austenite proportion
f_{A0}	1	initial austenite proportion
f_M	1	martensite proportion
$f_{equ}(T)$	1	(meta)stable equilibrium phase proportion
$f_i(\vec{\mathbf{r}})$	1	proportion of ith phase
$f_P(\vec{\mathbf{r}})$	1	local particle volume fraction
$f_P^*(\vec{\mathbf{r}})$	1	particle distribution regarding gravity force effects
$\vec{\mathbf{g}},\ g$	mm s^{-2}	gravity acceleration
h	mm	bead height
h_P	J g^{-1}	specific enthalpy of particles
j_E^0	W mm^{-2}	original power density of the laser beam
$\vec{\mathbf{j}}_E^L,\ j_E^L$	W mm^{-2}	energy flow density of the shadowed laser beam
$\vec{\mathbf{j}}_E^P,\ j_E^P$	W mm^{-2}	energy flow density transported by powder particles
$\vec{\mathbf{j}}_E^R,\ j_E^R$	W mm^{-2}	flux of energy loss by radiation or convection
$\vec{\mathbf{j}}_M,\ j_M$	g s^{-1}mm^{-2}	mass flow density of powder particles
$\vec{\mathbf{j}}_M^*,\ j_M^*$	g s^{-1}mm^{-2}	mass flow density of particles in the gravity field
k	1	capillarity parameter
$k_L(\dot{T})$	1	parameter in Leblond's model
m	1	scattering exponent
$n(T)$	1	Johnson-Mehl-Avrami exponent
$n_P(R_P)$	1	fraction of N_P particles which has radii less than R_P
p	Pa	pressure
p	1	Weibull parameter in (8.10)
$q_3(\vec{\mathbf{r}})$	W mm^{-3}	3D power density distribution
$q_2(\vec{\mathbf{r}})$	W mm^{-2}	2D power density distribution
r	mm	radial distance
$\vec{\mathbf{r}},\ \vec{\mathbf{r}}^*,\ \vec{\mathbf{r}}_0$	mm	point vectors
$\vec{\mathbf{r}}_N$	mm	centre of a coaxial nozzle
$\underline{\mathbf{s}}$	Pa	stress deviator (second rank tensor)
t	s	time
$\vec{\mathbf{u}}(\vec{\mathbf{r}})$	mm	displacement field
$\vec{\mathbf{v}} = v\,\vec{\mathbf{e}}_x$	mm s^{-1}	feed rate
$\vec{\mathbf{v}}_P,\ v_P$	mm s^{-1}	particle speed
v_M	mm s^{-1}	Marangoni flow velocity
v_r	mm s^{-1}	radial flow velocity
v_z	mm s^{-1}	axial flow velocity
w	mm	weld bead width
x	mm	coordinate in feed direction
$x_{sol}(z)$	mm	weld bead solidification line in the x-z plane
$x_{1,2,3}$	mm	x-coordinates of points $P_{1,2,3}$
y	mm	coordinate perpendicular to the feed direction
$y_{1,2}$	mm	lateral weld bead boundaries
z	mm	coordinate
z_0	mm	z-position of substrate surface
z_N	mm	distance of coaxial nozzle from substrate surface
Δ_M	mm	penetration depth of Marangoni flow

Table 8.2. *Continued*

Symbol	Unit	Meaning
Δt	s	particle dissolution time
$\Gamma(x)$	1	Gamma function
$\Theta(x)$	1	Heaviside's step function
$\Omega(\vec{r})$	sr	space angle of a domain seen from point $\vec{r}$
α	W mm^{-2} K^{-1}	heat transfer coefficient
α_i	K^{-1}	coefficient of thermal expansion of the i$^{\text{th}}$ phase
β	K^{-1}	Koistinen-Marburger parameter
χ	mm^2 s^{-1}	kinematic viscosity
δ	mm	skin depth
δ		variational principle (8.18)
$\delta(x)$		Dirac's delta-function
$\underline{\varepsilon}$	1	total strain tensor
$\underline{\varepsilon}^E$	1	elastic strain tensor
$\underline{\varepsilon}^{FF}$	1	fluid flow strain tensor
$\underline{\varepsilon}^I$	1	inelastic strain tensor
$\underline{\varepsilon}^M$	1	metallurgical strain tensor
$\underline{\varepsilon}^P$	1	plastic strain tensor
$\underline{\varepsilon}^{TP}$	1	transformation plasticity strain tensor
$\underline{\varepsilon}^T$	1	thermal strain tensor
$\varepsilon_0^{x,y}$	1	mean strain along x, y
ε_{eq}	1	equivalent strain
ε_{SB}	1	emissivity
$\Delta\varepsilon_{A\to F}^T$	1	change of thermal strain in the austenite$\to$ferrite transformation
$\gamma(T)$	s^{-1}	reciprocal recovery time
$\gamma_P(\vec{r})$	mm	free fall path of particles
η	1	dimensionless coordinate (y)
φ	rad	rotation angle
κ	mm^2 s^{-1}	thermal diffusivity
λ	W mm^{-1}K^{-1}	thermal conductivity
λ_L	Pa	Lagrangian multiplier
λ_P	(Pa s)$^{-1}$	proportionality factor (8.36)
$\overline{\lambda}$	W mm^{-1}K^{-1}	mean thermal conductivity
μ	1	relative magnetic permeability
μ_0	H m^{-1}	vacuum permeability
ν	1	Poisson's ratio
ϑ	rad	scattering angle
$\vartheta_{1,2}$	rad	boundary slope angles
ϑ_K	K	Kirchhoff's transform
ρ	g mm^{-3}	melt pool density
ρ_P	g mm^{-3}	particle density
ρ_{el}	Ω mm	electrical resistivity
σ	g s^{-2}	surface tension
$\Delta\sigma$	g s^{-2}	difference of surface tensions
$\underline{\sigma}$	Pa	stress tensor
σ_{eq}	Pa	equivalent stress

Table 8.2. *Continued*

Symbol	Unit	Meaning
σ_{SB}	W mm^{-2} K^{-4}	Stefan-Boltzmann constant
σ_Y	Pa	yield stress
σ_Y^A	Pa	yield stress of austenite
$\tau(T)$	s	temperature dependent relaxation time
τ_{TF}	Pa	shear stress in thermocapillary flow
ω	s^{-1}	angular frequency
$\omega_P(\vec{r})$	1	gravity force correction of particle density distribution
ξ	1	dimensionless coordinate (x)
ψ	1	shear parameter in the ellipsoid model
ψ_P	1	particle fraction within a prescribed size interval
ζ	1	dimensionless coordinate (z)
$\partial/\partial\vec{r}$	mm^{-1}	Nabla operator
$\vec{\mathbf{u}} \circ \vec{\mathbf{v}}$		dyadic vector product $u_i v_k$ yielding a second rank tensor
$\underline{\mathbf{C}} : \underline{\varepsilon}$		double dot product: $C_{ijkl}\varepsilon_{kl}$
$\underline{\mathbf{a}}, \underline{\tilde{\mathbf{a}}}$		second rank tensor and the related transposed tensor
$\langle x \rangle$		$x\Theta(x)$

The history of laser cladding simulations started as early as in the eighties of the last century with the pioneer work of Steen and co-workers [1–3] who calculated the laser induced temperature field by means of finite difference methods and used empirical relations in order to anticipate the required process parameter values.

During the nineties the interaction between the laser beam and the flying powder particles was studied very intensively [4–8]. These theories have been refined more recently by considering the heat exchange between the particles and the carrier gas, the influence of the nozzle geometry, and the evaporation of strongly heated particles [9–14].

Until 1994 energy and momentum transfer in the melt pool were investigated within the framework of two-dimensional numerical models [15–20]. In 1994 Picasso et al. [21] used three-dimensional analytical solutions of the heat flow equation in order to anticipate process parameters such as feed rate and powder rate.

A series of closed models that take into account the central processes in laser cladding, including powder preheating by the laser beam and the formation of the weld bead, have been published in recent years [22–33], though they cannot all be discussed in detail here.

In 2004/2005 a completely numerical model based on a finite difference approach was published by Han et al. [24–26]. Preheating of the powder particles by the laser beam, heat transfer, fluid flow, and phase transformations were simulated, and the evolution of the free melt pool surface was calculated by means of the level set method. The momentum transfer due to the

impinging particles was found to be responsible for fluctuations of the melt pool shape and of the fluid flow.

The first calculations of thermal stresses in laser cladding were published about ten years ago. At first, one-dimensional generalised plane strain finite element models (FEM) were used [34–37], which were later on extended to three dimensions by de Deus [38,39], Nickel [40,41] and others [42].

The interaction of two beads generated successively was investigated in 2003 and 2005 by Ghosh and Choi [43,44], who even took into account phase transformations and transformation plasticity.

Even now it is difficult to get crack-free coatings from cobalt or nickel based hard alloys on steel substrates if their hardness is greater than about 50 HRC. Recent work [45–49] showed that the reduction of temperature gradients by pre- or post-weld heating in a furnace or using electromagnetic induction can help to avoid cracks. Brückner et al. [23,50–52] studied the influence of various process parameters and material properties on stress and distortion in induction assisted laser cladding. Part of their work will be discussed in the last part of this chapter.

The aim of this chapter is to describe, as simply as possible, the interaction of powder particles and the laser beam, and the interrelation between melt pool shape and temperature field, as well as the evolution of thermal stress and distortion. Some of the models presented require the numerical evaluation of integrals or the numerical solution of ordinary differential equations, which, together with the associated graphical visualisation, can be done very quickly using modern computer algebra packages. Purely numerical calculations on the basis of finite difference or finite element codes, however, which are frequently not very transparent, are referred to here only briefly.

The models presented can be used for the prediction of the results of laser treatment as well as for a virtual trial and error approach to the required process parameter values on the computer. Short calculation times are therefore an essential requirement. Special attention is given to the prevention of cracks by inductive preheating.

8.2 Beam-Particle Interaction

8.2.1 Powder Mass Flow Density

In laser cladding different techniques are used to supply the powdery coating material: the method of off-axis supply (Fig. 8.1) for example can be adjusted very flexibly to suit the work piece geometry. Coaxial nozzles (Fig. 8.2) do not favour selected weld directions and thus are to be preferred if the weld beads are to follow curved or angular trajectories.

For simplicity it will be assumed that the powder particles are emitted by a point source, which is a good model even for off-axis supply. Powder particle distribution and mass flow density, as generated by a coaxial nozzle for
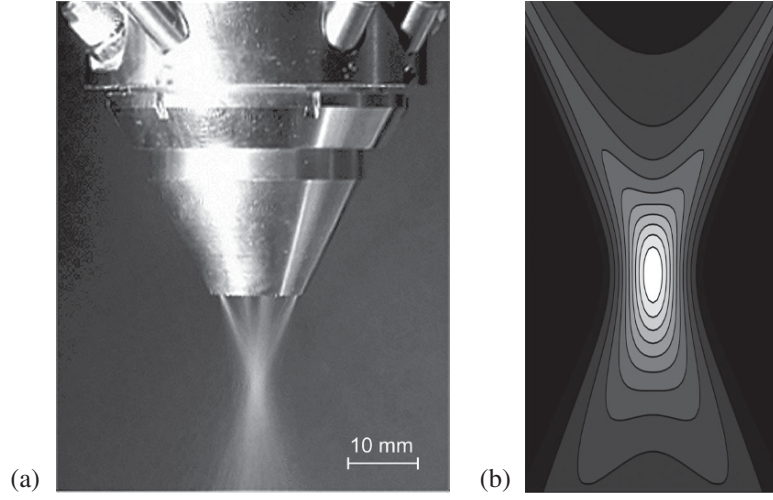
Fig. 8.2. Coaxial four-jet nozzle (left hand side) and side view of the particle volume fraction distribution (right hand side) for a coaxial nozzle with an axisymmetric powder ejection calculated by means of (8.2) and (8.3) for $m = 700$.

example, may be obtained by superposition of the contributions of appropriately distributed point sources.

Powder particles are ejected from the nozzle with an initial velocity v_P which is usually of the order of several meters per second and they scatter about an average direction which connects the nozzle outlet $\vec{r}_N$ with the target point $\vec{r}_0$. The powder mass flow density at the nozzle outlet can be described as a function of the scattering angle ϑ about this direction:

$$\vec{\mathbf{j}}_M\left(\vec{\mathbf{r}},\ \vec{\mathbf{r}}_N\right) = \frac{m+1}{2\,\pi}\ J\ \cos^m\vartheta\ \frac{\vec{\mathbf{r}} - \vec{\mathbf{r}}_N}{\left|\vec{\mathbf{r}} - \vec{\mathbf{r}}_N\right|^3}\ ,\quad \cos\vartheta = \frac{\left(\vec{\mathbf{r}} - \vec{\mathbf{r}}_N\right)}{\left|\vec{\mathbf{r}} - \vec{\mathbf{r}}_N\right|}\ \cdot\ \frac{\left(\vec{\mathbf{r}}_0 - \vec{\mathbf{r}}_N\right)}{\left|\vec{\mathbf{r}}_0 - \vec{\mathbf{r}}_N\right|}.$$
(8.1)

Here J is the total mass flow per unit time and m a scattering exponent to be determined from the area covered by the powder jet at the substrate surface. For a coaxial nozzle outlet with a radius R_N and the midpoint $\overline{\vec{\mathbf{r}}_N}$, lying in the x-y plane, we get accordingly

$$\vec{\mathbf{r}}_N \to \vec{\mathbf{r}}_N\left(\varphi\right) = \overline{\vec{\mathbf{r}}_N} + R_N\left(\vec{\mathbf{e}}_x\cos\varphi + \vec{\mathbf{e}}_y\sin\varphi\right),$$

$$\vec{\mathbf{j}}_M\left(\vec{\mathbf{r}},\vec{\mathbf{r}}_N\right) \to \int\limits_0^{2\pi}\frac{d\varphi}{2\pi}\vec{\mathbf{j}}_M\left[\vec{\mathbf{r}},\vec{\mathbf{r}}_N\left(\varphi\right)\right].$$
(8.2)

Figure 8.2 illustrates the powder stream of a coaxial four-jet nozzle and a calculated side view of the axisymmetric particle distribution for a coaxial nozzle showing a focus which is usually placed in the surface plane of the substrate.

The mass flow density $\vec{\mathbf{j}}_M(\vec{\mathbf{r}})$ obtained is related to the local volume fraction $f_P(\vec{\mathbf{r}}) = \overline{V_P}\, N_P/V$ of a cloud of N_P powder particles with the volume $\overline{V_P}$ as follows:

$$\vec{\mathbf{j}}_M(\vec{\mathbf{r}}, \vec{\mathbf{r}}_N) = \rho_P v_P f_P(\vec{\mathbf{r}}) \frac{\vec{\mathbf{r}} - \vec{\mathbf{r}}_N}{|\vec{\mathbf{r}} - \vec{\mathbf{r}}_N|},$$

$$f_P(\vec{\mathbf{r}}) = \frac{J}{\rho_P v_P} \frac{m+1}{2\pi} \frac{\left(\frac{\vec{\mathbf{r}} - \vec{\mathbf{r}}_N}{|\vec{\mathbf{r}} - \vec{\mathbf{r}}_N|} \cdot \frac{\vec{\mathbf{r}}_0 - \vec{\mathbf{r}}_N}{|\vec{\mathbf{r}}_0 - \vec{\mathbf{r}}_N|} \right)^m}{(\vec{\mathbf{r}} - \vec{\mathbf{r}}_N)^2}$$

(8.3)

(ρ_P: density of powder material, v_P: average initial particle speed at the nozzle). Particle collisions are neglected here, since in most cases the particle volume fraction is small ($f_P(\vec{\mathbf{r}}) \ll 1$), except perhaps immediately in front of the nozzle outlet.

8.2.2 Effect of Gravity on the Mass Flow Distribution

Powder mass flow and particle speed can be controlled by the carrier gas pressure. If the particle velocity, v_P, is less than or equal to about $1\ \mathrm{m\ s^{-1}}$, the influence of the gravitational force on the particle trajectories cannot be neglected. Advantage can be taken of such low velocities in order to allow the laser beam to melt the powder particles in transit before they arrive at the substrate surface.

In this section only, the direction of the gravitational acceleration vector $\vec{\mathbf{g}}$ will be taken to be the negative z-axis. Particles which would be found at position $\vec{\mathbf{r}}^*$ without the force of gravity reach the position

$$\vec{\mathbf{r}} = \vec{\mathbf{r}}^* + \frac{1}{2}\vec{\mathbf{g}}t^2(\vec{\mathbf{r}}^*) \equiv \vec{\mathbf{r}}^* + \gamma_P(\vec{\mathbf{r}}) \frac{\vec{\mathbf{g}}}{g}, \quad t(\vec{\mathbf{r}}^*) = \frac{|\vec{\mathbf{r}}^* - \vec{\mathbf{r}}_N|}{v_P}.$$

(8.4)

when it is taken into account. Here $t(\vec{\mathbf{r}}^*)$ is the flight time from the nozzle outlet to the point $\vec{\mathbf{r}}^*$. With the inclusion of the gravitational force it is possible to find those particles between positions z and $z + \Delta z$ which without the gravity force were between the positions $z + \gamma_P(x, y, z)$ and $z + \Delta z + \gamma_P(x, y, z + \Delta z)$, respectively. Hence, particles reaching points within a small interval of length Δz around z with gravity, would be found within an interval of length $\Delta z\,[1 + \partial\gamma_P/\partial z]$ without gravity. Thus the modified powder volume fraction $f_P^*(\vec{\mathbf{r}})$ and mass flow density $\vec{\mathbf{j}}_M^*(\vec{\mathbf{r}})$ are derived from (8.3) and (8.4) as follows:

$$f_P^*(\vec{\mathbf{r}}) = f_P(\vec{\mathbf{r}}^*) \left[1 + \frac{\partial\gamma_P(\vec{\mathbf{r}})}{\partial z} \right],$$

$$\vec{\mathbf{j}}_M^*(\vec{\mathbf{r}}) = \rho_P f_P^*(\vec{\mathbf{r}}) \left[v_P \frac{\vec{\mathbf{r}}^* - \vec{\mathbf{r}}_N}{|\vec{\mathbf{r}}^* - \vec{\mathbf{r}}_N|} + \vec{\mathbf{g}}\sqrt{\frac{2\,\gamma_P(\vec{\mathbf{r}})}{g}} \right].$$

(8.5)

Expression (8.4) leads to a quadratic equation for the free fall path γ_P:

$$\gamma_P(\mathbf{r}) = \frac{g}{2\,v_P^2}\,(\mathbf{r}^* - \mathbf{r}_N)^2 \;\Rightarrow\; \gamma_P^2 - 2\,\frac{\gamma_P}{g}\,\left[v_P^2 + \vec{\mathbf{g}}\cdot(\mathbf{r} - \mathbf{r}_N)\right] + (\mathbf{r} - \mathbf{r}_N)^2 = 0.$$

(8.6)

Of the two solutions $\gamma_P^{1,\,2}(\mathbf{r})$ of this quadratic equation, the one which vanishes at the position $\mathbf{r}_N$ of the nozzle outlet must be chosen. It is found to be given by

$$\gamma_P(\mathbf{r}) = \frac{v_P^2}{g\,(1 + \omega_P(\mathbf{r}))}\,\left\{\left[\frac{\vec{\mathbf{g}}}{v_P^2}\times(\mathbf{r} - \mathbf{r}_N)\right]^2 - \frac{\vec{\mathbf{g}}}{v_P^2}\cdot(\mathbf{r} - \mathbf{r}_N)\left[1 - \omega_P(\mathbf{r})\right]\right\},$$

$$\omega_P(\mathbf{r}) \equiv \sqrt{1 + 2\,\frac{\vec{\mathbf{g}}}{v_P^2}\cdot(\mathbf{r} - \mathbf{r}_N) - \left[\frac{\vec{\mathbf{g}}}{v_P^2}\times(\mathbf{r} - \mathbf{r}_N)\right]^2},$$

(8.7)

$$1 + \frac{\partial\,\gamma_P(\mathbf{r})}{\partial z} = \frac{1}{\omega_P(\mathbf{r})}.$$

Inserting this solution into expressions (8.5) for the powder volume fraction $f_P^*(\mathbf{r})$ and the powder mass flow $\vec{\mathbf{j}}_M^*(\mathbf{r})$ within the interaction zone gives

$$f_P^*(\mathbf{r}) = \frac{f_P\left(\mathbf{r} - \gamma_P(\mathbf{r})\,\dfrac{\vec{\mathbf{g}}}{g}\right)}{\omega_P(\mathbf{r})},$$

(8.8)

$$\vec{\mathbf{j}}_M^*(\mathbf{r}) = \rho_P\,f_P^*(\mathbf{r})\,\left[\sqrt{\frac{g}{2\,\gamma_P(\mathbf{r})}}\,(\mathbf{r} - \mathbf{r}_N) + \sqrt{\frac{\gamma_P(\mathbf{r})}{2\,g}}\,\vec{\mathbf{g}}\right].$$

The flight trajectory of a particle from the nozzle to a given point $\mathbf{r}$ is described by

$$\mathbf{r} = \mathbf{r}_N + \vec{\mathbf{v}}_P\left[\vartheta(\mathbf{r})\right]\,t + \frac{1}{2}\,\vec{\mathbf{g}}\,t^2,$$

(8.9)

$$\vec{\mathbf{v}}_P\left[\vartheta(\mathbf{r})\right] = \frac{\mathbf{r}^* - \mathbf{r}_N}{|\mathbf{r}^* - \mathbf{r}_N|}\,v_P = \sqrt{\frac{g}{2\,\gamma_P(\mathbf{r})}}\,(\mathbf{r} - \mathbf{r}_N) - \sqrt{\frac{\gamma_P(\mathbf{r})}{2g}}\,\vec{\mathbf{g}}.$$

Obviously, the gravity force can be neglected as long as the condition $g\,|\mathbf{r} - \mathbf{r}_N| \ll \nu_P^2$ holds.

8.2.3 Beam Shadowing and Particle Heating

Particles crossing the laser beam scatter and partly absorb the laser light. For that reason the beam is attenuated. At the same time the powder particles are heated reaching temperatures which depend on their size, speed, and flight trajectories.
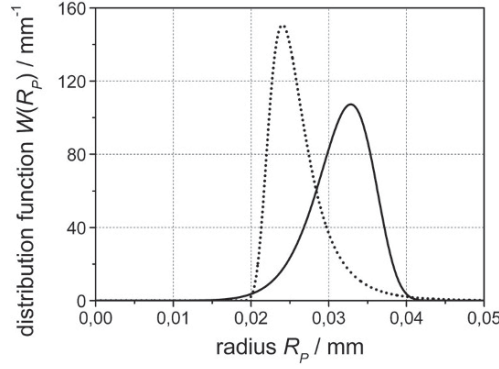
Fig. 8.3. Particle size distributions $W_1(R_P)$ [solid line] and $W_2(R_P)$ [dashed line] for $R_{min} = 0.02\,\text{mm}$, $R_{max} = 0.04\,\text{mm}$, and $\psi_P = 0.99$.

Strictly speaking, the interaction of the powder with the laser beam is more complicated owing to the diffraction phenomenon known as Mie scattering, which occurs if the particles are not much larger than about ten times the laser wave length, as is frequently observed in the case of cladding with CO_2-laser radiation.

Usually the particle size varies within certain limits. The fraction $n_P(R_P)$ of overall N_P particles with radii up to a certain value R_P may be described for example by one of the following Weibull type distributions, which are visualised in Fig. 8.3:

$$dn_p\left(R_P\right) = N_P W\left(R_P\right) dR_P, \quad \int\limits_0^\infty dR_P W\left(R_P\right) = 1,$$

$$W_1\left(R_P\right) = \frac{p}{R_0}\left(\frac{R_P}{R_0}\right)^{p-1}\exp\left[-\left(\frac{R_P}{R_0}\right)^p\right], \qquad (8.10)$$

$$W_2\left(R_P\right) = \frac{-p^2}{2R_0\Gamma\left(-2/p\right)}\left(\frac{R_0}{R_P}\right)^{p-1}\exp\left[-\left(\frac{R_0}{R_P}\right)^p\right].$$

The parameters R_0 and p can be determined from the known maximum and minimum values of the powder particle radius as follows:

$$W\left(R_{\min}\right) = W\left(R_{\max}\right), \quad \int\limits_{R_{\min}}^{R_{\max}} dR_P W\left(R_P\right) = \psi_P. \qquad (8.11)$$

Here ψ_P is the fraction of particles having radii within the interval $R_{min} < R_P < R_{max}$.
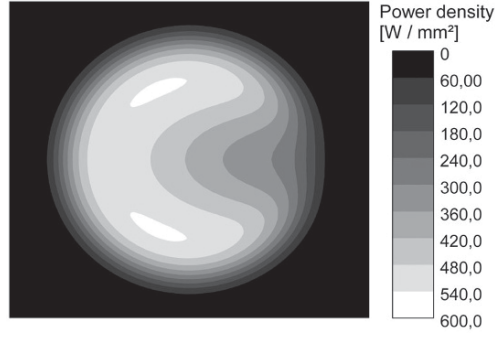
Fig. 8.4. Intensity distribution of a laser beam (top-hat) which is strongly attenuated by a transverse particle stream (off-axis powder supply) as calculated by (8.13).

Then the local volume fraction of particles within the size interval dR_P is given by

$$df_P^* (\vec{r}, R_P) = \frac{dR_P W(R_P) V_P(R_P)}{\overline{V_P}} f_P^* (\vec{r}),$$

$$\overline{V_P} \equiv \int_0^\infty dR_P W(R_P) V_P(R_P),$$

(8.12)

where $V_P(R_P)$ is the volume of a single particle with the radius R_P.

Let us consider a planar layer of volume V in the interaction zone with thickness dz along the beam direction, $\vec{e}_z$, which contains $dn_P(R_P)$ particles of radius R_P. Absorption and reflection cause the laser beam intensity to be reduced as follows:

$$\frac{dj_E}{j_E} = -dz \int dn_P(R_P) \frac{\overline{A_P}(R_P)}{V} = -dz\, f_P^*(\vec{r}) \int_0^\infty dR_P W(R_P) \frac{\overline{A_P}(R_P)}{\overline{V_P}},$$

$$\Rightarrow \vec{j}_E^L(\vec{r}) = j_E^0(x, y) \exp\left[-\int_{z_0}^z dz'\, f_P^*(x, y,\ z') \int_0^\infty dR_P W(R_P) \frac{\overline{A_P}(R_P)}{\overline{V_P}} \right] \vec{e}_z.$$

(8.13)

This yields the energy flow density, $\vec{j}_E^L(\vec{r})$, of the attenuated laser beam. $\overline{A_P}(R_P)$ is the mean cross section area of a rotating particle. Figure 8.4 shows an example of such a weakened power density distribution.

The heat balance of a small particle with radius R_P, moving along a given trajectory $\vec{r}(t)$ through the laser beam, leads to the following ordinary differential equation for the particle's specific enthalpy, $h_P[\vec{r}(t), R_P]$, and

temperature, T_P, even taking into account heat losses by convection and radiation:

$$\rho_P V_P(R_P) \frac{dh_P(t,\,R_P)}{dt} = \mathcal{A}\,\overline{A_P}(R_P)\,j_E^L\left[\vec{\mathbf{r}}(t)\right] - S_P(R_P)$$

$$\times \left[\alpha\,(T_P - T_a) + \varepsilon_{SB}\,\sigma_{SB}\left(\mathrm{T}_P^4 - \mathrm{T}_a^4\right)\right],$$

$$h_P(0,\,R_P) = c_P\left(T_P^i - T_0\right), \quad \mathbf{r}(t) = \vec{\mathbf{r}}_N + \vec{\mathbf{v}}_P\left[\vartheta(\tilde{\mathbf{r}})\right]t + \frac{1}{2}\vec{\mathbf{g}}\,t^2, \qquad (8.14)$$

$$h_P(t,\,R_P) = c_P\left[T_P(t,\,R_P) - T_0\right] + L_m\,\Theta\left[T_P(t,\,R_P) - T_m\right],$$

$$\mathrm{T}_{P,\,a} \equiv T_{P,\,a} + 273\,\mathrm{K}.$$

Thereby $\mathcal{A}$ is the absorptivity and ε_{SB} the emissivity of the particle surface, and σ_{SB} is the Stefan-Boltzmann constant. S_P denotes the particle surface area, α the heat transfer coefficient, T_a the ambient temperature, T_P^i the initial particle temperature, and T_0 an arbitrary reference temperature. Equations (8.14) contain also the relationship between the specific enthalpy h_P and the temperature T_P.

With the known particle enthalpies we calculate the energy flow density, $\vec{\mathbf{j}}_E^P$, transported by a cloud of preheated particles the size of which is distributed according to a function $W(R_P)$ as given in (8.10):

$$\vec{\mathbf{j}}_E^P(\vec{\mathbf{r}}) = \vec{\mathbf{j}}_M^*(\vec{\mathbf{r}}) \int_0^\infty dR_P\,W(R_P)\,h_P\left[t(\vec{\mathbf{r}}),\,R_P\right]\,V_P(R_P)\big/\overline{V_P},$$

$$\hspace{6cm} (8.15)$$

$$t(\vec{\mathbf{r}}) \;=\; \sqrt{\frac{2\,\gamma_P(\vec{\mathbf{r}})}{g}}.$$

In the case of coaxial or other distributed nozzles each point of the work piece surface is struck by particles which have travelled along different trajectories and thus reached different temperatures. Figure 8.5 shows the radial mass distribution of particles the temperatures of which exceed the value T given on the T-axis for a coaxial nozzle. The discontinuity at the melting temperature is due to the latent heat of melting.

8.3 Formation of the Weld Bead

The incident mass and energy flow densities given by (8.8), (8.13), and (8.15) are the input quantities of the subsequent self-consistent calculation of the bead shape and the steady state temperature field in the process zone. Part of the laser beam energy is lost from the process by reflection at the work piece surface.
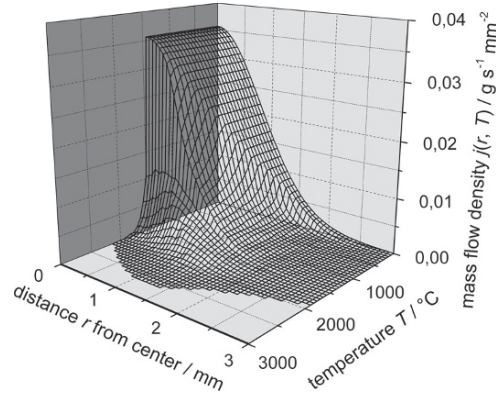
Fig. 8.5. Radial powder mass flow density $j_M(r, T)$ of those particles ejected by a coaxial nozzle the final temperatures of which exceed the corresponding axis value T. The discontinuous drop at the melting temperature $(1450\,°C)$ is due to the latent heat. Obviously, a small fraction of the particles is completely molten in this case.

8.3.1 Particle Absorption and Dissolution

Only those particles are able to penetrate into the melt pool which have enough kinetic energy to overcome the surface tension barrier at the melt pool surface. Of course, all those particles are absorbed in the melt pool which have already been melted by the laser beam during their flight. Liquid particles which strike a surface not melted by the laser beam can form a melt pool only if the substrate temperature exceeds the melting point of the coating material. In this case we get a soldered connection between substrate and coating which avoids material mixing and thus the undesired formation of brittle intermetallic compounds but does not have the strength of a welded joint. Solid particles are rejected by unmolten surface regions and are thus lost to the process.

After having entered the melt pool whose temperature is T_a, the particles are heated very rapidly from their initial temperature T_P to their melting point T_m. The dissolving of a spherical particle for example is described by the equation of heat flow taking into account the latent heat of melting L_m:

$$\rho \left[c_p + L_m \delta \left(T\left(r,t\right) - T_m\right)\right] \frac{\partial T\left(r,t\right)}{\partial t} = \frac{\lambda}{r} \frac{\partial^2}{\partial r^2} \left[rT\left(r,t\right)\right],$$

$$T\left(r,0\right) = T_P + \Theta\left(r - R_P\right)\left(T_a - T_P\right), \quad T\left(r \to \infty, t\right) = T_a. \tag{8.16}$$

There is no analytical solution of this strongly non-linear equation. For a numerical solution Dirac's delta-function has to be replaced by a very narrow Gaussian or similarly peaked function (width $\Delta T < 1$ K), and the partial differential equation (8.16) is transformed into a system of ordinary differential
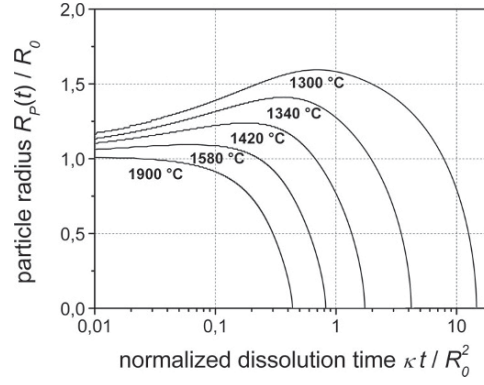
Fig. 8.6. Numerical solutions of (8.16) for the dissolution kinetics of particles, which were preheated by the laser beam up to $400\,^{\circ}\mathrm{C}$, for temperatures of the surrounding melt bath between $1300\,^{\circ}\mathrm{C}$ and $1900\,^{\circ}\mathrm{C}$ (latent heat over specific heat: $L_m/c_p = 222\,\mathrm{K}$, melting temperature of the particles: $T_m = 1280\,^{\circ}\mathrm{C}$, thermal diffusivity of the melt: $\kappa = 5\,\mathrm{mm}^2/\mathrm{s}$).

equations by discretising the spatial derivatives. Figure 8.6 shows normalised numerical solutions of this equation.

The melting time is found to be determined primarily by the initial particle radius, R_0, the latent heat of melting, L_m, and the melt pool temperature, T_a. Omitting numerical factors near to unity we get a rough estimate of the dissolution time Δt from the heat balance at the particle surface:

$$L_m\rho_P\frac{dR_P}{dt} \approx -\left.\lambda\frac{\partial T}{\partial r}\right|_{r=R_P} \approx -\lambda\frac{T_a - T_m}{R_P} \rightarrow \frac{\kappa\,\Delta t}{R_0^2} \approx \frac{L_m/c_P}{T_a - T_m}. \qquad (8.17)$$

For cobalt alloys and typical particle radii between $0.02\,\mathrm{mm}$ and $0.05\,\mathrm{mm}$ we find that the order of magnitude of the time taken to dissolve lies between 10^{-4} s and 10^{-3} s.

The melting of larger particles may however require several milliseconds if the ambient melt pool temperature T_a exceeds the melting point only slightly. Within that time these particles can be transported by the surface tension gradient driven flow (see Section 8.3.6) to the melt pool boundary where they remain. Hence, the capability of the melt pool to absorb powder particles is limited by its temperature.

8.3.2 Shape of the Cross Section of a Weld Bead

As a rule, only particles which penetrate into the melt pool contribute to the bead. Thus the bead width is given by the lateral melt pool boundaries y_1 and y_2. The cross sectional area follows from the absorbed powder mass per unit length. The cross section shape $z(y)$ of the solidifying melt pool is determined

by the balance of surface tension and gravity forces such that the melt pool energy consisting of the surface energy and the potential energy in the gravity field becomes a minimum:

$$\delta \int_{y_1}^{y_2} dy \left\{ \sigma\left[T\left(y\right)\right] \sqrt{1 + \left(\frac{dz}{dy}\right)^2} + \int_{z_0(y)}^{z(y)} dz' \left(\rho\, g\, z' + \lambda_L\right) \right\} = 0. \quad (8.18)$$

Here the Lagrangian multiplier λ_L has to be determined from the prescribed cross section area A. For a given value of A the melt pool shape $z(y)$ is most easily derived from Euler's equation for this variational principle with the boundary conditions $z(y_{1,2}) = z_0(y_{1,2})$ at the two bead margins $y_{1,2}$ where $z_0(y)$ gives the substrate surface:

$$\frac{d}{dy} \left\{ \frac{\sigma\left[T\left(y\right)\right] \frac{dz}{dy}}{\sqrt{1 + \left(\frac{dz}{dy}\right)^2}} \right\} - \rho\, g\, z\left(y\right) \;=\; \lambda_L, \int_{y_1}^{y_2} dy \left[z\left(y\right) - z_0\left(y\right)\right] = A, \quad (8.19)$$
$$z\left(y_{1,2}\right) = z_0\left(y_{1,2}\right).$$

The Lagrangian parameter, λ_L, is obtained by integrating (8.19) over the entire bead width. Introducing dimensionless coordinates

$$\eta \equiv y\,/\,w, \quad \zeta \equiv z\,/\,w, \quad w \equiv y_2 - y_1, \quad (8.20)$$

the boundary value problem (8.19) is transformed into an initial value problem, which can be solved numerically by means of computer algebraic methods starting from one or both boundaries:

$$-\frac{d^2\zeta}{d\eta^2} \Big/ \left[1 + \left(\frac{d\zeta}{d\eta}\right)^2\right]^{\frac{3}{2}} + k\left(\zeta - \frac{A^*}{w^2}\right) + \sin\vartheta_2 - \sin\vartheta_1 = 0,$$

$$A^* \equiv \int_{y_1}^{y_2} dy\, z\left(y\right),$$

$$\zeta\left(\eta_{1,2}\right) = \frac{z_0\left(\eta_{1,2}\right)}{w} \equiv \zeta_{1,2}, \qquad \frac{d\zeta}{d\eta}\left(\eta_{1,2}\right) = \tan\vartheta_{1,2}, \qquad k \equiv \frac{\rho\, g\, w^2}{\sigma},$$

$$(8.21)$$

$$\cos\vartheta_1 - \cos\vartheta_2 + \left(\zeta_1 - \zeta_2\right)\left[k\left(\frac{\zeta_1 + \zeta_2}{2} - \frac{A^*}{w^2}\right) - \left(\sin\vartheta_1 - \sin\vartheta_2\right)\right] = 0.$$

Here the surface tension σ has been assumed to be independent of y. The remaining unknown boundary slope angle, ϑ_1 or ϑ_2, is determined by trial and error such that the two branches of the solution meet each other with equal slope angles.
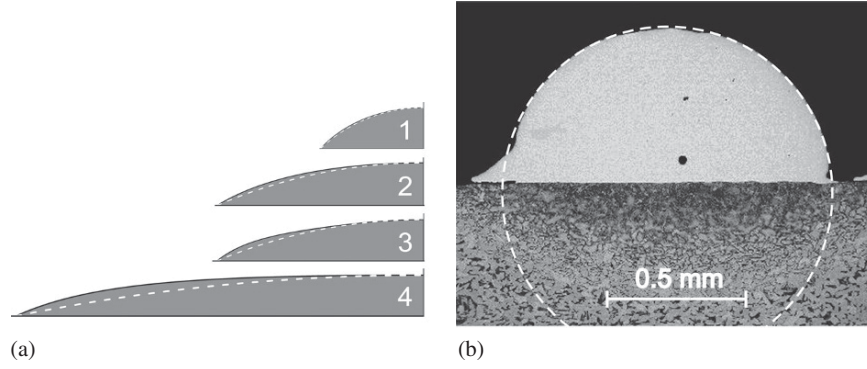
Fig. 8.7. a) Weld bead shape as derived from the pressure balance (8.21) for different values of the bead width w, which varies between 10 mm and 40 mm. The deviations from the circular arc become larger and larger with increasing bead width. In the case of the third bead the dynamic pressure due to the thermocapillary flow was accounted for in the pressure balance (surface tension σ: 1.8 N/m, density ρ: 7800 kg/m^3, bead height: 2 mm). b) The cross sectional contour of the bead in Fig. 8.7b is almost perfectly fitted by a circular arc.

Usually the capillarity parameter k is small in conventional laser cladding ($k \ll 1$) since the track width w is mostly restricted to a few millimeters (Fig. 8.7). The influence of the gravity force on the bead shape may therefore be neglected. This holds even for inclined substrate surfaces. For $k \ll 1$ (8.21) yields curves of constant curvature, i.e. circular arcs (see Fig. 8.7b). In induction assisted laser cladding (see Sect. 8.4.5) or when using PTA (plasma transferred arc) or even high-power lasers the increased heat input allows wider weld beads, and the force of gravity may have an influence on the bead shape as shown in Fig. 8.7a.

8.3.3 Three-Dimensional Model of the Melt Pool Surface

The size of the molten area on the substrate, which is able to absorb powder particles, is determined by the temperature field. Surface tension tends to minimise the curvature of the melt pool surface, whereas the gravitational force was found to be less important. In order to find an analytical expression of the three-dimensional melt pool surface we use, as a first trial, an ellipsoid-shaped surface morphing at the solidification front $x_{sol}(z) = x_3 + \psi(h-z)$ into an elliptical cylinder, which describes the solidified weld bead. Thereby x_3 is the x-position of the point P_3 in Fig. 8.8:

$$f(x, y, z) \equiv \Theta\left[x - x_{sol}(z)\right]\left(\frac{x - x_{sol}(z)}{a}\right)^2 + \left(\frac{y}{b}\right)^2 + \left(\frac{z + c - h}{c}\right)^2 - 1 = 0.$$
$$(8.22)$$
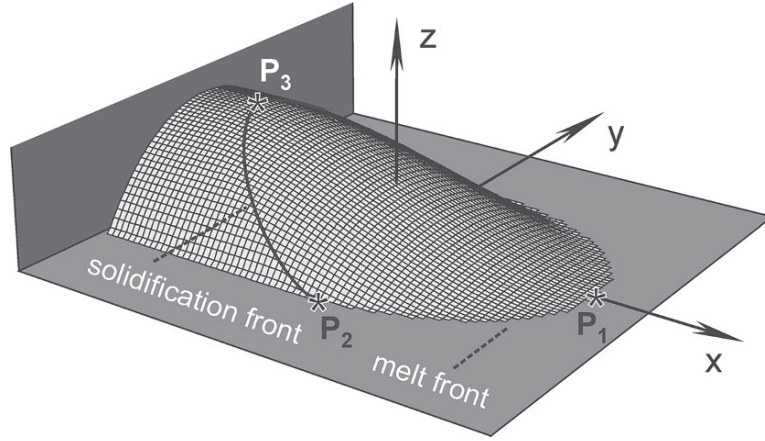
Fig. 8.8. Melt pool and bead surface according to the modified ellipsoid model.

$\Theta(x)$ is Heaviside's step function. The coordinate axes were chosen as shown in Fig. 8.8, the plane $y = 0$ being a plane of symmetry. The function (8.22) contains the half axes a, b, c, the bead height h, and the shear parameter ψ as unknown parameters.

The parameters b, c, and h are determined by inserting expression (8.22) with $x = x_3$ into the variational condition (8.18) using the known values of the bead width, w, and the bead cross section area, A, which follow from the temperature field and the mass deposited per unit length. The remaining two parameters, a and ψ, are obtained from the x-coordinates of the characteristic points $P_1 = (x_1,\, 0,\, 0)$, $P_2 = (x_2,\, w/2,\, 0)$ and $P_3 = (x_3,\, 0,\, h)$ on the melt pool boundary (see Fig. 8.8), which are determined by the temperature field, as follows:

$$x_2 = x_3 + \psi\, h\,, \quad x_1 = x_3 + \psi\, h + a\sqrt{1 - \left(1 - \frac{h}{c}\right)^2}\,. \qquad (8.23)$$

However, when passing from the substrate to the inclined ellipsoid surface, the direction of the surface normal changes discontinuously at the edge of the melt pool boundary. The same holds for the power absorbed per unit area. That may cause unrealistic minima of the calculated temperature distribution on the ellipsoid surface, which can even fall below the melting point. This effect becomes all the more pronounced the more the beam is screened by the powder particles. Function (8.22) has therefore to be modified in order to get a smooth transition from the substrate surface plane ($z = 0$) to the melt pool surface. To this end, the constant half axis length parameter a is replaced by a z-dependent function $a(z)$ such that the intersection line between the melt pool surface and the symmetry plane ($y = 0$) is described by a fourth-order polynomial with zero slopes at the front and rear boundaries of the

melt pool:

$$\frac{z}{h} = P\left(\frac{x - x_{sol}(z)}{x_1 - x_{sol}(0)}\right), \qquad a \to a(z) = \frac{x_1 - x_{sol}(0)}{\sqrt{1 - \left(\frac{z + c - h}{c}\right)^2}} P^{-1}\left(\frac{z}{h}\right),$$

$$P(\xi) = 3\xi^4 - 4\xi^3 + 1, \quad P^{-1}(\zeta) = \left[2 + \sqrt{u(\zeta)} - \sqrt{12 - u(\zeta) + \frac{16}{\sqrt{u(\zeta)}}}\right]\Bigg/ 6,$$

$$u(\zeta) \equiv 4 + 6\sqrt[3]{1 - \zeta}\left[\sqrt[3]{1 - \sqrt{\zeta}} + \sqrt[3]{1 + \sqrt{\zeta}}\right]. \tag{8.24}$$

Figure 8.8 shows the modified melt pool surface, which at the solidification front continuously and smoothly changes into a weld bead described by an elliptical cylinder. The correction (8.24) avoids unreasonable temperature minima as obtained with the unmodified ellipsoid model, which would disturb the convergence of the iterative approach to bead shape and temperature field.

   This conclusion concerning the melt pool shape, derived from a theoretical point of view, is supported by the high speed videos of Pirch et al. [32], who found these deviations from the ellipsoid model to increase with decreasing particle size.

8.3.4 Temperature Field Calculation using Rosenthal's Solution

Rosenthal's solution $G_R(\vec{r})$ [53] of the steady state heat flow equation for a point source moving with speed $\vec{v}$ is a powerful tool in calculating laser induced temperature fields:

$$G_R(\vec{r}) = \frac{\exp\left[-\frac{|\vec{v}|\,|\vec{r}| + \vec{v}\cdot\vec{r}}{2\,\kappa}\right]}{4\,\pi\,\lambda\,|\vec{r}|}, \quad \rho\,c\,\vec{v}\cdot\frac{\partial G_R(\vec{r})}{\partial\vec{r}} + \frac{\partial}{\partial\vec{r}}\cdot\lambda\frac{\partial G_R(\vec{r})}{\partial\vec{r}} + \delta(\vec{r}) = 0. \tag{8.25}$$

Here $\kappa = \lambda/\rho c$ is the heat diffusivity.

   Let us consider first an infinite flat plate in the x-y plane with thickness d. The temperature field of an arbitrary heat source with three-dimensional intensity distribution $q_3(\vec{r})$ moving with a constant speed $\vec{v}$ parallel to the plate surface is found by superposition of the fields of moving point sources. The boundary conditions at the plate surfaces (zero heat flow at both surfaces, $K = 1$, or zero heat flow at the top and zero heating rate at the bottom, $K = -1$) can be satisfied by introducing suitably arranged mirror source distributions. The steady state temperature at a point $\vec{r}$ in the moving

reference system is then given by

$$
T\left(\vec{\mathbf{r}}\right) = \sum_{j=-\infty}^{\infty} K^j \iint_{\infty} dx'\, dy' \int_0^d dz'\, G_R\left(\vec{\mathbf{r}} - \vec{\mathbf{r}}'\right)
$$

$$
\times \left[q_3\left(x',\, y',\, z' - 2j\,d\right) + q_3\left(x',\, y',\, -z' - 2j\,d\right)\right]. \qquad (8.26)
$$

Such a simple expression cannot be found for arbitrarily shaped domains; however, multiplying the steady state heat flow equation in the moving reference system,

$$
\rho\, c\, \vec{\mathbf{v}} \cdot \frac{\partial T}{\partial \vec{\mathbf{r}}} + \frac{\partial}{\partial \vec{\mathbf{r}}} \cdot \lambda \frac{\partial T}{\partial \vec{\mathbf{r}}} = 0, \qquad (8.27)
$$

by $G_R\left(\vec{\mathbf{r}} - \vec{\mathbf{r}}'\right)$ and integrating it twice by parts over the entire domain considered, yields the integral equation

$$
\left[T\left(\vec{\mathbf{r}}\right) - T_0\right] \frac{\Omega\left(\vec{\mathbf{r}}\right)}{4\pi} = \oiint_{domain} d\vec{\mathbf{S}}' \cdot \left\{ \lambda \frac{\partial G_R\left(\vec{\mathbf{r}} - \vec{\mathbf{r}}'\right)}{\partial \vec{\mathbf{r}}} \left[T\left(\vec{\mathbf{r}}'\right) - T_0\right] \right.
$$

$$
\left. - G_R\left(\vec{\mathbf{r}} - \vec{\mathbf{r}}'\right) \vec{\mathbf{j}}_E\left(\vec{\mathbf{r}}'\right) \right\} \qquad (8.28)
$$

with

$$
\vec{\mathbf{j}}_E\left(\vec{\mathbf{r}}\right) = -\lambda \frac{\partial T}{\partial \vec{\mathbf{r}}} - \rho c \vec{\mathbf{v}} \left[T\left(\vec{\mathbf{r}}\right) - T_0\right], \quad \frac{\Omega\left(\vec{\mathbf{r}}\right)}{4\pi} \equiv \int_{domain} \delta\left(\vec{\mathbf{r}} - \vec{\mathbf{r}}'\right) dV',
$$

$$
\qquad (8.29)
$$

External surfaces: $\vec{\mathbf{j}}_E\left(\vec{\mathbf{r}}\right) = \vec{\mathbf{j}}_E^L\left(\vec{\mathbf{r}}\right) + \left(\vec{\mathbf{j}}_E^P\left(\vec{\mathbf{r}}\right) - L_m \vec{\mathbf{j}}_M^*\right) - \vec{\mathbf{j}}_E^R\left(\vec{\mathbf{r}}\right),$

which holds for any point within the domain considered and on its surface; $\Omega\left(\vec{\mathbf{r}}\right)$ is the local space angle at which the domain is seen from the point $\vec{\mathbf{r}}$, and T_0 is an arbitrary reference temperature. The total energy flow density introduced, $\vec{\mathbf{j}}_E\left(\vec{\mathbf{r}}\right)$, contains contributions from the laser beam, $\vec{\mathbf{j}}_E^L\left(\vec{\mathbf{r}}\right)$, the penetrating particles, $\vec{\mathbf{j}}_E^P\left(\vec{\mathbf{r}}\right)$, and any losses, $\vec{\mathbf{j}}_E^R\left(\vec{\mathbf{r}}\right)$, by radiation or convection. The latent heat L_m is subtracted from the mean particle enthalpy in (8.29) since it is consumed during melting. It is set free again at the solidification front, but is neglected there since it has little influence on the bead shape because of the large temperature gradients.

Equation (8.28) yields the temperature values inside the domain directly when the heat flow and the temperature are known on the entire domain surface. It has to be evaluated in two steps therefore; first the unknown temperature and, if necessary, normal heat flow values are determined for positions $\vec{\mathbf{r}}$ on the surface only, solving the integral equation (8.28) numerically by spatial discretisation. Thereafter the temperatures inside the domain can be calculated directly. This numerical procedure is a special case of the well-known Boundary Element Method (BEM) [54]. Its main advantage is that only the domain surface has to be meshed. Hence, the number of algebraic

equations to be solved remains comparatively small. On the other hand, the matrix of the system of algebraic equations to be solved is very densely occupied and the calculation of the matrix elements requires some care because of the occurrence of singular integrals.

The use of Rosenthal's solution requires constant values for the heat conductivity and diffusivity. If there are various domains consisting of different materials, the substrate and coating for example, (8.28) has to be written down separately for each domain. The two resulting integral equations are coupled by the continuity conditions for the unknown values of the temperature and normal heat flow component at the interface.

For most metals the thermal conductivity depends strongly on the temperature. Although the thermal diffusivity also depends on the temperature, replacing it by a constant average value allows the effect of a temperature dependent conductivity to be approximately accounted for by Kirchhoff's transformation

$$\overline{\lambda}\,\vartheta_K\left[T\left(\vec{\mathbf{r}}\right)\right] \equiv \int_{T_1}^{T(\vec{\mathbf{r}})} dT'\,\lambda\left(T'\right), \quad \overline{\lambda} \equiv \int_{T_1}^{T_2} \frac{dT'}{T_2 - T_1}\,\lambda\left(T'\right)$$

$$\Rightarrow \overline{\lambda}\,\frac{\partial\vartheta_K}{\partial\vec{\mathbf{r}}} = \lambda\left(T\right)\,\frac{\partial T}{\partial\vec{\mathbf{r}}} \tag{8.30}$$

(with suitable integration limits T_1 and T_2). The latter transforms the heat diffusion equation (8.27) for the true temperature T, which is non-linear because of the temperature dependent conductivity $\lambda(T)$, into a linear one which can be solved for the transformed temperature $\vartheta_K(\vec{\mathbf{r}})$ by the method just described. Thereafter, the true temperature, T, is obtained by inverting Kirchhoff's transformation at each point. This procedure can improve the results considerably though the heat diffusivity κ is not really independent of temperature.

8.3.5 Self-Consistent Calculation of the Temperature Field and Bead Geometry

As already explained, bead shape and temperature field are strongly interrelated in laser cladding. Their calculation therefore requires either a completely numerical simulation including heat transfer, fluid flow, and the evolution of the free surface as carried out by [25, 26] or an iterative approach, based on an analytical model of the melt pool surface, with alternating calculations of the bead geometry and the related temperature field as proposed here. Starting from the temperature field of a laser beam moving over a plane substrate, we first calculate the bead shape on the basis of the modified ellipsoid model described above and then the corresponding temperature field. The latter requires corrections of the bead shape for which the temperature field has to be recalculated and so on until convergence is achieved.
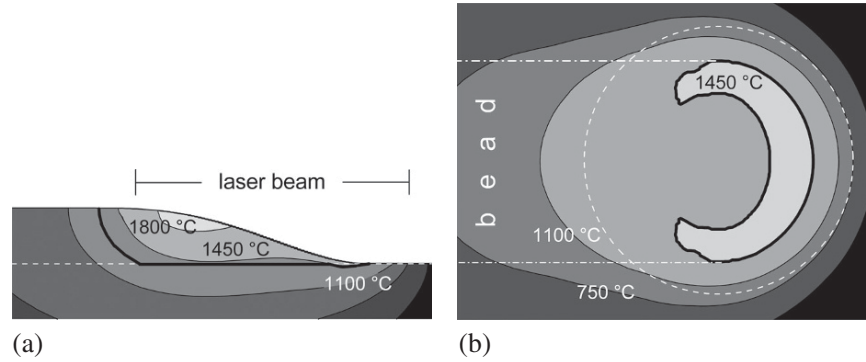
Fig. 8.9. Temperature field of a nascent weld bead on sections along its plane of symmetry (a) and on the interface between the substrate (AISI1045 steel) and the Stellite 21 coating (b). The heavily printed curves enclose the molten region, the lateral width of which determines the bead width. The dashed circle corresponds to the focal spot of the top-hat laser beam. Parameters: laser beam power P: 900 W, beam diameter: 2.6 mm, feed rate: $10\,\mathrm{mm\,s^{-1}}$, mass flow: $0.1\,\mathrm{g\,s^{-1}}$, powder jet diameter at the focus of the coaxial nozzle: 5.0 mm, absorptivity: 50%.

Figures 8.9 and 8.10 show the temperature distribution and bead geometry as calculated in this way for two different values of the laser beam power and otherwise equal process parameters.

The optimised power of 900 W (Fig. 8.9 and Fig. 8.10a) leads to a tight welding joint between substrate and bead with minimum dilution as shown in Fig. 8.10c, whereas an excess of power causes enhanced substrate melting and dilution (see Fig. 8.10b,d). Obviously, the shape of the interface between substrate and bead observed in Fig. 8.10d differs strongly from the calculated one shown in Fig. 8.10b. It cannot be explained by a purely conductive heat flow model and is probably caused by the convection in the melt pool.

8.3.6 Role of the Thermocapillary Flow

The effect of fluid flow in the melt pool on the temperature field was neglected in the preceding section for simplicity. Large temperature gradients at the melt pool surface, however, and the related gradients of the surface tension σ can cause a shear stress τ_{TF} which becomes responsible for a surface flow directed along the surface tension gradient, usually from hot to cold regions (Fig. 8.11). Large temperature differences can be partly compensated for by this flow. This thermocapillary flow or Marangoni flow [55,56] may reach comparatively large velocities v_M but is restricted to a very thin surface layer of thickness Δ_M. The speed of the back flow through the bulk is much lower and depends on the available space.
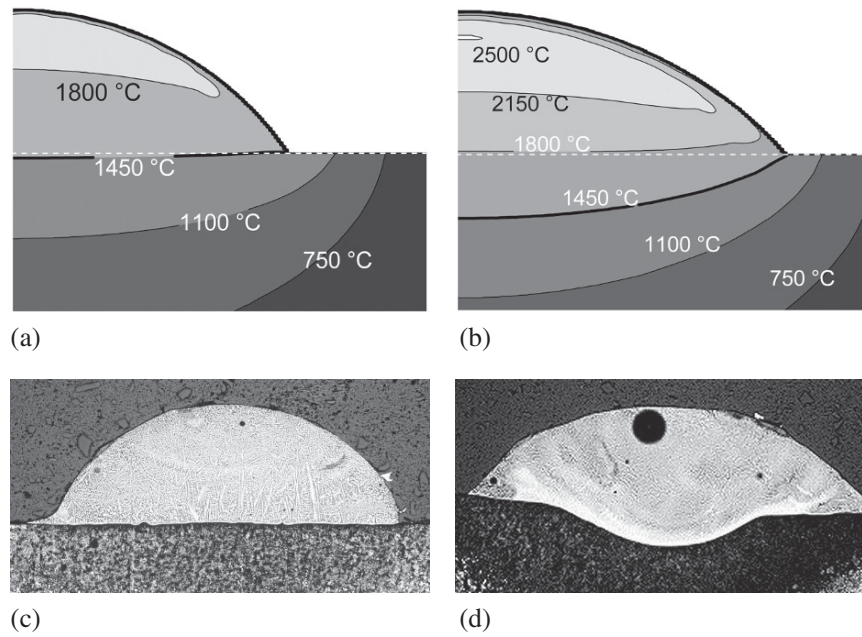
Fig. 8.10. Lines of constant local maximum temperature in a weld bead cross section (perpendicular to the feed direction) compared with bead cross section micrographs. Calculations were carried out with different values of the laser beam power P (900 W in Fig. 8.10a and 1200 W in Fig. 8.10b), other parameters as in Fig. 8.9.
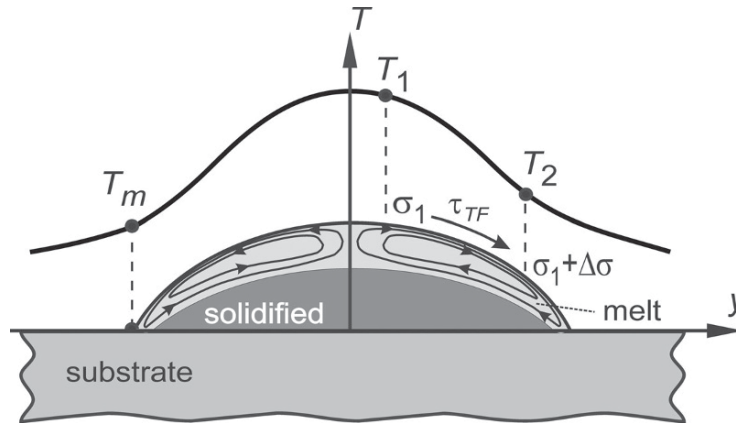
Fig. 8.11. Thermocapillary flow in laser cladding. The surface tension difference $\Delta\sigma$ causes a shear stress τ_{TF} which becomes the driving force of the surface flow.

Approximate expressions for the speed ν_M and the penetration depth Δ_M of a radial thermocapillary flow directed outward in a cylindrical melt pool of radius R may be obtained from the Navier-Stokes equations and the force

balance at the surface

$$v_r \frac{\partial v_r}{\partial r} + v_z \frac{\partial v_r}{\partial z} = -\frac{1}{\rho} \frac{\partial p}{\partial r} + \chi \left[\frac{\partial^2 v_r}{\partial z^2} + \frac{\partial}{\partial r} \frac{1}{r} \frac{\partial}{\partial r} (r\,v_r) \right], \left. \frac{\partial v_r}{\partial z} \right|_{z=0} = -\frac{1}{\rho\,\chi} \frac{d\sigma}{dr}$$

(8.31)

by simple dimensional considerations:

For reasons of mass conservation it follows that $v_r \sim v_M r/R$ in the central part of the melt pool. Then a dimensional analysis at the surface ($z = 0$, $v_z = 0$, $p = $ const.) yields

$$v_M \Delta_M^2 \sim \chi R, \quad \frac{v_M}{\Delta_M} \sim \frac{\Delta\sigma}{\rho\chi R} \Rightarrow v_M \sim Q^{\frac{2}{3}} \frac{\chi}{R}, \quad \Delta_{\mathrm{M}} \sim R\,Q^{-\frac{1}{3}}$$

$$Q \equiv \frac{\Delta\sigma}{\rho} \frac{R}{\chi^2} = \frac{\mathrm{Ma}}{\mathrm{Pr}}, \quad \mathrm{Ma} \equiv \frac{\Delta\sigma}{\rho} \frac{R}{\chi\,\kappa}, \quad \mathrm{Pr} \equiv \frac{\chi}{\kappa}. \qquad (8.32)$$

Here $\Delta\sigma$ is the surface tension difference between the outer border and the centre of the melt pool, and ρ and χ are the density and kinematic viscosity of the fluid, respectively. The number Q may be expressed in terms of the Marangoni number, Ma, and the Prandtl number, Pr. Inserting the material properties of cobalt and a radius $R = 1\,\mathrm{mm}$ gives $v_M \approx 1\ \mathrm{m\ s^{-1}}$ and $\Delta_M \approx 0.05\,\mathrm{mm}$ as orders of magnitude. Since melt pool depth and radius of curvature of the bead are accordingly much greater than the thickness Δ_M of the flow layer, (8.32) can even be applied to laser cladding.

The flow speed obtained is large enough to carry particles which have not dissolved after a time of about 1 ms to the melt pool boundaries.

Thermocapillary flow in a small laser-melted pool is difficult to observe. However, there is indirect evidence of its more significant effects; substrate melting leads to an almost uniform dilution of the coating with the substrate material as has been proved by EDX (energy dispersive X-ray spectroscopy). Furthermore, Fig. 8.12 demonstrates that the temperature distribution on the melt pool surface obtained by thermography does not show the pronounced temperature maximum predicted by the heat conduction model (Fig. 8.12b). Taking into account the thermocapillary flow in calculating the temperature field in a laser-melted pool may lead to maximum temperature values which are by several 100 K less than those obtained by means of a pure heat conduction model [58].

Despite the great influence of the thermocapillary flow on the temperature field in the melt pool, the heat conduction model can be advantageously used for the anticipation of process parameters under manufacturing conditions, since it describes the shape and size of the melt pool and weld bead almost correctly (see Fig. 8.12) and, moreover, can be handled much more easily than numerical calculations which take into account the thermocapillary flow. However, it should be kept in mind that the required laser beam power is usually overestimated by the heat conduction model.
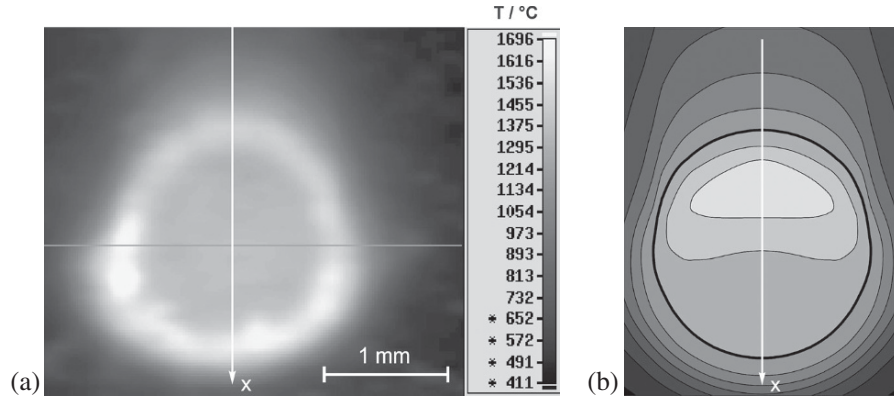
Fig. 8.12. Thermograph (left hand side) of the laser cladding process zone (reproduced by kind permission of G. Kirchhoff [57]) in comparison with the temperature field on the melt pool surface as calculated by means of the heat conduction model (right hand side). The halo at the melt pool borderline consists of solid agglomerates which appear bright since their emissivity is higher than that of the melt. The comparison shows a satisfactory agreement with respect to the size of weld bead and melt pool. However, the true melt pool surface temperature does not show a substantial maximum as is predicted by the heat conduction model.

8.4 Thermal Stress and Distortion

During cladding the coating solidifies and starts shrinking due to thermal contraction. At the same time, heat is conducted into the substrate, which first expands and later contracts according to the local thermal cycle. These phenomena lead to thermal stress and distortion and sometimes even to cracking and delamination, which are further influenced by thermally induced phase transformations and by accompanying phenomena such as plastic flow and transformation plasticity, which depend on the temperature, the temperature rate, and the phase proportions.

In order to prevent cracks or strong distortion it is therefore very important, but not easy, to understand the origin and the mechanisms of stress evolution in laser cladding.

8.4.1 Fundamentals of Thermal Stress

Inhomogeneous heating by the moving laser beam is the origin of various kinds of thermally induced inelastic strain in laser cladding. In contrast to the total strain $\underline{\varepsilon}$, the inelastic strain $\underline{\varepsilon}^I$ cannot be derived from a continuous displacement field. For that reason, neighbouring elements of inelastically strained bodies would no longer match if they were not held together by elastic stresses $\underline{\sigma}$ causing an additional elastic strain $\underline{\varepsilon}^E$ such that the symmetric total strain tensor, $\underline{\varepsilon} = \underline{\varepsilon}^I + \underline{\varepsilon}^E$, can be derived from a continuous displacement
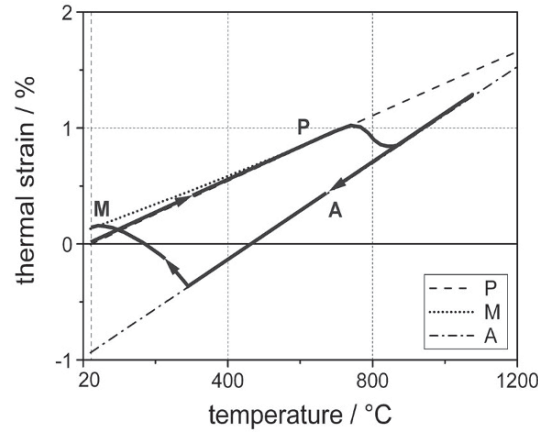
Fig. 8.13. Scheme of thermo-metallurgical strain changes in plain carbon steels during a thermal cycle with phase transformations from pearlite (P) via austenite (A) to martensite (M).

field $\vec{\mathbf{u}}\,(\vec{\mathbf{r}})$ and, therefore, must obey the so called compatibility conditions:

$$\underline{\varepsilon} = \frac{1}{2} \left[\frac{\vec{\partial}}{\partial \vec{\mathbf{r}}} \circ \vec{\mathbf{u}}\,(\vec{\mathbf{r}}) + \vec{\mathbf{u}}\,(\vec{\mathbf{r}}) \circ \frac{\overleftarrow{\partial}}{\partial \vec{\mathbf{r}}} \right] \Rightarrow \frac{\vec{\partial}}{\partial \vec{\mathbf{r}}} \times \underline{\varepsilon} \times \frac{\overleftarrow{\partial}}{\partial \vec{\mathbf{r}}} = \underline{\mathbf{0}}. \qquad (8.33)$$

Examples of inelastic strain are the thermal expansion, $\underline{\varepsilon}^T$, the metallurgical strain, $\underline{\varepsilon}^M$, caused by density differences due to phase transformations, the plastic strain, $\underline{\varepsilon}^P$, including the transformation plasticity, $\underline{\varepsilon}^{TP}$, as well as the fluid flow strain, $\underline{\varepsilon}^{FF}$, which occurs if parts of the body are temporarily melted or a coating is deposited in the liquid state. For a carbon steel Fig. 8.13 visualises the changes of the thermo-metallurgical strain during a thermal cycle with phase transformations from the pearlitic initial structure via austenite to a martensitic non-equilibrium structure.

Hook's tensor $\underline{\underline{\mathbf{C}}}$ describes the linear relationship between stress and elastic strain:

$$\underline{\sigma} = \underline{\underline{\mathbf{C}}} \; : \; \underline{\varepsilon}^E = \underline{\underline{\mathbf{C}}} \; : \; \left(\underline{\varepsilon} - \underline{\varepsilon}^T - \underline{\varepsilon}^M - \underline{\varepsilon}^P - \underline{\varepsilon}^{TP} - \underline{\varepsilon}^{FF} \right). \qquad (8.34)$$

If external forces are absent, the mechanical balance requires the total forces and moments acting on each finite or infinitesimal part of the body to vanish. For that reason the stress tensor has to be symmetric and its divergence and the integrals of the normal stress components over any cross section of the body have to be zero:

$$\underline{\sigma} = \underline{\tilde{\sigma}}, \quad \frac{\partial}{\partial \vec{\mathbf{r}}} \cdot \underline{\sigma} = 0, \quad \iint\limits_{\text{cross section}} d\vec{\mathbf{S}} \cdot \underline{\sigma} = 0, \quad \iint\limits_{\text{cross section}} d\vec{\mathbf{S}} \cdot (\vec{\mathbf{r}} \times \underline{\sigma}) = 0.$$
$$(8.35)$$

Driving forces of the evolution of thermal stress are the inelastic strain rates:

$$\frac{d\underline{\varepsilon}^T}{dt} = \frac{dT}{dt} \sum_i f_i\, \alpha_i\,(T), \qquad \frac{d\underline{\varepsilon}^M}{dt} = \sum_i \frac{df_i}{dt} \int_{T_i}^{T} dT'\alpha_i\,(T')\,,$$

$$\frac{d\underline{\varepsilon}^P}{dt} = \lambda_P \Theta \left[\sigma_{eq} - \sigma_Y\left(T, \varepsilon_{eq}^P\right)\right] \underline{s}\,, \qquad \frac{d\underline{\varepsilon}^{TP}}{dt} = 3\,\frac{\Delta\varepsilon_{A\to F}^T}{\sigma_Y^A}\,\ln(f_A)\,\frac{df_A}{dt}\,\underline{s},$$

$$\frac{d\underline{\varepsilon}^{FF}}{dt} = \left(\frac{d\underline{\varepsilon}}{dt} - \frac{d\underline{\varepsilon}^T}{dt}\right)\,\Theta\,(T\,-\,T_m)\,, \qquad \mathrm{Tr}\left(\underline{\varepsilon}^{FF}\right) = 0, \tag{8.36}$$

$$\underline{s} \equiv \underline{\sigma} - \frac{\mathrm{Tr}\,(\underline{\sigma})}{3}\,\mathbf{I}, \qquad \sigma_{eq} \equiv \sqrt{\frac{3}{2}\,\underline{s}:\underline{s}}\,, \qquad \frac{d\varepsilon_{eq}^P}{dt} + \gamma\,(T)\,\varepsilon_{eq}^P = \sqrt{\frac{3}{2}\,\frac{d\underline{\varepsilon}^P}{dt}:\frac{d\underline{\varepsilon}^P}{dt}}\,.$$

Thermal and metallurgical strain rates are caused by changes of the thermal strain, $d\varepsilon_i^T = \alpha_i(T)dT$, and of the volume fractions df_i of the various phases, respectively (Fig. 8.13). Nonzero plastic strain rates proportional to the stress deviator $\underline{s}$ occur when the equivalent stress σ_{eq} reaches the yield stress σ_Y [59]. The equivalent accumulated plastic strain ε_{eq}^P is a measure of the dislocation density produced and determines the influence of plastic strain on the yield stress (strain hardening). At elevated temperatures dislocations may anneal. This recovery is described in the differential equation (8.36) for ε_{eq}^P by a damping term with an Arrhenius type factor $\gamma(T)$. During phase transformations (in this case from the face-centred cubic austenite to a body-centred cubic phase in steels) additional plastic flow depending on transformation rates and density changes takes place at stresses much below the yield stress (transformation plasticity [60–65]). Temporarily molten regions or coatings deposited in the liquid state are able to adapt to the local strain state by fluid flow ($\underline{\dot{\varepsilon}}^{FF}$).

Any inelastic strain increment leads to changes of the distributions of stress and total strain. Since the plastic strain rate itself depends on the stress, this relationship becomes non-linear and stress calculations require an iterative approach.

8.4.2 Phase Transformations

A large number of materials undergo lattice transformations during heating and cooling (see also Chapter 7 of this book) which may be connected with changes of their thermo-physical and mechanical properties such as density, thermal expansion, and yield stress, as well as with recovery processes [66] and transformation plasticity [60–65]. Such phase transformations, in particular the formation of martensite in steels, may have a substantial influence on the stress history.

The transformation of ferritic steels to austenite during heating and the reverse transformations during cooling to ferrite/pearlite, bainite, or martensite are most important for technical applications. The formation of austenite is accompanied by a local increase in the density (Fig. 8.13) and a decrease of the yield stress leading to enhanced plastic deformation during thermal expansion or contraction. In the case of low cooling rates the austenite is transformed back by diffusion controlled mechanisms into the equilibrium phases ferrite and pearlite or the intermediate phase bainite. In the case of rapid cooling these processes are suppressed and the austenite is suddenly transformed by a military transformation into the hard non-equilibrium phase martensite, which contains a large excess content of carbon locked at interstitial places. Accordingly, the required volume per atom as well as the hardness and the yield strength are strongly enhanced by this transformation.

In the laser cladding of steels the strongly heated layer below the coating may be transformed into martensite during rapid cooling. The related volume expansion leads to local compressive stresses which are balanced by enhanced tensile stresses especially in the coating. Moreover, the substrate can be stiffened by this martensite layer, which therefore counteracts bending distortion caused by the contraction of the coating. Thus, suppressing the formation of martensite, by preheating for example (see Section 8.4.5), may have two effects: the reduction of stress and plastic strain in the coating on the one hand and an increased bending distortion on the other hand.

Simulation of the evolution of stress requires a detailed knowledge of the appropriate phase transformation kinetics. The kinetics of diffusion-controlled phase transformations can be modelled by means of the kinetic equations

$$\left(\frac{\partial f}{\partial t}\right)_T = n\left(T\right) \frac{f_{equ}\left(T\right) - f\left(T, t\right)}{\tau\left(T\right)} \left[\ln\left(\frac{f_{equ}\left(T\right)}{f_{equ}\left(T\right) - f\left(T, t\right)}\right)\right]^{1 - \frac{1}{n\left(T\right)}}$$

$$\xrightarrow[dT/dt=0]{} \qquad f\left(T\right) = f_{equ}\left\{1 - \exp\left[-\left(t/\tau\right)^n\right]\right\}, \tag{8.37}$$

given by Johnson, Mehl, Avrami [67–70], which describe the approach of the phase proportion $f(t)$ considered to that value $f_{equ}(T)$ which is thermodynamically (meta)stable at the given temperature T. The temperature dependent parameters $f_{equ}(T)$, $\tau(T)$, and $n(T)$ are derived from isothermal transformation diagrams. In the special case $n = 1$ we arrive at the Leblond model [71]

$$\frac{df\left[T\left(t\right), t\right]}{dt} = \frac{f_{equ}\left(T\right) - f\left[t\right]}{\tau\left(T\right)} k_L\left(\frac{dT}{dt}\right). \tag{8.38}$$

The factor $k_L(\dot{T})$ enables a more realistic application of this formula to continuous heating or cooling processes. The parameters $f_{equ}(T)$, $\tau(T)$, and $k_L(\dot{T})$ are usually obtained by fitting the solutions of (8.38) to adequate time-temperature dissolution and time-temperature transformation (TTT)

diagrams. Since laser cladding is a welding process the corresponding TTT diagrams should be used.

The formation of martensite during cooling depends on the temperature and the temperature rate only and is described by the Koistinen-Marburger formula [72],

$$\frac{df_M}{dt} = \beta \left\langle -\frac{dT}{dt} \right\rangle \{f_{A0} - f_M [T(t)]\}$$

$$\Rightarrow f_M [T(t)] = f_{A0} \{1 - \exp[\beta(T(t) - T_{MS})]\}, \qquad (8.39)$$

which can be extended as follows to the case when the formation of martensite is finished at a finite temperature T_{MF}:

$$\frac{df_M}{dt} = \beta \left\langle -\frac{dT}{dt} \right\rangle \frac{T_{MS} - T_{MF}}{T - T_{MF}} (f_{A0} - f_M)$$

$$\Rightarrow f_M = f_{A0} \left[1 - \left(\frac{T - T_{MF}}{T_{MS} - T_{MF}} \right)^{\beta(T_{MS} - T_{MF})} \right]. \qquad (8.40)$$

Here f_{A0} is the austenite proportion left over after cooling down to the martensite start temperature T_{MS}, and $\beta \approx 0.011\,\mathrm{K}^{-1}$ is a constant.

8.4.3 FEM Model and Results

Accurate calculations of laser induced stresses can be performed only by numerical techniques using a commercial finite element code for example. That requires the geometry of the work piece including the actual state of the coating and the effective heat source distribution to be known at each moment. One possibility for obtaining this information is to model the entire coating in an inactive state before starting the calculations. During the transient calculation the initially inactive elements of the bead are activated at that front at which the bead is actually generated, that is to say, at the moving melt pool surface (Fig. 8.8) calculated earlier by the process simulation. This activation is performed as a phase transition from a virtual initial phase having extremely low values of the specific heat and of Young's modulus, which ensures that no action can be exerted on the real work piece by these inactive elements.

Heat input at the melt pool surface has to be described by a body source within a thin transition layer instead of being given by a surface source as usual, since the front moves relative to the mesh which is fixed in the body, thereby crossing and activating its elements [23].

This layer fits the shape of the melt pool surface calculated previously and described by the function (8.22) with the correction (8.24), whereas the
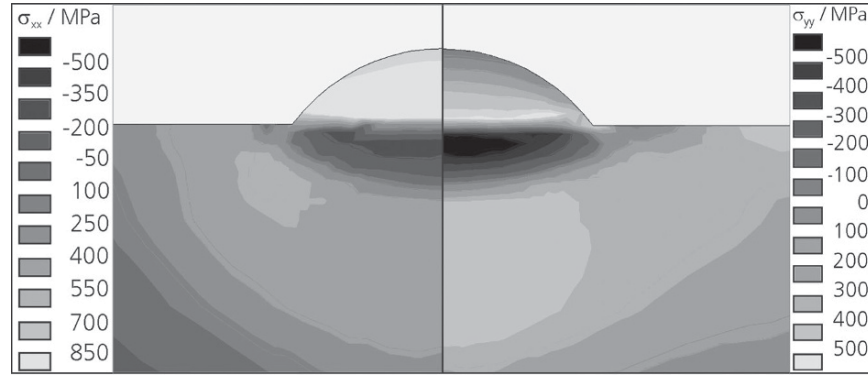
Fig. 8.14. Longitudinal (left hand side) and transverse (right hand side) residual stress distributions on a cross section through a single weld bead (Stellite 21 on AISI1045 steel, feed rate: $10\,\mathrm{mm\,s^{-1}}$, bead height: $0.5\,\mathrm{mm}$, bead width: $2\,\mathrm{mm}$), calculated by FEM.

projection of the power density distribution onto the $x - y$ plane (substrate surface plane z = 0)

$$q_2\left(x - v\,t,\, y\right)\ = j_E^L\left(x - v\,t,\, y,\, 0\right) + j_E^P\left(x - v\,t,\, y,\, 0\right) - L_m\,j_M^*\left(x - v\,t,\, y,\, 0\right),\tag{8.41}$$

is derived from the mass and heat flow densities (8.8), (8.13) and (8.15).

Care is required in choosing the size of the elements and the length of the time steps if phase transformations are involved. The martensite zone in particular has to be meshed very densely. Moreover, phase transformations occur in rather small temperature intervals, so serious errors can be caused by time steps which are too large if the automatic time step control does not take into account the phase transformation kinetics.

As an example of the results of such finite element stress calculations, Fig. 8.14 shows the computed distributions of the longitudinal stress, σ_{xx}, and of the transverse stress, σ_{yy}, for a single weld bead after cooling down to room temperature when a cobalt alloy coating was deposited on AISI1045 steel. Tensile stresses are found in the coating and in that part of the substrate which was plastically compressed during heating. Between these two tensile regions, close to the substrate surface, there is a strip with strong compressive stresses resulting from the formation of martensite. Weak compressive stresses extending from these zones are caused by the necessary mechanical balance. The longitudinal stress along a single bead is generally greater than the corresponding transverse stress [50].

A real coating consists of a lot of overlapping beads or even several layers deposited one over the other. The residual stress distribution in such a coating is sensitively influenced by the thermal and mechanical interaction
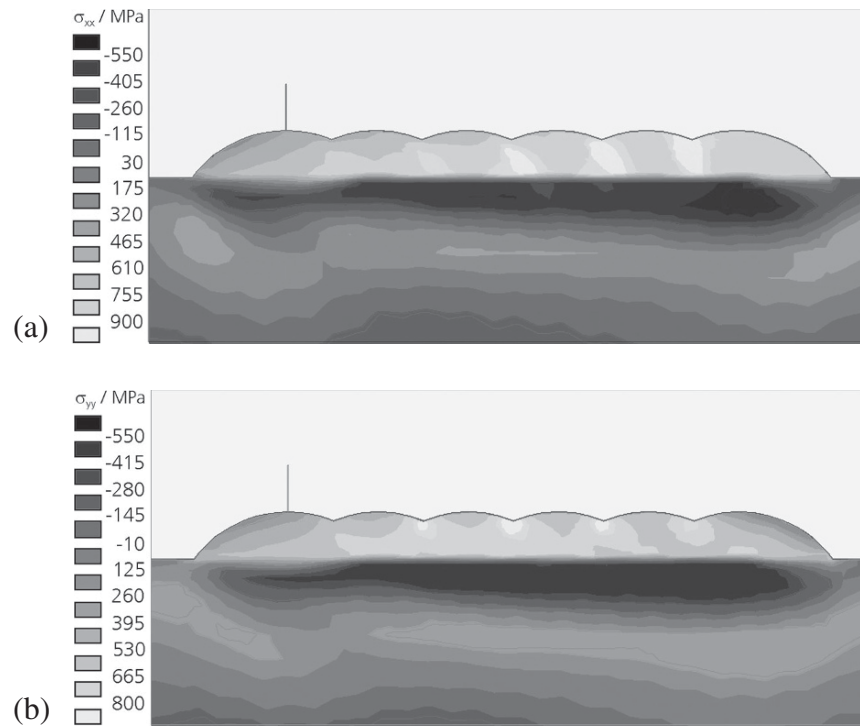
Fig. 8.15. Distributions of longitudinal (a) and transverse (b) residual stress on a cross section through six overlapping beads created one after the other from the left to the right (Stellite 21 on AISI1045 steel, feed rate: $10\,\mathrm{mm\ s^{-1}}$, bead height: $0.5\,\mathrm{mm}$, width of the first bead: $2\,\mathrm{mm}$), calculated by FEM.

of the various beads during reheating and cooling [51]. Figure 8.15 visualises the residual longitudinal and transverse stress distributions on a cross section through an ensemble of six overlapping beads obtained by means of FEM. Obviously, the largest tensile stresses are found in the overlap regions of neighbouring beads, which were strongly reheated and plastically compressed during the subsequent laser pass.

8.4.4 Simplified Heuristic Model

The finite element method is a very flexible and powerful tool, which is suitable even for very complex cases, but, unfortunately, it also has some disadvantages: performing accurate three-dimensional transient stress calculations with phase transformations for many overlapping weld beads requires a large number of elements and many time steps leading to a correspondingly substantial amount of computation time (several days on a personal computer). Parameter studies therefore become very expensive. Moreover, the
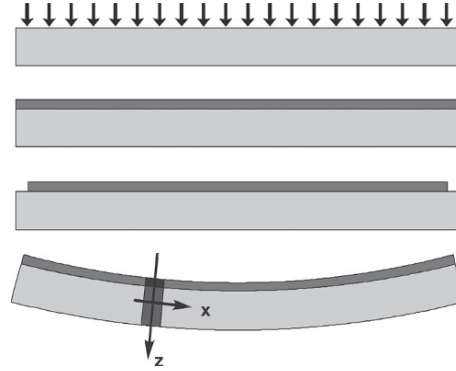
Fig. 8.16. Simplified heuristic model for an approximate estimation of stress and strain histories in laser cladding. Far away from the lateral boundaries of the plate, stresses and strains are merely functions of z and hence need to be calculated in the highlighted column only.

origin of the numerical results is not really transparent and it is difficult to detect hidden sources of error. Monitoring of intermediate results is not easy because of the large amount of data. For these reasons FEM calculations alone have only a restricted benefit for an improved understanding of the essentials of stress histories.

A much simplified model of the evolution of thermal stresses caused by coatings on planar substrates is therefore used as an additional tool, which is able to give qualitative impressions of the evolution of stress and strain profiles perpendicular to the surface considered and of their dependence on process parameters and material properties.

A planar plate is considered in the x-y plane whose thickness is d which is small compared to the other dimensions. One side of the plate is covered by an initially liquid coating in such a way that the derivatives of the resulting stress and strain components with respect to x and y are clearly smaller than those with respect to z. This condition is best satisfied at large Péclet numbers, $vw \gg \kappa$, meaning that feed rates are large and the beads wide. Except at the lateral plate boundaries, the normal stress σ_{zz} is nearly zero under these conditions, and the total strain components in the x-y plane are linear functions of z describing homogeneous bending and lateral expansion (Fig. 8.16):

$$\varepsilon_{xx} = \varepsilon_0^x + \frac{z}{R_x}, \quad \varepsilon_{yy} = \varepsilon_0^y + \frac{z}{R_y},$$

$$\sigma_{xx}(z) = \frac{E[T(z)]}{1-\nu}\left(\varepsilon_{xx} - \varepsilon_{xx}^I\right), \quad \sigma_{yy}(z) = \frac{E[T(z)]}{1-\nu}\left(\varepsilon_{yy} - \varepsilon_{yy}^I\right), \qquad (8.42)$$

$$\sigma_{zz}(z) = 0.$$
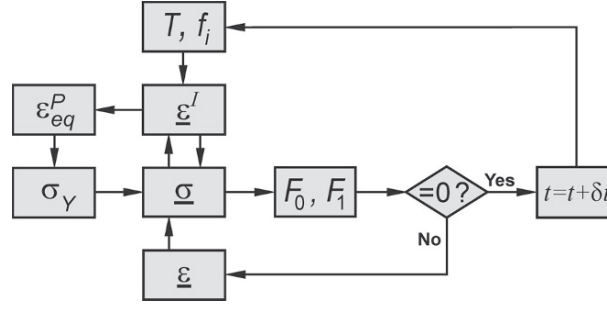
Fig. 8.17. Scheme of stress calculation in the heuristic model.

Equivalently, any straight line crossing the plate must remain straight during thermal treatment. This is a rather stringent restriction which may lead to an overestimate of stresses and plastic strain. The mean strain values, ε_0^x and ε_0^y, as well as the radii of curvature, R_x and R_y, have to be determined from the integral conditions of the mechanical balance (8.35); in the absence of external forces, they read:

$$
\begin{pmatrix} F_n^x \\ F_n^y \end{pmatrix} \equiv \int_{-d/2}^{d/2} dz\, z^n \begin{pmatrix} \sigma_{xx}(z) \\ \sigma_{yy}(z) \end{pmatrix} = \int_{-d/2}^{d/2} dz\, z^n \frac{E\,[T\,(z)]}{1-v} \begin{pmatrix} \varepsilon_0^x + \dfrac{z}{R_x} - \varepsilon_{xx}^I(z) \\ \varepsilon_0^y + \dfrac{z}{R_y} - \varepsilon_{yy}^I(z) \end{pmatrix}
$$

$$
= \begin{pmatrix} 0 \\ 0 \end{pmatrix}, n = 0,\ 1. \tag{8.43}
$$

Stress and strain in the plate can now be calculated as shown in Fig. 8.17.

First the three-dimensional steady state temperature field caused by the moving laser beam, including the local heating and cooling rates, is determined by means of Rosenthal's solution, (8.26). Then the kinetic equations (8.37) to (8.40) provide the related local changes in the proportions of phases, which are used to calculate the thermo-metallurgical strain increments at the given time by means of (8.36). The stresses are determined from (8.42) using the total strains from the last iteration or the last time step. If the resulting equivalent stress reaches the yield stress, the plastic strain rate also has to be computed. If the residual forces $F_{0,\,1}^{x,\,y}$ do not vanish the constants $\varepsilon_0^{x,y}$ and $R_{x,y}$ have to be recalculated by solving (8.43), and stresses, inelastic strains, and the yield stress (in the case of strain hardening) are corrected accordingly, etc. This cycle ends and the next time-step is initiated when the residual forces fall below a prescribed threshold.

Note: the derivatives in the x-y plane are only neglected in the mechanical calculations. The phase transformation kinetics and thus the thermo-metallurgical strain, which is the origin of stress, are therefore calculated correctly. The lateral heat flow in the plate, which causes gradual work
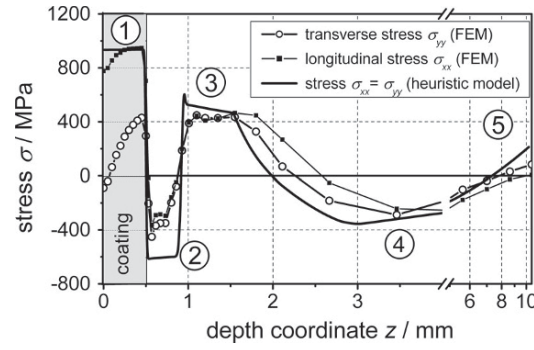
Fig. 8.18. Longitudinal and transverse stress profiles below a single bead across the plate (calculated by FEM) and stress profile across a completely coated plate obtained by the heuristic model. The figure shows the influence of the simplifications of the heuristic model on the stress profile. Feed rate: $10\,\mathrm{mm\,s^{-1}}$, coating thickness: $0.5\,\mathrm{mm}$, plate thickness: $10\,\mathrm{mm}$.
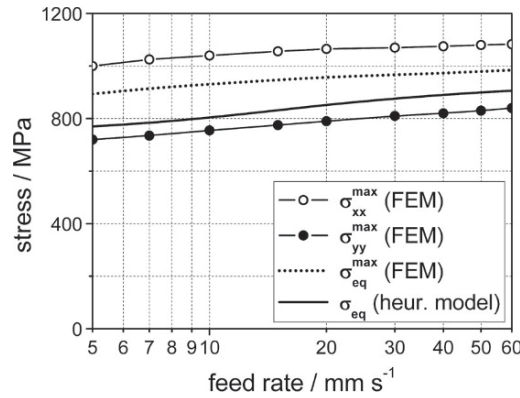
Fig. 8.19. Maximum values of longitudinal (σ_{xx}), transverse (σ_{yy}), and equivalent stress (σ_{eq}) in a single bead vs feed rate as calculated by FEM [23], compared with the equivalent stress of the heuristic model. Feed rate: $10\,\mathrm{mm\ s^{-1}}$, plate thickness: $20\,\mathrm{mm}$, bead height: $0.5\,\mathrm{mm}$, bead width: $2\,\mathrm{mm}$.

piece heating, is taken into account. Errors can however occur in calculating total strain, plastic strain, and stress, especially at low Péclet numbers.

The heuristic model therefore yields rough but qualitatively correct estimates of stress and strain profiles across the plate (Fig. 8.18) and of their dependence on process parameters (Fig. 8.19) and material properties, but no precise stress values. Stress and plastic strain may be overestimated. The model enables very fast calculations (within a few seconds) and an improved understanding of those physical processes which are essential for stress
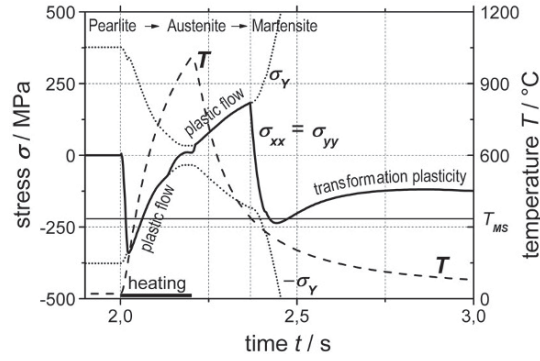
Fig. 8.20. Part of the stress history $\sigma_{xx}(t) = \sigma_{yy}(t)$ in a depth $z = 0.25\,\mathrm{mm}$ below the coating (Stellite 21) in a AISI1045 steel substrate, showing the influence of the temperature $T(t)$, the phase transformations, the yield stress $\sigma_Y(t)$, and the transformation plasticity (heuristic model).

evolution (Fig. 8.20), but for safety occasional spot checks by FEM are required. This model, however, is not able to describe local variations of stress and strain within the x-y plane, caused, for example, by overlapping tracks as in Fig. 8.15, or by the stresses at the lateral boundaries of the plate or the coating!

The following examples demonstrate various applications of the model.

In Fig. 8.18 longitudinal and transverse stress profiles below a single bead across the plate, obtained by an FEM calculation, are compared with the corresponding result for a completely coated plate obtained by means of the heuristic model. In the coating all these profiles show tensile stresses (1) due to thermal contraction. A martensite layer with pronounced compressive stresses (2) exists below the coating followed by a region (3) with tensile stresses due to plastic compression during heating. Soft compressive stresses are found in the middle of the substrate (4) for reasons of mechanical balance. Besides, tensile stresses (in the case of a single bead transverse tensile stress only) may occur at the bottom of thin plates (5) due to plate bending.

Figure 8.19 compares the results of the FEM [23] model and of the heuristic model for the dependence of the stresses in a single bead on the feed rate. All curves show approximately the same slope. The equivalent stress obtained by the heuristic model appears smaller than the corresponding FEM result since the latter gives the maximum stress values in the bead, whereas the heuristic model yields average values. The FEM calculation time amounted to about one week, the heuristic model needed three minutes.

Figure 8.20 visualises the evolution of stress in the substrate just below the coating showing the influence of the various phase transformations, of plastic flow during heating and cooling, and of transformation plasticity during laser treatment and immediately afterwards.
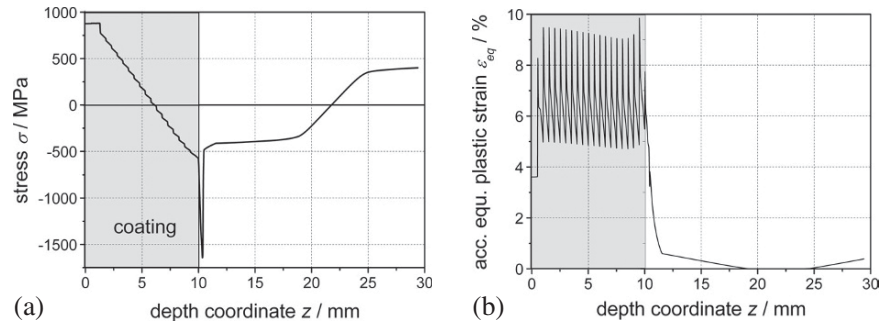
Fig. 8.21. Stress and accumulated plastic strain profiles for a 10 mm thick coating (Stellite 21) consisting of 20 single layers on a 20 mm thick substrate (AISI1045).

The build-up of three-dimensional structures by laser cladding requires the deposition of a large number of layers. Their stress states are changed substantially by every new passage of the laser beam as a consequence of reheating, thermal expansion and contraction, as well as plastic deformation. Hence, after the end of treatment the greatest tensile stresses will be found in the uppermost layers, which have contracted with respect to the layers below. Large compressive stresses may arise in the substrate and in the first deposited layers, since the zero stress level is permanently changed according to the integral conditions (8.35) of the mechanical balance. The simulation of these processes by a finite element calculation would be very time-intensive.

Figure 8.21 shows profiles of the stress and the equivalent plastic strain after the deposition of 20 layers forming a 10 mm thick coating on a 20 mm thick substrate, calculated by means of the heuristic model. Repeated reheating and cooling leads to substantial plastic strain which may cause cracking. The related structural damage, however, may also anneal during reheating to high temperatures. This last effect has not been considered in Fig. 8.21 since the required material data is not yet available.

8.4.5 Crack Prevention by Induction Assisted Laser Cladding

Cracks will arise in a coating if the ultimate tensile strength or the fracture strain of the material are exceeded. In order to reduce the danger of cracking the laser induced temperature gradients should be minimised and phase transformations with large density changes, as in the formation of martensite for example, should be suppressed. This can be realised by preheating the entire work piece in a furnace or by local preheating of the process zone by means of an inductor (see Fig. 8.22).

Preheating in a furnace yields a uniform preheating temperature throughout the entire work piece but can hardly be integrated into a technological process.
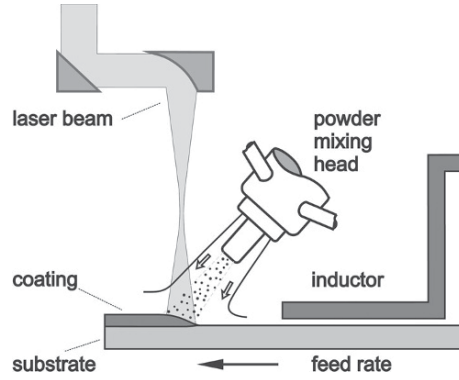
Fig. 8.22. Scheme for laser cladding with inductive preheating.

Resistive heating due to electromagnetic induction generates the following three-dimensional heat source within a narrow surface layer of thickness δ (skin effect),

$$q_3\left(x,\,y,\,z\right) = q_2\left(x,\,y\right)\exp\left(-\frac{z}{\delta}\right), \quad \delta = \sqrt{\frac{\rho_{el}\left(T\right)}{2\,\mu\left(T\right)\,\mu_0\omega}}, \qquad (8.44)$$

where $q_2(x,\,y)$ depends on the inductor shape and ω is the angular frequency of the alternating current applied. The penetration depth δ depends on the electrical resistivity ρ_{el} and the magnetic permeability μ and thus on the temperature. Hence δ is continuously rising during heating and will strongly increase in ferromagnetics when the Curie point is exceeded. This effect can be approximately accounted for in (8.44) by using a penetration depth which increases overtime according to the rise of temperature in the skin layer. Then the temperature distribution needed for the calculation of stress and strain is obtained by means of Rosenthal's solution (8.26).

The level of residual stress is found to decrease only slightly with increasing preheating temperature in a Stellite coating on the ferritic AISI1045 steel but very strongly if the substrate consists of the austenitic AISI304 steel (Fig. 8.23).

The reason for this effect is, that there are two different sources of tensile stress in a coating which was deposited in the liquid state; the first one is the thermal contraction during rapid cooling down to the average temperature of the body, for example the temperature up to which the body was preheated in a furnace. The second source operates only if the coating contracts more strongly than the substrate. In that case the tensile stress in the coating continues increasing when the whole body is uniformly cooling down to the ambient temperature. In the opposite case the stress in the coating decreases. Preheating can only reduce stresses caused by the first of these two
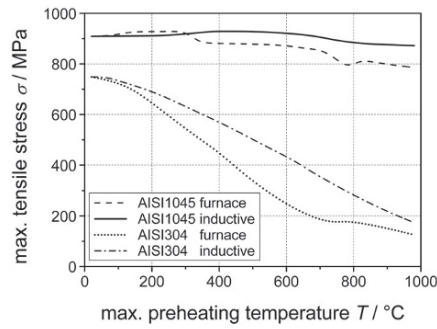
Fig. 8.23. Influence of the maximum (inductive or furnace) preheating temperature on the maximum stress in a Stellite 21 coating on AISI1045 and AISI304 steels (calculated by means of the heuristic model).
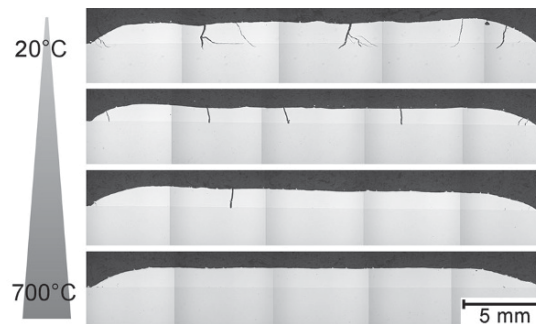
Fig. 8.24. Decrease of the crack probability with increasing temperature of inductive preheating as observed for Stellite 20 coatings ($\approx$58 HRC), consisting of four layers, on AISI1045 steel (feed rate: $10\,\mathrm{mm\ s^{-1}}$).

mechanisms. The effect of preheating on the stress level in the coating can therefore differ markedly for the various material pairs.

Furthermore, preheating has to ensure that no martensite is formed in the substrate since the latter tends to amplify the tensile stresses in the coating by reasons of the required mechanical balance.

Nevertheless, cracks were found to be successfully suppressed by preheating (see Fig. 8.24) even for Stellite coatings on AISI1045 or similar steels [45–48]. Apparently, the plastic deformation, which causes structural damage especially in high-strength materials, is responsible for the occurrence of cracks (see Fig. 8.25).

Thus the effect of inductive preheating can be understood as follows.

Thermal expansion due to inductive preheating may cause an outwards convex curvature of the substrate surface. The coating material, which is initially liquid, adapts by fluid flow to the actual strain of that surface. Thus a coating of given thickness contains more material after inductive preheating
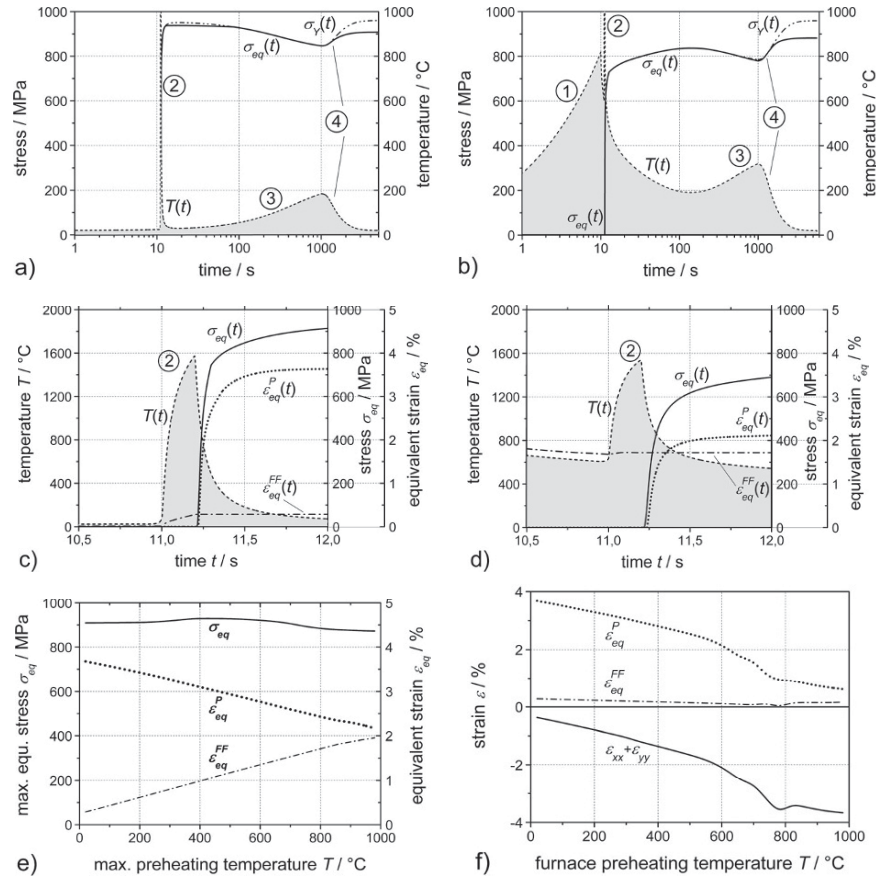
Fig. 8.25. Reduction of stress and plastic strain by (inductive) preheating: The diagrams show on different time scales the temperature-time cycles (grey areas) at the interface between the substrate (AISI1045 steel) and the coating (Stellite 21) as well as the evolution of the equivalent stress (solid lines) at the bottom of the coating without preheating (a, c) and with inductive preheating up to a maximum temperature of 820 °C (b, d). At the position considered the coating is generated in the time interval $11.0\,\mathrm{s} < t < 11.2\,\mathrm{s}$. The temperature-time cycles (a, b) show peaks due to preheating (1), laser treatment (2), and work piece heating by the lateral heat flow (3) as well as the growth of stress during cooling after the laser was shut off (4). For comparison the influence of the maximum preheating temperature on the various kinds of strain is shown in Fig. 8.25e for inductive and in Fig. 8.25f for furnace preheating. With rising preheating temperature the role of the plastic strain ε^P is partially overtaken by the fluid flow strain ε^{FF} in the case of inductive preheating (c, d, e) and by the total strain after furnace preheating (f). Parameter values: inductor size: $100\,\mathrm{mm} \times 20\,\mathrm{mm}$, AC frequency: $10\,\mathrm{kHz}$, coating thickness: $0.5\,\mathrm{mm}$, plate thickness: $10\,\mathrm{mm}$, feed rate: $10\,\mathrm{mm\,s^{-1}}$.

as it would on an unstrained substrate. After solidification this fluid flow strain $\underline{\varepsilon}^{FF}$ is frozen in. If the initially convex bending of the plate is reversed later on during cooling, the excess material in the coating layer softens the tensile stress arising from thermal contraction. The fluid flow strain is able to reduce tensile stresses exactly as a plastic strain but it has the advantage that it does not damage the structure.

Figure 8.25e shows that the fluid flow strain in the coating grows with increasing temperature of the inductive preheating in the same way that the plastic strain decreases. Moreover, at higher temperatures the structural damage caused by plastic strain might be further reduced by dislocation annealing, which, however, has not been taken into account here.

After uniform preheating in a furnace, fluid flow strain does not play a significant role in the coating. In this case the amount of total strain increases with rising preheating temperature to the same extent that plastic strain decreases (Fig. 8.25f). Thus distortion may be strongly enhanced by uniform preheating, whereas the corresponding negative effect on the distortion is much lower in the case of inductive preheating.

8.5 Conclusions and Future Work

The optimisation of processing in laser cladding is a difficult task because of the large number of process parameters involved. Modelling can assist it successfully using analytical as well as numerical methods. In this chapter a series of compatible (semi-)analytical models have been described one being based on the other. They help in the understanding of the physical phenomena involved in laser cladding, enable a rough estimate of the most important quantities, and even allow the possibility of anticipating the required process parameter values by using a computer with a trial and error approach.

The knowledge obtained can help to avoid welding defects on the one hand and substantial dilution on the other hand, to prevent cracking and delamination, and to increase the usable feed rates in order to facilitate the integration of the technology into complex manufacturing lines.

The agreement of the results with experiments is satisfactory but not always very good. The most crucial discrepancies are caused by the thermocapillary flow, which up to now cannot be described by a simple analytical model.

Not all the problems have been satisfactorily solved which are important in the search for optimised sets of process parameters, by far. Laser beam power and spot size, feed rate, and powder rate are the most important process parameters in laser cladding. The bead size is mainly determined by the laser spot width and the amount of powder deposited per unit time, which depends on feed rate and powder rate and on the melt pool temperature. The most critical parameter is the laser beam power density which, together

with the feed rate, determines the temperatures at the melt pool surface and at the interface between substrate and coating and hence is responsible for welding defects or substrate melting and dilution. To a certain extent, it can be optimised by means of the proposed BEM model, thereby approximately taking into account the effect of thermocapillary flow by an enhanced thermal conductivity of the melt pool.

In addition, particle size and speed, the particle trajectories, and the properties of the gases used influence the results. Preheated or even melted powder particles improve the process efficiency and the bead quality since they are easily absorbed by the melt pool. Small and slow particles are preheated greatly by the laser beam, which, however, may thereby be screened to such an extent that the remaining power density is not sufficient for substrate melting. This will happen especially at very high feed rates when the powder rate J has to be substantially increased.

Several problems still have to be solved in order to achieve greater feed rates, which would be very desirable from a technological point of view. The reduction of beam shadowing requires comparatively large and fast powder particles. The related increase of the momentum and kinetic energy transfer to the melt pool may disturb the bead formation and thus reduce the quality. Moreover, high feed rates imply large temperature gradients. Thus the achievable bead height becomes smaller, and it will be more difficult to avoid both substrate melting and welding defects.

Large temperature gradients are also the cause of stress and distortion. Preheating by means of inductors which can be directly integrated into the cladding process has been found to be an appropriate tool to reduce temperature gradients, to avoid cracks, and even to reach higher feed rates. However, the suppression of bending distortion when coatings are deposited on thin sheets remains an unsolved problem.

A simple heuristic model has been used here for quick parameter studies in order to understand rather better the influence of material properties and process parameters, and the effect of inductive preheating on the evolution of stresses, plastic strain, and bending distortion in a planar plate during cladding.

Further refinements of the theory could include the thermal and mechanical interaction of the gas flow with the particles during their flight and the influence of thermocapillary flow on the temperature field, bead shape, dilution, and solidification structure.

Most of the models presented refer to the generation of one single bead. This is sufficient for a better understanding of the most important physical phenomena. For more complex cases simplified models are needed which are, nevertheless, able to describe the effects connected with bead overlap and repeated reheating during a large number of laser passes in an acceptable calculation time.

References

1. Li L, Steen WM, Hibberd RB (1990) Computer aided laser cladding. In: Bergmann HW, Kupfer R (eds): Proc. ECLAT'90, Erlangen (D), Arbeitsgemeinschaft Wärmebehandlung und Werkstofftechnik e.V. (AWT) 1: 355–369
2. Steen WM (1986) Laser surface cladding. In: Draper and Mazzold (eds), Laser Surface Treatment of Metals, Martinus Nijhoff, Dordrecht, 369–387
3. Weerasinghe VM, Steen WM (1983) Computer simulation model for laser cladding. ASME HTD 29: 15–23
4. Li W-B, Engström H, Powell J, Tan Z, Magnusson C (1995) Modelling of the laser cladding process – preheating of the blown powder material. Lasers in Engineering 4: 329–341
5. Gedda H, Li W-B, Engström H, Magnusson C, Powell J, Wahlström G (2001) Energy redistribution during CO_2 laser cladding. Proc ICALEO 2001, Jacksonville (USA) 701
6. Marsden CF, Frenk A, Wagnière J-D, Dekumbis R (1990) Effects of injection geometry on laser cladding. In: Bergmann HW and Kupfer R (eds): Proc. ECLAT'90, Erlangen (D), Arbeitsgemeinschaft Wärmebehandlung und Werkstofftechnik e.V. (AWT) 1: 535–542
7. Marsden CF, Houdley AFA, Wagnière J-D (1990) Characterisation of the laser cladding process. In: Bergmann HW and Kupfer R (eds): Proc. ECLAT'90, Erlangen (D), Arbeitsgemeinschaft Wärmebehandlung und Werkstofftechnik e.V. (AWT) 1: 543–553
8. Marsden CF, Frenk A, Wagnière J-D (1992) Power absorption during the laser cladding process. In: Mordike BL (ed) Laser Treatment of Materials, Proc. ECLAT'92, Göttingen (D), DGM-Informationsgesellschaft Verlag: 375–380
9. Lin J (1999) A simple model of powder catchment in coaxial laser cladding. Optics & Laser Technology 31(3): 233–238
10. Lin J (1999) Temperature analysis of the powder streams in coaxial laser cladding. Optics & Laser Technology 31: 565–570
11. Lin J, Hwang B-C (1999) Coaxial laser cladding on an inclined substrate. Optics & Laser Technology 31: 571–578
12. Lin J, Hwang B-C (2001) Clad profiles in edge welding using a coaxial powder filler nozzle. Optics & Laser Technology 33: 267–275
13. Liu C-Y, Lin J (2003) Thermal processes of a powder particle in coaxial laser cladding. Optics & Laser Technology 35(2): 81–86
14. Yoshida T, Akashi K (1977) Particle heating in a radio-frequency plasma torch. J Appl Phys 48(6): 2252–2260
15. Hoadley AFA, Rappaz M (1992) A thermal model of laser cladding by powder injection. Metall Trans B 23B(5): 631–642
16. Ollier B, Pirch N, Kreutz EW, Schlüter H (1992) Cladding with laser radiation: properties and analysis. In: Mordike BL (ed) Laser Treatment of Materials, Proc. ECLAT'92, Göttingen (D), DGM-Informationsgesellschaft Verlag:687-692
17. Ollier B, Pirch N, and Kreutz EW (1995) Ein numerisches Modell zum einstufigen Laserstrahlbeschichten (A numerical model of single-stage laser cladding). Laser und Optoelektronik 27(1): 63–70
18. Picasso M, Hoadley AFA (1994) Finite element simulation of laser surface treatments including convection in the melt pool. Int J Num Meth Heat Fluid Flow 4: 61–83

19. Pirch N, Kreutz EW, Möller L, Gasser A, and Wissenbach K (1990) Melt dynamics in surface processing with laser irradiation. In: Bergmann HW, Kupfer R (eds): Proc. ECLAT'90, Erlangen (D), Arbeitsgemeinschaft Wärmebehandlung und Werkstofftechnik eV (AWT) 65–80

20. Schmitter H (1994) Simulation des einstufigen Laserbeschichtens mit FIDAP (Simulation of the single-stage laser cladding). Student research project, IFSW Stuttgart (D)

21. Picasso M, Marsden CF, Wagniere J-D, Frenk A, Rappaz M (1994) A simple but realistic model for laser cladding. Metallurgical and Materials Transactions B 25B: 281–291

22. Ahlström J, Karlsson B, Niederhauser S (2004) Modeling of laser cladding of medium carbon steel - a first approach. J Phys IV France 120: 405–412

23. Brückner F, Lepski D, Beyer E (2007) Modeling the influence of process parameters and additional heat sources on residual stresses in laser cladding. J Thermal Spray Technology 16(3): 355–373

24. Choi J, Han L, Hua Y (2005) Modeling and experiments of laser cladding with droplet injection. Trans ASME 127: 978–986

25. Han L, Liou FW, Phatak KM (2004) Modeling of laser cladding with powder injection. Metallurgical and Materials Transactions B 35B: 1139–1150

26. Han L, Phatak KM, Liou FW (2005) Modeling of laser deposition and repair process. J Laser Applications 17(2): 89–99

27. Kaplan AFH, Groboth G (2001) Process analysis of laser beam cladding. Journal of Manufacturing Science and Engineering 123: 609–614

28. Lepski D, Eichler H, Fux V, Scharek S, Beyer E (2001) Calculating temperature field and single track bead shape in laser cladding with Marangoni flow using Rosenthal's solution. Proc LIM - Lasers in Manufacturing, Wissenschaftliche Gesellschaft Lasertechnik e.V. (WLT), Munich (D) 167–177

29. Lepski D, Eichler H, Fux V, Scharek S, Beyer E (2002) Simulation of the powder injection laser beam cladding process. Proc Internat Conf THE Coatings in Manufacturing Engineering and EUREKA Partnering Event, Thessaloniki (GR) 529–538

30. Lepski D, Eichler H, Scharek S, Fux V, Zoestbergen E, Beyer E (2003) Simulation software for laser beam cladding in manufacturing. Proc 16th Meeting on Mathematical Modeling of Materials Processing with Lasers (M⁴PL16), Igls (A)

31. Lepski D, Eichler H, Scharek S, Fux V, Nowotny St, Beyer E (2003) Simulation of laser beam cladding by powder injection. Int Conf Laser 2003 – World of Photonics, Munich (D)

32. Pirch N, Mokadem S, Keutgen S, Wissenbach K, Kreutz EW (2004) 3D-model for laser cladding by powder injection. In: Geiger M and Otto A (eds): Laser Assisted Net Shape Engineering 4, Proc LANE 2004, Erlangen (D) 851–858

33. Toyserkani E, Khajepour A, Corbin S (2004) 3-D finite element modeling of laser cladding by powder injection: effects of laser pulse shaping on the process. Optics and Lasers in Engineering 41: 849–867

34. Chin RK (1998) Thermomechanical modelling of residual stresses in layered manufacturing with metals. PhD Thesis, Carnegie Mellon University

35. Chin RK, Beuth JL, Amon CH (1996) Thermomechanical modelling of successive material deposition in layered manufacturing, Proc Solid Freeform Fabrication Symposium, Austin (USA) 507–514

36. Klingbeil NW (1998) Residual stress induced warping and interlayer debonding in layered manufacturing. PhD Thesis, Carnegie Mellon University

37. Klingbeil NW, Beuth JL, Chin RK, Amon CH (1998) Measurement and modelling of residual stress-induced warpage in direct metal deposition processes. Proc Solid Freeform Fabrication Symposium, Austin (USA) 367–374
38. de Deus AM (2004) A thermal and mechanical model of laser cladding. PhD Thesis, University of Illinois
39. de Deus AM, Mazumder J (1996) Two-dimensional thermo-mechanical finite element model for laser cladding. Proc ICALEO 1996, Detroit (USA) 174–183
40. Nickel AH (1999) Analysis of thermal stresses in shape deposition manufacturing of metal parts. PhD Thesis, Stanford University
41. Nickel AH, Barnett DM, Prinz FB (2001) Thermal stresses and deposition patterns in layered manufacturing. Material Science and Engineering A317: 59–64
42. Kahlen FJ, Kar A (2001) Residual stresses in laser-deposited metal parts. J Laser Applications 13(12): 60–69
43. Ghosh S, Choi J (2003) Three-dimensional transient residual stress finite element analysis for laser aided direct metal deposition process, Proc ICALEO 2003, Orlando (USA), CD-Rom No. 908
44. Ghosh S, Choi J (2005) Three-dimensional transient finite element analysis for residual stresses in the laser aided direct metal/material deposition process. J Laser Application 17(3): 144–158
45. Brenner B, Fux V (1999) Induktiv unterstütztes Laserauftragschweißen – ein neues Verfahren zur effektiven Erzeugung hochverschleißbeständiger Randschichten (Induction assisted laser cladding – a new technology for the efficient generation of highly wear protective coatings). Stahl 48–50
46. Brenner B, Fux V, Wetzig A, Nowotny St (1996) Induktiv unterstütztes Laserauftragschweißen - eine Hybridtechnologie überwindet Anwendungsgrenzen (Induction assisted laser cladding - a hybrid technology expands limits of application). Proc ECLAT'96, Stuttgart (D) 1: 469–476
47. Brenner B, Fux V, Wetzig A (1997) Induktiv unterstütztes Laserauftragschweißen (Induction assisted laser cladding). Härterei-Techn. Mitteilungen 52(4): 221–225
48. Fux V und Brenner B (1999) Leistungsfähige Beschichtungsprozesse durch induktiv unterstütztes Laserauftragschweißen (High performance coating technologies by induction assisted laser cladding). Freiberger Forschungshefte B297: 121–130
49. Zhang Y, Xianghua Z, Xiangkai Y (2001) Elimination of laser cladding cracks: thermal control and stress analysis. Proc. ICALEO 2001, Orlando (USA), 705
50. Brückner F, Lepski D, Beyer E (2006) Finite element studies of stress evolution in induction assisted laser cladding. Proc SPIE – XVI Internat Symp on Gas Flow and Chemical Lasers & High Power Lasers Conf., Gmunden (A), paper 63461D
51. Brückner F, Lepski D, Beyer E (2007) FEM calculations of thermally induced stresses in laser cladded coatings. In: F. Vollertsen (ed.) Proc LIM, Lasers in Manufacturing, Munich (D) 97–103
52. Brückner F, Lepski D, Beyer E (2007) Simulation of thermal stress in induction-assisted laser cladding. Proc ICALEO 2007, Laser Institute of America, Orlando (USA), paper 1301: 647–656
53. Rosenthal D (1941) Mathematical theory of heat distribution during welding and cutting. Welding J 20(5): 222–234

54. Bausinger R, Kuhn G, Bauer W, Seeger G, Möhrmann W (1987) Die Boundary-Element-Methode – Theorie und industrielle Anwendung. Expert-Verlag, Ehningen

55. Mazumder J (1987) An overview of melt dynamics in laser processing. Proc High Power Lasers SPIE, The Hague 225

56. Tsotridis G, Rother H, and Hondros ED (1989) Marangoni flow and the shape of the laser melted pools. Naturwiss 76: 216

57. Kirchhoff G (2000) private communication

58. Zoestbergen E, Lepski D, Beyer E (2003) Dual reciprocity BEM applied to temperature field calculations in a laser melt pool. Proc 16th Meeting on Mathematical Modeling of Materials Processing with Lasers (M4PL16), Igls (A)

59. von Mises R (1913) Mechanik der festen Körper im plastisch deformablen Zustand. Göttinger Nachrichten math-phys Kl.: 582–592

60. Fisher FD, Sun QP, Tanaka K (1996) Transformation –induced plasticity (TRIP), ASM 49: 317–364

61. Greenwood GW, Johnson RH (1965) The deformation of metals under small stresses during phase transformations, Proc Roy Soc London Series A, Mathematical and Physical Sciences 283: 403–422

62. Leblond J-B, Mottet G, Devaux JC (1986) A theoretical and numerical approach to the plastic behaviour of steels during phase transformations I: derivation of general relations. Journal of the Mechanics and Physics of Solids 34(4): 395–409

63. Leblond J-B, Mottet G, and Devaux JC (1986) A theoretical and numerical approach to the plastic behaviour of steels during phase transformations II: study of classical plasticity for ideal plastic phases. J Mechanics and Physics of Solids 34(4): 411–432

64. Leblond J-B, Devaux J, Devaux JC (1989) Mathematical modelling of transformation plasticity in steels I: case of ideal plastic phases. Int J Plasticity 5: 551–572

65. Leblond J-B, Devaux J, Devaux JC (1989) Mathematical modelling of transformation plasticity in steels II: coupling with strain hardening phenomena. Int J Plasticity 5: 573–591

66. Aubry C, Denis S, Archambault P, Simon A, Ruckstuhl F (1997) Modelling of tempering kinetics for the calculation of heat treatment residual stresses in steels. In: Ericsson T, Oden M, Andersson A (eds): Proc ICRS-5, 1: 412–417

67. Avrami M (1939) Kinetics of phase change I: general theory. J Chem Phys 7: 103–112

68. Avrami M (1940) Kinetics of phase change II: transformation-time relations for random distribution of nuclei. J Chem Phys 8: 212–224

69. Johnson WA, Mehl RF (1939) Reaction kinetics in process of nucleation and growth. Trans AIME 135: 416–458

70. Mehl RF (1938) The physics of hardenability and the mechanism and the rate of the decomposition of austenite. Proc Symp Hardenability of Alloy Steels, 20th Annual Convention of the American Society of Metals, Detroit

71. Leblond J-B, Devaux J (1984) A new kinetic model for anisothermal metallurgical transformations in steels including effect of austenite grain size. Acta Metall 32(1): 137–146

72. Koistinen DP, Marburger RE (1959) A general equation describing extend of austenite-martensite transformation in pure Fe-C alloys and plain carbon steels. Acta metall 7: 59–60

9

Laser Forming

Thomas Pretorius

BIAS Bremer Institut für angewandte Strahltechnik GmbH, Klagenfurther Straße 2, 28359 Bremen, Germany. `pretorius@bias.de`

Abstract. The use of a laser beam in forming processes was introduced at the end of 20th century and is still under development. The laser beam makes forming technology applicable for industrial use, which formerly had to be done manually due to the lack of reproducibility or flexibility of the heat source used (e.g. straightening of distortion by heating with a gas torch). The main advantages of thermal forming processes are the fact that there's no spring-back effect and that tool and work piece are not in contact during the process. The latter fact also increases the flexibility of the processes, because no special tool is needed. Different geometries, therefore, can be produced by using the same set-up and changing only the process parameters.

Thermal forming is based on the generation of stress and strain fields by elevated local temperatures. The different mechanisms can be grouped as direct thermal forming mechanisms (temperature gradient, residual stress point, upsetting and buckling mechanisms) and indirect thermal forming mechanisms (residual stress relaxation and martensite expansion mechanisms), where the distinguishing criterion is the driving force for the forming process. In addition to the thermal forming mechanisms a non-thermal laser beam forming mechanism (shock wave mechanism) is described in this chapter.

Potential applications arise in the fields of forming, straightening and adjustment for both macro and micro components. Some examples are: rapid prototyping, precision adjustment, removing distortion and creating 3D complex shapes. Current research is concentrating on the mechanisms of thermal forming, on the prediction of the strains and on the heating strategies and path planning in order to obtain a given shape. For the latter especially, a precise prediction of the forming results is necessary. This can be done by modelling the process numerically, which is often done by finite element methods nowadays. The calculation results of FEM simulation of thermal forming processes have a high degree of accuracy if the material parameters and the boundary conditions are defined correctly.

A list of notation and abbreviations is given in Table 9.1.

9.1 History of Thermal Forming

Thermal forming processes have been applied for a long time in various industries. In ship building for example, the flame straightening of welded

Table 9.1. Table of notation and abbreviations.

a	thermal diffusivity
b_1	depth of structure
b_2	width of structure
A	absorption coefficient
BM	buckling mechanism
c_p	specific heat capacity
d_l	laser beam spot diameter on the surface of the sheet = width of the irradiated region
E	elastic modulus
FEM	finite element modelling
k_f	flow stress
l	half width of plastic zone
l_m	width of phase transformation zone
MEM	martensite expansion mechanism
N	numerical parameter
p_l	laser beam power
r_n	normalised laser beam radius
RSPM	residual stress point mechanism
RSRM	residual stress relaxation mechanism
s_0	sheet thickness
s_1	depth of plastic zone
SWM	shock wave mechanism
t	time
$T(x, y, z, t_e)$	temperature at position (x, y, z) after heating for time t_e
T_b	boundary temperature for plastic deformation
t_e	duration of laser heating
TGM	temperature gradient mechanism
UM	upsetting mechanism
v_l	process speed = velocity of the laser beam spot on the surface of the sheet
x, y, z	spatial coordinates
α_b	bending angle
α_{th}	thermal expansion coefficient
ε_{max}	maximum of plastic strain
ε_{pl}	plastic strain
$\varepsilon_{\mathrm{th}}$	thermal strain
λ	heat conductivity
ρ	density

structures is a well-known technique. However, due to difficulties in the reproducibility of the energy output and distribution of the gas torch used and the fact of manual application, the quality of the result depends highly on the skill and experience of the workers. Different heat sources can be used to generate thermal stress in the material which can generate plastic deformation. Some of these sources are: gas torch, induction coil, electron beam, laser beam and plasma jet. Flame bending, the oldest technology, uses a gas torch.

It has some limitations in connection with the variation of process parameters and reproducibility. Induction bending has the advantage of inducing the energy directly into the volume of the work piece, which is beneficial especially for forming of thick parts and/or the application of the upsetting mechanism. Consequently, an application of the induction coil as a heat source is tube bending. An electron beam is possibly the most flexible heat source available for thermal bending. Due to the fact that the beam can be moved very fast to different positions on the surface of the specimen, nearly any power distribution on the surface can be generated. The electron beam has some disadvantages, however, which prevent its application, especially in industrial uses. The most important is surely the fact that for the generation of the electron beam and to preserve the beam quality a vacuum is needed. A vacuum chamber represents considerable expenditure of money and effort on the creation of an environment which may often be unsuitable or impractical, especially for the processing of large parts. With the ongoing development of lasers to higher output powers, cheaper systems and higher beam quality, the application of the laser beam for materials processing became more and more favourable. Systematic research of laser beam bending and forming processes started in the mid of the 1980s [1, 2]. Research activity continues to increase steadily, as can be seen from the number of publications in this field [3]. In combination with scanner systems, the laser beam has a flexibility with regard to processing parameters which is nearly as high as for the electron beam, but without the need of a vacuum. For induction bending on the contrary, the size and shape of the heat source is fixed by the shape of the coil used. The energy transferred into the specimen by a laser beam can be controlled very precisely, if necessary by a closed-loop control, which guarantees a very high reproducibility. The development of new generations of lasers enabled new processes to be economical. The high power CO_2, diode, fibre and disc lasers became efficient heat sources for the processing of larger parts, whereas increasing beam quality enables very small laser spots on the surface of the part to be achieved and therefore enables the processing of small parts. In 1988 a plasma jet was introduced as an alternative heat source for straightening of thin sheets [4]. A systematic research of plasma jet bending was done later by Male et al. [5] and Pretorius et al. [6]. Using a plasma jet offers cheap thermal energy, compared to the application of laser or electron beam systems, but also has some limitations with regard to reproducibility and variability.

Today, thermal forming is evolving into a highly sophisticated manufacturing technology. Well-defined heat sources like laser beams, plasma jets and induction allow for precise and reproducible heating of a highly localised area and enable process automation. Thermal forming has the potential to be applied in high-volume production of automotive parts and microelectronic devices. Moreover, for line bending and spatial forming of metal components thermal forming can avoid disadvantages of mechanical forming processes such as the spring-back effect, and overcomes accessibility limits, thus enabling the forming of shapes which are unattainable by other methods.

Prediction of the forming result is necessary for process planning, especially for path planning in order to generate 3D shapes. For this task analytical models had to be used for a long time. For curved irradiation paths and complex geometries especially, the process becomes too complicated to be calculated analytically. For these cases numerical modelling is the only possibility for calculating the deformation. With increasing speed and development of fast algorithms, and the construction of computers that can handle large models, numerical simulation of the processes became usable. Nowadays standard FEM simulation is in wide use to calculate the time dependent temperature and stress and strain fields during the process, as well as the residual state. Nevertheless the calculation time can be rather long, which limits the ability to make parameter studies for complex processes. The development of fast calculation methods is therefore a subject of current research activities [7, 8].

9.2 Forming Mechanisms

For laser beam forming processes the thermal forming mechanisms, which can also be activated using other heat sources, can be utilised. The thermal forming mechanisms can be grouped by the driving force, which is responsible for the development of the deformation. The group of mechanisms which can be called *direct* thermal forming mechanisms consists of the mechanisms which use the local thermal expansion which is hindered by some internal or external force, and therefore produces thermal stress which itself results in local plastic deformation if the yield stress of the material is exceeded locally. These mechanisms are:

- temperature gradient mechanism (TGM),
- residual stress point mechanism (RSPM),
- upsetting mechanism (UM),
- buckling mechanism (BM).

If the driving force is not the thermal expansion, but some deformation potential which is already in the material before the process starts and is released due to the local heating of the material, the thermal forming mechanisms can be called *indirect*. This holds for the mechanisms:

- residual stress relaxation mechanism (RSRM),
- martensite expansion mechanism (MEM).

A different way to group the thermal forming mechanisms, which is related to the existence of a temperature gradient in the material thickness direction, was introduced by Vollertsen [9]. For TGM, RSPM and MEM a thermal gradient is necessary, whereas for UM, BM and RSRM a temperature gradient is not necessary. This kind of grouping focuses on the activation of the mechanisms with respect to the process and material parameters.
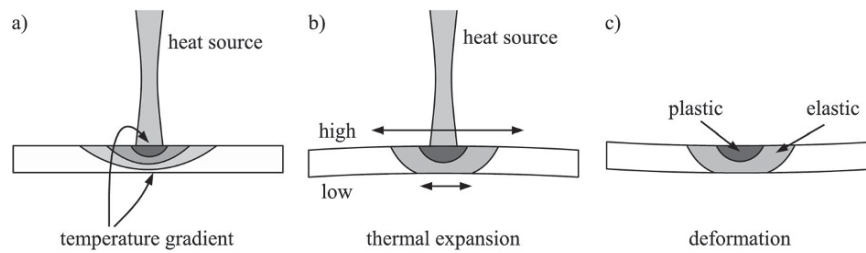
Fig. 9.1. Schematic illustration of TGM.

Additionally to the thermal forming mechanisms, there is also one laser forming mechanism for which no heating of the specimen is necessary. This is therefore a non-thermal forming mechanism:

- shock wave mechanism (SWM).

Laser assisted forming processes are processes in which the laser beam is not used to deform the material, but to change the material parameters in the desired way to enhance the deformation caused by other mechanisms. Examples are laser assisted drilling, forming, cutting or machining of metals. In these processes the laser is used to heat the material locally, which reduces the yield stress and improves the formability of the material. This leads to lower machine forces, longer lifetime of the tools and a reduced cracking risk. Being an additional investment for the equipment, the processes described are an option for such cases, where conventional processes reach their limits.

In this section the different mechanisms are described separately. This facilitates the understanding of the mechanisms, but in real thermal forming processes typically more that one mechanism will be activated. This holds for example for most applications of UM: if the material is heated only from one side a small temperature gradient cannot be avoided, which will activate TGM additionally to UM. If MEM is activated by locally heating steel components, the temperature gradient induced also generates thermal stress, which can be large enough to activate TGM. In this case, which mechanism produces larger deformation and therefore dominates the process depends strongly on the process parameters. As the bending direction of MEM is opposite to the one for TGM not only the bending angle reached but also the direction of the bending depends critically on the process parameters [10].

9.2.1 Temperature Gradient Mechanism

TGM is the thermal forming mechanism mainly used in sheet metal bending and forming. The principle of this mechanism is shown in Fig. 9.1.

The laser beam energy is absorbed locally at the upper surface of the specimen. This induces a temperature gradient over the thickness of the specimen in the irradiation zone; see Fig. 9.1a. Due to the positive thermal expansion

coefficient of most materials the thermal expansion in the irradiated region on the upper side of the sheet is larger than the expansion of the lower side. The different expansions induce a bending of the sheet away from the laser beam (Fig. 9.1b, counter-bending). This bending is not free, because the irradiated region is fixed inside the surrounding parts of the specimen. Stress is therefore induced in the irradiated region of the specimen, which is compressive on the upper side. Additionally, clamping of the specimen can increase this effect. If this thermal stress stays below the yield stress of the material, which is altered (decreased for many materials) due to the local change of the temperature, the deformation of the specimen is fully elastic. After switching off the laser beam and cooling of the specimen no deformation remains in this case. If, on the contrary, the local stress exceeds the temperature dependent yield stress in the irradiated region on the upper side of the sheet, a local upsetting of the material occurs. This means that the upper side of the irradiation region is plastically deformed, i.e. it is shortened and slightly thickened. After switching off the laser beam and cooling of the specimen the thermal expansion of the irradiated region vanishes and the plastic deformation of the upper side remains. This results in a bending of the specimen towards the laser beam; see Fig. 9.1c.

Analytical Modelling of the Temperature Gradient Mechanism

In Vollertsen and Rödle [11] and Vollertsen [9] an analytical model for the calculation of the bending angle produced by the application of TGM in laser beam bending processes is presented. The model consists of two parts: the mechanical calculation and the temperature field calculation.

For the mechanical calculation a model by Hänsch [12] is used. If the plastic zone is smaller than the sheet thickness, the bending angle α_b can be calculated by (radiant measure)

$$\alpha_b = \frac{\varepsilon_{\max} l s_1}{s_0^3}(3\pi s_0 - 8s_1), \tag{9.1}$$

where $2l$ is the width, s_1 the depth of the plastic zone and s_0 the sheet thickness. The maximum plastic strain at the irradiated surface $\varepsilon_{\max}$ is given by

$$\varepsilon_{\max} = \alpha_{th}T(0,0,0,t_e) - \frac{k_f}{E}, \tag{9.2}$$

where α_{th} is the thermal expansion coefficient, k_f the flow stress and E the elastic modulus at the average surface temperature $T(0,0,0,t_e)$ in the centre of the beam.

The time of heating t_e is given by the fraction of the laser beam spot diameter on the surface of the sheet d_l and the process speed v_l

$$t_e = \frac{d_l}{v_l}. \tag{9.3}$$

The temperature field calculation is done by a superposition of the Fourier solution for point heat sources for three-dimensional heat conduction, to make the model usable for finite area heat sources. The result is a function, which is solvable only numerically, but can be approximated in the range which is relevant for laser beam bending processes. Using further simplifications which are necessary to preserve the analytical solvability of the function the spatial distribution of the temperature field in the y and z-directions can be described by

$$T(z,t) = \frac{3}{4} N r_n^{\frac{2}{3}} \exp\left(-\frac{4\sqrt{2}z}{d_l}\right) \tag{9.4}$$

and

$$T(y,t) = \frac{3}{4} N r_n^{\frac{2}{3}} \exp\left(-\sqrt{2r_n}\left(\frac{2z}{d_l}\right)^2\right), \tag{9.5}$$

where the parameter N is calculated as

$$N = \frac{8 A p_l \sqrt{a t_e}}{\pi \lambda d_l^2} \tag{9.6}$$

and the normalised laser beam radius r_n as

$$r_n = \frac{d_l}{4\sqrt{a t_e}}, \tag{9.7}$$

where A is the absorption coefficient, p_l the laser beam power, a the thermal diffusivity and λ the heat conductivity. The average surface temperature in the middle of the laser beam spot at the end of the heating $T(0, 0, 0, t_e)$ can be calculated as

$$T(0,0,0,t_e) = \frac{3}{4} N r_n^{\frac{2}{3}}. \tag{9.8}$$

The width $2l$ and depth s_1 of the plastic region are calculated assuming that the plastic region is equal to the region where the temperature at the end of the heating $T(x, y, z, t_e)$ exceeds a boundary temperature T_b. Inside this region

$$\varepsilon_{pl} = -\varepsilon_{th} \tag{9.9}$$

is assumed, whereas outside the plastic strain ε_{pl} equals zero. An estimation of the size of the plastic zone is given by

$$s_1 = -\ln\left(\frac{4T_b}{3N} r_n^{-\frac{2}{3}}\right) \frac{\sqrt{2 r_n a t}}{2} \tag{9.10}$$

and

$$l = r_n \sqrt{4at} \sqrt{-\frac{1}{\sqrt{2r_n}} \ln\left(\frac{4T_b}{3N} r_n^{-\frac{2}{3}}\right)}. \tag{9.11}$$

The lower limit for the boundary temperature T_b can be assumed to be

$$T_b = \frac{k_f}{E\alpha_{th}}. \tag{9.12}$$

The fact that the surrounding region of the plastic zone is not ideally rigid increases the boundary temperature and makes the determination of the correct value difficult. The boundary temperature, which leads to the correct bending angle, has been found to be dependent on the boundary conditions of the process. The boundary temperature therefore has to be determined by empirical methods, which prevents a direct, accurate analytical calculation of the bending angle depending on the process parameters. For the steels St14 and St37 the boundary temperature lies in the range of $250\,^{\circ}$C to $450\,^{\circ}$C.

Due to the fact that, for a precise calculation, the shape of the specimen and the complex time dependency have to be taken into account for both the temperature field and the mechanical calculations, accurate predictions for the forming results (i.e. the bending angle achieved) can only be made by simulating the process. Analytical calculations can only be used to get results for simple geometries and a limited process parameter range. Effects like the temperature dependency of the material parameters especially (e.g. the decrease of the yield stress with increasing temperature), which can have a significant effect on the result, cannot be considered in analytical calculations in an adequate way.

Numerical Modelling of the Temperature Gradient Mechanism

In the following, the results of a calculation of a laser beam bending process of a sheet will be presented. The material parameters chosen represent an artificial steel material: thermal conductivity $= 40\,\mathrm{W\,m^{-1}\,K^{-1}}$, density $= 8000\,\mathrm{kg\,m^{-3}}$, Young's modulus $= 200\,\mathrm{GPa}$, Poisson's ratio $= 0.3$, thermal expansion coefficient $= 15\,10^{-6}\,\mathrm{K^{-1}}$ and specific heat $= 500\,\mathrm{J\,kg^{-1}\,K^{-1}}$. Most material parameters were taken to be independent of temperature, only in the case of the yield stress was temperature dependency allowed for: yield stress $400\,\mathrm{MPa}$ ($0\,^{\circ}$C), $100\,\mathrm{MPa}$ ($1000\,^{\circ}$C), $50\,\mathrm{MPa}$ ($1500\,^{\circ}$C). As a simplification, ideal plasticity has been assumed, i.e. no work hardening is taken into account. The distribution of the laser beam power inside the spot at the surface of the sheet is assumed to be even. For simulations which predict the bending angle achieved and the resulting shape of the specimen, the temperature dependency of all material parameters should be allowed for. Furthermore, the power distribution of the laser beam on the surface of the specimen and the hardening of the material during the plastic deformation should be taken into account. All necessary parameters for these tasks can be determined independently of the specific forming process. Often the absorption coefficient of the laser light at the material surface, which can be very sensitive to the state of the surface (i.e. clean or with an oxide layer, polished or rough), is the only parameter to be calibrated.
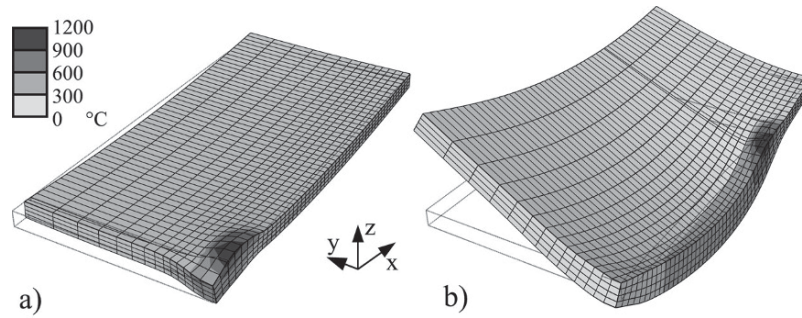
Fig. 9.2. Numerical modelling of TGM: Temperature field after 0.2 s a) and after 1.5 s b). Transferred laser beam power: 800 W, laser beam radius: 3 mm, laser spot velocity: $25\,\mathrm{mm\,s^{-1}}$, deformation scale factor: 50. The dotted lines indicate the initial state.

The numerical model was set up using the FEM-software ABAQUS with 2800 elements (8 node brick, type C3D8T). The coupled thermo-mechanical simulation required about 80 minutes of calculation time on a PC with 4 GB RAM and a 2.4 GHz Intel Core2 quad CPU using 3 cores.

In Fig. 9.2 the results of a calculation of a bending process of a sheet with sample geometry length 50 mm, width 50 mm and thickness 2 mm and a laser beam with spot radius 3 mm and a transferred beam power of 800 W are shown. The velocity of the laser beam spot on the sheet surface was chosen to be $25\,\mathrm{mm\,s^{-1}}$. Due to symmetry only half of the sample has been modelled. No clamping that could generate additional forces is included in the model. In a) the temperature distribution and the deformation after 0.2 s are displayed. In b) the situation after 1.5 s (i.e. the laser beam spot has moved over three quarters of the length of the sheet) is displayed. The deformation has been scaled by a factor of 50. For a more detailed analysis of the different states, cross-sectional cuts perpendicular to the direction of motion of the laser beam spot at the position of the spot and along the heating line are displayed in Figs. 9.3 and 9.4.

As can be seen in Figs. 9.2a and 9.3a the situation after 0.2 s corresponds to the state (b) in Fig. 9.1. The laser heats mainly the upper side of the sheet and a bending away from the laser is the result of the larger thermal expansion of the upper side of the sheet (counter-bending). This is true not only perpendicular to the direction of motion of the laser beam (i.e. y-direction) but also in the x-direction, as can be seen in Fig. 9.3b. This figure also indicates that the deformation of the heated region affects the whole sheet immediately. A slight bending at the end of the sheet can be observed.

When the laser beam spot moves further on, the bending angle develops at the starting side of the sheet. This bending effects the whole sheet, so that after 1.5 s of laser irradiation (see Figs. 9.2b and 9.4) not only the region behind the laser beam positions is bent, but also in front of the spot position.
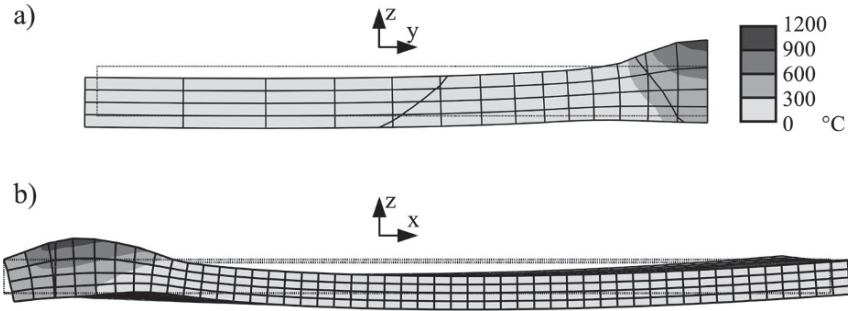
Fig. 9.3. Numerical modelling of TGM: Temperature field after 0.2 s. Cross-sectional cut at the beam position a) and longitudinal cut along the heating line b). Process parameters as in Fig. 9.2, deformation scale factor: 50. The dotted lines indicate the initial state.
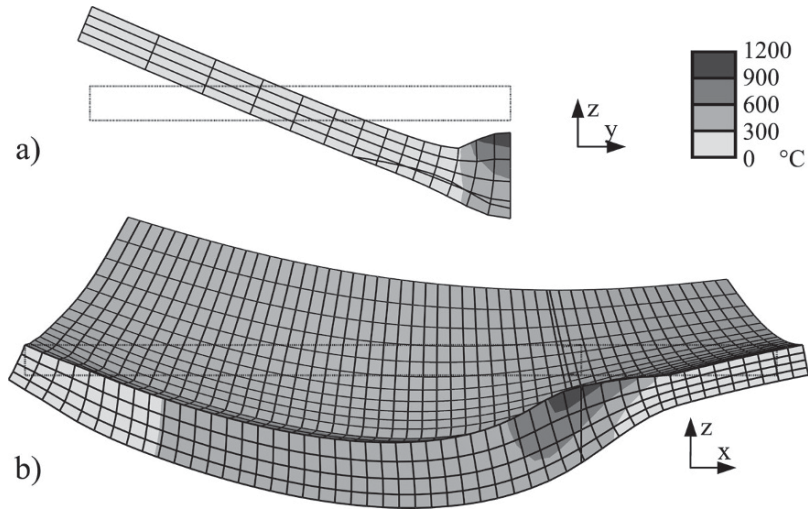
Fig. 9.4. Numerical modelling of TGM: Temperature field after 1.5 s. Cross-sectional cut at the beam position a) and longitudinal cut along the heating line b). Process parameters as in Fig. 9.2, deformation scale factor: 50. The dotted lines indicate the initial state.

This is a result of the stiffness of the parts of the sheet to the side of the irradiated region. This bending overcompensates the bending away from the laser beam due to the larger thermal expansion of the upper side of the sheet; the effect of the counter-bending, visible in Figs. 9.1b and 9.2a, can therefore only be observed at the beginning of sheet bending.

In Fig. 9.4b a significant bending in the longitudinal direction can be observed additionally to the development of the bending angle of the sheet. The reason for this is the fact that the thermal stress active in bending with
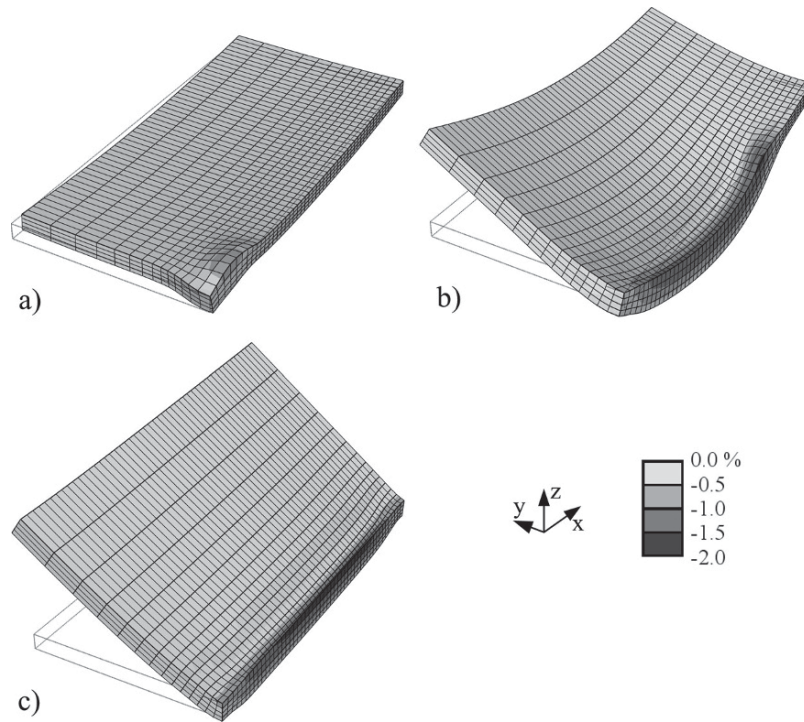
Fig. 9.5. Numerical modelling of TGM: Plastic Strain in the y-direction after 0.2 s a), after 1.5 s b) and after reaching an equilibrium temperature c). Process parameters as in Fig. 9.2, deformation scale factor: 50. The dotted lines indicate the initial state.

TGM acts not only perpendicular to the direction of motion of the laser beam spot, but also in this direction. Due to the stiffness of the sheet and the larger extension of the heated region in the x-direction (in comparison to the extension in the y-direction) the bending in the longitudinal direction is significantly smaller than the bending perpendicular to the direction of motion of the beam spot (typically one or two orders of magnitude smaller). Nevertheless without additional forces this bending occurs and influences the final shape of the sheet.

In Fig. 9.5 the local plastic deformation in the y-direction is illustrated. After 0.2 s the temperature dependent yield stress has been exceeded in a small region at the upper side of the sheet; see Fig. 9.5c. The situation after 1.5 s illustrates how the process is quasi stationary in the middle of the sheet, producing a constant plastic deformation in the y-direction of about 1.5% at the upper side of the sheet. After cooling the plastic deformation remains and the bending angle increases further, due to the vanishing of the difference in thermal expansion at the upper and lower side of the sheet. The bending angle in the middle of the sheet after one irradiation is 0.85°. Typical values

of the bending angle for sheet bending making use of TGM are up to about 2°. Depending on the process parameters smaller angles can be generated, which makes the mechanism applicable for adjustment processes. To generate larger bending angles, the irradiation can be repeated until the desired angle is reached. In many applications the bending angle per irradiation changes only slightly from irradiation to irradiation.

For the accurate prediction of the deformation result of a thermal forming process it is important to include the correct boundary conditions and the temperature dependencies in the model. Simplifications can have a significant influence on the accuracy of the results. If, in the calculation described earlier in this section, the yield stress had been taken to be independent of temperature (400 MPa), the resulting bending angle would have been only 0.62°, which corresponds to an error larger that 25%.

9.2.2 Residual Stress Point Mechanism

RSPM is very similar to TGM. The main difference is that the heat source (i.e. the laser beam spot on the surface of the sheet) does not move during the heating. The bending principle of TGM shown in Fig. 9.1 applies also for RSPM. The induced energy, which was controlled by laser beam power and beam spot velocity for TGM, is controlled for RSPM by laser beam power and irradiation duration. For a detailed investigation of the mechanism the results of a numerical calculation for RSPM are analysed.

Numerical Modelling of the Residual Stress Point Mechanism

For this calculation, the same material parameters and sample geometry were used as for the numerical model for TGM: thermal conductivity $= 40\,\mathrm{W\,m^{-1}\,K^{-1}}$, density $= 8000\,\mathrm{kg\,m^{-3}}$, Young's modulus $= 200\,\mathrm{GPa}$, Poisson's ratio $= 0.3$, thermal expansion coefficient $= 15\,10^{-6}\,\mathrm{K^{-1}}$, specific heat $= 500\,\mathrm{J\,kg^{-1}\,K^{-1}}$ and yield stress $= 400\,\mathrm{MPa}$ ($0\,°\mathrm{C}$), $100\,\mathrm{MPa}$ ($1000\,°\mathrm{C}$) and $50\,\mathrm{MPa}$ ($1500\,°\mathrm{C}$). The sample geometry was chosen as: length 50 mm, with 50 mm and thickness 2 mm. The laser beam with spot radius was 5 mm and the transferred beam power was 800 W. The total heating duration was 1.0 s. For symmetry reasons only one half of the sheet was modelled. Actually, one quarter of the sheet would have been sufficient. No clamping that could generate additional forces was included in the model. The numerical model was set up using the FEM-software ABA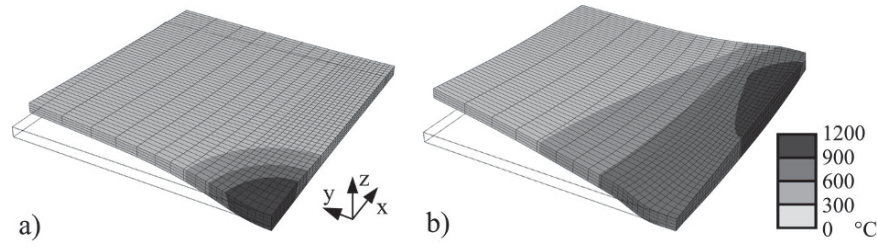QUS with 2800 elements (8 node brick, type C3D8T). The coupled thermo-mechanical simulation required about 10 minutes of calculation time on a PC with 4 GB RAM and a 2.4 GHz Intel Core2 quad CPU using 3 cores. Comparing the calculation time with the one needed for the simulation of TGM shows that the movement of the laser beam decreases the calculation speed of the simulation significantly.

In Fig. 9.6 the temperature field and the deformation of the sheet is illustrated after 0.2 s and 1.0 s of heating. To make the illustration clearer,
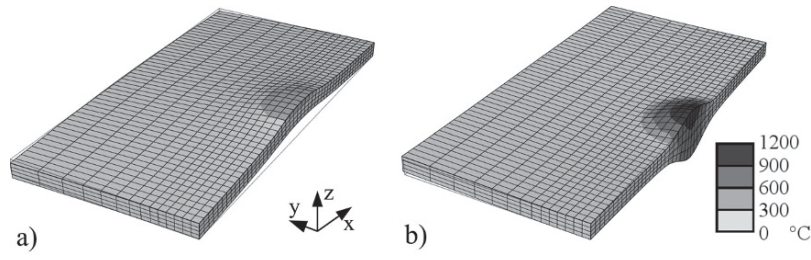
Fig. 9.6. Numerical modelling of RSPM: Temperature field after 0.2 s a) and after 1.0 s b). Transferred laser beam power: 800 W, laser beam radius: 5 mm, deformation scale factor: 50. The dashed lines indicate the initial state.
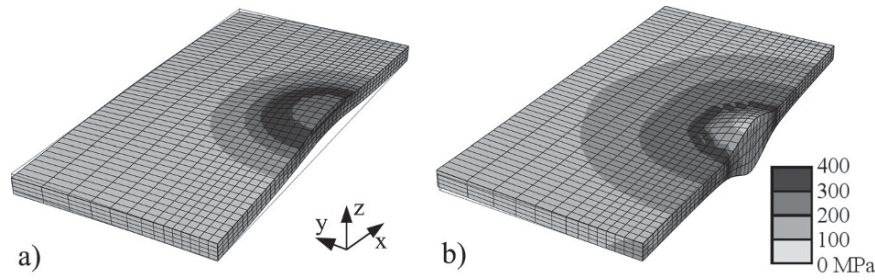
Fig. 9.7. Numerical modelling of RSPM: Stress field (von Mises) after 0.2 s a) and after 1.0 s b). Process parameters as in Fig. 9.6, deformation scale factor: 50. The dashed lines indicate the initial state.

the deformation is scaled by a factor of 50. After 0.2 s of heating the temperature at the upper side of the sheet has increased to about 400 °C. The counter-bending can be observed in this state. In contrast to the theoretical assumption that the counter-bending remains until the laser power is switched off, the bending decreases with further heating. After heating the sample for 1.0 s almost no general bending of the sheet remains (Fig. 9.6b). The reason for this can be identified by observing the stress field.

In Fig. 9.7a it can be seen that after 0.2 s of heating the highest stress occurs in the irradiated region at the upper side of the sheet. This stress is compressive due to the fact that it is generated by the thermal expansion (thermal stress). Already it can be seen here that a slight decrease of the stress occurs in the centre of the irradiated region on the upper surface of the sheet. The reason for this decrease of the stress is the temperature dependant yield stress, which decreases with increasing local temperature. In the region with higher temperature the plastic deformation occurs at lower stress levels and limits the stress level to the yield stress. The maximal stress in the sheet depends therefore not only on the thermal expansion but also on the local yield stress. As a result the maximal compressive stress is shifted from the upper side of the sheet to somewhere in the middle of the sheet; see Fig. 9.7b.
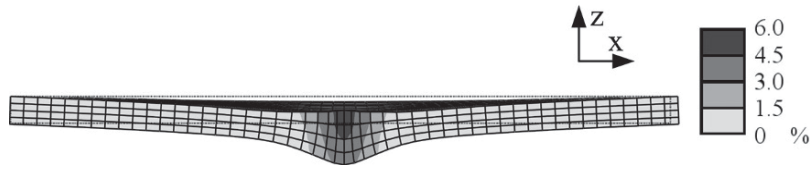
Fig. 9.8. Numerical modelling of RSPM: Plastic deformation in the y-direction after reaching an equilibrium temperature. Process parameters as in Fig. 9.6, heating duration 1 s, deformation scale factor: 50. The dotted lines indicate the initial state.
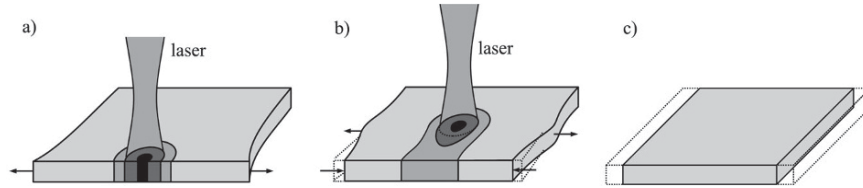
Fig. 9.9. Schematic illustration of UM for sheet material. The dotted lines indicate the initial size of the sheet.

This is the reason why the general bending of the sample nearly vanishes for longer heating durations in the case described.

During the cooling of the sheet the thermal expansion vanishes and the bending angle develops as predicted theoretically – cf. Fig. 9.1c. As can be observed in Fig. 9.8 the largest plastic deformation occurs in the centre of the heated region at the upper side of the sheet, where the highest temperatures had been reached. Also clearly visible is the local thickening of the sheet in the plastically deformed region, which is typical for forming processes making use of TGM, RSPM or UM. This is an advantage in comparison to mechanical bending processes, where the bending region is often thinned during the forming process and is therefore weakened.

9.2.3 Upsetting Mechanism

To activate UM no temperature gradient over the thickness of the sample should exist. For most processes this requirement cannot be fulfilled completely, which leads to the activation of other thermal forming mechanisms (i.e. TGM) additionally to UM. A possibility that allows activation of UM in practice is to use a laser beam spot with a diameter which is significantly larger than the thickness of the sample. Additionally, a high thermal conductivity of the sample material facilitates the activation of UM.

For the ideal case, in which no temperature gradient in the thickness direction of a sheet exists, the thermal expansion of the material in the heated region cannot generate stress which leads to a bending of the sheet: Fig. 9.9a). The expansion of the heated region in the sideways direction is uniform

over the thickness and produces compressive stress due to the fact that the expansion is hindered by the stiffness of the surrounding material. A clamping of the sample can increase this effect significantly. If the local compressive stress in the heated region exceeds the temperature dependent yield stress, plastic upsetting of the material occurs. When the laser spot moves further on over the surface of the sheet as in Fig. 9.9b, the material cools down behind the spot position and the thermal expansion decreases, while plastic upsetting remains. This leads to a shortening of the sheet perpendicular to the direction of motion of the laser beam spot. When the laser beam spot has moved over the total length of the sheet, it is shorter in the sideways direction and slightly thickened in the region that had been heated.

UM can also be activated by heating with a static heat source (like RSPM, but without a temperature gradient). In this case shortening will occur circularly in every direction around the heated region, which will generate tensile stress. UM using a static heat source can therefore be used to reduce or eliminate local buckles in a sheet [13, 14].

Analytical Modelling of the Upsetting Mechanism

UM is often used for bending tubes or forming 3D-structures. In Geiger et al. [15] and Vollertsen [9] an analytical model for the calculation of the bending angle for rectangular structures is described. The model makes the following assumptions:

- For all material parameters except the Young's modulus and the yield stress the values for ambient temperature are used. For Young's modulus and the yield stress the values for the highest temperature reached in the heated region are used.
- For the heated region the deformation is assumed to be elastic-ideal plastic in the heating phase and totally elastic in the cooling phase.
- For the unheated regions the material is assumed to be rigid.
- In the thickness direction an infinite thermal conduction and in the lateral direction no thermal conductivity at all is assumed.
- Heat losses due to thermal conductivity and to radiation and convection are neglected.
- Bending occurs along a bending edge at the rear of the profile (see Fig. 9.10).
- Time dependent effects are neglected.

The procedure for the bending process assumed is as follows: The laser beam heats the irradiation zone (marked light grey in Fig. 9.10) including the parts of the zone at the sides of the structure. Expansion of the material is prevented by the rigid surrounding regions of the structure. This generates thermal compressive stress, which leads to an upsetting of the material if the decreased yield stress (due to the higher temperature) is exceeded. After the laser is switched off, the irradiated region cools down. This cooling is assumed
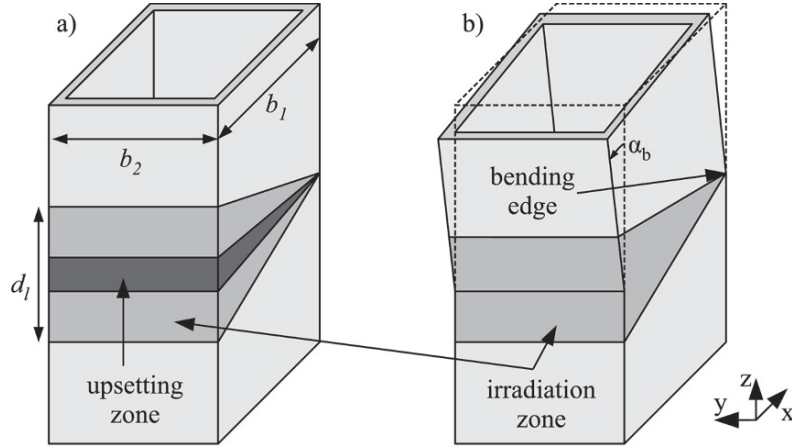
Fig. 9.10. Schematic illustration of the bending of profiles applying UM.

to be ideal and homogeneous, and produces no further stress. Bending occurs along a straight bending edge at the back of the structure. Bending stiffness there is neglected. After the cooling is complete the bending angle α_b can be calculated as:

$$\tan\frac{\alpha_b}{2} = \frac{d_l\varepsilon_{pl}}{2b_1}, \tag{9.13}$$

where d_l is the width of the irradiation zone and equals the diameter of the laser beam spot on the surface of the structure, ε_{pl} the plastic strain and b_1 the depth of the structure in the x-direction. The width of the upsetting zone (i.e. the shortening) at the front side is $\varepsilon_{pl}d_l$. For small bending angles (which, using this model, will be regarded typically as of the order of $0.1°$) the simplification $\tan\alpha_b = \alpha_b$ can be used. Using analogue methods to calculate the plastic upsetting and the maximal temperature reached in the irradiated zone as for the analytical calculation for TGM (section 9.2.1) the bending angle can be calculated as (radiant measure)

$$\alpha_b = \frac{4}{\pi}\frac{\alpha_{th}}{c_p\rho}\frac{Ap_l}{v_l}\frac{1}{b_1s_0} - \frac{d_l}{b_1}\frac{k_f\left(T_{\max}\right)}{E\left(T_{\max}\right)} \tag{9.14}$$

where α_{th} is the coefficient of thermal expansion, c_p the specific heat capacity, ρ the density, A the absorption coefficient of the laser light, p_l the laser beam power, v_l the velocity of the laser spot on the surface of the structure, s_0 the thickness of the material, $k_f(T_{max})$ the flow stress and $E(T_{max})$ the elastic modulus at the maximal temperature reached.

The accuracy of the result of the analytical calculation varies for different process parameters and materials. For steel the bending angle can be calculated with a sufficient accuracy for various process parameters, whereas for aluminium the calculated angles are generally too large by a factor of 2.

For this case the neglect of the thermal flow inside the material is not permitted due to the high thermal conductivity of aluminium.

Numerical Modelling of the Upsetting Mechanism

As already shown for TGM and RSPM numerical calculations can be used to model thermal processes in a detailed way, where the geometry can be as complex as necessary to include all substantial effects and particular features. To calculate the upsetting in a simple sheet is already very complex due to initiation and termination effects at the beginning and the end of the heating regime, edge effects, the stress distribution in the sheet, which depends highly on the boundary conditions and the question of whether UM, TGM or BM is activated in the process. In the following, the results of a calculation of a laser beam upsetting process of a sheet will be presented. To activate UM some changes were made to the model used for TGM:

- The thermal conductivity of the material was increased by a factor of 10 and the spot size of the laser beam on the surface of the sheet by a factor of 3 to reduce the temperature gradient in the thickness direction of the sheet.
- To achieve nearly stationary process conditions in the middle of the sheet, a pre-heating phase with a stationary laser beam spot was included at the beginning of the process and the laser beam power was increased significantly. This is necessary to compensate for the larger heat losses due to the increased thermal conductivity.
- The width of the sheet was increased to enlarge the stiffness of the sideways regions of the sheet and therefore to generate higher stress in the heated region.
- The irradiation stops 7.5 mm before the rear edge of the sheet to prevent overheating due to the missing thermal flow in front of the laser beam spot.

The material parameters chosen are therefore: thermal conductivity $= 400\,\mathrm{W\,m^{-1}\,K^{-1}}$, density $= 8000\,\mathrm{kg\,m^{-3}}$, Young's modulus $= 200\,\mathrm{GPa}$, Poisson's ratio $= 0.3$, thermal expansion coefficient $= 15\,10^{-6}\,\mathrm{K^{-1}}$ and specific heat $= 500\,\mathrm{J\,kg^{-1}\,K^{-1}}$. Again the yield stress was modelled as temperature dependent: 400 MPa (0 °C), 100 MPa (1000 °C), 50 MPa (1500 °C) and ideal plasticity has been assumed. The distribution of the laser beam power inside the spot at the surface of the sheet is assumed to be even. The sample geometry is: length 50 mm, width 100 mm and thickness 2 mm (due to symmetry only half of the geometry is modelled); the laser beam spot radius is 9 mm and the transferred beam power 6000 W. The velocity of the laser beam spot on the sheet surface was chosen to be $25\,\mathrm{mm\,s^{-1}}$, which is the same as for the modelling of TGM. No clamping that could generate additional forces is included in the model. The numerical model was set up using the FEM-software ABAQUS with 3800 elements (8 node brick, type C3D8T).

Fig. 9.11. Numerical modelling of UM: Temperature field after 0.8 s a) and after 2.5 s b). Transferred laser beam power: 6000 W, laser beam spot radius: 9 mm, laser spot velocity 25 mm s^{-1}, waiting time before spot movement 0.8 s, deformation scale factor: 25. The dashed lines indicate the initial state.

The coupled thermo-mechanical simulation required about 70 minutes of calculation time on a PC with 4 GB RAM and a 2.4 GHz Intel Core2 quad CPU using 3 cores. A pre-heating phase of 0.8 s with a stationary laser beam spot (centre of the spot at the edge of the sheet) heats the centre of the irradiated region to a temperature of about 1200 °C; see Fig. 9.11a. During the subsequent movement of the laser spot over the sheet the maximum temperature does not increase further.

The resulting temperature field and deformation of the numerical calculation of UM is shown in Fig. 9.11 after 0.8 s, i.e. at the end of the pre-heating phase (a), and after 2.5 s when the laser beam spot has been moved near to the rear edge of the sheet. As theoretically predicted, the thermal expansion of the irradiation region causes a widening of the sheet at the starting edge in the y-direction at the beginning of the process; cf. Fig. 9.9a. Additionally, a significant expansion of the irradiated region in the x-direction can be observed. Due to the fact that the edge of the sheet is free, no compressive stress is generated in the x-direction. The next theoretical phase, where the expansion moves on with the laser beam spot and the material shrinks behind the moving spot position, is hard to identify because the temperature decreases only slowly; therefore the upsetting cannot be fully observed until the sheet has cooled down to ambient temperature.

In Fig. 9.12 the plastic deformation and the spatial displacement (i.e. the amount of upsetting) in the y-direction is illustrated. It can be observed that the local plastic shrinkage in the upsetting zone reaches values up to 4%. Although the maximum temperature along the irradiation path is kept nearly constant the process is not quasi-stationary in the middle of the sheet. This can be clearly seen by observing the plastic deformation as seen in Fig. 9.12a, which increases from the starting edge of the sheet up to the position where the laser beam is switched off. In addition to upsetting in the y-direction a slight bending upwards can be observed. This bending is caused by an activation of TGM additionally to UM. Nevertheless the bending angle is significantly smaller than the one achieved using the process parameters of the model in section 9.2.1: $\alpha_b = 0.2°$. This shows that it is not necessary to distinguish
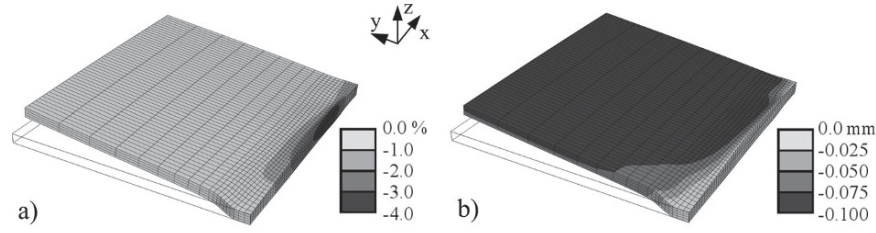
Fig. 9.12. Numerical modelling of UM: Plastic deformation a) and spatial displacement b) in the y-direction after reaching equilibrium temperature. Process parameters as in Fig. 9.11, deformation scale factor: 25. The dashed lines indicate the initial state.
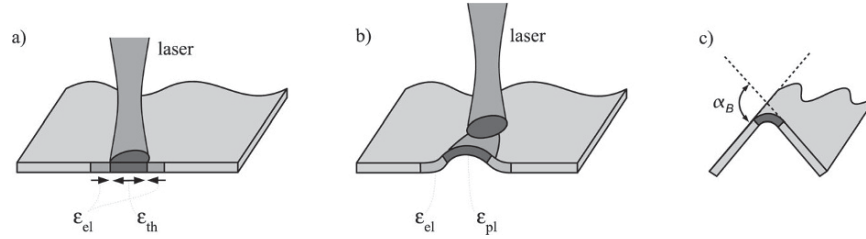
Fig. 9.13. Schematic illustration of BM for sheet bending.

between the thermal forming processes to set up a numerical model for the calculation of the forming result. On the contrary, the calculation result can be used to identify the activated mechanisms and to determine the dominant one.

9.2.4 Buckling Mechanism

BM can be activated if conditions are similar to those which lead to the activation of UM but the stiffness of the material in the heated region is not sufficient to prevent a local buckling of the sheet. The main conditions are therefore: no temperature gradient in the thickness direction and large size of the laser beam spot moving on the surface of the specimen, compared to the sheet thickness.

In Fig. 9.13 bending of sheet material by activating BM is illustrated schematically. At the beginning of the heating the thermal expansion ε_{th} in the irradiated region is compensated for by an elastic compression ε_{el} of the surrounding material: Fig. 9.13a. This produces compressive stress, which is nearly constant over the thickness of the sheet. Local deviations in the thickness direction can produce forces perpendicular to the sheet, which lead to the formation of a buckle. The thermal stress is converted to a convex deformation of the centre and a concave deformation of the surrounding region. The centre region is deformed plastically whereas the surrounding region is deformed elastically, because the stress is higher and the yield stress is lower
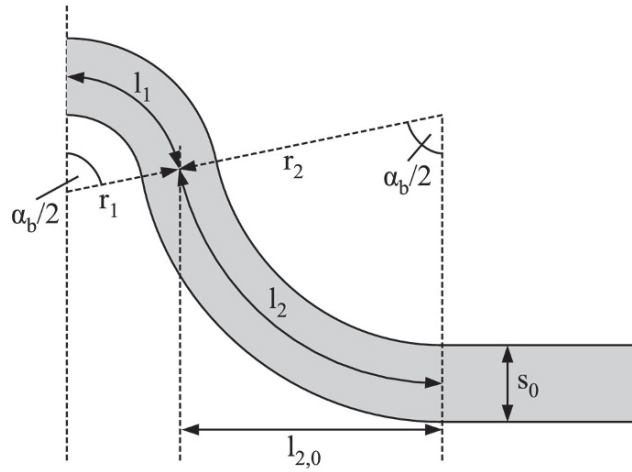
Fig. 9.14. Schematic illustration for the analytical calculation of the bending angle applying BM.

in the centre due to the higher temperature. Due to the movement of the laser beam spot the buckle is elongated in the movement direction as seen in Fig. 9.13b. With the elongation of the buckle the elastic deformation, which is caused by the stiffness of the sides of the sheet, decreases and the bending angle develops. After the laser beam spot has moved over the total length of the sheet the elastic deformation has vanished and the bending process is completed – Fig. 9.13c. Typical bending angles, which can be generated by activation of BM are in the range of $0.1°$ to $15°$.

Due to the fact that the direction of the buckling depends on local deviation from symmetry in the irradiated region it is difficult to predict the direction of the bending. Causes which influence the direction can be small distortions of the sheet, material inhomogenieties or residual stress, which exist in the material before processing begins.

Analytical Modelling of the Buckling Mechanism

Vollertsen [9] presented an analytical calculation for the estimation of the bending angle for BM. The geometrical model uses temperature-independent material parameters and simplifications of the temperature field. It is assumed that buckling occurs.

Considering the process phase where the buckle is fully developed but the side regions of the sheet are still straight allows calculation of the bending angle. Using the definitions in Fig. 9.14 the bending angle α_b can be calculated as

$$\frac{\alpha_b}{2} = \frac{l_1}{r_1} = \frac{l_2}{r_2}. \tag{9.15}$$

Considering that the bending moments are equal at the point of junction of l_1 and l_2 and assuming that along l_1 the material is purely plastically deformed and along l_2 purely elastically, the radius r_2 can be calculated as

$$r_2 = \frac{Es_0}{3k_f(T_{\max})},\tag{9.16}$$

where E is the elastic modulus at ambient temperature, s_0 the thickness of the sheet and $k_f(T_{max})$ the yield stress at the highest temperature reached in the irradiated region. The length l_2 can be calculated using the assumption that the total thermal elongation of the sheet in the heated region is divided evenly between l_1 and l_2 (l_2 is significantly longer than l_1 but along l_1 the temperatures are higher) as

$$l_2 = r_2 \sin\left(\frac{\alpha_b}{2}\right) + \frac{1}{2}\frac{\alpha_{th}Ap_l}{2c_p\rho s_0 v_l},\tag{9.17}$$

where α_{th} is the thermal expansion coefficient, A the absorption coefficient of the laser light on the surface of the sheet, p_l the laser power, c_p the specific heat capacity, ρ the density, s_0 the thickness of the sheet and v_l the velocity of the laser beam spot. The bending angle is now described by

$$\frac{\alpha_b}{2} = \sin\left(\frac{\alpha_b}{2}\right) + \frac{3\alpha_{th}Ap_l k_f(T_{\max})}{4Es_0^2 c_p\rho v_l}.\tag{9.18}$$

To solve (9.18) with respect to α_b the series expansion of the sine function up to the second term is used. Including only the first term, i.e. $\sin x = x$, would not be sufficient because the bending angles for BM are typically about $10°$. The resulting bending angle is (radiant measure)

$$\alpha_b = \left(36\frac{\alpha_{th}k_f(T_{\max})}{c_p\rho E}\frac{Ap_l}{v_l}\frac{1}{s_0^2}\right)^{\frac{1}{3}}.\tag{9.19}$$

A verification of the analytical model is difficult, because the maximum temperature and therefore the yield stress cannot be determined exactly. Additionally, a possible upsetting before the buckle develops is not taken into account; it would decrease the elongation of l_1 and l_2. The bending angles calculated by (9.19) are therefore generally too large compared to measured bending angles.

Numerical Modelling of the Buckling Mechanism

Analogous to TGM, RSPM and UM, BM can be modelled numerically using finite element methods. For the activation of BM the material properties chosen are the same as for the activation of TGM and RSPM.
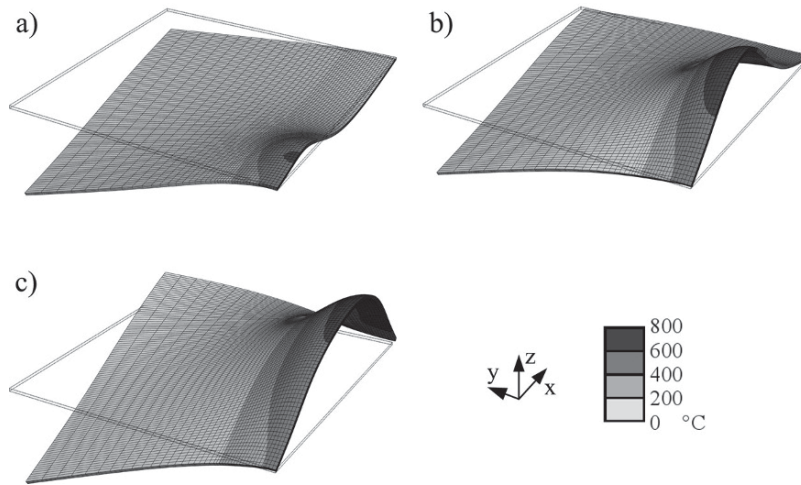
Fig. 9.15. Numerical modelling of BM: Temperature field after $0.5\,\mathrm{s}$ a), after $1.0\,\mathrm{s}$ b) and after $2.0\,\mathrm{s}$ c). Transferred laser beam power: $500\,\mathrm{W}$, laser beam spot radius: $8\,\mathrm{mm}$, laser spot velocity: $25\,\mathrm{mm\,s^{-1}}$, deformation scale factor: 10. The dotted lines indicate the initial state.

Therefore the material parameters are: thermal conductivity $= 40\,\mathrm{W\,m^{-1}\,K^{-1}}$, density $= 8000\,\mathrm{kg\,m^{-3}}$, Young's modulus $= 200\,\mathrm{GPa}$, Poisson's ratio $= 0.3$, thermal expansion coefficient $= 15\,10^{-6}\,\mathrm{K^{-1}}$ and specific heat $= 500\,\mathrm{J\,kg^{-1}\,K^{-1}}$. The yield stress was modelled as temperature dependent: $400\,\mathrm{MPa}$ ($0\,^{\circ}\mathrm{C}$), $100\,\mathrm{MPa}$ ($1000\,^{\circ}\mathrm{C}$), $50\,\mathrm{MPa}$ ($1500\,^{\circ}\mathrm{C}$) and ideal plasticity has been assumed. The distribution of the laser beam power inside the spot at the surface of the sheet is assumed to be even. The sample geometry is: length $50\,\mathrm{mm}$, width $100\,\mathrm{mm}$ and thickness $0.5\,\mathrm{mm}$, which is 4 times thinner than in the model for TGM, RSPM and UM (due to symmetry only half of the geometry is modelled), the laser beam has a spot radius of $8\,\mathrm{mm}$ and the transferred beam power is $500\,\mathrm{W}$. The velocity of the laser beam spot on the sheet surface was chosen as $25\,\mathrm{mm\,s^{-1}}$, which is the same as for the other mechanisms modelled. No clamping that could generate additional forces is included in the model. The numerical model was set up using the FEM-software ABAQUS with 16000 elements (8 node brick, type C3D8T). The coupled thermo-mechanical simulation required about 100 minutes of calculation time on a PC with $4\,\mathrm{GB}$ RAM and a $2.4\,\mathrm{GHz}$ Intel Core2 quad CPU using 3 cores.

In Fig. 9.15 the development of the temperature field and of the deformation of the sheet can be observed. The deformation is scaled by a factor of 10. After $0.5\,\mathrm{s}$ the temperature in the centre of the irradiation zone is about $600\,^{\circ}\mathrm{C}$ and a buckle is developing; see Fig. 9.15a. The initial model includes no asymmetries or residual stress, which could influence the direction of the buckling. The asymmetric condition perpendicular to the sheet surface is the
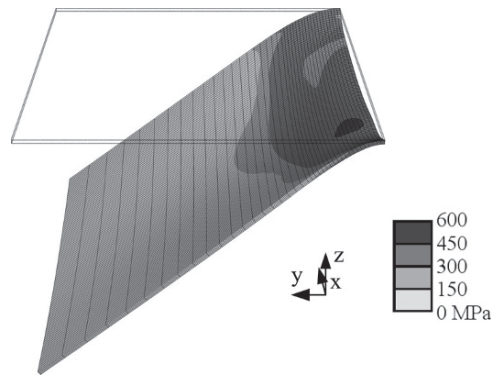
Fig. 9.16. Numerical modelling of BM: Residual stress (von Mises). Process parameters as in Fig. 9.15, deformation scale factor: 10. The dotted lines indicate the initial state.

laser beam heating, which is done only from one side. A temperature gradient is therefore induced at the start of the heating, which decreases with further irradiation of the sheet. Nevertheless, a counter-bending (as described for TGM in section 9.2.1) of the sheet occurs during the initial phase of the process. This counter-bending moves the side regions of the sheet away from the laser beam. At this time the critical conditions for buckling are reached and the buckle develops upwards. The situation described can be generalised: For ideal sheets (i.e. no material inhomogeneities, residual stress or initial distortion) the counter-bending produces a bending in the opposite direction if BM is activated rather than TGM. In Fig. 9.15b,c the buckle elongates in the x-direction and also increases in height. Additionally to the bending in the y-direction a significant local bending in the x-direction (i.e. the direction of motion of the laser beam spot) can be observed. The stiffness of the side regions of the sheet prevents the development of a bending angle in this direction. After the laser beam spot has left the sheet and it has cooled down to ambient temperature the buckle has vanished and a bending angle of 4.7° (measured in the middle of the sheet) remains. In Fig. 9.16 the final geometry and the residual stress, which is induced in the sheet by the bending process, can be seen.

9.2.5 Residual Stress Relaxation Mechanism

The principle of RSRM is the fact that residual stress in a material can be relaxed at increased temperature. Any thermal treatment (local or global) can therefore influence the residual stress field of a specimen. Global heating to a material-specific annealing temperature when held at this temperature will cause the residual stress to vanish. Nevertheless a fast or inhomogeneous
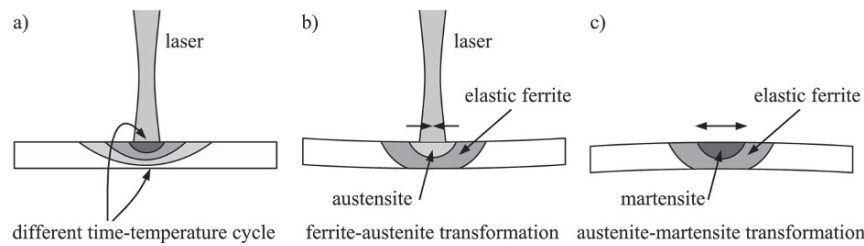
Fig. 9.17. Schematic illustration of MEM for bending of steel sheets.

cooling of the specimen can produce new stress. A change of the stress field of a specimen generally causes an instantaneous change of its shape. The relaxation of residual stress therefore generally causes a deformation of the specimen. In contrast to the thermal forming mechanisms described earlier, the driving force for the deformation is not generated during the process (i.e. the thermal stress for TGM, RSPM, UM and BM), but already resides in the specimen before the process begins. It follows that a repetition of the process will not cause the same (or nearly the same) deformation. In contrast, for an ideal process, if the residual stress is relaxed completely and no new stress is generated, no further change of the shape of the specimen will be caused by repeating the process.

To use RSRM for active bending processes is difficult because the residual stress field of the specimen has to be known. This is only possible if the production history of the component is known in detail. If the residual stress is mainly generated by preceding process steps in a production process chain it can be possible to simulate the preceding steps and thereby gain knowledge of the residual stress field. Measurement of the surface stress of a specimen will generally not be sufficient to be able to determine the shape changes which will be caused by a relaxation of the residual stress.

Even in cases in which the mechanism cannot be used for active forming of a specimen, it nonetheless cannot be ignored when local laser beam heating is applied in order to activate other thermal forming mechanisms. RSRM will be activated in addition to the desired mechanism if residual stress is present and will influence the forming result, at least at the beginning of the process. For multi-pass processes (e.g. if a line is subsequently heated several times to activate TGM) the influence of RSRM will decrease with every repetition of the process.

9.2.6 Martensite Expansion Mechanism

The principle of the bending of steel sheers by activation of MEM is illustrated in Fig. 9.17. A laser irradiation on one side of the sheet induces a temperature gradient in the thickness direction of the sheet, the same as for the activation of TGM.
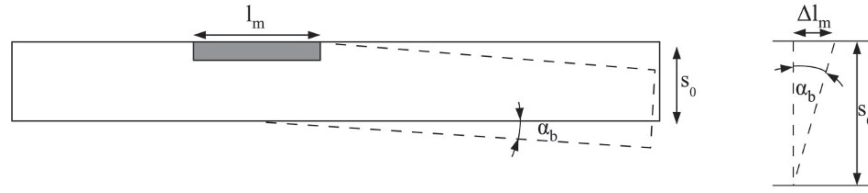
Fig. 9.18. Schematic illustration for the estimation of the maximal bending angle applying MEM.

The different time-temperature cycles in the upper and the lower region of the sheet can lead to the formation of different phases in the direction of the temperature gradient. In the lower region the highest temperature reached is lower than in the upper region; see Fig. 9.17a. During laser beam heating the critical temperature for phase transformation (i.e. the formation of austenite) can be exceeded for a sufficient time in the upper region of the sheet. In the lower region the highest temperature reached is lower and the initial ferrite phase survives. Due to the volume change from ferrite to austenite, shrinkage of the upper region occurs, which is the opposite effect from the counter-bending observed with TGM. When the laser is switched off the irradiated region of the sheet cools down. For laser beam processes the cooling rate can be high due to the self-quenching effect of the surrounding regions of the sheet. In this case the austenite in the upper region transforms to martensite. The volume change from austenite to martensite, which is even larger than the one from ferrite to austenite, causes the upper region to extend. This causes a bending of the sheet away from the laser beam.

An estimation of the upper limit for the bending angle α_b can be done by assuming a total transformation of the material in the upper region of the sheet (grey zone in Fig. 9.18) from ferrite to martensite and neglecting the stiffness:

$$\tan \alpha_{b,\mathrm{max}} = \frac{\Delta l_m}{s_0}. \tag{9.20}$$

Values of $\alpha_{b,max}$ can be of the order of magnitude of 0.1° [10] for a sheet thickness of 5 mm and a width of the irradiated region of 6 mm. In practice the stiffness of the material reduces the bending angle significantly. The measured values for the bending angle are therefore one order of magnitude smaller in the case described. Additionally, TGM can be activated which can reduce the bending angle further, or even overcompensate the bending due to MEM.

9.2.7 Shock Wave Mechanism

SWM is based on the formation of laser shock waves [9, 16]. In contrast to the thermal forming mechanisms described in this chapter SWM is a non-thermal forming mechanism, where the shock wave is the energy source for
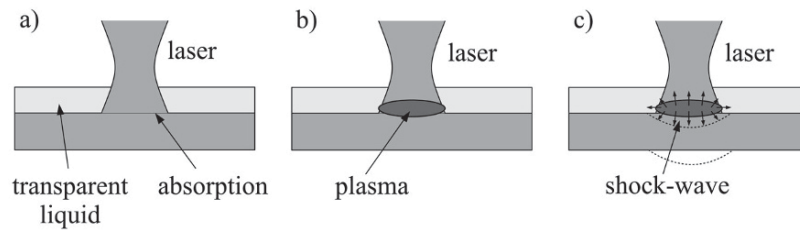
Fig. 9.19. Schematic illustration of SWM.

the forming process. The forming behaviour can be compared to that of a high speed forming process like electromagnetic forming or explosive forming. The sheet metal in the laser stretch-forming process is wetted by a transparent liquid film in order to generate confined plasma, placed on a die and clamped by a blank holder. In Fig. 9.19 the plasma and shock-wave formation are illustrated.

A single excimer or CO_2-laser pulse passes through the transparent liquid, hits the surface of the sheet metal and causes the formation of a plasma bubble above the surface. The explosion-like expansion of this bubble emits a shock-wave, which exerts pressure on the sheet surface. The liquid increases this pressure significantly. Due to the fact that the sheet is clamped by die and blank holder (not shown in Fig. 9.19) a hemispherical dome is formed.

Excimer laser stretch-forming by a single laser pulse usually leads to a uniform dome shape using water as the film liquid [17, 18]. Multiple laser pulses can lead to local deformations or to a perforation of the sheet. The local deformations could be explained by the fact that the surface of the sheet is locally pre-damaged by the first laser pulse, due to ablation. This leads to surface modification, resulting in higher local absorptivity. The second laser pulse consequently causes significantly higher ablation than the first laser pulse, which induces local thinning and can result in perforation for multiple pulses.

9.3 Applications

Since the development of lasers in the 1960's a continuous flow of new applications has occurred in all fields of production technology. Processes related to metal forming have been implemented in tool making and tool repair, cutting of blanks and formed parts and welding of blanks as well as laser assisted and laser induced forming. The development of new generations of lasers has enabled new processes to be very economical. New high power lasers, such as the diode laser [19, 20] and fibre laser (with powers up to 17 kW and very good beam quality) [21] have been developed and became efficient heat sources for applications on larger areas.
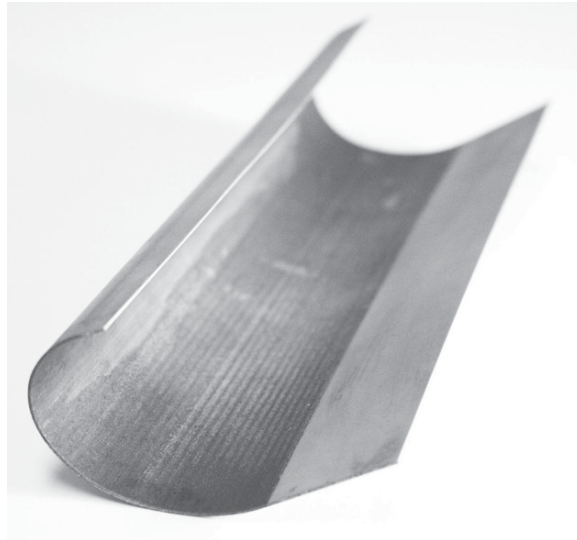
Fig. 9.20. Laser-bent steel sheet. Laser beam power $4.5\,\mathrm{kW}$, beam velocity $1500\,\mathrm{mm\,s^{-1}}$, distance between irradiation lines $2\,\mathrm{mm}$, 3 irradiations per line, carbon coating, sheet thickness $0.8\,\mathrm{mm}$, material hot-rolled steel.

In some fields of micro engineering laser bending is already in or ready for industrial use: fields which have benefited include the adjustment of electronic components (e.g. reed switches [22]), precision engineering, optics and mechatronics – particularly for mass production [23, 24]. For large scale applications laser bending processes can be integrated into production lines (e.g. for high volume automotive application [25]). Processes are under development which can even comply with the rigorous demands of the aircraft industry [26].

In the remainder of this section some general possibilities for the application of laser bending or forming processes are described as examples. The focus lies not on particular applications, but on the systematic use of the activation of bending mechanisms for different purposes.

9.3.1 Plate Bending

This is possibly the application of laser forming which has been investigated most (e.g. [27]–[29]). The laser beam spot is moved over the surface of a sheet metal to activate TGM. The movement can be done mechanically, which has limitations in the speed of the movement, or by using a scanner system, with which velocities of the laser beam spot of about $1\,\mathrm{m\,s^{-1}}$ can be realised. Not only can a simple bending of a sheet along a bending edge be done with this technique, but also the forming of complex shapes with different local curvatures, as shown if Fig. 9.20. The shape has been generated by a heating
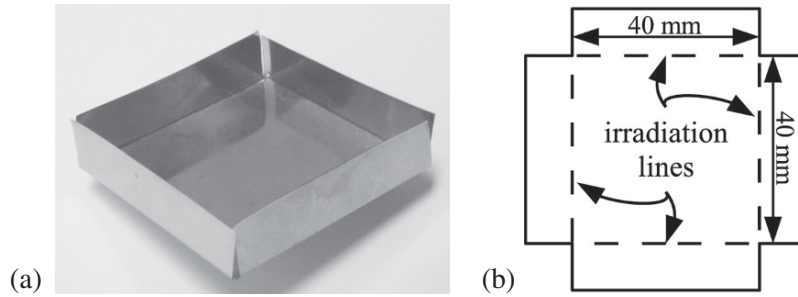
Fig. 9.21. Box produced by laser bending a) and sheet geometry before bending. Laser beam power 100 W, 50 irradiations per side, spot size 0.03 mm, beam velocity 500 mm s^{-1}, stainless steel (1.4310).

of multiple lines using a CO_2-laser with a scanner, starting on the left hand edge of the sheet. The total bending angle of the geometry is larger that 180°; a mechanical forming would have required several deformation steps in addition to geometry-dependent tools to produce the same result.

Even though the bending angle that can be achieved by one irradiation is not very large ($\sim$2° for TGM, 0.1° for UM), the ability to repeat the process and achieve nearly a constant bending angle per irradiation cycle when applying TGM, UM or RSPM allows for the formation of large bending angles. In Fig. 9.21 a box is illustrated which is created by bending a sheet at the dashed lines; the initial geometry is shown in Fig. 9.21b. At each line the sheet was irradiated 50 times with a fibre laser in combination with a scanner system, which produced the bending angle of 90° visible in Fig. 9.21a. The bending angle per irradiation cycle was therefore 1.8° applying TGM. Due to the use of a scanner system no movement of the sheet and no special clamping were necessary. The only clamping needed was a small weight in the middle of the sheet.

9.3.2 Tube Bending/Forming

The bending of tubes can be done by the application of the upsetting mechanism similarly to the situation in Fig. 9.10 but with a direction of motion of the heat source in the longitudinal direction of the tube, indicated by the dashed line in Fig. 9.22a. The heated part of the cross-section of the tube is shortened by the activation of UM, which leads to a bending of the tube. The bending radius can be controlled by varying the induced laser power or the velocity of the laser beam spot.

Laser forming of pipes can be used not only for bending the pipe, but also for forming of the cross-section by activation of TGM, as described by Osakada et al. [30] and illustrated in Fig. 9.22b. In this example three scanning regions (each with a range of 30°) where heated using a 50 W pulsed Nd:YAG laser
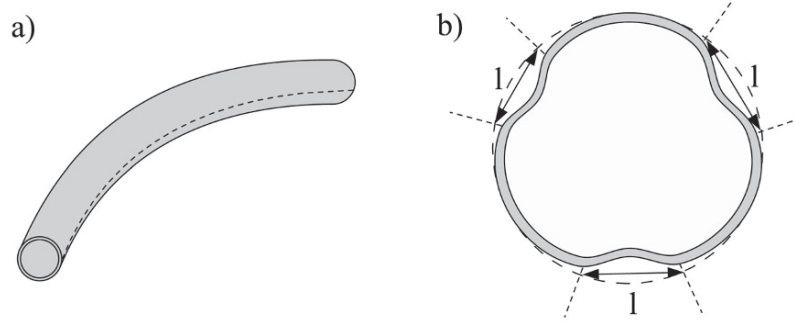
Fig. 9.22. Schematic illustration of tube bending a) and forming of the cross-section b).

(1 kW peak power, pulse length 1 ms, laser beam spot diameter 0.8 mm, pulse frequency 50 Hz). The heating was done by irradiating multiple scan lines with an angular distance of $0.2°$ and a scanning velocity of $40\,\mathrm{mm\,s^{-1}}$. The material used was stainless steel (18Cr-8Ni) with outer diameter of the tube 20 mm and wall thickness 0.5 mm. As a result, a combination of convex and concave sections of the cross-section of the tube can be achieved. With this method a complex shaped cross-section can be formed without the need of special tools and, even more, the shape of the cross-section can be modified along the length of the tube.

9.3.3 High Precision Positioning Using Actuators

Many applications have an increasing demand for high precision positioning, especially in the ongoing miniaturisation of functional parts in electronic, optical and mechanical devices. For high precision adjustment special structures can be included in the design of components, which allow movement in different spatial directions and around different axes by applying UM, TGM or RSPM [31, 32]. By using devices known as actuators accuracies in the sub-micron range can be reached [33]. A simple actuator geometry is the bridge actuator. It consists of a sheet with a recess, so that the free side of the sheet (right hand side in Fig. 9.23) is attached by two bridges with the stationary part. If one bridge is heated by laser irradiation UM can be activated and the bridge will be shortened, which leads to bending around the recess (see bending angle α_b in Fig. 9.23).

In order to optimise the design of actuators appropriate modelling is necessary. Widaszewski [34] describes an analytical-numerical model for the calculation of the bending angle. The model assumes a one-dimensional heat flux in the irradiated bridge and uses some simplifications for the calculation of the stress state and the amount of plastic deformation. These assumptions are similar to the ones described for the numerical models in sections 9.2.1, 9.2.3 and 9.2.4. A satisfactory accuracy for the description of the deformations
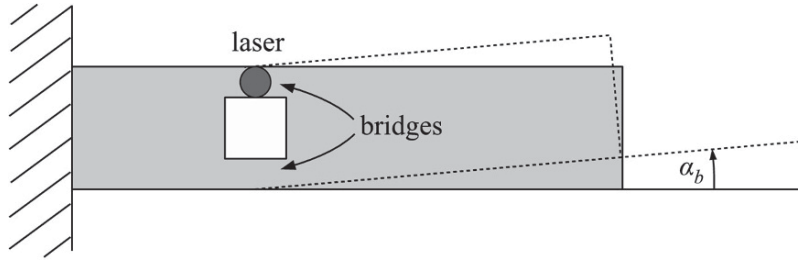
Fig. 9.23. Schematic illustration of a bridge actuator.
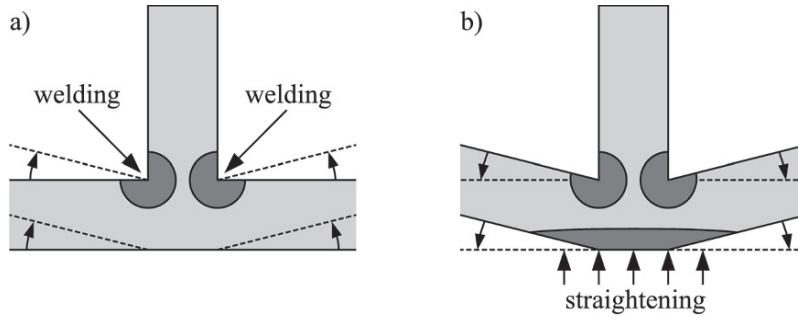
Fig. 9.24. Schematic illustration of the straightening of the weld distortion of a T-joint.

of the bridge actuator can be achieved if the actuator geometry complies with the assumptions and restrictions. A more detailed model is presented by Sakkiettibutra and Vollertsen [35] where the temperature, stress and strain field is calculated numerically. The numerical model allows for a detailed investigation of the process, with which the dependency of the bending angle on the induced laser power and heating duration can be determined.

9.3.4 Straightening of Weld Distortion

For many applications in the aircraft and shipbuilding industries thin sheet-metal structures with reinforcements have been used to reduce weight. The production of these has the general problem of deformation of the outer surface caused by the welding process, where deformation appears locally in the weld region as well as globally. The reason for this deformation is illustrated schematically in Fig. 9.24a. The welding process induces local tensile residual stress, which leads to bending along the weld lines similar to bending due to TGM.

Engler [36] described a method for correcting this distortion. By locally heating the surface of the sheet opposite the reinforcement as shown in Fig. 9.24b, local tensile residual stress is induced at the outer surface of the sheet by line heating with activation of TGM, which compensates for the
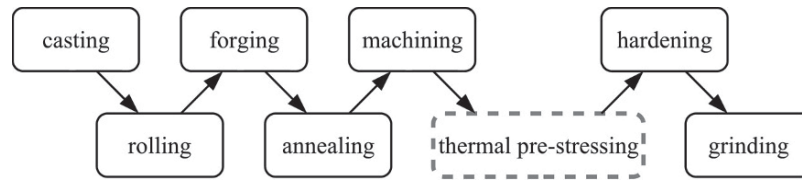
Fig. 9.25. Simplified production process chain for steel components with distortion manipulation enhancement (thermal pre-stressing).
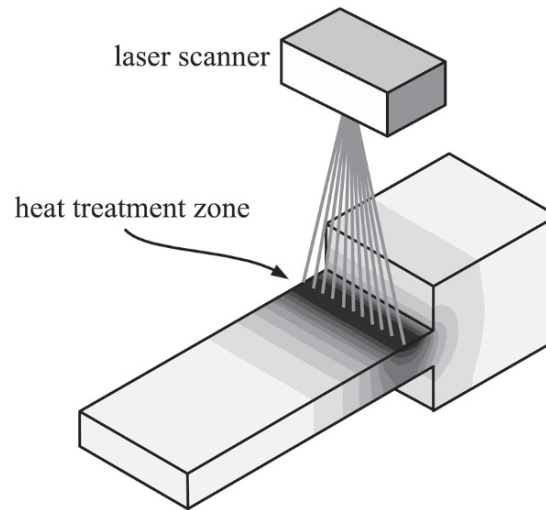
Fig. 9.26. Schematic illustration of the local laser heat treatment for thermal pre-stressing of an idealised gear wheel tooth.

bending caused by the welding process. The applicability of this method was proved by numerical modelling and experimental realisation of the welding and straightening of a titanium lightweight structure for use in the aircraft industry.

9.3.5 Thermal Pre-Stressing

Thermal treatments of steel components with the goal of hardening often result in distortion by releasing the residual stress (activation of RSRM), which is introduced into the specimen during the preceding processing steps. A correction of this distortion after the hardening can only be done by grinding and is therefore limited. This means that the prevention or compensation of distortion in the production process of components is preferable. Causes of distortion can be found in every step of the manufacturing process chain. In Fig. 9.25 the simplified production process chain according to Hoffmann et al. [37] of steel components (e.g. gear wheels) is illustrated. Towards the

end of the process chain – in the heat-hardening treatment – the distortion potential, which is generated in the preceding steps, is released. The final step – grinding – can only be used to correct very small distortions.

As an additional process step thermal pre-stressing can be used to manipulate the distortion potential of the component before the heat-hardening treatment [10]. At this position in the process chain TGM, MEM and RSRM can be activated and have to be taken into account in order to minimise the final distortion of the component at the end of the process chain. Thermal pre-stressing can be done by local heating of the component with a laser beam which is moved by means of a scanner system as illustrated in Fig. 9.26. Local heating induces a temperature gradient inside the component which can activate TGM and MEM. RSRM can additionally be activated during the thermal pre-stressing and the heat-hardening treatment. The combined activation of different mechanisms and the fact that multiple process steps have to be taken into account to determine the final distortion make it difficult to choose optimal process parameters for the thermal pre-stressing. The only possible way to predict the dependence of the distortion on the process parameters is by numerical modelling in which the model has to include the evolution of the micro-structure (i.e. phase changes) in addition to the thermo-mechanical calculation.

References

1. Namba Y (1985) Laser Forming in Space. In: Proc. Lases'85 403–407
2. Namba Y (1987) Laser Forming of Metals and Alloys. In: Laser Advanced Materials Processing LAMP'87, High Temp. Soc. of Japan and Japan Laser Processing Soc 601–606
3. Vollertsen F, Pretorius P (2005) Thermal Bending: History and Perspectives. In: Vollertsen F, Seefeld T (eds) Thermal Forming, Proceedings of the IWOTE'05, BIAS-Verlag, Bremen 1–19
4. Uelze A (1988) Thermisches Richtpunkten von gebeulten Feinblechfeldern. Schweißtechnik, vol 38 no 4, Berlin-Ost 166–168
5. Male AT, Li PJ, Chen YQ, Zhang YM (1999) Flexible Forming of Sheet Metal Using Plasma Arc. ASME/MED 10: 935–940
6. Pretorius T, Woitschig J, Vollertsen F (2005) Fast Simulation of the Temperature Field for Plasma Jet Forming. In: Vollertsen F, Seefeld T (eds) Thermal Forming, Proceedings of the IWOTE'05, BIAS-Verlag, Bremen 203–210
7. Komlódi A, Otto A (2005) Acceleration of the Simulation of Laser Beam Bending – Challenges and Possibilities. In: Vollertsen F, Seefeld T (eds) Thermal Forming, Proceedings of the IWOTE'05, BIAS-Verlag, Bremen 211–220
8. Grden M, Vollertsen F (2008) Fast Simulation Method of Thermal Bending along Curved Irradiation Paths. In: Vollertsen F, Sakkiettibutra J (eds) Proc. of the IWOTE'08, BIAS-Verlag, Bremen 289–296
9. Vollertsen F (1996) Laserstrahlumformen – Lasergestützte Formgebung: Verfahren, Mechanismen, Modellierung. Meisenbach, Bamberg

10. Pretorius T, Woitschig J, Habedank G, Vollertsen F (2006) Thermal generation of residual stress fields for purpose of distortion minimization. Materialwissenschaft und Werkstofftechnik 37(1): 85–91

11. Vollertsen F, Rödle M (1994) Model for the temperature gradient mechanism of laser bending. In: Geiger M, Vollertsen F (eds) Laser Assisted Net shape Engineering LANE'94, vol I, Meisenbach, Bamberg 371–378

12. Hänsch H (1984) Schweißeigenspannungen und Formänderungen an stabilen Bauteilen. DVS/VEB Verlag Technik, Berlin

13. Koerdt M, von Beren JD, Schilf M, Vollertsen F (2007) Straightening of ship structures using a laser beam. In: Vollertsen F, Emmelmann C, Schmidt M, Otto A (eds.) Proc. of Lasers in Manufacturing LIM 2007, Munich, Germany 517–522

14. Koerdt M, von Beren JD, Schilf M, Vollertsen F (2008) Richten mit dem Laserstrahl. Schiff & Hafen, February 2008, 2: 64–67

15. Geiger M, Kraus J, Pohl T, Hoffmann P, Vollertsen F (1994) Analytisches Modell für das Laserstrahlbiegen von Profilen. Laser Magazin 10(6): 18–25

16. Zhou JZ, Yang JC, Zhang YK, Zhou M (2002) A Study on Super-Speed Forming of Metal Sheet by Laser Shock Waves. Journal of Materials Processing Technology 129: 241–244

17. Schulze Niehoff H, Vollertsen F (2005) Non-thermal Laser Stretch-Forming, In: Geiger M, Duflou J, Kals HJJ, Shirvani B, Singh UP (eds) 11th Int. Conf. on Sheet Metal, Advanced Materials Research 6–8: 433–440

18. Vollertsen F (2005) Laser Induced and Laser Assisted Forming Technologies. In: Bariani, PF (ed) Advanced Technology of Plasticity, Proceedings of the 8th ICTP, Verona p557

19. Reinhart G, Härtl J, Lehner C (2001) New Ways for a Reliable Laser Beam Welding Process. In: Geiger M, Otto A (eds) Laser Assisted Net Shape Engineering 3, Proc. of 3rd LANE, Erlangen, Meisenbach-Verlag, Bamberg 687–696

20. Reinhart G, Härtl J (2004) The Usage of Active Gases to Elevate the Efficiency of Welding with High Power Diode Lasers. Annals of the German Academic Society for Production Engineering 11(2): 79–82

21. Thomy C, Seefeld T, Vollertsen, F (2005) Application of High-Power Fiber Lasers for Joining of Steel and Aluminium Alloys. In: Proc. of 3rd Int. WLT-Conf. Lasers in Manufacturing, AT-Fachverlag, Stuttgart 27–32

22. Verhoeven ECM, de Bie HFP, Hoving W (2000) Laser Adjustment of Reed Switches: Micron Accuracy in Mass Production. LIA, Laser Inst. of Am 90B: 21–30

23. Hoving W (1997) Accurate Manipulation Using Laser Technology. In Proc. SPIE–Int. Soc. for Optical Eng 3097: 284–295

24. Geiger M, Hennige T, Huber A, Müller B (1999) Laserstrahlumformen als Innovation für das Justieren vormontierter Systeme. Umformtechnik 2000 Plus:149–162

25. Peck DE, Deysel P (2001) Beam Spring Flexible Manufacturing Production Line. In: Proceedings of 20th ICALEO 2001, Laser Institute of Amarica, Orlando, USA, CD-ROM F209

26. Hornfeck T, Silvanus J, Zaeh MF, Schoberth A (2005) EcoShape – a robust laser beam forming process of aluminium alloys for aerospace applications. In: Vollertsen F, Seefeld T (eds) 1st International Workshop on Thermal Forming IWOTE'05. BIAS-Verlag, Bremen 139–147

27. Geiger M, Vollertsen F, Amon S (1991) Flexible Blechumformung mit Laserstrahlung – Laserstrahlbiegen. Blech, Rohre, Profile 38(11): 856–861
28. Mucha Z, Hoffmann J, Kalita W, Mucha S (1997) Laser Forming of Thick Free Plates. In: Proc. of LANE, Laser Assisted Net Shape Engineering, CIRP Int. Seminar on Manufacturing Systems 30: 383–392
29. Bartkowiak K, Edwardson SP, Borowski J, Dearden G, Watkins KG (2005) Laser forming of thin metal components for 2D and 3D applications using a high beam quality, low power Nd:YAG laser and rapid scanning optics. In: Vollertsen F, Seefeld T (eds) 1st International Workshop on Thermal Forming IWOTE'05. BIAS-Verlag, Bremen 111–129
30. Osakada K, Otsu M, Matsumoto R (2005) Thermal Forming of Pipes. In: Vollertsen F, Seefeld T (eds) Thermal Forming, Proceedings of the IWOTE'05, BIAS-Verlag, Bremen 131–138
31. Olowinsky A, Gillner A, Poprawe R (1997) Mikrojustage durch Laserstrahlumformen. In: Proc. of Sensor 97, Nürnberg, May 1997, AMA Fachverband für Sensorik 133–137
32. Hagenah H, Wurm T (2005) Problem Specific Design of Actuators for Micro Adjustment. Advanced Materials Research 6–8: 271–278
33. Zimmermann M, Dirschel M, Stark M (2006) Mikrojustierung mit Licht. Mikroproduktion 2: 32–35
34. Widaszewski J (2005) Micro Adjustment by Thermal Upsetting. In: Vollertsen F, Seefeld T (eds) Thermal Forming, Proceedings of the IWOTE'05, BIAS-Verlag, Bremen 93–109
35. Sakkiettibutra J, Vollertsen F (2008) Effects of Varying Heating Duration on Thermal Upsetting. In: Vollertsen F, Sakkiettibutra J (eds) Proc. of the IWOTE'08, BIAS-Verlag, Bremen 45–54
36. Engler I (1999) Verfahrenskombination Laserstrahlschweißen und -richten am Beispiel einer Titan-Leichtbaustruktur. Dissertation University of Bremen, Strahltechnik vol 12, BIAS-Verlag, Bremen
37. Hoffmann F, Keßler O, Lübben T, Mayr P (2002) Distortion Engineering – Verzugsbeherrschung in der Fertigung. HTM 57(3): 213–217

Femtosecond Laser Pulse Interactions with Metals

Bernd Hüttner

DLR – Institute of Technical Physics, Pfaffenwaldring 38-40, 70569 Stuttgart, Germany. `bernd.huettner@dlr.de`

Abstract. A new era of fundamental research and its application to surface processing has been created by the invention of femtosecond laser pulses. Theoretical aspects of these processes are considered in this chapter. The differences between these very short pulses and the more conventional longer pulses are discussed, including the electron-electron scattering time and the non-equilibrium electron distribution. The material properties of objects exposed to femtosecond laser pulses are discussed with particular reference to their optical and thermal properties. The problem of determining the electron and phonon temperature distributions is addressed by means of the two-temperature model and the extended two-temperature model.

10.1 Introduction

The invention of femtosecond laser pulses opened a new era of basic research and surface processing. Laser ablation, the removal of matter by means of a laser beam, is one of the most promising technologies among femtosecond laser applications, because the ablation physics of extremely short pulses is very different from that of longer laser pulses. During the last thirty years great advances have been achieved both in theoretical descriptions and in experimental investigations. Nevertheless, a complete understanding of the whole process is not available yet. This is due to the complicated nature of the process. One has to take into account not only the processing conditions but also the material properties like, for example, absorption, heat conduction and plasma formation. These properties are, however, in many cases not given by their steady state values, or cannot be described by equations derived under the assumption of local thermal equilibrium. They are modified due to the lack of equilibrium that is characteristic of ultrashort time laser material interaction. Both the optical and the thermodynamic properties of the solid are affected by the modifications. In addition, the presence of strong nonlinear processes caused by the temperature dependence of quantities like
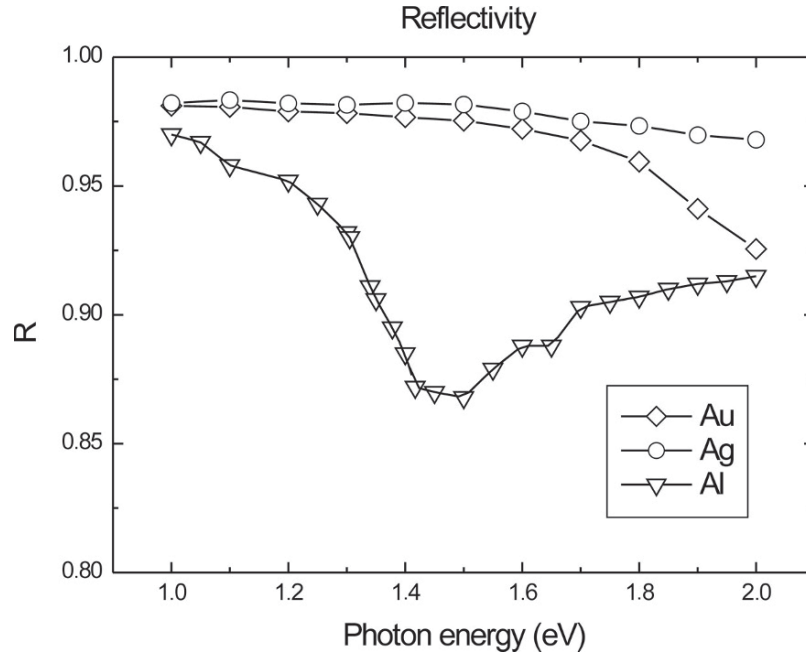
Fig. 10.1. Reflectivity of gold, silver and aluminium between 1 and 2 eV. Data taken from [4].

the absorption or the electronic thermal conductivity makes the problem no easier.

Today several laser systems are available for the generation of femtosecond laser pulses. For example, Ti:sapphire, dye, excimer and free electron lasers are among those. In the following, however, attention will be restricted to the examination of the Ti:sapphire laser because it is used in most experiments but also with the aim of making a comparison between different experiments more transparent. Furthermore, in many experiments the same pulse duration of $\tau_L = 100\,\mathrm{fs}$ was often used but not always the same wavelength. In the ground mode the Ti:sapphire laser possesses a working range of about $\lambda = 650\,\mathrm{nm}$ (1.91 eV) to $\lambda = 1100\,\mathrm{nm}$ (1.13 eV). Compared to the rare-earth doped gain materials like Nd:YAG or Nd:YLF this is very broad and results from the expanded gain bandwidth of the Ti^{3+} ion. The maximum gain and laser efficiency is achieved, however, around 800 nm. In noble metals the optical properties are usually not very sensitive to a variation of the wavelength in this range. For aluminium, however, one has to be careful because it possesses an interband transition and therefore a drastic change of the reflectivity emerges around 820 nm as can be seen in Fig. 10.1.

Another important aspect is that femtosecond lasers can deliver very high intensities in the focal spot of up to $I = 10^{20}\,\mathrm{W\,cm^{-2}}$ at present. The light

pressure $p = I/c$ at this intensity is $p = 3 \times 10^{15}$ Pa $= 30$ Gbar. This is higher than the typical value of yield stress for metals.

Even at much lower intensities, say $I = 10^{14}$ W cm^{-2}, interesting phenomena appear both for basic investigations and technological applications. In a very small volume, calculated as the laser spot size times skin depth, the electrons can reach temperatures of some tens of thousands Kelvin during the laser pulse while the lattice basically remains thermally undisturbed. Photoemission of electrons starts if the electron kinetic energy becomes larger than the work function. After the termination of the laser pulse the phonon temperature can rise rapidly close to or even above the critical temperature caused by the phonon emission during the energy relaxation of the electrons. The metal is then in an unstable nonequilibrium state leading to ejection of material driven by the high critical pressure followed by a rapid quenching. Therefore, a great part of the absorbed laser energy can be removed from the bulk during the ablation process by the ejected material. This is the origin of one of the great advantages of femtosecond laser applications compared to nanosecond lasers, since the dissipation of energy due to thermal conduction plays a minor role. The remaining heat affected zone therefore becomes quite small and only very little collateral damage may appear. Depending on the process conditions, this can be used for the processing of smooth and sharp structures in practically any material. Moreover, the optimum ablation efficiency, defined as the ratio of the volume of ablated matter to the laser pulse energy, was found for femtosecond lasers [1].

10.2 What is Different Compared to Longer Pulses?

10.2.1 The Electron-Electron Scattering Time

The phenomena of femtosecond laser interaction with metals are drastically different from those related to laser pulses longer, say, than 100 ps. There is, however, in the following no sharp boundary between the two pulse ranges because it depends on the material and the property under investigation. Nevertheless, it will be assumed that long pulse behaviour is established if a local thermal equilibrium exists between the electron and phonon subsystems during the laser pulse, equivalently, both systems have the same local temperature. This implies that for ultrashort laser pulses the electron temperatures are higher than the phonon temperatures because the electromagnetic laser fields couple only with the electrons. Indeed, the electron temperature can increase to values far above the critical temperature of metals. In this way, the electron-electron scattering, usually of less importance than the electron-phonon scattering time as a result of Pauli's exclusion principle [2], becomes significant or even dominant. In the frame of the Fermi liquid theory, the

Electron-electron scattering time
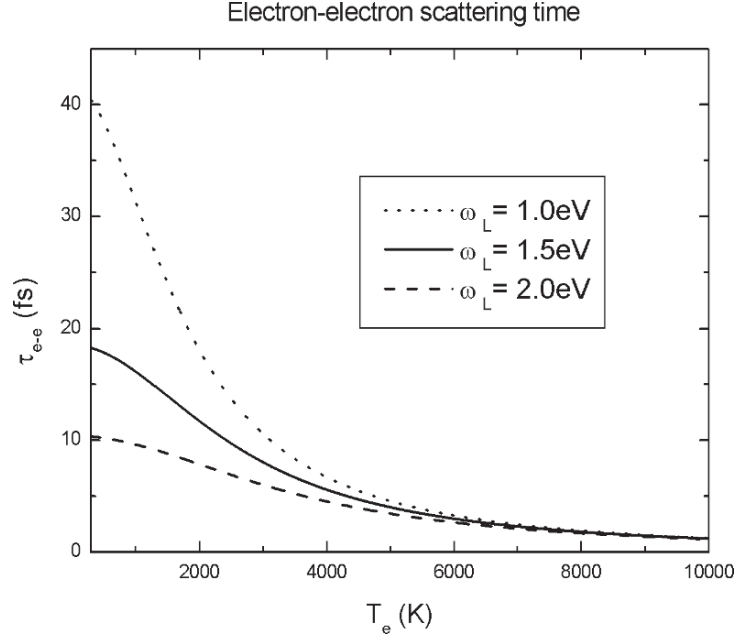
Fig. 10.2. Electron-electron scattering time of gold for three laser energies as a function of electron temperature.

electron-electron scattering time is defined by

$$\tau_{e-e} = \frac{1}{a\left(E - E_F\right)^2 + b\left(k_B T_e\right)^2} = \frac{1}{\beta\left[\left(E - E_F\right)^2 + 4\pi^2 T_e^2\left(eV\right)\right]} \quad (10.1)$$

where the constants a and b are independent of the electron energy, E, and the electron temperature, T_e. For normal transport, remembering $T = 300\,\mathrm{K}$ corresponds to $0.03\,\mathrm{eV}$, the electron energy is very close to the Fermi energy, E_F, leading to a rather large value for the electron-electron scattering time. In the case of laser excitation, however, the electron energy is approximately Fermi energy plus photon energy. Consequently, the denominator may become large and, therefore, τ_{e-e} small. Furthermore, since electron temperatures of some thousand degrees Kelvin are quite normal for femtosecond laser metal interaction, the second temperature dependent part also contributes remarkably to the reduction of the scattering time. Physically speaking, far above the Fermi energy the phase space for scattering is huge and is essentially not restricted by Pauli's principle since there are a lot of empty places available for scattering events. Figure 10.2 shows, as an example, the electron-electron scattering time of gold for three energies above the Fermi energy as a function of the electron temperature; the value for the constant β has been taken from Parkins et al. [3].

From Fig. 10.2 it can be concluded that the electron-electron scattering time for high temperatures becomes quite short and has, therefore, been taken into account explicitly in the consideration of the interaction of femtosecond laser pulses with metals. In the following, many examples will be found of changes in the behaviour of properties that can be traced back to the enhanced effect of the electron-electron scattering time.

Although laser energy is absorbed by the electrons in a thin layer for both long and ultrashort pulses with an optical penetration depth that is typically of the order of 10–20 nm, there is a large difference in the energy density near the surface. There are two quite different causes. First, it is well-known that absorption increases slightly with temperature in metals for frequencies far away from interband transitions. For aluminium at wavelengths of about 800 nm, however, the greatest part of the absorption is governed by the interband transition, which is decreasing with the phonon temperature due to band broadening [5]. This effect, however, has to be taken into account for long pulses only because, on the femtosecond scale, the phonon temperature is changed little or not at all. On the other hand, the increase of the electrical resistivity caused by stronger electron-electron scattering for femtosecond pulses can even induce an increase in absorption [6, 7]. Experimentally, such changes can be seen in transient thermal reflectivity pump and probe measurements in which the metal is heated with a strong pump laser and the change of reflectivity is detected; in most cases this is done at another wavelength, by a weak probe laser at the surface. For very thin films, one can also determine the transient thermal transmission by the same method at the rear.

Note that the absorption of the pump laser is not measured, only the optical response at the probe wavelength. There are, however, also measurements with the same wavelengths for the pump and probe laser but with different angles of incidence [8]. Figure 10.3 presents an example of the relative change of the reflectivity of gold film (180 nm) pumped by a 400 nm Ti:sapphire laser and probed at 800 nm. The pulse duration in the experiment was 130 fs (FWHM) and the energy for the excitation was 4.8 μJ [9]. The theoretical curves have been calculated with the equations provided by Hüttner [7] where the electron and phonon temperatures were either evaluated by means of the extended two temperature model (ETTM) [10] or with the more familiar two-temperature model (TTM) [11]. The differences between these models will be discussed in more detail in Sect. 10.4.

The second factor is related to the electronic thermal diffusivity defined by

$$k_e = \lambda_e / c_e, \tag{10.2}$$

the ratio of the electronic thermal conductivity to the electronic specific heat. From this quantity which is of the order of $100 \, \text{cm}^2 \text{s}^{-1}$ for metals at room temperature, the thermal diffusion length,

$$L_{th} = \sqrt{2 k_e \tau_L}, \tag{10.3}$$

Relative reflectivity of gold
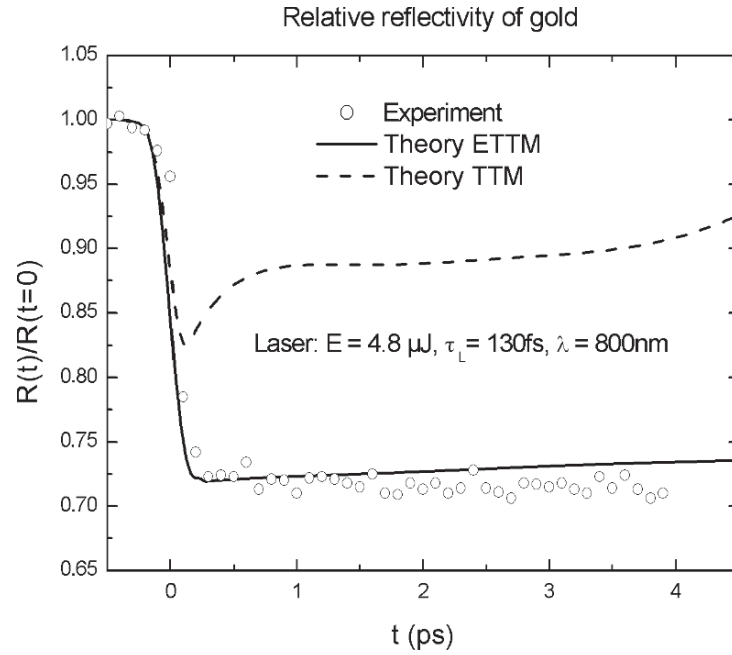
Fig. 10.3. The relative change of the reflectivity, $R(t)/R(t = 0)$, of aluminium after excitation with pulse energy of $4.8\,\mu$J at 400 nm with a pulse duration of 130 fs (FWHM) probed at 800 nm. The points are values measured by Funk et al. [9] and are compared with theoretical calculations; for details see text.

can be estimated to be approximately 45 nm for $\tau_L = 100$ fs but as $1.4\,\mu$m for $\tau_L = 100$ ps.

Consequently, for the same delivered laser pulse energy, the mean energy density is significantly higher in the femtosecond case because of a much smaller heated volume and by potentially increased absorption. The same will clearly be true for the electron temperatures after a short thermalisation time in the order of a few multiples of ten femtoseconds mainly caused by the electron-electron scattering.

10.2.2 The Nonequilibrium Electron Distribution

As mentioned above, the electron and phonon temperatures can be very different in the case of femtosecond laser pulses; the difference between them depends on the heat energy exchange coefficient. This important quantity will be discussed in more detail in the next section. In addition, after excitation with femtosecond pulses the electrons have a nonequilibrium distribution whereas for longer pulses they are governed by the Fermi-Dirac distribution. It is important to note that the occurrence of the nonequilibrium distribution is not dependent on the laser intensity, as seen in experiments [12] where
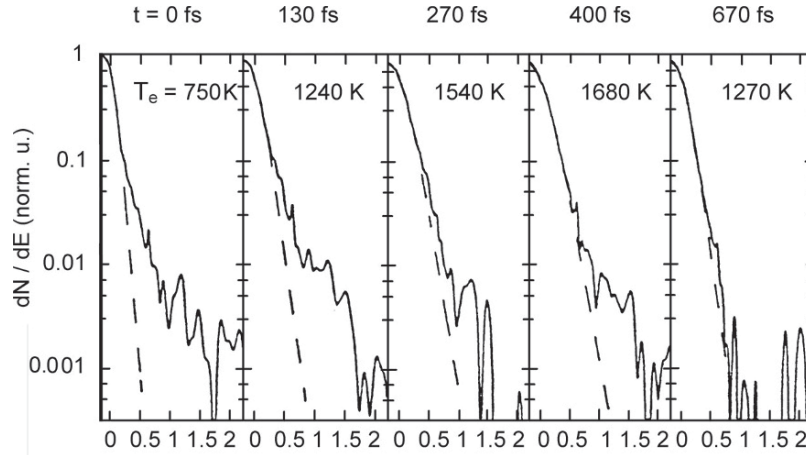
Fig. 10.4. Electron energy distribution function vs energy with $120\,\mu\mathrm{J\,cm^{-2}}$ absorbed laser fluence at five time delays. The dashed line is the best Fermi-Dirac fit and the corresponding electron temperature T_e, is shown. The vertical scale is in units of the density of states. *Reprinted with permission from [13]. Copyright 1992 by the American Physical Society.*

the electron temperature increased only by about 20 K. The reason is the excitation discussed above of the electrons in energy band states higher than the Fermi energy. Figure 10.4 presents a time-resolved photoemission spectroscopy of the time evolution of the electron energy distribution following ultrashort laser pulse excitation of a gold sample [13, 14]. The 30 nm gold film was excited with a photon energy of 1.84 eV, a fluence of $F = 300 \pm 90\,\mu\mathrm{J\,cm^{-2}}$ and a laser pulse duration of 180 fs. The deviations from the Fermi-Dirac distribution up to 1.84 eV can be seen clearly in the figure. The electron-electron scattering time is given in the paper in a slightly modified form, $\tau_{e-e} = \tau_0\left[E_F/E - E_F\right]^2$. If one substitutes in this equation the experimentally determined value $\tau_0 = 5$ fs and $E_F = 5.53$ eV [2] one obtains $\tau_{e-e} = 11.2$ fs in good agreement with the room temperature value from Fig. 10.2.

The authors model the nonequilibrium distribution by assuming that it is composed of a thermal and a nonthermal part. The thermal part is described by the Fermi-Dirac distribution. For the other, they choose a nascent distribution as the initial condition together with the additional assumption of an instantaneous excitation at $t = 0$ fs. Another theoretical explanation without these assumptions for the time dependence of the relaxation of the nonequilibrium distribution has been published by Hüttner [15]. The key point in this work consists of a combination of the development of the Boltzmann equation up to the second order together with the calculation of the electron temperature by means of the ETTM. For this purpose a photon operator, first proposed by Zinoviev et al. [16], has been incorporated in the Boltzmann equation. The resulting theoretical curves are plotted in Fig. 10.5.
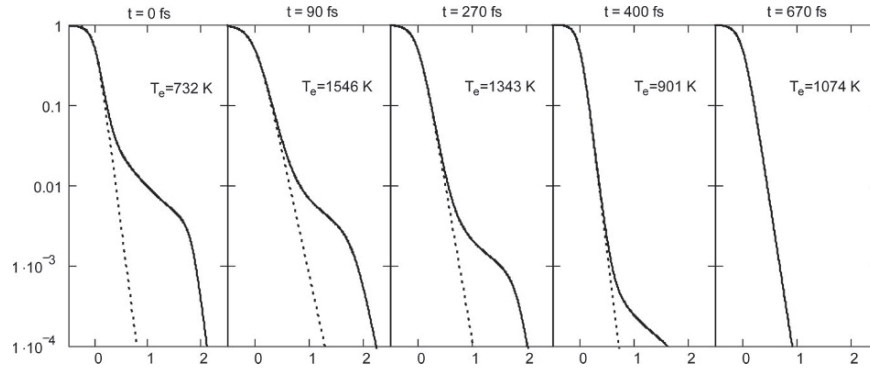
Fig. 10.5. Theoretical electron energy distribution function vs energy with $300\,\mu\mathrm{J\,cm^{-2}}$ absorbed laser fluence at five time delays. The dashed line is the Fermi-Dirac function and the corresponding electron temperature T_e is shown.

A closer inspection of Figs. 10.4 or 10.5 reveals a further remarkable feature. The maximum of the electron temperature appears at times long after the termination of the laser pulse. The agreement between the experimental and theoretical curves is satisfactory although the maximum of the temperature appears a little bit later in the theoretical calculation. The enhancement of the temperature at later times is a consequence of the heat wave, predicted by the ETTM, and the concomitant reflection of the temperature wave from the rear side. The slight discrepancy between experiment and theory can have several causes. It may reflect a weakness of the ETTM or it could be a result of the relatively large experimental uncertainty of 30% in the absorbed fluence.

Nevertheless, a maximum of the electron temperature after the laser pulse cannot occur in a diffusive model as given by the classical equation of heat conduction. This point will be considered in detail below when the evaluation of the electron and phonon temperatures is discussed.

10.3 Material Properties Under Exposure to Femtosecond Laser Pulses

In the preceding section some changes of material properties under the special conditions of femtosecond laser pulses were sketched. This will now be extended for both the optical and thermal properties.

10.3.1 Optical Properties

The calculation of all optical properties is practicable if one knows the complex dielectric function of the metal as a function of the photon frequency and of

the electron and phonon temperatures. It should be noted that the dielectric function becomes implicitly time dependent as a result of its dependence on the temperatures. Using the familiar relation between the complex dielectric function and the complex frequency dependent conductivity,

$$\varepsilon\left(\omega, T_e, T_{ph}\right) = \varepsilon_0 + i\frac{4\pi}{\omega}\sigma\left(\omega, T_e, T_{ph}\right), \tag{10.4}$$

the problem is shifted to the determination of the complex conductivity for the case of local thermal nonequilibrium. Since noble metals have no interband transition close to the range of Ti:sapphire wavelengths the free electron model, as dealt with in textbooks on solid state physics, this offers a good starting point. One has, however, to bear in mind that the usual temperature (local thermal equilibrium) must be replaced by the electron and phonon temperatures and that electron-electron scattering has to be included. As is well-known, the real and imaginary parts of the refractive index, respectively, are related to the complex dielectric function by

$$n\left(\omega, T_e, T_{ph}\right) = \mathrm{Re}\left\{\sqrt{\varepsilon\left(\omega, T_e, T_{ph}\right)}\right\}, \quad k\left(\omega, T_e, T_{ph}\right) = \mathrm{Im}\left\{\sqrt{\varepsilon\left(\omega, T_e, T_{ph}\right)}\right\}. \tag{10.5}$$

The absorption depth and the absorption are connected with (10.5) and (10.4), respectively, by the expressions

$$\delta\left(\omega, T_e, T_{ph}\right) = \frac{c}{\omega\, k\left(\omega, T_e, T_{ph}\right)}, \quad A\left(\omega, T_e, T_{ph}\right) = 1 - \left|\frac{\sqrt{\varepsilon\left(\omega, T_e, T_{ph}\right)}-1}{\sqrt{\varepsilon\left(\omega, T_e, T_{ph}\right)}+1}\right|^2. \tag{10.6}$$

The modified equations for all optical quantities were derived and evaluated in the case of gold in [7]. Unfortunately, the terms are rather long and so will not be repeated here. The interested reader is referred to the original paper. To give an indication, the results for the absorption in Fig. 10.6 are reprinted and the relative changes of the quantities at the end of the laser pulse presented in Table 10.1. The laser data used for the photon energy, pulse duration and absorbed intensity were $\omega = 1\,\mathrm{eV}$, $\tau_L = 500\,\mathrm{fs}$, $I_{abs} = 10\,\mathrm{GWcm}^{-2}$ and $I_{abs} = 20\,\mathrm{GW\,cm}^{-2}$, respectively, and a top-hat profile was applied for the time dependence of the laser pulse for the calculations. In this way, the intrinsic time dependence of the properties can be assessed more easily because it is not masked by the shape of the laser pulse. The time dependence of the electron and phonon temperature was determined by means of the ETTM and then inserted in the optical equations. The cusp of the absorption reflects the sharp cut-off of the top-hat profile. In the case of Drude absorption σ was replaced by the Drude conductivity

$$\sigma_D = \frac{ne^2\tau_D\left(T_{ph}\right)}{m} \tag{10.7}$$
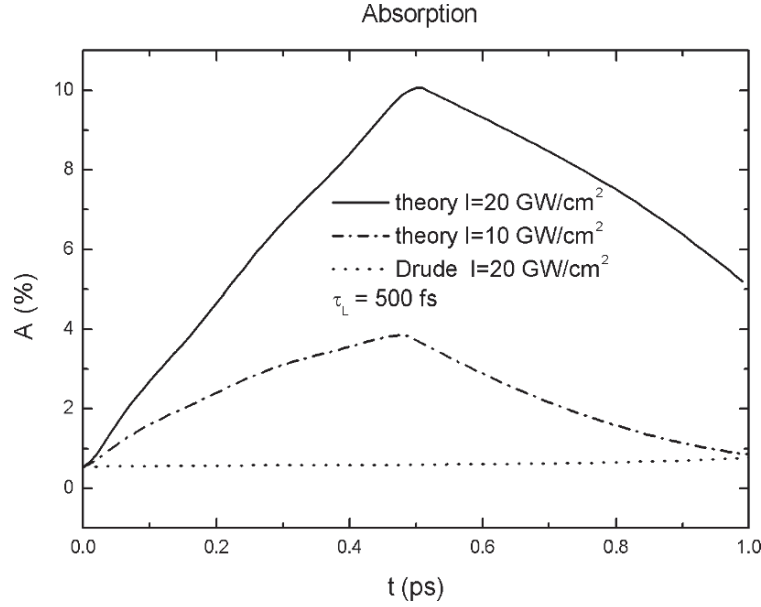
Absorption

Fig. 10.6. Absorption of gold: full and dashed curves display the theory up to a second, dash-dotted curve Drude's theory (depending only on T_{ph}).

Table 10.1. Relative change, $\Delta x/x = [x(\tau_L) - x(0)]/x(0)$, of the electron and phonon temperature (T_e, T_{ph}), the real and imaginary part of the conductivity (σ', σ''), the dielectric function (ε', ε'') and the refractive index (n, k), the absorption depth (δ) and the absorption (A) for $I = 10\,\mathrm{GWcm}^{-2}$ (second line), and $I = 20\,\mathrm{GW\,cm}^{-2}$ (third line), respectively.

$\dfrac{\Delta T_e}{T_e}$	$\dfrac{\Delta T_{ph}}{T_{ph}}$	$\dfrac{\Delta\sigma'}{\sigma'}$	$\dfrac{\Delta\varepsilon''}{\varepsilon''}$	$\dfrac{\Delta n}{n}$	$\dfrac{\Delta A}{A}$	$\dfrac{\Delta\sigma''}{\sigma''}$	$\dfrac{\Delta\sigma''}{\sigma''}$	$\dfrac{\Delta\varepsilon'}{\varepsilon'}$	$\dfrac{\Delta k}{k}$	$\dfrac{\Delta\delta}{\delta}$
15.94	0.100	5.67	5.67	5.79	5.88	−0.042	0.042	−0.018	0.018
29.23	0.127	14.73	14.73	16.20	17.59	−0.208	0.210	−0.086	0.094

depending explicitly only on the electron-phonon scattering and implicitly on the phonon temperature.

Table 10.1 reveals that the greatest relative change, an increase by a factor of almost 20, appears in the case of the absorption. Such an enhancement and the corresponding decrease of the reflection have been observed in many experiments [17–19].

One should, however, be careful in a direct comparison of the theory with the experiment because there are differences in the materials; polycrystalline metals with rough surfaces have a higher absorption at room temperature in contrast to theoretical single-crystalline ones with perfect smooth surfaces. Furthermore, the probe wavelength may be different and/or much larger delays of some tens to some hundreds of picoseconds between pump and probe may be used.

Nevertheless, the changes demonstrate in a clear manner the effect of decoupling the electron and phonon temperatures. They also demonstrate the fact that the electron-electron scattering rate becomes comparable or even greater than the electron-phonon scattering rate with increasing electron temperatures and starts to dominate the interactions.

10.3.2 Thermal Properties

The properties of the specific heat, thermal conductivity and thermal diffusivity of the electrons will be discussed next. It follows from the Fermi-Dirac distribution that the specific heat of free electrons is given by

$$c_e = \frac{\pi^2}{2} \frac{n k_{k_B}^2}{E_F} T_e \tag{10.8}$$

where n is the electron density and k_B the Boltzmann constant. Such linear temperature dependence is used in almost all papers for the calculation of the electron temperatures although at very high temperatures deviations may appear. Band structure calculations of gold revealed that the value of the specific heat near $T_e = 10000\,\mathrm{K}$ is about 2.5 times larger than (10.8) would produce [20]. The enhancement follows from a thermal excitation of the d-band electrons $2.2\,\mathrm{eV}$ below the Fermi energy. Analogous calculations for other metals were not reported. Starting from the expression of the thermal conductivity of a gas one can derive a simple linear relation between the electronic thermal conductivity and the electron temperature,

$$\lambda = \lambda_0 \frac{T_e}{T_0}. \tag{10.9}$$

The same expressions can be obtained from the Wiedemann-Franz law, $\lambda = \sigma T L_0$, where σ is the electrical conductivity and L_0 the Lorenz number. Although relation (10.9) is used in many papers one has to be very careful since it is only valid for a restricted temperature range up to few thousand Kelvin. Better equations applicable for a wider temperature range were proposed in [21] and [22]. In the latter paper the thermal conductivity was calculated by a Sommerfeld expansion up to the second order including the electron-electron scattering time, (10.1). The equation reads

$$\lambda_e = \lambda_{LTE} \frac{T_e\, G(T_e)}{T_{ph}\,(1 + z\,(T_e, T_{ph}))} \left\{ 1 + \frac{1}{G(T_e)^2} \left[\frac{\pi^2\, k_B^2\, T_e^2}{24\, E_F^2} + \frac{7\pi\, k_B^4\, T_e^4}{480\, E_F^4} \right] \right\}. \tag{10.10}$$

The prefactor λ_{LTE} is the conductivity related to the case of local thermal equilibrium $(T_e = T_{ph})$ without the contribution of the electron-electron scattering and is given by

$$\lambda_{LTE} = \frac{\pi^2}{3} \frac{k_B^2}{e^2} T_{ph} \sigma_D\,; \tag{10.11}$$

Thermal conductivity of gold
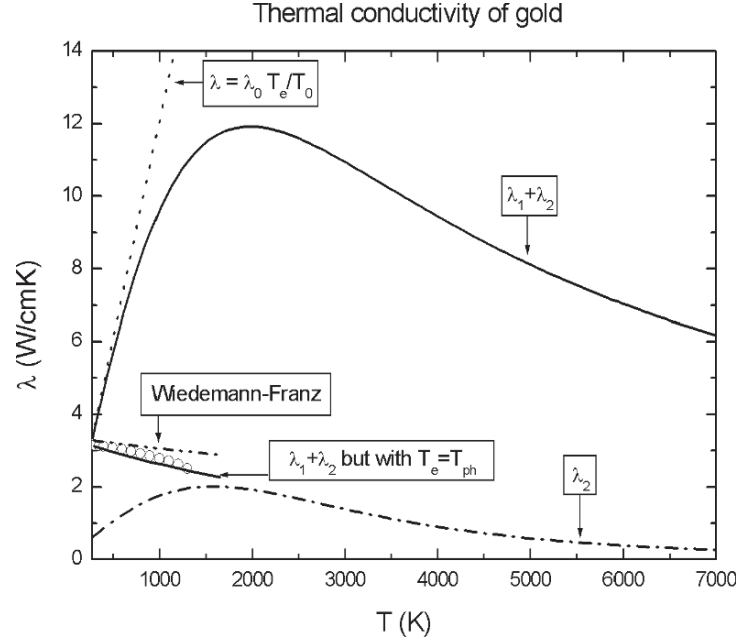
Fig. 10.7. Thermal conductivity of gold as a function of the electron temperature. The upper full curve shows the first and second order contribution for fixed $T_{ph} = 300\,\mathrm{K}$. The dotted curve presents the behaviour according to (10.9). The dashed-dotted curve is the second order contribution. The lower full curve is the first and second order contribution for the case of local thermal equilibrium ($T_e = T_{ph}$). The Wiedemann-Franz curve corresponds to (10.11). The experimental results are given by (o).

the function $G(T_e)$ and $z(T_e, T_{ph})$ are defined by

$$G\left(T_e\right) = \sqrt{1 - \frac{\pi^2\, k_B^2\, T_e^2}{12\, E_F^2} - \frac{7\pi^4\, k_B^4\, T_e^4}{360\, E_F^4}}\ . \qquad (10.12)$$

and

$$z\left(T_e, T_{ph}\right) = \frac{\tau_D}{\tau_{Te}} = 4\pi^2 \tau_D \beta T_e^2 \qquad (10.13)$$

where τ_{Te} is the temperature dependent part of the electron-electron scattering time.

   The result for gold is plotted in Fig. 10.7. The full curve represents the electronic short-time temperature dependence as a function of the electron temperature at a fixed phonon temperature of $T_{ph} = 300\,\mathrm{K}$ where λ_1 and λ_2 stand for the first and second order contributions respectively. A deviation from the linear increase predicted by (10.9) (dotted curve) can be recognised around 1000 K and for temperatures above about 2000 K a completely different behaviour appears. The lower full curve is the calculated thermal conductivity

Thermal diffusivity of gold
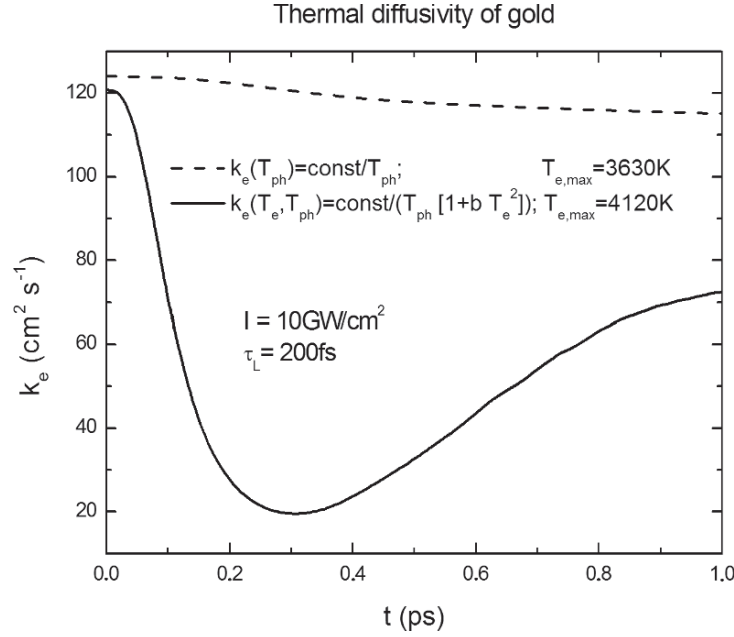
Fig. 10.8. Calculated electronic thermal diffusivity of gold as a function of time. The absorbed intensity is $10\,\mathrm{GW/cm^2}$ and 200 fs pulse duration.

if both temperatures are equal as happens during measurement under steady state conditions. The good agreement with the experimental values (o) taken from Weast [23] confirms the correctness of the constant β, (10.1), and underlines the necessity of already including the electron-electron scattering in the case of local thermal equilibrium, $T_e = T_{ph} = T$. Considering electron-phonon scattering only, one obtains the curve indicated as the Wiedemann-Franz prediction, for which values for the thermal conductivity are too large.

10.3.3 Electronic Thermal Diffusivity

The electronic thermal diffusivity is defined in (10.2) where the large difference for the thermal diffusion length between femtosecond and picosecond laser pulses was estimated. The dependence of the electronic thermal diffusivity of gold on the electronic temperature is plotted in Fig. 10.8 both for the thermal conductivity to (10.9) and the full expression (10.10). The used laser data are given in the figure.

   The decrease of the diffusivity with increasing electron temperatures is a direct result of the corresponding decline of the electron-electron scattering time due to the temperature dependent part of (10.1). There is, of course, a positive feedback to the temperature itself because a decreasing diffusion length induces a stronger confinement of the energy close to the surface and

therefore a further enhancement of the temperature. The thermal diffusivity can also be written as $k_e = v^2 \tau$ in one dimension where v is the Fermi velocity of the electrons, in contrast to the thermal velocity of classical particles not dependent on the square root of the temperature.

The information needed for the calculation of the electron and phonon temperature distributions in a metal during and after the interaction with a femtosecond laser pulse has been assembled, and their determination can now be considered.

10.4 Determination of the Electron and Phonon Temperature Distribution

10.4.1 The Two-Temperature Model

The two-temperature model is widely used for the calculation of the electron and phonon temperatures after interaction with ultrashort laser pulses. In its present form it was introduced by Anisimov et al. [11]. The main idea, the description of the electron and phonon subsystems by different temperatures, can be traced back, however, to Kaganov et al. [24]. One is able to reduce the treatment of the problem to one spatial dimension as long as the diameter of the laser focus is much broader than the skin depth or the electron thermal diffusion length as estimated in §10.1. Even for a spatial Gaussian pulse it has been shown that the radial temperature gradient can be neglected compared to the gradient in the normal direction [17]. This is, of course, not valid for arbitrarily long times but these are often not of interest for femtosecond laser pulse experiments. The two temperature equations are usually written in the following form,

$$c_e\left(T_e\right) \frac{\partial T_e}{\partial t} - \frac{\partial}{\partial x}\left(\lambda_e\left(T_e\right)\frac{\partial T_e}{\partial x}\right) = S\left(x,t\right) - h_{ex}\left(T_e - T_{ph}\right)$$
$$c_{ph}\frac{\partial T_{ph}}{\partial t} = h_{ex}\left(T_e - T_{ph}\right). \tag{10.14}$$

This is a nonlinear, inhomogeneous system of coupled differential equations for the electron and phonon temperatures where $S(x,t)$ is the source term and h_{ex} is the heat exchange coefficient. The neglect of phonon diffusion in the second equation is justified due to the smallness of the phonon temperature gradient compared to the gradient of the electron temperature and by the fact that the electron thermal conductivity is about two orders higher than in the phonon case. The source term can be written as

$$S\left(x,t\right) = \left(1 - R\right)\alpha e^{-\alpha x} I_0 g_L\left(x,t\right) \tag{10.15}$$

where R is the reflectivity, α the absorption coefficient, I_0 the maximum of the laser intensity and $g_L(x,t)$ a function describing the spatial and time dependence of the laser pulse.

Table 10.2. The coefficient of electronic specific heat, the mean square of phonon frequencies, the electron-phonon coupling constant, the heat exchange coefficient, the temperature relaxation time (10.17), Drude's relaxation time (10.7), the thermal conductivity and the absorption coefficient of some selected metals. The data for γ_e, λ_e and τ_D are taken from Ashcroft and Mermin [2], the other values from Brorson et al. [44] if not otherwise stated; α is determined from values in American Institute of Physics Handbook [43].

Metal	$\gamma_e \cdot 10^{-5}$ (J cm^{-3}K^{-2})	$\langle \Omega^2 \rangle$ (meV^2)	Λ_{e-ph}	h_{ex} (GW cm^{-3}K^{-1})
Au	6.7	178	0.15	26
Ag	6.5	344	0.12	35
Cu	9.7	377	0.1	94
Al	12.7		0.43	380[a]
Nb	71.7	275	1.04	3888
Pb	16.0	31	1.55	122
Ti	8.5	601	0.54	1207
V	117.7	352	0.82	5571
W	13.7	425	0.26	259

Metal	τ_e ($T = 300$ K) (fs)	τD ($T = 273$ K) (fs)	λ_e (W cm^{-1}K^{-1})	$\alpha \times 10^5$ (cm^{-1})
Au	773	30	3.1	7.31
Ag	557	40	4.18	8.56
Cu	310	27	3.85	7.60
Al	100	8	2.38	11.00
Nb	55	4.2	0.52	4.78
Pb	366	1.4	0.38	6.66
Ti	21	0.4	0.22	6.30
V	63	0.9	0.31	5.10
W	159	4.2	1.74	4.34

a: Fisher et al. [6].

The essential new quantity in (10.14) is the heat exchange coefficient given by

$$h_{ex} = \frac{3\hbar}{\pi k_B} \left\langle \Omega^2 \right\rangle \Lambda_{e-ph} \gamma_e. \tag{10.16}$$

It is very remarkable that the product of the averaged square of the phonon frequency and of the electron-phonon coupling constants, $\left\langle \Omega^2 \right\rangle \Lambda_{e-ph}$, is an important parameter in the theory of superconductivity [25]. In this way, a deeper understanding of the properties of metals from very low to very high temperatures is obtained. As a rule of thumb, good conductors have small electron-phonon coupling constants, low superconducting transition temperatures and modest heat exchange coefficients and vice versa. The third quantity in addition to the constants is the coefficient of the electronic specific heat. Values for the heat exchange coefficient are listed in Table 10.2. If the first

equation of (10.14) is divided by the electronic specific heat, $c_e(T_e)$, Allen's temperature relaxation time [26] is found on the right-hand side.

$$\tau_e = \frac{c_e\left(T_e\right)}{h_{ex}} = \frac{\gamma_e T_e}{h_{ex}} \, , \tag{10.17}$$

which is proportional to the electron temperature since h_{ex} can be regarded as constant in most cases. Deviations from it appear if d-band electrons are involved as already discussed for the electronic specific heat. The temperature dependence was observed in experiments [27, 28].

As can been seen from (10.14) the left hand side of the electron part corresponds to the parabolic heat conduction equation (the classical Fourier law). This equation, however, as discussed in many papers has a well-known shortcoming, namely the infinite speed of propagation of heat. Consequently, the energy is transported away from the surface faster in diffusive models, e.g. the TTM, compared to the ETTM, so lower temperatures are obtained close to the surface compared to the ETTM for the same experimental conditions. One has to state, however, that such a difference in the temperature is not sufficient to distinguish between the models or even to prefer one of the approaches. Indeed, some authors conclude that the TTM is also able to describe the transport on a femtosecond scale [29, 30]. Other authors, however, come to the conclusion that the TTM fails on a subpicosecond time scale [13, 28, 31]. An experimental result that can definitely not explained by the TTM is the ballistic transport of electrons. In this case the mean square of the thermal displacement of the electrons is proportional to the square of the time. In contrast, a diffusive model like the TTM predicts that the mean square is proportional to the time. By measuring the travel time as a function of the thickness of gold films a linear time dependence was observed with a thermal velocity of the electrons of about 70% of the Fermi velocity [32]. Although the ETTM possesses a principal solution with a ballistic behaviour at very short times as shown by Metzler and Compte [33], the calculated thermal velocities are of the order of about 50% of the Fermi velocity.

10.4.2 The Extended Two-Temperature Model

The ETTM is based on the hyperbolic heat conduction equation and predicts, therefore, that heat travels in damped waves. Comprehensive collections of papers related to this subject were published by Joseph and Preziosi [34, 35]. The basic idea can be traced back to Maxwell [36] who derived Fourier's law with an additional term

$$\tau \frac{\partial \vec{q}}{\partial t} + \vec{q} = -\lambda \nabla T. \tag{10.18}$$

In his discussion of the result he dropped the first term of (10.18) with the statement, "The first term may be neglected, as the rate of conduction will rapidly establish itself." Maxwell's conclusion may have been justified then,

but it is not so on the femtosecond time scales that are of interest now. Later this term was rediscovered independently from each other by Vernotte [37] and Cattaneo [38] with the aim of eliminating the "paradox" of the infinite speed of propagation of thermal phenomena. A modern derivation of (10.18) is provided by the theory of extended thermodynamics [39]. Using (10.18) and the energy conservation condition, the electron system is seen to be governed by the equations

$$
\tau \frac{\partial \vec{q}_e}{\partial t} + \vec{q}_e = -\lambda_e \left(T_e \right) \nabla T_e
$$

$$
\nabla \vec{q}_e + \frac{\partial u_e \left(T_e \right)}{\partial t} = S \left(x, t \right) - h_{ex} \left(T_e - T_{ph} \right)
$$

(10.19)

where $u_e \left(T_e \right) = 0.5 \cdot \gamma_e T_e^2$ is the internal energy of the electrons. The phonon part is unchanged and corresponds to the second equation of (10.14). After some manipulation to eliminate the heat flow in favour of the temperature one gets the following system of coupled differential equations,

$$
\tau \frac{\partial^2 u_e \left(T_e \right)}{\partial t^2} + \frac{\partial u_e \left(T_e \right)}{\partial t} - \frac{\partial \lambda_e \left(T_e \right)}{\partial x} \frac{\partial T_e}{\partial x} - \lambda_e \left(T_e \right) \frac{\partial^2 T_e}{\partial x^2} =
$$

$$
\left(1 + \tau \frac{\partial}{\partial t} \right) S \left(x, t \right) - h_{ex} \left(1 + \tau \frac{\partial}{\partial t} \right) \left(T_e - T_{ph} \right)
$$

(10.20)

$$
c_{ph} \frac{\partial T_{ph}}{\partial t} = h_{ex} \left(T_e - T_{ph} \right)
$$

It should be noted, however, that (10.20) in this form can be derived only if τ is taken as constant otherwise the term $\nabla \tau \dot{\vec{q}}_e$ cannot be cancelled. Equation (10.20) is a hyperbolic partial differential equation similar to the telegraph equation and therefore predicts the existence of temperature waves. In the limit as τ to zero, it becomes the classical parabolic equation of heat conduction. Several ways of deriving a non-Fourier heat equation are proposed in the literature. An illustrative example is to assume a non-local relation between the heat flow and the gradient of temperature, e.g.,

$$
\vec{q}(t) = - \int_{-\infty}^{t} \lambda \left(t - t' \right) \nabla T \left(t' \right) dt' .
$$

(10.21)

If the memory kernel is defined as

$$
\lambda \left(t - t' \right) = \lambda \frac{1}{\tau_h} \exp \left(-\frac{t - t'}{\tau_h} \right) ,
$$

(10.22)

the first equation of (10.19) is found immediately by differentiation with respect to the upper bound of the integral in (10.21). Physically this means

that the generation of a heat flow occurs with a characteristic time τ_h because it cannot be established in arbitrarily short times. Up to this point, by and large, there is a consensus in the literature, but very different answers exist to the question of what the characteristic time τ_h is. Zhang et al. [40] say τ_h is the relaxation time needed for the target temperature to reach a new equilibrium after the surface experiences a very high temperature gradient; they estimate its value to lie in the range from 10^{-14} s to 10^{-8} s for homogeneous materials. Other explanations are that τ_h is the mean free time in the energy carrier's collision process and is calculated by dividing the mean free path by the energy carrier's speed [41]; this gives, for example, a time of 10^{-12} s for nickel. Alternatively, τ_h is the free electron relaxation time in metals corresponding to $\tau_D(T_{ph})$ of (10.18) [42]. These times are quite short as can be seen from Table 10.2. The first equation of (10.19) has been derived from the Boltzmann equation in reference [15] where it was shown, furthermore, that τ_h corresponds to Allen's temperature relaxation time, (10.17). This time appears quite naturally on the right side of (10.20) if the whole expression is divided by $c_e(T_e)$. In this way, as few assumptions as possible are made in the sense of Ockham's razor or the "law of succinctness". A more physical motivation is provided by the following consideration. After the excitation, the temperature as an intensive quantity is approximately the same over the range of optical penetration. The specific heat of the electrons is, however, an extensive quantity proportional to the electron density. Due to the exponential decrease of the absorbed energy (Beer's law), the specific heat has an exponential distribution after the excitation and therefore it is higher close to the surface than it is deeper inside the metal. Consequently, it takes more time for the temperature to relax near the surface than further away from it, causing the build-up of an electron temperature gradient.

From Table 10.2 one can see that there are great differences between the temperature relaxation times of metals. From the discussion above it is clear that the ETTM reduces to the TTM in the limit $\tau_h = \tau_e = 0$. Therefore, the temperature distributions found from the two models become closer the smaller τ_e is and vice versa. This conjecture is in agreement with experimental observations. For example, Yoo et al. [45] found for the same laser conditions that the peak temperature of the electrons is 1660 K for copper but only 580 K for niobium. The phonon peak temperatures showed the opposite behaviour namely 360 K for niobium and 344 K for copper. The reasons for it are: (1) it takes a longer time for energy relaxation from the electrons to the phonons to occur for copper than for niobium. Therefore, hot copper electrons can move a greater distance before they lose their energy. For a fixed energy an increase in volume means, of course, a decrease in temperature. (2) Niobium has a higher specific heat for the electrons but a smaller one for the phonons compared to copper. The first property reduces the electron temperature, the second increases that for the phonons.

The Fig. 10.9 shows a comparison of the experimental results taken from Wang et al. [20] with the theoretical calculations based on the ETTM using

Electron surface temperature
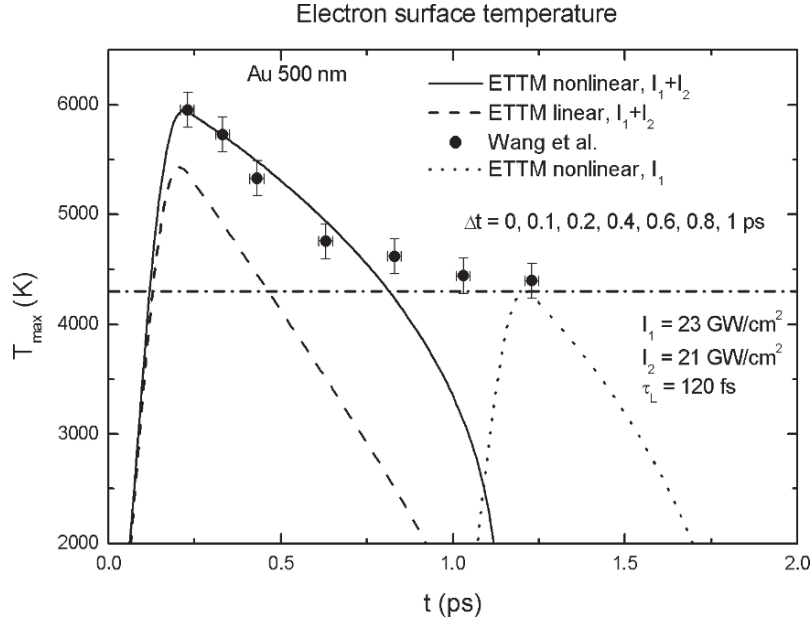
Fig. 10.9. Maximum electron temperature of gold as a function of the delay time, experimental (•) and calculated behaviour; for details see text.

both the linear thermal conductivity model, (10.9), and the nonlinear one, (10.10) [46].

The gold sample with a thickness of 500 nm has been irradiated with two almost identical pulses at different delay times Δt as indicated in Fig. 10.9. The theoretical curves were calculated for two delays ($\Delta t = 0$ and $\Delta t = 1.25$ ps) by means of the extended two temperature model (ETTM) both with the linear approximation for λ (dashed curve) and with the nonlinear expression (solid and dotted curve). The horizontal curve corresponds to the maximal electron temperature reachable with the single laser pulse I_1. For two delayed pulses this means that the temperature produced by the first pulse has relaxed completely before the second pulse arrives. As can be seen from the experiment this takes more than 1.25 ps. The agreement with the theory for one pulse (maximum of the dotted curve) is satisfactory. The same is true for two pulses with zero delay (solid curve). For the linear relation (dashed curve), however, the electron temperature stays well below the maximum because transport into the metal is too fast at high electron temperatures. It should be mentioned that the TTM gives values that are much too low even if we take into account the nonlinear thermal conductivity. The physical origin lies in the implicit prediction by the model that a temperature gradient arises instantaneously. Now we are in a position to understand the physical origin of the two theoretical curves in Fig. 10.3. The change of reflectivity is mainly

determined by the temperature dependent part of the electron-electron scattering time. Due to the delay for heat transport in the ETTM higher electron temperatures are achieved at the surface compared to the TTM. Consequently, the change in reflectivity is more pronounced. The slower decrease of the electron temperature in Fig. 10.3 compared to Fig. 10.9 is caused by the higher intensity and by the smaller film thickness.

10.5 Summary and Conclusions

In this chapter some aspects of the interaction of femtosecond laser pulses with metals has been considered and compared with the effects of longer pulses. The most important point is, perhaps, that metals exposed to femtosecond laser pulses are no longer in local thermal equilibrium. On short time scales the electron and phonon subsystem are decoupled and may have very different temperatures. For the description of this phenomenon the TTM was introduced about 30 years ago. However, as also stated by others, "one should say that the two-temperature model is derived under the assumption that the classical Fourier law describes the electron and phonon energy transports. It is applicable for times, which are longer than characteristic relaxation time τ_e within the electron gas. This time depends on the electronic temperature (i.e. the laser fluence). It typically comprises a few hundred femtoseconds" [47].

Moreover, the electrons are governed by a nonequilibrium distribution and not by the Fermi-Dirac distribution even for low intensities. In many cases, depending on the value of the electron temperature relaxation time, the parabolic heat conduction model (TTM) is no longer suitable for the determination of the electron temperature distribution and should be replaced by the ETTM. In this way, the electron temperature no longer possesses the usual diffusive spreading but follows a wavelike behaviour damped by phonon emission. For thin metal films, not considered here for lack of space, this may be of special importance because of the reflection of the wave at the rear. Furthermore, the electron-electron scattering, even though of minor significance in solid state physics under steady state conditions, becomes important for high electron temperatures in particular. Many thermal and optical properties are drastically changed in the case of thermal nonequilibrium ($T_e \neq T_{ph}$) and often have nonlinear temperature dependence.

Finally, it should be mentioned that only some selected aspects and problems of the interaction of femtosecond laser pulses with metals have been considered. The distinctions between experiments performed in air or vacuum, plasma formation, the determination of thresholds for ablation and many other phenomena, have not been discussed. Nevertheless, femtosecond lasers are a very promising tool for material treatments on small spatial scales.

Experimental investigations and theoretical considerations have gone a long way in the last three decades very successfully, but both are long way from providing a complete understanding.

References

1. Semerok A, Chaleard C, Detalle V, Lacour J-L, Mauchien P, Meynadier P, Nouvellon C, Salle B, Palianov P, Perdrix M and Petite G (1999) Experimental investigations of laser ablation efficiency of pure metals with femto, pico and nanosecond pulses. Applied Surface Science 138–139: 311–314
2. Ashcroft NW and Mermin ND (1976) Solid State Physics, Saunders, Philadelphia, 2: 346–348
3. Parkins GR, Lawrence EW, Christy RW (1981). Intraband optical conductivity $\sigma(\omega,T)$ of Cu, Ag, and Au: Contribution from electron-electron scattering. Physical Review B23: 6408–6415
4. Palik ED (ed) (1985) Handbook of Optical Constants of Solids. Academic Press
5. Hüttner B (1994) Optical properties of polyvalent metals in the solid and liquid state: aluminium. J Phys Condens Matter 6: 2459–2474
6. Fisher D, Fraenkel M, Henis Z, Moshe E, Eliezer S (2001) Interband and intraband (Drude) contributions to femtosecond laser absorption in aluminum. Physical Review E 65: 016409–8
7. Hüttner B (2002) Optical properties under exposure to ultrashort laser pulses. J Phys Condens Matter 14: 6689–6700
8. Hohlfeld J, Conrad U and Matthias E (1996) Does femtosecond time-resolved second-harmonic generation probe electron temperatures at surfaces? Appl Phys B63: 541–544
9. Funk DJ, Moore DS, McGrane SD, Reho, JH and Rabie RL (2004). Proc SPIE 5448: 182-192 and private communication
10. Hüttner B, Rohr G (1996) On the theory of ps and sub-ps laser pulse interaction with metals I. Surface temperature distribution. Applied Surface Science 126: 269–274
11. Anisimov SI, Bonch-Bruevich AM, El'yashevich MA, Imas YaA, Pavlenko NA and Romanov GS (1967) Effect of powerful light fluxes on metals. Soviet Physics Technical Physics 11: 945–952
12. Sun C K, Vallee F, Acioli LH, Ippen EP and Fujimoto JG (1994) Femtosecond-tunable measurement of electron thermalisation in gold. Physical Review B50: 15337–15348
13. Fann WS; Storz R, Tom HWK, Bokor J (1992) Direct measurement of non-equilibrium electron-energy distributions in subpicosecond laser-heated gold films. Physical Review Letters 68: 2834–2837
14. Fann WS; Storz R, Tom HWK, Bokor J (1992) Electron thermalisation in gold. Physical Review B 46: 13592–13595
15. Hüttner B (1999) Thermodynamics and transport properties in the transient regime. J Phys Condens Matter 11: 6757–6777
16. Zinoviev AV, Kulagin IA. Lugovskoy AV, Usmanov T (1980) Nonequilibrium excitation of electrons by high-intensity monochromatic radiation. Sov Phys Tech Phys 25: 953–956
17. Bonn M, Denzler DN, Funk S, Wolf M, Wellershoff S-S, Hohlfeld J (2000) Ultra-fast electron dynamics at metal surfaces: Competition between electron-phonon coupling and hot-electron transport. Physical Review B 61: 1101–1105
18. Fedosejevs R, Ottmann R, Sigel R, Kühnle G, Szatmari S, Schafer FP (1990) Absorption of Subpicosecond Ultraviolet Laser Pulses in High-Density Plasma. Appl Phys B 50: 79–99

19. Price DF, More RM, Walling RS, Guethlein G, Shepherd RL, Stewart RE, White WE (1995) Absorption of Ultrashort Laser Pulses by Solid Targets Heated Rapidly to Temperatures 1–1000 eV. Phys Rev Letters 75: 252–255
20. Wang XY, Riffe DM, Lee Y-S and Downer MC (1994) Time-resolved electron-temperature measurement in a highly excited gold target using femtosecond thermionic emission. Physical Review B50: 8016–8019
21. Rethfeld B (1999) Dissertation TU Braunschweig
22. Hüttner B (1998) On the temperature dependence of the electronic thermal conductivity in metals when the electron and phonon subsystems are not in local equilibrium. J Phys Condens Matter 10: 6121–6141
23. Weast RC (ed) (1982) CRC Handbook of Chemistry and Physics. CRC Press, West Palm Beach Vol 62, p E-9
24. Kaganov MI, Lifshitz IM, Tanatarov LV (1957) Relations between electrons and the crystalline lattice. Soviet Physics JETP 4: 173–178
25. McMillan WL (1968) Transition temperature of Strong-Coupled Superconductors. Physical Review 167: 331–344
26. Allen PB (1987) Theory of thermal relaxation of electrons in metals. Physical Review Letters 59: 1460–1463
27. Schoenlein RW, Lin WZ, Fujimoto JG, Eesley G L (1987) Femtosecond Studies of Nonequilibrium Electronic Processes in Metals. Physical Review Letters 58: 1680–1683
28. Groeneveld RHM, Sprik R, Lagendijk Ad (1995) Femtosecond spectroscopy of electron-electron and electron-phonon energy relaxation in Ag and Au. Phys Rev B51: 11433–11445
29. Hohlfeld J, Wellershoff S-S, Güdde J, Conrad U, Jahnke V, Matthias E (2000) Electron and lattice dynamics following optical excitation of metals. Chem Phys 251: 237–258
30. Wellershoff S-S, Hohlfeld J, Güdde J, Matthias E (1999) The role of electron–phonon coupling in femtosecond laser damage of metals. Appl Phys A 69: 99–107
31. Schmidt V, Husinsky W, Betz G (2002) Ultrashort laser ablation of metals: pump–probe experiments, the role of ballistic electrons and the two-temperature model. Applied Surface Science 197–198: 145–155
32. Suarez C, Bron WE and Juhasz T (1995) Dynamics and Transport of Electronic Carriers in Thin Gold Films. Phys Rev Letters 75: 4536–4539
33. Metzler R, Compte A (1999) Stochastic foundation of normal and anomalous Cattaneo-type transport. Physica A268: 454–468
34. Joseph DD and Preziosi L (1989) Heat waves. Reviews of Modern Physics 61: 41–73
35. Joseph DD and Preziosi L (1990) Heat waves. Reviews of Modern Physics 62: 375–391
36. Maxwell JC (1867) On the Dynamical Theory of Gases. Phil Trans Roy Soc 157: 49–88
37. Vernotte P (1958) Paradoxes in the Continuous Theory of the Heat Equation. C R Acad Sci 246: 3154–3155
38. Cattaneo C (1958) A Form of Heat Equation which Eliminates the Paradox of Instantaneous Propagations. C R Acad Sci 247: 431–433
39. Jou D, Casas-Vazquez J, Lebon G (1999) Extended irreversible thermodynamics revisited (1988–98). Rep Prog Phys 62: 1035–1142

40. Zhang DM, Li L, Li ZH, Guan L, Tan X, Liu D (2006) Non-Fourier heat conduction studying on high-power short-pulse laser ablation considering heat source effect. Eur Phys J Appl Phys 33: 91–96
41. Wang X and Xu X (2001) Thermoelastic wave induced by pulsed laser heating. Appl Phys A 73: 107–114
42. Qiu TQ, Tien CL (1994) Femtosecond laser heating of multi-layer metals-I Analysis. Int J Heat Mass Transfer 37: 2789–2797
43. American Institute of Physics Handbook (1972). Third edition
44. Brorson SD, Kazeroonian A, Moodera JS, Face DW, Cheng TK, Ippen EP, Dresselhaus MS, Dresselhaus G (1990) Femtosecond Room-Temperature Measurement of the Electron-Phonon Coupling Constant λ in Metallic Superconductors. Physical Review Letters 64: 2172–2175
45. Yoo KM, Zhao XM, Siddique M, Alfano RR, Osterman DP, Radparvar M, Cunniff J (1990) Femtosecond thermal modulation measurements of electron-phonon relaxation in niobium. Appl Phys Lett 56: 1908–1910
46. Hüttner B (2004) The change of thermal properties under exposure to fs-laser pulses. In: High-Power Laser Ablation V, ed Phipps CR, Proc SPIE 5448: 103–109
47. Luk'yanchuk BS, Anisimov SI, Lu YF (2001) Dynamics of Subpicosecond Laser Ablation, Examined by Moments Technique. Nonresonant Laser-Matter Interaction (NLMI-10), ed Libenson MN, Proc. SPIE vol 4423: 141–152

11

Comprehensive Numerical Simulation of Laser Materials Processing

Markus Gross

University of Cambridge, Innovative Manufacturing Research Centre, Department of Engineering, Unit 26A Cambridge Science Park, Cambridge, CB4 0FP, UK. `msg30@cam.ac.uk`

Abstract. The previous chapter concluded the physical discussion of laser materials processing (LMP). In this chapter no new physical concepts or theory of physical phenomena will be introduced. The objective of this chapter is rather to give an overview of how to analyse the complex system that is Laser Materials Processing. As has been shown in great detail, the physical level of complexity is deep and analysis becomes extremely cumbersome if it is pursued on an analytical level. Albeit giving great insight into the detailed phenomena, whole processes and their sensitivity to ambient conditions and changes in process parameters or physical setup cannot be investigated using these methods alone. Here numerical simulation comes into play for the scientist investigating processes from an engineering point of view. Numerical simulation has an almost endless scope for system complexity and is only limited by the resources available and the time the investigator is prepared to wait for results. This final chapter should be read as a guide to how to get started. Some fundamental principles of discrete numerical modelling will be introduced and reference made to work by other authors. This, in the space available, can by no means be a comprehensive review, or a textbook of all the methods available and required. Nevertheless it should be seen as a starting point for investigators, at the doctoral student level, trying to get to terms with the task ahead, or for the researcher trying to move from practice to theory, from experiment to simulation, looking for a guide on what to look out for, where to go and which pitfalls to avoid.

11.1 Motivation – The Pursuit of Ultimate Understanding

It is the intention of this chapter to stimulate the intelligent development of comprehensive methods. The strength of numerical simulation should not be underestimated if performed properly. Experimentation can only draw conclusions from correlations. Experimental results are correlated with a variation in input parameters and in consequence hypotheses are formed or overturned. Experiments, especially in LMP are extremely difficult to set up, perform and evaluate. The combination of extremes on a small scale, short to ultra short

time frames and high intensities of power call for the most skilled of investigators who often have to employ expensive equipment in order to obtain results with measurable errors, repeatability and confidence. They may be forgiven if they take the results and the conclusions drawn at face value.

In an ideal world we would like to go further. We would like to measure the turbulence in the melt flow, the exact state of ionisation in the keyhole, or we want to know if what we see is just an oscillatory process too fast for our diagnostic tools or really a continuous forcing/feedback scenario. Too often these questions have to remain unanswered as it is not possible or not feasible to obtain the required data from the experiment. Ideas then form in the investigator's mind, of a continuous melt film flowing down kerfs cut by lasers for example; models based on aggregate mass conservation may even seem to reinforce points of view.

Simulation is different from modelling. Even though both terms are often used interchangeably it is worthwhile to make the distinction and to be conscious of the advantages, merits and faults of both. Modelling is in a sense closer to experiments. The investigator decides which effects, parameters, dimensions etc are important, discards the rest and builds a mathematical model around the "understanding" of the process in order to obtain further insight. This often yields very elegant and fast results. These can, if interpreted correctly, yield understanding and we can correlate the observed results with the results from the model. The process is summarised in an excellent fashion by Abraham Kaplan in "The Conduct of Inquiry" [1]:

> Models are undeniably beautiful, and a man may justly be proud
> to be seen in their company. But they may have their hidden vices.
> The question is, after all, not only whether they are good to look at,
> but whether we can live happily with them.

We can learn a lot from models. Nevertheless we always have to be on guard not to take the results further than the modelling assumptions allow. With the complexity of the process as it is, it will become very difficult to ascertain the impact of the simplifications introduced and evaluate the results in the correct light, as Mandelbrot remarked[1] succinctly: "... the research carried out so far has proved ineffective because so many fixes and twiddles are added [...] until it works. That leaves you with a [model] that is out of shape. You don't know which is more important, the things you started with or all the fixes and twiddles".

If the system under investigation is very unstable, even small effects which may be deemed negligible if only compared in their magnitude, may make the process change from one with a very broad parameter window to a very narrow one, if the process performs at all.

Simulation can reveal forcing and feedback scenarios, allowing the investigator to sample at will and provide insight into the causes of events. Therefore

---

[1] NewScientist, 13 Nov 2004, p52.

knowledge can be derived from analysing the chain of events, the transfer of momentum, mass and energy in all its detail. Combined with classical experiments, which validate the overall process results, this can lead to ultimate understanding, transform hypotheses into theory and provide discriminating evidence where before there was only associative evidence. Associative evidence only links chosen inputs to certain observed families of output parameters which together form the result, by means of correlation – not causation. In simulation the causal relationships are often immediately obvious as the transient history is available and measurements can be taken everywhere.

11.2 Review

Literature concerning the modelling of laser cutting (or LMP in general) is summarised in Table 11.1 on the following page. These publications are concerned with cutting (a bias originating from the author's research field) or LMP in general. Broadly speaking, every welding simulation should be capable of simulating the cutting process, provided that the gas dynamics is capable of simulating the compressible gas jet at sufficient pressures; a selection of welding papers is therefore presented in Table 11.2 on page 346. Analytical models[2] have been excluded, despite their elegance and low demand for computational resources, since they are limited in their flexibility with regard to geometry and non-uniform material parameters. Examples of such models can be found in [2–27].

In Tables 11.1 and 11.2 the following terminology is used.

- model: title of the publication
- author
- dim: what is the dimensionality of the model described?
- transient (yes/no): have transient effects been considered?
- assumed kerf: is kerf geometry presumed *a priori*?
- moving source: does the source or work piece move?
- Fresnel: is Fresnel absorption considered?
- melt: is a model for the melt dynamics included (a free surface has to be considered as well – in the rare case that a free surface was not considered this indicated by *no f.s.*)? *Y* indicates a full Navier-Stokes treatment, *m.b.* indicates mass balance considerations, *pot* indicates a potential theory approach.
- evaporation: is a model of evaporation included? *N*=no, *phen*=phenomelogical evaporation (see below), *kin*=kinematic theory approach, *vac*=evaporation into vacuum (classical Hertz-Knudsen), *vp*=evaporation is only considered by applying the vapour pressure as boundary condition

---

[2] Including energy balance iterative numerical models.

Table 11.1: Literature review – cutting and LMP in general.

Model	Author	dim (1,2 or 3)	transient (Y/N)	assumed kerf (Y/N)	moving source (Y/N)	fresnel (Y/N)
Analysis of striation formation in laser material cutting process	Chung et al. [29]	1	Y	N	Y	N
A numerical investigation into cutting front mobility in CO_2 laser cutting	Di Pietro et al. [30]	2	Y	N	Y	N
A three-dimensional analysis of gas entrainment operating during the laser-cutting process	O'Neill and Steen [31]	3	N	Y	N	N
Computational Model for High-Energy Laser-Cutting Process	Kim et al. [32]	2	Y	N	Y	N
Estimation of heat conduction losses in laser cutting	Prusa et al. [33]	2(3)	N	Y	Y	Y
Finite element analysis of evaporative cutting with a moving high energy pulsed laser	Kim et al. [34]	2	Y	N	Y	N
Finite Element Modelling of the Laser Cutting Process	Kim et al. [35]	2	Y	N	Y	N
Gas jet effects on laser cutting	Chryssolouris et al. [36]	1	N	Y	Y	N
Gas jet-workpiece interactions in laser machining	Chen et al. [37]	3	N	Y	N	N
Heat transfer model for cw laser materials processing	Mazumder et al. [38]	3	N	N	Y	N
Hydrodynamical instability of melt flow in laser cutting	Vicanek et al. [39]	2	N	Y	N	N
Interactive effects of reactivity and melt flow in laser machining	Chen et al. [40]	2	Y	N	N	N
Investigation into the development of liquid layer and formation of surface plasma during CO_2 Laser cutting process	Yilbas et al. [41]	2	N	Y	Y	N
Investigation of striation formation in thin stainless steel tube during pulsed Nd: YAG laser cutting process by numerical simulation	Kim et al. [42]	3	Y	N	Y	N
Mathematical modeling of melting during laser materials processing	Xie and Kar [43]	1	Y	N	N	N
Melt flow characteristics in gas-assisted laser cutting	Rao et al. [44]	1	N	N	N	N
Momentum and heat transfer of an inert gas jet to the melt in laser cutting	Vicanek et al. [45]	2	N	Y	N	N
Nozzle design and simulation of gas flow for the laser cutting process	Leidinger et al. [46]	n.k.	N	Y	N	N

melt (Y/N)	evaporation (N,phen, kin,vac,vp)	gas dynamics (class,sc,bl)	stress (Y/N)	reaction kinetics (Y/N)	radiation heat transfer (Y/N)	viscous forcing (Y/N)	convective cooling (Y/N)	temp. dep. material prop. (Y/N)
Y	VP	N	N	Y	N	Y	N	N
m . b .	N	N	N	Y	Y	N	Y	N
N	N	class inc	N	N	N	Y	N	N
N	phen	N	N	N	Y	N	Y	N
N	N	N	N	N	N	N	Y	N
N	phen	N	N	N	N	N	Y	N
Y	phen	N	N	N	Y	N	Y	N
m . b	N	b . l	N	N	N	N	N	N
N	N	class	N	N	N	N	Y	N
Y	phen	N	N	N	Y	N	Y	N
Y	N	bl	N	N	N	Y	N	N
Y	N	bl	N	Y	N	Y	N	N
m . b	N	b . l	N	N	N	Y	N	N
N	N	N	N	Y	N	N	Y	Y
N	N	N	N	N	N	N	N	N
Y	N	N	N	N	N	Y	N	N
N	N	pot	N	N	N	Y	N	Y
N	N	class mod	N	N	N	N	N	N

Table 11.1: *Continued*

Model	Author	dim (1,2 or 3)	transient (Y/N)	assumed kerf (Y/N)	moving source (Y/N)	fresnel (Y/N)
Numerical modeling laser thermochemical processes on metals surface	Bukharov et al. [47]	2	Y	N	N	N
Numerical simulation of oxidation effects in the laser cutting process	Chen et al. [48]	2	Y	N	Y	N
Numerical studies of gas jet/molten layer interaction during laser cutting	Lim et al. [49]	2	Y	N	Y	N
On the gas kinetics of laser-induced evaporation of metals	Finke et al. [50]	1	N	N	N	N
Optimisation of Melt Removal in Laser Cutting	Rand et al. [51]	3	N	Y	N	N
Steady-state laser cutting modeling	Mas et al. [52]	0	N	N	Y	Y
Temporal evolution of the temperature field in the beam interaction zone during laser material processing	Semak et al. [53]	1	Y	N	N	N
Thermal and efficiency analysis of CO_2 laser cutting process	Yilbas et al. [54]	2	N	Y	Y	N
The role of recoil pressure in energy balance during laser materials processing	Semak et al. [55]	1	N	N	N	N
Three-dimensional transient model for laser machining of ablating/decomposing materials	Modest [56]	3	Y	N	Y	Y
Transient Elastic Thermal Stress Development During Laser Scribing of Ceramics	Modest and Mallison [57]	3	Y	N	Y	Y
Transient evaporative laser-cutting with boundary boundary element method	Kim [58]	2	Y	N	Y	N

- gas dynamic: is a gas dynamic model included? *class* = classical method (finite difference etc), *class inc*=classical method but incompressible, *class mod*=classical method slightly modified for better shock capture, *sr*=shock relations, *bl*=boundary layer theory and *sc*=shock capturing
- stress: is three dimensional stress analysis included?
- reaction kinetics: has the chemical interaction of the melt with ambient/shield/assist gas been considered?
- radiation heat transfer: are there heat losses into the ambient air?
- viscous forcing: have shear stress effects been exerted by the assist gas jet on the free surface?
- convective cooling: is there convective heat transfer from/into the gas jet?
- have temperature dependent material properties been considered?

melt (Y/N)	evaporation (N,phen, kin,vac,vp)	gas dynamics (class,sc,bl)	stress (Y/N)	reaction kinetics (Y/N)	radiation heat transfer (Y/N)	viscous forcing (Y/N)	convective cooling (Y/N)	temp. dep. material prop. (Y/N)
N	N	N	N	N	N	N	N	N
b . l	N	N	N	Y	N	N	N	Y
Y	N	class	N	Y	Y	Y	N	Y
N	kin	clss	N	N	N	N	N	N
N	N	class	N	N	N	Y	N	N
N	phen	sr	N	N	N	N	N	N
Y	phen	N	N	N	N	N	N	N
m . b	N	b . l	N	N	N	Y	N	N
Y	phen	N	N	N	N	N	Y	N
N	phen	N	Y	N	N	N	N	N
N	phen	N	Y	N	N	N	N	N
N	phen	N	N	N	N	N	Y	N

Additional terminology has been used in the table: *n.m.,phenomelogical evaporation* and *n.k.* Their meaning is detailed below.

- *n.m.* – denotes not mentioned but likely to be included,
- *phenomelogical evaporation* – used for models in which the evaporation is treated in simplified ways, ranging from the application of a rate law to the removal of mass above the evaporation temperature. This has severe implications since it has been shown that the mass transport in the gas phase can significantly increase the mass removal rate [28].
- *n.k.* – not known, since occasionally nozzle flow simulations have been reported using a two dimensional simulation, no inference on the dimensionality of the model is made. In cases where the dimensionality was not stated n.k. has been inserted in the table.

Table 11.2: Literature review – welding.

Model	Author	dim (1,2 or 3)	transient (Y/N)	moving source (Y/N)	fresnel (Y/N)
A generalized thermal modeling for laser drilling process	Ganesh et al. [59][60]	2	Y	N	N
An analytical model for the laser drilling of metals with absorption within the vapour	Solana et al. [61]	2	Y	N	N
Effect of surface tension gradient driven convection in a laser melt pool: Three-dimensional perturbation model	Chan et al. [62]	3	N	Y	N
Effects of Surface Depression on Pool Convection and Geometry in Stationary GTAW	Ko et al. [63]	2	Y	N	N
Finite element analysis of flow heat transfer and free interfaces in an electron-beam vaporization system for metals	Westerberg et al. [64]	2	N	N	N
Finite element modelling of tungsten inert gas welding of aluminum alloy 2024	Preston et al. [65]	3	Y	Y	N
Mathematical modeling of the dynamic behavior of gas tungsten arc weld pools	Ko et al. [66]	3	Y	N	N
Modeling and simulation of short pulse laser ablation with feeding speed	Callies et al. [67]	3	Y	Y	N
Modeling of Hybrid Laser-MIG Keyhole Welding Process	Zhou et al. [68]	3	Y	Y	Y
Modeling of laser keyhole welding	Ki et al. [69][70][22]	3	Y	Y	N
Modeling of the compressible vapor flow induced in a keyhole during laser welding	Amara et al. [71]	2	N	Y	N
Modeling of Weld Pool Dynamics during Dual-Beam Laser Welding Process	Hu et al. [72]	3	Y	N	N
The transient behavior of weldpools with a deformed free surface	Thompson et al. [73]	2	Y	N	N
Three-dimensional axisymmetric model for convection in laser-melted pools	Chan et al. [74]	3	N	Y	N
Three-dimensional model for convection in laser weld pool	Chan et al. [75]	3	N	Y	N

When reading carefully through Table 11.1 it becomes clear that most of the available work uses some sort of simplification. It shows that the choice of simplification is a choice guided by the preference of the author and that the need for both, for simulation in general and for a non-biased simulation in particular, is real.

From Table 11.2 it can be seen that most welding models do not consider gas dynamics in the process, which, in theory, limits these models

melt (Y/N)	evaporation (N,phen, kin,vac,vp)	gas dynamics (class,sc,bl)	stress (Y/N)	reaction kinetics (Y/N)	radiation heat transfer (Y/N)	viscous forcing (Y/N)	convective cooling (Y/N)	temp. dep. material prop. (Y/N)
Y	phen	N	N	N	N	N	N	N
N	phen	N	N	N	N	N	N	N
Y (no f . s .)	N	N	N	N	Y	N	N	N
Y	N	N	N	N	N	N	N	N
Y	phen	N	N	N	Y	N	N	Y
N	N	N	Y	N	N	N	N	Y
Y	N	N	N	N	N	N	N	N
N	phen	N	N	N	N	N	N	N
Y	N	N	N	N	Y	N	N	N
Y	kin	class	N	N	Y	N	N	N
Y	vac	class	N	N	N	n . m .	N	N
Y	N	N	N	N	N	N	N	N
Y	N	N	N	N	N	N	N	N
Y (no f . s .)	N	N	N	N	Y	N	N	N
Y (no f . s .)	N	N	N	N	Y	N	N	N

to conduction welding only. Despite this, most publications discuss the keyhole effect, which is intrinsically vaporisation dependent and therefore a gas dynamic phenomenon. Laser attenuation and blanketing effects cannot be captured without modelling the vapour plume and – if used in the process – shield gases. The pressure of the escaping vapour has a strong influence on the evaporation process as well and hence the neglect of gas dynamics is even more severe. Furthermore, thermal properties are often considered to be

constant and the evaporation model often assumes a vacuum. This leads to the conclusion that the welding models available in the literature cannot be easily extended to cover cutting processes.

11.3 Correlation, the Full Picture

There are two motivations for performing numerical analysis. The first, possibly the one most readers aim for initially, is a wish to reproduce an experiment. This is referred to in the following as *industrial analysis*, analysis which may aim at optimising a product, improving performance by small margins to obtain a competitive lead etc. Here it is required that the simulation represents the experiment closely, otherwise the aim may not be achieved. It may be sufficient to fine tune the model to capture experimental results and then determine how the system would respond if some of the parameters were altered slightly (most optimisation projects do not have much scope for modification due to other engineering constraints at the outset). However, to assume from this that we always need to replicate experimental results exactly with the results from numerical simulation is wrong. If we can learn from the simulation about different dynamic regimes, if we can learn about what can occur, it can help immensely when analysing experimental results and trying to understand what happened in the experiment. In these, the kind of simulation which may be termed *academic analysis*, we do not need to require the exact one-to-one match of analysis result and experimental result. It is sufficient to create the awareness that there may be more to the process than initially thought, that there are more complex interactions than previously fathomed, to make these investigations worthwhile as well. Coming back to industrial analysis, a mistake often made is that the correlation of experimental analysis with numerical analysis is taken for granted if only a few experimental points can be found to fit the numerical result. Two things have to be remembered here, that a) correlation requires a match for every experimental result and b) that even if correlation is proved, this does not reveal the cause of the effect observed. This is sometimes referred to as "Correlation does not imply causation", which should be rephrased more accurately: "Empirically observed covariation is a necessary but not sufficient condition for causality" [76]. If the aim is not just to improve the performance marginally, but rather to reinvent, to innovate, the correlation of experiments with numerical results does not lead to the desired result. We have to understand the causes of the effects and then create systems around this knowledge. To match points and lines will not lead us there.

11.4 Introduction to Numerical Techniques

In the following the basic ideas of discrete numerical simulation will be introduced. The techniques required to solve the partial differential equations

arising from a mathematical formulation of the system under investigation will be detailed and examples given. This will mainly focus on solutions for the melt and gas flow. A variant of the most famous and long standing technique for solving incompressible flow, the semi-implicit method for the solution of pressure linked equations (SIMPLE) method, will be introduced, as it is an ideal candidate for teaching the main basic principles and the interested reader can follow this up by reading the excellent book written by the inventor of this method himself, S.V. Patankar [77]. Up until recently the SIMPLE method was the default method in many commercial computational fluid dynamics (CFD) codes, like FLUENT^{TM} etc. Methods for compressible gas flow will then be touched upon and a scheme for linking the individual models into a simulation will be presented.

Then, continuing with a brief section on the modelling of laser beam propagation and phase changes this chapter will conclude with notes on best practice and high performance computing.

The careful reader will have noticed that the term model was used above, in spite of the distinction and differentiation made in the previous sections. This is mainly because the simulation, which in itself should replicate the subject under investigation, is a collection of models. These, suitably combined, then provide the simulation. There will always be models, turbulence models, assumptions about phase changes and mathematical approximations to intermolecular processes such as evaporation. This will be valid until the point comes where it will be possible to compute the interaction, to simulate the process, from first principles, i.e. from computing the interaction of every single electron, photon and phonon. Even then we will still need a model for this interaction. The investigator has to take great care however that the model does not imprint itself onto the process under investigation so that we can still clearly say that the computer program computing the solutions to the differential equations is a simulation, representing the process.

11.4.1 The Method of Discretisation

Rather than seeking closed continuous solutions to the partial differential equations (PDEs) when dealing with systems on the scale of the ones alluded to above there is no choice but to use approximate methods. The solution will not be found in terms of equations describing the result in every possible position in space and time, but rather only on discrete points. On these points we can write the conservation laws in terms of sums, easily performed by computers, nearly irrespective of how many sums are required. These points form meshes and examples of how to solve the differential equations on these meshes are given in the following sections.

11.4.2 Meshes

In this section the PDEs are solved on meshes, sometimes also called grids. These meshes are the basis for the discretisation of the PDEs. The outline

of the mesh defines the geometry under investigation and appropriate boundary conditions have to be formulated there. On the interior the solution is defined by a discrete approximation to the physics taking place, by solving the differential equations, i.e. by evaluating the gradients of field quantities and computing the respective change with respect to time due to the gradients. The gradients are approximated for each vertex in finite difference methods, for each edge (in 2D) or each face (in 3D) in finite volume methods. The finer the mesh the more accurately the gradients can be resolved. However, with a finer mesh longer computation times are encountered. Therefore the difficulty is to create a mesh fine enough where necessary and as coarse as possible elsewhere. The so called "grid independence" has to be verified by studies with finer and finer meshes. Only when the solution does not change any more with increased mesh size can the solution be assumed reliable. This information is often missing in publications, significantly reducing the value of the contribution, making it like a solution to the formulated problem without a proof. Adaptive mesh refinement helps a little bit as it aims at automating the process of refining and coarsening the mesh.

The mesh is not always a static entity. So called Langrangian meshes are frequently used (compared to the static Euler meshes) which move with the flow, or deform to accommodate a free surface for example. Whilst extremely elegant and simplifying the treatment of jump conditions at surfaces, these codes require a lot of care and computation time to ensure that the mesh does not deteriorate in shape and frequent "remeshing" will be necessary, to create new meshes accommodating the new geometry. Keeping in mind the complex melt flows observed in LMP, Lagrangian meshes seem less appealing. It is convenient therefore to use one grid which spans the whole domain of interest. On this grid the different states (solid/liquid/gas) can then be defined by scalar functions, which in the simplest form assume integer values for the respective phase. This will be revisited when the treatment of the free surface is discussed later.

11.4.3 Explicit versus Implicit

As long as the characteristic velocities are not too large and the required mesh resolution is not too high, explicit methods yield results in acceptable times and the programming effort is relatively low. New physical phenomena can be included easily as every step is additive and only depends on the previous time step. However, stability limitations require Courant numbers (sometimes also called Courant-Friedrichs-Lewy number (CFL), from the names of the three authors of the original paper [78, 79]) of less than one. This means that the time-step is restricted to Δ/v with Δ denoting the smallest grid dimension and v the maximum velocity in the domain. This, especially if supersonic vapour jets are present and the resolution is high to capture steep temperature gradients, will eventually result in unfeasibly small time steps. For example, assume melt velocities of say $10\,\mathrm{ms}^{-1}$, which are not uncommon.

If we require submicron resolution, a grid spacing of $0.1\,\mu$m say, due to high temperature gradients at high laser powers or due to the need to resolve thin melt films, a CFL requirement of unity will lead to a time-step limit of less than $10^{-7}/10$. Assuming the solution of each time step takes one second, which is optimistic for typical mesh sizes of several million cells, the solution of one second real time will take 10^8 seconds. Since one day only has 8.64×10^4 s, this leads to 1158 days or 3.17 years – a long wait even for the most patient scientist.

The solution to this problem is a formulation of the equations in their implicit form. This means that the gradients will be evaluated at the new time step, i.e. the field variables are functions of the field variables at the current and previous timesteps:

$$\text{Explicit:}\ \ \Phi\left(x,y,z,t+\delta t\right) = f\left(\Phi\left(x,y,z,t\right)\right) \tag{11.1}$$

$$\text{Implicit:}\ \ \Phi\left(x,y,z,t+\delta t\right) = f\left(\Phi\left(x,y,z,t\right),\Phi\left(x,y,z,t+\delta t\right)\right). \tag{11.2}$$

As a result a system of equations has to be solved and iteration is needed due to the nonlinearity. The convective part of the momentum equation is a transport equation of itself[3], i.e. the resulting system is nonlinear. The system of equations has to be updated at every iteration until a steady solution for the particular time step is reached. All other coupled systems have to be included in an overall iteration loop, for example if the viscosity depends on temperature in the chosen model, once the flow problem is solved, the energy equation needs to be solved again; this in turn may result in a new temperature profile, which will require a new iteration loop over the flow problem to accommodate the change in viscosity. It can be readily seen that the effort is much greater and that instabilities can interfere with the overall convergence.

11.4.4 Discretisation of Transport pde's

The momentum equation for an incompressible fluid can be solved using a power law scheme (e.g. [77]). Here, the discrete momentum equation is solved simultaneously with the mass balance. The combined equations represent an equation for pressure which will be subsequently referred to as the pressure equation, illustrated using an explicit time integration scheme. The surface pressure of the previous time step is applied as a boundary condition to the pressure equation. Krylov-Subspace solvers (e.g. generalized minimal residual algorithm (GMRES) [80]) can then be used efficiently to solve the pressure equation. The hypre library[4], developed at Lawrence Livermore National

---

[3] Usually a convection equation convects a field variable according to a give velocity field, a problem which results in a linear set of equations. In the momentum equation this velocity field is not given, it is the result of solving the momentum equation – the convection problem.

[4] www.llnl.gov/CASC/hypre/.
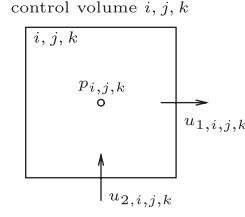
Fig. 11.1: Assignment of field variables to control volumes.
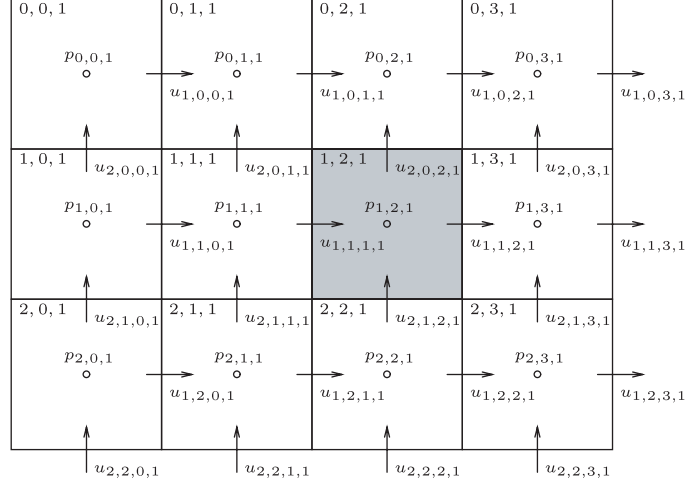
Fig. 11.2: Control volume for mass conservation equation.

Laboratory, is an example of an easy-to-use freely available solver package. The pressure equation is essentially an augmented mass conservation equation as shown below. For incompressible matter the mass conservation equation is:

$$\frac{\partial u_1}{\partial x_1} + \frac{\partial u_2}{\partial x_2} + \frac{\partial u_3}{\partial x_3} = 0. \tag{11.3}$$

This equation can be obtained by substituting the discrete momentum equation into the discretised form of the mass conservation equation. This method is similar to the pressure correction equation as derived by Patankar in [77] which, in the context of an implicit scheme, only describes an intermediate state in the iterative procedure. This explicit scheme yields the pressures for the next time step. The variables are discretised on a staggered grid. The discrete velocities are defined on the cell boundaries and pressures on the cell centre as shown in Fig. 11.1. In order to differentiate between the velocities new indices need to be introduced. The velocity u_1 at the boundary of the cell with the coordinates i, j, k is denoted $u_{1,i,j,k}$ and the pressure p in the centre of cell i, j, k is denoted $p_{i,j,k}$. The control volume for the mass conservation equation coincides with the discrete volumes (see Fig. 11.2), whereas the
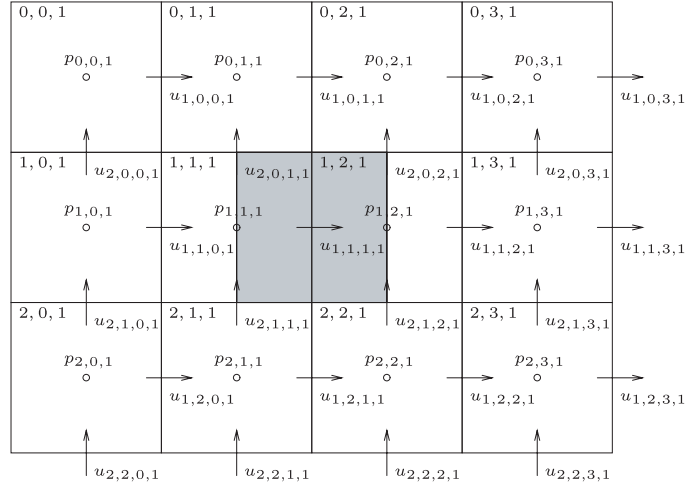
Fig. 11.3: Control volume for momentum equation.

control volume for the momentum equation is staggered, i.e., for the velocity $u_{1,1,1,1}$ the control volume is made up of half the cell $1, 1, 1$ and half of $1, 2, 1$ (see Fig. 11.3). The discretised mass conservation equation reads (according to Fig. 11.2):

$$\frac{1}{\Delta}\left(u_{1,1,2,1} - u_{1,1,1,1}\right) + \frac{1}{\Delta}\left(u_{2,0,2,1} - u_{2,1,2,1}\right) + \frac{1}{\Delta}\left(u_{3,1,2,0} - u_{3,1,2,1}\right) = 0 \tag{11.4}$$

where Δ represents the vertex length of the cell (assuming equidistant cells). Multiplying the discretised mass conservation equation by Δ^3 leads to:

$$\Delta^2\left(u_{1,1,2,1} - u_{1,1,1,1}\right) + \Delta^2\left(u_{2,0,2,1} - u_{2,1,2,1}\right) + \Delta^2\left(u_{3,1,2,0} - u_{3,1,2,1}\right) = 0. \tag{11.5}$$

The discretised momentum equation (for the x_1 direction[5] as shown in Fig. 11.3) is:

$$a_P u_{1,1,1,1} = a_E u_{1,1,2,1} + a_W u_{1,1,0,1} + + a_N u_{1,0,1,1} + a_S u_{1,2,1,1}$$
$$+ a_T u_{3,1,2,0} + a_B u_{3,1,2,1} + S_c \Delta^3 + a_0 u_{1,1,1,1}^0 \tag{11.6}$$

$$a_0 = \frac{\rho \Delta^3}{\Delta t} \tag{11.7}$$

$$S_c = \frac{P_{1,2,1} - P_{1,1,1}}{\Delta} \tag{11.8}$$

$$a_P = a_E + a_W + a_N + a_S + a_T + a_B + a_0 \tag{11.9}$$

where $a_E, a_W, a_N, a_S, a_T, a_B, a_0$ represent the integration coefficients (see [77]) at the respective east, west, north, south, top and bottom face and at

---

[5] All other directions can be derived by cyclic permutation of the indices.

the central point. We obtain:

$$u_{1,1,1,1} = \frac{a_E u_{1,1,2,1}}{a_P} + \frac{a_W u_{1,1,0,1}}{a_P} + \frac{a_N u_{1,0,1,1}}{a_P} + \frac{a_S u_{1,2,1,1}}{a_P} + \frac{a_T u_{3,1,2,0}}{a_P}$$

$$+ \frac{a_B u_{3,1,2,1}}{a_P} + \frac{P_{1,2,1}\Delta^2}{a_P} - \frac{P_{1,1,1}\Delta x^2}{a_P} + \frac{a_0 u^0_{1,1,1,1}}{a_P}. \qquad (11.10)$$

From (11.10) the coefficients for the pressure equation can be derived directly. Equivalent expressions for $u_{2,1,2,1}, u_{1,1,2,1}$ and $u_{2,0,2,1}$ can be written and substituted into 11.5. To identify the different factors of a_P, the grid location in the subscript is added, e.g., a_P for gridpoint $(1,1,1)$ is $a_{P,1,1,1}$. Hence the coefficients of the pressure equation are:

$$
\left.
\begin{aligned}
a_W^{\text{press}} &= \frac{\left(\Delta^2\right)^2}{a_{P,1,1,1}}, \quad a_E^{\text{press}} = \frac{\left(\Delta^2\right)^2}{a_{P,1,2,1}} \\[2mm]
a_N^{\text{press}} &= \frac{\left(\Delta^2\right)^2}{a_{P,0,2,1}}, \quad a_S^{\text{press}} = \frac{\left(\Delta^2\right)^2}{a_{P,1,2,1}} \\[2mm]
a_T^{\text{press}} &= \frac{\left(\Delta^2\right)^2}{a_{P,1,2,0}}, \quad a_B^{\text{press}} = \frac{\left(\Delta^2\right)^2}{a_{P,1,2,1}} \\[2mm]
a_P^{\text{press}} &= -a_W^{\text{press}} - a_E^{\text{press}} - a_N^{\text{press}} - a_S^{\text{press}} - a_T^{\text{press}} - a_B^{\text{press}} \\[2mm]
b_{\text{transient}} &= \Delta^2 \left(\frac{a_0 u^0_{1,1,2,1}}{a_{P,1,2,1}} - \frac{a_0 u^0_{1,1,1,1}}{a_{P,1,1,1}} \right) \\[2mm]
&+ \Delta^2 \left(\frac{a_0 u^0_{2,0,2,1}}{a_{P,0,2,1}} - \frac{a_0 u^0_{2,1,2,1}}{a_{P,1,2,1}} \right) \\[2mm]
&+ \Delta^2 \left(\frac{a_0 u^0_{3,1,2,0}}{a_{P,1,2,0}} - \frac{a_0 u^0_{3,1,2,1}}{a_{P,1,2,1}} \right)
\end{aligned}
\right\} \qquad (11.11)
$$

and the pressure equation reads:

$$a_P^{\text{press}} P_P = a_E^{\text{press}} P_E + a_W^{\text{press}} P_W + a_N^{\text{press}} P_N + a_S^{\text{press}} P_S$$

$$+ a_T^{\text{press}} P_T + a_B^{\text{press}} P_B + b_{\text{transient}}. \qquad (11.12)$$

The pressures resulting from the solution of these discrete equations can then be used to evaluate the momentum equations, yielding the velocities at this time step.

11.4.5 Schemes of Higher Order

Particularly in cases with low viscosity, in the gas problem for example, it very soon becomes evident that first order upwind solutions are not sufficient.

The use of upwind quantities ensures that the schemes are very stable and obey the transportiveness requirement (i.e., they allow for the direction of flow), but their first order accuracy makes them prone to numerical diffusion errors [81].

The error introduced by the lack of "transverse coupling" will result in wrong solutions. This is most evident in flows at a 45 degree angle to the mesh axis. Here a numerical viscosity will lead to diffusion of the transport variables, turning circular flow profiles (such as from a nozzle for example) into ellipses or, even worse, into star-shaped profiles.

This can be reduced by applying higher order interpolation functions and then integrating these over the face of the control volume. An established method is the quadratic upstream interpolation for convective kinematics (QUICK) scheme by Leonard [82–84]. Several versions of this scheme exist. In this case only the multidimensional version (i.e. with transverse curvature in the interpolant) will be presented. The theories for limiter functions/algorithms will be omitted as well for sake of brevity. It should be noted that care has to be taken in the choice of limiters since they have to represent the multidimensional nature accurately and sometimes are not applicable to compressible flow [85].

Cell-averaged quantities $\bar{\Phi}$ of field variables Φ are introduced as:

$$\bar{\Phi}_{\text{cell}} = \frac{1}{h^2} \int \int_{\text{cell}} \Phi(x, y) \, \mathrm{d}x \mathrm{d}y \tag{11.13}$$

and the effective face value is:

$$\Phi_f^{\text{eff}} = \frac{1}{h} \int_{-h/2}^{h/2} \Phi(h/2, y) \, \mathrm{d}y \quad u > 0 \tag{11.14}$$

with h denoting the cell width. The field variable Φ is approximated using the quadratic equation:

$$\Phi(x, y) = C_0 + C_1 x + C_2 x^2 + C_3 y + C_4 y^2. \tag{11.15}$$

With h denoting the equidistant grid spacing, a system of linear equations can be written:

$$\bar{\Phi}_{i,j} = \frac{1}{h^2} \int_{-h/2}^{h/2} \int_{-h/2}^{h/2} \Phi(x, y) \, \mathrm{d}y \mathrm{d}x$$

$$\bar{\Phi}_{i-1,j} = \frac{1}{h^2} \int_{-3h/2}^{-h/2} \int_{-h/2}^{h/2} \Phi(x, y) \, \mathrm{d}y \mathrm{d}x \tag{11.16}$$

$$\bar{\Phi}_{i,j-1} = \frac{1}{h^2} \int_{-h/2}^{h/2} \int_{-3h/2}^{-h/2} \Phi(x, y) \, \mathrm{d}y \mathrm{d}x$$

$$\bar{\Phi}_{i+1,j} = \frac{1}{h^2} \int_{h/2}^{3h/2} \int_{-h/2}^{h/2} \Phi(x,y) \, \mathrm{d}y\mathrm{d}x$$

$$\bar{\Phi}_{i,j+1} = \frac{1}{h^2} \int_{-h/2}^{h/2} \int_{h/2}^{3h/2} \Phi(x,y) \, \mathrm{d}y\mathrm{d}x$$

(11.17)

and solved for $C_0, \ldots, C_4$ which then leads to a simple polynomial for Φ_f^{eff}:

$$\Phi_f^{\mathrm{eff}} = \frac{1}{2} \left(\bar{\Phi}_{i+1,j} + \bar{\Phi}_{i,j} \right) - \frac{1}{8} \left(\bar{\Phi}_{i+1,j} - 2\bar{\Phi}_{i,j} + \bar{\Phi}_{i-1,j} \right)$$

$$+ \frac{1}{24} \left(\bar{\Phi}_{i,j+1} - 2\bar{\Phi}_{i-1,j} + \bar{\Phi}_{i,j-1} \right). \tag{11.18}$$

This value for the field variable represents the integral more accurately.

Whilst this is an improvement, i.e. it reduces the numerical viscosity, interpolations of higher order are prone to overshoots in the interpolant. This can be reduced by introducing monotonicity-preserving constraints on Φ_f^{eff}.

11.4.6 The Multi Phase Problem

Several different methods exist addressing the modelling of the different phases, solid, melt and gas. In general we have the following multiphase scenarios:

- Mixtures: The fluids mix on an atomic level and can hence be characterised by material properties according to the volume fraction of the constituents. This model can be used for example for the effects of shielding (oxygen atmosphere and inert process gas) or the vapour phase in the ambient gas phase. Only one momentum equation and one energy equation needs to be solved along with a transport equation for each of the constituents.
- Dispersive systems: The fluid contains discrete particles. Here the momentum equation has to be augmented by additional terms representing the dynamics of the dispersed phase. It cannot be assumed that the mixture behaves in a homogeneous fashion. This means that additional momentum equations are required for the behaviour of the suspended particles. For example heavy particles may settle in a horizontal flow and hence modify the vertical distribution. This approach would be required if for example condensation is to be included in the model.
- Immiscible fluids: Two fluids which do not mix, like water and oil or as in LMP melt and gas. If the material properties do not vary greatly, only one momentum equation is sufficient, with an advection equation defining the two liquids. However, if – as in LMP – the properties of the liquids vary greatly this will yield dramatically wrong results at the interface.

To ensure that the melt velocities at the interface are correct the following procedure was developed. Two momentum equations are solved, one compressible for the gas flow (mixture multiphase) and one incompressible momentum

equation for the melt flow (single phase). Both are discretised across the whole domain. For the gas flow the velocity is required to be zero at control volumes where there is solid material, and equal to the melt velocity (i.e. effectively zero as the melt velocity is usually orders of magnitude lower than the gas velocity) in cells containing melt. For the melt the scenario is reversed. The momentum equation is solved in all molten cells. At gas cells the velocity profile has a zero gradient boundary condition and the pressure from the gas flow solution is imposed, combined with source terms representing the curvature, recoil from evaporation and shear. At solid control volumes the velocity is zero and a mushy-zone may be modelled at the solid-melt interface. In essence the melt acts like a wall boundary on the gas and the gas represents a pressure force on the melt. The melt velocities are then extended into the gas domain to allow for advection of the chosen representation of the interface (volume of fluid or level set).

Volume of Fluid

The volume of fluid (VOF) method is a popular method for the simulation of free surface flows. The underlying principle is as follows. A scalar is introduced as an additional field variable of the problem. This scalar can attain any value between zero and one. Zero represents zero fluid in the control volume, i.e. air in most cases, and one will represent a cell fully filled with liquid. This scalar is then advected with the flow. As mass conservation holds, the VOF value should remain one inside the liquid body and the surface is described by a value between zero and one. In reality however, it is not as straightforward to develop advection schemes which will be capable of keeping the surface well defined. The VOF value will be "smeared out", leading to immediate problems. To avoid this, several algorithms have been developed which will only allow advection from surface cells to other surface cells or from full cells into either surface cells or empty cells. This strategy however has the following drawbacks:

- It will only be accurate to first order, leading to numerical diffusion.
- The accuracy is compromised when a cell is "over emptied" (i.e. more fluid should have left the cell than the combination of fluid in the cell and fluid gained by the cell from neighbours during this time step) or "overfilled" during one time step.
- As most of these corrections are based on an evaluation of the "wet faces" of a cell and then using this information in order to limit the advection (i.e. no advection across a "dry" face for example) it follows immediately that a limit has to be placed on the CFL number. These algorithms can only work for a CFL of less than unity (see section 11.4.3 on page 350 for a discussion of the implications).

Due to the fact that the scalar defines only the fill level of the cell a decision has to be made with regard to the "state" of the cell faces. How much of

the face is available for convection, is the face of the control volume fully submerged in the liquid or not? Too often the algorithms utilise `if` loops, which can potentially be biased towards the `if` statements at the top of the chain, or rounding errors, leading to a drift of the mass towards one side of the simulation domain. (It is sometimes enlightening to run a problem which should be symmetric in a full 3D computation, ignoring potential time saving available through utilising the symmetry. Sometimes the results will not be symmetric and often this will be due to bias in the algorithms or hitherto hidden programming errors[6]).

In most VOF algorithms the VOF value will be reset, i.e. slightly larger than one will be reset to 1 and close to zero will have to be reset to zero. This will lead to – at best – an erroneous fluctuation of mass in the system or even a steady depletion or steady increase of mass. For the simulation of laser cutting this is not an overly significant problem, as the melt is generated at the cut front and, several hundred timesteps later, leaves the simulation domain for ever. Any error incurred during this transition will not accumulate. In welding however, where the melt is stirred continuously by Marangoni or electromagnetic effects, this is different. Any error will accumulate and can severely alter the results.

The reaction of the melt to the gas pressure is strong, especially in laser cutting. The pressure variations of several bar will lead to high velocities in the melt and hence the surface has to be described as accurately as possible. This is very difficult to achieve with a VOF approach.

Level Set

The level set method as introduced by Setian and Osher [86] addresses most of these issues satisfactorily. The core of this method is that the surface is described by the zero isosurface of a distance function. This field variable describes the distance from any of the discrete volume centres to the surface. The sign of this function defines whether the cell is in the liquid or air domain. This field variable can then be advected using the standard schemes for scalar advection without any special attention required to keep the interface sharp.

Surface cells can be uniquely and unambiguously defined by extrapolating the level set function onto the control volume corners and requiring that at least one of the corner level set values has to be negative and at least one positive for surface cells. The curvature and surface normals can be readily computed from the level set.

There is no need to clean up the data as in the VOF scheme. Occasionally the level set deteriorates. In that case the level set has to be re–initialised, which is a simple advection routine. Similar advection schemes

---

[6] Drifts can of course occur due to instabilities intrinsic to the system under investigation. This however can only be assumed after length sanity checks and algorithm testing

Table 11.3: Comparison of a numerical computation of the free surface position following one time step using an uncorrected explicit first order upwind discretisation.

	$-2dx$	$-1dx$	0	$1dx$	$2dx$
$t = t_1$	-2	-1	0	1	2
$t = t_1 + \delta t$	-2.5	-1.5	-0.5	0.5	1.5

(a) level set

	$-2dx$	$-1dx$	0	$1dx$	$2dx$
$t = t_1$	1	1	0.5	0	0
$t = t_1 + \delta t$	1	1	0.75	0.25	0

(b) VOF

are also used to extend variables from the interface into the control volumes close to the surface, which is sometimes required for boundary conditions. For optimum speed the level set equations are often only solved in the proximity of the surface, which is called the fast-marching scheme. For more details and an excellent implementation of the level set scheme see lmslib at: http://www.princeton.edu/~ktchu/software/lsmlib/ .

A Numerical Example

Assume a problem as follows. A one dimensional representation of the position of a surface is subject to advection by a flow field. The grid spacing dx is $1\,\mathrm{m}$, the flow velocity is $0.5\,\mathrm{ms}^{-1}$ and the time-step δt is $1\,\mathrm{s}$. Then, assuming a first order upwind scheme without any further modifications, the advection step at $t = t_1 + \delta t$ yields the values in Table 11.3. It is obvious that the surface position in the VOF case is not clearly defined any more, whereas it is accurate in the level set computation.

11.5 Solution of the Energy Equation and Phase Changes

The discretisation of the energy equation consists of two parts: a convective/conductive part and a source term. The convective/conductive contribution reads:

$$\frac{\partial}{\partial x_i}\left(\rho u_i T\right) = \frac{\partial}{\partial x_i}\left(\Gamma \frac{\partial T}{\partial x_i}\right), \tag{11.19}$$

with Γ denoting the diffusion coefficient and T the temperature. The exact solution to this problem over a domain with $0 \leq x \leq L$ is utilised. This exact solution (for the one dimensional case) is:

$$\frac{T\left(x\right) - T\left(x = 0\right)}{T\left(x = L\right) - T\left(x = 0\right)} = \frac{\exp\left(P_e x/L\right) - 1}{\exp\left(P_e\right) - 1}, \tag{11.20}$$

with the Péclet number P_e defined by:

$$P_e = \frac{\rho u L}{\Gamma}. \tag{11.21}$$

As shown by Patankar, the exact solution can now be used to compute the total convective/conductive flux across the cell boundaries. Hence the temperature field can be determined by introducing the requirement of flux balance within the control volume cell. In order to achieve an expression which is less computationally intensive, the exact solution given by (11.20) is replaced by a piecewise polynomial fit[7] which represents the exponential expression occurring in (11.20). The temperature field is then represented by a piecewise linear equation:

$$(a_E + a_W + a_N + a_S + a_T + a_B) T_P = a_E T_E + a_W T_W + a_N T_N$$
$$+ a_S T_S + a_T T_T + a_B T_B, \quad (11.22)$$

with $a_{E,W,N,S,T,B}$ representing the same coefficients as in Patankar [77]. To capture transient behaviour the derivative of temperature with respect to time has to be added to (11.22) which is discretised as:

$$\rho \frac{\partial T}{\partial t} = \rho \frac{\Delta^3}{\delta t} T_p^t - \rho \frac{\Delta^3}{\Delta t} T_P^{t - \delta t}, \quad (11.23)$$

with δt denoting the discrete time step. Radiation losses are modelled using a sink term. The heat flux for radiation can be described by the Stefan-Boltzmann law:

$$q_r = \sigma_r (T + 273.15)^4, \quad (11.24)$$

with $\sigma_r = 5.67051 \times 10^{-8}$ W m^{-2} K^{-4}. This has to be linearised in order to be incorporated in the set of linear equations. This can be done in the following manner:

$$q_r = \sigma_r T_{k-1}^4 + \frac{\partial q_r}{\partial T} \times (T - T_{k-1}), \quad (11.25)$$

where T_{k-1} is the temperature at the previous $(k-1)$ iteration. This yields:

$$q_r = \sigma_r T_{k-1}^4 + 4 \sigma_r T_{k-1}^3 T - 4 \sigma_r T_{k-1}^3 T_{k-1}. \quad (11.26)$$

Equation (11.26) is then subtracted from the right hand side and added to the coefficient of T_p in the linear system of equations subsequent to premultiplication by $A_f A_{surf}/c_p$. $A_f A_{surf}$ is the surface area available for radiation losses with A_f and A_{surf} denoting the surface area of one face of the cell, i.e., Δ^2, and the area fraction which allows for inclined surfaces respectively. The energy input from the laser source can then be modelled as a surface boundary flux. In the modelling method presented (finite volume or control volume method) this is *equivalent* to modelling the heat source as a volume source with an extent of one cell in thickness. This has to be revised once the resolution of the discrete model falls below the optical penetration of the laser into the solid. According to the position of the surface cell the reflectivity can be calculated using the Fresnel laws and the local laser intensity is evaluated assuming the shape of a Gaussian beam or via ray tracing.

---

[7] This power-law scheme is the same as the one applied in the solution of the momentum equation. For a detailed derivation see Patankar [77] pp. 79–102.

Energy Balance with Phase Change

In the enthalpy formulation, the energy equation is initially cast in terms of the total enthalpy h. By splitting the total enthalpy into the enthalpy and the latent heat l due to the phase change, a unified formulation to describe the energy transport in both phases can be found. Phase boundaries can be captured and determined as part of the solution. The phase fraction is based on the volume fraction occupied by a given phase. This two-phase approach is particularly suitable for alloys where phase change generally occurs over a temperature range, forming a zone in which both phases can coexist [87]. For homogenous single element materials, this zone is a by-product of the modelling procedure. The governing equation reads:

$$\frac{\partial \rho h}{\partial t} = \frac{\partial}{\partial x_i}\left(k\frac{\partial}{\partial x_i}T\right) , \qquad (11.27)$$

with $h = c_p T + fl$:

$$\frac{\partial (\rho c_p T)}{\partial t} = \frac{\partial}{\partial x_i}\left(k\frac{\partial}{\partial x_i}T\right) - l\frac{\partial (\rho f)}{\partial t} , \qquad (11.28)$$

where l is the specific latent heat, and $0 \leq f \leq 1$ is the phase fraction of melt. This can then be discretised in a suitable manner as:

$$a_P T_P^k = \sum a_{nb} T_{nb} - \rho l \frac{\Delta^3}{\delta t}\left[f_P^{k-1} - f_P^{n-1}\right] , \qquad (11.29)$$

where the superscript k denotes the current iteration value at time step n and superscript $n-1$ represents the previous time step. Subscript P represents the node (grid) point for which the phase fraction and temperature is to be evaluated and subscript nb refers to all neighbours of this point. Subsequent to the solution of the energy equation an update procedure is performed as follows. First, the total enthalpy is calculated:

$$h_P^k = c_p T_P^k + f_P^{k-1} l \qquad (11.30)$$

and then the phase fraction is updated according to:

$$f_P^k = \begin{cases} 0 & , \quad h_P^k < h_s , \\ \dfrac{h_P^k - h_s}{h_l - h_s} & , \quad h_s \leq h_P^k \leq h_l , \\ 1 & , \quad h_P^k > h_l \end{cases} \qquad (11.31)$$

with h_s and h_l representing the enthalpy values at the solidus and liquidus line and h_P denoting the total enthalpy at node P respectively. The above assumes that the liquid is motionless until the complete control volume is molten. For evaporation of the melt this does not hold true. The characteristic

equation reads:

$$\frac{\partial \left(\rho c_p T\right)}{\partial t} + u_i \frac{\partial c_p T}{\partial x_i} + u_i l \frac{\partial f}{\partial x_i} = \frac{\partial}{\partial x_i}\left(k\frac{\partial}{\partial x_i}T\right) - l\frac{\partial \left(\rho f\right)}{\partial t} \qquad (11.32)$$

with l in this case denoting the latent heat of evaporation. Under the assumption that, due to the high vapour and recoil pressure, the velocity is predominately perpendicular to the surface, and the fact that the sink term has to be included for the sake of the evaporation kinetics and not in order to represent the specific heat correctly[8], the convective contribution can therefore most often be neglected and simplified to:

$$S_{\mathrm{ev}} = -\frac{\Delta^3}{\delta t}\frac{\Delta H_l^g}{c_p}\rho V\, dV \qquad (11.33)$$

with S_{ev} denoting a volumetric sink term due to evaporation (which appears on the right hand side vector of the discrete equations) and, following Iida [88]:

$$\Delta H_l^g = \Delta_l^g H_m - K_e\left(T - T_m\right), \quad K_e = \frac{\Delta_l^g H_m - \Delta_l^g H_b}{T_b - T_m}, \qquad (11.34)$$

with $\Delta_l^g H_m$, $\Delta_l^g H_b$, T_m, T_b, V, dV and K_e denoting the enthalpies of evaporation and temperatures at the melting and boiling point, volume of the cell, volume change with time and the enthalpy temperature dependence (usually in the order of 4–30 J mol^{-1}K^{-1} for metals [88]), respectively.

11.5.1 Gas Dynamics

The gas dynamic problem can be modelled as a first approximation by the non-viscous Euler equations for compressible gas dynamics. The Euler equations describe conservation of mass, momentum, and energy for an ideal fluid in three-dimensions, i.e.

$$\frac{\partial \rho}{\partial t} + \frac{\partial \rho u_i}{\partial x_i} = 0 \qquad (11.35)$$

$$\frac{\partial \rho u_j}{\partial t} + \frac{\partial \rho u_i u_j}{\partial x_i} = 0 \qquad (11.36)$$

---

[8] The reason for adding a convective part for the latent heat is the assumption of a partial constant specific heat with three discrete levels: solid, melt and vapour. The contributions of each of these phases is then represented by the respective phase fraction to form an average specific heat for the cell. In the case presented the vapour leaves the domain and hence is not considered in the subsequent solution of the energy equation. It therefore does not have any influence on the average specific heat, which could be convected, as with any other state variable. It acts rather as a damping factor in the evaporation associated with the extraction of energy due to the evaporated mass, which is a local effect.

$$\frac{\partial \rho E}{\partial t} + \frac{\partial \left(\rho E + P\right) u_i}{\partial x_i} = 0 \tag{11.37}$$

$$E = \epsilon + \frac{1}{2}\left|v\right|^2 \tag{11.38}$$

$$P = \left(\gamma - 1\right)\rho\epsilon \tag{11.39}$$

$$\frac{\partial \rho X_l}{\partial t} + \frac{\partial \rho X_l u_j}{\partial x_i} = 0 \tag{11.40}$$

with ρ, E, ϵ, γ, X and P denoting density, sum of internal and kinetic energy, internal energy, ratio of specific heats, mass fraction of species and pressure, respectively.

In an explicit fashion these can be solved successfully using the piecewise parabolic method (PPM) scheme. This scheme, developed by Colella and Woodward [89], utilises a higher order polynomial for the computation of the fluxes. However, as opposed to calculating face integrals for the control volume, as in the QUICK scheme introduced previously, the field variable at the new time-step is calculated directly from the polynomial. Keeping in mind that the problem to be solved is basically:

$$\frac{\partial \Phi}{\partial t} + u\frac{\partial \Phi}{\partial x} = 0 \tag{11.41}$$

the new value $\bar{\Phi}^{n+1}$ (at time-step $n+1$) can be calculated from the current value $\bar{\Phi}^n$ at time-step n from:

$$\bar{\Phi}^{n+1} = \frac{1}{h}\int_{x-h/2}^{x+h/2} \Phi^n\left(x - u\delta t\right) \mathrm{d}x. \tag{11.42}$$

The interpolation polynomial is:

$$\Phi^n\left(x\right) = \Phi_L + x\left(\left(\Phi_R - \Phi_L\right) + 6\left(\bar{\Phi}^n - \frac{1}{2}\left(\Phi_L + \Phi_R\right)\right)\left(1 - x\right)\right) \tag{11.43}$$

with x representing the normalised distance from the left face of the control volume to the right face. The variables Φ_R and Φ_L denote the value of the field quantity at the right and left control volume face respectively. These can be calculated from the averages $\bar{\Phi}^n$ by interpolating a quadratic polynomial and subsequent differentiation to obtain Φ_R. It follows that:

$$\Phi_R = \bar{\Phi}_j^n + \frac{1}{2}\left(\bar{\Phi}_{j+1}^n - \bar{\Phi}_j^n\right) - \frac{2}{9}\left(\delta\Phi_{j+1}^n - \delta\Phi_j^n\right) \tag{11.44}$$

with:

$$\delta\Phi_j^n = \begin{cases} \min\left(\left|\delta\Phi_{j,\mathrm{exact}}^n\right|, 2\left|\bar{\Phi}_j^n - \bar{\Phi}_{j-1}^n\right|\right)\mathrm{sgn}\left(\delta\Phi_{j,\mathrm{exact}}^n\right) \\ \qquad\qquad \text{if } \left(\bar{\Phi}_{j+1}^n - \bar{\Phi}_j^n\right)\left(\bar{\Phi}_j^n - \bar{\Phi}_{j-1}^n\right) > 0 \\ 0 \qquad\qquad\qquad \text{otherwise} \end{cases} \tag{11.45}$$

and:

$$\delta\Phi^n_{j,\text{exact}} = \frac{1}{2}\left[\left(\bar{\Phi}^n_{j+1} - \bar{\Phi}^n_j\right) + \left(\bar{\Phi}^n_j - \bar{\Phi}^n_{j-1}\right)\right] \tag{11.46}$$

where the use of $\delta\Phi^n_j$ instead of $\delta\Phi^n_{j,\text{exact}}$ ensures that $\bar{\Phi}^n_j \le \Phi_R \le \bar{\Phi}^n_{j+1}$ and in that sense limits the quadratic interpolant to avoid over- and undershoots. In order to ensure monotonicity, i.e. to ensure that the interpolation function does not have a value outside the range defined by Φ_L and Φ_R within the control volume, three further adjustments may be necessary:

$$\Phi_R = \Phi_L = \bar{\Phi}^n \qquad \text{if } \left(\Phi_R - \bar{\Phi}^n\right)\left(\bar{\Phi}^n - \Phi_L\right) \le 0$$

$$\Phi_L = 3\bar{\Phi}^n - 2\Phi_R \quad \text{if } \left(\Phi_R - \Phi_L\right)\left(\bar{\Phi}^n - \tfrac{1}{2}\left(\Phi_R + \Phi_L\right)\right) > \frac{\left(\Phi_R - \Phi_L\right)^2}{6}$$

$$\Phi_R = 3\bar{\Phi}^n - 2\Phi_L \quad \text{if } -\frac{\left(\Phi_R - \Phi_L\right)^2}{6} > \left(\Phi_R - \Phi_L\right)\left(\bar{\Phi}^n - \frac{1}{2}\left(\Phi_R + \Phi_L\right)\right)$$

$$\tag{11.47}$$

The explicit calculation of $\bar{\Phi}^{n+1}$ can then be expressed as:

$$\bar{\Phi}^{n+1}_j = \bar{\Phi}^n_j + \frac{1}{h}\left(\int_{h/2-u\delta t}^{h/2} \Phi^n_{j-1}\left(x\right)\mathrm{d}x - \int_{h/2}^{h/2+u\delta t} \Phi^n_j\left(x\right)\mathrm{d}x\right) \tag{11.48}$$

if $u > 0$ (for $u < 0$ the signs would change accordingly).

For improved shock-capturing by the numerical scheme a steepening algorithm is applied[9] to Φ_R and Φ_L prior to the monotonicity constraint 11.47 when a discontinuity (shock) was detected. This is based on three criteria:

- the third derivative is sufficiently large,
- the second derivative changes sign, and
- the first and third derivative have opposite sign.

This procedure and the necessary corrections are outlined in [89] (1.15–1.17). For hydrodynamics the values for Φ_R and Φ_L are then input to a Riemann-solver which advances the solution taking into account the shock physics. This is also detailed in [89].

11.5.2 Beam Tracing and Associated Difficulties

Due to the fact that the laser beam is the major driving force in the processes under investigation it is important to model it accurately. In the literature papers appear frequently concerning the "difficulty" of tracing straight rays through keyholes, using a keyhole geometry obtained from experimental observations. However, these publications are often of limited use as they detail the ray tracing procedure in great depth but do not address the real

---

[9] This is only applied to the density and only in the case of contact discontinuities.

issues in laser materials processing. The problem of tracing a straight ray through complex geometry was solved shortly after ray tracing was "invented" by Arthur Appel in 1968. In laser materials processing the rays are not straight lines as the refractive index changes with temperature, density and ionisation level (see [90]). Furthermore a static analysis cannot really reveal the complex interaction in the process under investigation. These dynamical influences are clearly of higher significance than the precise energy deposition and it may be argued that rather than investing in a ray tracing analysis, neglecting the dynamical influences, the beam should be treated as a steady Gaussian source with shadowing only as a hindrance to propagation and including the whole process dynamics in the analysis. This would however neglect the influence of wave-guiding, i.e. would not be applicable for deep section cutting or the drilling of deep holes. Another point to note is that ray tracing will give wrong results near the focus, where the energy distribution is dominated by diffraction, which is a problem for LMP simulations as most operations will be carried out at the focus. A solution of the Maxwell equations would solve this problem. This can be achieved via finite difference time domain simulations, as for example pursued by Mazumder. However, the high frequency of the light calls for an extremely high resolution of the mesh and short timescales, inconvenient for macro process simulation. From this we can surmise that a dynamical simulation is preferable; if ray tracing is included it should address the issues of variable refractive index.

Variable Refractive Index Ray Tracing

The path traversed by a ray of light obeys Fermat's principle. It requires that the ray follows the path of shortest time of travel. This is defined by the speed of light c along the ray-path and hence the refractive index n, where in a non-charged medium the Gladstone-Dale-Relationship [91]

$$c = \frac{c_0}{n}, \quad n = 1 + k\rho \tag{11.49}$$

holds, with c_0, k and ρ denoting the speed of light in a vacuum, the Gladstone-Dale constant, and density of the medium respectively. Then, following [92], the ray-path can be described by a second order differential equation:

$$\frac{d}{ds}\left(\frac{1}{v}\frac{dr}{ds}\right) = \nabla\left(\frac{1}{v}\right), \tag{11.50}$$

with $dr = \{x(s), y(s), z(s)\}$ and $v(x, y, z)$ denoting the coordinate vector and local speed of light. Defining the slowness vector $P(s)$ such that

$$P = \left(\frac{1}{v}\right)\left(\frac{dr}{ds}\right), \tag{11.51}$$

the above system simplifies to:

$$\frac{dr}{ds} = vP \qquad\qquad (11.52)$$

$$\frac{dP}{ds} = \nabla\left(\frac{1}{v}\right). \qquad\qquad (11.53)$$

Using $U = 1/v$, $P_x = U(dx/ds) = W_2$, $P_y = U(dy/ds) = W_4$, $P_z = U(dz/ds) = W_6$, $x = W_1$, $y = W_3$, $z = W_5$ and $P = \{P_x, P_y, P_z\} = \{W_2, W_4, W_6\}$ the following initial value problem (IVP) results:

$$
\begin{aligned}
W_1 &= x, & \frac{\partial W_1}{\partial s} &= vW_2 \\[2mm]
W_2 &= U\frac{\partial x}{\partial s}, & \frac{\partial W_2}{\partial s} &= \frac{\partial U(x,y,z)}{\partial x} \\[2mm]
W_3 &= y, & \frac{\partial W_3}{\partial s} &= vW_4 \\[2mm]
W_4 &= U\frac{\partial y}{\partial s}, & \frac{\partial W_4}{\partial s} &= \frac{\partial U(x,y,z)}{\partial y} \\[2mm]
W_5 &= z, & \frac{\partial W_5}{\partial s} &= vW_6 \\[2mm]
W_6 &= U\frac{\partial z}{\partial s}, & \frac{\partial W_6}{\partial s} &= \frac{\partial U(x,y,z)}{\partial z}.
\end{aligned}
\qquad (11.54)
$$

This initial value problem (IVP) can be solved using standard Runge-Kutta methods and appropriate interpolators to compute the intermediate function values of temperature, density and ionisation in between mesh points for the evaluation of the refractive index. RKSUITE [93] is an excellent collection of codes based on Runge-Kutta methods for the numerical solution of an IVP for a first order system of ordinary differential equations (ODEs) and is available in the public domain.

A Note About Ray Density and Multiple Reflections

It has to be noted that, if multiple reflections are important, the initial ray count has to be sufficiently high. If the beam is deflected from non-planar surfaces the rays will at some point diverge. This divergence cannot be allowed to become larger than one minimum grid spacing. Otherwise the energy deposition will be wrong. The algorithm will be further complicated by the fact that if one ray is reflected by a surface and the neighbouring ray is not, there may be an infinite or at least an unmanageable number, from the point of view of computational effort, of rays required in order to satisfy the afore-mentioned requirement. Ray-tracing attempts with only a couple of hundred rays should be considered with caution. Additionally it has to be noted that,

when multiple reflections are considered, ray-tracing only covers specular reflections, the diffuse part is neglected and heat transfer by radiation is likely to contribute as well – but is often ignored.

11.6 Program Development and Best Practice when Using Analysis Tools

A vast number of tools exist to aid the development process of software and the generation of data in general. Some of them enforce good practice by default, such as versioning systems which track and record changes in text files, like program codes for example. In the development process a lot of practice exists which originated at some point as a result of necessity, has by now been superseded, but still lingers on and is passed from teacher to student. Some of these pitfalls are summarised below together with hints and suggestions about available tools.

- Use concurrent versions system (CVS) to obtain a reversible record of modifications to files.
- Use `make` to keep track of dependencies.
- Write comments, a rule of one third program and two thirds comments is very good.
- Embed the CVS version strings from the source files into the output of your codes. This way you know exactly which version generated the output.
- Use journal files in American Standard Code for Information Interchange (ASCII) mode. This ensures repeatability, traceability and documentation on the fly. Make plenty of use of comments in the file. Record which software versions were used, in case "something changes" – it will – and explain what you have done. You will forget. In addition, if the application is discontinued or ceases to function, the ASCII file can always be adapted or translated to other software; binary files are often of little use without the application which generated them.
- Try to generate as much meta data as possible and do not worry about redundancy. It may be welcome in the last couple of hours before the deadline if it is over-clear, rather than a mystery, how something was generated or what some piece of data represents.
- Build parametric models where possible, only rarely will you want to explore one version of design/set up.
- Save frequently and use backups.
- The cleverest code is not the most cryptic but the one everybody understands.
- When things start to go wrong go home (assuming it is already very late).
- There is usually nothing wrong with long variable names "WeightAveragedInterpolantSumAcrossDomain" *is* okay "WAISAD" *is not*.

- Write and use test codes, prepare sample input files for subroutines and check if the output is as expected! Document these tests and if possible automate with a `Makefile` or similar for frequent automated code-sanity checks.
- Do not forget to use compiler optimisation. Codes will run 10–100 times faster by simply switching optimisation on.
- Know and use all compiler flags for debugging and code checking. Fortran compilers more often than c or c++ compilers have flags for simple tests.
- valgrind (http://valgrind.org/) your code.
- Do check the return status of functions where available

11.7 Introduction to High Performance Computing

In order to solve the mathematical models in sufficient resolution, more than the standard computing capacity is needed. Dedicated high performance computers are often called upon. These computers are different from the normal desktop computer in two ways. Firstly they have dedicated and expensive processors, specifically designed for a high throughput of floating point operations[10] and a close and fast access to memory. Desktop computers are often waiting for disk input/output (IO) to complete or for data to come in through the network so that the interprocessor or processor to memory speed and rate is not so important. This is not the case for high peformance computing (HPC) compute nodes which rarely use the hard disk. Secondly, they gain their computing capacity from calling upon, often, several thousand central processing unit (CPU) cores, all working on the same problem in parallel. Here it is differentiated between two classes of HPC systems. There are shared memory machines, where each CPU has access to one single pool of memory and distributed memory machines, where each CPU has its own local memory attached and CPUs have to access the memory on other CPUs via communication calls. The most powerful systems to date are often a hybrid of these two paradigms, i.e. clusters of shared memory computers, either clustered across one large machine room or even clustered across the globe by utilising high performance computer centres in the world and utilising their joint computational power for solving the problem at hand. For this reason programming these computers is slightly different from programming a normal sequential single CPU computer. In the following two de facto standards, openMP for shared memory programming and message passing interface (MPI) for distributed memory programming are introduced, following [94] closely.

---

[10] Most office applications and game operations – the main commercial reason to produce faster and faster desktop computers – require fast integer, but not floating point performance. This is unfortunate for the scientific world, which requires fast floating point calculations but is less dependent on fixed point computations whilst also representing only a comparatively insignificant market share.

11.7.1 MPI

Using MPI the programmer has to keep in mind constantly that the program is executed independently on each CPU and the parallelism has to be handled via programmed communication between the different copies of the program. This means that all variables are local to the particular copy of the program. Changing a variable on one CPU does not change it on the others. To aid the programming effort a lot of communication types are available as high level function call, making the task not as strenuous as it may sound in the above. Communication types available are for example broadcasts where one CPU broadcasts a variable value to all other CPUs or gathers, where all CPUs send their data to one specific CPU. This process is illustrated below in an example of computing π:

```
1    program numeric_pi
     include 'mpif.h'
     ! local variables

5    real(8) mypi, pi, w, sum, x, f, a
     integer n, myid, numprocs, i

     ! Start MPI, required at the beginning of every MPI program
     call MPI_INIT( ierr )
10   if(ierr.ne.0) STOP 'error when initialising MPI'

     ! Find out on which cpu this program runs, we need this below
     ! in order to distribute the work
     call MPI_COMM_RANK( MPI_COMM_WORLD, myid, ierr )
15
     ! Find out how many processors there are allotgether
     call MPI_COMM_SIZE( MPI_COMM_WORLD, numprocs, ierr )

     ! We have decided that CPU # 0 is managing the others
20   ! The code below will only be executed on cpu 0
     if ( myid .eq. 0 ) then
       print *, 'Enter number of intervals:'
       read *, n
     endif
25
     ! The information gathered above on cpu # 0 only now needs
     ! to be distributed (or braodcasted) to the other cpus
     call MPI_BCAST(n,1,MPI_INTEGER,0,MPI_COMM_WORLD,ierr)
     if(ierr.ne.0) STOP 'error in broadcast'
30
     ! Every cpu now calculates the interval size
     w = 1.0d0/DBLE(n)
```

```
      ! initialise the sum to zero
35    sum = 0.0d0

      ! Perform the integration on the interval for this CPU
      ! Note that every cpu will have a different interval!
      do i = myid+1, n, numprocs
40      x = w * (DBLE(i) - 0.5d0)
        sum = sum +  4.d0 / (1.d0 + x*x)
      enddo

      ! Now we have a local and partial result which we store
45    ! in the variable mypi

       mypi = w * sum

      ! The results from the other cpus have to be added to the
50    ! local result in form of a global sum. This is done below

      call MPI_REDUCE(mypi,pi,1,MPI_DOUBLE_PRECISION,MPI_SUM,0,
        MPI_COMM_WORLD,ierr)
      if(ierr.ne.0) STOP 'error in reduction'
55
      ! NOTE: This is a global reduction to cpu 0. This means that
      !       on all other cpus the variable pi is undefined! we
      !       would need to either broadcast the result subsequen-
      !       tly to MPI_REDUCE or use MPI_ALLREDUCE instead.
60
      ! CPU # 0 prints the answer.
      if (myid .eq. 0) then
        print *, 'pi =' , pi
      endif
65
      ! finalise MPI (every MPI program needs this at the end)
      call MPI_FINALIZE(ierr)
      if(ierr.ne.0) STOP 'error when finalising MPI'

70    end program numeric_pi
```

It is immediately obvious that there is added effort involved due to the necessity of setting up the problem in accordance with the number of processors used. A master CPU (sometimes called root CPU) is identified which performs the input and output operations. This is usually CPU 0 as it can be safely assumed that this will always exist. Since the data is not shared with the other processes the input parameters have to be explicitly broadcast.

Additionally the loop bounds have to be computed using the knowledge of the CPU number and the total number of CPUs working on the problem. This is where the parallelism comes in. The local fraction of the total sum will then be computed. A global summation is performed, with CPU 0 storing the result. Note that a) the result is not broadcast to the other CPUs and therefore the variable pi does hold a wrong value on those processors (which in other circumstances could lead to programming errors if it were to be assumed that it would be broadcast) and b) that the storage space for this variable on the other CPUs is wasted. This shows how in principle MPI programs need more memory than shared memory applications.

11.7.2 openMP

The same program as above is shown here programmed using openMP.

```
1    program numeric_pi
     integer n, i
     real(8) w, x, sum, pi, f, a

5    print *, 'Enter number of intervals: '
     read *,n

     ! calculate the interval size
     w = 1.0d0/DBLE(n)
10
     ! initialise sum to zero (do never assume the compiler does
       that)
     sum = 0.0d0

15   ! instruction to the compiler to paralise the subsequent loop
       and information
     ! on how to treat the variables
     !$OMP PARALLEL DO PRIVATE(x), SHARED(w), REDUCTION(+: sum)

20   do i = 1, n
       x   = w * (DBLE(i) - 0.5d0)
       sum = sum +  4.d0 / (1.d0 + x*x)
     enddo

25   pi = w * sum

     print *, 'pi =' , pi

     end program numeric_pi
```

It is significantly shorter and there is no great difference from a serial program, apart from the instruction to the compiler instructing it which loop to parallelise and how to treat the variables inside that loop. Note how the openMP lines are comment lines if the compiler is not instructed to treat the program as an openMP program!

The beginning of this program is executed in a serial fashion; the program is hence written in the standard sequential manner, reading values and writing results without any need for checks to avoid multiple outputs/reads. The parallel construct is in this case a parallel `do` loop. At run time this will be decomposed with private and public (reduction) variables. The reduction attribute takes an operator. At the end of the parallel region the private copies will be reduced to the master process using this operator (similar to the `MPI reduce` command used above). The compiler assigns the appropriate iterations to the individual processors, therefore the user need not even know how many processors the program runs on nor program the distribution by hand. The parallel region terminates with the end do. On exit from the parallel region, the master process resumes execution using its updated data environment. This model of execution is referred to as the fork/join model. Throughout the course of a program, the initial process can fork and join many times. The fork/join execution model makes it easy to get loop-level parallelism out of a sequential program. Unlike message passing, where the program must be completely decomposed for parallel execution, the shared-memory model makes it possible to parallelise just at the loop level without decomposing the whole data structure.

This ease of programming comes at a price of course; this program will only run on shared memory systems which are usually expensive and limited in maximum processor count. The most powerful supercomputers to date are clusters of shared memory computers which then call for MPI programming as well. But if there is no intention to use systems of that size and if the shared memory resource is available, or if the aim is simply to make more use of the dual core processor in the desktop, then openMP may be the more rewarding paradigm with respect to programming effort. For the latter it may be interesting to investigate the "auto-paralleliser" capability of the compiler, which may yield a performance increase.

11.7.3 Performance

When discussing the performance of parallel programs the points have to be noted:

- An overhead due to communication and data transfer exists; it cannot be assumed that the scaling will be linear. It is very difficult to achieve economical scaling with more than several hundred CPUs. National super computing centres usually provide expert advice and assistance to

Table 11.4: Performance comparison of mpi and openMP on a 4 CPU shared memory system.

	1 CPU	2 CPUs	3 CPUs	4 CPUs	8 CPUs
mpi	10.240s	5.287s	3.690s	2.963s	1.790s
openMP	11.313s	5.677s	3.859s	2.910s	
automatic parallelisation	10.074s	5.105s	3.447s	2.598s	
none	10.033s				
ideal	10.033s	5.016s	3.344s	2.508s	1.254s

researchers who want to execute their codes on more than several hundred CPUs.

- At times "superlinear" scaling can be observed. This occurs when the data structures are of such a size that they can make best use of the cache structure of that particular architecture and more than balance the communication overhead.
- Despite linear scaling, the time versus CPU count curve is not linear. It will become more and more expensive to achieve noticeable differences in computational time, even if the code scales well. For example, if a simulation requires 10 days of computation on 1 CPU, 5 days can be saved by moving to two CPUs. However, only an additional 2.5 days will be saved by moving to 4 CPUs and so on.
- Some applications are "embarrassingly" parallel (like the one presented above). This means they are particularly suited for parallelisation as they have no great need for communication (dependency in the data). Explicit codes are more embarrassingly parallel than implicit codes for example as no communication is required when integrating the fields with respect to time; only at the update phase, once the new solution is established, is communication required.

As shown in Table 11.4, the communication overhead leads to a less than ideal scaling. However, considering the length of the program these results are acceptable. Of course, these result do not present openMP as being the better way forward or vice versa. Performance results will depend on the problem, the skill of the programmer and the particular hardware used. Potential gains in performance have to be balanced against development time and cost as well.

At first glance it may seem a good idea to attempt to program a cluster of shared memory computers in a mixed mode, using the shared memory where available and communicating with MPI across the node boundaries. This however has so far only proved successful in rare cases. To use MPI only is often the more promising method on such machines. This problem is currently being addressed by some commercial developments like "Cluster openMP".

11.8 Visualisation Tools

Visualisation is the key to successful numerical analysis as it is often the only sensible method to analyse the vast amounts of data generated. Visualisation tools broadly fall into two categories, volume rendering and graph plotting tools. The former are used to render field variables and isosurfaces and depict vector quantities using arrow glyphs. The latter will plot time series data at a specific location in the multidimensional domain, histories of residuals etc. Thanks to the Open Source movement there are plenty of good tools available at no cost to the investigator. One thing to keep in mind when choosing visualisation tools is the ability to write scripts. If the user has to click hundreds of buttons in order to produce plots without any option of automation, the tool should possibly be avoided as it will be a sink of valuable research time wasted by doing the same task over and over again. Even worse, it leaves no trace or "evidence" of what was done, so if the same graph needs to be reproduced later for whatever reason, it may take some time to remember how exactly it was done. For line plotting tasks a tool very much worth mastering is `gnuplot`[11]. Albeit being perhaps a bit cryptic to begin with it is a powerful tool to plot graphs of numeric data or simple analytical expressions quickly. Once the analysis is complete it is only a matter of minutes to convert the "quick plot" into a professional quality graph, ready for print publication. For more complex tasks `xmgrace`[12] is a tool with plenty of options and a graphical user interface. For volume data a standalone solution worth investing some time into is `opendx`[13]. In opendx a "visualisation network" is created using a graphical representation of the dataflow. Different operations on the data are represented by blocks which the user adds to the network and connects the inputs and outputs according to the flow of data with lines. This first block will be an import module, reading the data into `opendx`. Then some operations will be performed, like the computation and colouring of isosurfaces for example. The final block will be an image block, which is responsible for displaying the visualisation on the screen. The user has no programming to perform in the traditional sense. If a visualisation is to be integrated into an analysis code it will possibly pay off to learn `vtk` from scratch. `Paraview`[14] and `visit`[15], based on `vtk`, are two examples of "`opendx` like" visualisation tools. The commercial system `avs`[16] is based on a similar flow-diagram programming language as opendx.

---

[11] http://www.gnuplot.info/
[12] http://plasma-gate.weizmann.ac.il/Grace/
[13] http://www.opendx.org/
[14] http://www.paraview.org
[15] https://wci.llnl.gov/codes/visit
[16] http://www.avs.com

11.9 Summary and Concluding Remarks

In summary, this chapter has provided an overview over the salient features of a LMP simulation. It was shown how to solve the melt dynamics problem and track the free surface, how to model the temperature distribution, laser beam absorption and assist gas dynamics. This places the reader into a position to start experimenting and to extend the model to include more and more process physics, until a fully comprehensive description is achieved.

A simulation such as the one envisaged in the context of this chapter comes at a price of course. Simulation, especially in LMP, becomes very compute intensive very quickly, calling for state of the art multiple CPU systems running continuously for days or weeks. Hence investigators often find themselves in the situation where they have to fit their model to the computational resources at hand, sacrificing detail and ignoring non-convergence of their solutions. In doing so they progress, backwards, from simulation to modelling. As was demonstrated in this chapter, most of the present literature can only be classed as modelling, not simulation. As such, a lot of care has to be taken when the results are compared with experiments. Often experimenters feel obliged to present "at least one" "correlation" of their results with experiments. That in itself is a pointless exercise of course, a sign of overly confident investigators who do not appreciate the shortcomings of their simplifications.

Mainly because of the price of comprehensive simulation, it is still a young field, not pursued by many researchers. The rewards are potentially very large but there may also still be a while to wait before they can be claimed. It is hoped that this discussion provides a fertile ground for the enterprising investigator to start building simulation codes and start investigating and exploring, in pursuit of ultimate understanding. If quick results are expected, this is possibly not a path for the less patient to follow. For the researcher with sufficiently patience however, this may be the starting point for an exiting and rewarding journey into the intricacies of LMP, with many "established ideas" waiting to be challenged and overturned by new results, opening up the details of the process like a book waiting to be read.

In conclusion, following the thoughts of Rapaport [95], the state of the computer will be elevated from being purely a tool to perform calculations, to that of a laboratory, where experiments can be conducted in a similar fashion to the way it is done in the real world. With a numerical experiment the problem can be approached in all its detail, without the obscuring haze of simplification and assumption.

References

1. Kaplan A (1964) Conduct of Inquiry: Methodology for Behavioral Science. Chandler Publishing Company, p 288 para 32. Reprinted (1998) Transaction Publishers, p 288.

2. Dowden JM (200) The Mathematics of Thermal Modeling. Chapman & Hall/CRC

3. Dowden J, Davis M, Kapadia P (1985) The flow of heat and the motion of the weld pool in penetration welding with a laser. J Appl Phys, 57(9): 4474–4479

4. Dowden J, Postacioglu N, Davis M, Kapadia P (1987) A keyhole model in penetration welding with a laser. J Physics D: Appl Phys, 20(1): 36–44

5. Dowden J, Kapadia P, Postacioglu N (1989) An analysis of the laser-plasma interaction in laser keyhole welding. J Physics D: Appl Phys, 22(6): 741–749

6. Postacioglu N, Kapadia P, Dowden JM (2000) Distortion generated by a moving weld pool of elliptical cross section in the welding of thin metal sheets. J Physics D: Appl Phys, 33(14): 1739–1746

7. Postacioglu N, Kapadia P, Dowden J (1989) Capillary waves on the weld pool in penetration welding with a laser. J Physics D: Appl Phys, 22(8): 1050–1061

8. Postacioglu N, Kapadia P, Dowden J (1991) Theory of the oscillations of an ellipsoidal weld pool in laser welding. J Physics D: Appl Phys, 24(8): 1288–1292

9. Postacioglu N, Kapadia P, Davis M, Dowden J (1987) Upwelling in the liquid region surrounding the keyhole in penetration welding with a laser. J Physics D: Appl Phys, 20(3): 340–345

10. Wei PS, Chang CY (1996) Surface ripple in electron-beam welding solidification. J Heat Transfer – Trans ASME, 118(4): 960–969

11. Wei PS, Shian MD (1993) 3-dimensional analytical temperature-field around the welding cavity produced by a moving distributed high-intensity beam. Journal Heat Transfer – Trans ASME, 115(4): 848–856

12. Colla TJ, Vicanek M, Simon G (1994) Heat transport in melt flowing past the keyhole in deep penetration welding. J Physics D: Appl Phys, 27(10): 2035–2040

13. Matsunawa A, Semak V (1997) The simulation of front keyhole wall dynamics during laser welding. J Physics D: Appl Phys, 30(5): 798–809

14. Kroos J, Gratzke U, Vicanek M, Simon G (1993) Dynamic behaviour of the keyhole in laser welding. J Physics D: Appl Phys, 26(3): 481–486

15. Kroos J, Gratzke U, Simon G (1993) Towards a self-consistent model of the keyhole in penetration laser beam welding. J Physics D: Appl Phys, 26(3): 474–480

16. Fabbro R, Chouf K (2000) Keyhole modeling during laser welding. J Appl Phys, 87(9): 4075–4083

17. Ducharme R, Williams K, Kapadia P, Dowden J, Steen W, Glowacki M (1994) The laser welding of thin metal sheets: an integrated keyhole and weld pool model with supporting experiments. J Physics D: Appl Phys, 27(8): 1619–1627

18. Steen WM, Dowden JM, Davis M, Kapadia PD (1988) A point and line source model of laser keyhole welding. J Physics D: Appl Phys, 21(8): 1255–1260

19. Davies M, Kapadia P, Dowden J (1986) Modeling the fluid-flow in laser-beam welding. Welding J, 65(7): S167–S174

20. Akhter R, Davis M, Dowden J, Kapadia P, Ley M, Steen WM (1989) A method for calculating the fused zone profile of laser keyhole welds. J Physics D: Appl Phys, 21: 23–28

21. Gratzke U, Kapadia PD, Dowden JM, Kroos J, Simon G (1992) Theoretical approach to the humping phenomenon in welding processes. J Physics D: Appl Phys, 25(11): 1640–1647

22. Ki H, Mohanty P, Mazumder J (2002) Multiple reflection and its influence on keyhole evolution. J Laser Appl, 14: 39–45

23. Kar A, Mazumder J (1995) Mathematical modeling of key-hole laser welding. J Appl Phys, 78(11): 6352–6360
24. Farooq K, Kar A (1999) Effects of laser mode and scanning direction on melt pool shape. J Appl Phys, 85(9): 6415–6420
25. Choi JH, Lee J, Yoo CD (2001) Dynamic force balance model for metal transfer analysis in arc welding. J Physics D: Appl Phys, 34(17): 2685–2664
26. Tsai FR, Kannatey-Asibu E (2000) Modeling of conduction mode laser welding process for feedback control. Trans ASME, 122: 420–428
27. Kaplan A (1994) A model of deep penetration laser welding based on calculation of the keyhole profile. J Physics D: Appl Phys 27(9): 1805–1814
28. Schubart D, Otto A (1997) Process development of laser melt ablation. In: Laser Assisted Net shape Engineering 2 (LANE 97), 865–876
29. Chung JD, Lee JS, Whang KH, Kim TH (1996) Analysis of striation formation in laser material cutting process. J Mater Process Manuf Sci 5: 3–15
30. DiPietro P, Yao YL (1995) A numerical investigation into cutting front mobility in co-2 laser cutting. International Journal of Machine Tools & Manufacture 35(5): 673–688
31. O'Neill W, Steen WM (1995) A three-dimensional analysis of gas entrainment operating during the laser-cutting process. J Physics D: Appl Phys 28(1): 12–18
32. Kim MJ, Majumdar P (1995) Computational model for high-energy laser-cutting process. Numerical Heat Transfer, Part A 27: 717–733
33. Prusa JM, Venkitachalam G, Molian PA (1999) Estimation of heat conduction losses in laser cutting. International Journal of Machine Tools & Manufacture 39(3): 431–458
34. Kim MJ, Zhang J (2001) Finite element analysis of evaporative cutting with a moving high energy pulsed laser. Appl Math Modelling 25(3): 203–220
35. Kim MJ, Chen ZH, Majumdar P (1993) Finite element modelling of the laser cutting process. Computers & Structures 49(2): 231–241
36. Chryssolouris G, Choi WY (1989) Gas jet effects on laser cutting. In: Proc. SPIE, vol 1042 of Proc. SPIE, pages 86–96
37. Chen K (2000) Gas jet-workpiece interactions in laser machining. J Manuf Sci and Engineering-Trans ASME 122(3): 429–438
38. Mazumder J, Steen WM (1980) Heat transfer model for cw laser materials processing. J Appl Phys 51(2): 941–947
39. Vicanek M, Simon G, Urbassek HM, Decker I (1987) Hydrodynamical instability of melt flow in laser cutting. J Physics D: Appl Phys 20(1): 140–145
40. Chen K, Yao YL (2000) Interactive effects of reactivity and melt flow in laser machining. High Temp Mater Process 4: 227–252
41. Yilbas BS, Davies R, Gorur A, Yilbas Z, Begh F, Akcakoyun N, Kalkat M (1992) Investigation into the development of liquid layer and formation of surface plasma during co2 laser cutting process. Proceedings of the Institution of Mechanical Engineers, Part B: Journal of Engineering Manufacture 206(B4): 287–298
42. Kim BC, Kim TH, Jang YS, Chung KH (2001) Investigation of striation formation in thin stainless steel tube during pulsed nd : Yag laser cutting process by numerical simulation. Metall Mater Trans A-Phys Metall Mater Sci 32: 2623–2632
43. Xie J, Kar A (1997) Mathematical modeling of melting during laser materials processing. J Appl Phys 81(7): 3015–3022

44. Rao BT, Nath AK (2002) Melt flow characteristics in gas-assisted laser cutting. Sadhana 27(5): 569–575
45. Vicanek M, Simon G (1987) Momentum and heat transfer of an inert gas jet to the melt in laser cutting. J Physics D: Appl Phys 20(9): 1191–1196
46. Leidinger D, Schuoecker D, Deinzer G, Geiger M, Haensel A, Herbig N (1994) Nozzle design and simulation of gas flow for the laser cutting process. In: Proc. SPIE vol 2207 of Proc. SPIE, pages 469–479
47. Bukharov NN, Barinov VV, Mishina MV, Prokoshev VG, Arakelian SM (1997) Numerical modeling laser thermochemical processes on metals surface. In: Laser Assisted Net shape Engineering 2 (LANE 97), 683–686
48. Chen K, Yao YL, Modi V (1999) Numerical simulation of oxidation effects in the laser cutting process. Int J Advanced Manufacturing Technology 15(11): 835–842
49. Lim CK, Molian PA, Brown RC, Prusa JM (1998) Numerical studies of gas jet/molten layer interaction during laser cutting. J Manuf Sci and Engineering, Trans ASME 120(3): 496–503
50. Finke BR, Simon G (1990) On the gas kinetics of laser-induced evaporation of metals. J Physics D: Appl Phys 23(1): 67–74
51. Rand C, Sparkes M, O'Neill W, Sutcliffe C, Brookfield D (2003) Optimisation of melt removal in laser cutting. In: ICALEO 2003 Congress Proceedings. LIA, Orlando
52. Mas C, Fabbro R, Gouédard Y (2003) Steady-state laser cutting modeling. J Laser Applics 15(3): 145–152
53. Semak VV, Damkroger B, Kempka S (1999) Temporal evolution of the temperature field in the beam interaction zone during laser material processing. J Physics D: Appl Phys 32: 1819–1825
54. Yilbas BS, Kar A (1998) Thermal and efficiency analysis of co2 laser cutting process. Optics and Lasers in Engineering 29(1): 17–32
55. Semak V, Matsunawa A (1997) The role of recoil pressure in energy balance during laser materials processing. J Physics D: Appl Phys 30(18): 2541–2552
56. Modest M (1996) Three-dimensional, transient model for laser machining of ablating/decomposing materials. Int J Heat Mass Transfer 39(2): 221–234
57. Modest MF, Mallison TM (2001) Transient elastic thermal stress development during laser scribing of ceramics. J Heat Transfer 123(1): 171–177
58. Kim MJ (2000) Transient evaporative laser-cutting with boundary element method. Appl Math Modelling 25(1): 25–39
59. Ganesh RK, Faghri A (1997) A generalized thermal modeling for laser drilling process – ii. numerical simulation and results. Int J Heat Mass Transfer 40(14): 3361–3373
60. Ganesh RK, Faghri A, Hahn Y (1997) A generalized thermal modeling for laser drilling process – i. mathematical modeling and numerical methodology. Int J Heat Mass Transfer 40(14): 3351–3360
61. Solana P, Kapadia P, Dowden JM, Marsden PJ (1999) An analytical model for the laser drilling of metals with absorption within the vapour. J Physics D: Appl Phys 32(8): 942–952
62. Chan CL, Mazumder J, Chen MM (1988) Effect of surface tension gradient driven convection in a laser melt pool: Three-dimensional perturbation model. J Appl Phys 64(11): 6166–6174
63. Ko SH, Choi SK, Yoo CD (2001) Effects of surface depression on pool convection and geometry in stationary gtaw. Welding research supplement pp 39s–45s

64. Westerberg K, McClelland M, Finlayson B (1998) Finite element analysis of flow, heat transfer, and free interfaces in an electron-beam vaporization system for metals. Int J Numer Methods Fluids 26: 637–655
65. Preston RV, Shercliff HR, Withers PJ, Smith SD (2003) Finite element modelling of tungsten inert gas welding of aluminum alloy 2024. Science and Technology of Welding and Joining 8(1): 10–18
66. Koo SH, Farson DF, Choi SK, Yoo CD (2000) Mathematical modeling of the dynamic behavior of gas tungsten arc weld pools. Metallurgical and Materials Transactions B-Process Metallurgical and Materials Processing Science 31(6): 1465–1473
67. Callies G, Schittenhelm H, Berger P, Hügel H (1997) Modeling and simulation of short pulse laser ablation with feeding speed. In: Laser Assisted Net shape Engineering 2 (LANE 97) 825–834
68. Zhou J, Wang PC (2003) Modeling of hybrid laser-mig keyhole welding process. In: ICALEO 2003 Congress Proceedings
69. Ki H, Mohanty PS, Mazumder J (2002) Modeling of laser keyhole welding: Part ii. simulation of keyhole evolution, velocity, temperature profile, and experimental verification. Metallurgical and Materials Transactions A-Physical Metallurgical and Materials Science 33(6): 1831–1842
70. Ki H, Mohanty PS, Mazumder J (2002) Modeling of laser keyhole welding: Part i. mathematical modeling, numerical methodology, role of recoil pressure, multiple reflections, and free surface evolution. Metallurgical and Materials Transactions A-Physical Metallurgical and Materials Science 33(6): 1817–1830
71. Amara EH, Fabbro R, Bendib A (2003) Modeling of the compressible vapor flow induced in a keyhole during laser welding. J Appl Phys 93(7): 4289–4296
72. Hu J, Tsai HL, Lee YK (2003) Modeling of weld pool dynamics during dual-beam laser welding process. In: ICALEO 2003 Congress Proceedings
73. Thompson ME, Szekely J (1989) The transient behavior of weldpools with a deformed free surface. Int J Heat Mass Transfer 32(6): 1007–1019
74. Chan CL, Mazumder J, Chen MM (1987) Three-dimensional axisymmetric model for convection in laser-melted pools. Materials Science and Technology 3(4): 306–311
75. Chan CL, Zehr R, Mazumder J, Chen MM (1986) Three-dimensional model for convection in laser weld pool. In: Proc. 3rd conf modeling & control of casting & welding processes pp 229–246
76. Tufte ER (2006) The Cognitive Style of PowerPoint: Pitching Out Corrupts Within. Graphics Press
77. Patankar SV (1997) Numerical Heat Transfer and Fluid Flow. Series in computational methods in mechanics and thermal sciences. Hemisphere Publishing Corporation
78. Courant R, Friedrichs K, Lewy H (1928) über die partiellen differenzengleichungen der mathematischen physik. Mathematische Annalen 100(1): 32–74
79. Courant R, Friedrichs K, Lewy H (1967) On the partial difference equations of mathematical physics. IBM Journal 215–234
80. Saad Y, Schultz MH (1986) Gmres: A generalized minimal residual algorithm for solving nonsymmetric linear systems. SIAM J Sci Stat Comput 7(3): 856–869
81. Versteeg HK, Malalasekera W (1995) An introduction to computational fluid dynamics The finite volume method. Prentice Hall

82. Leonard BP (1979) A stable and accurate convective modelling procedure based on quadratic upstream interpolation. Comput Methods Appl Mech Eng 19: 59–98
83. Leonard BP (1991) The ultimate conservative difference scheme applied to unsteady one-dimensional advection. Comput Meth Appl Mech Eng 88: 17–74
84. Leonard BP (1988) Simple high-accuracy resolution program for convective modelling of discontinuities. Int J Numerical Methods in Fluids 8: 1291–1318
85. Thuburn J (1996) Multidimensional flux-limited advection schemes. J Comput Phys 123: 74–83
86. Osher S, Sethian JA (1988) Fronts propagating with curvature-dependent speed: Algorithms based on hamilton-jacobi formulations. J Comp Phys 79: 12–49
87. Shyy W, Udaykumar HS, Rao MM, Smith RW (1996) Computational fluid dynamics with moving boundaries. Taylor & Francis
88. Iida T, Guthrie RI (1988) The Physical Properties of Liquid Metals. Oxford Science Publications
89. Colella P, Woodward PR (1984) The piecewise parabolic method (ppm) for gas-dynamical simulations. J Comput Phys 54: 174–201
90. Ducharme R, Kapadia PD, Dowden JM (1993) A mathematical model of the defocusing of laser light above a workpiece in laser material processing. In: Proc ICALEO, vol 75 of Proc ICALEO, pp 187–197. Laser Institute of America
91. Gladstone JH, Dale TP (1863) Researches on the refraction, dispersion and sensitiveness of liquids. Phil Trans Roy Soc 153: 317–343
92. Lee WHK, Stewart SW (1981) Principles and applications of microearthquake networks. Adv Geophys Supplement No. 2 p 293
93. Brankin RW, Gladwell I (1994) A fortran 90 version of rksuite: an ode initial value solver. Ann Numer Math 1: 363–375
94. Dagum L, Menon R (1998) Openmp: An industry-standard api for shared-memory programming. IEEE Computational Science & Engineering pages 46–55
95. Rapaport DC (2004) The Art of Molecular Dynamics Simulation. Cambridge University Press

Index

Springer Series in

MATERIALS SCIENCE

Editors: R. Hull   R.M. Osgood, Jr.   J. Parisi   H. Warlimont

Springer Series in
MATERIALS SCIENCE

Editors: R. Hull   R.M. Osgood, Jr.   J. Parisi   H. Warlimont